MOLECULAR MECHANISMS OF NOCICEPTION

EDITED BY: Fabien Marchand and Cyril Goudet
PUBLISHED IN: Frontiers in Molecular Neuroscience

frontiers Research Topics

ISSN 1664-8714
ISBN 978-2-83250-255-6
DOI 10.3389/978-2-83250-255-6

About Frontiers

Frontiers is more than just an open-access publisher of scholarly articles: it is a pioneering approach to the world of academia, radically improving the way scholarly research is managed. The grand vision of Frontiers is a world where all people have an equal opportunity to seek, share and generate knowledge. Frontiers provides immediate and permanent online open access to all its publications, but this alone is not enough to realize our grand goals.

Frontiers Journal Series

The Frontiers Journal Series is a multi-tier and interdisciplinary set of open-access, online journals, promising a paradigm shift from the current review, selection and dissemination processes in academic publishing. All Frontiers journals are driven by researchers for researchers; therefore, they constitute a service to the scholarly community. At the same time, the Frontiers Journal Series operates on a revolutionary invention, the tiered publishing system, initially addressing specific communities of scholars, and gradually climbing up to broader public understanding, thus serving the interests of the lay society, too.

Dedication to Quality

Each Frontiers article is a landmark of the highest quality, thanks to genuinely collaborative interactions between authors and review editors, who include some of the world's best academicians. Research must be certified by peers before entering a stream of knowledge that may eventually reach the public - and shape society; therefore, Frontiers only applies the most rigorous and unbiased reviews.
Frontiers revolutionizes research publishing by freely delivering the most outstanding research, evaluated with no bias from both the academic and social point of view. By applying the most advanced information technologies, Frontiers is catapulting scholarly publishing into a new generation.

What are Frontiers Research Topics?

Frontiers Research Topics are very popular trademarks of the Frontiers Journals Series: they are collections of at least ten articles, all centered on a particular subject. With their unique mix of varied contributions from Original Research to Review Articles, Frontiers Research Topics unify the most influential researchers, the latest key findings and historical advances in a hot research area! Find out more on how to host your own Frontiers Research Topic or contribute to one as an author by contacting the Frontiers Editorial Office: frontiersin.org/about/contact

MOLECULAR MECHANISMS OF NOCICEPTION

Topic Editors:
Fabien Marchand, INSERM U1107 Douleur et Biophysique Neurosensorielle (Neuro-Dol), France
Cyril Goudet, INSERM U1191 Institut de Génomique Fonctionnelle (IGF), France

Citation: Marchand, F., Goudet, C., eds. (2022). Molecular Mechanisms of Nociception. Lausanne: Frontiers Media SA. doi: 10.3389/978-2-83250-255-6

Table of Contents

frontiers | Frontiers in Molecular Neuroscience

TYPE Editorial
PUBLISHED 06 September 2022
DOI 10.3389/fnmol.2022.1025230

OPEN ACCESS

EDITED AND REVIEWED BY
Robert John Vandenberg,
The University of Sydney, Australia

*CORRESPONDENCE
Cyril Goudet
cyril.goudet@igf.cnrs.fr
Fabien Marchand
fabien.marchand@uca.fr

SPECIALTY SECTION
This article was submitted to Pain Mechanisms and Modulators, a section of the journal Frontiers in Molecular Neuroscience

RECEIVED 22 August 2022
ACCEPTED 23 August 2022
PUBLISHED 06 September 2022

CITATION
Goudet C and Marchand F (2022) Editorial: Molecular mechanisms of nociception.
Front. Mol. Neurosci. 15:1025230.
doi: 10.3389/fnmol.2022.1025230

Editorial: Molecular mechanisms of nociception

Cyril Goudet[1]* and Fabien Marchand[2]*

[1]IGF, University of Montpellier, CNRS, INSERM, Montpellier, France, [2]Université Clermont Auvergne, Inserm U1107 Neuro-Dol, Pharmacologie Fondamentale et Clinique de la Douleur, Clermont-Ferrand, France

KEYWORDS

pain, nociception, chronic pain, physiopathologic mechanism, therapeutic targets, analgesic

Editorial on the Research Topic
Molecular mechanisms of nociception

Nociception is the perception of noxious stimuli (chemical, thermal, or mechanical) by neurons of the nociceptive system through the peripheral and central nervous system. This is a highly complex phenomena involving different key molecules, activating different types of neurons and pathways. In addition, the nociceptive system is dysregulated in a context of chronic pain altering the process as a whole. Getting insights into nociceptive processes will lead to a better understanding of chronic pain physiopathology and will certainly lead to the discovery of new therapeutic targets.

This Research Topic covers a large spectrum of nociceptive mechanisms, from the periphery to the brain, proposing new mechanisms and/or potential new therapeutic targets.

First, we gathered articles investigating nociception through a developmental perspective such as Tröster et al. who studied the impact of axon bifurcation on sensory processing in adulthood or how transcription factors such as PRDM12 are required for nociceptor function throughout life (Kokotović et al.).

Some of these articles investigated the modulation of the nociceptive message at the spinal cord level. Leonardon et al. nicely demonstrated that NMDA receptors modulate GABAergic transmission reinforcing the role of plastic changes in synaptic inhibition which can be ultimately involved in the development and maintenance of chronic pain. Another study by Comitato et al. showed that 5-HT7 receptors also regulate excitatory-inhibitory balance in mouse spinal dorsal horn. These two studies highlight the role of the imbalance of inhibition and excitation and their mutual regulation underlying chronic pain development and/or maintenance.

Then, nociceptive signal reaches the brain where it is integrated. Here, Presto and Neugebauer observed a sexual dimorphic function of CGRP in the amygdala, indicating that CGRP1 receptors could be potential therapeutic targets for neuropathic pain relief, particularly in female. Two others studies investigated molecular changes in the locus coeruleus and the prelimbic cortex. Short-term pain seems to lead to an increase of markers of excitatory synapses in the perisomatic region of noradrenergic cells in the locus coeruleus, an effect that is lost after long-term pain, which appears

to rather activate apoptosis (Bravo et al.). In the other hand, Fan et al. demonstrated that persistent hyperphosphorylation of p38MAPK in the prelimbic cortex underlies aggravated nociceptive responses in rats with chronic inflammatory pain. Overall, these studies highlight how chronic pain altered the functioning of different brain area.

A better understanding of the factors and receptors leading to chronic pain will be also clearly helpful. In the last decade, lipids have emerged as potential contributors of chronic pain. Pidoux et al. found that a single intraplantar injection of lysophosphatidyl-choline through peripheral ASIC3 activation lead to an increase of dorsal horn neuronal activity, underlining the potential of modulating lipids for chronic pain treatment.

Unfortunately, chronic pain treatments lack of efficacy and often lead to adverse effects. Here, Oehler et al. and Notartomaso et al. demonstrated the potential of botulinum toxin A1 and cinnabaric acid, respectively, to reduce chronic pain. These two studies also improved our understanding of their mechanisms of actions. Conversely, a better knowledge of the mechanism of action of efficacious analgesic could allow to target specific neuronal subpopulation and/or pathways. Thus, Ma et al. observed that the population of *Trpv1* and *Oprm1* co-expressing neurons may explain the remarkable efficacy of opioid drugs administered at the level of the DRG-spinal synapse, and that this subpopulation of *Trpv1*+ neurons is responsible for registering tissue damage. In addition, Petitjean et al. reviewed the analgesics properties of monoterpenes through their modulation of TRP channels activity and the importance and the potential of characterizing new plant extracts for the development of ethnopharmacology-based innovative treatments for chronic pain.

Finally, relevant rodent models of chronic pain inspired by patients will definitely help to improve the translational quality of preclinical studies. In this Research Topic, Xue et al. provided genetic evidence that the SCN9AR185H point mutation of Nav1.7 channel plays an important role in nociception and in pain experienced by patients with small fiber neuropathy suffering from this mutation. These findings should help to further explore pain treatments based on the Nav1.7 channel.

In conclusion, we hope that this Research Topic, which covers a large spectrum of nociceptive mechanisms, will be useful for scientists interested in understanding the physiopathology of chronic pain and the identification of potential therapeutic targets.

Author contributions

Both authors listed have made a substantial, direct, and intellectual contribution to the work and approved it for publication.

Conflict of interest

The authors declare that the research was conducted in the absence of any commercial or financial relationships that could be construed as a potential conflict of interest.

Publisher's note

frontiers in Molecular Neuroscience

ORIGINAL RESEARCH
published: 08 February 2018
doi: 10.3389/fnmol.2018.00019

The Absence of Sensory Axon Bifurcation Affects Nociception and Termination Fields of Afferents in the Spinal Cord

Philip Tröster[1], Julia Haseleu[2], Jonas Petersen[3,4], Oliver Drees[4], Achim Schmidtko[3,4], Frederick Schwaller[2], Gary R. Lewin[2], Gohar Ter-Avetisyan[1], York Winter[5], Stefanie Peters[6], Susanne Feil[6], Robert Feil[6], Fritz G. Rathjen[1] and Hannes Schmidt[1]*†*

[1] Developmental Neurobiology, Max Delbrück Center for Molecular Medicine in the Helmholtz Association, Berlin, Germany, [2] Molecular Physiology of Somatic Sensation, Max Delbrück Center for Molecular Medicine in the Helmholtz Association, Berlin, Germany, [3] Institute of Pharmacology, College of Pharmacy, Goethe University, Frankfurt am Main, Germany, [4] Institute of Pharmacology and Toxicology, Zentrum für Biomedizinische Ausbildung und Forschung (ZBAF), Witten/Herdecke University, Witten, Germany, [5] Cognitive Neurobiology, Humboldt University of Berlin, Berlin, Germany, [6] Interfaculty Institute of Biochemistry, University of Tübingen, Tübingen, Germany

OPEN ACCESS

Edited by:
Simone Di Giovanni,
Imperial College London,
United Kingdom

Reviewed by:
Lars Klimaschewski,
Innsbruck Medical University, Austria
Christian Gonzalez-Billault,
Universidad de Chile, Chile

***Correspondence:**
Fritz G. Rathjen
rathjen@mdc-berlin.de
Hannes Schmidt
hannes.schmidt@uni-tuebingen.de

†Present Address:
Hannes Schmidt,
Interfaculty Institute of Biochemistry,
University of Tübingen, Tübingen,
Germany

Received: 18 October 2017
Accepted: 15 January 2018
Published: 08 February 2018

Citation:
Tröster P, Haseleu J, Petersen J, Drees O, Schmidtko A, Schwaller F, Lewin GR, Ter-Avetisyan G, Winter Y, Peters S, Feil S, Feil R, Rathjen FG and Schmidt H (2018) The Absence of Sensory Axon Bifurcation Affects Nociception and Termination Fields of Afferents in the Spinal Cord. Front. Mol. Neurosci. 11:19. doi: 10.3389/fnmol.2018.00019

A cGMP signaling cascade composed of C-type natriuretic peptide, the guanylyl cyclase receptor Npr2 and cGMP-dependent protein kinase I (cGKI) controls the bifurcation of sensory axons upon entering the spinal cord during embryonic development. However, the impact of axon bifurcation on sensory processing in adulthood remains poorly understood. To investigate the functional consequences of impaired axon bifurcation during adult stages we generated conditional mouse mutants of Npr2 and cGKI (*Npr2*$^{fl/fl}$;*Wnt1*^{Cre} and *cGKI*$^{KO/fl}$;*Wnt1*^{Cre}) that lack sensory axon bifurcation in the absence of additional phenotypes observed in the global knockout mice. Cholera toxin labeling in digits of the hind paw demonstrated an altered shape of sensory neuron termination fields in the spinal cord of conditional Npr2 mouse mutants. Behavioral testing of both sexes indicated that noxious heat sensation and nociception induced by chemical irritants are impaired in the mutants, whereas responses to cold sensation, mechanical stimulation, and motor coordination are not affected. Recordings from C-fiber nociceptors in the hind limb skin showed that Npr2 function was not required to maintain normal heat sensitivity of peripheral nociceptors. Thus, the altered behavioral responses to noxious heat found in *Npr2*$^{fl/fl}$;*Wnt1*^{Cre} mice is not due to an impaired C-fiber function. Overall, these data point to a critical role of axonal bifurcation for the processing of pain induced by heat or chemical stimuli.

Keywords: sensory neurons, axon bifurcation, Npr2, cGKI, development, nociception and pain, axonal pathfinding

INTRODUCTION

The primary sensory representation of the body within the central nervous system is based on the intricate innervation patterns of dorsal root ganglion (DRG) neurons into the spinal cord. This projection represents an attractive system to study the branching of axons and has enabled the characterization of a cGMP-dependent signaling cascade essential for the bifurcation of sensory axons. This specific form of neuronal branching proceeds during embryonic development

at the so-called dorsal root entry zone (DREZ) where axons of DRG neurons split into ascending and descending stem axons that grow along the lateral margin of the spinal cord (Brown, 1981). Previous investigations showed that the cGMP signaling cascade composed of C-type natriuretic peptide (CNP), the receptor guanylyl cyclase Npr2 (also designated GC-B or Npr-B), and the cGMP-dependent protein kinase I (cGKI, also known as PKGI) are essential for the bifurcation of axons from DRG as well as cranial sensory ganglion neurons (Schmidt et al., 2002, 2007, 2009; Zhao and Ma, 2009; Zhao et al., 2009; Ter-Avetisyan et al., 2014). In the absence of any one of these components sensory axons no longer bifurcate and instead turn either in a rostral or caudal direction. Consistent with these observations is the timing and pattern of localization of CNP in the dorsal spinal cord and Npr2 and cGKI in sensory neurons (Schmidt et al., 2009). A critical missing link of the Npr2-mediated cGMP signaling pathway is the characterization of phosphorylation targets of cGKIα in sensory growth cones that mediate axon bifurcation. Such data might provide mechanistic insights into the machinery for bifurcation. The nitric oxide-sensitive guanylyl cyclases (NO-GCs) are not expressed in embryonic DRG neurons and thus not implicated in sensory axon branching *in vivo* (Schmidt et al., 2007, 2009). Also, variations in cGMP levels caused by the absence of phosphodiesterase 2A do not interfere with proper bifurcation of sensory axons (Schmidt et al., 2016). Notably, collateral sprouting originating from the stem axons as well as branch formation in the periphery of the body are not affected by the absence of Npr2-mediated cGMP signaling (Schmidt et al., 2007, 2009; Ter-Avetisyan et al., 2014).

Additionally, CNP and Npr2 are also involved in the process of endochondral ossification which is essential for long bone growth. Consequently, biallelic loss-of-function mutations including missense, nonsense, frame-shift mutations, insertions and deletions, and splice site mutations in the human *Npr2* gene result in acromesomelic dysplasia type Maroteaux (AMDM; OMIM602875), a skeletal dysplasia with an extremely short and disproportionate stature (Bartels et al., 2004; Potter, 2011; Kuhn, 2016). Whether AMDM patients also reveal bifurcation errors of sensory axons when entering the spinal cord is currently not known and unfortunately, neurological qualities have so far not been characterized on patients with mutations in the *Npr2* gene. Similarly to human patients, constitutive Npr2-deficient mice show dwarfism (Chusho et al., 2001; Tamura et al., 2004; Tsuji and Kunieda, 2005). Due to their decreased survival rate at post-weaning stages, *Npr2* global mouse knockouts are of limited use for further anatomical, physiological, and behavioral studies. Furthermore, the disproportionate bone growth in Npr2-deficient mice might cause the vertebrate column to squeeze on spinal or cranial nerves which in turn might affect sensation. Unlike Npr2 and its ligand CNP, cGKI is not implicated in long bone growth. However, constitutive cGKI-deficient mice have a number of other deficits including gastrointestinal and cardiovascular impairments which limits their use for investigations on the impact of disturbed axon bifurcation on sensory information processing (Hofmann et al., 2006).

To study the functional consequences of the absence of axon bifurcation in the spinal cord in the absence of other phenotypes that may complicate the interpretation of results, we have generated floxed alleles of *Npr2* and *cGKI* for conditional inactivation of *Npr2* or *cGKI* in DRG neurons at early stages. As in constitutive *Npr2* or *cGKI* knockout mice, DRG axons from mice with a conditional inactivation of *Npr2* or *cGKI* in the neural crest completely lack bifurcations which was associated with altered spinal termination patterns. Behavioral testing indicated that noxious heat sensation as well as nociception induced by chemical irritants was impaired, whereas the behavior driven by mechanical stimulation or balance of body position and motor coordination remained unchanged in mice without sensory axon bifurcations.

MATERIALS AND METHODS

Mice

Generation of *Npr2$^{fl/fl}$* Mice

Based on the bacterial artificial chromosome clone bMQ331a20 (BioScience) two loxP sites were inserted by standard procedures into the intronic sequences flanking exons 17 and 18 of the murine *Npr2* gene to generate the target construct. R1 embryonic stem cells (ESCs) (129X1x129S1) were electroporated and clones that had incorporated the targeting vector into their genome were selected by G418 and analyzed for homologous recombination after digestion with EcoRV or BlnI by Southern blotting using either the 3′ or 5′ probe as indicated in **Figure 1A**. ESCs were injected into blastocysts from C57Bl/6 mice and chimera that transmitted the floxed *Npr2* allele were identified by Southern blotting and by PCR genotyping using the following primer sequences: P1 5-GCCACTTTTGCACCCGGATG-3, P2 5-GTGACGCTGTCGAAGGCCTC-3, P3 5-CCTGCTTTGATG CCATTATCG-3, and P4 5-CTGCAACAACCAAAGCTCAG-3. Crossbreeding with Flpe-deleter mice induced the excision of the neomycin cassette flanked by FRT sites (B6; 129S7-*Npr2$^{tm4(flox)Fgr}$*).

Genotyping of the floxed cGKI mouse (B6.129-*Prkg1^{tm2Naw}*) (Wegener et al., 2002) (RRID:MGI:2668654), *Thy1-YFP-H* (*Tg(Thy1-YFP)H$^{Jrs/J}$*) (Feng et al., 2000) (RRID:IMSR_JAX:003782), *Wnt1-Cre (Tg(Wnt1-Cre)11Rth)* (Danielian et al., 1998) (RRID:IMSR_JAX:003829), FLPE-deleter strain (B6.129S4-*Gt(ROSA)26Sor$^{tm1(FLP1)Dym}$*/RainJ; The Jackson Laboratories) (Farley et al., 2000) (RRID:IMSR_JAX:009086), *TrkA-Cre* mice (B6;129S4-*Ntrk1$^{tm1(cre)Lfr}$*/Mmucd; Mutant Mouse Regional Resource Centers, https://www.mmrrc.org/) (Quina et al., 2015) (RRID:MMRRC_015500-UCD), *TrkC-Cre* mice (B6.129X1-*Ntrk3$^{tm1(cre)Lfr}$*/Mmucd, originating in the laboratory of Louis Reichardt, provided by Karina Gültig, University of Tübingen) (Funfschilling et al., 2004) (RRID:MMRRC_000364-UCD), *Npr2-LacZ* (B6.129P2-*Npr2$^{tm1.1(nlslacZ)/Fgr}$*) (Ter-Avetisyan et al., 2014) (RRID:MGI:5568090), *Npr2-CreERT2* (B6.129S7-*Npr2$^{tm1.2(CreERT2)/Fgr}$*) (Ter-Avetisyan et al., 2014) or *Rosa26-tdTomato* (B6.Cg-*Gt(ROSA)26Sor$^{tm14(CAG-TdTomato)Hze}$*/J) (Madisen et al., 2010) (RRID:IMSR_JAX:007914) was performed by PCR as described.

Animals were housed on a 12/12 h light/dark cycle with free access to food. The animal procedures were performed according

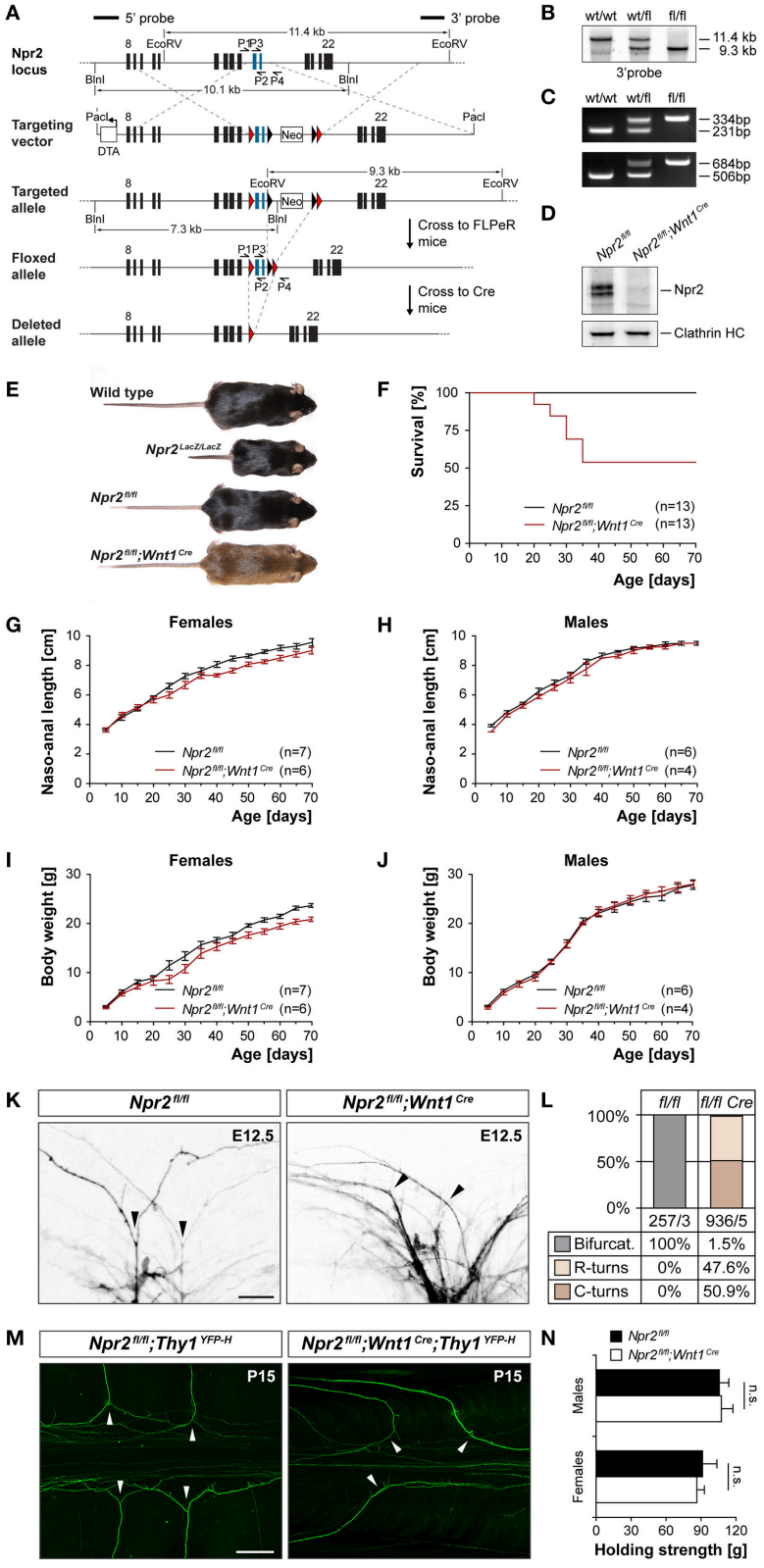

FIGURE 1 | *(Continued)*

FIGURE 1 | Generation of a conditional *Npr2*-deficient mouse mutant and analysis of sensory axon bifurcation at the DREZ. **(A)** Targeting strategy for the generation of the floxed *Npr2* allele and inactivation by Wnt1-Cre. **(B)** Southern blotting of the wild type, heterozygotes, and homozygous floxed allele using genomic DNA isolated from liver tissue. **(C)** PCR genotyping of wild type, heterozygotes and homozygous allele. Upper panel primer P1 and P2 flanking the loxP1 site, lower panel primer P3 and P4 flanking loxP2. **(D)** Western blotting of membrane fractions from E13.5 DRGs demonstrating the absence of Npr2 protein after recombination with Wnt1-Cre. The heavy chain of clathrin served as loading control. **(E)** Depiction of wild type, $Npr2^{LacZ/lacZ}$, $Npr2^{fl/fl}$ or $Npr^{2fl/fl};Wnt1^{Cre}$ mice of mature stages (see also **Figure S1**). **(F)** Survival rate of $Npr2^{fl/fl}$ or $Npr2^{fl/fl};Wnt1^{Cre}$ mice at different ages. Numbers of animals inspected are given in parenthesis. **(G–J)** Naso-anal length and body weight of $Npr2^{fl/fl}$ or $Npr2^{fl/fl};Wnt1^{Cre}$ males and females at different ages. **(K)** Analysis of DRG axon bifurcation by DiI tracing in $Npr2^{fl/fl}$ or $Npr2^{fl/fl};Wnt1^{Cre}$ E12.5 embryos (see also **Figure S2**). Arrow heads mark bifurcations or turns of sensory axons in wild type or mutants, respectively. Bar, 25 μm. **(L)** Quantification of bifurcation errors demonstrated the complete absence of DRG axon bifurcation in $Npr2^{fl/fl};Wnt1^{Cre}$ E12.5 embryos. The numbers of counted axons and embryos are indicated below the columns. **(M)** Bifurcation errors persisted at mature stages (P15) as indicated by the reporter *Thy1-YFP-H* in the $Npr2^{fl/fl};Wnt1^{Cre};Thy1^{YFP-H}$ mouse. Arrow heads mark bifurcations or turns of sensory axons in wild type or mutants, respectively. Bar, 250 μm. **(N)** Analysis of grip strength revealed indistinguishable maximal muscle strength (mean ± SEM) of the forelimbs between mature $Npr2^{fl/fl}$ ($n = 6$ males and 6 females) and $Npr2^{fl/fl};Wnt1^{Cre}$ ($n = 8$ males and 7 females) of both sexes (paired *t*-test; $p = 0.90$ and 0.72 in males and females, respectively).

to the guidelines from directive 2010/63/EU of the European Parliament on the protection of animals used for scientific purposes. All experiments were approved by the local authorities of Berlin(LaGeSO) (numbers T0313/97, 0143/07, G0370/13, G0239/11, X9014/15, and G0222/14), the Landesamt für Natur, Umwelt und Verbraucherschutz Nordrhein-Westfahlen (number 84-02.04.2012.A422), and Regierungspräsidium Darmstadt (number FU/1102). All experiments were also approved by the local Ethics Committee for Animal Research and adhered to the guidelines of the Committee for Research and Ethical Issues of the International Association for the Study of Pain.

Axon Tracing by DiI, Immunohistochemistry, and Western Blotting

DiI tracing and immunofluorescent staining of cryostat sections (16 μm) from paraformaldehyde-fixed tissue were performed as described previously (Schmidt et al., 2007; Schmidt and Rathjen, 2011).

The following primary and secondary antibodies using the indicated concentrations or dilutions were applied to tissue sections or Western blotting: Guinea pig antiserum to the extracellular domain of Npr2 (dilution: 1:5,000) (Ter-Avetisyan et al., 2014), guinea pig antiserum to amino acids 2-89 of cGKIα (1:25,000 for immunofluorescence staining), affinity-purified rabbit antibody to amino acids 2-89 of cGKIα (0.25 μg/ml for Western blot analysis), rabbit antibody to full length cGKIα expressed in Sf9 cells (1 μg/ml of the IgG fraction for Western blot analysis), chicken anti-β-galactosidase (1:5,000; Abcam, ab 9361; RRID:AB_307210), mouse anti-clathrin heavy chain (0.05 μg/ml; BD Biosciences, 610499; RRID:AB_397865), mouse anti-GAPDH (1:7,500; Novus Biologicals, NB300-221; RRID:AB_10077627), rabbit anti-PGP9.5 (1:1,000, Dako, Z5116, RRID:AB_2622233), rabbit anti-trkA (1:1,000; Millipore, 06-574; RRID:AB_310180), rabbit anti-parvalbumin (1:1,000; Swant, PV28; RRID:AB_2315235), rabbit anti-CGRP (1:1,000; Chemicon, AB1971; RRID:AB_2313629), rabbit anti-red fluorescent protein (1:2,500, ABIN129578; RRID:AB_10781500), isolectin GS-IB4-Alexa-488 (1:50; Life Technologies; RRID:AB_2314662), donkey anti-chick-IgY-Cy3 (1:1,000; Dianova), goat-anti-rabbit-Alexa488 (1:1,000; Dianova), goat anti-guinea pig-Alexa488 (1:1,000; Dianova), donkey anti-guinea pig-HRP (Dianova), goat anti-rabbit-HRP, and goat anti-mouse-HRP (all 1:20,000; Dianova,). 0.1 mg per g body weight of tamoxifen was applied by oral gavaging as described (Ter-Avetisyan et al., 2014).

Microscopic images were obtained at room temperature by confocal imaging using a Carl Zeiss LSM 710 NLO Laser Scanning Microscope equipped with ZEN 2010 software and the following lenses: a Plan-Neofluar 10x/0.30 NA objective, a Plan-Achromat 40x/1.40 NA oil objective, or a Plan-Achromat 63x/1.40 NA oil objective (all from Carl Zeiss MicroImaging, GmbH). Images were imported into Photoshop CS5 (Adobe) for uniform adjustment of contrast and brightness. Figures were assembled using Illustrator CS5 (Adobe).

Transganglionic Labeling Using Cholera Toxin Subunit B, Optical Clearing, and Imaging of Fixed Spinal Cord Tissue

Five to six-week old mice of either sex were anesthetized by an intraperitoneal injection of ketamine (100 mg/kg) and xylazine (10 mg/kg). 0.2 μl of 1.5% cholera toxin subunit B conjugated with Alexa Fluor 594 (CTB-AL594) (Wan et al., 1982; Robertson and Arvidsson, 1985; Conte et al., 2009) in 0.1 M phosphate buffered saline (PBS) were injected subcutaneously into the plantar surface of the left second hindpaw digit using a pulled glass capillary attached to a Hamilton microliter syringe. The glass capillary was inserted into the most distal interphalangeal crease and advanced under the skin toward the next proximal crease where the tracer was slowly injected. Five days post-injection, allowing for transganglionic transport of the tracer, mice were transcardially perfused with PBS and ice-cold 4% paraformaldehyde (PFA). Subsequently, the lumbar spinal cord was dissected out and post-fixed overnight in 4% PFA at 4°C. Fixed spinal cords were washed three times with 0.1 M PBS for 10 min each at RT. Subsequently, the tissue was immersed in ascending concentration series of 2,2'-thiodiethanol (TDE) (Staudt et al., 2007; Kloepper et al., 2010; Aoyagi et al., 2015; Costantini et al., 2015) for 24 h each at RT. The applied concentrations were 10, 25, 50, and 97% TDE diluted with 0.1 M PBS. During all incubation steps, the samples were kept on a vibrating table in the dark. For two-photon imaging, the cleared spinal cords were mounted on glass slides in 97% TDE which has a refractive index of 1.52 (Staudt et al., 2007) using press-to-seal silicone isolators with the dorsal surface facing up.

Two-photon imaging was performed using a laser scanning microscope equipped with a tunable Ti:sapphire laser. Two channels were recorded sequentially to collect Alexa Fluor 594 fluorescence (excitation wavelength: 810 nm; emission range: 600–735 nm) and tissue autofluorescence (excitation wavelength: 810 nm; emission range: 505–575 nm). A 25x multi-immersion objective (0.8 numerical aperture) was used with immersion oil for cleared sample imaging. Tiled stacks were taken through the spinal cord dorsal horn (pixel size: 0.5 × 0.5 µm; z step size: 1.5 µm). All images were processed using ImageJ (Schneider et al., 2012). Tiled stacks were stitched using either the imaging software ZEN 2010 or the ImageJ plugin "Stitching 2D/3D" (Preibisch et al., 2009). Subsequently, images were cropped to the same size and reduced to the same slice number. Next, background fluorescence was reduced by subtracting the autofluorescence channel from the CTB-AL594 channel. Using stack histogram-based thresholding, the image stacks were binarized. The threshold was set as the mean gray value plus three times the standard deviation. Finally, single pixels were removed to reduce noise, e.g., hot pixels. In order to enable comparative analyses of spinal terminal fields of cutaneous myelinated afferents, the three-dimensional centers of mass of the voxel clouds representing CTB-AL594 labeled fiber terminals were determined using the ImageJ plugin "3D ImageJ Suite" (Ollion et al., 2013). All images were aligned to the center of mass of the voxel cloud, i.e., images were cropped to the same size and reduced to the same slice number around the respective centers of mass. Summed dorsoventral, rostrocaudal, and/or mediolateral projections of the binary image stacks were constructed to enable two-dimensional visualization of terminal fields.

Morphometric Analysis of Spinal Terminal Fields

Mediolateral, rostrocaudal, and dorsoventral spans of the terminal fields were measured in summed dorsoventral and rostrocaudal projections of binary image stacks. Summed projections were thresholded with the threshold being set as the mean gray value plus one standard deviation. Subsequently, the dimensions of the bounding rectangles enclosing all pixels representing CTB-AL594 labeled fiber terminals were measured.

Density Analysis of Spinal Terminal Fields

Areal densities (as voxels per area) of spinal terminal fields were calculated in summed dorsoventral, mediolateral, and rostrocaudal projections of binary image stacks. Using the ImageJ plugin "3D ImageJ Suite" (Ollion et al., 2013), the total number of voxels representing CTB-AL594 labeled fiber terminals was determined in binary image stacks. Subsequently, the number of voxels was divided by the area (in μm^2) that was occupied by positive pixels in summed dorsoventral, mediolateral, and rostrocaudal projections, respectively.

Ex Vivo Skin Nerve Preparation

Ex vivo skin nerve preparations were performed as described (Moshourab et al., 2013). Briefly, mice were sacrificed and the glabrous skin on the left hindlimb was removed. The saphenous nerve was exposed dissected free along the lower leg up. Subsequently, the skin was carefully removed from the musculoskeletal and the connective tissue of the paw. The skin-nerve preparation was placed in an organ bath filled with oxygenated 32°C warm synthetic interstitial fluid (SIF) consisting of 123 mM NaCl, 3.5 mM KCl, 0.7 mM $MgSO_4$, 1.7 mM NaH_2PO_4, 2.0 mM $CaCl_2$, 9.5 mM sodium gluconate, 5.5 mM glucose, 7.5 mM sucrose and 10 mM HEPES, at a pH of 7.4. Using insect needles, the skin was mounted in the organ bath with its epidermis facing the bottom of the chamber, exposing the dermis to the solution. The nerve was pulled through a hole into the adjacent recording chamber which was filled with mineral oil. Finally, using fine forceps the nerve was desheathed by removing its epineurium and small filaments were teased of the nerve. Throughout the whole experiment the skin was superfused with oxygenated SIF at a flow rate of 15 ml/min.

Single-Unit Recordings

Single receptor units were recorded as previously described (Moshourab et al., 2013). Teased filaments were attached to a recording electrode and the receptive fields (RF) of individual units were identified by manually probing the skin with blunt forceps. To probe for heat-responsive units, 1 ml of hot (48°C) SIF buffer was washed over the surface of the skin. For immediate visual identification of single units, whole action potential waveforms were resolved on an oscilloscope. Data was acquired using a PowerLab 4/30 system which was controlled with the software LabChart 7.1.The conduction velocities (CVs) of single fibers were determined by evoking a local action potential with a platinum iridium electrode. The electrical impulse was conducted nearly instantaneously through the solution whereas the triggered action potential conducted by the fiber was delayed depending on the fiber type and the distance of the fiber's receptive field from the electrode. Hence, the distance between the RF of a unit to the electrode was measured and the CV was calculated as distance divided by time delay. Fibers with CVs below 1.3 m/s were classified as C-fibers.

Stimulation Protocols

A Peltier device (custom device built by the Yale School of medicine Instrument Repair and Design) was used to apply warm or cool stimulation parameters to the RFs of cutaneous afferent fibers. Two heat ramps were applied to skin: firstly a ramp and hold stimulus from 32 to 48°C with a 0.5 s ramp, followed by a 3 s hold time and a further 0.5 s ramp; and secondly a slow 15 s ramp from 32 to 48°C. Two cold ramps were also applied: first a ramp and hold stimulus from 32 to 12°C with a 0.5 s ramp, followed by a 3 s hold time, and a further 0.5 s ramp; and secondly a slow 15 s ramp from 32 to 12°C.

A computer-controlled Nanomotor (Kleindieck, Germany) was used to apply controlled mechanical stimuli of known amplitude and velocity to the RF of afferent fibers. Four 3 s ramp and hold stimuli were applied to the RF of each afferent fiber, each increasing in amplitude (40, 75, 150, 220 mN).

Analysis of Extracellular Afferent Recordings

Thermosensitive C-fibers were searched for in recordings and for further analysis. Spike sorting was performed with a spike analysis plug-in of the LabChart software (AD Instruments).

C-mechanoheat (C-MH), C-mechanoheatcold (C-MHC), and C-mechanocold (C-MC) fibers were pooled in each experimental group (Milenkovic et al., 2014). Thermal thresholds represent the temperature required to cause the first action potential spike in slow (15 s) heat and cold ramp protocols. Mechanical thresholds represent the average force required to cause the first action potential spike over the four ramp and hold stimuli. Mean group data were compared using *t*-tests and two-way repeated measures ANOVA tests.

Behavioral Testing

Littermate mice of either sex were used in all behavioral tests (8 to 10-weeks old). The $Npr2^{fl/fl};Wnt1^{Cre}$ mice were on a mixed genetic background (Bl6/SV129) and $cGKI^{KO/fl};Wnt1^{Cre}$ mice were on a Bl6 background. Animals were habituated to the experimental room and were investigated by observers blinded for the genotype.

Hot Plate Test

Mice were placed into a Plexiglas cylinder on a metal surface maintained at 50, 52, or 54°C (Hot Plate; Ugo Basile, Comerio Italy). Cut-off times were 60, 40, and 20 s, respectively, to prevent tissue damage. The time between placement and shaking or licking of the hindpaws or jumping off the plate was recorded.

Acetone Test

For acetone-evoked evaporative cooling, animals were habituated in a glass enclosure on a mesh floor, a drop of acetone (50 μl) was applied to the plantar side of a hindpaw and responses were observed for 1 min. The responses were scored as follows: 0, no response (sniffing or walking was not considered nociceptive); 0.5, a licking response; 1, flinching and brushing of the paw; 2, strong flinching (Caspani et al., 2009).

Capsaicin Test

Capsaicin (5 μg dissolved in 10 μl of a solution consisting of 90% sterile saline, 5% ethanol, and 5% Tween 80) was injected subcutaneously (s.c.) into the dorsal surface of a hindpaw. The time spent licking the capsaicin-injected paw and the number of shakes of the injected paw was recorded for 5 min.

Formalin Test

Formalin (20 μl of a 0.5% formaldehyde solution) was s.c. injected into the dorsal surface of a hindpaw (Braz and Basbaum, 2010). The time spent licking the formalin-injected paw was recorded in 5 min intervals up to 60 min after formalin injection.

Hargreaves Test

The Hargreaves test was performed with an idle value of 5% and a stimulus value of 50% of the maximum intensity as described (Hargreaves et al., 1988). The withdrawal reaction induced by heat stimulation was measured 25 times per animal over period of 3 consecutive days using model 400 Heated Base (IITC Life Science Inc.).

Dynamic Plantar Test

The mechanical sensitivity of the plantar side of a hindpaw was assessed with an automated von Frey-type testing device (Dynamic Plantar Aesthesiometer; Ugo Basile). This device pushes a thin probe (0.5 mm diameter) with increasing force through a wire-grated floor against the plantar surface of the paw from beneath, and it automatically stops and records the latency time, after which the animal withdraws the paw. The force increased from 0 to 5 g within 10 s (0.5 g/s ramp) and was then held at 5 g for an additional 10 s (Lu et al., 2015). The paw withdrawal latency was calculated as the mean of five to six consecutive trials with at least 20 s in-between.

Balance and Motor Coordination in the Absence of Npr2

Grip Strength Assay

Motor functions were assessed using the grip strength assay that measures maximal muscle strength of the forelimbs (TSE Grip Strength Meter). An animal holding onto the meter handle was pulled backwards steadily in horizontal orientation, and the mean of three maximum force measurements was recorded.

Balance and coordination were examined using the beam walking test, rotarod performance test, staircase test, adhesion removal test, food grasping and reaching test, and walking track (MouseWalker) which provide readouts for general motor performance.

The Beam Walking Test

The beam walking test assesses motor coordination and balance from the ability of mice to traverse a series of narrow, horizontal beams graded in diameter. Wooden beams were 1 m × 10 or 15 or 20 mm diameter at 50 cm height with one starting end (with a 60 W aversive light) and the other end attached to an escape box. Mice were trained for 2 days with four trials per day, motivated by a reward in the escape box until traversing took < 20 s. On the test day (day 3) mice received two consecutive trials per beam, progressing from wide to narrow, allowing up to 60 s for a traversal. A fall off counted as incomplete trial. Durations of beam traversals und instances of hind feet slipping off the beam were recorded (Carter et al., 2001; Luong et al., 2011).

The Staircase Test

The staircase test (Campden Instruments) allows measurement of lateralized effects on skilled motor function required for reaching and grasping a food pellet from variable distance. Food was removed from subjects' home cages 4–6 h before first training and prior to later experiments animals were fed one pellet of regular feed. Animals were habituated to sucrose pellet rewards at least three times prior to testing to avoid food neophobia. Mice were trained for 3 days in the staircase test box with the double, eight-step staircase baited with two pellets per step (16 on each side, total 32). Testing was conducted with one pellet per step and sessions lasted for 15 min. We recorded collected pellets, and maximum distance reached.

The Adhesion Removal Test

The adhesion removal test assesses sensory and motor deficits related to paw and mouth coordination. It was performed in an empty mouse cage where a mouse received two adhesive tape strips (3 × 4 mm) onto the hairless part of the forepaws. The time to first contact reaction was recorded for both paws, as well as the time to tape removal.

The Reaching and Grasping Test

The reaching and grasping test was performed with an automated forepaw reaching chamber (Campden Instruments) providing sensitive measures of fine motor coordination (Marques and Olsson, 2010). Prior to testing subjects were habituated to sucrose pellets. Four days before testing, animals were trained daily to reach for pellets, each training lasting until either 10 pellets were retrieved or 10 min had passed. During the test one pellet at a time was placed in the tray. Reaching attempts were counted until the pellet was removed. Performance parameters were latency to first reach, reaching accuracy (pellets retrieved per reach attempt), latency to first pellet retrieval, interval to retrieve five pellets after the first pellet had been retrieved.

The Rotarod Test

The Rotarod test was performed using Rota-Rod 47600 (Ugo Basile) with an acceleration of the rotating cylinder from 5 to 40 rpm in 360 s. Animals were given 2 days of habituation to the Rotarod (same protocol as in test). Four recordings per day were done.

The mouse's gait was tested using a home-made *MouseWalker* as described in Mendes et al. (2015). This system is based on the total internal reflection of light on transparent plates. Paw contacts of the mice disrupt this reflection and generate scattered light which is then detected by a high speed digital camera. Parameters such as foot print clustering and stance linearity were evaluated.

Experimental Design and Statistical Analysis

Sample size for behavioral experiments and for analysis of axon branching was deduced from previously published studies (Schmidt et al., 2007) or in publications listed above in the subsection on behavioral testing. No further statistical methods were used to predetermine sample size. Sample size are given directly in the figures or in the legends. Experiments were done blind with respect to genotype. Littermates were used as control. Statistical analysis was performed with SPSS software (RRID:SCR_002865) using the Student's *t*-test for paired comparisons or Mann-Whitney *U*-test. Power analysis of statistical data was performed with the software "nQuery + nTerim 4.0." Depending on the equality or inequality of variances and on the equality and inequality of the number of measurements *t*-test or Satterthwaite *t*-test were applied.

RESULTS

Conditional Inactivation of *Npr2* in DRG Neurons Interrupted Sensory Axon Bifurcation

To generate a conditional allele of *Npr2*, two loxP sites were introduced into the introns flanking exons 17 and 18 of the mouse *Npr2* gene which encode the guanylyl cyclase domain of Npr2. The neo selection cassette flanked by two FRT sites was removed by crossing this mouse line with a FLPE-deleter strain. The resulting floxed *Npr2* allele contains two loxP sites surrounding exon 17 and 18 (**Figure 1A**). The correct integration of the loxP sites was verified by Southern blotting using (**Figure 1B**) a probe as indicated in **Figure 1A** and PCR was applied for genotyping using two distinct primer pairs that amplify genomic regions including loxP1 or loxP2, respectively (**Figure 1C**). Conditional inactivation of *Npr2* in DRG neurons at early embryonic stages when sensory axons enter the spinal cord was obtained by crossbreeding with the *Wnt1-Cre* transgenic mouse line. At early embryonic stages Wnt1 is restricted to the midbrain, dorsal spinal cord and DRGs as detected by the *Wnt1-lacZ* reporter mouse (Echelard et al., 1994). Cre-mediated excision of the exon 17 and exon 18 generated a frameshift in exon 19 which leads to a premature stop codon. This resulted in nearly undetectable expression of Npr2 protein in DRGs as indicated by Western blotting using antibodies to the extracellular domain of Npr2 (**Figure 1D**).

About 50% of these Wnt1-Cre inactivated *Npr2* mutants developed normally as demonstrated by a nasal to anal body length and a body weight that were indistinguishable from wild type or the homozygous floxed strain (**Figures 1E–J**). Furthermore, grip strength in these mutant mice appeared normal (**Figure 1N**). However, about 50% of $Npr2^{fl/fl};Wnt1^{Cre}$ mice were retarded in their development which revealed also a reduced survival rate at post-weaning stages (**Figure 1F**). Premature death of these mutants was accompanied by a severe malocclusion of the upper and lower incisors and intestinal distension which both affected normal nutrition (**Figure S1**). These mice were excluded from further testing. A malocclusion in conditional mutants of the Npr2 ligand CNP (Nakao et al., 2015) and milk retention in the stomach and intestinal distension have also been observed in the *Npr2* mutant *slw/slw* (Sogawa et al., 2010).

Analysis of sensory axon bifurcation by DiI tracing at embryonic day 12.5 or by the reporter line *Thy1-YFP-H* at postnatal day P15 indicated a complete absence of axon bifurcation at the dorsal root entry zone of the spinal cord in the conditional mutant but not in the homozygous floxed allele (**Figures 1K–M**). DRG axons turn either in a rostral or caudal direction at the lateral margin of the cord. In contrast, the formation of collaterals from stem sensory axons in the dorsal funiculus is not impaired in the absence of Npr2 (data not shown) indicating that this type of branch formation is not dependent on Npr2 signaling as described previously (Schmidt et al., 2007). In contrast to conditional inactivation of *Npr2* by Wnt1-Cre the use of other Cre-lines such as *trkA-Cre* or *trkC-Cre* did not induce bifurcation errors most likely due to later initiation of Cre expression with respect to Npr2 in embryonic DRG neurons (**Figure S2**). Overall, our data indicate that the $Npr2^{fl/fl};Wnt1^{Cre}$ mutant is a suitable model to study the consequences of impaired axon bifurcation in adult mice.

Receptive Fields in the Spinal Cord Are Altered in the Absence of Sensory Axon Bifurcation

Sensory information from a large number of afferent axons converges within the spinal cord in nociceptive,

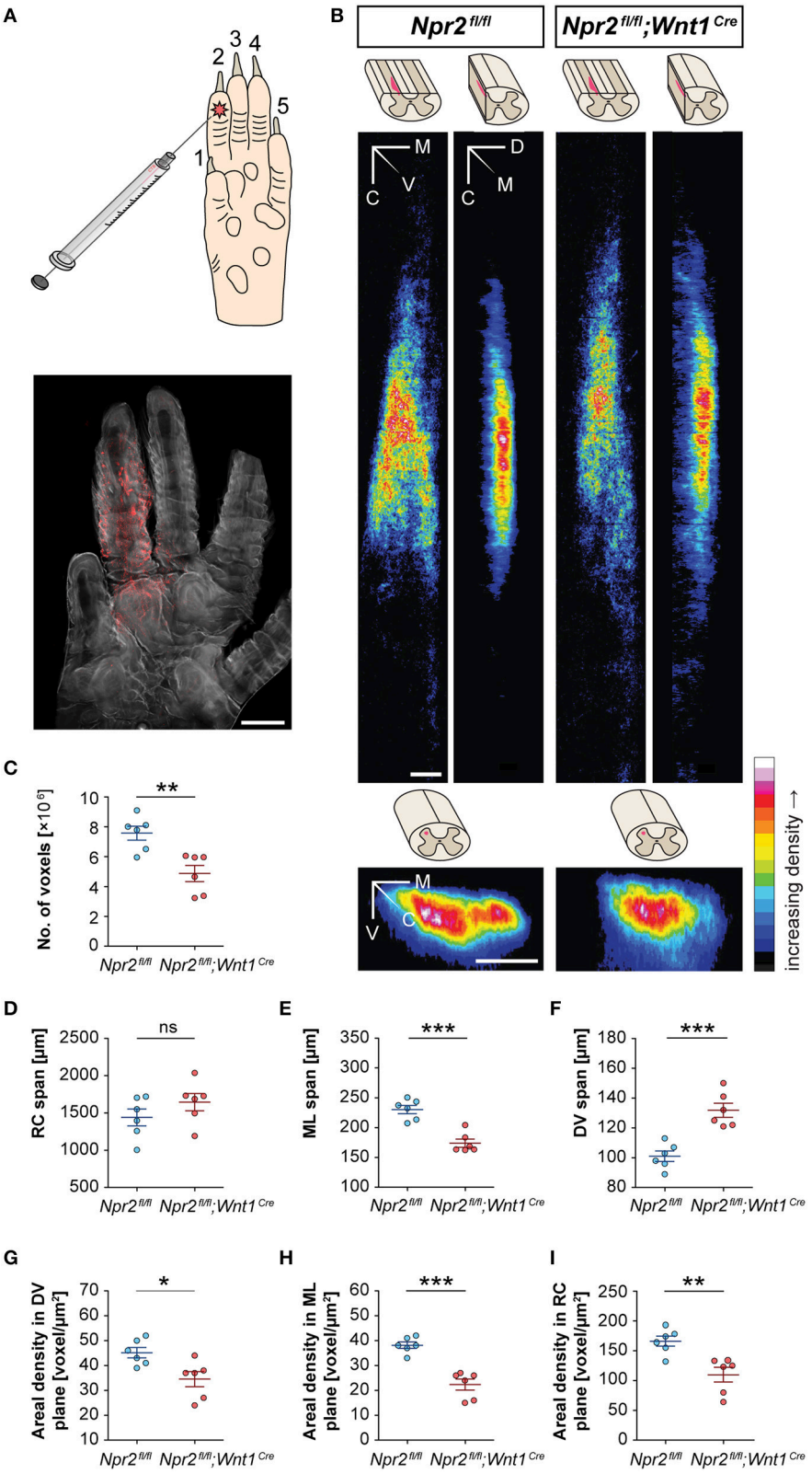

FIGURE 2 | *(Continued)*

FIGURE 2 | Receptive fields of spinal terminations of tactile afferents from the hindpaw in wild type and Npr2-deficient conditional mice. **(A)** Subcutaneous injection of 0.3 μl of CTB conjugated to AL594 into the second digit of the left hind paw in order to label the terminal fields of cutaneous myelinated afferents in the spinal cord dorsal horn. A fluorescent micrograph of the left hind paw is shown. Scale bar, 1 mm. **(B)** Heat maps of averaged summed projections of spinal terminal fields in $Npr2^{fl/fl};Wnt1^{Cre}$ and $Npr2^{fl/fl}$ control mice. Terminal fields of fibers innervating the second digit of the left hind paw appear different in $Npr2^{fl/fl};Wnt1^{Cre}$ mice ($n = 6$) than in $Npr2^{fl/fl}$ mice ($n = 6$) in dorsoventral, mediolateral, and rostrocaudal projections. The ImageJ color lookup table "16 Colors" was applied (see color map). The color code in each pixel denotes the number of voxels found in corresponding positions along different axes averaged across mice. Scale bars, 100 μm. **(C)** In $Npr2^{fl/fl};Wnt1^{Cre}$ mice, the number of voxels representing CTB-labeled fibers is significantly lower compared to those in $Npr2^{fl/fl}$ mice. **(D–F)** Morphometrics of spinal terminal fields in $Npr2^{fl/fl};Wnt1^{Cre}$ and $Npr2^{fl/fl}$ control mice. Spinal terminal fields of fibers innervating the second digit of the left hind paw span similarly far in the **(D)** RC dimension but in a significantly different range in the **(E)** ML and further in the **(F)** DV dimension in $Npr2^{fl/fl};Wnt1^{Cre}$ (red, $n = 6$) as compared to $Npr2^{fl/fl}$ (blue, $n = 6$) mice. **(G–I)** Areal densities of spinal terminal fields in $Npr2^{fl/fl}$ and $Npr2^{fl/fl};Wnt1^{Cre}$ mice. The areal densities of terminal fields innervating the second digit of the left hind paw digit were significantly lower in **(G)** the dorsoventral projection, **(H)** the mediolateral projection, and **(I)** the rostrocaudal projection in $Npr2^{fl/fl};Wnt1^{Cre}$ (red, $n = 6$) as compared to $Npr2^{fl/fl}$ (blue, $n = 6$) mice. Individual data points and mean values ± SEM are shown. Each data set was compared using a two-tailed unpaired *t*-test (*$p < 0.05$; **$p < 0.01$; ***$p < 0.001$). CTB, cholera toxin subunit B; WT, wild type; M, medial; V, ventral; C, caudal; D, dorsal; RC, rostrocaudal; ML, mediolateral; DV, dorsoventral.

mechanoreceptive or proprioceptive fields by the generation of collaterals that terminate in specific layers. Bifurcation of sensory axons at the DREZ contributes to this overall representational organization (Brown, 1981). The normal body length of the conditional *Npr2* mutant allowed us to clarify whether the absence of bifurcation affects the size or shape of termination fields of afferents from the skin. A lack of bifurcation at the DREZ predicts altered receptive fields and less overlap between different sensory modalities. Therefore, we mapped the spinal terminations of cutaneous myelinated afferents from the hind paw in wild type and $Npr2^{fl/fl};Wnt1^{Cre}$ mice. The topography of primary afferent termination was visualized by transganglionic transport of fluorescently labeled cholera toxin B (CTB) subcutaneously injected into the second digit of the left hind paw of 5-week old mice (**Figure 2A**). CTB binds to the ganglioside GM1 which is highly expressed on axons (Kobbert et al., 2000). Injection in digit two resulted in a characteristic fork-like afferent fiber termination field in control $Npr2^{fl/fl}$ spinal cords (**Figure 2B**). Total number of positive voxels representing CTB-labeled fibers as well as spans and area densities in dorso-ventral, medio-lateral, and rostro-caudal planes were calculated (**Figures 2C–I**). The total number of voxels was reduced to 64% for the 2nd digit (**Figure 2C**) indicating that the number of incoming sensory axons and collaterals were strongly reduced in comparison to wild type - surprisingly not to 50% as one might have been expected from the total lack of bifurcation at the DREZ. This observation might be explained by an increase in the density of collaterals protruding from the stem axons or by an increase in the terminal branching of collaterals in the mutant. Interestingly, the dorsoventral span of fluorescence intensity was increased to about 131% of control for the 2nd digit in the mutant whereas the medial-to-lateral distribution of terminal field was decreased by 25%. No difference was observed in the rostral-to-caudal span of the projection (**Figures 2D–F**). The density, the voxels per area, decreased to 66 and 58% in the rostrocaudal and in the mediolateral direction, respectively, whereas the dorsoventral direction decreased only to 76% (**Figures 2G–I**) for digit two. In summary, the absence of bifurcation caused decreased projection intensities together with a reduction in the mediolateral span as well as an increase in the dorsoventral extension of sensory afferent termination fields in the spinal cord.

Balance and Motor Coordination Is Not Impaired in the Absence of Sensory Axon Bifurcation

Since axon bifurcation is compromised in all DRG neurons of Npr2-deficient mice we asked whether proprioception might be impaired. Therefore, balance and motor coordination in $Npr2^{fl/fl};Wnt1^{Cre}$ mice was examined using the balance beam test, rotarod, staircase assay, food grasping and reaching assay, and walking track analysis (MouseWalker). Balance beam and rotarod measure the ability to perform complex and coordinated movements. Npr2-deficient mice did not show a reduced latency to fall off or to slip off the beam (**Figures 3A,B**) or to fall off the rotating rod (**Figure 3C**). Similarly, no deficits were observed in the staircase and reaching and grasping test (**Figures 3E–I**), indicating that motor coordination was not altered in the absence of sensory axon bifurcation. To assess sensory and motor abilities related to the forepaw and mouth coordination the adhesion removal test was performed. Adhesive tape was fixed gently to the hairless parts of the forepaws and the time to first contact and the removal of both adhesive strips was recorded. Control mice and Npr2 mutants made regular attempts to remove the tape (**Figure 3D**). To ask whether the absence of sensory axon bifurcation interferes with the control of locomotion we applied the MouseWalker system which allows a comprehensive and quantitative description of parameters of freely walking Npr2-deficient mice (**Figures 3J–L**).

In summary, no deficits were observed in these behavioral assays in conditional *Npr2* mutants (**Figure 3**). Npr2-deficient mutants possess considerable coordination capabilities.

Heat Sensation Is Impaired in the Absence of Sensory Axon Bifurcation in $Npr2^{fl/fl};Wnt1^{Cre}$ mice

To assess the consequences of impaired axonal bifurcation of sensory neurons for pain processing *in vivo*, we analyzed the nociceptive behavior of $Npr2^{fl/fl};Wnt1^{Cre}$ and respective control mice in various animal models of pain. We tested both male and female mice, but no significant effects of sex were detected in any assay.

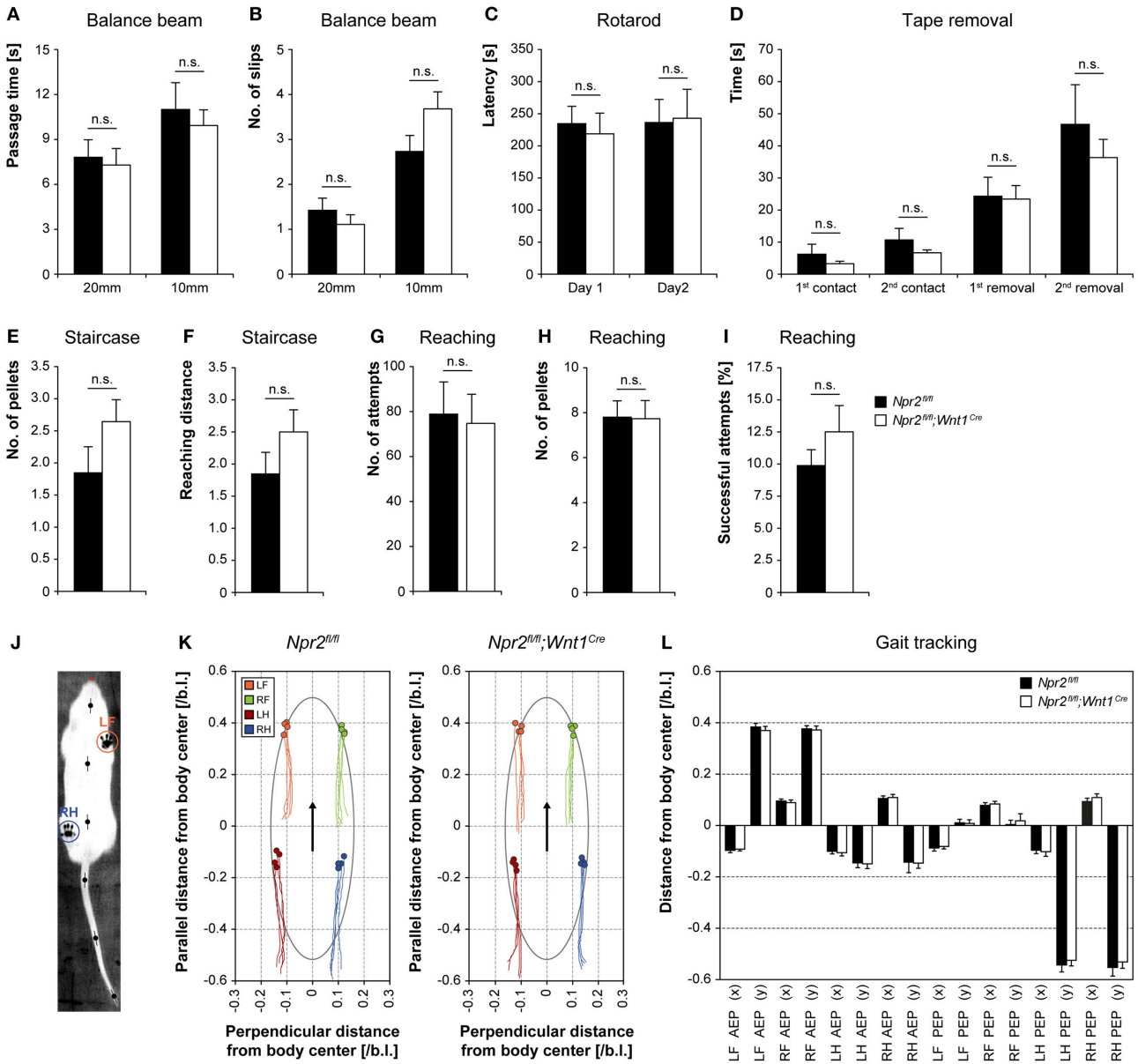

FIGURE 3 | Analysis of balance and motor coordination in the absence of *Npr2*$^{fl/fl}$;*Wnt1*^{Cre}. Balance and motor coordination in Npr2-deficient mice was not altered in the absence of DRG axon bifurcation using the **(A)** beam walking test ($n = 13$ *Npr2*$^{fl/fl}$ and 14 *Npr2*$^{fl/fl}$;*Wnt1*^{Cre}), passage time and **(B)** number of slips, **(C)** rotarod performance test ($n = 5$), **(D)** tape removal test ($n = 13$ *Npr2*$^{fl/fl}$ and 14 *Npr2*$^{fl/fl}$;*Wnt1*^{Cre}), **(E)** staircase test, no. of pellets and **(F)** reaching distance ($n = 13$ *Npr2*$^{fl/fl}$ and 14 *Npr2*$^{fl/fl}$;*Wnt1*^{Cre}), **(G)** food grasping and reaching, number of attempts, **(H)** number of pellets and **(I)** successful attempts ($n = 10$ *Npr2*$^{fl/fl}$ and 15 *Npr2*$^{fl/fl}$;*Wnt1*^{Cre}), **(J)** walking track analysis using the MouseWalker, **(K)** Plots of stand traces of free walking animals and **(L)** summary of paw positioning in *Npr2*$^{fl/fl}$ ($n = 4$) and *Npr2*$^{fl/fl}$;*Wnt1*^{Cre} ($n = 4$) are shown. AEP, anterior extreme position; PEP, posterior extreme postion; L, left; R, right; F, forepaw; H, hind paw; error bar: SEM. No significant differences were observed between *Npr2*$^{fl/fl}$ and *Npr2*$^{fl/fl}$;*Wnt1*^{Cre} mice in any of these tests.

We first determined the acute pain thresholds for noxious thermal stimuli in *Npr2*$^{fl/fl}$;*Wnt1*^{Cre} and littermate control mice using the hot plate test (50–54°C). *Npr2*$^{fl/fl}$;*Wnt1*^{Cre} mice displayed typical nocifensive behaviors (shaking or licking of the hindpaws or jumping off the plate), but at all tested temperatures they did so at consistently longer latencies than control mice (**Figure 4A**). Paw withdrawal responses to radiant heat (Hargreaves method) were also significantly increased in *Npr2*$^{fl/fl}$;*Wnt1*^{Cre} mice as compared to control mice (**Figure 4B**). In contrast to the impaired heat sensitivity, responses to acetone-evoked evaporative cooling were normal in *Npr2*$^{fl/fl}$;*Wnt1*^{Cre} mice in the group tested (**Figure 4C**; $p = 0.295$). Moreover, mechanical sensitivity of the hindpaw assessed using a dynamic plantar aesthesiometer was similar in *Npr2*$^{fl/fl}$;*Wnt1*^{Cre} and

control mice (**Figure 4D**). Together, these data suggest that the loss of axonal bifurcation impairs the rapid response to avoid noxious heat, whereas behavioral thresholds and response latencies to cold or mechanical stimuli were not affected.

We next examined the tonic pain behavior in $Npr2^{fl/fl};Wnt1^{Cre}$ and control mice after injection of capsaicin or formalin into a hindpaw. The capsaicin injection (5 μg) resulted in licking and shaking the injected paw in both genotypes. Whereas, the licking behavior was not statistically different between groups ($p = 0.104$), the number of paw shakes was significantly reduced in $Npr2^{fl/fl};Wnt1^{Cre}$ mice compared to control mice in the test group (**Figure 4E**). Injection of 0.5% formalin into a hindpaw resulted in the typical biphasic paw licking. In the first phase (1–10 min), which results from acute activation of nociceptors, the licking behavior of $Npr2^{fl/fl};Wnt1^{Cre}$ and control littermates was comparable (**Figure 4F**). However, the formalin-induced paw licking behavior was significantly reduced in $Npr2^{fl/fl};Wnt1^{Cre}$ mice in the second phase (11–60 min), which involves a combination of ongoing afferent firing and central sensitization (Shields et al., 2010). These data indicate that nociception induced by the chemical irritants capsaicin or formalin are impaired by the loss of axonal bifurcation. Consistent with these results are our previously published electrophysiological recordings on global *Npr2* and *CNP* knockouts which revealed a reduced number of neurons in the dorsal spinal cord responding to capsaicin (Schmidt et al., 2007, 2009).

Npr2 Expression in DRGs Declines Postnatally

In addition to its role in sensory axon bifurcation Npr2 could potentially have an acute function in the processing of sensory information for example in noxious heat perception or nociception induced by chemical irritants. Furthermore, the second messenger cGMP and cGKI contribute to the processing of inflammatory and neuropathic pain in the spinal cord (Tegeder et al., 2004; Schmidtko et al., 2008, 2009; Luo et al., 2012). To further explore whether the measured deficits in pain behaviors in *Npr2* mutants are caused by the absence of sensory axon bifurcation or by changes in primary acute pain perception, we studied the developmental expression profile of Npr2 in DRGs by histochemical determination of β-galactosidase activity in cryostat sections from the $Npr2^{wt/lacZ}$ reporter mouse and by Western blot analysis of tissue extracts of DRGs (Ter-Avetisyan et al., 2014). Consistent with our previous *in situ* hybridization data we observed that all DRG neurons strongly express Npr2 at early embryonic stages when sensory axons enter the spinal cord (**Figures 5A**, **C–E**). At postnatal stages, however, the level and the number of Npr2 expressing cells gradually decreases in DRGs and at post-natal day 75 only 10% were positive for Npr2. Similar results were obtained by analyzing red fluorescent protein expression in DRGs at P75 which was induced by crossing the *Rosa26-tdTomato* reporter mouse line with *Npr2-CreERT2* and tamoxifen application at 3 consecutive days (P71, P72, and P73) (data not shown). Further analysis revealed that Npr2 is not confined to a specific subset of DRG neurons. It is expressed in a small group of trkA-, parvalbumin-, CGRP-, or IB4-expressing DRG neurons. The percentage of Npr2-positive cells in these subpopulations - except for parvalbumin - decreased during maturation (**Figures 5F–I**).

Cutaneous C-Fiber Thermal and Mechanical Sensitivity Is Normal in Npr2 Mutants

Co-stainings indicated that a small percentage of Npr2-positive DRG neurons at P75 express parvalbumin or trkA; therefore, it is possible that changes in peripheral nociceptor function may underlie altered heat sensitivity in $Npr2^{fl/fl};Wnt1^{Cre}$ mice. To test this, extracellular recordings from single C-fiber units in the hindpaw skin were performed using the *ex vivo* skin nerve preparation. C-fiber responses to heat, cold and mechanical stimulation of receptive fields were characterized in a total of 24 thermal-responsive C-fibers in $Npr2^{fl/fl};Wnt1^{Cre}$ mice, and 33 units in littermate control mice (**Table S1**). Example heat-evoked firing activity of single C-fibers in $Npr2^{fl/fl};Wnt1^{Cre}$ mice and littermate controls are shown in **Figure 6A**.

C-fiber heat thresholds, defined as the temperature required to evoke the first action potential, did not differ between $Npr2^{fl/fl};Wnt1^{Cre}$ mice and littermate controls (**Figure 6B**). Similarly, there was no significant difference in the number of action potentials in C-fibers during heat stimulation between $Npr2^{fl/fl};Wnt1^{Cre}$ mice and littermate controls in response to suprathreshold heat stimulation (**Figure 6C**, exemplified in **Figure 6A**). Cold thresholds of C-fibers were also not different between $Npr2^{fl/fl};Wnt1^{Cre}$ mice and littermate controls (**Figure 6D**). Mechanical thresholds and suprathreshold mechanical stimulus-evoked firing activity of C-fibers also did not differ between $Npr2^{fl/fl};Wnt1^{Cre}$ mice and littermate controls (**Figures 6E,F**). Example mechanical-evoked firing activity of a C-fibers recorded from a $Npr2^{fl/fl};Wnt1^{Cre}$ mouse is shown in **Figure 6G**. These data indicate that thermal and mechanical coding properties of cutaneous C-fibers are not functionally impaired in *Npr2* mutant mice.

Conditional Inactivation of cGKI Abolishes Sensory Axon Bifurcation and Partially Mimics the Phenotype of *Npr2* Mutants in Pain-Related Behavior

cGKI is an essential signaling component downstream of Npr2 to induce sensory axon bifurcation as shown previously (Schmidt et al., 2002, 2007; Zhao et al., 2009). However, the developmental expression profile of cGKI is distinct from Npr2. At early embryonic stages when sensory axons are bifurcating in the spinal cord a complete overlap between Npr2 and cGKIα in all sensory neurons was observed (**Figures 5B,D,E**). In contrast to Npr2, cGKIα remains expressed in all sensory neurons also at mature stages suggesting that its function might be regulated by other cGMP synthesizing enzymes than by Npr2 in adult mice.

The absence of cGKI in a constitutive knockout does not interfere with bone growth but shows deficits in the regulation of smooth muscle contraction with vascular and intestinal dysfunctions which cause pre-mature death (Hofmann et al., 2006). Behavioral testing therefore also required conditional

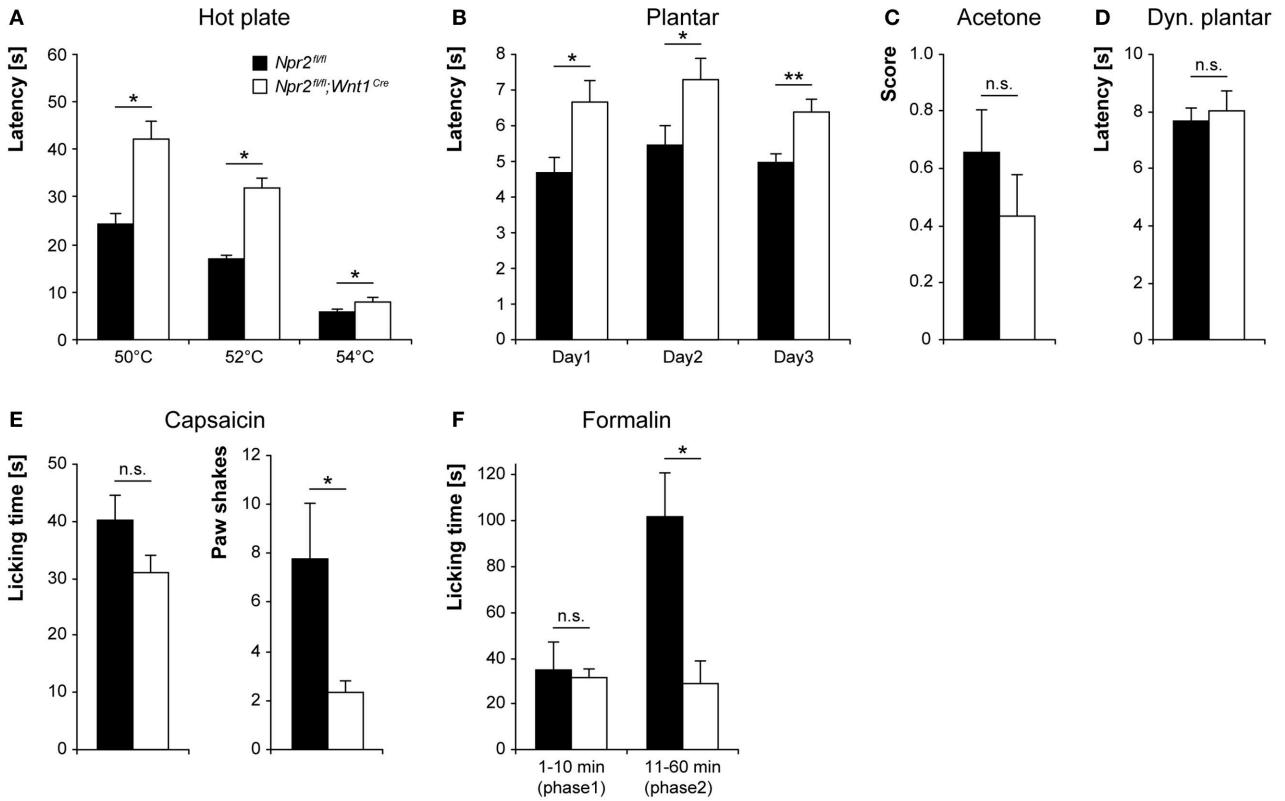

FIGURE 4 | Pain behavior in $Npr2^{fl/fl};Wnt1^{Cre}$ and littermate control mice. **(A)** Thermal heat pain was assessed on a 50, 52, and 54°C hot plate ($n = 15$–16; $^*p < 0.05$; power 97, 99, and 53% for 50, 52, and 54°C, respectively). **(B)** Thermosensation by the Hargreaves method (Plantar test) performed at 3 consecutive days ($n = 8$; $^*p < 0.05$ and $^{**}p < 0.01$; power 70, 56, and 85% for day 1, 2, and 3, respectively). **(C)** Cold pain was investigated using acetone-evoked evaporative cooling ($n =$ 15–16, power 17%). **(D)** Mechanical sensitivity was measured using a dynamic plantar test ($n = 11$, power 11%). **(E,F)** The nocifensive response to chemical pain stimuli was determined by injection of 5 μg capsaicin ($n = 9$, power 36 and 55% for licking and paw shakes, respectively) or 0.5% formalin ($n = 5$, power 5 and 84% for phase 1 and 2, respectively) into a hindpaw. $^*p < 0.05$.

inactivation of cGKI in DRG neurons, which was obtained by a floxed allele of the *cGKI* gene (Wegener et al., 2002) and using *Wnt1-Cre* as described for *Npr2*. This resulted in a complete loss of cGKI protein in DRGs as indicated by Western blotting using antibodies to cGKI (**Figure 7A**). Consequently, sensory axons failed to form bifurcational branches at the DREZ (**Figures 7B,C**). In contrast to conditional Npr2 mutants, no decrease in the survival rate or any problems on the health status of 23 inspected $cGKI^{KO/fl};Wnt1^{Cre}$ animals in which cGKI was conditionally inactivated was observed. In some tissues Npr2-induced cGMP signals are mediated by the cGKII instead of cGKI which might explain these phenotypic differences on the survival rate between cGKI and Npr2.

To estimate whether the observed Npr2-dependent changes in pain processing are mediated by a Npr2/cGMP/cGKI signaling pathway, we analyzed the nociceptive behavior of $cGKI^{KO/fl};Wnt1^{Cre}$ and littermate control mice ($cGKI^{KO/fl}$). In the hot plate test, $cGKI^{KO/fl};Wnt1^{Cre}$ mice demonstrated reduced noxious heat sensation (**Figure 8A**), albeit with significant differences compared to control mice only at 50 and 54°C. In the acetone test (**Figure 8B**) and dynamic plantar test (**Figure 8C**), the responses to cold and mechanical stimuli were normal in $cGKI^{KO/fl};Wnt1^{Cre}$ mice. After capsaicin injection into a hindpaw, the paw licking behavior of $cGKI^{KO/fl};Wnt1^{Cre}$ mice was reduced as compared to $cGKI^{KO/fl}$ control mice (**Figure 8D**). Altogether, both $Npr2^{fl/fl};Wnt1^{Cre}$ and $cGKI^{KO/fl};Wnt1^{Cre}$ mice demonstrated impaired responses to noxious heat and chemical stimuli but normal responses to cold and mechanical stimuli, suggesting that the loss of bifurcation causes specific deficits in nociceptive processing.

DISCUSSION

Previous studies using knockout mice and axon tracing methods have implicated a cGMP signaling cascade composed of the ligand CNP, the receptor guanylyl cyclase Npr2 and the cGMP-dependent kinase I in bifurcation of DRG and cranial sensory ganglia (Schmidt and Rathjen, 2010; Gibson and Ma, 2011; Ter-Avetisyan et al., 2014). Since constitutive knockouts of *Npr2* and *cGKI* are not suitable for further anatomical and behavioral studies on the consequences of the primary defect, the branching error at the DREZ, we generated mouse models

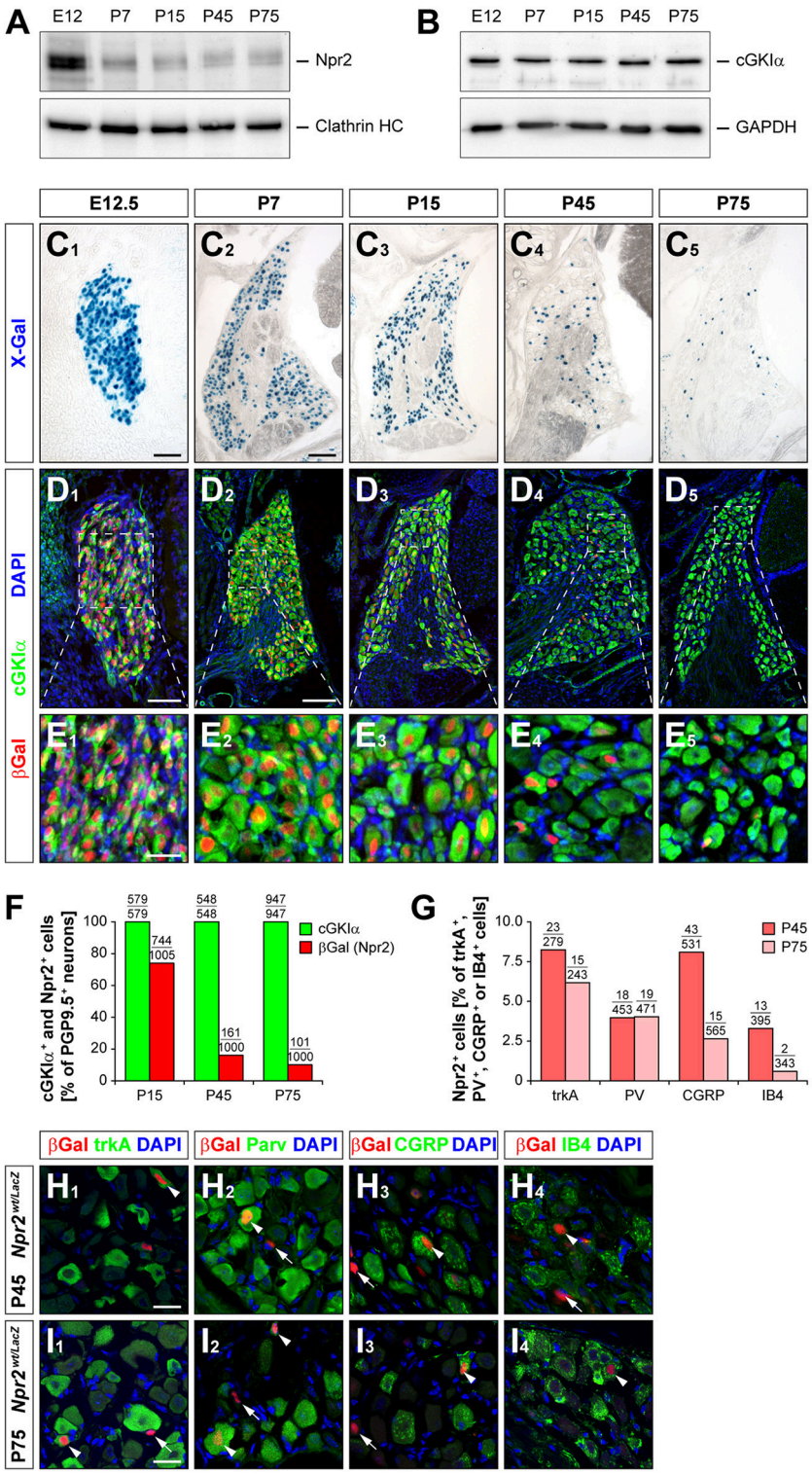

FIGURE 5 | Expression of Npr2 and cGKIα in DRGs at different developmental stages. **(A,B)** Western blot of membrane or cytosolic fractions of DRGs using antibodies to Npr2 or to cGKIα, respectively. The heavy chain of clathrin or GAPDH served as loading control. **(C–E)** Sections through thoracic DRGs at different stages. Localization of anti-βGal staining indicating Npr2-expression is demonstrated in the *Npr2*$^{wt/LacZ}$-mouse reporter and localization of cGKIα by a polyclonal antibody to mouse cGKIα. Scale bars in **(C_1,D_1)**, 50 μm; in **(C_2-C_5,D_2-D_5)**, 100 μm; in **(E)** 25 μm. **(F)** Quantification of Npr2-positive and cGKIα-positive neurons in DRGs counterstained with an antibody to PGP9.5 at different stages. **(G–I)** A small proportion of Npr2-positive DRG neurons at P45 and P75 express trkA, parvalbumin, CGRP or IB4. Scale bars in **(H,I)**, 20 μm.

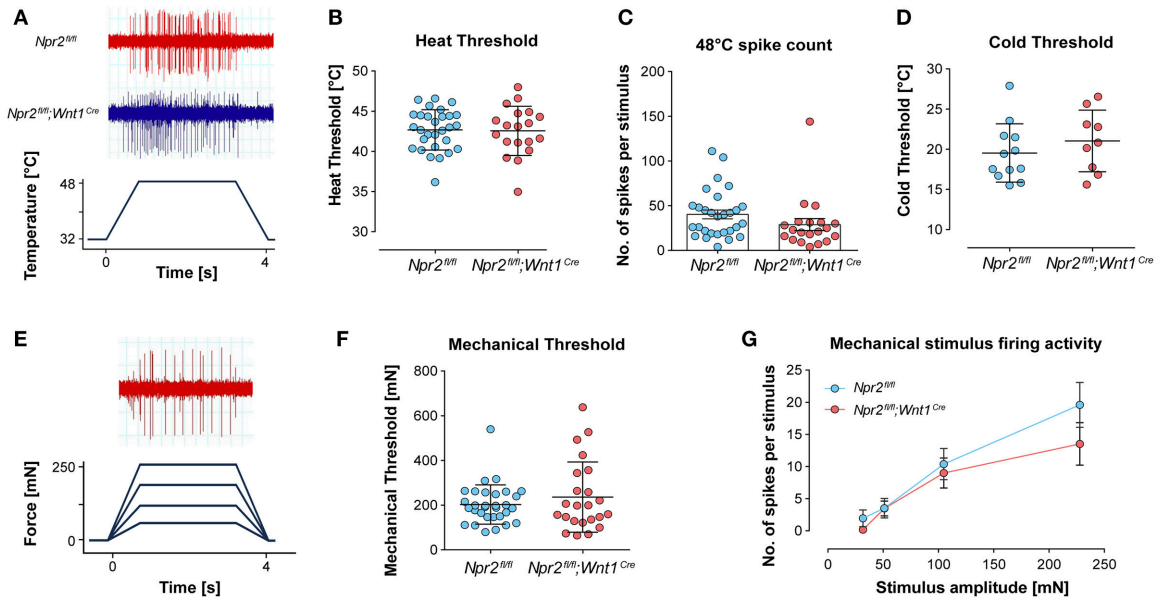

FIGURE 6 | Responses of cutaneous hindpaw C-fibers to mechanical and thermal stimuli. Hindpaw cutaneous C-fibers with receptive fields on hairy foot skin were recorded from *Npr2*$^{fl/fl}$;*Wnt1*^{Cre} mice and littermate controls using the *ex vivo* skin nerve preparation. **(A)** Example traces of C-fiber firing activity recorded from *Npr2*$^{fl/fl}$;*Wnt1*^{Cre} mice and littermate controls in response to heat stimulation. **(B)** Heat thresholds of C-fibers were investigated using a 32–48°C 15 s heat ramp protocol. **(C)** The total number of spikes were quantified over the 4 s heat stimulus shown in **(A)**. **(D)** Cold thresholds were investigated using a 32–12°C 15 s heat ramp protocol. **(E)** The total numbers of spikes were quantified over the 4 s heat stimulus shown in **(A)**. **(F)** Mechanical thresholds of C-fibers. **(G)** Mechanical stimulus-evoked firing activity of C-fibers was quantified in response to four ramp and hold stimuli and compared between groups (see also **Table S1**).

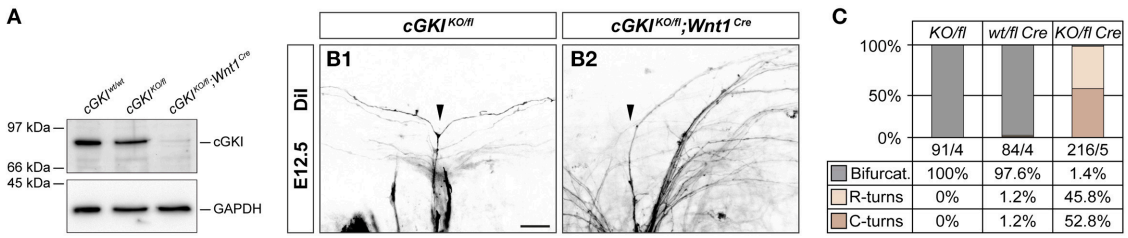

FIGURE 7 | Conditional inactivation of *cGKI*. **(A)** Conditional inactivation by Wnt1-Cre results in the complete absence of cGKI protein in embryonic DRGs as revealed by Western blot detection of cGKI in cytosolic fractions of E13.5 DRG from *cGKI*$^{wt/wt}$, *cGKI*$^{KO/fl}$, and *cGKI*$^{KO/fl}$;*Wnt1*^{Cre} mice. Equal loading was demonstrated by reprobing of the blot with an antibody to GAPDH. **(B,C)** Complete absence of sensory axon bifurcation in *cGKI*$^{KO/fl}$;*Wnt1*^{Cre} and quantification. The numbers of counted axons and embryos are indicated below the columns. Scale bar, 25 μm.

that allowed an inactivation of Npr2 or cGKI specifically in embryonic DRGs at very early developmental stages before sensory axons enter the spinal cord. The *Wnt1-Cre* line was suitable to completely inactivate Npr2 or cGKI resulting in a complete lack of bifurcation for all DRG axons as previously described for the constitutive knockouts. Other Cre lines such as *trkA-Cre* or *trkC-Cre* did not induce bifurcation errors most likely by mediating recombination at relatively late stages of development and therefore cannot be used to assess a role of axonal bifurcation. The conditional inactivation of Npr2 by *Wnt1-Cre* allowed us to study the behavioral consequences and additional anatomical changes in the termination fields in the spinal cord caused by the disturbed axon bifurcation at the DREZ.

Due to the lack of axon bifurcation a reduction in the number of collaterals originating from primary afferents of DRG neurons within the spinal cord is not unexpected. However, the observed reduction to 64% of control values and not to 50% when total voxels numbers were summed up points to compensatory mechanisms such as an increase in the density of collaterals on stem axons, increased terminal branching of collaterals in spinal target areas or increased cell number in DRGs. The latter can be excluded since numbers were unchanged in the absence of cGMP signaling (Schmidt et al., 2002). Topographic representation of the sensory periphery within the spinal cord is of fundamental importance for information processing (Brown et al., 1991; Florence et al., 1991; Levinsson et al., 2002; Schouenborg, 2004; Granmo et al., 2008). Our work

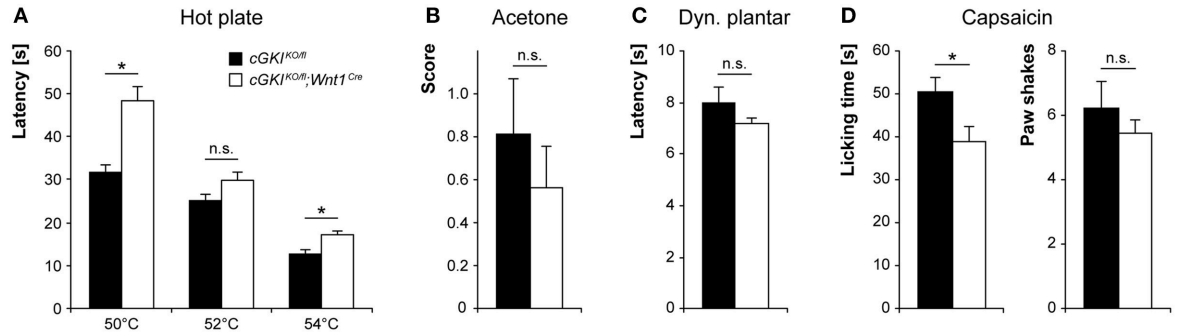

FIGURE 8 | Pain behavior in $cGKI^{KO/fl};Wnt1^{Cre}$ and littermate control mice. **(A)** Thermal heat pain was assessed on a 50, 52, and 54°C hot plate ($n = 16$; $^*p < 0.05$; power 99, 47, and 90% for 50, 52, and 54°C, respectively). **(B)** Cold pain was investigated using acetone-evoked evaporative cooling ($n = 16$, power 11%). **(C)** Mechanical sensitivity was measured using a dynamic plantar test ($n = 12$, power 20%). **(D)** The nocifensive response to a chemical pain stimulus was determined by injection of 5 μg capsaicin ($n = 9$, power 61% for licking and 12% for paw shakes) into a hindpaw. $^*p < 0.05$.

reported here showed that not only a quantitative reduction of incoming fibers but also a change in the pattern in the termination fields was detected in the absence of bifurcation. Npr2-deficiency caused an increase of the dorsoventral span to 131% of the termination field of digit two of the hindpaw whereas the mediolateral extension was narrowed by 25%. In principle pre- and postsynaptic mechanisms contribute to the formation of terminal fields. In the *Npr2* mutants the balance between these interacting structures is disordered in the spinal cord. Our observations suggest that the incoming sensory axons and most likely less the postsynaptic neurons within the spinal cord might be the causative determinants on the development of these modified fields. Less sensory collaterals compete for postsynaptic neurons which might result in an increase of terminal branching in dorsoventral direction. In other words, in *Npr2* mutants collaterals project not just to the normal zone of responding postsynaptic cells. The opposite is found for the mediolateral extension and no change was observed for the rostrocaudal span. The latter was expected since the longitudinal growth of the stem axons was not diminished in the absence of cGMP signaling (Schmidt et al., 2002).

In behavioral assays responses to noxious heat and chemical stimuli were impaired by the loss of axonal bifurcation either by the absence of Npr2 or cGKI which is in line with our previously published patch clamp recordings in Npr2- or CNP-deficient slices of the dorsal horn of the spinal cord. A reduced number of responding cells upon capsaicin treatment was measured in both mutants in comparison to wild type tissue, whereas synaptic transmission *per se* was not affected (Schmidt et al., 2007, 2009). In addition, in a recent study using global *Npr2* mutants - in which, however, bone growth is disturbed - deficits in the auditory system have been described (Lu et al., 2014). Although the downstream effector cGKI shows a widespread pattern of localization in DRGs that is distinct from the more restricted expression of Npr2 in mature stages, similar - however not fully identical - deficits in nociception were observed in the behavioral tests upon the conditional ablation of cGKI. Its widespread localization in mature DRG neurons, its multiple phosphorylation targets (Hofmann and Wegener, 2013) and its involvement in synaptic potentiation in spinal neurons (Luo et al., 2012) might contribute to the differences in the licking time vs. paw shakes that were observed upon capsaicin treatment in *Npr2* and *cGKI* conditional mutants. Our interpretation that the deficits in noxious heat perception in *Npr2* and *cGKI* mutated mice were caused by the absence of axon bifurcation are in line with studies on a mouse mutant in which cGKI was inactivated by a Cre recombinase under control of the $Na_v1.8$ promoter (*SNS-Cre*). These mice do not show axon bifurcation defects at the DREZ due to the expression of the Cre recombinase after the ingrowth of sensory axons. They responded normally to noxious heat as measured by paw withdrawal to radiant heat (Hargreaves method) (Luo et al., 2012). In contrast to nociception, balance and motor performance appear normal in the conditional absence of Npr2-mediated bifurcation suggesting that pain processing might be more sensitive to a lack of bifurcation than proprioception. Moreover, nociceptors and other chemoreceptors have small-diameter axons which are either unmyelinated or thinly myelinated and therefore conduct action potentials more slowly. In contrast, proprioception, which is mediated by myelinated axons with a large diameter, might be more flexible due to fast conductance of action potentials and might therefore adjust more rapidly. It is also conceivable that elaborate compensatory mechanisms are implemented in the proprioceptive system to reorganize neuronal circuits in the absence of bifurcation. These compensational mechanisms might be less active in the nociceptive system.

It also cannot be excluded that the significant differences observed between nociception and proprioception in the absence of bifurcation might be related to the experimental systems that were applied. Pain was always analyzed by paw withdrawal reactions and a time delay in responses was measured (Weng and Schouenborg, 1998). In such a system pain perception needs to be transferred to muscle activity and this might require axon bifurcation at the DREZ to be well-coordinated and effectively executed. Further tactile feedback might be important for the nociceptive withdrawal reflex system. In

addition accurate pain signaling might involve the integration of sensory information from several afferent subtypes and might require a complex crosstalk between spinal interneurons which might not be fully developed in the absence of axon bifurcation.

An acute or a morphological role of Npr2 on interneurons in the spinal cord or in the brain which might contribute to the measured behavioral deficits cannot currently be fully excluded. However, we never observed any changes in the arrangement of specific cell layers in the spinal cord, in the overall growth of proprioceptive collaterals or any synaptic deficits in the absence of Npr2 or CNP (Schmidt et al., 2007, 2009). Bifurcation errors of sensory axons were the only changes in the absence of the CNP/Npr2/cGKI signaling cascade we observed in the nervous system so far. Our electrophysiological recordings on the C-fibers in the nerve-skin preparation make it unlikely that Npr2 has an acute function in the conduction of sensory information. Nevertheless, a detailed pattern of expression of Npr2 in the developing and mature brain and spinal cord remains to be established including investigations on a co-localization with cGKI and Wnt1-Cre recombinase. In the future selective inactivation of Npr2 in spinal interneurons but not in DRG neurons might further substantiate or relativize our interpretations on the deficits caused by axonal bifurcation.

In humans, loss-of-function mutations in the *NPR2* gene cause a skeletal dysplasia, termed acromesomelic dysplasia type Maroteaux (AMDM) with an extremely short and disproportionate stature (Bartels et al., 2004). AMDM is a rare autosomal-recessive genetic disorder with a prevalence of one out of 1,000,000. Point mutations leading to single amino acid exchanges were found throughout the NPR2 protein including the ligand binding, kinase homology or guanylyl cyclase domain (for a synopsis of human *NPR2* mutations see Vasques et al., 2014). A number of these *NPR2*-missense mutations resulted in retention of the protein in the endoplasmic reticulum and poor targeting of the protein to the plasma membrane (Hume et al., 2009; Vasques et al., 2013; Amano et al., 2014; Wang et al., 2016) while others reached the cell surface (Dickey et al., 2016). Radiographic images demonstrated abnormal growth plates and short bones in the limbs detectable by two years of age. Carrier parents of individuals with AMDM and heterozygous mutations in *NPR2* are associated with a slight reduction in height in comparison to the population average (Olney et al., 2006; Vasques et al., 2013; Hisado-Oliva et al., 2015) which was also found for mice heterozygous for *Npr2* (Tamura et al., 2004). Heterozygosity in *Npr2* or *cGKI* does not affect axonal bifurcation in mice (Schmidt et al., 2007). In contrast, *NPR2* gain-of-function mutations result in an overgrowth syndrome (Miura et al., 2014). Currently, it can only be hypothesized whether the absence of the Npr2-mediated cGMP signaling axis in DRG neurons causes branching errors of sensory axons within the spinal cord in these patients. In addition, detailed neurological tests which might reveal neurological deficits have not been performed in AMDM patients so far. However, studies on mutations in rodents on axonal guidance factors have established a good correlation between animal models and human diseases (Jen et al., 2004; Engle, 2010; Srour et al., 2010; Depienne et al., 2011; Nugent et al., 2012; Chedotal, 2014). Our data using mouse genetics indicated deficits in noxious heat perception and nociception induced by the chemical irritants capsaicin or formalin. These observations might provide a framework for future studies to characterize neurological qualities of human patients with mutations in the *NPR2* gene.

AUTHOR CONTRIBUTIONS

PT, JH, JP, OD, FS, GT-A, SP, SF, FR, and HS performed experiments. Conception, drafting, approval, and agreement to be accountable for all aspects of the work in ensuring that questions related to the accuracy or integrity of any part of the work are appropriately investigated and resolved: PT, JH, JP, OD, AS, FS, GL, GT-A, YW, SP, SF, RF, FR, and HS.

FUNDING

This work was supported by the MDC and DFG grants SFB 665 (grant B2 and B6 to FR and GL, respectively) and FOR 2060 (FE 438/5-1 and FE 438/6-1 to RF, and SCHM 2371/1 to HS, and SCHM 2629/3-1 to AS).

ACKNOWLEDGMENTS

The technical help of Madlen Driesner, Mechthild Henning, and Karola Bach is greatly acknowledged. We thank Melissa Long from the Animal Outcome Core Facility (Charité Universitätsmedizin Berlin) for her dedicated support. We thank Dr. Christina Eichhorn (MDC) for help on statistical evaluations of data, Dr. César S. Mendes (Universida de Nova, Lisboa) for discussions on the MouseWalker and Drs. Carmen Birchmeier (MDC, Berlin) and Marina Gültig (University of Tübingen) for mice.

SUPPLEMENTARY MATERIAL

The Supplementary Material for this article can be found online at: https://www.frontiersin.org/articles/10.3389/fnmol.2018.00019/full#supplementary-material

Figure S1 | Severe malocclusions of P22 $Npr2^{fl/fl};Wnt1^{Cre}$ mice which prevents normal nutrition and correlated with premature death. Such animals have been excluded from behavioral testing.

Figure S2 | No bifurcation errors of DRG axons were observed when the *Npr2-flox* line was crossbred with *trkA-Cre* or *trkC-Cre*. **(A)** Example of a DiI-labeled axon from E12.5 $Npr2^{fl/fl};trkA^{Cre}$. Scale bar, 50 μm. **(B)** Quantification of bifurcation behavior of DRG axons in $Npr2^{fl/fl}$ and $Npr2^{fl/fl};trkA^{Cre}$ embryos at E12.5. Numbers below the columns indicate counted axons and embryos. **(C)** Dorsolateral view of DRG axons at the dorsal root entry zone of a $Npr2^{fl/fl};trkC^{Cre};Thy1^{YFP-H}$ mouse at P21. Bar, 100 μm.

Table S1 | C-fiber *ex vivo* skin nerve preparation recorded from the hindpaw hairy skin. C-mechanoheat (CMH), C-mechanoheatcold (CMHC), and C-mechanocold (CMC) fibers were recorded from $Npr2^{fl/fl};Wnt1^{Cre}$ mice and littermate controls. Mean CVs are shown ± SEM.

REFERENCES

Amano, N., Mukai, T., Ito, Y., Narumi, S., Tanaka, T., Yokoya, S., et al. (2014). Identification and functional characterization of two novel NPR2 mutations in Japanese patients with short stature. *J. Clin. Endocrinol. Metab.* 99, E713–E718. doi: 10.1210/jc.2013-3525

Aoyagi, Y., Kawakami, R., Osanai, H., Hibi, T., and Nemoto, T. (2015). A rapid optical clearing protocol using 2,2'-thiodiethanol for microscopic observation of fixed mouse brain. *PLoS ONE* 10:e0116280. doi: 10.1371/journal.pone.0116280

Bartels, C. F., Bükülmez, H., Padayatti, P., Rhee, D. K., van Ravenswaaij-Arts, C., Pauli, R. M., et al. (2004). Mutations in the transmembrane natriuretic peptide receptor NPR-B impair skeletal growth and cause acromesomelic dysplasia, type Maroteaux. *Am. J. Hum. Genet.* 75, 27–34. doi: 10.1086/422013

Braz, J. M., and Basbaum, A. I. (2010). Differential ATF3 expression in dorsal root ganglion neurons reveals the profile of primary afferents engaged by diverse noxious chemical stimuli. *Pain* 150, 290–301. doi: 10.1016/j.pain.2010.05.005

Brown, A. G. (1981). *Organization in the Spinal Cord*. Berlin; Heidelberg; New York, NY: Springer.

Brown, P. B., Gladfelter, W. E., Culberson, J. C., Covalt-Dunning, D., Sonty, R. V., Pubols, L. M., et al. (1991). Somatotopic organization of single primary afferent axon projections to cat spinal cord dorsal horn. *J. Neurosci.* 11, 298–309.

Carter, R. J., Morton, J., and Dunnett, S. B. (2001). Motor coordination and balance in rodents. *Curr. Protoc. Neurosci.* Chapter 8:Unit. doi: 10.1002/0471142301.ns0812s15

Caspani, O., Zurborg, S., Labuz, D., and Heppenstall, P. A. (2009). The contribution of TRPM8 and TRPA1 channels to cold allodynia and neuropathic pain. *PLoS ONE* 4:e7383. doi: 10.1371/journal.pone.0007383

Chedotal, A. (2014). Development and plasticity of commissural circuits: from locomotion to brain repair. *Trends Neurosci.* 37, 551–562. doi: 10.1016/j.tins.2014.08.009

Chusho, H., Tamura, N., Ogawa, Y., Yasoda, A., Suda, M., Miyazawa, T., et al. (2001). Dwarfism and early death in mice lacking C-type natriuretic peptide. *Proc. Natl. Acad. Sci. U.S.A.* 98, 4016–4021. doi: 10.1073/pnas.071389098

Conte, W. L., Kamishina, H., and Reep, R. L. (2009). Multiple neuroanatomical tract-tracing using fluorescent Alexa Fluor conjugates of cholera toxin subunit B in rats. *Nat. Protoc.* 4, 1157–1166. doi: 10.1038/nprot.2009.93

Costantini, I., Ghobril, J. P., Di Giovanna, A. P., Allegra Mascaro, A. L., Silvestri, L., Mullenbroich, M. C., et al. (2015). A versatile clearing agent for multi-modal brain imaging. *Sci. Rep.* 5:9808. doi: 10.1038/srep09808

Danielian, P. S., Muccino, D., Rowitch, D. H., Michael, S. K., and McMahon, A. P. (1998). Modification of gene activity in mouse embryos *in utero* by a tamoxifen-inducible form of Cre recombinase. *Curr. Biol.* 8, 1323–1326. doi: 10.1016/S0960-9822(07)00562-3

Depienne, C., Cincotta, M., Billot, S., Bouteiller, D., Groppa, S., Brochard, V., et al. (2011). A novel DCC mutation and genetic heterogeneity in congenital mirror movements. *Neurology* 76, 260–264. doi: 10.1212/WNL.0b013e318207b1e0

Dickey, D. M., Edmund, A. B., Otto, N. M., Chaffee, T. S., Robinson, J. W., and Potter, L. R. (2016). Catalytically active guanylyl cyclase b requires endoplasmic reticulum-mediated glycosylation, and mutations that inhibit this process cause dwarfism. *J. Biol. Chem.* 291, 11385–11393. doi: 10.1074/jbc.M115.704015

Echelard, Y., Vassileva, G., and McMahon, A. P. (1994). Cis-acting regulatory sequences governing Wnt-1 expression in the developing mouse CNS. *Development* 120, 2213–2224.

Engle, E. C. (2010). Human genetic disorders of axon guidance. *Cold Spring Harb. Perspect. Biol.* 2:a001784. doi: 10.1101/cshperspect.a001784

Farley, F. W., Soriano, P., Steffen, L. S., and Dymecki, S. M. (2000). Widespread recombinase expression using FLPeR (flipper) mice. *Genesis* 28, 106–110. doi: 10.1002/1526-968X(200011/12)28:3/4<106::AID-GENE30>3.0.CO;2-T

Feng, G., Mellor, R. H., Bernstein, M., Keller-Peck, C., Nguyen, Q. T., Wallace, M., et al. (2000). Imaging neuronal subsets in transgenic mice expressing multiple spectral variants of GFP. *Neuron* 28, 41–51. doi: 10.1016/S0896-6273(00)00084-2

Florence, S. L., Wall, J. T., and Kaas, J. H. (1991). Central projections from the skin of the hand in squirrel monkeys. *J. Comp. Neurol.* 311, 563–578. doi: 10.1002/cne.903110410

Funfschilling, U., Ng, Y. G., Zang, K., Miyazaki, J., Reichardt, L. F., and Rice, F. L. (2004). TrkC kinase expression in distinct subsets of cutaneous trigeminal innervation and nonneuronal cells. *J. Comp. Neurol.* 480, 392–414. doi: 10.1002/cne.20359

Gibson, D. A., and Ma, L. (2011). Developmental regulation of axon branching in the vertebrate nervous system. *Development* 138, 183–195. doi: 10.1242/dev.046441

Granmo, M., Petersson, P., and Schouenborg, J. (2008). Action-based body maps in the spinal cord emerge from a transitory floating organization. *J. Neurosci.* 28, 5494–5503. doi: 10.1523/JNEUROSCI.0651-08.2008

Hargreaves, K., Dubner, R., Brown, F., Flores, C., and Joris, J. (1988). A new and sensitive method for measuring thermal nociception in cutaneous hyperalgesia. *Pain* 32, 77–88.

Hisado-Oliva, A., Garre-Vazquez, A. I., Santaolalla-Caballero, F., Belinchon, A., Barreda-Bonis, A. C., Vasques, G. A., et al. (2015). Heterozygous NPR2 mutations cause disproportionate short stature, similar to leri-weill dyschondrosteosis. *J. Clin. Endocrinol. Metab.* 100, E1133–E1142. doi: 10.1210/jc.2015-1612

Hofmann, F., and Wegener, J. W. (2013). cGMP-dependent protein kinases (cGK). *Methods Mol. Biol.* 1020, 17–50. doi: 10.1007/978-1-62703-459-3_2

Hofmann, F., Feil, R., Kleppisch, T., and Schlossmann, J. (2006). Function of cGMP-dependent protein kinases as revealed by gene deletion. *Physiol. Rev.* 86, 1–23. doi: 10.1152/physrev.00015.2005

Hume, A. N., Buttgereit, J., Al-Awadhi, A. M., Al-Suwaidi, S. S., John, A., Bader, M., et al. (2009). Defective cellular trafficking of missense NPR-B mutants is the major mechanism underlying acromesomelic dysplasia-type Maroteaux. *Hum. Mol. Genet.* 18, 267–277. doi: 10.1093/hmg/ddn354

Jen, J. C., Chan, W. M., Bosley, T. M., Wan, J., Carr, J. R., Rüb, U., et al. (2004). Mutations in a human ROBO gene disrupt hindbrain axon pathway crossing and morphogenesis. *Science* 304, 1509–1513. doi: 10.1126/science.1096437

Kloepper, J. E., Biro, T., Paus, R., and Cseresnyes, Z. (2010). Point scanning confocal microscopy facilitates 3D human hair follicle imaging in tissue sections. *Exp. Dermatol.* 19, 691–694. doi: 10.1111/j.1600-0625.2010.01110.x

Kobbert, C., Apps, R., Bechmann, I., Lanciego, J. L., Mey, J., and Thanos, S. (2000). Current concepts in neuroanatomical tracing. *Prog. Neurobiol.* 62, 327–351. doi: 10.1016/S0301-0082(00)00019-8

Kuhn, M. (2016). Molecular physiology of membrane guanylyl cyclase receptors. *Physiol. Rev.* 96, 751–804. doi: 10.1152/physrev.00022.2015

Levinsson, A., Holmberg, H., Broman, J., Zhang, M., and Schouenborg, J. (2002). Spinal sensorimotor transformation: relation between cutaneous somatotopy and a reflex network. *J. Neurosci.* 22, 8170–8182.

Lu, C. C., Cao, X. J., Wright, S., Ma, L., Oertel, D., and Goodrich, L. V. (2014). Mutation of Npr2 leads to blurred tonotopic organization of central auditory circuits in mice. *PLoS Genet.* 10:e1004823. doi: 10.1371/journal.pgen.1004823

Lu, R., Bausch, A. E., Kallenborn-Gerhardt, W., Stoetzer, C., Debruin, N., Ruth, P., et al. (2015). Slack channels expressed in sensory neurons control neuropathic pain in mice. *J. Neurosci.* 35, 1125–1135. doi: 10.1523/JNEUROSCI.2423-14.2015

Luo, C., Gangadharan, V., Bali, K. K., Xie, R. G., Agarwal, N., Kurejova, M., et al. (2012). Presynaptically localized cyclic GMP-dependent protein kinase 1 is a key determinant of spinal synaptic potentiation and pain hypersensitivity. *PLoS Biol.* 10:e1001283. doi: 10.1371/journal.pbio.1001283

Luong, T. N., Carlisle, H. J., Southwell, A., and Patterson, P. H. (2011). Assessment of motor balance and coordination in mice using the balance beam. *J. Vis. Exp.* e2376 doi: 10.3791/2376

Madisen, L., Zwingman, T. A., Sunkin, S. M., Oh, S. W., Zariwala, H. A., Gu, H., et al. (2010). A robust and high-throughput Cre reporting and characterization system for the whole mouse brain. *Nat. Neurosci.* 13, 133–140. doi: 10.1038/nn.2467

Marques, J. M., and Olsson, I. A. (2010). Performance of juvenile mice in a reach-to-grasp task. *J. Neurosci. Methods* 193, 82–85. doi: 10.1016/j.jneumeth.2010.08.016

Mendes, C. S., Bartos, I., Marka, Z., Akay, T., Marka, S., and Mann, R. S. (2015). Quantification of gait parameters in freely walking rodents. *BMC Biol.* 13:50. doi: 10.1186/s12915-015-0154-0

Milenkovic, N., Zhao, W. J., Walcher, J., Albert, T., Siemens, J., Lewin, G. R., et al. (2014). A somatosensory circuit for cooling perception in mice. *Nat. Neurosci.* 17, 1560–1566. doi: 10.1038/nn.3828

Miura, K., Kim, O. H., Lee, H. R., Namba, N., Michigami, T., Yoo, W. J., et al. (2014). Overgrowth syndrome associated with a gain-of-function mutation of

the natriuretic peptide receptor 2 (NPR2) gene. *Am. J. Med. Genet. A* 164A, 156–163. doi: 10.1002/ajmg.a.36218

Moshourab, R. A., Wetzel, C., Martinez-Salgado, C., and Lewin, G. R. (2013). Stomatin-domain protein interactions with acid-sensing ion channels modulate nociceptor mechanosensitivity. *J. Physiol.* 591, 5555–5574. doi: 10.1113/jphysiol.2013.261180

Nakao, K., Osawa, K., Yasoda, A., Yamanaka, S., Fujii, T., Kondo, E., et al. (2015). The Local CNP/GC-B system in growth plate is responsible for physiological endochondral bone growth. *Sci. Rep.* 5:10554. doi: 10.1038/srep10554

Nugent, A. A., Kolpak, A. L., and Engle, E. C. (2012). Human disorders of axon guidance. *Curr. Opin. Neurobiol.* 22, 837–843. doi: 10.1016/j.conb.2012.02.006

Ollion, J., Cochennec, J., Loll, F., Escude, C., and Boudier, T. (2013). TANGO: a generic tool for high-throughput 3D image analysis for studying nuclear organization. *Bioinformatics* 29, 1840–1841. doi: 10.1093/bioinformatics/btt276

Olney, R. C., Bukulmez, H., Bartels, C. F., Prickett, T. C., Espiner, E. A., Potter, L. R., et al. (2006). Heterozygous mutations in natriuretic peptide receptor-B (NPR2) are associated with short stature. *J. Clin. Endocrinol. Metab.* 91, 1229–1232. doi: 10.1210/jc.2005-1949

Potter, L. R. (2011). Guanylyl cyclase structure, function and regulation. *Cell. Signal.* 23, 1921–1926. doi: 10.1016/j.cellsig.2011.09.001

Preibisch, S., Saalfeld, S., and Tomancak, P. (2009). Globally optimal stitching of tiled 3D microscopic image acquisitions. *Bioinformatics* 25, 1463–1465. doi: 10.1093/bioinformatics/btp184

Quina, L. A., Tempest, L., Ng, L., Harris, J. A., Ferguson, S., Jhou, T. C., et al. (2015). Efferent pathways of the mouse lateral habenula. *J. Comp. Neurol.* 523, 32–60. doi: 10.1002/cne.23662

Robertson, B., and Arvidsson, J. (1985). Transganglionic transport of wheat germ agglutinin-HRP and choleragenoid-HRP in rat trigeminal primary sensory neurons. *Brain Res.* 348, 44–51. doi: 10.1016/0006-8993(85)90357-9

Schmidt, H., and Rathjen, F. G. (2010). Signalling mechanisms regulating axonal branching *in vivo*. *Bioessays* 32, 977–985. doi: 10.1002/bies.201000054

Schmidt, H., and Rathjen, F. G. (2011). DiI-labeling of DRG neurons to study axonal branching in a whole mount preparation of mouse embryonic spinal cord. *J. Vis. Exp.* e3667. doi: 10.3791/3667

Schmidt, H., Peters, S., Frank, K., Wen, L., Feil, R., and Rathjen, F. G. (2016). Dorsal root ganglion axon bifurcation tolerates increased cyclic GMP levels: the role of phosphodiesterase 2A and scavenger receptor Npr3. *Eur. J. Neurosci.* 44, 2991–3000. doi: 10.1111/ejn.13434

Schmidt, H., Stonkute, A., Juttner, R., Koesling, D., Friebe, A., and Rathjen, F. G. (2009). C-type natriuretic peptide (CNP) is a bifurcation factor for sensory neurons. *Proc. Natl. Acad. Sci. U.S.A.* 106, 16847–16852. doi: 10.1073/pnas.0906571106

Schmidt, H., Stonkute, A., Juttner, R., Schaffer, S., Buttgereit, J., Feil, R., et al. (2007). The receptor guanylyl cyclase Npr2 is essential for sensory axon bifurcation within the spinal cord. *J. Cell Biol.* 179, 331–340. doi: 10.1083/jcb.200707176

Schmidt, H., Werner, M., Heppenstall, P. A., Henning, M., More, M. I., Kuhbandner, S., et al. (2002). cGMP-mediated signaling via cGKIalpha is required for the guidance and connectivity of sensory axons. *J. Cell Biol.* 159, 489–498. doi: 10.1083/jcb.200207058

Schmidtko, A., Gao, W., Konig, P., Heine, S., Motterlini, R., Ruth, P., et al. (2008). cGMP produced by NO-sensitive guanylyl cyclase essentially contributes to inflammatory and neuropathic pain by using targets different from cGMP-dependent protein kinase I. *J. Neurosci.* 28, 8568–8576. doi: 10.1523/JNEUROSCI.2128-08.2008

Schmidtko, A., Tegeder, I., and Geisslinger, G. (2009). No NO, no pain? The role of nitric oxide and cGMP in spinal pain processing. *Trends Neurosci.* 32, 339–346. doi: 10.1016/j.tins.2009.01.010

Schneider, C. A., Rasband, W. S., and Eliceiri, K. W. (2012). NIH Image to ImageJ: 25 years of image analysis. *Nat. Methods* 9, 671–675. doi: 10.1038/nmeth.2089

Schouenborg, J. (2004). Learning in sensorimotor circuits. *Curr. Opin. Neurobiol.* 14, 693–697. doi: 10.1016/j.conb.2004.10.009

Shields, S. D., Cavanaugh, D. J., Lee, H., Anderson, D. J., and Basbaum, A. I. (2010). Pain behavior in the formalin test persists after ablation of the great majority of C-fiber nociceptors. *Pain* 151, 422–429. doi: 10.1016/j.pain.2010.08.001

Sogawa, C., Abe, A., Tsuji, T., Koizumi, M., Saga, T., and Kunieda, T. (2010). Gastrointestinal tract disorder in natriuretic peptide receptor B gene mutant mice. *Am. J. Pathol.* 177, 822–828. doi: 10.2353/ajpath.2010.091278

Srour, M., Riviere, J. B., Pham, J. M., Dube, M. P., Girard, S., Morin, S., et al. (2010). Mutations in DCC cause congenital mirror movements. *Science* 328:592. doi: 10.1126/science.1186463

Staudt, T., Lang, M. C., Medda, R., Engelhardt, J., and Hell, S. W. (2007). 2,2′-thiodiethanol: a new water soluble mounting medium for high resolution optical microscopy. *Microsc. Res. Technol.* 70, 1–9. doi: 10.1002/jemt.20396

Tamura, N., Doolittle, L. K., Hammer, R. E., Shelton, J. M., Richardson, J. A., and Garbers, D. L. (2004). Critical roles of the guanylyl cyclase B receptor in endochondral ossification and development of female reproductive organs. *Proc. Natl. Acad. Sci. U.S.A.* 101, 17300–17305. doi: 10.1073/pnas.0407894101

Tegeder, I., Del, T. D., Schmidtko, A., Sausbier, M., Feil, R., Hofmann, F., et al. (2004). Reduced inflammatory hyperalgesia with preservation of acute thermal nociception in mice lacking cGMP-dependent protein kinase I. *Proc. Natl. Acad. Sci. U.S A.* 101, 3253–3257. doi: 10.1073/pnas.0304076101

Ter-Avetisyan, G., Rathjen, F. G., and Schmidt, H. (2014). Bifurcation of axons from cranial sensory neurons is disabled in the absence of Npr2-induced cGMP signaling. *J. Neurosci.* 34, 737–747. doi: 10.1523/JNEUROSCI.4183-13.2014

Tsuji, T., and Kunieda, T. (2005). A loss-of-function mutation in natriuretic peptide receptor 2 (Npr2) gene is responsible for disproportionate dwarfism in cn/cn mouse. *J. Biol. Chem.* 280, 14288–14292. doi: 10.1074/jbc.C500024200

Vasques, G. A., Amano, N., Docko, A. J., Funari, M. F., Quedas, E. P., Nishi, M. Y., et al. (2013). Heterozygous mutations in natriuretic peptide receptor-B (NPR2) gene as a cause of short stature in patients initially classified as idiopathic short stature. *J. Clin. Endocrinol. Metab.* 98, E1636–E1644. doi: 10.1210/jc.2013-2142

Vasques, G. A., Arnhold, I. J., and Jorge, A. A. (2014). Role of the natriuretic peptide system in normal growth and growth disorders. *Horm. Res. Paediatr.* 82, 222–229. doi: 10.1159/000365049

Wan, X. C., Trojanowski, J. Q., and Gonatas, J. O. (1982). Cholera toxin and wheat germ agglutinin conjugates as neuroanatomical probes: their uptake and clearance, transganglionic and retrograde transport and sensitivity. *Brain Res.* 243, 215–224. doi: 10.1016/0006-8993(82)90244-X

Wang, W., Song, M. H., Miura, K., Fujiwara, M., Nawa, N., Ohata, Y., et al. (2016). Acromesomelic dysplasia, type maroteaux caused by novel loss-of-function mutations of the NPR2 gene: Three case reports. *Am. J. Med. Genet. A* 170A, 426–434. doi: 10.1002/ajmg.a.37463

Wegener, J. W., Nawrath, H., Wolfsgruber, W., Kuhbandner, S., Werner, C., Hofmann, F., et al. (2002). cGMP-dependent protein kinase I mediates the negative inotropic effect of cGMP in the murine myocardium. *Circ. Res.* 90, 18–20. doi: 10.1161/hh0102.103222

Weng, H. R., and Schouenborg, J. (1998). On the cutaneous receptors contributing to withdrawal reflex pathways in the decerebrate spinal rat. *Exp. Brain Res.* 118, 71–77. doi: 10.1007/s002210050256

Zhao, Z., and Ma, L. (2009). Regulation of axonal development by natriuretic peptide hormones. *Proc. Natl. Acad. Sci. U.S.A.* 106, 18016–18021. doi: 10.1073/pnas.0906880106

Zhao, Z., Wang, Z., Gu, Y., Feil, R., Hofmann, F., and Ma, L. (2009). Regulate axon branching by the cyclic GMP pathway via inhibition of glycogen synthase kinase 3 in dorsal root ganglion sensory neurons. *J. Neurosci.* 29, 1350–1360. doi: 10.1523/JNEUROSCI.3770-08.2009

Conflict of Interest Statement: The authors declare that the research was conducted in the absence of any commercial or financial relationships that could be construed as a potential conflict of interest.

frontiers in Molecular Neuroscience

ORIGINAL RESEARCH
published: 22 March 2018
doi: 10.3389/fnmol.2018.00085

Hypersensitivity of Prelimbic Cortex Neurons Contributes to Aggravated Nociceptive Responses in Rats With Experience of Chronic Inflammatory Pain

Xiao-Cen Fan[1], Su Fu[1], Feng-Yu Liu[1], Shuang Cui[1], Ming Yi[1] and You Wan[1,2]**

[1]*Neuroscience Research Institute and Department of Neurobiology, School of Basic Medical Sciences, Peking University, Beijing, China,* [2]*Key Laboratory for Neuroscience, Ministry of Education/National Health and Family Planning Commission, Peking University, Beijing, China*

Previous experience of chronic pain causes enhanced responses to upcoming noxious events in both humans and animals, but the underlying mechanisms remain unclear. In the present study, we found that rats with complete Freund's adjuvant (CFA)-induced chronic inflammatory pain experience exhibited aggravated pain responses to later formalin test. Enhanced neuronal activation upon formalin assaults and increased phosphorylated cAMP-response element binding protein (CREB) were observed in the prelimbic cortex (PL) of rats with chronic inflammatory pain experience, and inhibiting PL neuronal activities reversed the aggravated pain. Inflammatory pain experience induced persistent p38 mitogen-activated protein kinase (MAPK; p38) but not extracellular regulated protein kinase (ERK) or c-Jun N-terminal kinase (JNK) hyperphosphorylation in the PL. Inhibiting the p38 phosphorylation in PL reversed the aggravated nociceptive responses to formalin test and down-regulated enhanced phosphorylated CREB in the PL. Chemogenetics identified PL–periaqueductal gray (PAG) but not PL–nucleus accumbens (NAc) as a key pathway in inducing the aggravated formalin pain. Our results demonstrate that persistent hyperphosphorylation of p38 in the PL underlies aggravated nociceptive responses in rats with chronic inflammatory pain experience.

Keywords: pain, chronic pain, prelimbic cortex, prefrontal cortex, p38

OPEN ACCESS

Edited by:
Ildikó Rácz,
Universitätsklinikum Bonn, Germany

Reviewed by:
Esperanza Bas Infante,
University of Miami, United States
Sangsu Bang,
Duke University, United States

****Correspondence:***
Ming Yi
mingyi@bjmu.edu.cn
You Wan
ywan@hsc.pku.edu.cn

Received: *26 November 2017*
Accepted: *05 March 2018*
Published: *22 March 2018*

Citation:
Fan X-C, Fu S, Liu F-Y, Cui S, Yi M and Wan Y (2018) Hypersensitivity of Prelimbic Cortex Neurons Contributes to Aggravated Nociceptive Responses in Rats With Experience of Chronic Inflammatory Pain. Front. Mol. Neurosci. 11:85. doi: 10.3389/fnmol.2018.00085

INTRODUCTION

Chronic pain is one of the most prevalent clinical situations. The experience of chronic pain affects physiological states of the individual, even after the pain has perceptually recovered. A subject with chronic pain experience frequently shows enhanced responses to following noxious events, reflected in lower pain thresholds and increased pain ratings (Bachiocco et al., 1993; Lidow, 2002; Ren et al., 2004; Hermann et al., 2006; Wegner et al., 2015). In animal studies, enhanced formalin-evoked pain behaviors are also observed in adult rats with chronic inflammatory pain experience (Li et al., 2012). However, mechanisms underlying deteriorated pain responses following previous pain experience are not well illustrated.

Medial prefrontal cortex (mPFC) shows long-term morphological and functional changes in chronic pain (Apkarian et al., 2004; Metz et al., 2009; Seminowicz et al., 2009; Lim et al., 2016), which parallel long-term behavioral patterns such as anxiety, stress and depression

(Negrón-Oyarzo et al., 2014; Fitzgerald et al., 2015; Moench and Wellman, 2015; Seo et al., 2017). Even when the chronic pain has been well treated, the neuroanatomical abnormality could only be partly reversible (Seminowicz et al., 2011). Prelimbic cortex (PL) is part of the rodent mPFC and plays a critical role in perceptual and emotional aspects of chronic pain (Baliki et al., 2012; Wang et al., 2015; Wu et al., 2016). Excitability of layer 4/5 pyramidal neurons in the PL increases in complete Freund's adjuvant (CFA)-induced inflammatory mice (Wu et al., 2016), and bilateral lesions of the PL attenuate CFA-induced heat hyperalgesia (Wang et al., 2015). PL may regulate pain through its projections to a number of other brain areas (Kucyi et al., 2013; Khan et al., 2014; Yu et al., 2014; Lee et al., 2015; Vachon-Presseau et al., 2016), including amygdala, nucleus accumbens (NAc), hippocampus and in particular periaqueductal gray (PAG), a critical component of the descending pain modulatory system (Umana et al., 2017).

Several molecular signaling pathways underlie the altered neuronal activities in the PL in chronic pain. The mitogen-activated protein kinase (MAPK), including extracellular regulated protein kinase (ERK), p38 MAPK (p38) and c-Jun N-terminal kinase (JNK), is a family of serine/threonine protein kinases that transduces extracellular stimuli into intracellular post-translational and transcriptional responses (Seger and Krebs, 1995; Widmann et al., 1999; Johnson and Lapadat, 2002; Obata and Noguchi, 2004). Besides its role in chronic stress, depression and fear conditioning (Sherrin et al., 2011; Ferland et al., 2014; Pochwat et al., 2017), the MAPK also contributes to pain hypersensitivity by regulating neuronal plasticity and inflammatory responses in dorsal root ganglion (DRG), spinal cord and cerebral cortex (Impey et al., 1999; Ji and Woolf, 2001; Kumar et al., 2003; Gao and Ji, 2008; Ji et al., 2009). Chronic pain is accompanied by hyperphosphorylation of MAPKs in both peripheral and central nervous system (Zhuang et al., 2005; Crown et al., 2006, 2008; Cao et al., 2014), whereas inhibition of MAPKs impairs neuronal excitability and relieves pain (Hu and Gereau, 2003; Wynne, 2006; Toyoda et al., 2007; Zhang et al., 2007; Pucilowska et al., 2012).

Based on the findings above, we hypothesize that persistent functional alterations in the PL facilitate nociceptive responses to subsequent noxious exposure, even after the perceptual recovery of chronic pain. To test this hypothesis, we examined molecular changes of the PL in rats with experience of CFA-induced chronic inflammatory pain, and observed sustained PL hyper-reactivity which mediated the vulnerability to formalin pain test in these rats.

MATERIALS AND METHODS

Animals

Adult male Sprague-Dawley rats (230–250 g at the beginning of experiments) were provided by the Department of Laboratory Animal Sciences, Peking University Health Science Center (Beijing, China). All animals were housed in standard cages with a 12-h alternating light/dark cycle and food and water available *ad libitum*. All experimental procedures were approved by the Animal Care and Use Committee of our University, according to the guidelines of the International Association for the Study of Pain. By the end of the experiment, euthanasia was performed with 1% pentobarbital sodium (1 ml/100 g, *i.p.*).

Establishment of CFA-Induced Inflammatory Pain Model of Rats

Following our previous protocol (Yue et al., 2017; Zhang C. et al., 2017), the rat was anesthetized with isoflurane. The plantar surface of left hindpaw was cleaned by 75% ethanol before a total of 100 μL CFA was injected intraplantarly. For control, an equal volume of normal saline was injected.

Measurement of Thermal and Mechanical Pain Thresholds

The rat was handled for 10 min, and adapted in a plexiglas box for 30 min per day for three consecutive days before the first measurement. Thermal or mechanical pain thresholds were measured as previously described (Chaplan et al., 1994; Zhang et al., 2016) while the rat was calm and awake. Paw withdrawal latencies (PWLs) to thermal stimuli were measured by a focused radiant heat (40 W of power) applied to either hindpaw (Hargreaves Method, IITC 390). PWLs were recorded three times and averaged as the thermal pain threshold. A cut-off value of 30 s was set to avoid any possible tissue injuries.

Fifty percent paw withdrawal thresholds (50% PWTs) to mechanical stimuli were measured by *von* Frey hairs (0.41–15.1 g; North Coast, Gilroy, CA, USA). The *von* Frey hair was applied to the central plantar surface of either hindpaw. The 50% PWTs were calculated by the "up and down" method as described by Chaplan et al. and in our lab (Chaplan et al., 1994; Zhang et al., 2016). Thermal hyperalgesia and mechanical allodynia were measured 1 day before and 1, 3, 7, 14, 21 and 28 days after CFA injection.

Hot Plate Test

The rat was handled for 10 min and adapted in the hot plate for 10 min per day for three consecutive days before the test. Rats were placed individually onto the center of the hot plate (49°C) and the latency of the first sign of hind paw licking or jumping to avoid heating pain was recorded as an index of the nociceptive threshold (Luo et al., 2004; Yu et al., 2008). A cut-off value of 30 s was set to avoid any possible tissue injuries. The hot plate was cleaned by 75% ethanol between tests.

Open Field Test

The rat was placed in a 100 × 100 × 50 cm box exposed to 50 lux illumination, with its activities videotaped for 10 min (Zhang M. et al., 2017; Zhang Y. et al., 2017). Time spent (C.Time) and distance traveled (C.Dis) in the central area (60 × 60 cm), and

total distance traveled (T.Dis) in the field were measured using the SMART software (v2.5.21, Panlab, Harvard Apparatus). The box was cleaned by 75% ethanol between tests.

Elevated Plus-Maze Test

The elevated plus-maze test was carried out on the next day of the open field test (Li et al., 2017; Zhang M. et al., 2017). The maze was placed 50 cm above the floor in a 30 lux illuminated room and consisted of two open arms and two closed arms (48 × 8 cm, and 40 cm wall height for the closed arms). The rat was placed onto the center area, heading toward the same open arm, and videotaped in the following 10 min. Time spent (O.Time) and numbers of entries (O.Entries) into open arms and total arm entries (T.Entries) were analyzed. The maze was cleaned by 75% ethanol between tests.

Formalin Test

Formalin test was performed 30 days after the CFA injection. Rats were handled for 10 min and adapted in a plexiglas chamber for 20 min per day for 3 days before test. The rat received an injection of 100 μL of 5% standard formalin solution into the plantar surface of right hindpaw (the opposite hindpaw of CFA/saline injection), with its behavior videotaped in the following 60 min. Time spent on licking and lifting the formalin injected paw were counted, and the formalin pain score was calculated as previously described: (time lifting + 2 × time licking)/total time (Yi et al., 2011; Zhang et al., 2014). The chamber was cleaned by 75% ethanol between tests.

Brains were removed 45 min after formalin injection for Western blotting and immunostaining, or 90 min after formalin injection for c-Fos immunostaining.

To test anxiety-like behaviors of rats after the formalin injection, open field and elevated plus-maze tests were performed 1 and 2 days after formalin injection, respectively.

Capsaicin Test

Capsaicin test was performed 30 days after the CFA injection. The plantar surface of right hindpaw was cleaned by 75% ethanol before a total of 5 μg (0.1 μg/μl) capsaicin was injected intraplantarly (Chen et al., 2006). Evoked nociceptive responses were measured by focused radiant heat (as described above) 15, 30, 60, 90 and 120 min after capsaicin injection (Soliman et al., 2005).

Cannula Implantation and Drug Microinjection

The rat was anesthetized deeply with 1% sodium pentobarbital (0.5 ml/100 g, *i.p.*) and positioned in a stereotaxic frame (RWD, Shenzhen, China). A guide cannula (O.D. 0.48 mm/I.D. 0.34 mm, C.C 1.2 mm, RWD, Shenzhen, China) was implanted 1.5 mm above PL [anterior-posterior (AP) + 2.9 mm; medial lateral (ML) ± 0.6 mm from Bregma; dorsal-ventral (DV) −2.5 mm from brain surface] (Zhang et al., 2016). Four skull screws were used for securing the guide cannula to the skull surface with dental acrylic. The matching cap (0.5 mm below the guide cannula, RWD, Shenzhen, China) was inserted into the guide cannula. All animals were given at least 1 week for recovery from surgery before further experiments. The injection needle (1.5 mm below the guide cannula, RWD, Shenzhen, China) was used for microinjection with a polyethylene catheter connecting a micro-syringe. $GABA_AR$ agonist muscimol (1 μg/μl, 0.5 μl/side, Tocris Bioscience), p38 inhibitor SB203580 (1 μg/μl, 0.5 μl/side, Sigma-Aldrich) or vehicle (artificial cerebrospinal fluid, aCSF, 0.5 μl/side) was injected into PL of either side over 2 min. The injection needle was held on for at least 2 min to allow drug diffusion. The behavioral tests were performed 30 min after drug/vehicle injection. Rats with incorrect site of the guide cannula were excluded from analysis.

Stereotaxic Microinjection of Adeno-Associated Virus (AAV) Vectors Into PL

AAV5-CaMKIIα-hM4D(Gi)-mCherry and AAV5-CaMKIIα-mCherry viruses were packaged and purchased from the University of North Carolina Vector Core Facilities (Zhang Y. et al., 2017). AAV virus solution was microinjected into PL (AP +2.7/3.2 mm; ML ± 0.6 mm from Bregma; DV −2.5 mm from brain surface) with 0.5 μl/hole, 2 holes/side, at a speed of 0.1 μl/min after being anesthetized with 1% sodium pentobarbital (0.5 ml/100 g, *i.p.*). The needle was kept on the site for 3 min to allow for virus diffusion and gradually withdrawn over 1 min to prevent possible leakage from the needle track. The behavioral tests were performed 6 weeks after virus injection.

Stereotaxic Microinjection of Clozapine-N-Oxide (CNO)

For local clozapine-N-Oxide (CNO) delivery, a guide cannula (O.D. 0.48 mm/I.D. 0.34 mm, C.C 1.6 mm, RWD, Shenzhen, China) was implanted 2 mm above ventrolateral periaqueductal gray matter (vlPAG; AP −7.8 mm; ML ± 0.8 mm from Bregma; DV −6.0 mm from brain surface), and guide cannula (O.D. 0.48 mm/I.D. 0.34 mm, C.C 3, 0 mm, RWD, Shenzhen, China) was implanted 2 mm above NAc core (AP +1.5 mm; ML ± 1.5 mm from Bregma; DV −7.7 mm from brain surface). CNO (1 mmol/L, 0.5 μl/side, Tocris Bioscience) was injected into vlPAG or NAc core slowly. Behavioral tests were performed 30 min after the CNO injection.

Western Blotting

The rat brain was removed, embedded in optimum cutting temperature compound (catalog #0201 08926, Leica), and frozen in liquid nitrogen immediately. PL tissues were taken out by using No.9 puncture needles in a cryostat microtome according to the stereological location (Zheng et al., 2017). Protein was extracted by RIPA (C1053, Applygen Technologies Inc.) and mixed with a 6× loading buffer (DE0105, Beijing BioDee BioTech Corporation Ltd.). Thirty microgram protein in each hole was separated in 10% SDS-PAGE gel and transferred onto polyvinylidene fluoride membrane (ISEQ00010, Merck Millipore). The membrane was blocked with 5% bull serum albumin at room temperature for 1 h, then

incubated with rabbit anti-p38 antibody (1:1000, 8690, Cell Signaling Technology), or anti-p-p38 antibody (1:1000, 4511, Cell Signaling Technology), or anti-cAMP-response element binding protein (CREB) antibody (1:1000, 9197, Cell Signaling Technology), or anti-p-CREB antibody (1:1000, 9198, Cell Signaling Technology), or anti-ERK antibody (1:1000, 4695, Cell Signaling Technology), or anti-p-ERK antibody (1:1000, 4370, Cell Signaling Technology), or anti-JNK antibody (1:1000, 9252, Cell Signaling Technology), anti-p-JNK antibody (1:1000, 9251, Cell Signaling Technology), anti-β-tubulin antibody (1:2000, 2128, Cell Signaling Technology) or anti-GAPDH (1:5000, 2118, Cell Signaling Technology) at 4°C for 20 h, washed in Tris-buffered saline and Tween-20 (TBST), and then incubated with horseradish peroxidase-conjugated goat anti-rabbit IgG antibody (1:2000, 111–035–003, Jackson ImmunoResearch) at room temperature for 1 h. Protein bands were detected using Western blotting luminol reagent (sc-2048, Santa Cruz). Data were analyzed with the ImageJ software.

Immunostaining

The rat was anesthetized with 1% pentobarbital sodium and intracardially perfused with 4% paraformaldehyde (PFA, in 0.1 M phosphate buffer, pH 7.4). The brain was post-fixed with 4% PFA for 12 h, and cryoprotected in 20% and 30% sucrose solutions in turn. 35 μm sections were sliced coronally using a cryostat microtome (Model 1950, Leica Instrument Co., Ltd.) throughout the entire PL (Zheng et al., 2017). Free-floating sections were washed in the phosphate buffered saline (PBS), blocked with a buffer containing 3% bull serum albumin and 0.3% triton X-100 for 1 h, and incubated with the following primary antibodies in 4°C for 24 h: rabbit anti-c-Fos antibody (1:300, sc-52, Santa Cruz), or rabbit anti-p-p38 antibody (1:500, 4511, Cell Signaling Technology), or goat anti-glutamate transporter (EAAC1) antibody (1:1000, AB1520, Merck Millipore), or mouse anti-GFAP antibody (1:1000, 3670, Cell Signaling Technology), or goat anti-Iba1 antibody (1:800, ab5076, Abcam) or mouse anti-GAD67 antibody (1:1000, ab26116, Abcam). Sections were then washed in PBS and incubated with secondary antibodies at room temperature for 90 min: Alexa Fluor 594-conjugated donkey anti-rabbit IgG (1:300, A21207, Invitrogen), or Alexa Fluor 488-conjugated donkey anti-goat IgG (1:300, A11055, Invitrogen) or Alexa Fluor 488-conjugated goat anti-mouse IgG (1:300, ab150113, Abcam). For p-p38 and glutamate transporter staining, sections were incubated in EDTA antigen retrieval solution at 98°C for 30 min to expose epitopes in DNA before blocked with serum. For co-staining of p-p38 and Iba1, antigen retrieval was not applied to avoid poor coloration of Iba1. Images were taken by a laser scanning confocal microscope (model FV1000, Olympus Co., Ltd.).

Statistical Analysis

Data were presented as means ± SEM. Unpaired or paired two-tailed *t* tests and one-way analysis of variance (ANOVA) with Bonferroni *post hoc* tests were used for the comparison

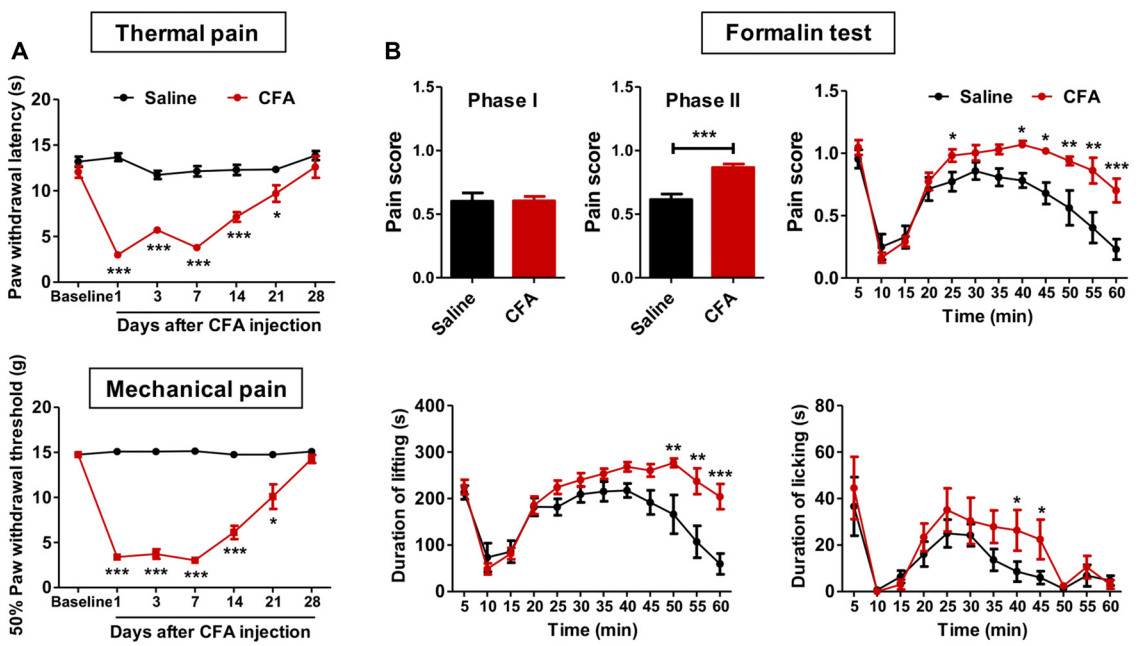

FIGURE 1 | Aggravated formalin-induced pain in rats with chronic inflammatory pain experience. **(A)** Thermal hyperalgesia (top) and mechanical allodynia (bottom) in complete freund's adjuvant (CFA)-induced chronic inflammatory pain recovered to the baseline level 28 days after CFA injection. $n = 8$ in each group. $^{*}p < 0.05$, $^{***}p < 0.001$, CFA vs. Saline, analyses of variance (ANOVA) with repeated measures and Bonferroni *post hoc* test. **(B)** Increased pain scores in the phase II of the formalin test (top) in rats with chronic inflammatory pain experience. The elevated pain score involved increased durations of both paw lifting behavior (bottom, left) and paw licking behavior (bottom, right). $n = 8$ in each group. $^{*}p < 0.05$, $^{**}p < 0.01$, $^{***}p < 0.001$, CFA vs. Saline, *t* test, ANOVA with repeated measures and Bonferroni *post hoc* test.

of two groups. Comparisons of two groups with different time points were performed using two-way ANOVA or ANOVA with repeated measures and Bonferroni *post hoc* test. The differences were calculated with software GraphPad Prism 5.0 and statistical significance was defined as $p < 0.05$.

RESULTS

Aggravated Nociceptive Responses in Rats With CFA Chronic Pain Experience

To examine whether chronic pain experience would affect upcoming nociceptive assaults, we first established chronic inflammatory pain with intraplantar CFA injection. These animals showed significant thermal hyperalgesia (group effect: $F_{(1,90)} = 130.1$, $p < 0.001$; time effect: $F_{(6,90)} = 29.27$, $p < 0.001$; interaction: $F_{(6,90)} = 21.77$, $p < 0.001$; **Figure 1A**) and mechanical allodynia (group effect: $F_{(1,96)} = 273.6$, $p < 0.001$; time effect: $F_{(6,96)} = 65.37$, $p < 0.001$; interaction: $F_{(6,96)} = 70.02$, $p < 0.001$; **Figure 1A**), which recovered to the baseline level 28 days after CFA injection. PWLs and PWTs of the contralateral paw remained unchanged throughout this period (data not shown). Inflammatory rats exhibited significant paw swelling after CFA injection (on day 1: 3613.0 ± 100.6 vs. 1587.0 ± 60.9 mm^3; on day 28: 2601.0 ± 49.8 vs. 2042.0 ± 56.9 mm^3; CFA vs. Saline group).

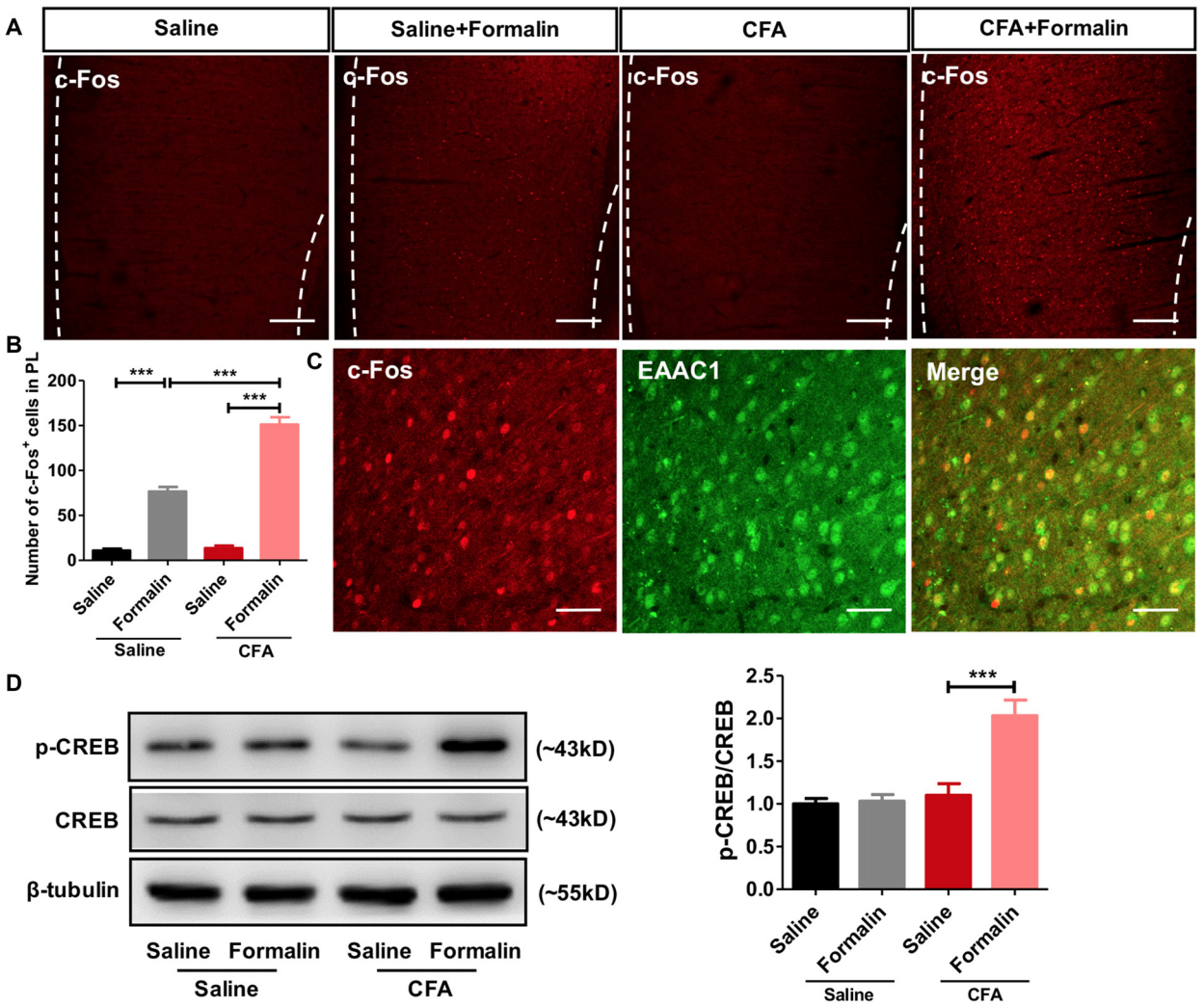

FIGURE 2 | Enhanced activation of prelimbic cortex (PL) neurons to formalin pain in rats with chronic pain experience. **(A)** Representative immunofluorescence images showing c-Fos$^+$ neurons in the PL of rats in CFA and saline groups, with or without formalin injection. Scale bars: 200 μm. **(B)** Quantitative analysis of images in **(A)**. Formalin injection induced significant c-Fos expression in the PL, especially in rats with chronic pain experience. $n = 6$ in each group. $^{***}p < 0.001$, CFA+Formalin vs. Saline+Formalin, CFA vs. CFA+Formalin, Saline vs. Saline+Formalin, one-way ANOVA. **(C)** The majority (93.70 ± 1.53%) of c-Fos$^+$ neurons (red) in PL in CFA+formalin group co-labeled with EAAC1$^+$ neurons (green). Scale bars: 50 μm. **(D)** Increased PL p-CREB with formalin injection after chronic pain recovery. Chronic pain experience or formalin injection alone did not affect p-CREB expression in PL in rats. Representative Western blots of p-CREB, CREB and β-tubulin were shown above the corresponding histogram. $n = 6$ in each group. $^{***}p < 0.001$, CFA+Formalin vs. CFA+Saline, one-way ANOVA.

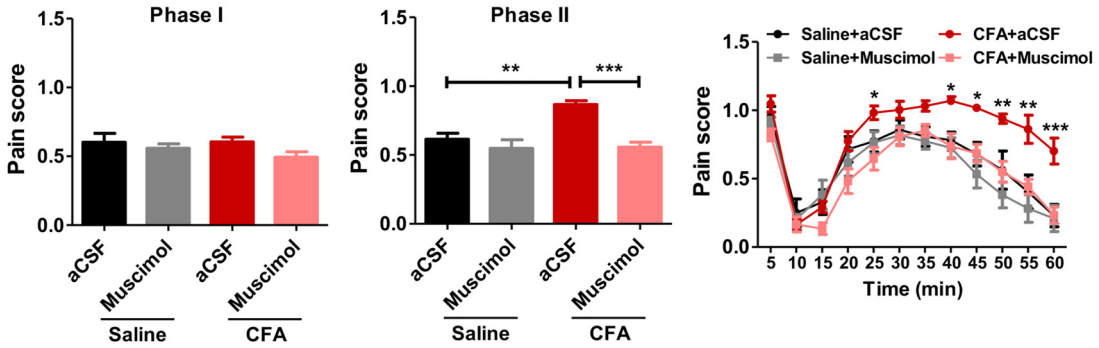

FIGURE 3 | Inhibiting PL reverses aggravated formalin pain in rats with chronic pain experience. Inhibiting PL activities by muscimol relieved the aggravated phase II formalin pain in CFA (the middle column), but not saline (the right column) group. No significant differences in phase I of formalin pain were observed among groups (the left column). $n = 8$ in each group. In the middle column: $^{***}p < 0.001$, CFA+aCSF vs. CFA+Muscimol. $^{**}p < 0.01$, CFA+aCSF vs. Saline+aCSF, one-way ANOVA. In the right column: $^{*}p < 0.05$, $^{**}p < 0.01$, $^{***}p < 0.001$, CFA+aCSF vs. CFA+Muscimol, ANOVA with repeated measures and Bonferroni *post hoc* test.

Anxiety is a common co-morbidity of chronic pain (Zheng et al., 2017). To examine anxiety-like behaviors, we performed open field and elevated plus-maze tests on days 29 and 31 after CFA or saline injection, respectively. We did not observe significant differences between CFA and saline groups at this time point (open field: C.Time, $t_{(16)} = 0.38$, $p > 0.05$; C.Dis, $t_{(16)} = 0.14$, $p > 0.05$; T.Dis, $t_{(16)} = 1.92$, $p > 0.05$; elevated plus-maze: O.Time, $t_{(16)} = 0.59$, $p > 0.05$; O.Entries, $t_{(16)} = 0.14$, $p > 0.05$; T.Entries, $t_{(16)} = 0.63$, $p > 0.05$; **Supplementary Figures S1A,B**). These results indicate full recovery of thermal hyperalgesia, mechanical allodynia and anxiety-like behaviors in CFA-induced chronic inflammatory pain 28 days after CFA injection.

We next examined these animals' responses to formalin and capsaicin tests. Rats with CFA pain experience showed significantly higher pain scores in the formalin test (phase I: $t_{(15)} = 0.04$, $p > 0.05$; phase II: $t_{(15)} = 5.00$, $p < 0.001$; **Figure 1B**), as revealed by increased duration of lifting time and licking time (lifting: group effect: $F_{(1,165)} = 12.03$, $p < 0.01$; time effect: $F_{(11,165)} = 20.67$, $p < 0.001$; interaction: $F_{(11,165)} = 4.10$, $p < 0.001$; licking: group effect: $F_{(1,165)} = 1.79$, $p > 0.05$; time effect: $F_{(11,165)} = 9.80$, $p < 0.001$; interaction: $F_{(11,165)} = 0.77$, $p > 0.05$; **Figure 1B**). Similarly, aggravated thermal hyperalgesia in the capsaicin test was also observed in rats with chronic pain experience (group effect: $F_{(5,70)} = 27.56$, $p < 0.01$; baseline: $t_{(14)} = 0.03$, $p > 0.05$; 15 min: $t_{(14)} = 2.56$, $p < 0.05$; 30 min: $t_{(14)} = 2.65$, $p < 0.05$; 60 min: $t_{(14)} = 3.40$, $p < 0.01$; 90 min: $t_{(14)} = 5.10$, $p < 0.001$; 120 min: $t_{(14)} = 3.53$, $p < 0.01$; **Supplementary Figure S2**). However, no differences of anxiety-like behaviors were observed after formalin injection between CFA and saline treated rats (elevated plus-maze: O.Time, $t_{(13)} = 0.72$, $p > 0.05$; O.Entries, $t_{(13)} = 0.23$, $p > 0.05$; T.Entries, $t_{(13)} = 0.10$, $p > 0.05$; open field: T.Dis, $t_{(13)} = 0.69$, $p > 0.05$; **Supplementary Figure S3**).

Together, these results indicate aggravated nociceptive responses to following noxious assaults in rats with prior chronic pain experience. Given the similar findings from formalin and capsaicin tests, only the formalin test was performed in further experiments.

Enhanced Activation of PL Neurons Upon Formalin Assaults in Rats With Chronic Pain Experience

To examine whether PL participated in the observed aggravated nociceptive responses, we first performed c-Fos protein mapping after formalin injection. After saline injection, PL showed little c-Fos protein expression in rats with or without chronic pain experience. By contrast, formalin injection induced significant c-Fos expression in PL, especially in rats with chronic pain experience ($F_{(3,85)} = 159.5$, $p < 0.001$; **Figures 2A,B**). The majority (93.70 ± 1.53%) of c-Fos positive neurons in PL co-labeled with EAAC1, a marker of excitatory glutamatergic neurons (**Figure 2C**).

Meanwhile, we observed significantly up-regulated phosphorylation of CREB, a marker of neuronal activation, in PL of rats receiving formalin injection with chronic pain experience. However, formalin alone was not sufficient to elevate the content of p-CREB in the PL ($F_{(3,26)} = 15.45$, $p < 0.001$; **Figure 2D**). These findings indicate stronger activation of PL by formalin pain in rats with chronic pain experience than in those without.

Inhibiting PL Reverses Aggravated Formalin Pain in Rats With Chronic Pain Experience

To examine whether PL contributed to aggravated nociceptive responses, we injected muscimol, a $GABA_A$ receptor agonist, into PL before the formalin test. Muscimol significantly relieved formalin-induced pain behaviors in rats with chronic pain experience, but not in those without (phase I: $F_{(3,33)} = 1.35$, $p > 0.05$; phase II: $F_{(3,33)} = 11.62$, $p < 0.001$; right: group effect: $F_{(3,330)} = 11.32$, $p < 0.001$; time effect: $F_{(11,330)} = 55.07$, $p < 0.001$; interaction: $F_{(33,330)} = 2.47$, $p < 0.001$; **Figure 3**). These results indicate that PL contributes to aggravated nociceptive

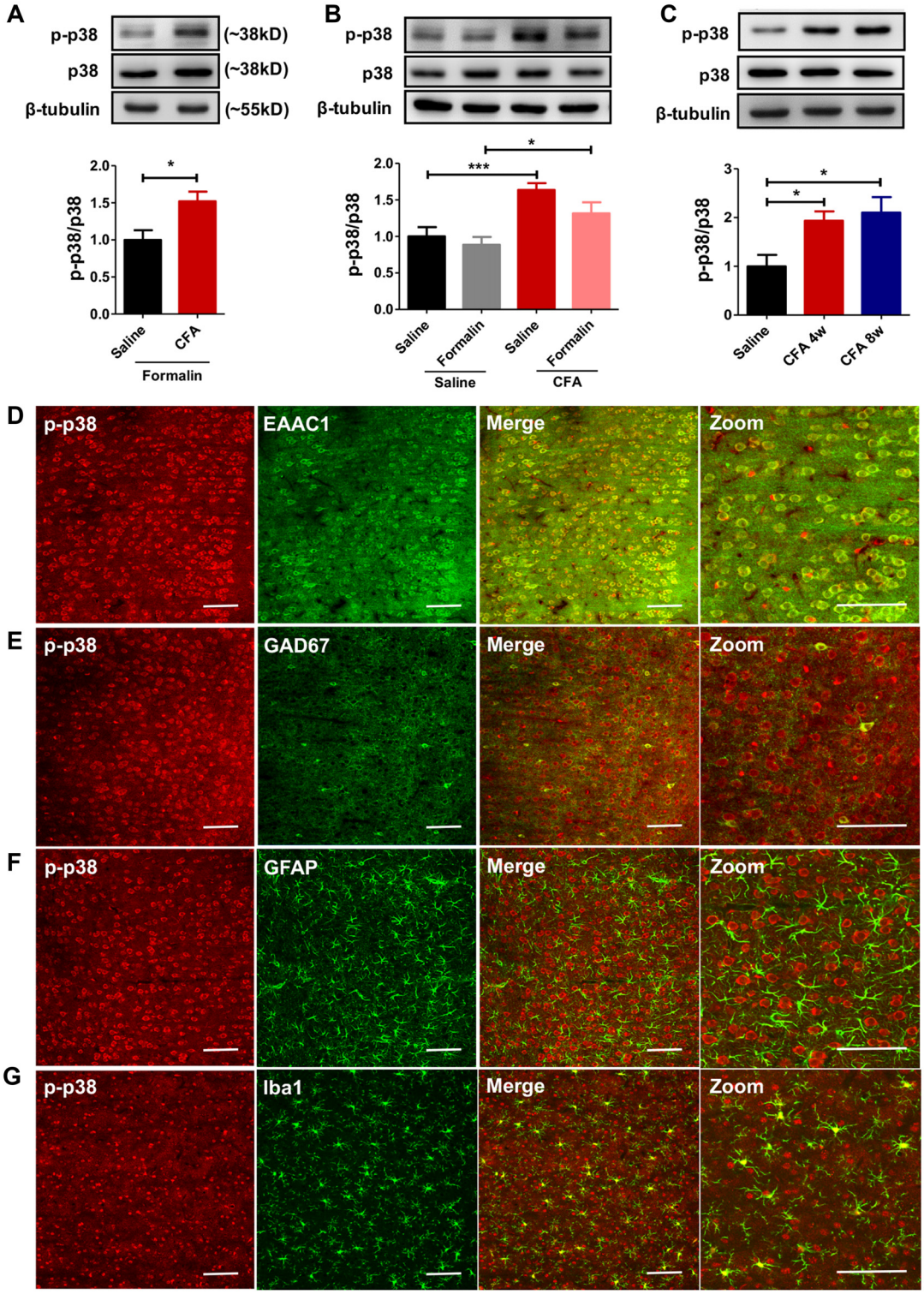

FIGURE 4 | Persistent hyperphosphorylation of p38 accompanies aggravated formalin pain in rats with chronic pain experience. **(A)** Increased PL p-p38 after formalin injection in rats with chronic pain experience. Representative Western blots of p-p38, p38 and β-tubulin were shown above the corresponding histogram. $n = 7$ in each group. $^{*}p < 0.05$, CFA+Formalin vs. Saline+Formalin, *t* test. **(B)** p-p38 in the PL increased in rats with chronic pain experience, with or without formalin injection. Formalin injection alone did not obviously influence the expression of p-p38 in PL. Representative Western blots of p-p38, p38 and β-tubulin were shown above the corresponding histogram. $n = 8$ in each group. $^{***}p < 0.001$, CFA vs. Saline, $^{*}p < 0.05$, CFA+Formalin vs. Saline+Formalin, one-way ANOVA.

(*Continued*)

FIGURE 4 | Continued
(C) Hyperphosphorylation of p38 in PL maintained for at least 8 weeks after CFA injection. Representative Western blots of p-p38, p38 and β-tubulin were shown above the corresponding histogram. $n = 6$ in each group. $^*p < 0.05$ CFA 1 m/CFA 2 m vs. Saline, one-way ANOVA. **(D)** Representative immunofluorescence images showing that the majority (87.86 ± 0.84%) of p-p38$^+$ neurons (red) co-labeled with EAAC1$^+$ neurons (green, a marker of glutamatergic neurons). Scale bars: 100 μm. **(E)** Representative immunofluorescence images showing that few (2.56 ± 0.51%) p-p38$^+$ neurons (red) co-labeled with GAD67$^+$ neurons (green, a marker of gabaergic neurons). Scale bars: 100 μm. **(F,G)** Representative immunofluorescence images showing that a small proportion of p-p38$^+$ neurons (red) co-labeled with GFAP$^+$ (1.23 ± 0.16%, green, a marker of astrocytes) and Iba1$^+$ cells (8.35 ± 0.66%, green, a marker of microglia). Scale bars: 100 μm.

formalin pain responses in rats with chronic inflammatory pain experience.

Persistent Hyperphosphorylation of p38 Accompanies Aggravated Formalin Pain in Rats With Chronic Pain Experience

To explore molecular mechanisms of PL's contribution to aggravated pain, we examined protein contents of MAPKs (including ERK, p38 and JNK) and their phosphorylation in bilateral PL. MAPKs are key players in nociceptive sensitization, which are activated by various second-messenger signal transduction cascades (Edelmayer et al., 2014). Western blotting showed significantly up-regulated phosphorylation of p38 in PL of rats with chronic pain experience after formalin injection ($t_{(12)} = 2.80$, $p < 0.05$; **Figure 4A**). Indeed, the up-regulated phosphorylation of p38 was apparent in the PL of rats with chronic pain even without formalin injection ($F_{(3,34)} = 7.57$, $p < 0.001$; **Figure 4B**). The up-regulated p-p38 was apparent 7 days after CFA injection ($F_{(6,34)} = 6.25$, $p < 0.001$; **Supplementary Figure S4**), and lasted minimally 8 weeks ($F_{(2,17)} = 5.51$, $p < 0.05$; **Figure 4C**). By contrast, no significant differences in the content of ERK, p-ERK, JNK or p-JNK were detected (p-ERK/ERK: $F_{(3,33)} = 1.24$, $p > 0.05$; p-JNK/JNK: $F_{(3,37)} = 1.23$, $p > 0.05$; **Supplementary Figures S5A,B**). Immunofluorescence showed that the majority (87.86 ± 0.84%) of p-p38 positive neurons in PL co-labeled with EAAC1 (**Figure 4D**), and only a small proportion (2.56 ± 0.51%) with GAD67, a marker of interneurons (**Figure 4E**). Few astrocytes or microglial cells (GFAP$^+$ and Iba1$^+$ cells, 1.23 ± 0.16% and 8.35 ± 0.66%, respectively) showed co-expression with p-p38 (**Figures 4F,G**). These findings indicate that previous chronic pain experience induces sustained hyperphosphorylation of p38 after pain recovery.

Inhibiting p38 Phosphorylation Reverses Aggravated Formalin Pain in Rats With Chronic Pain Experience

To examine whether the hyperphosphorylated p38 contributed to sensitized pain behaviors in rats with chronic pain experience, we micro-injected SB203580, a specific inhibitor of p38 phosphorylation, into bilateral PL 30 min before the formalin test (**Figure 5A**). SB203580 inhibited the hyperphosphorylation of p38 after chronic pain recovery (left: $t_{(10)} = 5.27$, $p < 0.001$; right: $t_{(10)} = 4.17$, $p < 0.01$; **Figures 5B,C**) and down-regulated formalin-induced p-CREB ($t_{(6)} = 2.72$, $p < 0.05$; **Figure 5D**).

Behaviorally, SB203580 reversed the aggravated formalin pain in rats with chronic pain experience, but not in those without (phase I: $F_{(3,25)} = 4.19$, $p < 0.05$; phase II: $F_{(3,28)} = 83.37$, $p < 0.001$; right: group effect: $F_{(3,275)} = 96.95$, $p < 0.001$; time effect: $F_{(11,275)} = 95.58$, $p < 0.001$; interaction: $F_{(33,275)} = 2.64$, $p < 0.001$; **Figure 5E**).

These results suggest that persistent hyperphosphorylation of p38 in the PL contributes to the hypersensitized formalin pain in rats with chronic pain experience.

PL–PAG Pathway Mediates Aggravated Formalin Pain in Rats With Chronic Pain Experience

PL projects to several brain areas that modulate pain. We further investigated the neural pathways that aggravated formalin pain in rats with chronic pain experience (**Figure 6A**). We chemogenetically inhibited the PL–PAG pathway (**Figure 6B**), which is essential for descending pain modulation, and observed an relieved effect on the aggravated formalin pain in rats with chronic pain experience (phase I: $F_{(3,31)} = 5.07$, $p < 0.01$; phase II: $F_{(3,31)} = 19.05$, $p < 0.001$; right: group effect: $F_{(3,308)} = 19.04$, $p < 0.001$; time effect: $F_{(11,308)} = 74.70$, $p < 0.001$; interaction: $F_{(33,308)} = 2.23$, $p < 0.001$; **Figure 6C**). By contrast, inhibiting the PL–PAG pathway did not affect physiological pain in rats with chronic pain experience (mCherry: $t_{(21)} = 1.11$, $p > 0.05$; hM4Di: $t_{(5)} = 1.75$, $p > 0.05$; **Supplementary Figures S6A,B**), nor the development of CFA induced chronic inflammatory pain ($p > 0.05$; **Supplementary Figures S7A,B**).

In contrast, chemogenetic inhibition of the PL–NAc core pathway did not relieve the aggravated formalin pain in rats with chronic pain experience (phase I: $F_{(3,27)} = 0.81$, $p > 0.05$; phase II: $F_{(3,28)} = 0.52$, $p > 0.05$; right: group effect: $F_{(3,275)} = 0.16$, $p > 0.05$; time effect: $F_{(11,275)} = 76.15$, $p < 0.001$; interaction: $F_{(33,275)} = 1.27$, $p > 0.05$; **Supplementary Figures S8A,B**).

These findings indicate that PL–mediated aggravated formalin pain in rats with chronic pain experience is achieved through the PL–PAG pathway, but not the PL–NAc core pathway.

DISCUSSION

PL Contributes to Aggravated Nociceptive Formalin Pain Responses in Rats With Chronic Inflammatory Pain Experience

Prior pain experience alters future responses to painful stimuli in both human and animals (Bachiocco et al., 1993; Lidow, 2002; Ren et al., 2004; Hermann et al., 2006; Li et al., 2012; Wegner et al., 2015). In the present study, we identified PL as a key region in regulating the aggravated formalin-induced pain in rats after the recovery from CFA-induced chronic inflammatory pain. Rats

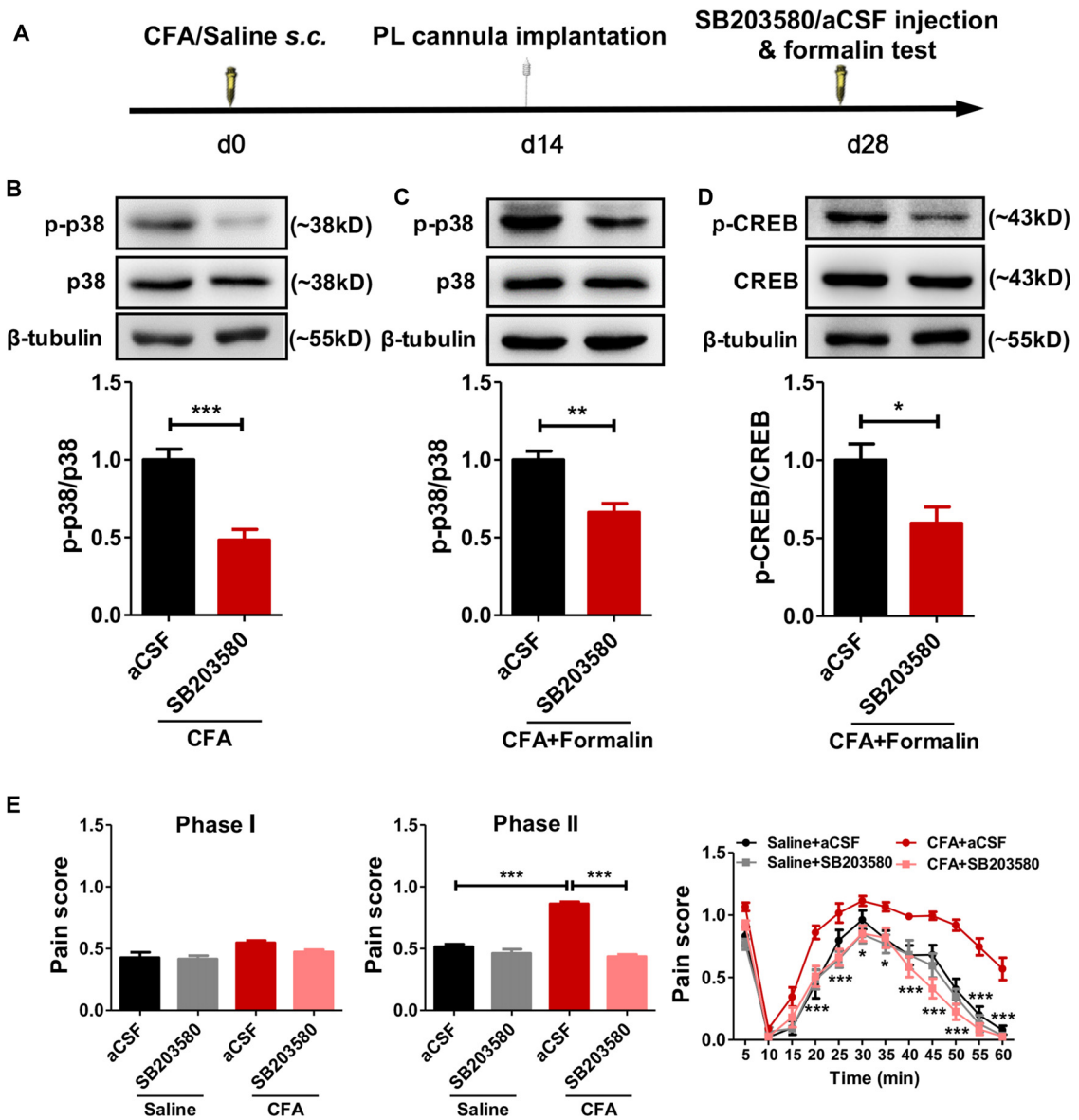

FIGURE 5 | Inhibiting the phosphorylation of p38 reverses aggravated formalin pain in rats with chronic pain experience. **(A)** A diagram showing the experiment time line. SB203580/aCSF micro-injection and formalin test were performed 28 d after CFA/saline injection. The cannula implantation surgery was performed 2 weeks before behavior tests. **(B,C)** SB203580 micro-injection into PL inhibited the hyperphosphorylation of p38 in rats with chronic pain experience, without **(B)** or with formalin injection **(C)**. Representative Western blots of p-p38, p38 and β-tubulin were shown above the corresponding histogram. $n = 6$ in each group. $^{***}p < 0.001$, CFA+aCSF vs. CFA+SB203580. $^{**}p < 0.01$, CFA+aCSF+Formalin vs. CFA+SB203580+Formalin, *t* test. **(D)** SB203580 micro-injection into PL inhibited the hyperphosphorylation of cAMP-response element binding protein (CREB) after formalin injection in rats with chronic pain experience. Representative Western blots of p-CREB, CREB and β-tubulin were shown above the corresponding histogram. $n = 6$ in each group. $^{*}p < 0.05$, CFA+aCSF+Formalin vs. CFA+SB203580+Formalin, *t* test. **(E)** Inhibiting the phosphorylation of p38 in PL by SB203580 reversed the aggravated phases II formalin pain in the CFA group, but not the saline group (the middle column). Detailed pain scores shown in every 5 min (the right column). $n = 6$ in each group. In the middle column: $^{***}p < 0.001$, Saline + aCSF/CFA+SB203580 vs. CFA+aCSF, one-way ANOVA. In the right column: $^{*}p < 0.05$, $^{***}p < 0.001$, CFA+aCSF vs. CFA+SB203580, ANOVA with repeated measures and Bonferroni *post hoc* test.

with chronic pain experience showed elevated pain scores in the second, but not the first, phase of formalin pain. The second phase of formalin pain reflects the development of inflammation and central sensitization, and indicates the involvement of the central nervous system in the aggravated pain (Shibata et al., 1989; Vaccarino and Melzack, 1992).

Structural and functional changes in several brain regions persist long after pain recovery. For example, reduced gray matter densities in chronic back pain patients are observed in the middle cingulate gyrus, thalamus and prefrontal cortex (Ivo et al., 2013), and an increase of gray matter density is found in PAG, thalamus and cerebellum months

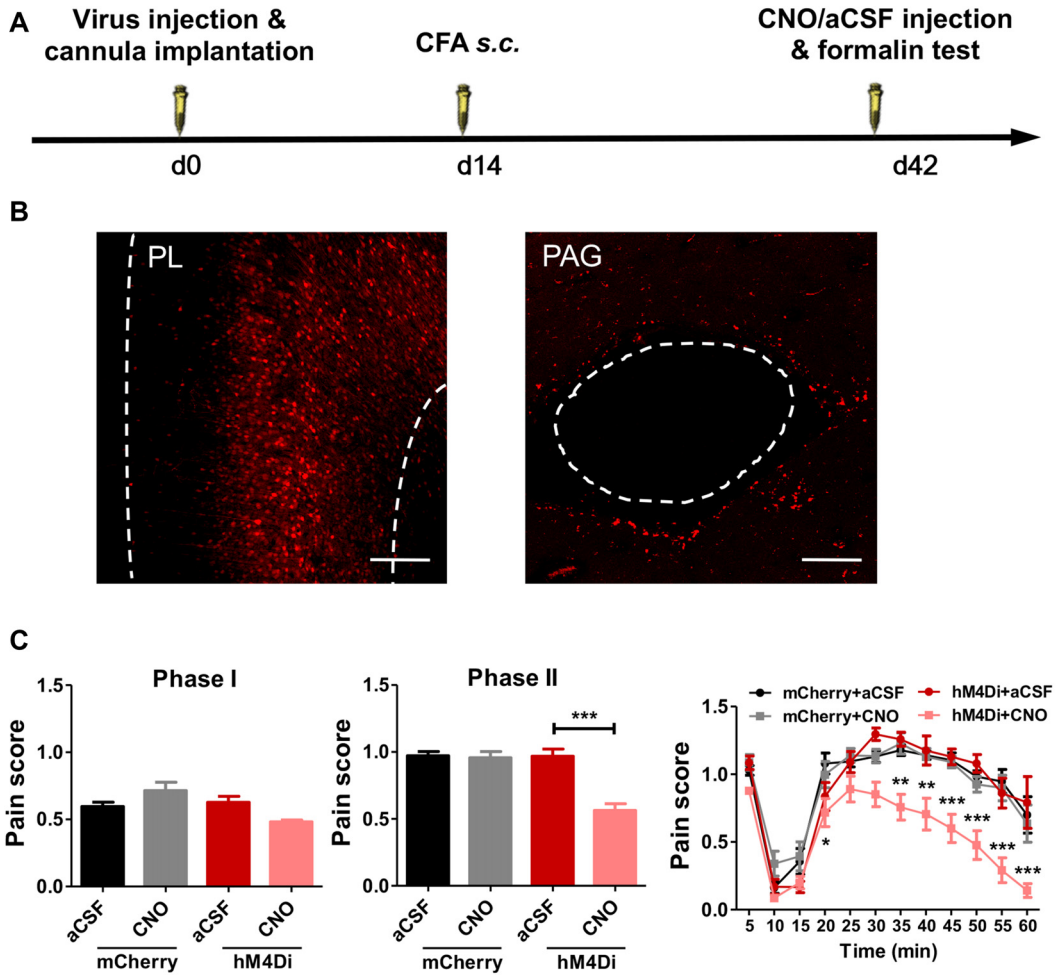

FIGURE 6 | PL–periaqueductal gray (PAG) pathway mediates aggravated formalin pain in rats with chronic pain experience. **(A)** A diagram showing the experiment time line. The clozapine-N-Oxide (CNO)/aCSF micro-injection and formalin test were performed 42 days after virus injection and cannula implantation surgery. CFA injection was performed 28 days before formalin test. **(B)** AAV5-CaMKIIα-hM4D(Gi)-mCherry virus expression in PL (red, left), expression of hM4Di in PL projection in PAG (red, right). Scale bars: 200 μm. **(C)** Compared to the control, inhibiting PL–PAG pathway relieved the aggravated phases II formalin pain in the CFA group (the middle column). Detailed pain scores were shown in every 5 min (the right column). $n = 8$ in each group. In the middle column: $^{***}p < 0.001$, hM4Di+aCSF vs. hM4Di+CNO, one-way ANOVA. In the right column: $^{*}p < 0.05$, $^{**}p < 0.01$, $^{***}p < 0.001$, hM4Di+aCSF vs. hM4Di+CNO, ANOVA with repeated measures and Bonferroni *post hoc* test.

after whiplash injury and after the headache subsided in most patients with posttraumatic headache (Obermann et al., 2009). Chronic back pain also alters the human brain chemistry: reduction of *N*-acetyl aspartate and glucose is demonstrated in the dorsolateral prefrontal cortex, but not cingulate, sensorimotor and other brain regions (Grachev et al., 2000). In animals, long-term neuropathic pain decreases frontal cortex volumes several months after nerve injury (Seminowicz et al., 2009), and increases basal dendrites of neurons and spine densities in the PL (Metz et al., 2009). These structural and functional changes are accompanied by altered synaptic plasticity and neuronal excitability (Metz et al., 2009; Baliki et al., 2014). Taken together, PL is a brain region particularly vulnerable to chronic pain, regardless of pain recovery or not (Grachev et al., 2000; Apkarian et al., 2004). Some evidences show that pain-induced functional and structural abnormalities in the PFC are at least partially reversible by effective pain treatment (Rodriguez-Raecke et al., 2009; Seminowicz et al., 2011). However, we demonstrated persistent hypersensitivity of PL neurons in rats with chronic pain experience to following pain assaults.

However, we do not consider PL to be the only brain region that contributes to the aggravated nociceptive responses in rats with experience of chronic inflammatory pain. Other areas such as anterior cingulate cortex (ACC) and infralimbic cortex (IL), insular cortex and thalamus are densely connected with PL and undergo plastic changes in chronic pain (Obermann et al., 2009; Ivo et al., 2013; Lin, 2014; Zhuo, 2016; Yue et al., 2017).

Persistent Hyperphosphorylation of p38 Contributes to Aggravated Formalin Pain in Rats With Chronic Pain Experience

p38 is one of the major MAPK members crucial for generating pain hypersensitivity through transcription-dependent and -independent means (Ji and Woolf, 2001; Crown et al., 2006; Wynne, 2006; Toyoda et al., 2007; Ji et al., 2009). In both peripheral and central nervous system, such as spinal cord and ACC, p38 is activated following pain stimulations, and the activation lasts for more than 3 weeks after chronic constriction injury or spinal nerve ligation (Toyoda et al., 2007; Crown et al., 2008; Cao et al., 2014). Inhibiting p38 in spinal cord or ACC alleviates both subacute and chronic pain (Kumar et al., 2003; Crown et al., 2008; Cao et al., 2014). In the present study, p-p38$^+$ neurons are mostly glutamatergic neurons in PL. Under persistent noxious stimulation, hyperphosphorylated p38 can be invoked to activate the downstream signal pathway, including p-CREB and c-Fos, and the activation of nociceptive neurons further sensitizes pain. Inhibiting the phosphorylation of p38 relieves the aggravated formalin pain in rats with chronic pain experience and down-regulates the phosphorylation of its downstream effector CREB and the neuronal activity. The persistent hyperphosphorylation of p38 in PL in rats with chronic pain experience does not directly contribute to pain responses unless a strong stimulus such as formalin injection is performed. These findings indicate that some endogenous inhibitors overlay sensitized p-p38 to keep the balanced "recovery" state.

One candidate of such inhibitors would be layer V pyramidal neurons in the IL, which directly innervate inhibitory interneurons in the PL (Saffari et al., 2016). In addition to pain (Baliki et al., 2012; Wang et al., 2015; Wu et al., 2016), PL also regulates other long-term cognitive behaviors including fear conditioning, working memory, drug addiction and chronic stress (Gisquet-Verrier and Delatour, 2006; Lasseter et al., 2010; Negrón-Oyarzo et al., 2014; Fitzgerald et al., 2015; Moench and Wellman, 2015; Seo et al., 2017). PL neuronal activities maintain freezing behaviors in fear conditioning, whereas extinction induces a novel inhibitory learning in the IL, which antagonize PL pyramidal neuronal activities through local interneurons (Ji and Neugebauer, 2012). These facts lead to an intriguing proposal that the recovery from chronic pain represents pain extinction, instead of simple oblivion of the pain memory (Apkarian et al., 2009; Yi and Zhang, 2011).

PL–PAG Pathway Mediates Aggravated Formalin Pain in Rats With Chronic Pain Experience

PL has direct projections to several nuclei, including ACC, NAc, amygdala and PAG. Previous studies have revealed roles of PL–NAc and PL–PAG pathways in regulating chronic pain (Kucyi et al., 2013; Yu et al., 2014; Lee et al., 2015). Activation of the PL to NAc core circuit inhibits persistent neuropathic pain and relieves the affective symptoms associated with chronic pain (Lee et al., 2015). Functional and structural connectivity between PAG and mPFC relates to individual differences in attention to pain (Kucyi et al., 2013). PAG is a critical component of the descending pain modulatory system, and usually exerts an inhibitory effect on nociceptive transmission (Umana et al., 2017). Evidence shows that glutamatergic projections from mPFC act to inhibit PAG function (Franklin et al., 2017). Pharmacogenetic inhibition of the projections from PL to PAG therefore disinhibits PAG, and in turn relieves the aggravated formalin-induced pain. The finding that paw lifting behaviors in response to formalin injection, indicating peripheral reflexes, increase in rat with chronic pain experience also supports the involvement of the descending pathway.

Different from the role of PAG in perceptual part of pain, NAc is more involved in pain affection, such as depression-like behaviors in the chronic neuropathic pain state (Goffer et al., 2013; LeBlanc et al., 2015; Navratilova et al., 2015; Kaneko et al., 2017). The present study shows that PL–PAG, but not PL–NAc, pathway regulates the aggravated formalin pain in rats with chronic pain experience, which reflects mostly aggravated pain sensation.

PL as a Potential Therapeutic Target

Patients with chronic pain have less PFC deactivation than controls during cognition or visual attention tasks (Baliki et al., 2008; Seminowicz et al., 2011), in keeping with our results that the PL is more strongly activated during the following noxious assault in rats with chronic pain experience. Previous work has identified the PL as a target for pain treatment. Repetitive transcranial magnetic stimulation, deep brain stimulation, cognitive-behavioral therapy or other therapies can lead abnormal function of prefrontal cortex to stable or normal state (Fierro et al., 2010; Seminowicz et al., 2013; Boccard et al., 2015), thus relieves the aggravated nociceptive responses in patients with chronic pain experience.

In conclusion, our present study demonstrates that persistent hyperphosphorylation of p38 in the PL underlies aggravated nociceptive responses in rats with chronic inflammatory pain experience, and indicates inhibiting the activity of PL as a promising option for treating hyperalgesia in patients with chronic pain experience.

AUTHOR CONTRIBUTIONS

X-CF, MY and YW designed experiments and wrote the manuscript; X-CF, SF, F-YL and SC performed the experiments and analyzed the data; YW and MY supervised the experiments.

ACKNOWLEDGMENTS

This study was supported by grants from the Ministry of Science and Technology of China (2014CB548200 and 2015CB554503), the National Natural Science Foundation of China (91732107, 81571067 and 81521063), the Beijing Natural Science Foundation (5182013) and the "111" Project of Ministry of Education of the People's Republic of China.

SUPPLEMENTARY MATERIAL

The Supplementary Material for this article can be found online at: https://www.frontiersin.org/articles/10.3389/fnmol.2018.00085/full#supplementary-material

FIGURE S1 | Similar levels of anxiety-like behaviors in chronic pain rats 30 days after CFA injection. **(A)** Rats showed similar levels of anxiety-like behaviors in the open field test 30 days after CFA injection, indicated by similar time spent (C.Time, left) and distance traveled (C.Dis, middle) in the central area of the open field between groups. Total distance traveled (T.Dis, right) in the field were not affected either. $n = 8$ in each group. CFA vs. Saline, *t* test. **(B)** Rats showed similar levels of anxiety-like behaviors in the elevated plus-maze test 30 days after CFA injection, indicated by similar time spent (O.Time, left) and entries (O.Entries, middle) into the open arms between groups. Total arm entries (T.Entries, right) were not affected either. $n = 8$ in each group. CFA vs. Saline, *t* test.

FIGURE S2 | Aggravated capsaicin-induced pain in rats with chronic inflammatory pain experience. Rats with chronic inflammatory pain experience showed increased thermal hyperalgesia 15, 30, 60, 90 and 120 min after capsaicin injection. $n = 8$ in each group. $p < 0.01$, Saline+Capsaicin vs. CFA+Capsaicin, one-way ANOVA; $^{*}p < 0.05$, $^{**}p < 0.01$, $^{***}p < 0.001$, Saline+Capsaicin vs. CFA+Capsaicin, *t* test.

FIGURE S3 | Similar levels of anxiety-like behaviors after formalin injection between CFA chronic pain group and saline control group. **(A)** Rats with chronic pain experience showed similar levels of anxiety-like behaviors in the elevated plus-maze test after formalin injection, indicated by similar time spent (O.Time, left) and entries (O.Entries, middle) into the open arms between groups. Total arm entries (T.Entries, right) were similar either. $n = 8$ in each group. CFA+Formalin vs. Saline+Formalin, *t* test. **(B)** Similar levels of locomotion after formalin injection between CFA and saline groups, indicated by similar total distance traveled (T.Dis) in the field. $n = 8$ in each group. CFA+Formalin vs. Saline+Formalin, *t* test.

FIGURE S4 | Increased levels of p-p38 in the PL after CFA injection. p-p38 in the PL increased in chronic pain rats 7 days after CFA injection, and maintained for at least 28 days. Representative Western blots of p-p38, p38 and β-tubulin were shown above the corresponding histogram. $n = 5$ in each group. $^{***}p < 0.001$, $^{**}p < 0.01$, vs. Saline, one-way ANOVA.

FIGURE S5 | Chronic pain experience and formalin injection do not affect the phosphorylation of ERK1/2 and JNK in PL. **(A)** Similar levels of p-ERK1/2 in PL in rats with chronic pain experience. Formalin injection did not affect the phosphorylation of ERK1/2 in PL in rats with or without chronic pain experience. Representative Western blots of p-ERK1/2, ERK1/2 and β-tubulin were shown above the corresponding histogram. $n = 8$ in each group, one-way ANOVA. **(B)** Lack of significant changes of p-JNK in PL in rats with chronic pain experience. Formalin injection did not affect the phosphorylation of JNK in PL in rats with or without chronic pain experience. Representative Western blots of p-JNK, JNK and GAPDH were shown above the corresponding histogram. $n = 8$ in each group, one-way ANOVA.

FIGURE S6 | Inhibiting PL–PAG pathway does not affect physiological pain after chronic inflammatory pain recovery. **(A)** A diagram showing the time line of the experiment. The CNO/aCSF micro-injection and hot plate test were performed 28 days after CFA injection. Virus injection and cannula immplantation surgery were performed 14 days before CFA injection. **(B)** Compared to the control, inhibiting PL–PAG pathway did not affect physiological pain after chronic inflammatory pain recovery. $n = 6$ in each group. Before vs. After CNO injection, paired *t* test.

FIGURE S7 | Inhibiting PL–PAG pathway does not affect thermal hyperalgesia in the development of CFA-induced chronic inflammatory pain. **(A)** A diagram showing the experiment time line. CNO/aCSF micro-injection and thermal hyperalgesia test were performed 1 day before and 1, 3, 7, 14, 21 and 28 days after CFA injection. Virus injection and cannula implantation surgery were performed 6 weeks before CFA injection. **(B)** Compared to the control, inhibiting PL–PAG pathway did not influence thermal hyperalgesia in the development of CFA-induced chronic inflammatory pain. $n = 7$ in each group. Before vs. After CNO injection, paired *t* test.

FIGURE S8 | PL–NAc core pathway does not affect aggravated formalin pain in rats with chronic pain experience. **(A)** Confirmation of AAV5-CaMKIIα-hM4D(Gi)-mCherry virus expression in PL projection in NAc core (red). Scale bars: 100 μm. **(B)** Inhibiting PL–NAc core pathway did not relieve the aggravated formalin pain in either phase I (the left column) or phase II (the middle column) in CFA group. $n = 8$ in each group, one-way ANOVA. Detailed pain scores were shown in every 5 min (the right column). $n = 8$ in each group, ANOVA with repeated measures and Bonferroni *post hoc* test.

REFERENCES

Apkarian, A. V., Baliki, M. N., and Geha, P. Y. (2009). Towards a theory of chronic pain. *Prog. Neurobiol.* 87, 81–97. doi: 10.1016/j.pneurobio.2008.09.018

Apkarian, A. V., Sosa, Y., Sonty, S., Levy, R. M., Harden, R. N., Parrish, T. B., et al. (2004). Chronic back pain is associated with decreased prefrontal and thalamic gray matter density. *J. Neurosci.* 24, 10410–10415. doi: 10.1523/JNEUROSCI.2541-04.2004

Bachiocco, V., Scesi, M., Morselli, A. M., and Carli, G. (1993). Individual pain history and familial pain tolerance models: relationships to post-surgical pain. *Clin. J. Pain* 9, 266–271. doi: 10.1097/00002508-199312000-00008

Baliki, M. N., Geha, P. Y., Apkarian, A. V., and Chialvo, D. R. (2008). Beyond feeling: chronic pain hurts the brain, disrupting the default-mode network dynamics. *J. Neurosci.* 28, 1398–1403. doi: 10.1523/JNEUROSCI.4123-07.2008

Baliki, M. N., Mansour, A. R., Baria, A. T., and Apkarian, A. V. (2014). Functional reorganization of the default mode network across chronic pain conditions. *PLoS One* 9:e106133. doi: 10.1371/journal.pone.0106133

Baliki, M. N., Petre, B., Torbey, S., Herrmann, K. M., Huang, L., Schnitzer, T. J., et al. (2012). Corticostriatal functional connectivity predicts transition to chronic back pain. *Nat. Neurosci.* 15, 1117–1119. doi: 10.1038/nn.3153

Boccard, S. G., Pereira, E. A., and Aziz, T. Z. (2015). Deep brain stimulation for chronic pain. *J. Clin. Neurosci.* 22, 1537–1543. doi: 10.1016/j.jocn.2015.04.005

Cao, H., Zang, K. K., Han, M., Zhao, Z. Q., Wu, G. C., and Zhang, Y. Q. (2014). Inhibition of p38 mitogen-activated protein kinase activation in the rostral anterior cingulate cortex attenuates pain-related negative emotion in rats. *Brain Res. Bull.* 107, 79–88. doi: 10.1016/j.brainresbull.2014.06.005

Chaplan, S. R., Bach, F. W., Pogrel, J. W., Chung, J. M., and Yaksh, T. L. (1994). Quantitative assessment of tactile allodynia in the rat paw. *J. Neurosci. Methods* 53, 55–63. doi: 10.1016/0165-0270(94)90144-9

Chen, S. C., Liu, B. C., Chen, C. W., and Wu, F. S. (2006). Intradermal pregnenolone sulfate attenuates capsaicin-induced nociception in rats. *Biochem. Biophys. Res. Commun.* 349, 626–633. doi: 10.1016/j.bbrc.2006.08.076

Crown, E. D., Gwak, Y. S., Ye, Z., Johnson, K. M., and Hulsebosch, C. E. (2008). Activation of p38 MAP kinase is involved in central neuropathic pain following spinal cord injury. *Exp. Neurol.* 213, 257–267. doi: 10.1016/j.expneurol.2008.05.025

Crown, E. D., Ye, Z., Johnson, K. M., Xu, G. Y., McAdoo, D. J., and Hulsebosch, C. E. (2006). Increases in the activated forms of ERK 1/2, p38 MAPK and CREB are correlated with the expression of at-level mechanical allodynia following spinal cord injury. *Exp. Neurol.* 199, 397–407. doi: 10.1016/j.expneurol.2006.01.003

Edelmayer, R. M., Brederson, J. D., Jarvis, M. F., and Bitner, R. S. (2014). Biochemical and pharmacological assessment of MAP-kinase signaling along pain pathways in experimental rodent models: a potential tool for the discovery of novel antinociceptive therapeutics. *Biochem. Pharmacol.* 87, 390–398. doi: 10.1016/j.bcp.2013.11.019

Ferland, C. L., Harris, E. P., Lam, M., and Schrader, L. A. (2014). Facilitation of the HPA axis to a novel acute stress following chronic stress exposure modulates histone acetylation and the ERK/MAPK pathway in the dentate gyrus of male rats. *Endocrinology* 155, 2942–2952. doi: 10.1210/en.2013-1918

Fierro, B., De Tommaso, M., Giglia, F., Giglia, G., Palermo, A., and Brighina, F. (2010). Repetitive transcranial magnetic stimulation (rTMS) of the dorsolateral

prefrontal cortex (DLPFC) during capsaicin-induced pain: modulatory effects on motor cortex excitability. *Exp. Brain Res.* 203, 31–38. doi: 10.1007/s00221-010-2206-6

Fitzgerald, P. J., Giustino, T. F., Seemann, J. R., and Maren, S. (2015). Noradrenergic blockade stabilizes prefrontal activity and enables fear extinction under stress. *Proc. Natl. Acad. Sci. U S A* 112, E3729–E3737. doi: 10.1073/pnas.1500682112

Franklin, T. B., Silva, B. A., Perova, Z., Marrone, L., Masferrer, M. E., Zhan, Y., et al. (2017). Prefrontal cortical control of a brainstem social behavior circuit. *Nat. Neurosci.* 20, 260–270. doi: 10.1038/nn.4470

Gao, Y. J., and Ji, R. R. (2008). Activation of JNK pathway in persistent pain. *Neurosci. Lett.* 437, 180–183. doi: 10.1016/j.neulet.2008.03.017

Gisquet-Verrier, P., and Delatour, B. (2006). The role of the rat prelimbic/infralimbic cortex in working memory: not involved in the short-term maintenance but in monitoring and processing functions. *Neuroscience* 141, 585–596. doi: 10.1016/j.neuroscience.2006.04.009

Goffer, Y., Xu, D., Eberle, S. E., D'Amour, J., Lee, M., Tukey, D., et al. (2013). Calcium-permeable AMPA receptors in the nucleus accumbens regulate depression-like behaviors in the chronic neuropathic pain state. *J. Neurosci.* 33, 19034–19044. doi: 10.1523/JNEUROSCI.2454-13.2013

Grachev, I. D., Fredrickson, B. E., and Apkarian, A. V. (2000). Abnormal brain chemistry in chronic back pain: an *in vivo* proton magnetic resonance spectroscopy study. *Pain* 89, 7–18. doi: 10.1016/s0304-3959(00)00340-7

Hermann, C., Hohmeister, J., Demirakça, S., Zohsel, K., and Flor, H. (2006). Long-term alteration of pain sensitivity in school-aged children with early pain experiences. *Pain* 125, 278–285. doi: 10.1016/j.pain.2006.08.026

Hu, H. J., and Gereau, R. W. (2003). ERK integrates PKA and PKC signaling in superficial dorsal horn neurons. II. Modulation of neuronal excitability. *J. Neurophysiol.* 90, 1680–1688. doi: 10.1152/jn.00341.2003

Impey, S., Obrietan, K., and Storm, D. R. (1999). Making new connections: role of ERK/MAP kinase signaling in neuronal plasticity. *Neuron* 23, 11–14. doi: 10.1016/S0896-6273(00)80747-3

Ivo, R., Nicklas, A., Dargel, J., Sobottke, R., Delank, K. S., Eysel, P., et al. (2013). Brain structural and psychometric alterations in chronic low back pain. *Eur. Spine J.* 22, 1958–1964. doi: 10.1007/s00586-013-2692-x

Ji, R. R., Gereau, R. W., Malcangio, M., and Strichartz, G. R. (2009). MAP kinase and pain. *Brain Res. Rev.* 60, 135–148. doi: 10.1016/j.brainresrev.2008.12.011

Ji, G., and Neugebauer, V. (2012). Modulation of medial prefrontal cortical activity using *in vivo* recordings and optogenetics. *Mol. Brain* 5:36. doi: 10.1186/1756-6606-5-36

Ji, R. R., and Woolf, C. J. (2001). Neuronal plasticity and signal transduction in nociceptive neurons: implications for the initiation and maintenance of pathological pain. *Neurobiol. Dis.* 8, 1–10. doi: 10.1006/nbdi.2000.0360

Johnson, G. L., and Lapadat, R. (2002). Mitogen-activated protein kinase pathways mediated by ERK, JNK and p38 protein kinases. *Science* 298, 1911–1912. doi: 10.1126/science.1072682

Kaneko, H., Zhang, S., Sekiguchi, M., Nikaido, T., Makita, K., Kurata, J., et al. (2017). Dysfunction of nucleus accumbens is associated with psychiatric problems in patients with chronic low back pain: a functional magnetic resonance imaging study. *Spine* 42, 844–853. doi: 10.1097/BRS.0000000000001930

Khan, S. A., Keaser, M. L., Meiller, T. F., and Seminowicz, D. A. (2014). Altered structure and function in the hippocampus and medial prefrontal cortex in patients with burning mouth syndrome. *Pain* 155, 1472–1480. doi: 10.1016/j.pain.2014.04.022

Kucyi, A., Salomons, T. V., and Davis, K. D. (2013). Mind wandering away from pain dynamically engages antinociceptive and default mode brain networks. *Proc. Natl. Acad. Sci. U S A* 110, 18692–18697. doi: 10.1073/pnas.1312902110

Kumar, S., Boehm, J., and Lee, J. C. (2003). p38 MAP kinases: key signalling molecules as therapeutic targets for inflammatory diseases. *Nat. Rev. Drug Discov.* 2, 717–726. doi: 10.1038/nrd1177

Lasseter, H. C., Xie, X., Ramirez, D. R., and Fuchs, R. A. (2010). Prefrontal cortical regulation of drug seeking in animal models of drug relapse. *Curr. Top. Behav. Neurosci.* 3, 101–117. doi: 10.1007/7854_2009_19

LeBlanc, D. M., McGinn, M. A., Itoga, C. A., and Edwards, S. (2015). The affective dimension of pain as a risk factor for drug and alcohol addiction. *Alcohol* 49, 803–809. doi: 10.1016/j.alcohol.2015.04.005

Lee, M., Manders, T. R., Eberle, S. E., Su, C., D'Amour, J., Yang, R., et al. (2015). Activation of corticostriatal circuitry relieves chronic neuropathic pain. *J. Neurosci.* 35, 5247–5259. doi: 10.1523/JNEUROSCI.3494-14.2015

Li, M. J., Liu, L. Y., Chen, L., Cai, J., Wan, Y., and Xing, G. G. (2017). Chronic stress exacerbates neuropathic pain via the integration of stress-affect-related information with nociceptive information in the central nucleus of the amygdala. *Pain* 158, 717–739. doi: 10.1097/j.pain.0000000000000827

Li, S. G., Wang, J. Y., and Luo, F. (2012). Adult-age inflammatory pain experience enhances long-term pain vigilance in rats. *PLoS One* 7:e36767. doi: 10.1371/journal.pone.0036767

Lidow, M. S. (2002). Long-term effects of neonatal pain on nociceptive systems. *Pain* 99, 377–383. doi: 10.1016/s0304-3959(02)00258-0

Lim, M., Kim, J. S., Kim, D. J., and Chung, C. K. (2016). Increased low- and high-frequency oscillatory activity in the prefrontal cortex of fibromyalgia patients. *Front. Hum. Neurosci.* 10:111. doi: 10.3389/fnhum.2016.00111

Lin, C. S. (2014). Brain signature of chronic orofacial pain: a systematic review and meta-analysis on neuroimaging research of trigeminal neuropathic pain and temporomandibular joint disorders. *PLoS One* 9:e94300. doi: 10.1371/journal.pone.0094300

Luo, H., Cheng, J., Han, J. S., and Wan, Y. (2004). Change of vanilloid receptor 1 expression in dorsal root ganglion and spinal dorsal horn during inflammatory nociception induced by complete Freund's adjuvant in rats. *Neuroreport* 15, 655–658. doi: 10.1097/00001756-200403220-00016

Metz, A. E., Yau, H. J., Centeno, M. V., Apkarian, A. V., and Martina, M. (2009). Morphological and functional reorganization of rat medial prefrontal cortex in neuropathic pain. *Proc. Natl. Acad. Sci. U S A* 106, 2423–2428. doi: 10.1073/pnas.0809897106

Moench, K. M., and Wellman, C. L. (2015). Stress-induced alterations in prefrontal dendritic spines: implications for post-traumatic stress disorder. *Neurosci. Lett.* 601, 41–45. doi: 10.1016/j.neulet.2014.12.035

Navratilova, E., Atcherley, C. W., and Porreca, F. (2015). Brain circuits encoding reward from pain relief. *Trends Neurosci.* 38, 741–750. doi: 10.1016/j.tins.2015.09.003

Negrón-Oyarzo, I., Pérez, M. A., Terreros, G., Muñoz, P., and Dagnino-Subiabre, A. (2014). Effects of chronic stress in adolescence on learned fear, anxiety and synaptic transmission in the rat prelimbic cortex. *Behav. Brain Res.* 259, 342–353. doi: 10.1016/j.bbr.2013.11.001

Obata, K., and Noguchi, K. (2004). MAPK activation in nociceptive neurons and pain hypersensitivity. *Life Sci.* 74, 2643–2653. doi: 10.1016/j.lfs.2004.01.007

Obermann, M., Nebel, K., Schumann, C., Holle, D., Gizewski, E. R., Maschke, M., et al. (2009). Gray matter changes related to chronic posttraumatic headache. *Neurology* 73, 978–983. doi: 10.1212/WNL.0b013e3181b8791a

Pochwat, B., Rafalo-Ulinska, A., Domin, H., Misztak, P., Nowak, G., and Szewczyk, B. (2017). Involvement of extracellular signal-regulated kinase (ERK) in the short and long-lasting antidepressant-like activity of NMDA receptor antagonists (zinc and Ro 25–6981) in the forced swim test in rats. *Neuropharmacology* 125, 333–342. doi: 10.1016/j.neuropharm.2017.08.006

Pucilowska, J., Puzerey, P. A., Karlo, J. C., Galán, R. F., and Landreth, G. E. (2012). Disrupted ERK signaling during cortical development leads to abnormal progenitor proliferation, neuronal and network excitability and behavior, modeling human neuro-cardio-facial-cutaneous and related syndromes. *J. Neurosci.* 32, 8663–8677. doi: 10.1523/JNEUROSCI.1107-12.2012

Ren, K., Anseloni, V., Zou, S. P., Wade, E. B., Novikova, S. I., Ennis, M., et al. (2004). Characterization of basal and re-inflammation-associated long-term alteration in pain responsivity following short-lasting neonatal local inflammatory insult. *Pain* 110, 588–596. doi: 10.1016/j.pain.2004.04.006

Rodriguez-Raecke, R., Niemeier, A., Ihle, K., Ruether, W., and May, A. (2009). Brain gray matter decrease in chronic pain is the consequence and not the cause of pain. *J. Neurosci.* 29, 13746–13750. doi: 10.1523/JNEUROSCI.3687-09.2009

Saffari, R., Teng, Z., Zhang, M., Kravchenko, M., Hohoff, C., Ambrée, O., et al. (2016). NPY^{+}-, but not PV^{+}-GABAergic neurons mediated long-range inhibition from infra- to prelimbic cortex. *Transl. Psychiatry* 6:e736. doi: 10.1038/tp.2016.7

Seger, R., and Krebs, E. G. (1995). The MAPK signaling cascade. *FASEB J.* 9, 726–735. doi: 10.1096/fasebj.9.9.7601337

Seminowicz, D. A., Laferriere, A. L., Millecamps, M., Yu, J. S., Coderre, T. J., and Bushnell, M. C. (2009). MRI structural brain changes associated with

sensory and emotional function in a rat model of long-term neuropathic pain. *Neuroimage* 47, 1007–1014. doi: 10.1016/j.neuroimage.2009.05.068

Seminowicz, D. A., Shpaner, M., Keaser, M. L., Krauthamer, G. M., Mantegna, J., Dumas, J. A., et al. (2013). Cognitive-behavioral therapy increases prefrontal cortex gray matter in patients with chronic pain. *J. Pain* 14, 1573–1584. doi: 10.1016/j.jpain.2013.07.020

Seminowicz, D. A., Wideman, T. H., Naso, L., Hatami-Khoroushahi, Z., Fallatah, S., Ware, M. A., et al. (2011). Effective treatment of chronic low back pain in humans reverses abnormal brain anatomy and function. *J. Neurosci.* 31, 7540–7550. doi: 10.1523/JNEUROSCI.5280-10.2011

Seo, J. S., Wei, J., Qin, L., Kim, Y., Yan, Z., and Greengard, P. (2017). Cellular and molecular basis for stress-induced depression. *Mol. Psychiatry* 22, 1440–1447. doi: 10.1038/mp.2016.118

Sherrin, T., Blank, T., and Todorovic, C. (2011). c-Jun N-terminal kinases in memory and synaptic plasticity. *Rev. Neurosci.* 22, 403–410. doi: 10.1515/RNS.2011.032

Shibata, M., Ohkubo, T., Takahashi, H., and Inoki, R. (1989). Modified formalin test: characteristic biphasic pain response. *Pain* 38, 347–352. doi: 10.1016/0304-3959(89)90222-4

Soliman, A. C., Yu, J. S., and Coderre, T. J. (2005). mGlu and NMDA receptor contributions to capsaicin-induced thermal and mechanical hypersensitivity. *Neuropharmacology* 48, 325–332. doi: 10.1016/j.neuropharm.2004.10.014

Toyoda, H., Zhao, M. G., Xu, H., Wu, L. J., Ren, M., and Zhuo, M. (2007). Requirement of extracellular signal-regulated kinase/mitogen-activated protein kinase for long-term potentiation in adult mouse anterior cingulate cortex. *Mol. Pain* 3:36. doi: 10.1186/1744-8069-3-36

Umana, I. C., Daniele, C. A., Miller, B. A., Abburi, C., Gallagher, K., Brown, M. A., et al. (2017). Nicotinic modulation of descending pain control circuitry. *Pain* 158, 1938–1950. doi: 10.1097/j.pain.0000000000000993

Vaccarino, A. L., and Melzack, R. (1992). Temporal processes of formalin pain: differential role of the cingulum bundle, fornix pathway and medial bulboreticular formation. *Pain* 49, 257–271. doi: 10.1016/0304-3959(92)90150-a

Vachon-Presseau, E., Tetreault, P., Petre, B., Huang, L., Berger, S. E., Torbey, S., et al. (2016). Corticolimbic anatomical characteristics predetermine risk for chronic pain. *Brain* 139, 1958–1970. doi: 10.1093/brain/aww100

Wang, G. Q., Cen, C., Li, C., Cao, S., Wang, N., Zhou, Z., et al. (2015). Deactivation of excitatory neurons in the prelimbic cortex via Cdk5 promotes pain sensation and anxiety. *Nat. Commun.* 6:7660. doi: 10.1038/ncomms8660

Wegner, A., Elsenbruch, S., Rebernik, L., Roderigo, T., Engelbrecht, E., Jager, M., et al. (2015). Inflammation-induced pain sensitization in men and women: does sex matter in experimental endotoxemia? *Pain* 156, 1954–1964. doi: 10.1097/j.pain.0000000000000256

Widmann, C., Gibson, S., Jarpe, M. B., and Johnson, G. L. (1999). Mitogen-activated protein kinase: conservation of a three-kinase module from yeast to human. *Physiol. Rev.* 79, 143–180. doi: 10.1152/physrev.1999.79.1.143

Wu, X. B., Liang, B., and Gao, Y. J. (2016). The increase of intrinsic excitability of layer V pyramidal cells in the prelimbic medial prefrontal cortex of adult mice after peripheral inflammation. *Neurosci. Lett.* 611, 40–45. doi: 10.1016/j.neulet.2015.11.030

Wynne, P. (2006). p38 mitogen-activated protein kinase: a novel modulator of hyperpolarization-activated cyclic nucleotide-gated channels and neuronal excitability. *J. Neurosci.* 26, 11253–11254. doi: 10.1523/jneurosci.3852-06.2006

Yi, M., and Zhang, H. (2011). Nociceptive memory in the brain: cortical mechanisms of chronic pain. *J. Neurosci.* 31, 13343–13345. doi: 10.1523/JNEUROSCI.3279-11.2011

Yi, M., Zhang, H., Lao, L., Xing, G. G., and Wan, Y. (2011). Anterior cingulate cortex is crucial for contra- but not ipsi-lateral electro-acupuncture in the formalin-induced inflammatory pain model of rats. *Mol. Pain* 7:61. doi: 10.1186/1744-8069-7-61

Yu, R., Gollub, R. L., Spaeth, R., Napadow, V., Wasan, A., and Kong, J. (2014). Disrupted functional connectivity of the periaqueductal gray in chronic low back pain. *Neuroimage Clin.* 6, 100–108. doi: 10.1016/j.nicl.2014.08.019

Yu, L., Yang, F., Luo, H., Liu, F. Y., Han, J. S., Xing, G. G., et al. (2008). The role of TRPV1 in different subtypes of dorsal root ganglion neurons in rat chronic inflammatory nociception induced by complete Freund's adjuvant. *Mol. Pain* 4:61. doi: 10.1186/1744-8069-4-61

Yue, L., Ma, L. Y., Cui, S., Liu, F. Y., Yi, M., and Wan, Y. (2017). Brain-derived neurotrophic factor in the infralimbic cortex alleviates inflammatory pain. *Neurosci. Lett.* 655, 7–13. doi: 10.1016/j.neulet.2017.06.028

Zhang, Y., Cai, G., Ni, X., and Sun, J. (2007). The role of ERK activation in the neuronal excitability in the chronically compressed dorsal root ganglia. *Neurosci. Lett.* 419, 153–157. doi: 10.1016/j.neulet.2007.04.040

Zhang, C., Chen, R. X., Zhang, Y., Wang, J., Liu, F. Y., Cai, J., et al. (2017). Reduced GABAergic transmission in the ventrobasal thalamus contributes to thermal hyperalgesia in chronic inflammatory pain. *Sci. Rep.* 7:41439. doi: 10.1038/srep41439

Zhang, Y., Jiang, Y. Y., Shao, S., Zhang, C., Liu, F. Y., Wan, Y., et al. (2017). Inhibiting medial septal cholinergic neurons with DREADD alleviated anxiety-like behaviors in mice. *Neurosci. Lett.* 638, 139–144. doi: 10.1016/j.neulet.2016.12.010

Zhang, Y., Liu, F. Y., Liao, F. F., Wan, Y., and Yi, M. (2014). Exacerbation of tonic but not phasic pain by entorhinal cortex lesions. *Neurosci. Lett.* 581, 137–142. doi: 10.1016/j.neulet.2014.05.015

Zhang, M., Liu, J., Zhou, M. M., Wu, H., Hou, Y., Li, Y. F., et al. (2016). Elevated neurosteroids in the lateral thalamus relieve neuropathic pain in rats with spared nerve injury. *Neurosci. Bull.* 32, 311–322. doi: 10.1007/s12264-016-0044-7

Zhang, M., Liu, J., Zhou, M. M., Wu, H., Hou, Y., Li, Y. F., et al. (2017). Anxiolytic effects of hippocampal neurosteroids in normal and neuropathic rats with spared nerve injury. *J. Neurochem.* 141, 137–150. doi: 10.1111/jnc.13965

Zheng, J., Jiang, Y. Y., Xu, L. C., Ma, L. Y., Liu, F. Y., Cui, S., et al. (2017). Adult hippocampal neurogenesis along the dorsoventral axis contributes differentially to environmental enrichment combined with voluntary exercise in alleviating chronic inflammatory pain in mice. *J. Neurosci.* 37, 4145–4157. doi: 10.1523/JNEUROSCI.3333-16.2017

Zhuang, Z. Y., Gerner, P., Woolf, C. J., and Ji, R. R. (2005). ERK is sequentially activated in neurons, microglia and astrocytes by spinal nerve ligation and contributes to mechanical allodynia in this neuropathic pain model. *Pain* 114, 149–159. doi: 10.1016/j.pain.2004.12.022

Zhuo, M. (2016). Contribution of synaptic plasticity in the insular cortex to chronic pain. *Neuroscience* 338, 220–229. doi: 10.1016/j.neuroscience.2016.08.014

Conflict of Interest Statement: The authors declare that the research was conducted in the absence of any commercial or financial relationships that could be construed as a potential conflict of interest.

frontiers in Molecular Neuroscience

ORIGINAL RESEARCH
published: 27 September 2021
doi: 10.3389/fnmol.2021.720973

PRDM12 Is Transcriptionally Active and Required for Nociceptor Function Throughout Life

*Tomislav Kokotović [1,2,3], Michiel Langeslag [4,5,6], Ewelina M. Lenartowicz [1,3], John Manion [7], Christopher W. Fell [1,2,3], Elham Alehabib [8], Abbas Tafakhori [9], Hossein Darvish [10], Eric J. Bellefroid [11], G. Gregory Neely [7], Michaela Kress [4], Josef M. Penninger [12,13] and Vanja Nagy [1,2,3]**

[1] Ludwig Boltzmann Institute for Rare and Undiagnosed Diseases, Vienna, Austria, [2] CeMM Research Center for Molecular Medicine of the Austrian Academy of Sciences, Vienna, Austria, [3] Department of Neurology, Medical University of Vienna, Vienna, Austria, [4] Department of Physiology and Medical Physics, Institute of Physiology, Medical University of Innsbruck, Innsbruck, Austria, [5] Institute of Pharmacy and Center for Molecular Biosciences Innsbruck (CMBI), University of Innsbruck, Innsbruck, Austria, [6] Department of Pharmacology, Medical University of Innsbruck, Innsbruck, Austria, [7] Charles Perkins Centre, Dr. John and Anne Chong Lab for Functional Genomics, Centenary Institute, and School of Life and Environmental Sciences, University of Sydney, Camperdown, NSW, Australia, [8] Student Research Committee, Department of Medical Genetics, School of Medicine, Shahid Beheshti University of Medical Sciences, Tehran, Iran, [9] Iranian Center of Neurological Research, Neuroscience Institute, Tehran University of Medical Sciences, Tehran, Iran, [10] Neuroscience Research Center, Faculty of Medicine, Golestan University of Medical Sciences, Gorgan, Iran, [11] ULB Neuroscience Institute (UNI), Université Libre de Bruxelles (ULB), Gosselies, Belgium, [12] Institute of Molecular Biotechnology of the Austrian Academy of Sciences, VBC – Vienna BioCenter, Vienna, Austria, [13] Department of Medical Genetics, Life Science Institute, University of British Columbia, Vancouver, BC, Canada*

OPEN ACCESS

Edited by:
Cyril Goudet, INSERM U1191 Institut de Génomique Fonctionnelle (IGF), France

Reviewed by:
Fabien Marchand, INSERM U1107 Douleur et Biophysique Neurosensorielle (Neuro-Dol), France
Erin E. Young, University of Kansas Medical Center, United States

***Correspondence:**
Vanja Nagy
vanja.nagy@rud.lbg.ac.at

Specialty section:
This article was submitted to Pain Mechanisms and Modulators, a section of the journal Frontiers in Molecular Neuroscience

Received: *05 June 2021*
Accepted: *20 August 2021*
Published: *27 September 2021*

Citation:
Kokotović T, Langeslag M, Lenartowicz EM, Manion J, Fell CW, Alehabib E, Tafakhori A, Darvish H, Bellefroid EJ, Neely GG, Kress M, Penninger JM and Nagy V (2021) PRDM12 Is Transcriptionally Active and Required for Nociceptor Function Throughout Life. Front. Mol. Neurosci. 14:720973. doi: 10.3389/fnmol.2021.720973

PR domain-containing member 12 (PRDM12) is a key developmental transcription factor in sensory neuronal specification and survival. Patients with rare deleterious variants in *PRDM12* are born with congenital insensitivity to pain (CIP) due to the complete absence of a subtype of peripheral neurons that detect pain. In this paper, we report two additional CIP cases with a novel homozygous *PRDM12* variant. To elucidate the function of PRDM12 during mammalian development and adulthood, we generated temporal and spatial conditional mouse models. We find that PRDM12 is expressed throughout the adult nervous system. We observed that loss of PRDM12 during mid-sensory neurogenesis but not in the adult leads to reduced survival. Comparing cellular biophysical nociceptive properties in developmental and adult-onset PRDM12 deletion mouse models, we find that PRDM12 is necessary for proper nociceptive responses throughout life. However, we find that PRDM12 regulates distinct age-dependent transcriptional programs. Together, our results implicate PRDM12 as a viable therapeutic target for specific pain therapies even in adults.

Keywords: ***Prdm12*, *TRPV1*, capsaicin, pain, nociception, CIP, dorsal root ganglia**

INTRODUCTION

Congenital insensitivity to pain (CIP), a subtype of hereditary sensory and autonomic neuropathies (HSAN), primarily affects the peripheral nervous system (PNS). Recently, mutations in methyltransferase PR domain-containing member 12 (PRDM12) have been demonstrated to cause CIP, which based on clinical symptoms was subtyped as HSAN type VIII (OMIM 616488) (Chen et al., 2015). PRDM12 belongs to a large family of transcription factors responsible for cell fate

decisions (Hohenauer and Moore, 2012). At present, there are 24 reported patients with PRDM12-CIP, including the complete absence of all modalities of acute and chronic pain perception, frequently accidental or self-inflicted injuries, frequent bone fractures, the absence of corneal reflex and impaired tear production, and skin ulcerations and recurrent bacterial infections often requiring amputations. Unlike the association of CIP syndromes with other genes, such as nerve growth factor beta (*NGFβ*), a very few PRDM12-CIP patients present with central nervous system (CNS) symptoms, such as intellectual disability (ID) (Chen et al., 2015; Imhof et al., 2020). Skin biopsies of patients revealed the absence of protein gene product 9.5- (PGP9.5) reactive nerve fiber endings in the epidermis, suggesting the participation of PRDM12 in nociceptor development or the survival in humans (Chen et al., 2015).

Nociceptors are pseudounipolar primary afferent sensory neurons in the PNS that detect noxious, potentially tissue-damaging, and painful stimuli. Their somata reside in the dorsal root ganglia (DRG) and trigeminal ganglion, with one axonal process in the periphery and one that synapses in the spinal cord (SC) or brain stem. Nociceptors express a variety of specialized noxious stimuli receptors for their function. These include transient receptor potential (TRP) cation channels, including TRPV1 and TRPA1 activated by capsaicin (Caterina et al., 1997) or noxious cold or electrophilic chemicals such as allyl isothiocyanate and cinnamaldehyde (Bandell et al., 2004; Julius, 2013). Additionally, potentially tissue-damaging temperatures are detected by a variety of voltage-gated Na^+ channels, including $Na_v1.7$, $Na_v1.8$, and $Na_v1.9$. Indeed, deleterious variants in genes encoding for $Na_v1.7$ (*SCN9A*) and $Na_v1.9$ (*SCN11A*) were also identified to be causative for a type of CIP (OMIM 243000 and OMIM 615548, respectively). Strong noxious stimulation of nociceptors will trigger afferent action potentials (APs) that send nociceptive signals to the CNS to induce the conscious sensation of pain.

PR domain-containing member 12 had no intrinsic enzymatic activity and was reported to recruit euchromatic histone-lysine N-methyltransferase 2 (EHMT2), also known as G9a, for the trimethylation of histone 3 lysine 9 (H3K9me3) resulting in subsequent regulation of target genes (Yang and Shinkai, 2013; Matsukawa et al., 2015). Detailed studies on *Danio rerio*, *Xenopus laevis,* and *Drosophila melanogaster* demonstrated that PRDM12 regulates a transcriptional program critical in cell fate decisions during early sensory neuronal development required for the specification and function of nociceptors (Matsukawa et al., 2015; Nagy et al., 2015; Thelie et al., 2015). Reduction of Hamlet, an ortholog of *PRDM12*, in *D. melanogaster* sensory neurons caused reduced nociceptive responses to noxious heat in fly embryos, a phenotype that could not be rescued by reconstitution with human *PRDM12* disease-causing variants, providing evidence of the contribution of variants to pathology (Nagy et al., 2015).

In mammals, embryonic mouse studies demonstrated that PRDM12 is expressed in DRGs and is necessary for the initiation and maintenance of an NGF-β receptor, neurotrophic receptor tyrosine kinase 1 (TrkA), by modulating neurogenins 1 and 2 (Ngn1 and Ngn2) activity, thereby promoting nociceptive lineage from neural crest cell progenitors (Kinameri et al., 2008; Bartesaghi et al., 2019; Desiderio et al., 2019). Correspondingly, the analysis of DRG from constitutive knock-out (KO, $Prdm12^{-/-}$) mice revealed a significant reduction in DRG size, decreased density of cutaneous myelinated sensory branches and the absence of nociceptor-specific markers, all suggesting the absence of nociceptors (Bartesaghi et al., 2019; Desiderio et al., 2019). This specific reduction in nociceptor lineage seems to be a result of a proliferation defect during neurogenesis (Bartesaghi et al., 2019; Landy et al., 2021), however, an increase in apoptotic cell death with no change in proliferation was also reported (Bartesaghi et al., 2019; Desiderio et al., 2019). Constitutive embryonic PRDM12 deficiency resulted in early neonatal death suggesting that in mice, unlike humans, PRDM12 function is essential for survival (Bartesaghi et al., 2019; Desiderio et al., 2019).

Here, we aim to understand the functional role of PRDM12 in nociception in the mammal system. We first present two patients from a large consanguineous family with typical CIP symptoms, including the complete absence of pain perception, confirmed to have a previously unreported homozygous variant in *PRDM12*. To clarify the role played by PRDM12 in pain perception, we developed several different mouse models. To model human patient variants, we generated a mouse model with the previously reported CIP W160C PRDM12 single base-pair mutation ($Prdm12^{W160C}$) and S159AfsTer2 ($Prdm12^{S159AFsTer2}$) using clustered regularly interspaced short palindromic repeats- (CRISPR-) associated system 9 (Cas9) genome editing (Chen et al., 2015; Nagy et al., 2015). We additionally generated conditional mouse mutants, and therefore crossed $Prdm12^{fl/fl}$ to *Sox10-Cre* ($Prdm12^{fl/fl}$; *Sox10-Cre*) to ablate PRDM12 expression in the neural crest cell population during embryonic development, to *Avil-Cre* ($Prdm12^{fl/fl}$; *Avil-Cre*) to ablate PRDM12 expression in the developing DRG and to tamoxifen- (TAM-) inducible *Rosa26-CreER*^{T2} mice ($Prdm12^{fl/fl}$; *Rosa26-CreER*^{T2}) to be able to induce whole-body PRDM12 KOs in adults. To combine genetic, cellular, electrophysiological, and molecular approaches, we were able to ascertain that PRDM12 is critical for survival and functional nociception in mice. Additionally, we were able to delineate the transcriptional program regulated by PRDM12, in developing and adult mammalian systems containing both core-PRDM12 regulated genes and those that are age-specific.

MATERIALS AND METHODS

Patients and Whole-Exome Sequencing

Following informed consent and approval from patients and participating relatives, all procedures were performed. The procedures are in accordance with the ethical standards and approval of the Shahid Beheshti University of Medical Sciences ethics board and with the current update of the Declaration of Helsinki.

Whole-exome sequencing (WES) was performed at the Biomedical Sequencing Facility (BSF) in CeMM Center for Molecular Medicine of the Austrian Academy of Sciences (CeMM). Briefly, genomic DNA was extracted from the whole blood of patients, parents, and participating siblings using

the QIAamp DNA Mini Kit (Qiagen, Hilden, Germany). The quantity and quality of DNA from index patient 1 were assessed by the Qubit 2.0 Fluorometric Quantitation system (Life Technologies, Carlsbad, CA, USA). Libraries were prepared using the Nextera DNA Flex Exome Library Prep Kit (Illumina, San Diego, CA, USA). Briefly, genomic DNA was tagmented, size-selected, and amplified followed by the two rounds of hybridization with biotinilated baits and capturing with streptavidin-conjugated magnetic beads. After enrichment, library fragments represented in the total 45 Mb coding region were amplified and size-selected. Final library pools were quality controlled and sequenced on a HiSeq 3000 instrument (Illumina, San Diego, CA, USA) using 75-bp paired-end chemistry. DNA sequences were mapped to GRCh37 (hg19) version of a human reference genome using a Burrows–Wheeler Aligner with default parameters. Single-nucleotide variants (SNVs) and indels were annotated with SNPEff (Cingolani et al., 2012), Combined Annotation Dependent Depletion (CADD; Kircher et al., 2014), the single-nucleotide polymorphism database (dbSNP; Sherry et al., 2001), the genome aggregation database (gnomAD; https://gnomad.broadinstitute.org/) (Karczewski et al., 2020), and ClinVar (Landrum et al., 2018) data. Subsequent filtering of the remaining variants of interest was based on a homozygous inheritance pattern, a variant type, the population frequency, and the gene lists of interest in relation to the symptoms of the patient. Further, the segregation analysis was performed in patient 2, as well as in both sets of parents and participating siblings by the conventional Sanger sequencing.

Animals

Prdm12^{W160} experiments were approved by the University of Sydney Animal Ethics Committee under the animal ethics protocol (938), and the reporting complies with the animals in research: reporting *in vivo* experiments (ARRIVE) guidelines. Experimentation protocols comply with National Health and Medical Research Council (NHMRC) guidelines. Mice were housed in specific pathogen-free facilities at Australian BioResources, The Charles Perkins Centre and the Medical Foundation Building at the University of Sydney, Australia. *Prdm12*^{W160} mice were generated by CRISPR Cas9-mediated genome editing and were confirmed by the Sanger sequencing using the following primers: forward primer 5′-CTGCTTGGGAGTCTCTTAGAGAG-3′; reverse primer 5′-ATACAGCTGAACGAGGGTGA-3′; and sequencing primer (forward) 5′- TGACTCTCTATTGATCTTTTGCTTC-3′.

Prdm12$^{-/-}$ or *Prdm12*$^{fl/fl}$ mice were generated on C57BL/6 background using the promoter-driven knockout-first gene trap technique with En2SA-IRES-LacZ cassette in first intron and loxP sites around the second exon as described previously (Desiderio et al., 2019). Female mice carrying an conditional allele were crossed to *Advillin-Cre* or *Rosa26-Cre-ER*^{T2} male mice to generate corresponding developmental or TAM-inducible *Prdm12* conditional knockout offspring. Both *Prdm12*$^{fl/fl}$; *Rosa26-CreER*$^{T2+}$ and their *Prdm12*$^{fl/fl}$; *Rosa26-CreER*$^{T2-}$ littermates received 80 mg/kg intraperitoneal injections of TAM (Sigma-Aldrich, St. Louis, MO, USA) once per day for 4 consecutive days. TAM-injections were carried out at the age of 8 weeks, and animals were then tested 3 weeks following injections. TAM-injected *Prdm12*$^{fl/fl}$; *Rosa26-CreER*$^{T2-}$ animals are referred to as "controls." These mice were housed at the Animal Facility of the Medical University of Vienna, and Comparative Medicine Mousehouse Vienna Biocenter, Vienna, Austria. All mice were maintained at a 12-h light/dark cycle and provided with food and water *ad libitum*. Experiments were approved by the Bundesministerium fur Wissenschaft, Forschung und Wirtschaft (BMWFW-66.015/0011-WF/V/3b/2017) and were carried out according to EU-directive 2010/63/EU. Genotyping was determined using the primers as follows: for *Cre*, forward primer 5′-GCTCGACCAGTTTAGTTACCC-3′, reverse primer 5′-TCGCGATTATCTTCTATATCTTCAG-3′; for *Prdm12* forward primer 5′-GCTGATCGAGTCCAGGAGAC-3′, reverse primer 5′-CCAAACATCCACAACCTTCA-3′. Select animals in each cohort were confirmed by qRT-PCR of DRG or whole brain (WB) tissue.

Western Blotting

Tissue samples were collected in an RIPA (Sigma-Aldrich, St. Louis, MO, USA) buffer with Proteinase and Phosphatase inhibitor cocktail (Thermo Fischer Scientific, Waltham, MA USA) and homogenized using a Precellys 24 Tissue Homogenizer (Bertin Instruments, Frankfurt, Germany, 3 s × 20 s, 5,000 rpm). Protein concentration was measured using the Bradford assay (Bio-Rad, Hercules, CA, USA). Laemmli buffer- (Sigma-Aldrich, St. Louis, MO, USA) treated samples with standardized concentration of 1 μg/μl were incubated at 95°C for 5 min. About 25 μg of protein per lane was loaded on a 10% polyacrylic acid (PAA) gel, followed by protein transfer to a methanol-activated poly vinylidene fluoride (PVDF) membrane (GE Healthcare Life Sciences, Marlborough, MA, USA) for 10 h at 4°C with a constant current of 0.12 A. The membrane was then blocked with 5% bovine serum albumin (BSA) in TBS-T (0.01% Tween 20) for 1 h at room temperature (RT). Anti-PRDM12 (1:500, Santa Cruz, sc-130242) and loading control anti-HSP90α/β (1:1000, Santa Cruz, sc-13119) primary antibodies were incubated for 12 h at 4°C, followed by 1 h of incubation at RT with anti-mouse horseradish peroxidase- (HRP-) conjugated secondary antibody (1:30000, Sigma-Aldrich, St. Louis, MO, USA; GENA931). To control e specificity of the anti-PRDM12 antibody, human embryonic kidney (HEK) cell lysates overexpressing complementary DNA (cDNA) of human wild type (WT) PRDM12 (PRDM12^{WT}) as a positive control or CIP-causing PRDM12 variant PRDM12^{S58fs} previously determined (Nagy et al., 2015) not to have a protein product, as a negative control were run alongside tissue lysates as labeled. The signal was visualized using a chemiluminescent reagent (ECL, GE Healthcare Life Sciences, Marlborough, MA, USA) and imaged using the ChemiDoc Imaging System (Bio-Rad, Hercules, CA, USA).

Immunohistochemistry

Lumbar DRG from WT mice were dissected into ice cold phosphate-buffered saline (PBS), fixed in 4% formaldehyde for 20 min, and washed with PBS. Following cryopreservation in 30% sucrose, 20-μm sections were cut on a Microm Cryostat (HM560,

Microm) at the Histopathology Service Facility in the Vienna Biocenter Core Facilities (VBCF), the member of the Vienna Biocenter (VBC), Austria, and stored in −80°C until needed. PBS hydrated tissue was permeabilized with 0.5% TritonX-PBS for 15 min and blocked for 1 h at RT with blocking buffer 10% normal goat serum in 0.25% TritonX-PBS. Following 2 × 3 min washes in 0.1% Tween20-PBS, the sections were incubated for 1 h at RT with goat F(ab) anti-mouse IgG (1:2000, Abcam, ab6668, Cambridge, UK) in 0.1% Tween20-PBS. Primary antibodies raised against IB4 (1:1000, Thermo Fisher, I21412, Waltham, MA, USA), $Na_v1.8$ (1:200, Sigma-Aldrich Handels GmbH, Vienna, Austria, S2071), TrkA (1:200, GeneTex GTX54856, Irvine, CA, USA), or CGRP (1:500, Millipore, Burlington, MA, USA), with Guinea pig polyclonal anti-PRDM12 (1:10,000, clone 910) (Desiderio et al., 2019), diluted in a blocking buffer were incubated O/N at 4°C. Following 3 × 3 min washes in 0.01% TritonX-PBS, appropriate secondary antibodies (1:500 goat anti-mouse or anti-rabbit Alexa Fluor 488 or 546, Invitrogen, Waltham, MA, USA) diluted in 0.01% TritonX-PBS were incubated for 1 h at RT. Finally, following 3 × 3 min washes in 0.01% TritonX-PBS, the sections were mounted and imaged on the Zeiss LSM780 confocal microscope.

Skin biopsies were collected from hind paws, and flattened and fixed in 4% formaldehyde in PBS O/N at 4°C. Following cryopreservation in 30% sucrose, 20-μm sections were prepared as described above and stored at −80°C. Tissue was hydrated in PBS, incubated in 50 mM glycine/PBS for 1 h at RT, and blocked with 10% normal goat serum and 1% BSA in 0.1% TritonX-PBS. The sections were then incubated at 4°C O/N with a primary antibody raised against PGP9.5 (1:200, Zytomed 516-3344, Berlin, Germany) in blocking buffer. The sections were washed 3 × 3 min in 0.01% TritonX/PBS, followed by appropriate secondary antibody and nuclear label DAPI (1:2000, Carl Roth, Karlsruhe, Germany) in 0.01% TritonX-PBS and incubated for 1 h at RT. Following 3 × 3 min washes with 0.01% TritonX-PBS, the sections were mounted and imaged as mentioned earlier.

Behavioral Assays

Behavioral assays were performed on both male and female mice at 8–15 weeks of age separated by at least 24 h between the tests to reduce handling stress. Experimenter was blind to the genotype of the test subjects.

Intraplantar capsaicin injections: about 1 μg of capsaicin (Sigma, St. Louis, MO, USA) diluted in 15 μl of normal saline was injected intraplantar in the hind paw of the animal. The animal was then observed for a total of 5 min, which is the time for the duration of reaction to the injection. Counted reactions included licking, shaking, or lifting of the injected paw. At the completion of 5 min, the animal was returned to its home cage. $Prdm12^{fl/fl}$; $Avil\text{-}Cre^{+}$ $N = 33$ was compared to the corresponding control littermates; and $N = 26$ of $Prdm12^{fl/fl}$; $Rosa26\text{-}CreER^{T2+}$ to $N = 35$ of their corresponding control littermates.

Von frey test: the measurements were performed according to Lau et al. (2019). Briefly, mice were habituated on 3 separate days and then tested three times with filaments ranging from 0.04 to 2 g with 10 applications per filament.

The Hargreaves test: mice were habituated on 3 separate days and then tested on 3 consecutive days with a low and a high input resistance (IR) intensity. The number of test animals in both von Frey and Hargraves assays was $N = 16$, compared to $N = 18$ of littermate controls.

Open-field test (*OFT*) was performed by the Preclinical Phenotyping Facility at the VBCF, the member of the Vienna Biocenter (pcPHENO, VBCF), Austria. Briefly, mice were placed in a 28 × 28 cm gray, plexi-glass arena and allowed to freely explore for 5 min. Time spent in the center or along the walls of the arena, as well as the distance traveled during exploration, were measured using an automated activity system (TSE-Systems, Bad Homburg, Germany). Reluctance to enter the center of the arena as compared to controls was scored and interpreted as the levels of anxiety. Distance traveled during the test was compared to controls and used as a readout for locomotion deficits.

Morris water maze: mice were trained in the Morris water maze (pcPHENO, VBCF) as described previously (Nagy et al., 2019). Briefly, mice were trained for two sessions a day, with four trials per session, using alternating entry points in different quadrants for each trial. Mice were video tracked using the software Topscan 3.0 (Cleversys, Inc., Reston, VA, USA). On day 1, the visual capacity of the mice was checked by making the platform visible with a black flag and letting the mice explore the pool for 1 min or until they reached the platform (data not shown). Short-term memory test was performed after the last trial, on days 8 and 11 to test for long-term memory. The time spent on searching the target quadrant and target zone (exact location of the platform) was recorded and used as a readout for memory. For both, OFT and Morris water maze $N = 8$ of $Prdm12^{fl/fl}$; $Rosa26\text{-}CreER^{T2+}$ were compared to $N = 12$ of their corresponding control littermates.

Micro CT Imaging

For microscopic x-ray imaging, samples were contrasted with IKI (Lugol's iodine solution) (Metscher, 2009) and mounted in an aqueous medium (Metscher, 2011). MicroCT images were acquired using the Xradia MicroXCT system (www.zeiss.com/microscopy/int/x-ray.html) in the Theoretical Biology Department at the University of Vienna. Scans were made with the source settings of 60 kVp at 133 μA and source-sample-detector distances chosen to optimize the field of view for the sample. Tomographic slices were reconstructed using the Xradia XMReconstructor software and saved as TIFF image stacks with an isotropic voxel size of 7.5 μm. The segmentation and processing of images were performed manually using Amira Software 6.4.

Single-Cell Electrophysiology

Sensory neuron culture: lumbar DRG were harvested from adult mice (age > 8 weeks) as discussed in previous publications (Langeslag et al., 2014; Namer et al., 2017). The sensory neurons were plated on glass coverslips coated with poly-L-lysine/laminin-1 (Sigma-Aldrich, Merck, Burlington, MA, USA) and cultivated in supplemented neruronal culture media (TNB) (Biochrom) containing 25 ng/ml mNGF 2.5S (Alomone Labs,

Jerusalem, Israel) at 37°C and 5% CO_2 in a humidified incubator for 16–24 h.

Cultured sensory neurons were used for electrophysiological experiments 16–24 h after seeding. Only DRG neurons with size smaller than <35 μm were selected, representing the small- to medium-sized neurons. Glass coverslips were mounted in a recording chamber and placed on a Zeiss Axiovert 200 microscope. All measurements were recorded with an EPC 10 and the Patchmaster v2.73 software (HEKA) at RT. For more details on the methodology for single-cell recordings, please see **Supplementary Materials**.

From the isolated sensory neurons, cellular voltage and current recordings were performed in a whole-cell patch-clamp configuration. The DRG neurons were kept in extracellular solution (ECS) containing (in mM); NaCl (150), KCl (5), $CaCl_2$ (2), $MgCl_2$ (1), HEPES (10), glucose (10), and the pH was set to 7.3 with NaOH. Borosilicate glass pipettes (Science Products) were pulled with a horizontal puller (P-97, Sutter Instrument Company, Novato, CA, USA) and filled with intracellular solution (ICS) containing (in mM); K-gluconate (98), KCl (50), $CaCl_2$ (0.5), $MgCl_2$ (2), EGTA (5), HEPES (10), MgATP (2), NaGTP (0.2), and the pH was adjusted to 7.3 with KOH.

In current-clamp recordings, the recorded neurons were kept at the holding current of 0 pA. The IR of sensory neurons was determined by four increasing hyperpolarizing current injections (Δ-5 pA from a holding current of 0 pA, 5 kHz).

The minimal current to evoke a single AP within 50 ms (I_{AP}) for each neuron was obtained by 5 pA stepwise increasing, depolarizing instanteous, block pulses, and APs were recorded at 20 kHz. The amplitudes of 5 s ramp-shaped depolarizations were set at 1x, 2x, and 3x I_{AP} and sampled at 5 kHz. The amplitude of the 20 s depolarizing pulse was set to 2x I_{AP} for the corresponding neuron, and the voltage changes were recorded at 5 kHz.

A seven-barrel system with the common outlet was used for the heat stimulation of single neurons (Dittert et al., 1998). In voltage clamp recordings, the neurons were clamped at a holding potential of −60 mV. Heat-activated inward currents (I_{Heat}) were elicited by applying ramp-shaped heat stimuli at 60 s intervals (linear temperature increases from RT to 50°C within 5 s). Neurons were assigned as heat responsive when they showed a non-linear inward current with a threshold below −0.2 nA from the baseline current.

Electrophysiological Analysis

Action potential analysis: the average IR was calculated according to Ohm's law. From the AP evoked by injecting depolarizing current pulses (50 ms, sampled at 20 kHz), the resting membrane potential (V_{mem}), afterhyperpolarization (AHP), and overshoot (OS) of *Prdm12*$^{fl/fl}$; *Avil-Cre*$^{+}$ and *Prdm12*$^{fl/fl}$; *Avil-Cre*$^{-}$ DRG neurons were determined. From the first derivative of the evoked APs, the maximal speeds of depolarization (S1) and of the biphasic repolarization (S2 and S3) were derived. Further, the time between S1, S2, and/or S3 (t1-t2; t2-t3; and t1-t3) was determined to compare AP width. The corresponding membrane voltage was deducted at the point where the falling slope of the 1st derivative reversed into a rising slope, and the AP threshold was determined (Langeslag et al., 2014; Namer et al., 2017).

RNA Sequencing and Real-Time qPCR

RNA isolation: lumbar DRG tissues were dissected from 10 to 14-week-old animals, immediately placed in RNALater solution (Ambion, Austin, TX, USA), and snap frozen in liquid nitrogen until further isolation. Tissues were lysed using Precellys 24 Tissue Homogenizer (Bertin Instruments, Paris, France) 3×30 s at 5000 rpm, by QIAshredder (Qiagen, Valencia, CA, USA) homogenization. RNA was isolated using the RNeasy Mini Kit (Qiagen, Valencia, CA, USA) with on-column DNease treatment with RNase-Free Dnase Set (Qiagen, Valencia, CA, USA). A minimum of three biological replicates per genotype were used.

Real-time q-PCR: reverse transcription was performed using the qScript cDNA Synthesis Kit (Quantabio, Beverly, MA, USA) with an input amount of 200 ng of RNA, as per the instructions of the manufacturer. Real-time quantitative PCRs (RT-qPCRs) were done using an iTaq Universal SYBR Green Supermix (Bio Rad, Los Angeles, CA, USA) and run on a StepOnePlus Real-Time PCR System (Applied Biosystems, Darmstadt, Germany). The comparative Ct method (ΔΔCt) was used to determine relative gene expression, normalizing to GAPDH. The primers used for qPCR are *Gapdh* forward: 5'-GGTCGTATTGGGCGCCTGGTCACC-3'; reverse: 5'-CACACCCATGACGAACATGGGGGC-3'; *Prdm12* (exon 3) forward: 5'-CTACATCAAGTGTGCCCGGA−3'; reverse: 5'-TGGCCTTGTAGAAGATGCTCG-3'.

RNA sequencing: the amount of RNA was quantified using a Qubit 2.0 Fluorometric Quantitation System (Life Technologies, Carlsbad, CA, USA), and an Experion Automated Electrophoresis System (Bio-Rad, Hercules, CA, USA) was used to calculate the RNA integrity score. RNA-sequencing (RNA-seq) libraries were prepared using the TruSeq Stranded messenger RNA (mRNA) LT sample preparation kit Illumina, San Diego, CA, USA) using Sciclone and Zephyr liquid handling robotics (PerkinElmer, Spokane, WA, USA) at pre- and post-PCR steps. Library concentrations were determined using a Qubit 2.0 Fluorometric Quantitation system (Life Technologies, Carlsbad, CA, USA), and the distribution of sizes was determined using an Experion Automated Electrophoresis System (Bio-Rad, Hercules, CA, USA). For sequencing, the 14 libraries were pooled, diluted to equimolar amounts, and sequenced on an Illumina HiSeq 3000/4000 using 50-bp single-end chemistry. Base calls provided by the real-time analysis (RTA) software (Illumina, San Diego, CA, USA) were converted into a multiplexed, unaligned BAM format before demultiplexing into sample-specific unaligned BAM files.

Transcriptome Analysis

Next generation sequencing (NGS) samples (passing quality filtering) were aligned to the UCSC Genome Browser (*Mus musculus* genome assembly mm10, Mus musculus transcriptome mm10_e100) of the genome reference consortium (GrCh38/GrCm38) using the STAR alignment tool (Dobin et al., 2013). The Bioconductor DESeq2 package (Love et al., 2014) was

used for testing differentially expressed genes (DEGs) using the negative binomial distribution.

Transcriptome Enrichment Analysis

Overrepresentation analysis of the unranked list of significantly (FDR < 0.05) DEGs common to both animal models was performed. The analysis utilized g:profiler package (version e103_eg50_p1) (Reimand et al., 2007), specifically g:GOSt Functional profiling tool with the Benjamini-Hochberg FDR threshold cutoff of 0.05. Gene sets utilized in analysis included gene ontology molecular function (GO:MF) and Kyoto Encyclopedia of Genes and Genomes (KEGG) pathway sets. The 10 most enriched terms for both GO:MF and KEGG pathways were represented in a decreasing order using –log10(FDR) value.

Gene set enrichment analysis (GSEA) was performed using the GSEA software. As GSEA input expression data set values, DeSeq2 normalized counts were used. The analysis performed for MSigDB gene sets (Subramanian et al., 2005; Liberzon et al., 2011) from C2: KEGG pathways, C5: GO:MF, and cutoffs for the value of $p < 0.05$ and FDR < 0.25. GO:MF gene sets were further imported into Cytoscape (v.3.8.2) (Shannon et al., 2003), and the pathways were clustered into networks using EnrichmentMap (v.3.3.1) (Merico et al., 2010). For network generation (Reimand et al., 2019), a similarity cutoff of 0.375 for combined Overlap+Jaccard score and combined score of 0.5 was used.

Data-Analyses and Statistics

All electrophysiological data were analyzed using the Origin software (Originlab, Origin Pro 8, North Hampton, NH, USA). Statistical analysis (Graphpad Prism 7.0, GraphPad Software Inc., San Diego, CA) was performed by either the Mann–Whitney test in case of non-normal-distributed data or *t*-test for normal-distributed data (Shapiro–Wilk). The distribution of heat-responsive sensory neurons was tested using a Fisher's exact test. Statistical analysis of behavioral data and qPCR was performed by unpaired Student's *t*-test (capsaicin injections, Von Frey assay, Hargreaves test, and OFT, qRT-PCR). For Morris water maze, unpaired Student's *t*-test was used to analyze the short- and long-term memory data and two-way ANOVA with Sidak's multiple comparisons test for the latency to reach the platform.

RESULTS

Identification of Novel Splice-Site Variant in Two Related Cases of CIP

Currently, there are 24 known PRDM12-CIP patients from different ethnic backgrounds (**Figure 1A**). To contribute a better understanding of prevalence and the contribution of a PRDM12 variant to nociceptive dysfunction, we present two cases harboring an unreported *PRDM12* variant. Two affected first-order male cousins from an Iranian Farsi consanguineous family presented to the clinics with the absence of acute and chronic pain perception starting from birth (**Figure 1B**, **Table 1**). There is no history of CIP in the family. Index patient [patient 1 (P1)] was first presented with a tongue ulceration, and was later confirmed to have disturbed temperature and vibration sensation, sensorineural deafness, corneal abrasions, frequent skin and bone infections, and scoliosis. Patient 2 (P2) exhibited very similar symptoms with a few minor differences (**Table 1**). While both patients were determined to exhibit autism spectrum disorder (ASD), ID, and muscular weakness, patient 1 also presented with mild cortical malformation as evaluated by MRI (data not shown). Due to clinical similarity to other PRDM12-CIP cases, the targeted Sanger sequencing was performed on the DNA sample from patient 1 that revealed a homozygous splice acceptor site variant within intron 1 of *PRDM12* NM_021619:c.224-2 A>T (chr9: 133541993) (**Figure 1B**). Considering that ASD and ID are not commonly associated with PRDM12-CIP, and to rule out any other known CIP-causing gene contribution, we performed WES on the DNA sample from patient 1. WES analysis confirmed the presence of the *PRDM12* variant with a CADD score (Kircher et al., 2014) of 29.4. Subsequently, we confirmed that the variant segregated with the disease in a recessive fashion: in a homozygous state in patients 1 and 2 and in a heterozygous state in each of the four parents (**Figure 1B**). A different homozygous variant in the same position (c.224-2A>G) has previously been published in a patient suffering from CIP accompanied with global developmental delay, similarly to the patients we describe (Saini et al., 2017). Subsequent filtering of the WES failed to detect any additional rare, high CADD-PHRED scoring variants within the other known CIP genes, including *NGF, NTRK1, SCN9A, SCN11A, ZFHX2, FAAHP1*, and *CLTCL1*. To identify potential variants contributing to the autism and ID phenotype, we performed a search for rare variants in the genes associated with ASDs and ID as per PanelApp corresponding panels (Martin et al., 2019). The analysis identified rare variants within nine genes confirmed or predicted to be causative for ADD and/or ID in patient 1, however, subsequent Sanger sequencing of these loci in patients 1 and 2 revealed that none were shared (**Table 2**).

PRDM12 Is Expressed in the Mouse Nervous System Through Life

To understand PRDM12 expression pattern in the mouse, we performed the western blotting analysis of various tissues harvested from adult WT mice. HEK293 cell lysates overexpressing either WT PRDM12 ($PRDM12^{WT}$) or previously published frameshift mutation $Prdm12^{S58fs}$ ($PRDM12^{S58fs}$) that leads to no protein product (Nagy et al., 2015) were blotted to ensure antibody specificity (**Figure 2A**). In addition, low expression in the heart, we did not detect PRDM12 immunoreactivity in any other non-nervous tissue we examined (**Figure 2A**, upper panel). We detected PRDM12 immunoreactivity in both peripheral and CNS tissue samples (**Figure 2A**, lower panel). Interestingly, PRDM12 expression was noted in all brain regions examined. As previously reported in embryonic tissue, immunohistochemical double labeling of adult WT DRG sections revealed PRDM12 to remain co-expressed with various polymodal nociceptive markers, including IB4, $Na_V1.8$, CGRP, and TRKA (**Figures 2B–E**) (Desiderio et al., 2019).

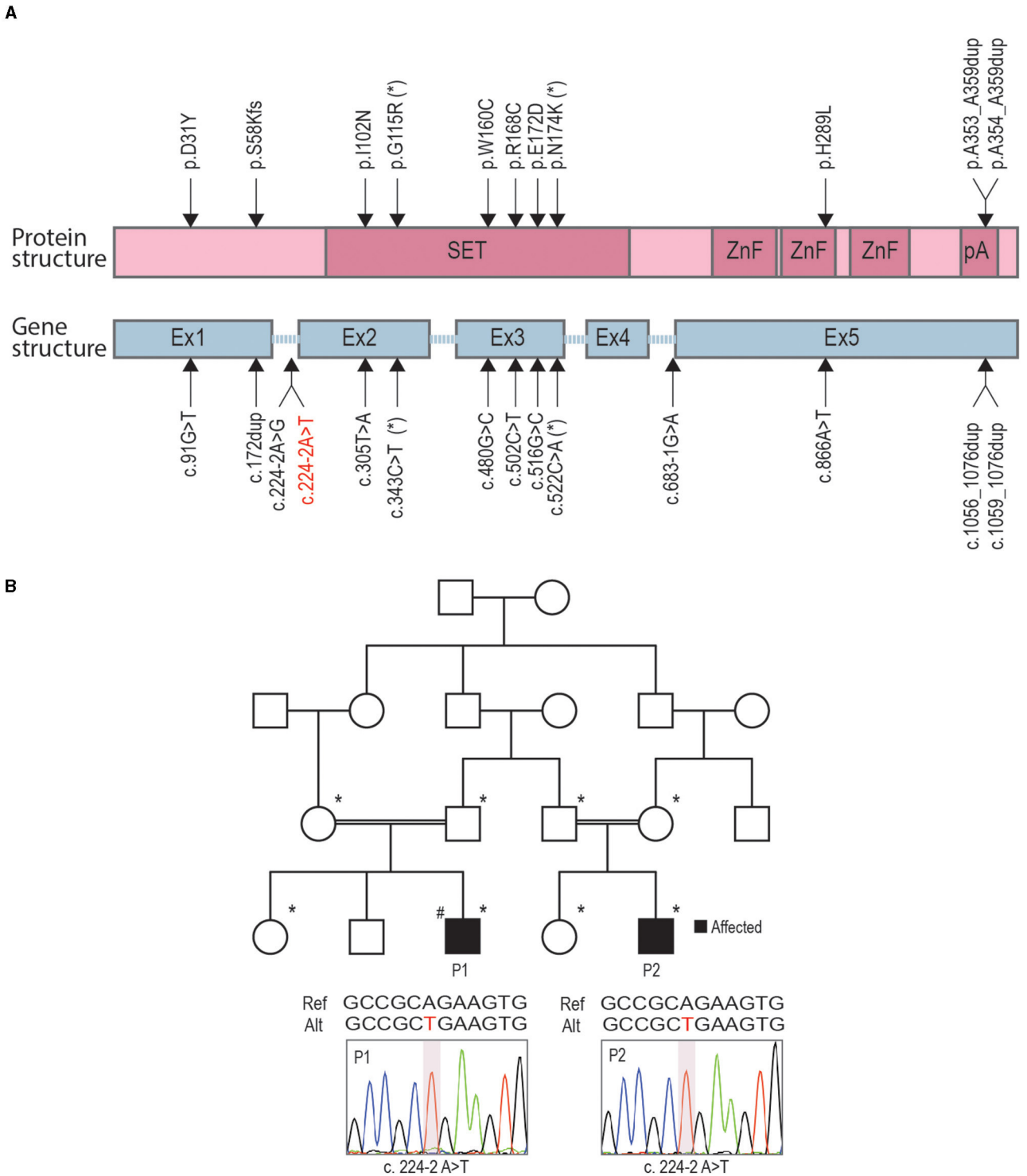

FIGURE 1 | Identification of novel variants in two related congenital insensitivity to pain (CIP) cases. **(A)** A schematic representation of PR-domain containing member 12 (PRDM12) protein domain structure (pink) and gene structure (blue) with marked locations of previously published causative CIP variants and a novel splice-site variant reported here (red letters). **(B)** Family pedigree, with affected individuals shaded in black; family members included in segregation analysis indicated with asterisks; hashtag denotes index patient (patient 1, P1) for which whole-exome sequencing (WES) was performed. The position of the missense mutation is depicted below the family pedigree for patients 1 (P1) and 2 (P2) with an illustrative Sanger chromatogram of genomic PCR amplicons.

TABLE 1 | Clinical synopsis of patients 1 and 2.

Patient		P1	P2
Ethnic origin		Farsi	Farsi
Sex		M	M
Age		19	9
Parental consanguinity		4th degree consanguinity (first cousins)	4th degree consanguinity (first cousins)
Gene		*PRDM12*	*PRDM12*
Variant zygosity		Homozygous	Homozygous
Genomic change (GRCh37)		chr9:g.133541993A>T	chr9:g.133541993A>T
Variant cDNA position		ENST00000253008.2:c.224-2A>T	ENST00000253008.2:c.224-2A>T
Age of onset		At birth	At birth
First sign		Tongue ulceration	Tongue ulceration
Pain sensitivity	Acute	Absent	Absent
	Chronic	Absent	Absent
	Inflammatory	Absent	Absent
	Segmental or global	Global pain insensitivity	Global pain insensitivity
Thermosensitivity		Impaired	Impaired
Vibration		Impaired	Impaired
Proprioception		N/A	Yes
Touch		N/A	Yes
Corneal ulcerations		Yes	Yes
Hypo-/alacrimia		Yes	Yes
Smell		N/A	Hyposmia
Hearing		Sensineural deafness	Sensineural deafness
Deep tendon reflexes		Trace	Trace
Motor weakness		Mild	Mild
Life threatening hyperthermia		N/A	No
Intellectual disability		Moderate	Mild
Autism		Yes	Yes
Behavioral stereotypy		Yes	No
Brain MRI findings		Mild cortical malformation	No
Sensory nerve conduction		Impaired	Impaired
Ulcers and mutilation		Oral cavity, lips	Oral cavity, lips
Frequent skin infections		Yes	Yes
Bone infections		Yes	No
Other phenotypes		Hypertensia, scoliosis, hypersalivation	Hypertension, scoliosis

PRDM12 Loss During Embryogenesis but Not in Adult Mice Leads to Reduced Survival

Constitutive, "classic" KO (**Figure 3A**) of *Prdm12* (*Prdm12*$^{-/-}$) results in a significant reduction of DRG volume (**Figure 3B**) and early neonatal death of unknown cause (Desiderio et al., 2019). We were, therefore, motivated to generate a mouse model that more closely resembles human disease as most CIP-causing variants of *PRDM12* do not affect its protein expression (Nagy et al., 2015). Therefore, using the Cas9 methodology, we generated a frameshift at position c.537A_del (p.S159AfsTer2; *Prdm12*^{S159AfsTer2}) and point mutation at c.542G>C (p.W160C; *Prdm12*^{W160C}) in murine *Prdm12* gene (NM_001123362, **Supplementary Figure 1A**) to reflect the previously reported PRDM12-CIP mutation W160C (Nagy et al., 2015). To improve viability, mice were maintained on a mixed FVB/NJ/C57/BL6 background. *Prdm12*^{S159AfsTer2} mutation is predicted to cause an early stop codon and likely mimic the constitutive *Prdm12*$^{-/-}$ absence of PRDM12 protein expression. Both *Prdm12*^{S159AfsTer2} and *Prdm12*^{W160C} mice, similarly to the constitutive *Prdm12*$^{-/-}$, showed complete penetrance of prenatal lethality in homozygous mutants. Heterozygous *Prdm12*$^{S159AfsTer2+/-}$ mice had normal pain perception as compared to WT littermates when tested in acute pain assays (**Supplementary Figure 1B**).

To understand the functional role of PRDM12, we generated several conditional *Prdm12* mutant mouse models. We aimed to determine if PRDM12 function was necessary for pain perception when ablated during early development and/or in adults. We first crossed *Prdm12*$^{fl/fl}$ to *Sox10-Cre* (*Prdm12*$^{fl/fl}$; *Sox10-Cre*), thereby eliminating PRDM12 expression in the entire neural crest cell population during

TABLE 2 | Rare homozygous variants in autism and/or intellectual disability- (ID-) associated genes identified in patient 1 whole-exome sequencing (WES).

Gene	Zygosity	Genomic change (GRCh37)	P1 variant genotype	P2 variant genotype	PanelApp panel	OMIM gene entry	Inheritance	Segregation result
UNC80	Homozygous	chr2:g.210678477C>T	T/T	C/T	ID	612636	AR	Excluded
POLA2	Homozygous	chr11:g.65063046T>C	C/C	T/C	Autism candidate	N/A	N/A	Excluded
KCNK7	Homozygous	chr11:g.65363204C>T	T/T	C/T	Autism candidate	603940	N/A	Excluded
CEP290	Homozygous	chr12:g.88500631C>A	A/A	C/A	ID	610142	AR	Excluded
ACE	Homozygous	chr17:g.61566077G>C	C/C	G/G	Autism candidate	106180	N/A	Excluded
ARFGEF2	Homozygous	chr20:g.47632862A>G	G/G	A/G	ID	605371	AR	Excluded
PLA2G6	Homozygous	chr22:g.38508527C>T	T/T	C/C	ID	603604	AR	Excluded
BCOR	Homozygous	chrX:g.39932734G>C	C	G	ID	300485	XLD	Excluded
BRWD3	Homozygous	chrX:g.79938123T>C	T	C	ID	300553	XLR	Excluded

N/A, inheritance mode unknown.

embryonic development (**Figure 3C**). Notably, we did not detect any viable *Prdm12*$^{fl/fl}$; *Sox10-Cre*$^{+}$ offspring. Thermal and chemical acute pain tests (hot plate assay and capsaicin intraplantar injection, respectively) on heterozygous *Prdm12*$^{fl/+}$; *Sox10-Cre*$^{+}$ did not reveal any reduction in pain perception when compared to control littermates (data not shown).

We next sought to ablate PRDM12 expression specifically in the DRG, thus we crossed *Prdm12*$^{fl/fl}$ to *Avil-Cre* (*Prdm12*$^{fl/fl}$; *Avil-Cre*) to remove PRDM12 expression approximately at embryonic day 12.5 (**Figure 3C**) (Hasegawa et al., 2007; Desiderio et al., 2019). RT-qPCR and the western blotting of lumbar DRG tissue confirmed a significant reduction of Prdm12 transcript and protein expression, respectively (**Supplementary Figure 2A**). We noted a reduction of the survival of *Prdm12*$^{fl/fl}$*; Avil-Cre*$^{+}$ animals (**Supplementary Figure 2B**). The animals that died did so before weaning for reasons that have yet to be determined. In *Prdm12*$^{fl/fl}$; *Avil-Cre*$^{+}$ survivors, we noted corneal abrasions and facial scarring similar to PRDM12-CIP patients (**Supplementary Figure 2C**) (Desiderio et al., 2019; Chen et al., 2020).

To delete PRDM12 in adults, we crossed *Prdm12*$^{fl/fl}$ to TAM-inducible *Rosa26-CreER*^{T2} mice (*Prdm12*$^{fl/fl}$; *Rosa26-CreER*^{T2}). Following TAM injections at 8 weeks of age, we generated whole-body PRDM12 KOs in adults 3 weeks following injection as confirmed by RT-qPCR in lumbar DRG and WB tissue (**Figure 3C**, **Supplementary Figure 3A**). Unlike the constitutive (*Prdm12*$^{-/-}$) or neuronal crest cell progenitor PRDM12 KOs (*Prdm12*$^{fl/fl}$; *Sox10-Cre*$^{+}$), there was no noted reduction in the survival of adult TAM-injected *Prdm12*$^{fl/fl}$; *Rosa26-CreER*$^{T2+}$ as compared to control littermates. As PRDM12 is expressed in the mouse brain, we aimed to identify any confounding CNS effects that may have resulted by the reduction of PRDM12 expression in the CNS. OFT of TAM-injected *Prdm12*$^{fl/fl}$; *Rosa26-CreER*$^{T2+}$ revealed no deficiencies in the distance traveled or increased anxiety as compared to control littermates (**Supplementary Figure 3B**). Furthermore, the Morris water maze test and the gold standard for hippocampal-dependent spatial learning, revealed no deficiencies in swimming ability, learning acquisition, or short- or long-term memory retention (**Supplementary Figure 3C**).

To determine the effect of nociceptor development in our conditional mouse models and the extent to which they phenocopy the symptoms of patients, we performed the immunohistochemical analysis of hind paw skin biopsies from both *Prdm12*$^{fl/fl}$; *Avil-Cre* and TAM-injected *Prdm12*$^{fl/fl}$; *Rosa26-CreER*^{T2} adult mice with anti-PGP9.5 antibody, a marker for small caliber, intraepidermal nerve fibers. PGP9.5 immunostaining is considered as a diagnostic tool in the study of peripheral neuropathies, which, in PRDM12-CIP case, revealed the absence of PGP9.5 reactive nerve endings in patient epidermis (Chen et al., 2015; Van Acker et al., 2016). As it was noted for PRDM12-CIP patients, *Prdm12*$^{fl/fl}$*; Avil-Cre*$^{+}$ biopsies had no detectable PGP9.5 reactive fibers in the epidermis, in contrast to control littermates (**Figure 3D**). TAM-injected *Prdm12*$^{fl/fl}$; *Rosa26-CreER*$^{T2+}$, on the other hand, had normal epidermal PGP9.5^{+} innervation (**Figure 3D**).

PRDM12 Expression Is Required for Functional Nociceptors in Cultured DRG

To investigate the functional nociceptive role of PRDM12 in the two mouse models at a cellular level, we performed single-cell electrophysiological studies on cultured DRG. We isolated DRG from *Prdm12*$^{fl/fl}$*; Avil-Cre*$^{+}$ and TAM-injected *Prdm12*$^{fl/fl}$*; Rosa26-CreER*$^{T2+}$ and their respective controls and cultured them for ∼16 h. The resting membrane potential (V_{mem}) of *Prdm12*$^{fl/fl}$*; Avil-Cre*$^{+}$ DRG neurons was similar to *Prdm12*$^{fl/fl}$*; Avil-Cre*$^{-}$ DRG neurons in whole-cell current-clamp recordings (**Table 3**). However, the IR in the *Prdm12*$^{fl/fl}$*; Avil-Cre*$^{+}$ DRG neurons was significantly low. Consequently, the minimal current to evoke an AP within 50 ms (I_{AP}) was increased to more than two times in *Prdm12*$^{fl/fl}$*; Avil-Cre*$^{+}$ neurons. The ablation of the *Prdm12* gene after TAM-injection in *Prdm12*$^{fl/fl}$; *Rosa26-CreER*^{T2} DRG neurons, however, showed no differences in the resting membrane potential, IR and I_{AP} compared to DRG neurons were derived from control, TAM-injected *Prdm12*$^{fl/fl}$; *Rosa26-CreER*$^{T2-}$, mice (**Table 3**).

To investigate the properties of APs between the corresponding genotypes, we injected the currents at IAP

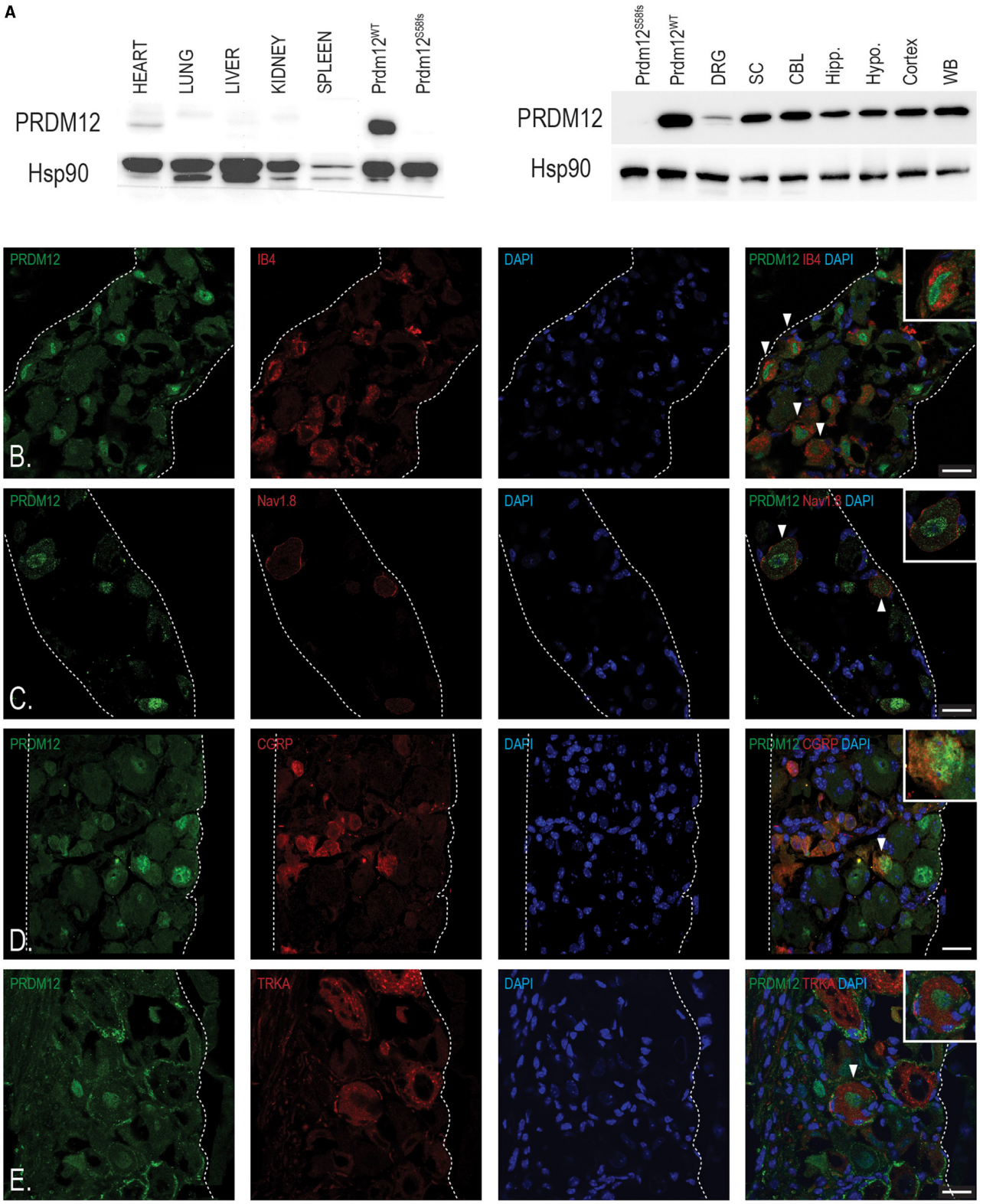

FIGURE 2 | Tissue analyses reveal PRDM12 expression in adult mouse peripheral and central nervous tissue. **(A)** Upper panel, western blot analysis shows a slight PRDM12 protein expression in adult heart tissue, but no detectable expression in the lungs, livers, kidneys, or spleen. Lower panel, western blot indicates PRDM12 protein level expression in the central nervous system (CNS): whole brain (WB), cortex, hypothalamus (Hypo.), hippocampus (Hipp.), cerebellum (CBL), and spinal cord

(Continued)

FIGURE 2 | (SC), as well as in peripheral nervous system (PNS), and dorsal root ganglia (DRG). Antibody positive control ($PRDM12^{WT}$) is HEK293 cell lysate overexpressing wild type (WT) PRDM12 complementary DNA (cDNA) and negative control ($PRDM12^{S58fs}$) is HEK203 cell lysate overexpressing $PRDM12^{S58fs}$ cDNA. HSP90 was used as loading control. **(B–E)** Representative immunohistochemical images of adult mouse lumbar DRG sections indicating PRDM12 co-expression with classical nociceptive markers: IB4, $Na_v1.8$, CGRP, and tyrosine kinase 1 (TRKA), as labeled. White arrows indicate cells with co-labeling, with digitally enlarged insets of select co-labeled cells. Scale bar in all images is 20 μm.

+ 10 pA of the recorded neurons. Remarkably, APs evoked from *Prdm12*$^{fl/fl}$*; Avil-Cre*$^{+}$ were significantly different from those derived from *Prdm12*$^{fl/fl}$*; Avil-Cre*$^{-}$. The AP width recorded from cultured *Prdm12*$^{fl/fl}$*; Avil-Cre*$^{+}$ DRG neurons was significantly smaller than those from *Prdm12*$^{fl/fl}$*; Avil-Cre*$^{-}$ neurons and seem to lack the typical biphasic repolarization phase (also known as "hump" or "shoulder"), which is a characteristic of nociceptive DRG (**Figure 4A**) (Ritter and Mendell, 1992). This reduction in AP width (t1–t3, **Table 3**) in *Prdm12*$^{fl/fl}$*; Avil-Cre*$^{+}$ is correlated with increased repolarization speeds (dV/dt min_1 and dV/dt min_2, **Table 3**), whereas the depolarization speed (dV/dt max) is unchanged. Additionally, the AP peak (OS) was significantly lower in *Prdm12*$^{fl/fl}$*; Avil-Cre*$^{+}$ DRG neurons, whereas the AHP was unchanged (**Figure 4A**, **Table 3**). The AP threshold did not differ between *Prdm12*$^{fl/fl}$*; Avil-Cre*$^{-}$ and *Prdm12*$^{fl/fl}$*; Avil-Cre*$^{+}$ DRG neurons. The AP characteristics V_{mem}, IR, and I_{AP} recorded from *Prdm12*$^{fl/fl}$; *Rosa26-CreER*$^{T2+}$ and *Prdm12*$^{fl/fl}$; *Rosa26-CreER*$^{T2-}$-derived neurons have not shown any differences (**Figure 4B**, **Table 3**).

We applied two different depolarization protocols to evaluate the excitability of the DRG neurons. During a ramp-shaped depolarization, the *Prdm12*$^{fl/fl}$*; Avil-Cre*$^{+}$ neurons generated fewer APs (**Figures 4C,D**, **Table 3**). Additionally, the number of APs generated in a 20-s long, block-shaped depolarization by *Prdm12*$^{fl/fl}$*; Avil-Cre*$^{+}$ neurons were significantly low (**Figure 4E**, **Table 3**) and the *Prdm12*$^{fl/fl}$*; Avil-Cre*$^{+}$ neurons predominantly fired within the seconds of the depolarization (**Table 3**). In contrast to *Prdm12*$^{fl/fl}$*; Avil-Cre*$^{+}$, the *Prdm12*$^{fl/fl;}$*Avil-Cre*$^{-}$ neurons generated more APs during ramp-shaped depolarizations and constantly during the long block-shaped depolarization. Meanwhile, there were no differences observed in the AP characteristics between TAM-injected *Prdm12*$^{fl/fl}$*; Rosa26-CreER*$^{T2+}$ and *Prdm12*$^{fl/fl}$*; Rosa26-CreER*$^{T2-}$ neurons, both excitability protocols showed a minor difference between the two genotypes. In the 1 × I_{AP} depolarizing ramp, the *Prdm12*$^{fl/fl}$; *Rosa26-CreER*$^{T2+}$ showed a reduced number of Aps, and additionally, in the prolonged 2× I_{AP} depolarization, they showed a reduced number of APs within the first few seconds (**Figure 4F**, **Table 3**).

Non-specific activation of Na+ channels by prepulse at −120 mV revealed larger currents in *Prdm12*$^{fl/fl}$*; Avil-Cre*$^{+}$ DRG neurons compared to controls (**Supplementary Figure 4A**). The difference was not observed between the TAM-injected *Prdm12*$^{fl/fl}$; *Rosa26-CreER*$^{T2+}$ and littermate controls. To determine the contribution of tetrodotoxin- (TTX-) sensitive and resistant inward currents observed in *Prdm12*$^{fl/fl}$*; Avil-Cre*$^{+}$, subsequent inhibition of TTX-sensitive inward currents was performed by 250 ms prepulse at −40 mV showing a reduction of inward currents only in *Prdm12*$^{fl/fl}$; *Avil-Cre*$^{+}$, and not in TAM-injected *Prdm12*$^{fl/fl}$; *Rosa26-CreER*$^{T2+}$ neurons (**Supplementary Figure 4B**), as compared to their respective littermate controls. These results imply a larger fraction of TTX-S Na+ channels in *Prdm12*$^{fl/fl}$*; Avil-Cre*$^{+}$ (**Supplementary Figures 4C–E**).

PR domain-containing member 12-deficient and control neurons were also tested for their thermal responsiveness by an increase in a ramp-shaped temperature. Strikingly, only a single *Prdm12*$^{fl/fl;}$*Avil-Cre*$^{+}$ neuron (of the 42 recorded neurons) responded to the thermal stimulus with a relatively high temperature threshold (>45.0°C, **Figure 4G**). From the *Prdm12*$^{fl/fl}$*; Avil-Cre*, ∼38% of the neurons responded with an averaged threshold temperature of 40.0°C. The percentage of thermal-responsive neurons was similar between TAM-injected *Prdm12*$^{fl/fl}$; *Rosa26-CreER*$^{T2+}$ and *Prdm12*$^{fl/fl}$; *Rosa26-CreER*$^{T2-}$ neurons and the temperature threshold of the thermal-activated currents (**Figures 4H,I**).

To determine the behavioral responses of our mouse models to noxious chemical stimuli, we injected intraplantar capsaicin, a pungent ingredient in chili peppers, and recorded the behavioral response. Capsaicin activates its receptor TrpV1 on nociceptive C-fibers, generating a painful sensation completely absent in CIP patients. We found that both conditional mouse models *Prdm12*$^{fl/fl}$*; Avil-Cre*$^{+}$ and TAM-injected *Prdm12*$^{fl/fl}$; *Rosa26-CreER*$^{T2+}$ had significantly reduced responses to capsaicin as compared to their respective control littermates (**Figures 4H,J**).

Developmental or Adult-Onset Deletion of PRDM12 Causes Different Effects in Downstream Gene Expression

To identify the effect of *Prdm12* deletion on the key genes responsible for acute pain perception between our two mouse models, we performed mRNA sequencing on bulk lumbar DRG samples from at least three animals of both models and corresponding controls. We sought to clarify the cellular phenotypic difference of the development and adult mouse model. *Prdm12*$^{fl/fl}$*; Avil-Cre*$^{+}$ had 5,851 significantly (false discovery rate, FDR < 0.05) DEGs as compared to corresponding controls, including markers of nociceptors, some of which including *Trpv1*, *Ntrk1*, *Calca*, and *Scn10a* are additionally validated by RT-qPCR (**Supplementary Figure 5A**). Out of 5,851 DEGs, 868 genes had an expression level fold change larger than 2 for upregulated DEGs, or smaller than −2 for downregulated DEGs (**Figure 5A**, top panel). In comparison, TAM-injected *Prdm12*$^{fl/fl}$; *Rosa26-CreER*$^{T2+}$ had 67 significantly (FDR < 0.05) DEGs (**Figure 5A**, bottom panel).

To gain insights into the possible contribution of DEGs to the PRDM12 core transcriptional program crucial for the function of nociceptors, we considered all 67 *Prdm12*$^{fl/fl}$; *Rosa26-CreER*$^{T2+}$ DEGs and 868 most significantly dysregulated genes

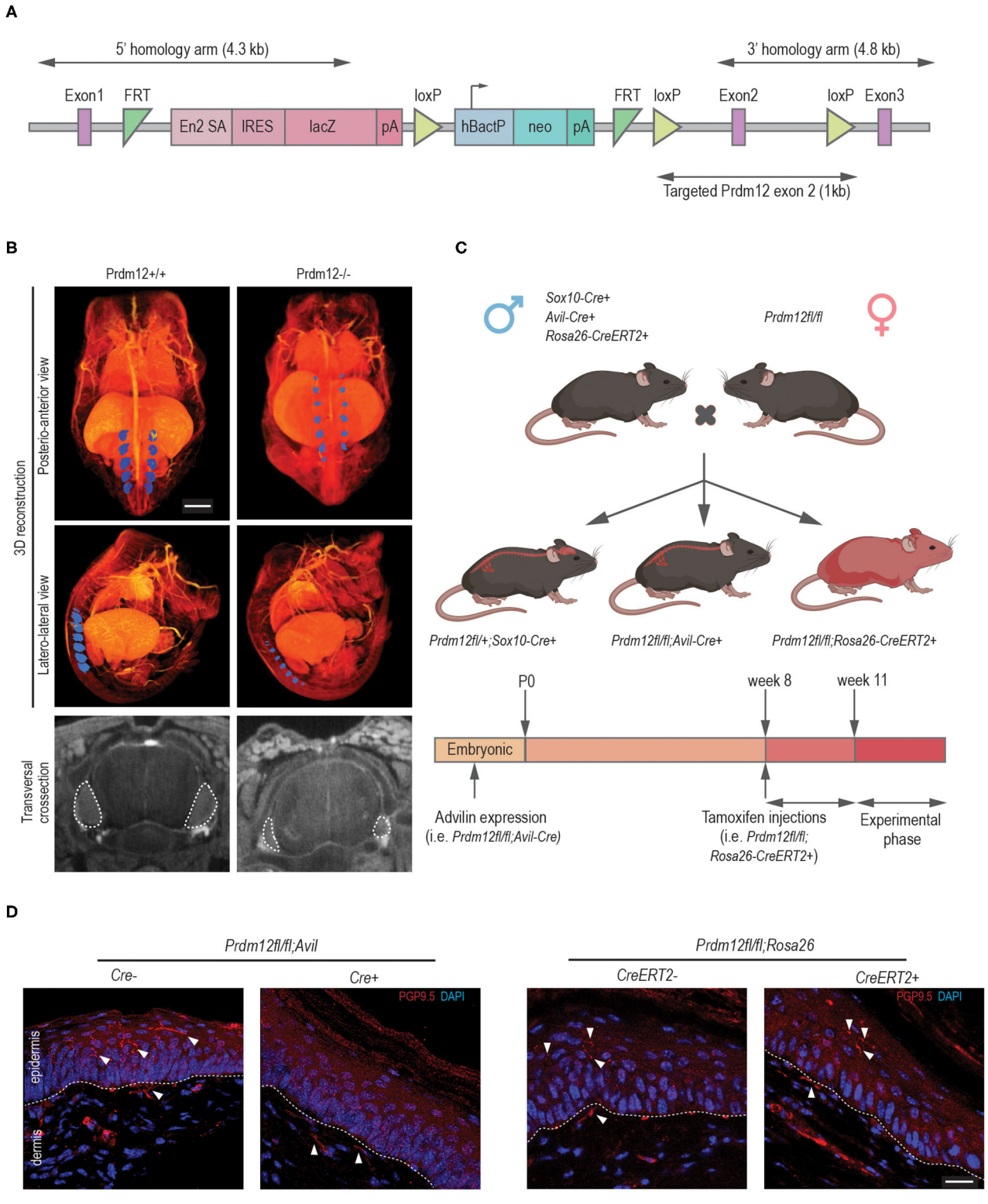

FIGURE 3 | Validation of animal models generated for the study. **(A)** A schematic representation of the lethal classical *Prdm12* knock-out (KO) allele. **(B)** Lower panels, representative lumbar DRG cross-section micro-CT images of WT and *Prdm12*$^{-/-}$ E15.5 embryos depicting a reduction of DRG volume in the *Prdm12*$^{-/-}$. Middle and upper panels—pseudocolored (blue) 3D reconstructed micro-CT images of lumbar DRG in WT and *Prdm12*$^{-/-}$ 15.5 embryos, as indicated—posteroanterior (upper panels) and latero-lateral view (middle panels). Scale bar is 1,000 μm. Transversal cross-section of the SC with DRG outlined with a white dotted line (bottom panel). **(C)** Schematic of the genetic crosses performed to generate developmental constitutive *Prdm12*$^{fl/fl}$; *Avil-Cre* and *Prdm12*$^{fl/fl}$;

(Continued)

FIGURE 3 | *Sox10-Cre*, and inducible *Prdm12*$^{fl/fl}$; *Rosa26-Cre*ER^{T2}, with the timeline of tamoxifen (TAM) injection, analysis or tissue harvest below. **(D)** Left two panels: representative immunohistochemical images of hind paw skin biopsy from *PRDM12*$^{fl/fl}$*; Avil-Cre*$^{+}$ show the complete absence of PGP9.5-reactive nerve fibers in the epidermal layer as compared to the *Cre*$^{-}$ controls. In contrast, PGP9.5-reactive nerve fibers are clearly visible in the epidermal layers in representative images of TAM-injected *Prdm12*$^{fl/fl}$; *Rosa26-CreER*$^{T2+}$ hind paw skin biopsy (right two panels) as compared to the *Cre*$^{-}$ controls. Dotted line delineates epidermis/dermis border. Scale bar is 20 μm.

TABLE 3 | Action potential (AP) characteristics of *Prdm12*$^{fl/fl}$*; Avil-Cre*$^{+}$ and *Prdm12*$^{fl/fl}$*; Rosa26-CreER*$^{T2+}$ nociceptive neurons and corresponding controls.

	***Prdm12*$^{fl/fl}$; *Avil-Cre*$^{-}$ (*N* = 32, *n* = 3)**	***Prdm12*$^{fl/fl}$; *Avil-Cre*$^{+}$ (*N* = 38, *n* = 3)**		***Prdm12*$^{fl/fl}$; *Avil-CreER*$^{T2-}$ (*N* = 37, *n* = 4)**	***Prdm12*$^{fl/fl}$; *Avil-Cre ER*$^{T2+}$ (*N* = 29, *n* = 3)**	
Action potential						
Input Resistance (GΩ)	1.53 ± 0.14	0.81 ± 0.11	***	1.33 ± 0.11	1.54 ± 0.18	n.s.
I_{AP} (pA)	69.84 ± 12.6	162.4 ± 20.9	***	47.16 ± 7.36	50.17 ± 11.9	n.s.
V_{mem} (mV)	−56.28 ± 1.42	−56.29 ± 0.90	n.s.	−51.34 ± 1.17	−52.52 ± 1.29	n.s.
OS (mV)	68.97 ± 0.52	49.89 ± 1.84	***	56.97 ± 0.54	56.90 ± 0.46	n.s.
AHP (mV)	−66.66 ± 0.81	−66.66 ± 0.48	n.s.	−66.71 ± 0.60	−66.30 ± 0.94	n.s.
AP Treshold (mV)	−28.98 ± 0.71	−30.89 ± 1.39	n.s.	−28.29 ± 0.92	−27.09 ± 0.88	n.s.
S1 (mV.ms^{-1})	127.64 ± 3.79	116.94 ± 5.44	n.s.	73.92 ± 2.63	72.63 ± 2.95	n.s.
S2 (mV.ms-^{1})	−38.80 ± 2.20	−92.89 ± 4.72	***	−20.95 ± 1.09	−20.10 ± 1.32	n.s.
S3 (mV.ms^{-1})	−30.87 ± 1.83	−73.63 ± 4.91	***	−27.23 ± 1.40	−23.91 ± 1.50	n.s.
t1-t2 (ms)	1.66 ± 0.10	0.79 ± 0.02	***	1.93 ± 0.06	2.17 ± 0.08	n.s.
t2-t3 (ms)	5.87 ± 0.98	1.51 ± 0.12	***	5.51 ± 0.21	5.88 ± 0.27	n.s.
t1-t3 (ms)	4.21 ± 0.89	0.70 ± 0.10	***	3.58 ± 0.18	3.70 ± 0.21	n.s.
Rheo ramp						
1xIAP	0.67 ± 0.36	5.09 ± 1.05	***	2.97 ± 0.88	6.24 ± 1.19	**
2xIAP	3.58 ± 1.57	13.71 ± 1.81	***	10.5 ± 1.75	14.65 ± 2.37	n.s.
3xIAP	7.78 ± 2.94	22.31 ± 2.60	***	18.41 ± 2.78	22.41 ± 3.26	n.s.
2xIAP Rheo20s						
0.0–2.5s	7.5 ± 2.15	11.25 ± 1.61	n.s.	9.41 ± 1.69	13.24 ± 2.05	*
2.5–5.0s	3.20 ± 1.48	13.06 ± 2.05	***	9.52 ± 1.87	13.44 ± 2.40	n.s.
5.0–7.5s	2.20 ± 1.15	15.21 ± 2.47	***	10.35 ± 1.91	14.20 ± 2.52	n.s.
7.5–10.0s	1.58 ± 0.82	16.75 ± 2.67	***	10.29 ± 1.78	13.58 ± 2.24	n.s.
10.0–12.5s	1.02 ± 0.59	16.09 ± 2.55	***	10.94 ± 1.76	13.72 ± 2.30	n.s.
12.5–15.0s	0.88 ± 0.53	14.28 ± 2.42	***	11.97 ± 1.86	13.96 ± 2.37	n.s.
15.0–17.5s	0.91 ± 0.60	12.96 ± 2.39	***	11.91 ± 1.80	16.06 ± 2.69	n.s.
17.5–20.0s	1.02 ± 0.72	12.06 ± 2.30	***	11.94 ± 1.75	16.48 ± 2.69	n.s.
Total #APs	16.35 ± 6.10	110.58 ± 16.9	***	86.35 ± 13.2	114.72 ± 15.3	n.s.

I_{AP}, minimal current to evoke a single AP within 50 ms; V_{mem}, resting membrane potential; OS, overshoot; AHP, afterhyperpolarization; S1, maximal speed of depolarization; S2 and S3, biphasic repolarization speeds; n.s, not significant.

**p > 0.05, **p > 0.01, ***p > 0.001, N, number of cells; n, number of mice.*

of the *Prdm12*$^{fl/fl}$*; Avil-Cre*$^{+}$ model and identified 35 transcripts common to both models, now referred to as PRDM12 core DEGs (**Figure 5B**). In addition to *Prdm12*, the core DEGs include the genes encoding for TRP channels and TRP channel-associated signaling including *Ntrk1*, *Trpm8*, *Adcy5*, *Prkcd*, and ion channels like *Kcnv1*, *Kcnb1*, *Scn4a*, and neurotransmitter receptor activity like *Grik1* and *Chrna7*. Overrepresentation analysis of MF and KEGG pathway gene sets with a g:profiler toolbox revealed that PRDM12 core DEGs are mainly involved in the function of ion channel activity, either passive or gated (**Figure 5C**). Among KEGG pathways, top enriched pathways are associated with synaptic signaling and pathways regulating TRP-mediated signaling (**Figure 5C**, bottom panel). DEG protein products included in TRP channel signaling are illustrated in **Figure 5D**, with the associated heat map representing DEGs from both mouse models.

To examine if dysregulated transcriptomes of *Prdm12*$^{fl/fl}$*; Avil-Cre*$^{+}$ and TAM-injected *Prdm12*$^{fl/fl}$; *Rosa26-CreER*$^{T2+}$ models vs. corresponding controls reflect transcriptome footprints of nociceptors or some other sensory cell types in the DRG as benchmark gene sets, we used the top 50 genes marking each of the 14 different distinct sensory cellular subtypes described by Sharma et al. (2020) and performed GSEA. *Prdm12*$^{fl/fl}$*; Avil-Cre*$^{+}$ model is predominantly enriched for the cell types associated with proprioception and mechanoreception (**Figure 6A**, top). Moreover, in both *Prdm12*$^{fl/fl}$*; Avil-Cre*$^{+}$ and *Prdm12*$^{fl/fl}$; *Rosa26-CreER*$^{T2+}$ experimental set-up, the subtypes of nociceptors were enriched in the corresponding

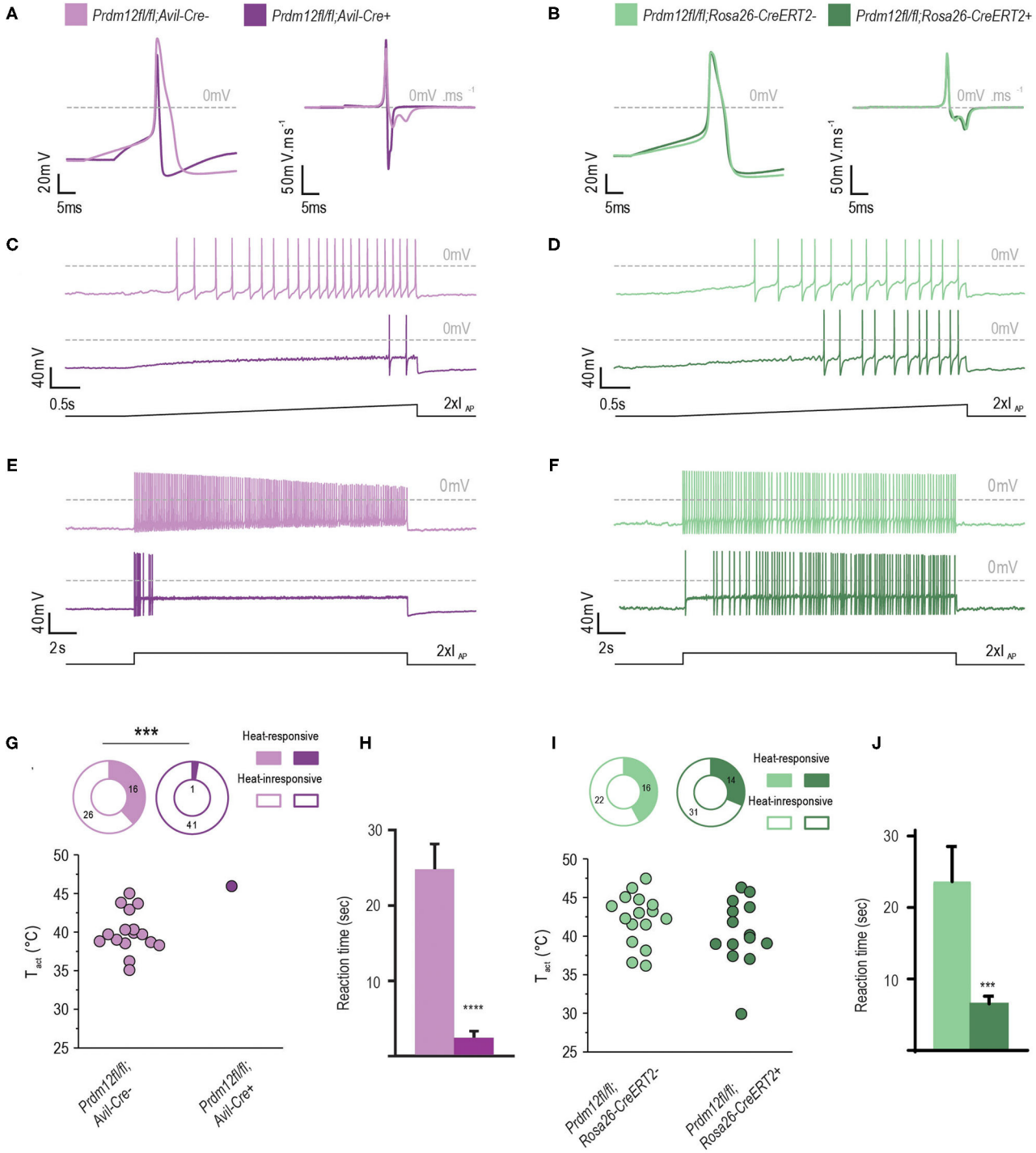

FIGURE 4 | PRDM12 expression is required for proper biophysical properties of cultured DRG. **(A)** and **(B)** Representative action potentials (APs) and their first derivatives from *Prdm12*$^{fl/fl}$*; Avil-Cre*$^{+}$ **[(A)**, dark purple trace], *Prdm12*$^{fl/fl}$*; Avil-Cre*$^{-}$ **[(A)**, light purple trace], *Prdm12*$^{fl/fl}$*; Rosa26-CreER*$^{T2+}$ **[(B)**, dark green trace], and *Prdm12*$^{fl/fl}$*; Rosa26-CreER*$^{T2-}$ **[(B)**, light green trace] cultured DRG neurons. Note the reduced AP width and lack of biphasic repolarization in *Prdm12*$^{fl/fl}$*; Avil-Cre*$^{+}$ **(A)**. **(C,D)** Typical examples of AP generation upon 2 x I_{AP} ramp-shaped depolarization showing the inability of *Prdm12*$^{fl/fl}$*; Avil-Cre*$^{+}$ DRG neurons to generate similar number of APs compared to the *Prdm12*$^{fl/fl}$*; Avil-Cre*$^{-}$ DRG neurons **(C)**. Note the delay of AP firing for initial 2 s in the ramp-shaped depolarization in *Prdm12*$^{fl/fl}$*; Avil-CreER*$^{T2+}$, as compared to littermate controls **(D)**. **(E)** *Prdm12*$^{fl/fl}$*; Avil-Cre*$^{+}$ neurons dot not generate APs over the full time course of 2 x I_{AP} current injection compared to *Prdm12*$^{fl/fl}$*; Avil-Cre*$^{-}$ neurons. **(F)** The TAM-injected *Prdm12*$^{fl/fl}$*; Rosa26-CreER*$^{T2+}$ and *Prdm12*$^{fl/fl}$*; Rosa26-CreER*$^{T2-}$ generate APs over the full length of 2 x I_{AP} current injection although the TAM-injected *Prdm12*$^{fl/fl}$*; Rosa26-CreER*$^{T2+}$ show a reduced number of APs in the beginning of the 2 x I_{AP} current injection. **(G,I)** Fraction of neurons that showed temperature-evoked currents (top panels) and temperature activation thresholds (T_{act}) of the recorded neurons (bottom panels). *Prdm12*$^{fl/fl}$*; Avil-Cre*$^{+}$ neurons do not respond to the applied ramp-shaped temperature increase **(G)**, whereas in both fractions of TAM-injected *Prdm12*$^{fl/fl}$;

(Continued)

FIGURE 4 | *Rosa26-CreER*$^{T2+}$ and *Prdm12*$^{fl/fl}$*; Rosa26-CreER*$^{T2-}$ neurons their respective T_{act} were similar **(I)**. **(H)** *Prdm12*$^{fl/fl}$*; Avil-Cre*$^{+}$ exhibited reduced behavioral reactions to intraplantar capsaicin injections as compared to their respective littermate controls ($N = 33$, mean values 12.38 ± 1.702 SEM vs. $N = 18$ 1.216 ± 0.4454 SEM). **(J)** TAM-injected *Prdm12*$^{fl/fl}$*; Rosa26-CreER*$^{T2+}$ exhibited reduced behavioral reactions to intraplantar capsaicin injections as compared to their respective littermate controls ($N = 26$, mean values 23.66 ± 4.887 SEM vs. $N = 35$ 6.555 ± 1.04 SEM). Values of $^{***}p \leq 0.005$, $^{****}p \leq 0.0001$, ns: not significant. Lower black traces are examples of the applied stimulus protocol.

controls as compared to the loss-of-function models (**Figure 6A**, **Supplementary Figures 5B–D**). This finding shows that the deletion of *Prdm12* depletes DRG of nociceptor-specific genes, and in particular the subtypes of somatostatin-positive and CGRP-positive nociceptors. Intriguingly, this observation is common to both the developmental *Prdm12*$^{fl/fl}$*; Avil-Cre*$^{+}$ as well as adult TAM-inducible *Prdm12*$^{fl/fl}$; *Rosa26-CreER*$^{T2+}$models. Recently, Landy et al. (2021) have reported a transcriptomic analysis of bulk RNA in DRG harvested from a spatially restricted adult-inducible Prdm12 KO (*Prdm12Avil*^{ERT2CKO}). Between 150 genes that were dysregulated in TAM-inducible *Prdm12Avil*^{ERT2CKO} described by Landy et al. (2021) and 67 DEGs that were found in our TAM-inducible *Prdm12*$^{fl/fl}$; *Rosa26-CreER*^{T2} model, we find an overlap in 2 genes—*Prdm12* and *Chrna6*. However, between DEGs in Landy et al. (2021) model and our *Prdm12*$^{fl/fl}$*; Avil-Cre* model, we identified 40 overlapping genes, 21 of which are expressed in the DRG, including *Prdm12*, *Chrna6*, *Trpm3*, and are important for the development of nervous system, such as *Nnat*. Mapping of the possible functional consequences of the DEGs in both models was performed by GSEA of GO MF (GO:MF) gene sets, followed by generating the clustered network of the enriched terms (**Figure 6B**). Developmental model *Prdm12*$^{fl/fl}$*; Avil-Cre*$^{+}$ vs. controls exhibited an enrichment in the control samples (conversely the depletion in *Prdm12*$^{fl/fl}$*; Avil-Cre*$^{+}$) for gene sets that cluster into networks including "ion channel activity," "neurotransmitter associated activity," and "neuropeptides" (**Figure 6B**). Clusters in the adult model TAM-injected *Prdm12*$^{fl/fl}$; *Rosa26-CreER*$^{T2+}$ vs. control maintain the depletion of gene sets associated with "ion channel activity" (**Figure 6A**).

To explore the enrichment patterns within ion channel activity clusters between the models, we investigated various gene sets to identify if any specific GO:MF terms are common in the two models. "Calcium activated ion channel activity" (**Figure 6C**) and "potassium channel activity" terms (**Figure 6D**, **Supplementary Figure 5E**) are enriched in controls of both models. Within the genes contributing to the leading edge of both models, 21 genes are common (**Figure 6D**, middle panel). Most of the common genes belong to the group of voltage-gated potassium channels (**Figure 6D**, right panel). To identify specific gene sets that differ between *Prdm12*$^{fl/fl}$*; Avil-Cre*$^{+}$ and *Prdm12*$^{fl/fl}$; *Rosa26-CreER*$^{T2+}$ models, we analyzed neuropeptide and neurotransmitter clusters in the *Prdm12*$^{fl/fl}$*; Avil-Cre*$^{+}$. Within a neuropeptide cluster, GO terms associated with neuropeptide binding were depleted in the *Prdm12*$^{fl/fl}$*; Avil-Cre*$^{+}$ (and enriched in the controls), with transcripts associated with opioid receptors *Oprm1* and *Oprk*, as well as galanin receptors *Galr1* and *Galr2* within the leading edge (**Figure 6E**, left panel). In the neurotransmitter cluster, genes associated with neurotransmitter-mediated ion channel activity were depleted in *Prdm12*$^{fl/fl}$*; Avil-Cre*$^{+}$ model as compared to controls, with the subunits of glutamate receptors (*Grin2c*, *Grik4*, *Grin2d*, and *Grik1*), cholinergic nicotinic receptors contributing the most to the leading edge (**Figure 6E**, right panel). Furthermore, the analysis of ion channel cluster in the *Prdm12*$^{fl/fl}$; *Rosa26-CreER*$^{T2+}$ model revealed the depletion of sodium channel activity genes, including markers of nociceptors, voltage-gated sodium channels encoded by *Scn11a*, and *Scn10a*, members of TRP pathways like acid sensing channels encoded by *Asic1* and *Asic3* as well as glutamate receptor subunits *Grik1*, *Grik4*, and *Grik5* (**Figure 6F**).

DISCUSSION

Here, we present two novel cases of CIP in a large, consanguineous family, exhibiting symptoms in line with defective nociception that share a novel homozygous variant in *PRDM12*. Generating several developmental and adult-onset deletion mouse models of *Prdm12,* we could determine that early developmental expression of PRDM12 is essential for survival in mice. We show that PRDM12 expression is essential for acute noxious pain detection throughout life. Detailed electrophysiological analyses revealed different but significantly altered biophysical properties of cultured DRG in the developmental and in the adult PRDM12 ablation models. Indeed, different transcriptional programs are regulated by PRDM12 at different maturation stages, accounting for a difference in the corresponding cellular phenotypes. Taken together, these data confirm that developmental PRDM12 is essential in pain perception in mice by regulating key nociceptor-specific genes required for the development and function of nociceptors. While PRDM12 expression in adults is no longer essential for survival or needed for certain types of CNS functions, it is still required for nociceptive responses.

Human PRDM12 expression is exclusive to the PNS making it a promising therapeutic target (Chen et al., 2015). However, considering the restricted PRDM12 expression, it is not clear why a small number of PRDM12-CIP patients, including those in this report, have CNS dysfunctions. The analysis of WES of patient 1 identified eight rare variants in genes associated with autism and/or ID, but these are not shared with patient 2 and are unlikely to explain the CNS symptoms in this family. Interestingly, a splice-site acceptor variant reported here is in the same position as an already reported PRDM12-CIP case of different ethnic background, presenting with typical CIP symptoms including ID (Saini et al., 2017). Why should variants at this position but not in others have an impact on CNS function is not clear. Therefore, the molecular mechanisms underlying CNS symptoms that are

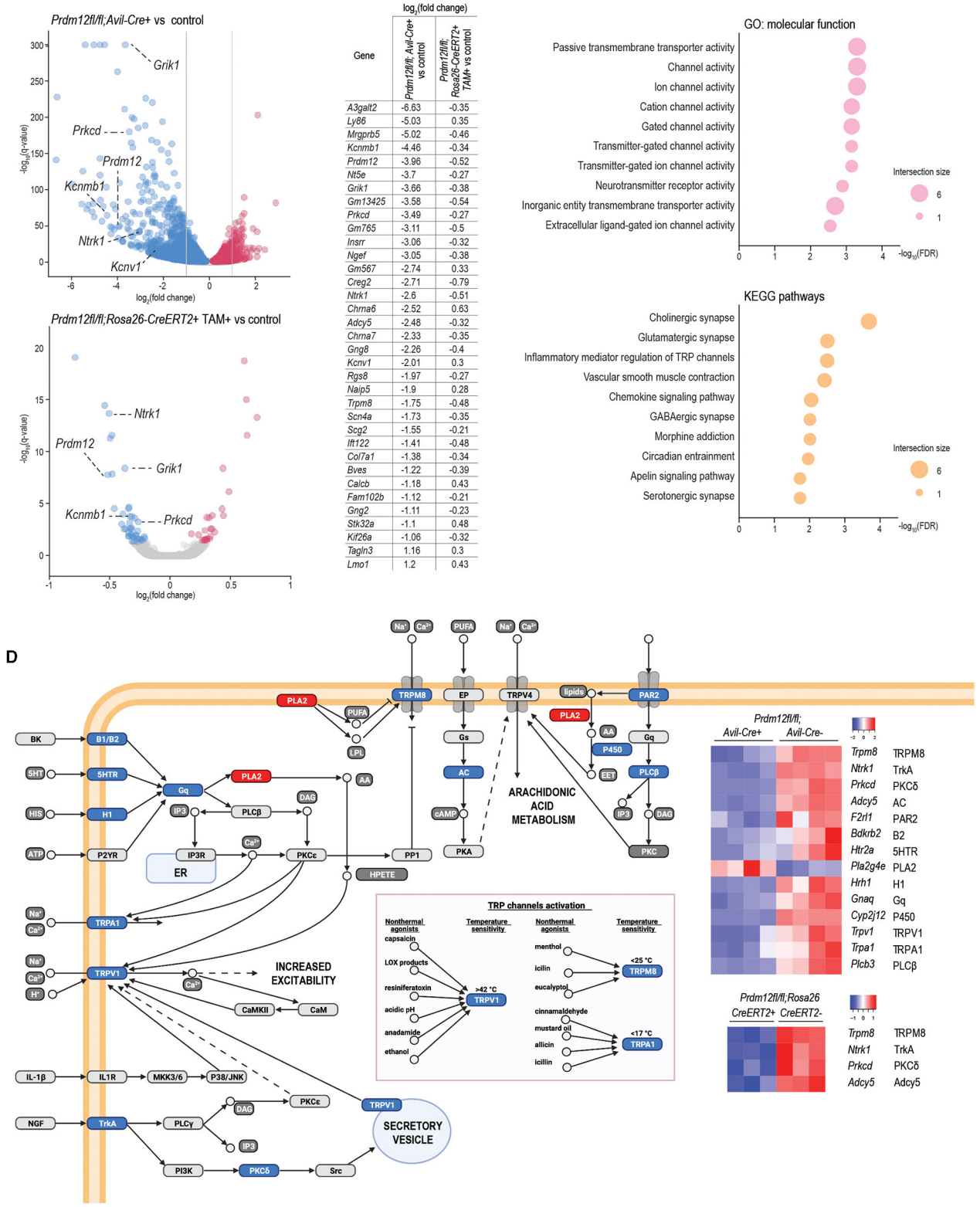

FIGURE 5 | Transcriptomics analysis of DRG of Prdm12-deficient animal models. **(A)** Volcano plot of differentially expressed genes (DEGs) depicts significantly upregulated and downregulated genes in pooled lumbar DRG isolated from adult *Prdm12*$^{fl/fl}$*; Avil-Cre*$^{+}$ (upper panel, four biological replicates) and *Prdm12*$^{fl/fl}$*; Rosa26-ER*$^{T2+}$ (lower panel, three biological replicates) as compared to their respective control littermates. X-axis represents $\log_2$ fold change and the y-axis

(Continued)

FIGURE 5 | represents $-\log_{10}(q\text{-values})$. Genes with the value of q (FDR) < 0.05 were considered differentially regulated, downregulated genes in blue and upregulated genes in red. Gray dotted lines in the top panel demark the cutoff for the most DEGs with at least 2-fold upregulation or downregulation. **(B)** The list of core DEGs (value of $q < 0.05$) common to both *Prdm12*$^{fl/fl}$*; Rosa26-ER*$^{T2+}$ and *Prdm12*$^{fl/fl}$*; Avil-Cre*$^{+}$ model, and the most DEGs (value of $q < 0.05$, |log2(fold change)|>1) of the *Prdm12*$^{fl/fl}$*; Avil-Cre*$^{+}$ model as compared to their corresponding controls. **(C)** About 10 most enriched terms in the overrepresentation analysis of the core DEGs for the GO:MF database (upper panel) and kyoto encyclopedia of genes and genomes (KEGG) pathways (lower panel). Values on the x-axis present –log10 of the Benjamini–Hochenberg FDR score for a particular pathway enrichment significance. **(D)** Transient receptor potential (TRP) channels pathway with heatplot of *Z*-scores for DEG members of the TRP pathway in both developmental and adult Prdm-12 deficiency model. Protein symbols corresponding to the dysregulated transcripts are denoted next to the transcript symbol, and colors within the pathway illustration correspond to the downregulation (blue) or upregulation (red) of the transcripts represented in the heatmap.

associated with PRDM12-CIP in a small number of cases remain to be elucidated.

We report PRDM12 expression in all adult mouse brain regions examined, suggesting a role for PRDM12 beyond nociception. Generating the *Prdm12*^{W160C} mouse model that proved to be neonatally lethal allowed us to conclude that fully functional PRDM12 is required for the survival in mice. While the cause of death is still not clear, lethality of the neuronal progenitor KO model *Prdm12*$^{fl/fl}$; *Sox10-Cre* leads us to posit that the PRDM12 essentiality may be intrinsic to the cells derived from the Sox10+ lineage, not necessarily of neuronal origin. The heart or brain, for example, expresses PRDM12 but also contain Sox10+ cardiomyocytes and glia, respectively (Kuhlbrodt et al., 1998; Montero et al., 2002; Sande-Melón et al., 2019; Tang et al., 2019). The role for PRDM12 in mouse CNS has recently gained attention. Hypothalamic PRDM12 regulates *Pomc* expression, food intake, adiposity, and weight (Chen et al., 2020; Woo et al., 2020). Here, we report no effect of ablating PRDM12 expression in adults on survival, locomotion, anxiety, or hippocampal-dependent learning. These results suggest that whatever the role for developmental PRDM12 is in the mouse CNS, it is no longer required for the behaviors tested here in the adult. It would be of great interest to fully characterize the role for PRDM12 in the mouse CNS, and in light of a growing number of PRDM12-CIP patients with CNS symptoms, to explore the possibility for its function in the human brain.

Analyses of PRDM12 developmental and adult-ablation models show a dependence of proper nociceptive responses on the presence of Prdm12. Contrary to our results, recent publication indicates that, while the adult murine model of Prdm12 deficiency has an effect on transcriptional regulation, it does not translate to the impairment of pain sensation behaviorally (Landy et al., 2021). We posit that these differences could be explained by the different experimental mouse models used in the two studies. TAM-inducible *Prdm12*$^{fl/fl}$; *Rosa26-CreER*$^{T2+}$ adult model used here targets *Prdm12* exon 2, mimicking the splice acceptor mutation described in our patients, under the ubiquitous *Rosa26* promoter, while Landy et al. (2021) describe a model that targets exon 5, and is under the TAM-inducible DRG-specific *Avil* promoter targeting a more specific cellular subtype only in the periphery. The reduction in behavioral responses to capsaicin injections together with the significant dysfunction of cultured nociceptor electrophysiological responses in our *Prdm12*$^{fl/fl}$; *Rosa26-CreER*$^{T2+}$ mouse model confirm PRDM12 nociceptive regulation in the PNS even in adults. However, a variety of behavioral pain responses were not observed in the DRG-specific adult-ablation model in Landy et al. (2021), implying a possible contribution of PRDM12 action in CNS pain responses that would warrant further study.

Electrophysiological studies of developmental homozygous mouse model clearly determined that it is the peripherally expressed PRDM12 during the embryonic/developmental stage that is required for the detection and signaling of nociceptive stimuli. We find that, while resting membrane potential is unaffected in the developmental PRDM12-ablation model, AP morphology is impaired, as well as the number of APs generated upon different stimulation protocols. Moreover, based on the prepulse inhibition experiments, we find that the ratio of currents generated by TTX-sensitive Na^+ channels is increased in *Prdm12*$^{fl/fl}$*; Avil-Cre*$^{+}$ neurons as compared to control littermates. A significant reduction of pain-related genes encoding for $Na_v1.8$, $Na_v1.9$, TrpV1, TrkA, and CGRP, in the *Prdm12*$^{fl/fl}$*; Avil-Cre*$^{+}$ strongly corroborates the electrophysiological nociceptive dysfunctions are due to the lack of nociceptors in developmental models as described previously (Desiderio et al., 2019).

Transcriptome analysis of the bulk DRG shows *Prdm12*$^{fl/fl}$*; Avil-Cre*$^{+}$ dysregulation of more than 5,000 genes, 868 of which are dysregulated by at least a 2-fold increase or decrease. Downregulated expression of nociceptor signature genes including *Ntrk1*, *Scn10a* and *Scn11a*, *Calca* in *Prdm12*$^{fl/fl}$*; Avil-Cre*$^{+}$ compared to controls is a consequence of the lack of nociceptor development as described previously (Desiderio et al., 2019), and confirmed by the lack of skin PGP9.5 positive innervation in *Prdm12*$^{fl/fl}$*; Avil-Cre*$^{+}$ animals. Nevertheless, as *Prdm12*$^{fl/fl}$; *Rosa26-CreER*$^{T2+}$ TAM-inducible model overlaps with *Prdm12*$^{fl/fl}$*; Avil-Cre*$^{+}$ in 35 DEGs, which in the overrepresentation analysis is associated with ion channels, and more specifically TRP channels pathways, indicate that Prdm12 maintains a role in regulating ion channels essential for the function of nociceptors even in the adulthood, supported by the electrophysiological and behavioral data. Indeed, the comparison of our *Prdm12*$^{fl/fl}$*; Avil-Cre* model transcriptomic data to adult TAM-inducible model *Prdm12Avil*^{ERT2CKO} proposed by Landy et al. (2021) shows an overlap in 40 DEGs, out of which 21 are DRG genes.

Gene set enrichment analysis highlights that both developmental and adult models share the depletion of the terms associated with an ion channel cluster. Many of these terms in adult model are the members of distinct subfamilies of voltage-gated potassium channels essential for the generation and propagation of APs, corroborating the electrophysiological changes and behavioral responses to capsaicin injections. In

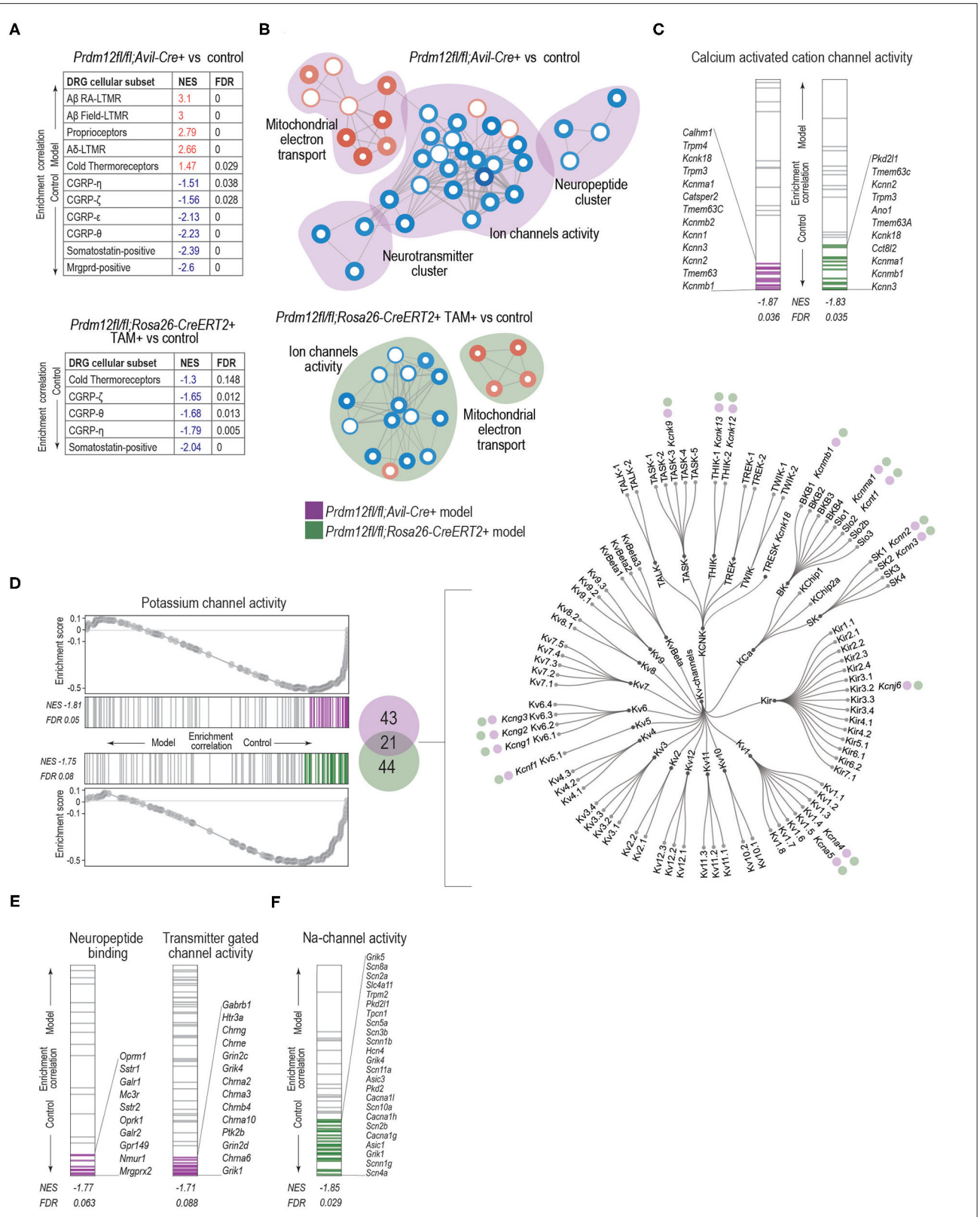

FIGURE 6 | GSEA analysis with enrichment mapping shows distinct clusters of dysregulated MF:GO terms. **(A)** Dysregulation of bulk RNA DRG transcriptomes as demarked by gene sets most significant by sensory neuron subtypes detected in the DRG, for both *Prdm12*$^{fl/fl}$*; Avil-Cre*$^{+}$ (top table) or TAM-injected *Prdm12*$^{fl/fl}$*; Rosa26-ER*$^{T2+}$ (bottom table) as detected by GSEA with the cutoff value of *p* of 0.05 and FDR cutoff of 0.25. **(B)** Clusters of GSEA enriched-term nodes in the GO:MF terms. Nodes in red either in *Prdm12*$^{fl/fl}$*; Avil-Cre*$^{+}$ (pink cloud, left) or in *Prdm12*$^{fl/fl}$*; Rosa26-ER*$^{T2+}$ (blue cloud, right) are enriched in DRG, while nodes in

(Continued)

FIGURE 6 | blue represent the depletion of MF terms, as labeled. Thickness of the node border corresponds to the $-\log_{10}$(FDR), while depth of the color corresponds to normalized enrichment score (NES) of a particular node as compared to the whole gene set. Thickness of the edge lines corresponds to the strength of the used similarity coefficient. Clusters of highly connected nodes are grouped together and annotated with the closest common functional term. **(C)** GSEA enrichment graphs showing the distribution of calcium-activated cation channel activity as an example of a significantly enriched GO:MF term common to both in *Prdm12$^{fl/fl}$; Avil-Cre^{+}* (left) or TAM-injected *Prdm12$^{fl/fl}$; Rosa26-ER^{T2+}* (right) showing genes contributing to the leading edge in purple and green for *Prdm12$^{fl/fl}$; Avil-Cre^{+}* and *Prdm12$^{fl/fl}$; Rosa26-ER^{T2+}*, respectively. NES and FDR values are denotated in the figure. **(D)** Enrichment graphs depicting the distribution of GOM:MF potassium channel activity genes enrichment in the controls of both *Prdm12$^{fl/fl}$; Avil-Cre^{+}* (left panel, top) and *Prdm12$^{fl/fl}$; Rosa26-ER^{T2+}* (left panel, bottom). Graphs for each model show running enrichment scores, as well as NES and FDR. Genes within the leading edge are colored purple and green for *Prdm12$^{fl/fl}$; Avil-Cre^{+}* and *Prdm12$^{fl/fl}$; Rosa26-ER^{T2+}* models, respectively. In the middle panel, Venn diagram depicts the number of genes within the leading edge of *Prdm12$^{fl/fl}$; Avil-Cre^{+}* (43 genes, purple) and *Prdm12$^{fl/fl}$; Rosa26-ER^{T2+}* (44 genes, green) and 21 overlapping genes. Dendogram of voltage-gated potassium channel families (right) denotes the type of Kv-channel transcripts shared between the two models, note the purple and green circles. **(E)** Enrichment graphs showing the distribution of terms specific for *Prdm12$^{fl/fl}$; Avil-Cre^{+}* model, showing the depletion of GO:MF neuropeptide binding genes and transmitter-gated channel activity genes in *Prdm12$^{fl/fl}$; Avil-Cre^{+}* model as compared to the corresponding controls. Positions of genes contributing to the significant enrichment are colored in purple. **(F)** Enrichment graphs showing the distribution of GO:MF sodium channel activity genes in the transcriptome of *Prdm12$^{fl/fl}$; Rosa26-ER^{T2+}* model, showing an enrichment in the controls as compared to the deficiency model. Positions of genes contributing to the significant enrichment are colored in green. NES and FDR values are denoted in the figures.

contrast, developmental model exhibits specific clusters of dysregulated gene sets including neurotransmitter- (e.g., *Grik1, Grik4, Grin2d*, and *Grin2c*) and neuropeptide- (e.g., *Oprm1*, *Oprk1, Galr1, Galr2,* and *Nmur1)* related clusters. Specific gene set that is selectively depleted in *Prdm12$^{fl/fl}$*; *Rosa26-CreER^{T2+}* but not in *Prdm12$^{fl/fl}$*; *Avil-Cre^{+}* is associated with sodium channel activity. Interestingly, these include nociceptor-specific genes *Scn10a*, encoding for $Na_v1.8$ and *Scn11a* encoding for $Na_v1.9$, possibly contributing to the observed differences in AP firing in TAM-injected *Prdm12$^{fl/fl}$*; *Rosa26-CreER^{T2+}* as compared to the corresponding controls.

PR domain-containing member 12 ablation in *Prdm12$^{fl/fl}$; Avil-Cre^{+}* animals results in electrophysiological and behavioral deficiencies and the lack of nociceptor skin innervation due to the essential role played by PRDM12 in the specification of nociceptor development. However, TAM-injected *Prdm12$^{fl/fl}$*; *Rosa26-CreER^{T2+}* adult-deletion model maintains a significant dysregulation of a small subset of genes involved in TRP channel and ion channel activities. Clearly, PRDM12 is an indispensable component of nociceptor specification and function required for pain perception throughout life. Together with its uniquely restricted expression in humans and the requirement for adult pain perception make it an intriguing therapeutic target with immense clinical potential.

DATA AVAILABILITY STATEMENT

The datasets presented in this study can be found in online repositories. The names of the repository/repositories and accession number(s) can be found at: https://www.ncbi.nlm.nih.gov/, PRJNA734482.

ETHICS STATEMENT

The studies involving human participants were reviewed and approved by Shahid Beheshti University of Medical Sciences ethics board (with the current update of the Declaration of Helsinki). Written informed consent to participate in this study and for the publication of any potentially identifiable images or data included in this article was provided by the participants' legal guardian/next of kin. The animal study was reviewed and approved by Bundesministerium fur Wissenschaft, Forschung und Wirtschaft (BMWFW-66.015/0011-WF/V/3b/2017), Austria and carried out according to EU-directive 2010/63/EU. Prdm12W160 and Prdm12S159AfsTer2+/- experiments were approved by the University of Sydney Animal Ethics Committee under animal ethics protocol (938) and reporting complies with the ARRIVE guidelines.

AUTHOR CONTRIBUTIONS

TK: curated data, performed the formal analysis, investigation, validation of the data, visualization, and assisted in writing the manuscript. ML: curated data, performed the formal analysis, investigation, and assisted in writing the manuscript. EL, JM, and CF: curated data, performed the formal analysis, and investigation. EA and AT: curated patient data. HD: participated in project administration and supervision. EB: provided resources. GN and MK: provided resources, project administration, supervision, and funding acquisition. JP: conceptualized the project and methodology, provided resources, and funding acquisition. VN: conceptualized the project and methodology, curated data, participated in the investigation, formal analysis, resources, project administration, supervision, funding acquisition, and wrote the manuscript. All authors contributed to the article and approved the submitted version.

FUNDING

This work was funded by Austrian Science Fund (FWF): P32924 and Ludwig Boltzmann Gesellschaft. TK was funded by a DOC-fellowship of the Austrian Academy of Sciences (OeAW): 25408; CF was funded by a DOC-fellowship of the Austrian Academy of Sciences (OeAW): 25525.

ACKNOWLEDGMENTS

We would like to thank patients and their families for participating in this study. WES was performed at the BSF in CeMM Center for Molecular Medicine of the Austrian Academy of Sciences (CeMM). We would like to thank Brian Metcher,

Department of Evolutionary Biology, University of Vienna, for his help with the microCT imaging and Sophie Imhof, Medical University of Vienna, for help with figure design. Figure illustrations were created with BioRender, Adobe Illustrator 2021, and Python (Pandas, Numpy, Seaborn libraries).

SUPPLEMENTARY MATERIAL

The Supplementary Material for this article can be found online at: https://www.frontiersin.org/articles/10.3389/fnmol.2021.720973/full#supplementary-material

REFERENCES

Bandell, M., Story, G. M., Hwang, S. W., Viswanath, V., Eid, S. R., Petrus, M. J., et al. (2004). Noxious cold ion channel TRPA1 is activated by pungent compounds and bradykinin. *Neuron* 41, 849–857. doi: 10.1016/S0896-6273(04)00150-3

Bartesaghi, L., Wang, Y., Fontanet, P., Wanderoy, S., Berger, F., Wu, H., et al. (2019). PRDM12 is required for initiation of the nociceptive neuron lineage during neurogenesis. *Cell Rep.* 26, 3484–3492.e4. doi: 10.1016/j.celrep.2019.02.098

Caterina, M. J., Schumacher, M. A., Tominaga, M., Rosen, T. A., Levine, J. D., and Julius, D. (1997). The capsaicin receptor: a heat-activated ion channel in the pain pathway. *Nature.* 389, 816–824. doi: 10.1038/39807

Chen, X., Wyler, S. C., Li, L., Arnold, A. G., Wan, R., Jia, L., et al. (2020). Comparative transcriptomic analyses of developing melanocortin neurons reveal new regulators for the anorexigenic neuron identity. *J. Neurosci.* 40, 3165–3177. doi: 10.1523/JNEUROSCI.0155-20.2020

Chen, Y.-C., Auer-Grumbach, M., Matsukawa, S., Zitzelsberger, M., Themistocleous, A. C., Strom, T. M., et al. (2015). Transcriptional regulator PRDM12 is essential for human pain perception. *Nat. Genet.* 47, 803–808. doi: 10.1038/ng.3308

Cingolani, P., Platts, A., Wang, L. L., Coon, M., Nguyen, T., Wang, L., et al. (2012). A program for annotating and predicting the effects of single nucleotide polymorphisms, SnpEff SNPs in the genome of *Drosophila melanogaster* strain. *Fly* 6, 80–92. doi: 10.4161/fly.19695

Desiderio, S., Vermeiren, S., Van Campenhout, C., Kricha, S., Malki, E., Richts, S., et al. (2019). Prdm12 directs nociceptive sensory neuron development by regulating the expression of the NGF receptor TrkA. *Cell Rep.* 26, 3522–3536.e5. doi: 10.1016/j.celrep.2019.02.097

Dittert, I., Vlachová, V., Knotková, H., Vitásková, Z., Vyklicky, L., Kress, M., et al. (1998). A technique for fast application of heated solutions of different composition to cultured neurones. *J. Neurosci. Methods*. 82, 195–201. doi: 10.1016/S0165-0270(98)00051-X

Dobin, A., Davis, C. A., Schlesinger, F., Drenkow, J., Zaleski, C., Jha, S., et al. (2013). STAR: Ultrafast universal RNA-seq aligner. *Bioinformatics* 29, 15–21. doi: 10.1093/bioinformatics/bts635

Hasegawa, H., Abbott, S., Han, B. X., Qi, Y., and Wang, F. (2007). Analyzing somatosensory axon projections with the sensory neuron-specific Advillin gene. *J. Neurosci.* 27, 14404–14414. doi: 10.1523/JNEUROSCI.4908-07.2007

Hohenauer, T., and Moore, A. W. (2012). The Prdm family: expanding roles in stem cells and development. *Dev.* 139, 2267–2282. doi: 10.1242/dev.070110

Imhof, S., Kokotović, T., and Nagy, V. (2020). PRDM12: new opportunity in pain research. *Trends Mol. Med.* 26, 895–897. doi: 10.1016/j.molmed.2020.07.007

Julius, D. (2013). TRP channels and pain. *Annu. Rev. Cell Dev. Biol.* 29, 355–384. doi: 10.1146/annurev-cellbio-101011-155833

Karczewski, K. J., Francioli, L. C., Tiao, G., Cummings, B. B., Alföldi, J., Wang, Q., et al. (2020). The mutational constraint spectrum quantified from variation in 141,456 humans, Genome Aggregation Database Consortium. *Nature* 581:19. doi: 10.1038/s41586-020-2308-7

Kinameri, E., Inoue, T., Aruga, J., Imayoshi, I., Kageyama, R., Shimogori, T., et al. (2008). Prdm proto-oncogene transcription factor family expression and interaction with the Notch-Hes pathway in mouse neurogenesis. *PLoS ONE* 3, 1–10. doi: 10.1371/journal.pone.0003859

Kircher, M., Witten, D. M., Jain, P., O'roak, B. J., Cooper, G. M., and Shendure, J. (2014). A general framework for estimating the relative pathogenicity of human genetic variants. *Nat. Genet.* 46, 310–315. doi: 10.1038/ng.2892

Kuhlbrodt, K., Herbarth, B., Sock, E., Hermans-Borgmeyer, I., and Wegner, M. (1998). Sox10, a novel transcriptional modulator in glial cells. *J. Neurosci.* 18, 237–250. doi: 10.1523/JNEUROSCI.18-01-00237.1998

Landrum, M. J., Lee, J. M., Benson, M., Brown, G. R., Chao, C., Chitipiralla, S., et al. (2018). ClinVar: improving access to variant interpretations and supporting evidence. *Nucleic Acids Res.* 46:gkx1153. doi: 10.1093/nar/gkx1153

Landy, M. A., Goyal, M., Casey, K. M., Liu, C., and Lai, H. C. (2021). Loss of Prdm12 during development, but not in mature nociceptors, causes defects in pain sensation. *Cell Rep.* 34:108913. doi: 10.1016/j.celrep.2021.108913

Langeslag, M., Malsch, P., Welling, A., and Kress, M. (2014). Reduced excitability of gp130-deficient nociceptors is associated with increased voltage-gated potassium currents and Kcna4 channel upregulation. *Pflugers Arch. Eur. J. Physiol.* 466, 2153–2165. doi: 10.1007/s00424-014-1443-0

Lau, M. T., Manion, J., Littleboy, J. B., Oyston, L., Khuong, T. M., Wang, Q. P., et al. (2019). Molecular dissection of box jellyfish venom cytotoxicity highlights an effective venom antidote. *Nat. Commun.* 10:1655. doi: 10.1038/s41467-019-09681-1

Liberzon, A., Subramanian, A., Pinchback, R., Thorvaldsdóttir, H., Tamayo, P., and Mesirov, J. P. (2011). Molecular signatures database (MSigDB) 3.0. *Bioinformatics* 27, 1739–1740. doi: 10.1093/bioinformatics/btr260

Love, M. I., Huber, W., and Anders, S. (2014). Moderated estimation of fold change and dispersion for RNA-seq data with DESeq2. *Genome Biol.* 15:8. doi: 10.1186/s13059-014-0550-8

Martin, A. R., Williams, E., Foulger, R. E., Leigh, S., Daugherty, L. C., Niblock, O., et al. (2019). PanelApp crowdsources expert knowledge to establish consensus diagnostic gene panels. *Nat. Genet.* 51, 1560–1565. doi: 10.1038/s41588-019-0528-2

Matsukawa, S., Miwata, K., Asashima, M., and Michiue, T. (2015). The requirement of histone modification by PRDM12 and Kdm4a for the development of pre-placodal ectoderm and neural crest in Xenopus. *Dev. Biol.* 399, 164–176. doi: 10.1016/j.ydbio.2014.12.028

Merico, D., Isserlin, R., Stueker, O., Emili, A., and Bader, G. D. (2010). Enrichment map: a network-based method for gene-set enrichment visualization and interpretation. *PLoS ONE* 5:13984. doi: 10.1371/journal.pone.0013984

Metscher, B. D. (2009). MicroCT for developmental biology: a versatile tool for high-contrast 3D imaging at histological resolutions. *Dev. Dyn.* 246, 368–380. doi: 10.1002/dvdy.21857

Metscher, B. D. (2011). X-ray microtomographic imaging of intact vertebrate embryos. *Cold Spring Harb. Protoc.* 2011:prot067033. doi: 10.1101/pdb.prot067033

Montero, J. A., Giron, B., Arrechedera, H., Cheng, Y. C., Scotting, P., Chimal-Monroy, J., et al. (2002). Expression of Sox8, Sox9 and Sox10 in the developing valves and autonomic nerves of the embryonic heart. *Mech. Dev.* 118, 199–202. doi: 10.1016/S0925-4773(02)00249-6

Nagy, V., Cole, T., Van Campenhout, C., Khoung, T. M., Leung, C., Vermeiren, S., et al. (2015). The evolutionarily conserved transcription factor PRDM12 controls sensory neuron development and pain perception. *Cell Cycle* 14, 1799–1808. doi: 10.1080/15384101.2015.1036209

Nagy, V., Hollstein, R., Pai, T. P., Herde, M. K., Buphamalai, P., Moeseneder, P., et al. (2019). HACE1 deficiency leads to structural and functional neurodevelopmental defects. *Neurol. Genet.* 5:e330. doi: 10.1212/NXG.0000000000000330

Namer, B., Ørstavik, K., Schmidt, R., Mair, N., Kleggetveit, I. P., Zeidler, M., et al. (2017). Changes in ionic conductance signature of nociceptive neurons underlying fabry disease phenotype. *Front. Neurol.* 8:335. doi: 10.3389/fneur.2017.00335

Reimand, J., Isserlin, R., Voisin, V., Kucera, M., Tannus-Lopes, C., Rostamianfar, A., et al. (2019). Pathway enrichment analysis and visualization of omics data using g:Profiler, GSEA, Cytoscape and EnrichmentMap. *Nat. Protoc.* 14, 482–517. doi: 10.1038/s41596-018-0103-9

Reimand, J., Kull, M., Peterson, H., Hansen, J., and Vilo, J. (2007). G: profiler-a web-based toolset for functional profiling of gene lists from large-scale experiments. *Nucleic Acids Res.* 35:W193. doi: 10.1093/nar/gkm226

Ritter, A. M., and Mendell, L. M. (1992). Somal membrane properties of physiologically identified sensory neurons in the rat: effects of nerve growth factor. *J. Neurophysiol.* 68, 2033–2041. doi: 10.1152/jn.1992.68.6.2033

Saini, A. G., Padmanabh, H., Sahu, J. K., Kurth, I., Voigt, M., and Singhi, P. (2017). Hereditary sensory polyneuropathy, pain insensitivity and global developmental delay due to novel mutation in PRDM12 gene. *Indian J. Pediatr.* 84, 332–333. doi: 10.1007/s12098-016-2284-y

Sande-Melón, M., Marques, I. J., Galardi-Castilla, M., Langa, X., Pérez-López, M., Botos, M. A., et al. (2019). Adult sox10+ cardiomyocytes contribute to myocardial regeneration in the Zebrafish. *Cell Rep.* 29, 1041–1054.e5. doi: 10.1016/j.celrep.2019.09.041

Shannon, P., Markiel, A., Ozier, O., Baliga, N. S., Wang, J. T., Ramage, D., et al. (2003). Cytoscape: a software environment for integrated models of biomolecular interaction networks. *Genome Res.* 13, 2498–2504. doi: 10.1101/gr.1239303

Sharma, N., Flaherty, K., Lezgiyeva, K., Wagner, D. E., Klein, A. M., and Ginty, D. D. (2020). The emergence of transcriptional identity in somatosensory neurons. *Nature* 577, 392–398. doi: 10.1038/s41586-019-1900-1

Sherry, S. T., Ward, M.-H., Kholodov, M., Baker, J., Phan, L., Smigielski, E. M., et al. (2001). dbSNP: the NCBI database of genetic variation. *Nucl. Acids Res.* 29, 308–11. doi: 10.1093/nar/29.1.308

Subramanian, A., Tamayo, P., Mootha, V. K., Mukherjee, S., Ebert, B. L., Gillette, M. A., et al. (2005). Gene set enrichment analysis: a knowledge-based approach for interpreting genome-wide expression profiles. *Proc. Natl. Acad. Sci. U. S. A.* 102, 15545–15550. doi: 10.1073/pnas.0506580102

Tang, W., Martik, M. L., Li, Y., and Bronner, M. E. (2019). Cardiac neural crest contributes to cardiomyocytes in amniotes and heart regeneration in zebrafish. *Elife.* 8:e47929. doi: 10.7554/eLife.47929.018

Thelie, A., Desiderio, S., Hanotel, J., Quigley, I., Driessche, B., Van Rodari, A., et al. (2015). Prdm12 specifies V1 interneurons through cross-repressive interactions with Dbx1 and Nkx6 genes in Xenopus. *Development* 142, 3416–3428. doi: 10.1242/dev.121871

Van Acker, N., Ragé, M., Sluydts, E., Knaapen, M. W. M., De Bie, M., Timmers, M., et al. (2016). Automated PGP9.5 immunofluorescence staining: a valuable tool in the assessment of small fiber neuropathy? *BMC Res. Notes*. 9:280. doi: 10.1186/s13104-016-2085-4

Woo, J., Kang, H., Lee, E. Y., Park, S., and Cho, Y. E. (2020). Investigation of PRDM7 and PRDM12 expression pattern during mouse embryonic development by using a modified passive clearing technique. *Biochem. Biophys. Res. Commun.* 524, 346–353. doi: 10.1016/j.bbrc.2019.12.133

Yang, C.-M., and Shinkai, Y. (2013). Prdm12 is induced by retinoic acid and exhibits anti-proliferative properties through the cell cycle modulation of P19 embryonic carcinoma cells. *Cell Struct. Funct.* 38, 197–206. doi: 10.1247/csf.13010

Conflict of Interest: The authors declare that the research was conducted in the absence of any commercial or financial relationships that could be construed as a potential conflict of interest.

Publisher's Note: All claims expressed in this article are solely those of the authors and do not necessarily represent those of their affiliated organizations, or those of the publisher, the editors and the reviewers. Any product that may be evaluated in this article, or claim that may be made by its manufacturer, is not guaranteed or endorsed by the publisher.

frontiers | Frontiers in Molecular Neuroscience

ORIGINAL RESEARCH
published: 26 May 2022
doi: 10.3389/fnmol.2022.909835

Evaluation of Recombinant Botulinum Neurotoxin Type A1 Efficacy in Peripheral Inflammatory Pain in Mice

Beatrice Oehler[1,2], Cindy Périer[3], Vincent Martin[3], Amy Fisher[4], Stéphane Lezmi[3], Mikhail Kalinichev[3] and Stephen B. McMahon[1]*

[1]Wolfson Center of Age-Related Diseases, IoPPN, Health and Life Science, King's College London, London, United Kingdom, [2]Department of Anaesthesiology, Heidelberg University Hospital, Heidelberg, Germany, [3]Ipsen Innovation, Les Ulis, France, [4]Transpharmation Ltd., London, United Kingdom

Well-established efficacy of botulinum neurotoxin type A (BoNT/A) in aesthetic dermatology and neuromuscular hyperactivity disorders relies on canonical interruption of acetylcholine neurotransmission at the neuromuscular junction at the site of the injection. The mechanisms and the site of activity of BoNT/A in pain, on the other hand, remain elusive. Here, we explored analgesic activity of recombinant BoNT/A1 (rBoNT/A1; IPN10260) in a mouse model of inflammatory pain to investigate the potential role of peripheral sensory afferents in this activity. After confirming analgesic efficacy of rBoNT/A1 on CFA-induced mechanical hypersensitivity in C57Bl6J mice, we used GCaMP6s to perform *in vivo* calcium imaging in the ipsilateral dorsal root ganglion (DRG) neurons in rBoNT/A1 vs. vehicle-treated mice at baseline and following administration of a range of mechanical and thermal stimuli. Additionally, immunohisochemical studies were performed to detect cleaved SNAP25 in the skin, DRGs and the spinal cord. Injection of CFA resulted in reduced mechanical sensitivity threshold and increased calcium fluctuations in the DRG neurons. While rBoNT/A1 reduced mechanical hypersensitivity, calcium fluctuations in the DRG of rBoNT/A1- and vehicle-treated animals were similar. Cleaved SNAP25 was largely absent in the skin and the DRG but present in the lumbar spinal cord of rBoNT/A1-treated animals. Taken together, rBoNT/A1 ameliorates mechanical hypersensitivity related to inflammation, while the signal transmission from the peripheral sensory afferents to the DRG remained unchanged. This strengthens the possibility that spinal, rather than peripheral, mechanisms play a role in the mediation of analgesic efficacy of BoNT/A in inflammatory pain.

Keywords: inflammation, nociception, analgesia, GCaMP, *in vivo* calcium imaging, hyperalgesia, sensitization, cleaved SNAP-25

OPEN ACCESS

Edited by:
Fabien Marchand, INSERM U1107 Douleur et Biophysique Neurosensorielle (Neuro-Dol), France

Reviewed by:
Siro Luvisetto, Institute of Cell Biology (CNR), Italy
Guang Yang, Columbia University Irving Medical Center, United States

****Correspondence:***
Beatrice Oehler
Beatrice.Oehler@med.uni-heidelberg.de

Specialty section:
This article was submitted to Pain Mechanisms and Modulators, a section of the journal Frontiers in Molecular Neuroscience

Received: *31 March 2022*
Accepted: *02 May 2022*
Published: *26 May 2022*

Citation:
Oehler B, Périer C, Martin V, Fisher A, Lezmi S, Kalinichev M and McMahon SB (2022) Evaluation of Recombinant Botulinum Neurotoxin Type A1 Efficacy in Peripheral Inflammatory Pain in Mice. Front. Mol. Neurosci. 15:909835. doi: 10.3389/fnmol.2022.909835

Abbreviations: AAV9, adeno-associated virus, serotype 9; BoNT, Botulinum neurotoxin; c-SNAP25, cleaved synaptosomal-associated protein 25; rBoNT/A1, recombinant botulinum neurotoxin, subtype A1; CFA, complete Freund's adjuvant; DRGs, dorsal root ganglion neurons; GCaMP6s, ultrasensitive genetically encoded calcium indicator; GFP-Calmodulin-Myosin light chain kinase M13, subtype 6s; GPB, gelatine-phosphate buffer; SNAP25, synaptosomal-associated protein 25.

INTRODUCTION

Pain remains an area of considerable unmet medical need. The Global Burden of Disease survey, which has been running for several decades, continues to show that pain, and particularly musculoskeletal pain, is among the leading causes of disability worldwide, accounting for more impairment than cardiovascular diseases and Alzheimer's disease combined (GBD 2019 Diseases and Injuries Collaborators, 2020). In developed countries, the anticipated prevalence of chronic pain is about 20% (Macfarlane, 2016; Kuehn, 2018). One major factor in poor pain management has been the slow development of novel classes of analgesic drugs. In this context there is a growing interest in analgesic potential of botulinum neurotoxin type A (BoNT/A), produced by *Clostridium botulinum*. For several decades this molecule has shown utility in aesthetic dermatology as well as in muscle or glandular hyperactivity conditions observed in patients with spasticity, dystonia, blepharospasm and others. It is well established that the activity of BoNT/A in these conditions relies on a blockade of acetylcholine neurotransmission at the neuromuscular junction in response to BoNT/A-mediated cleavage of the synaptic protein SNAP25.

There is growing clinical evidence that BoNT/A can show analgesic efficacy in a range of pain conditions which is largely independent of its muscle-relaxant properties (Finnerup et al., 2015; Herd et al., 2018). Based on several clinical trials and meta-analysis BoNT/A has been approved for treatment of some forms of migraine (Burstein et al., 2014; Blumenfeld et al., 2018; Herd et al., 2018). Randomized, placebo-controlled clinical trials have shown analgesic efficacy of BoNT/A in patients with posttraumatic, trigeminal and postherpetic neuralgias and diabetic neuropathy (Park and Park, 2017). Also, BoNT/A reduced pain in patients with low back pain, refractory shoulder pain as well as those suffering from osteoarthritic pain and pain linked to total knee arthroplasty (Singh et al., 2010; Intiso et al., 2015; Mendes et al., 2019). Analgesic efficacy of BoNT/A in the clinic is supported by the evidence from non-clinical studies in a wide range of rodent models of pain (Matak et al., 2019).

Despite growing evidence of analgesic efficacy of BoNT/A, the mechanisms and the site of activity remain elusive. On the one hand, there is evidence that analgesic efficacy of BoNT/A is linked to reduction of neurotransmitter release in peripheral terminals of nociceptors. BoNT/A blocked KCl-evoked release of CGRP and substance P in primary sensory neuronal cultures *in vitro* (Purkiss et al., 2000; Durham et al., 2004). Additionally, BoNT/A injection reduced bladder pain responses and inhibited CGRP release from nerve terminals (Chuang et al., 2004). BoNT/A injected *via* intraplantar route reduced nocifensive behaviors in the phase 2 of the formalin test and formalin-evoked glutamate release in the injected paw (Cui et al., 2004). On the other hand, there is evidence that analgesic efficacy of BoNT also involves spinal mechanisms. For example, intraplantar injection of BoNT/A reduced expression of Fos protein in the dorsal horn of the spinal cord and excitation of wide dynamic range neurons of the dorsal horn in phase 2 of the formalin response (Aoki, 2005). While initially spinal effects of BoNT were thought to be indirect, subsequent evidence of retrograde axonal transport of BoNT/A to the spinal cord, pointed at possibility of its direct central effects (Matak et al., 2014, 2019).

The aim of this study was to investigate whether analgesic efficacy of BoNT/A is associated with inhibition of functional hyperexcitability of peripheral nociceptors in a mouse model of inflammatory pain. We used intraplantar injection of complete Freund's adjuvant (CFA) to induce mechanical allodynia detectable by the von Frey test and compared the efficacy of rBoNT/A1 to vehicle. Persistent excitability of many peripheral nociceptors to mechanical and thermal stimuli applied to the inflamed paw was monitored simultaneously by *in vivo* calcium imaging in the cell bodies located in the ipsilateral dorsal root ganglion (DRG). Responses of CFA-exposed animals treated with either rBoNT/A or vehicle were compared to those without inflammation. In addition, we evaluated the effect of rBoNT/A1 on CFA-induced inflammatory responses in the skin and assessed the presence of cleaved synaptosomal-associated protein 25 (c-SNAP25), the target of BoNT/A, in the injected hind paw, DRGs, and the spinal cord.

MATERIAL AND METHODS

Animals

Adult male and pregnant female C57/Bl6 mice (gestational days 14–16) were purchased from Charles River Laboratories (Harlow, UK). For behavioral experiments and histological analysis, male mice were group-housed at the animal facility of the Royal Veterinary College. Animals were acclimated for at least 7 days prior to the experiments. For *in vivo* imaging experiments, pregnant mice were single-housed at the animal facility of King's College London. After birth, pups remained with the dam until weaning on day 21. Animals were kept on a 12 h light/dark cycle (lights on from 07:00 to 19:00) under a constant temperature (22 ± 2°C) and humidity (55% ± 5) with access to food and water *ad libitum*.

All animal experiments were performed under appropriate Home Offices licenses. Experimental protocols were in accordance with the international guidelines for the care and use of laboratory animals (EU Directive 2010/63/EU for animal experiments) and the Animal Research: Reporting of *in vivo* Experiments (ARRIVE) criteria. All animal monitoring was performed during daytime. Criteria for discontinuation of the experiments and humane end points were evaluated throughout the experiments. The taxonomy suggested by the International Association for the Study of Pain was used (Merskey and Bogduk, 1994).

Materials

AAV9-GCamP6s at a titer of $\geq 1 \times 10^{13}$ viral genomes/ml was obtained from Addgene (Watertown, MA, USA). CFA (F5881, Sigma, Manchester, UK) was stored at 4°C. rBoNT/A1 (IPN10260, Ipsen Bioinnovation, UK) was freshly dissolved prior to injection at 5 pg per 20 μl in vehicle solution based on a gelatine phosphate buffer (GPB) composed of gelatine 0.2% and disodium hydrogen phosphate 50 mM, at pH 6.5 (orthophosphoric acid).

Preparation of rBoNT/A1

rBoNT/A1 gene synthesis, expression of *E. coli*, and purification methods have been described previously (Hooker et al., 2016). Briefly, the BoNT/A1 protein sequence was back-translated and codon-optimized for expression in *E. coli*. The DNA sequence was synthetized in two parts and subsequently combined to create a coding sequence for a full-length neurotoxin. Repeated batches of consistent material were produced and showed equivalent activity to native BoNT/A1 in several biochemical assays (Hooker et al., 2016). rBoNT/A1 was shown to be comparable to native BoNT/A1 *In vitro* in inhibiting the acetylcholine release by cleaving SNAP25 in the rat embryonic spinal cord neurons and, *ex vivo*, in the mouse phrenic nerve hemidiaphragm assay. *In vivo*, equipotent effects of rBoNT/A1 and native BoNT/A1, injected intramuscularly, were demonstrated, and had similar onset and duration of action in the rat digit abduction assay in mice and rats (Périer et al., 2021). Furthermore, rBoNT/A1 injected into the gastrocnemius muscle of the rat, dose-dependently reduced muscle weight and volume, induced myofiber atrophy and cleaved SNAP25 at the neuromuscular junction and the peripheral nerves.

Measurement of Mechanical Allodynia With Von Frey Filaments: Experimental Design and Behavioral Assessment

Mice were habituated to the facility and the experimental setup, before being assessed for mechanical sensitivity by measurement of withdrawal threshold using calibrated von Frey filaments applied to the plantar surface of the left hind paw at baseline, on three consecutive days (Day-4, Day-3, and Day-2; Tough-Test Sensory Evaluator; Scientific Marketing Associates; Barnet, UK). The mean of Day-3 and Day-2 were considered as baseline (**Figure 1A**). Mechanical sensitivity was also tested on day 0 (before rBoNT/A1 or vehicle treatment) and on days 3 and 5. A series of graduated von Frey filaments (0.07, 0.16, 0.4, 0.6, and 1 g) were applied in sequence with a protocol of 1 s on/1 s off, repeated 10 times. Each filament was applied perpendicularly to the center of the ventral surface of the paw until it bent slightly. The force applied to the hind paw of the animal to induce 5 responses out of 10 trials was recorded as the paw withdrawal threshold.

Mice were injected intraplantarly with 20 μl of CFA (1.5 mg/ml) two days before rBoNT/A1 or vehicle treatment (day-2; **Figure 1A**). On day 0, animals received intraplantar injections of either rBoNT/A1 (5 pg/mouse) or vehicle (GPB) into the same ipsilateral hind paw ($n = 10$/group). All intraplantar injections were made at 20 μl volume and performed with a 30 G needle under a brief isoflurane anesthesia. Both experimental groups, rBoNT/A1- and vehicle-injected animals, were kept in the same cage. The experimenter was blinded to treatment. At the end of the experiment, mice were euthanized with CO_2.

In vivo Calcium Imaging in DRG Neurons

GCaMP6s Treatment

At the age of 2–5 days, pups received intraplantar injections of 5 μl AAV9-GCaMP6 into the left hind paw (ipsilateral site of rBoNT/A1 injection and *in vivo* imaging; see below). After reaching about 18–30 g bodyweight, animals were randomly allocated to their experimental groups. Animals were closely monitored throughout the experiment. If the bodyweight decreased below 20% of the initial weight, mice were euthanized. Depending on the litter size, the authors aimed to use siblings of the same sex within the same experimental day. At the end of the imaging session mice were humanely euthanized with an overdose of pentobarbital.

Animal Preparation for Imaging

In line with the behavioral setup, adult mice, treated with AAV9-GCaMP6 as neonates, received intraplantar injections of 20 μl CFA (1.5 mg/ml) into the left hind paw on day-2 (**Figure 1A**). Two days later (day 0), either rBoNT/A1 ($n = 5$) or vehicle (GPB; $n = 7$) were applied to the same site. An additional group of mice with the neonatal history of AAV9-GCaMP6 treatment ($n = 6$) received intraplantar injections of phosphate buffered saline (PBS; 20 μl) on day-2 and injections of vehicle (GPB) on day 0. On day 3 calcium transients were recorded in the L4 DRG neurons containing most of the somata of the peripheral terminals of the plantar surface of the murine hind paw. After induction of anesthesia with high Vol% Isoflurane in an induction box (Uno BV) the mice were, throughout the experiment, spontaneously breathing 1–1.5 Vol% isoflurane mixed with oxygen in a semi-closed anesthesia aperture at a flow rate of 1 l/min *via* a nose cone. Body temperature was controlled by a heat mat and rectal thermometer (FHC) and adjusted to initial levels, around 36°C. Eyes were kept moist with artificial tears and the mice received a subcutaneous injection of isotonic saline (10 μl/g bodyweight). After shaving the back, the skin above the vertebral column was incised from the lower thoracic to the sacral level. The rostral part of the vertebral column was clamped in a custom-made frame with forceps to decrease movement artifacts evoked by breathing excursions and positioned in a more lateral recumbent position to placing the DRG in a more horizontal position (Chisholm et al., 2018). On the left-hand site, around vertebrae L4, the fasciae and muscles covering the lateral processus were removed. With small rongeurs, the lateral part of the bone was gently cracked apart to uncover the L4 DRG. To prevent drying, tissue was coated with a thin layer of low melting agarose. The left hind paw was retroflexed, so the plantar surface was pointing upwards. We observed that animals were more likely to die under isoflurane anesthesia after receiving rBoNT/A1 due to weakness and quality of imaging decreased over time, e.g., by bleaching and drying of the tissue.

Stimulation Protocol

To evaluate the sensitivity of peripheral sensory nerve endings innervating the corresponding, ipsilateral hind paw, neuronal activity in the DRG neurons was recorded. After sampling baseline activity of the left L4 DRG neurons for 10 min, the left hind paw was stimulated first mechanically and then, after an extended interval, thermally (**Figure 1A**).

To assess the mechanical sensitivity, a custom-made, electrically-controlled stamp device was established (**Figure 2A**). The mechanical stimulator consisted of an electric motor that controls a lever *via* pinions, stored in a handle. The

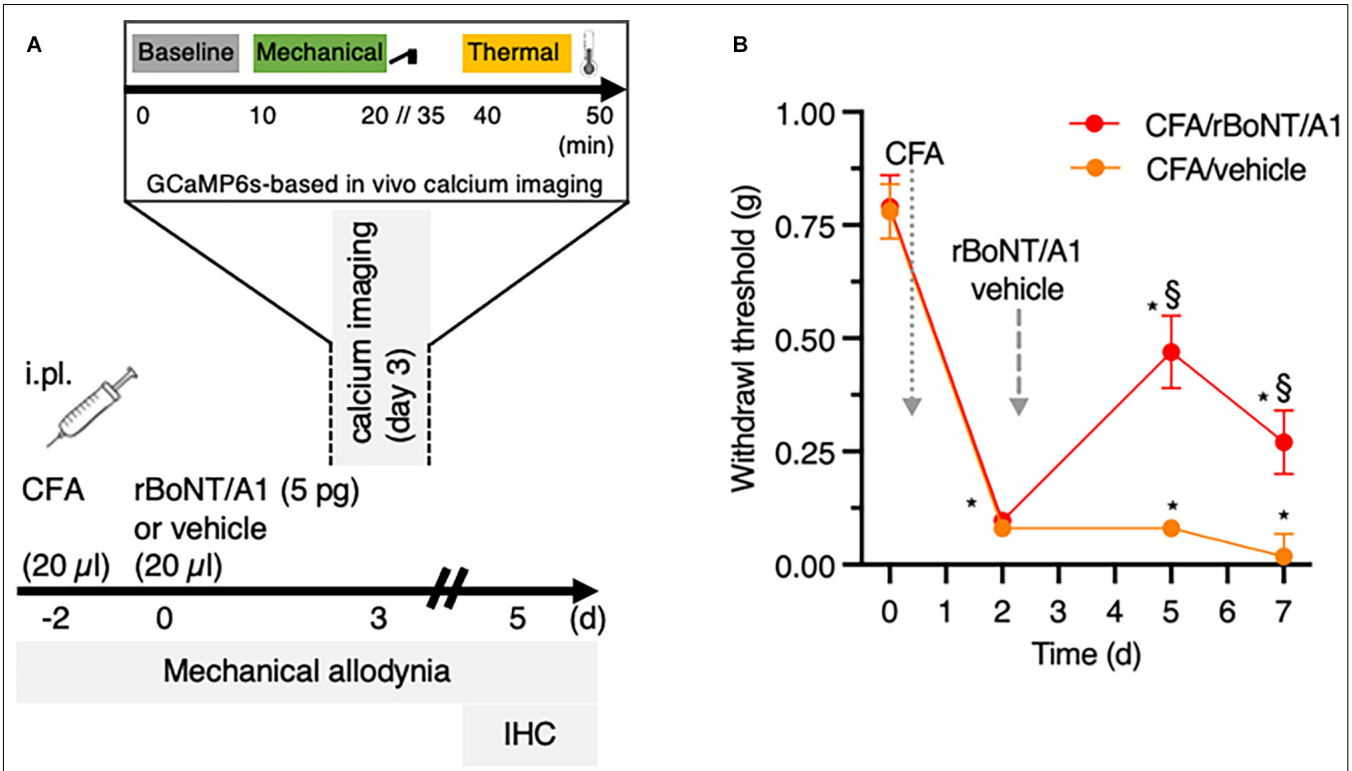

FIGURE 1 | rBoNT/A1 ameliorates mechanical allodynia in CFA-evoked local hind paw inflammation in mice. **(A)** Schematic representation of the experimental protocol used for *in vivo* calcium imaging, behavioral and histology experiments. CFA and rBoNT/A1 or vehicle (gelatine phosphate buffer; GPB) were injected on day -2 and day 0, respectively, followed by behavior measurements on day 3 and 5. *In vivo* calcium imaging was performed on day 3. Recordings at baseline were followed by mechanical and thermal stimulation. On day 5, tissues were collected for histological analysis. **(B)** Mechanical allodynia (g) was measured by von Frey filaments. Two-way ANOVA, *post hoc* Tukey. *(within groups to baseline) and §(across groups): $p < 0.05$. $N = 10$/group.

top-view shows a part of the handle and the lever attached in a 90° angle. The sideview depicts the ball joint and gives the range of motion of the lever, about 23°. A little stamp with 6 × 4 blunt pins, about 2 mm in height and 0.1 mm spaced apart, measuring about 6 × 4 mm, magnitudes smaller than a UK 1 pence coin, was magnetically attached to the distal end of the lever. Current applied to the electrically controlled lever was converted into movement. The stamp was positioned 1.5 mm above the plantar surface of the left hind paw without contact to the skin. Continuous contact of the stamp with the glabrous skin was avoided to prevent constant stimulation of the innervating nerve endings. Acceleration was neglectable. Calibration of the overall force of the plane surface of the lever on a kitchen scale revealed a minimum of 100 g (approx. 0.09 mN per pin). Application of the minimum pressure was followed by a 100 g increments, until reaching 1,000 g maximum (approx. 0.9 mN per pin) after one-minute intervals before applying the next stimulus (**Figure 2B**). Thermal stimuli were applied by a peltier device (TSAII, Medoc; Ramat Yishay, Israel) placed on the plantar surface of the concomitant, left hind paw. The temperature of the 16 × 16 mm probe was increased by ramps of 4°C/s from baseline (32°C) to 40°C, 45°C, and 50°C, respectively. Each heat stimulus was applied for 8 s followed by 60 s baseline before the next stimulus.

Data Acquisition

Data were acquired with a 10-fold dry objective attached to an upright Eclipse Ni-E FN confocal/multiphoton microscope (Nikon UK, Branch of Nikon Europe B.V., Amsterdam, The Netherlands) using a 488-nm Argon ion laser line. GCaMP signal was collected at 500–550 nm. Time series recordings were taken with an in-plane resolution of 512 × 256 pixels at an acquisition speed of 3–4 Hz. Data were saved with date and experiment number to encrypt the experiments and to impede a biased analysis.

Tissue Analyses

In line with behavior and imaging experiments, the same treatment protocol was used for tissue analysis in an independent cohort of 13 mice. On day five, CFA-exposed mice that were injected with either rBoNT/A or vehicle (n = 5/group) were euthanized, and tissues were collected for analyses. A group of untreated, untreated animals (n = 3) was added as absolute controls. The injected footpad (three tissues/section/animal), lumbar vertebrae including DRGs and the lumbar spinal cord (at least four tissues/section/animal) were fixed in 10% formalin for 48 h, decalcified and embedded in paraffin blocks. Histological slides were prepared. Footpad tissue sections were stained with haematoxylin and eosin (H&E) for standard histopathologic examination and

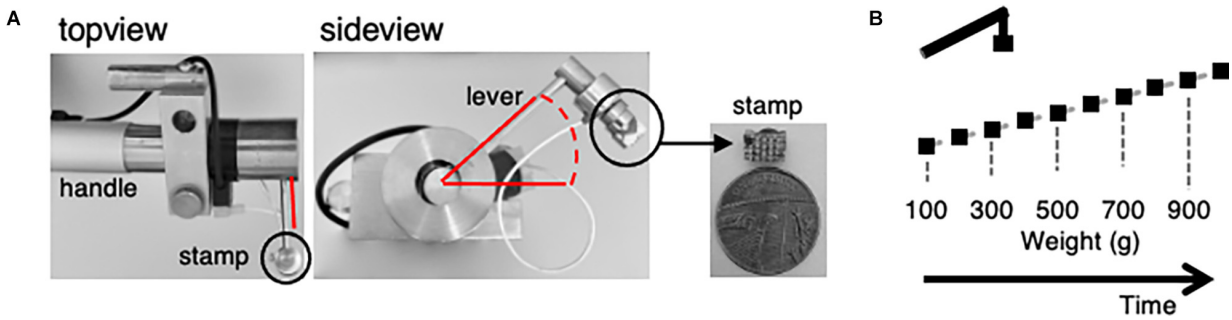

FIGURE 2 | A custom-made electronically controlled mechanical stimulator and the mechanical stimulation protocol for *in vivo* calcium imaging. **(A)** Photos of the electronically controlled mechanical stimulator and its stamp. Top view showing the lever attached to the handle, sideview giving insight into the rotation angle of the lever highlighted in red and the stamp attachment (black circle). Enlarged picture of the stamp in comparison to a one penny coin. **(B)** Illustration of the mechanical stimulation protocol. Weight was increased from 100 g (0.09 N) to 1,000 g (0.9 N) in 100 g increments every 60 s. Stimulus duration was about 1 s.

evaluation of the inflammatory process. Severity of lesions were classified using the following standard grading system: 0 (no lesions), 1 (minimal), 2 (mild), 3 (moderate), 4 (severe), 5 (marked).

The immunohistochemical staining for SNAP25 and cleaved SNAP25 were performed using a standard avidin-biotin-peroxidase procedure as previously described (Périer et al., 2021). After a heat-induced epitope retrieval step, endogenous peroxidases were blocked for 10 min in a 3% H_2O_2 solution in a TBS buffer. The sections were incubated with a non-commercial primary rabbit polyclonal antibody (EF14007, Ipsen Innovation, Les Ulis, France) which is specific for the cleaved form of SNAP25 by BoNT/A only or with an antibody directed against the N-terminal part of SNAP25, thus recognizing both SNAP25 full and cleaved forms (SYSY 111 008, Synaptic Systems, Göttingen, Germany; overnight incubation). Sections were then incubated with a biotinylated secondary antibody for 30 min (anti-rabbit IgG, Vector Laboratories, Burlingame, CA, USA), followed by a 30-min incubation with an amplification system (avidin-biotin) coupled to horseradish peroxidase (Vector Laboratories, Burlingame, CA, USA). Finally, sections were incubated for 5 min with a 0.02% diaminobenzidine solution (DAKO, Carpinteria, CA, USA). To counterstain, haematoxylin was used, and the slides were imaged with a light microscope.

For the quantification of the amount of cleaved SNAP25 in muscles, the number of stained neuromuscular junctions (NMJ), intensity of staining, the presence of staining in terminal nerve ending and larger intramuscular nerves was used as previously described (Périer et al., 2021). In the spinal cord, the intensity and density of cleaved SNAP25 positive nerve endings was graded as follows: 1 (minimal), 2 (mild), 3 (moderate), 4 (marked) on the 4 most intensely stained spinal cord sections; a cumulative score (0–16) was then calculated for each animal in the ipsilateral dorsal and ventral horns.

Statistical Analysis

For behavioral tests, the minimum number of animals to reach statistical significance was estimated by an *a priori* power analysis (Faul et al., 2009). For the statistical analysis, InVivoStat[1] (Clark et al., 2012) and Prism 7 for Mac OS X (GraphPad Software, San Diego, CA) were used to calculate a two-way repeated measures ANOVA followed by Tukey *post hoc* multiple comparison after normality check. Values given in the results section are the *P*-values for interaction within or across groups as indicated ($P < 0.05$).

Prior to statistical analysis of the *in vivo* calcium imaging experiments a mixture of published codes (Pachitariu et al., 2016) and custom written scripts in Python (python.org) and Matlab 2019a (MathWorks) were used to process the data. After exporting the nd2 files obtained during recording with Nikon Elements software (Nikon) as tiffs, data were loaded into Suite2p, a Python script to identify regions of interest (ROIs; Pachitariu et al., 2016). Threshold parameters were kept constant throughout analysis of all experiments. The results were then imported into Matlab to perform further analysis. In accordance with our previously performed analysis of *in vitro* calcium imaging (Martin et al., 2018), data were normalized to baseline fluorescence after correction for the neuropil, reflecting data points out of focus and scattered fluorescence from nearby processes (e.g., axons, dendrites, synaptic boutons) as well as subtraction of averaged baseline values. Then, cells with high initial calcium concentrations as well as those cells not returning to baseline 3 min after maximum stimulation were excluded. To compare the magnitude of responses for each stimulus, the area under curve (AUC) was calculated in each individual neuron for a 15 s period after stimulation, including the peak hight. The interval started 20 frames before and ended 35 frames after the stimulus. Only cells reaching at least calcium concentrations 25% above their baseline AUC at the maximum stimulus were considered as positive responders. Later, the size of the AUC was correlated with the different mechanical stimuli used. When the correlation coefficient was >0.7, suggesting a 70% probability of linear correlation, cells were counted as nociceptors and were therefore included into subsequent statistical analysis. Event counts were conducted on deconvoluted data, an analysis

[1] invivostat.co.uk

implemented in Suite2p (Pachitariu et al., 2016; Friedrich et al., 2017). The deconvolution of calcium transients into spikes was a tool implemented into the Suite2p analysis program. After extracting the information, the data were processed to generate a 1 or 0 code.

For histopathology and cleaved SNAP25 staining analyses, the mean of CFA/vehicle group was compared to the one of CFA/BoNT group using non-parametric Mann-Whitney test.

Statistical tests, indicated in the figure legends, were performed with GraphPad Prism (San Diego, CA, USA). Equally sized experimental groups were planned prior to the study aiming for eight mice per group. However, in the BoNT group mice were more vulnerable to anesthesia and therefore died early. To keeping the group size similar, fewer experiments than planned were conducted in the CFA plus vehicle and the control group. Throughout the analysis, data obtained in the same mice were used. Here, due to technical and methodological issues, the animal numbers included in each analysis varies. Even though we are aware of this problem, increasing group sizes to even out the statistical analysis would fail to prove that hypothesis that BoNT reduces CFA-mediated sensitization of peripheral nerve endings.

RESULTS

After obtaining baseline parameters on mechanical sensitivity by von Frey measurements, CFA was injected into the footpad (**Figure 1B**). The withdrawal thresholds dropped from 0.8 g at baseline by factor of 10 2 days later. Three days after, rBoNT/A1 or vehicle (GPB) application into the inflamed paws, the withdrawal thresholds in the rBoNT/A1-treated group increased significantly by a factor of five compared to mice receiving vehicle treatment only. Those thresholds remained at low levels. Changes in withdrawal thresholds in the CFA/rBoNT/A1 group declined on day five by 57%, still being 15-times above the control group.

To investigate the inhibition of inflammatory, mechanically evoked hypersensitivity in mice by rBoNT/A1 a custom made electrically controlled mechanical device was introduced (**Figure 2A**). Photos show the device (**Figure 2**). The top-view displays the handle and the rectangularly attached lever. The sideview depicts the ball joint and gives the range of motion of the lever. *via* a little stamp with blunt pins forces were applied to the footpad. Starting with a stimulus of 100 g (about 0.09 mN per pin) for a minimum contact time (approx. 1 s), the weight pushing onto the specimen was increased every minute by 100 g until reaching 1,000 g (0.9 mN per pin; **Figure 2B**). During the interval, the stamp was distanced from the skin.

Stills of DRG neurons extracted from the recordings in mice receiving CFA/rBoNT/A1 (top), CFA/vehicle (middle), or PBS (bottom), illustrate the increase in fluorescence signal upon maximum mechanical stimulation compared to baseline fluorescence in individual DRG neurons (**Figure 3A**). The fluorescence traces (ΔFoF) depict corresponding examples of intracellular calcium fluctuations upon mechanical stimulation over time (**Figure 3B**).

Forces from 100 g (0.09 mN) to 1,000 g (0.9 mN) were applied over 10 min. It appeared that the response patterns which lined up with the corresponding mechanical stimulus were different in mice treated with PBS in comparison to mice with an inflamed hind paw. To identify distinctive cell types, signals were sorted by different response patterns (**Figure 4**). The analysis of the individual traces confirmed a group recognized as "nociceptors" (**Figure 4A**).

Constantly rising force applied to the peripheral nerve endings in the footpad of the mice evoked a linear correlating increase in fluorescence intensities. In other neurons of the same DRG, either low and intermediate pressure already evoked a maximum response (**Figures 4B,C**) or the signal was constantly weak regardless the forces applied (**Figure 4D**). Counting the number of mechanically activated "nociceptive" neurons uncovered that 67% and 64% of all neurons respond to mechanical stimuli after induction of local, peripheral inflammation with CFA treated with rBoNT/A1 or vehicle, respectively (**Figure 5A**). In the group treated with PBS, approximately 40% of the "nociceptive" neurons responded to pressure. The averaged responses of the "nociceptors" were increased upon mechanical stimulation in mice with local CFA-evoked inflammation (**Figure 5B**). Differences were significant at high pressure, starting at 700 g ($p_{(CFA/rBoNT/A1)}$ = 0.44 and $p_{(CFA/vehicle)}$ = 0.04). Throughout the experiments, the averaged magnitude of responses was about two-fold increased under inflammatory conditions. Co-application of rBoNT/A1 failed to alter CFA-evoked responses. A detailed analysis of the data clouds unmasks an increased variance under inflammatory conditions (**Figure 5C**). The slopes of the rising responses in individual animals were significantly different between the CFA group and the control group (p = 0.04; **Figure 5D**). After identifying different subsets of neurons, fluorescence signals were analyzed in more detail. Randomly picked, individual fluorescence traces from DRG neurons of mice treated with CFA ± rBoNT/A1 or vehicle alone are displayed upon mechanical stimulation (**Figures 6A–C**).

Mechanical withdrawal thresholds in inflamed paws of freely moving mice were significantly ameliorated by rBoNT/A1. To evaluate whether the discharge in any mechanosensitive neuron was affected, we analyzed the different response patterns of all individual neurons activated by mechanical stimulation. High magnification analysis of the plotted traces uncovered that prolonged, unsteady calcium fluctuations were detected in some but not all neurons before the subsequent stimulus (**Figure 6B**). This observation prompted to the analysis of deconvoluted calcium events (**Figure 6D**). Raster plots uncovered that calcium fluctuations were prolonged in some individual neurons after mechanical stimulation. The number of cells with prolonged activity in CFA treated animals remained unaffected regardless the treatment with rBoNT/A1 or GPB but increased by 25% in comparison to the control (**Figure 6E**). A quantitative comparison of the activity of individual neurons in different animals verified that the median of the summed events per cell increased from 11.8 to 20 and 24.5 under inflammatory conditions (**Figure 6F**). However, also in this in-depth analysis, rBoNT/A1 failed to alter the median of in CFA-treated animals compared to the neurons of mice receiving CFA and vehicle treatment only (p = 0.07). Hence, rBoNT/A1 had no

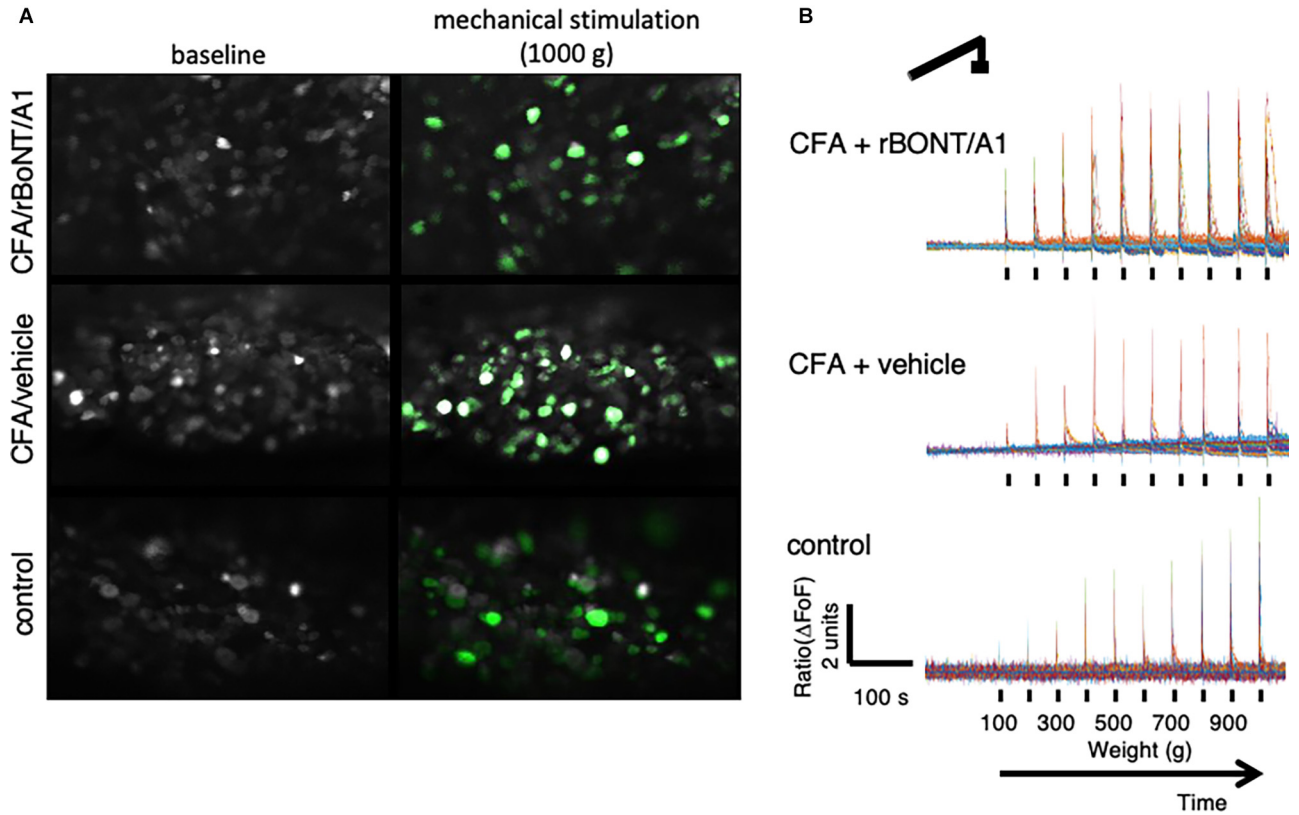

FIGURE 3 | Peripherally applied pressure to hind paws evokes calcium transients in dorsal root ganglion (DRG) neurons *in vivo*. **(A)** False color images of GCaMP6s-labeled DRG neurons *in situ* at baseline and after maximum mechanical stimulation (1,000 g/0.9 N). **(B)** Traces depict calcium transients normalize to baseline (ΔFoF) in individual neurons from mice treated with CFA and rBoNT/A1 (top), CFA and vehicle (GPB; middle), or control (PBS; bottom) upon mechanical stimulation as indicated over time.

effect on mechanically evoked responses under inflammatory conditions.

To assess changes in GCaMP6s fluorescence in DRG neurons upon thermal stimulation, the linked hind paw was stimulated every minute for eight seconds by increasing heat stimuli using a ramp protocol. Temperatures peaks were set to 40°C, 45°C, and 50°C, respectively after recoding baseline fluorescence at 32°C (**Figure 7A**). Plotted traces depict the rising fluorescence changes over time (ΔFoF) in line with the applied temperatures. Pictures from the top to the bottom show corresponding false-colored DRG neurons from mice who received CFA and rBoNT/A1, CFA and vehicle or PBS (**Figure 7B**). Fluorescence brightness changed dramatically upon noxious heat stimulation (50°C) compared to baseline. The pictures suggest an increase in numbers of responding neurons upon thermal stimulation depending on the local treatment. About 80% of the neurons responded to thermal stimuli under inflammatory conditions regardless the co-treatment with rBoNT/A1 or vehicle. Statistical analysis unmasks that the proportion of responding cells after CFA was only increased by less than 10% compared to control (**Figure 7C**). Under given treatment conditions, CFA sensitization evoked a significant increase in responses at noxious temperatures compared to the group without inflammatory responses (**Figure 7D**; PBS vs. CFA/BoNT: $p = 0.007$ or CFA/vehicle: $p = 0.01$). Responses in DRG neurons of mice treated with CFA significantly increased at noxious 50°C in comparison to 40°C (both: $p < 0.001$). rBoNT/A1 failed to inhibit these responses ($p > 0.99$). In the PBS group, changes in the magnitude of response were not significantly different at any time. Non-noxious temperatures (40°C) barely changed the calcium influx in DRG neurons regardless the treatment. Hence, the data confirmed that CFA sensitizes the terminal nerve endings resulting in an upregulated response upon hot temperature stimulation but rBoNT/A1 has no impact.

In the footpad of untreated mice uncleaved SNAP25 was identified in nerve fibers terminating in the epidermis (**Supplementary Figure 1A**), surrounding apocrine glands (**Supplementary Figure 1B**), in peripheral nerve bundles (**Supplementary Figure 1C**), in nerves innervating arteries (**Supplementary Figure 1D**) and at neuromuscular junctions (**Supplementary Figure 1E**). Cleaved SNAP25 (c-SNAP25), on the other hand, was not detected in any of the samples taken from mice treated with CFA/rBoNT/A1 (**Supplementary Figures 1F–I**) except at the neuromuscular junctions of the small muscles located in the footpad (**Supplementary Figure 1J**). Nothing was labeled by the

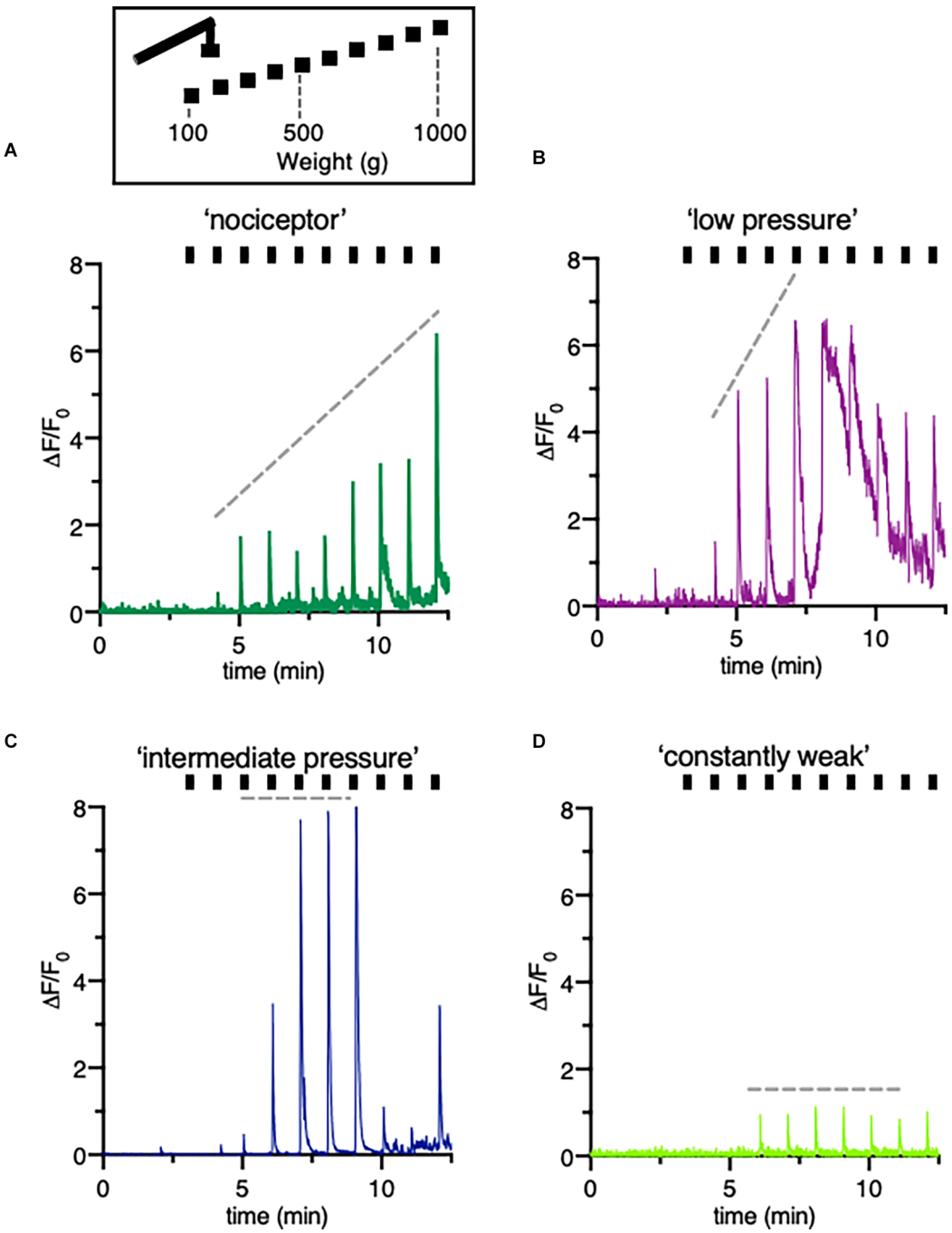

FIGURE 4 | Classification of different type of DRG neurons responsive to increasing pressure. **(A–D)** Schematic drawing of the mechanical stimulation protocol and example trace indicating a variety of fluorescence responses taken from individual neurons of a mouse treated with vehicle only. The hindpaw was stimulated with increasing pressure started at 100 g to a maximum of 1,000 g. Different patterns of changes in intracellular calcium concentrations reflect distinctive cell types, here called "nociceptors" **(A)** "low pressure" responders **(B)** "intermediate pressure" responders **(C)** and "constant weak" **(D)** responders. Ticks correspond to mechanical stimulation protocol.

isotype antibody, confirming the specificity of the staining (**Supplementary Figures 1K–O**). Quantification of the labeling showed significantly higher levels of c-SNAP25 in the neuromuscular junctions of CFA/rBoNT/A1-treated animals compared to CFA/vehicle-treated mice and absolute controls (**Supplementary Figure 1P**).

Specifically focussing on neuronal tissue, c-SNAP25 was lacking in DRG neurons but was identified in the

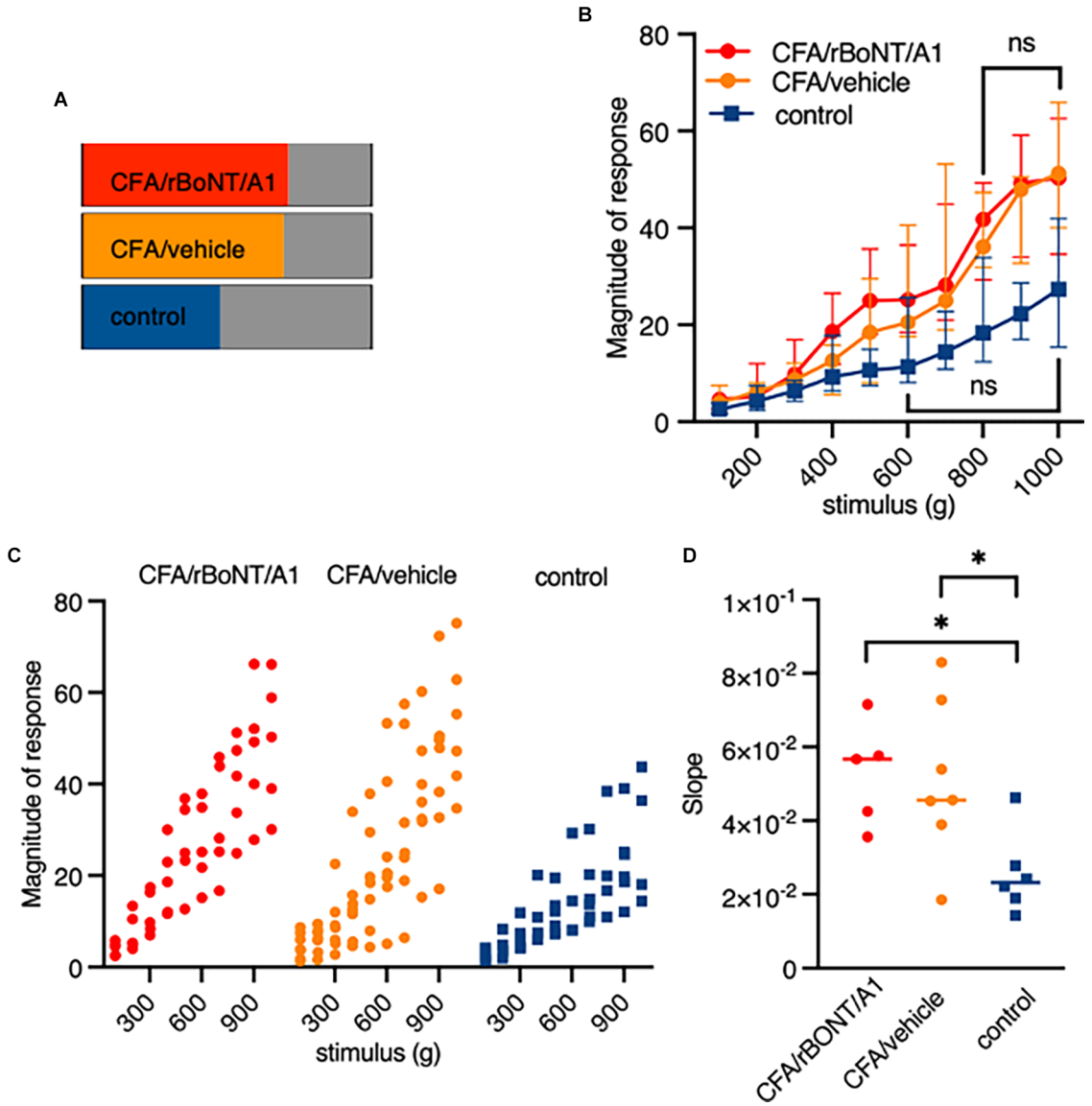

FIGURE 5 | Pressure responsive "noiceptors" are sensitized by inflammation but not inhibited by rBoNT/A1 on a cellular level. **(A)** Percentage of identified "nociceptors" under indicated conditions. **(B)** Magnitude of responses over stimulus in the three different treatment groups as median plus interquartile range. Significant difference between 100 and 700 g in CFA/rBoNT/A1 and CFA/vehicle as well as 100–500 g in control (PBS) group compared to maximum stimulus. Indication in graph highlights first stimulus that is not significantly different to 1,000 g. No difference in between the CFA/rBoNT/A1 and CFA/GPB treatment groups. Mixed-effect analysis, *post hoc* Tukey. $p < 0.05$. **(C)** Magnitude of responses in individual animals presented as data clouds over stimulus grouped by treatment. **(D)** Comparison of response/stimulus slopes from individual mice calculated from the median in **Figure 4B**. Welch ANOVA, *post hoc* Dunnett. $^*p < 0.05$. *n*(CFA/rBoNT/A1) = 5; *n*(CFA/vehicle) = 7; *n*(PBS) = 6. ns, not significant.

corresponding ipsilateral dorsal and ventral horns in animals treated with rBoNT/A1 (**Figures 8A,C,E**). There was no evidence of c-SNAP25 in untreated animals (**Figures 8B,D,F**). Quantification of the stainings revealed a significant increase of c-SNAP25 in the spinal cord that was modest in the ipsilateral dorsal horn (**Figure 8G**) and high in the ipsilateral ventral horn (**Figure 8H**) of the rBoNT/A1-injected animals in comparison to CFA/vehicle and untreated mice. This was also confirmed by the dorsal horn/ventral horn c-SNAP25 score ratio being inferior to 1 (**Figure 8I**).

H&E staining of the foot pad of mice clearly demonstrated that inflammation was present in CFA-treated animals (**Supplementary Figures 2A–C**), while being absent in controls (**Supplementary Figures 2D,E**). Immune cells infiltrated the site of lesion and formed foamy vacuoles containing a foreign substance, most likely CFA (**Supplementary Figures 2B,C**) but were absent in controls (**Supplementary Figure 2E**). The overall inflammation score in the CFA/rBoNT/A1 group equaled the CFA/vehicle group (**Supplementary Figure 2F**) even though, the number of neutrophils was slightly lower in

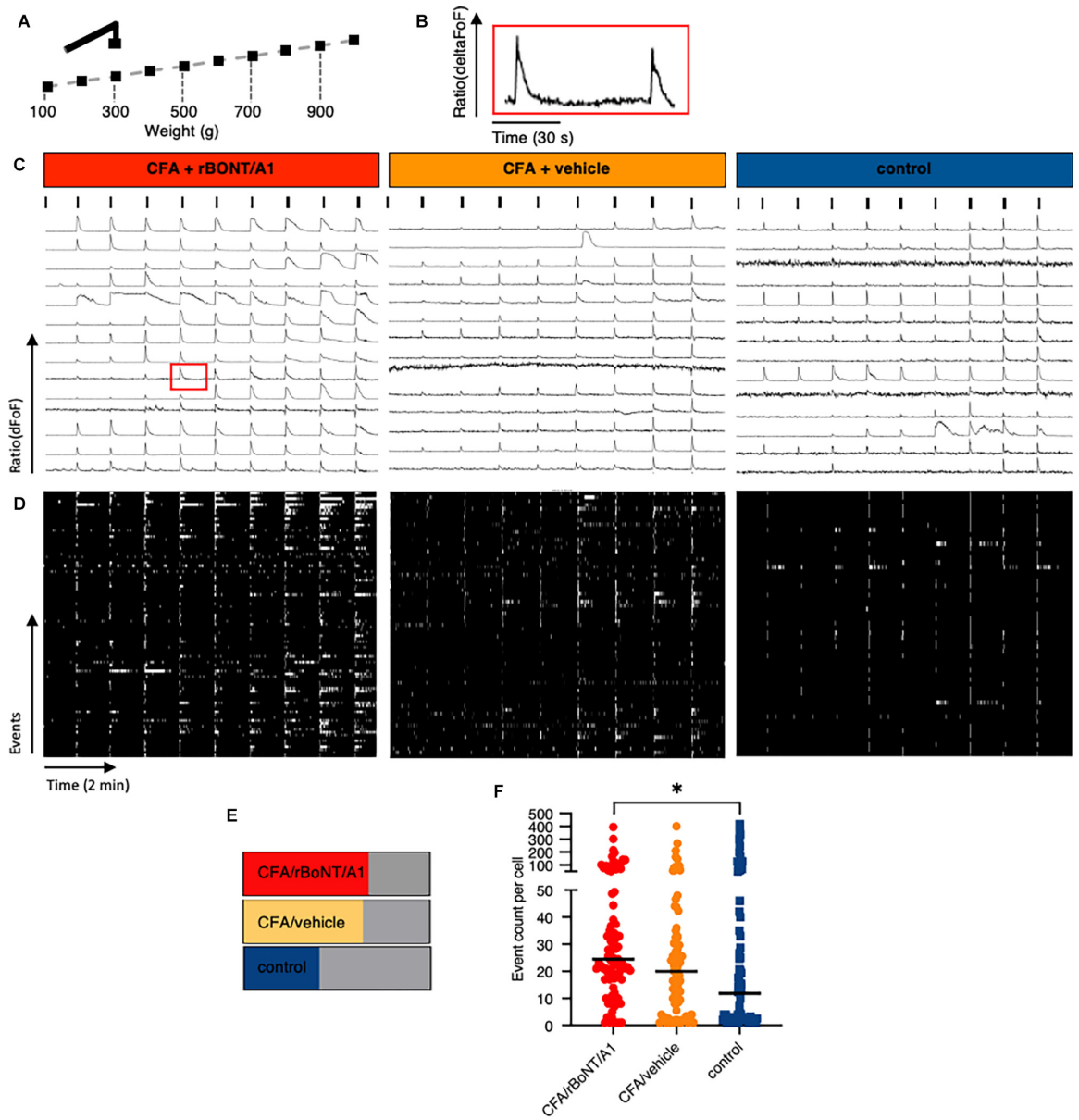

FIGURE 6 | Prolonged discharge of DRG neurons after mechanical stimulation in mice with local CFA-provoked inflammation uncovered by *in vivo* calcium imaging. **(A)** Schematic drawing of the mechanical stimulation protocol corresponding to the traces shown below. **(B)** Enlarged trace of a calcium transient taken from **(C)** (CFA/rBoNT/A1, 500–600 g, 9th cell, red square). **(C)** Example traces of fluorescence changes upon mechanical stimulation over time in any DRG neuron of three different mice treated as indicated. Ticks indicate mechanical event as shown in **(A)**. **(D)** Raster plots of deconvoluted data of calcium events corresponding to individual calcium traces shown in **(C)**. **(E)** Percentage of cells responding to mechanical stimuli under different treatment conditions as indicated. **(F)** Plot of summed deconvoluted events per cell and median taken from animals with indicated treatments. *n*(CFA/rBoNT/A1) = 189; *n*(CFA/vehicle) = 175; *n*(control) = 187 neurons of *n* = 3 mice per group. Kruskal-Wallis ANOVA, *post hoc* Dunn. $^*p < 0.05$.

inflamed tissue of rBoNT/A1- than in vehicle-treated mice. This trend failed to reach statistical significance ($p = 0.48$; **Supplementary Figure 2G**).

DISCUSSION

Here, we have used an *in vivo* optical imaging method to investigate whether analgesic activity of rBoNT/A1 was mediated by changes in the activity of peripheral nociceptors in a model of inflammatory pain. To achieve this, we simultaneously monitored activity in cell bodies of hundreds of sensory neurones located in the ipsilateral DRG of rBoNT/A- vs. vehicle-treated animals with CFA-evoked local inflammation. Peripherally evoked signals are transmitted *via* the afferent axon to the soma of the pseudo-unipolar DRG neurons. *In vivo* imaging of DRG neurons is used as a proxy for

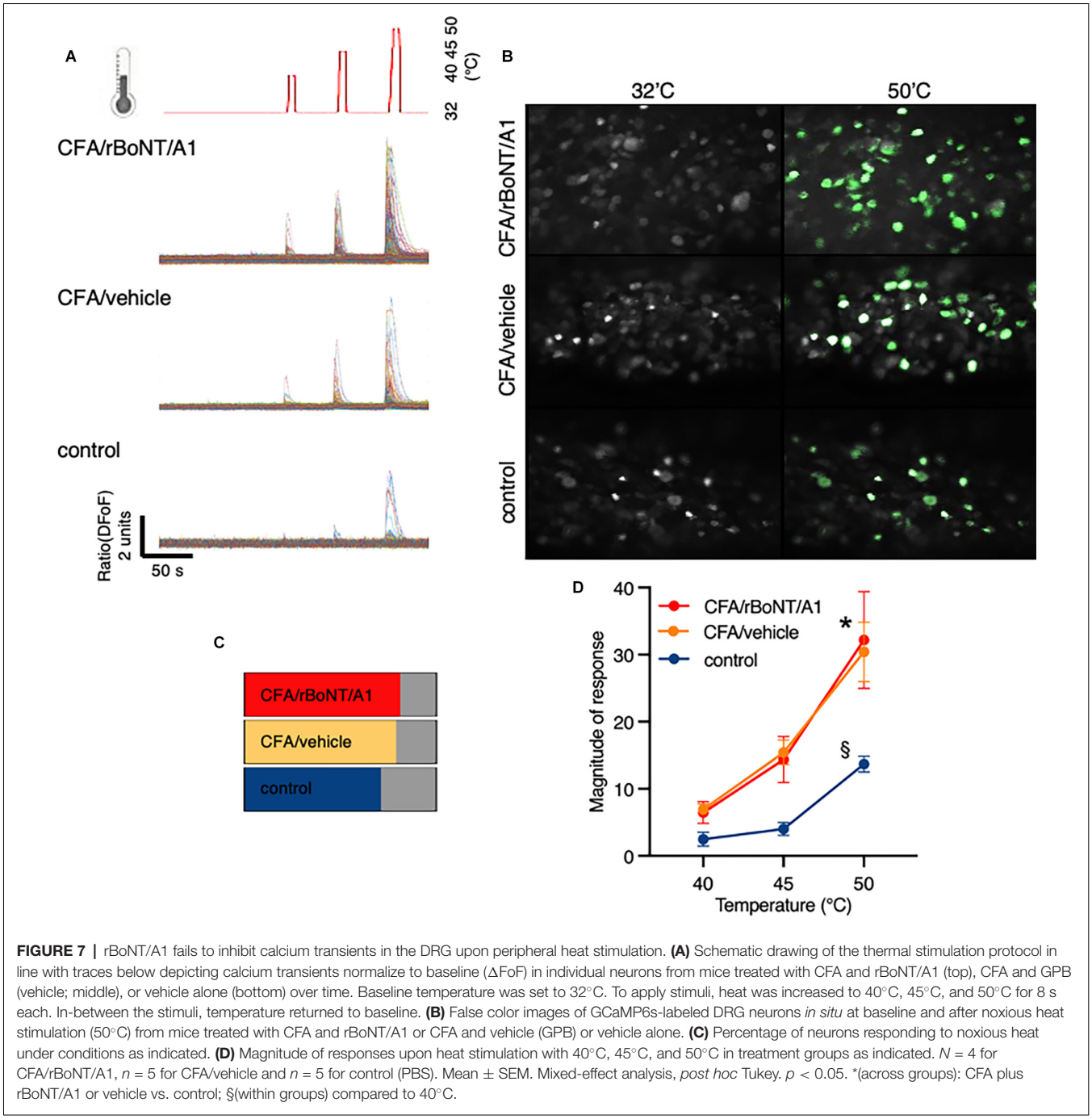

FIGURE 7 | rBoNT/A1 fails to inhibit calcium transients in the DRG upon peripheral heat stimulation. **(A)** Schematic drawing of the thermal stimulation protocol in line with traces below depicting calcium transients normalize to baseline (ΔFoF) in individual neurons from mice treated with CFA and rBoNT/A1 (top), CFA and GPB (vehicle; middle), or vehicle alone (bottom) over time. Baseline temperature was set to 32°C. To apply stimuli, heat was increased to 40°C, 45°C, and 50°C for 8 s each. In-between the stimuli, temperature returned to baseline. **(B)** False color images of GCaMP6s-labeled DRG neurons *in situ* at baseline and after noxious heat stimulation (50°C) from mice treated with CFA and rBoNT/A1 or CFA and vehicle (GPB) or vehicle alone. **(C)** Percentage of neurons responding to noxious heat under conditions as indicated. **(D)** Magnitude of responses upon heat stimulation with 40°C, 45°C, and 50°C in treatment groups as indicated. $N = 4$ for CFA/rBoNT/A1, $n = 5$ for CFA/vehicle and $n = 5$ for control (PBS). Mean ± SEM. Mixed-effect analysis, *post hoc* Tukey. $p < 0.05$. *(across groups): CFA plus rBoNT/A1 or vehicle vs. control; §(within groups) compared to 40°C.

events at the terminal nerve endings. Previous reports show an enhanced action potential firing upon local thermal stimulation of nerve terminals in inflamed paws of rodents (Djouhri et al., 2006). We found that CFA-mediated inflammation is also associated with increased calcium influx in the DRG neurons. In comparison to electrophysiological recordings, *in vivo* calcium imaging can be used for screening by recording signals of many neurons at the same time. To investigate whether the site of action of BoNT exerts from the periphery, we evaluated if upstream calcium signal responses in L4 dorsal root ganglion neurons (DRGs) were inhibited after local, peripheral injection of rBoNT/A1 into inflamed paws. Recorded calcium fluctuations linked to peripheral stimulation of the nerve terminals prompt to a peripheral mode of action while a lack of changed responses rather implicates a more upstream site of action of BoNT, which is likely to be in the spinal cord.

The primary purpose of this study was to ask if botulinum toxin prevents the transmission of the peripherally evoked signal in sensory nerve endings to their soma in the

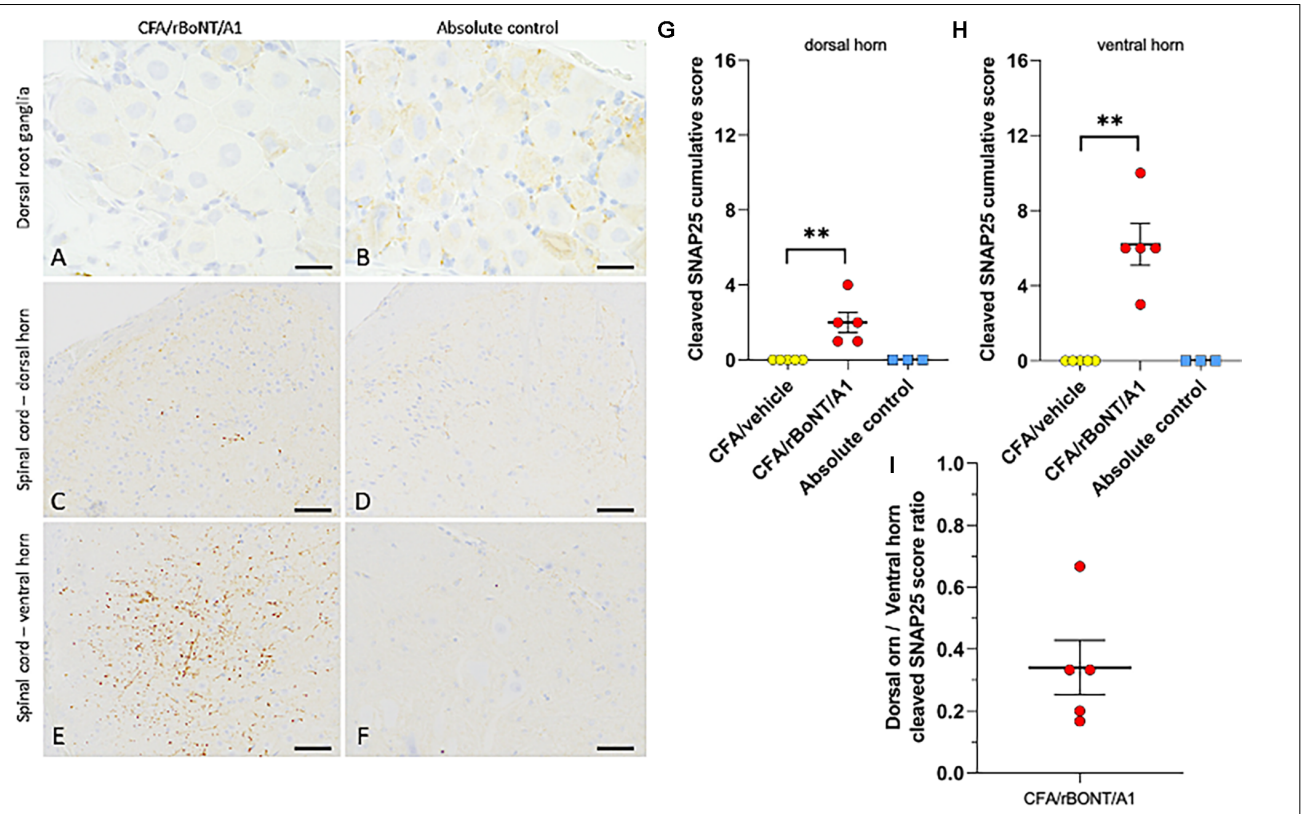

FIGURE 8 | Cleaved SNAP25 in the dorsal root ganglion (DRG) and the lumbar spinal cord. **(A,B)** Representative images of the dorsal root ganglion (DRG) and **(C–F)** of the spinal cord of mice treated with CFA/rBoNT/A1 or in untreated controls. Cleaved SNAP25 was absent in the DRG (despite higher background staining), while being present in the nerve ending-like structures in the ipsilateral dorsal **(C)** and ventral **(E)** horns of the lumbar spinal cord of CFA/rBoNT/A1-treated animals, but not in absolute controls. Bars **(A,B)** (20 μm), **(C–F)** (50 μm). **(G–I)** Quantification of cleaved SNAP25 in the lumbar spinal cord in CFA/rBoNT/A1-treated animals compared to CFA/vehicle and absolute controls. c-SNAP25 staining was moderate in the dorsal horn **(G)** and high in the ventral horn of the spinal cord **(H)** while being absent in CFA/vehicle-treated animals and in absolute controls. **(I)** The dorsal horn/ventral horn ratio of c-SNAP25 (< 1) indicates higher targeting of ventral vs. dorsal horn by rBoNT/A1. *N* = 5/group (CFA/rBoNT/A1, CFA/vehicle) and *N* = 3 (absolute control). Mean ± SEM. $^{**}p < 0.01$ CFA/rBoNT/A1 vs. CFA/vehicle; Mann-Whitney test.

DRG in an inflammatory model of pain in mice. BoNT has been used in several pre-clinical and clinical trials to reduce inflammatory and neuropathic pain (Yoo et al., 2014; Finnerup et al., 2015; Egeo et al., 2020). Behavioral studies in both, humans and rodents, suggest that BoNT suppresses hypersensitivity when applied locally into inflamed subcutaneous tissue (Shi et al., 2020). We confirmed that withdrawal reflexes upon mechanical stimulation were diminished in rBoNT/A1-treated animals in comparison to vehicle-treated controls. In line with our data, an investigation of the inhibitory profile of BiTox, a modified botulinum toxin, on CFA-evoked inflammatory pain revealed a reduction in mechanical hypersensitivity in rats while thermal responses remained unchanged (Mangione et al., 2016; Maiarù et al., 2018). In our study, the antinociceptive effect of rBoNT/A1 is not mediated by a reduced inflammation as proven by similar levels of inflammatory responses and neutrophils in rBoNT/A1- and vehicle-treated animals with local CFA-provoked hind paw inflammation.

The principal mode of action of BoNT/A1 is the cleavage of SNAP25, a component of the SNARE complex necessary for the calcium-mediated vesicular release of neurotransmitters and other proteins. Several studies have confirmed that BoNT/A1 reduces the CGRP release in migraine, its acknowledged pathophysiological mechanism, as well as the release of substance P, one of the major pain-related neuropeptides (Montecucco et al., 1996; Purkiss et al., 2000; Durham et al., 2004; Matak et al., 2017; Joussain et al., 2019). We endorse previous findings that the terminal nerve endings remain intact after local rBoNT/A1 injection (Paterson et al., 2014). The chilli receptor transient potential receptor channel vanilloid-type 1 (TRPV1) is one of the principal peripheral pain sensors responding to noxious heat. After BoNT/A1 treatment, the plasma membranes abundancy of TRPV1 is diminished on dorsal root ganglia (Xiao et al., 2013; Li and Coffield, 2016; Meng et al., 2016; Cao et al., 2017; Fan et al., 2017). A study on cultured DRG neurons showed a reduction in slowly adapting currents upon mechanical stimulation in cells treated with BoNT/A (Paterson et al., 2014). Conversely, in our study calcium transients in DRG neurons distant from the stimulation site were not reduced. Also, our data did not confirm a decreased responsiveness to thermal stimuli

after rBoNT/A1 application although our dosing regime was effective.

In addition to the peripheral effects, it has been shown that BoNT suppresses the neurotransmitter release in primary synapses in the spinal cord (Kim et al., 2015; Matak et al., 2017). There is evidence that unilateral peripheral injection of rBoNT/A1 into a hind paw of rats decreases hypersensitivity thresholds on the contralateral site in a model of chemotherapeutic-induced polyneuropathy (Favre-Guilmard et al., 2009, 2017). Our data imply that the analgesic effect rather might take place in the central nervous system consistent with the hypothesis that the toxin is retrogradely transported to its place of action in the spinal cord (Marinelli et al., 2012; Papagiannopoulou et al., 2016). This is strengthened by our data revealing the total absence of c-SNAP25 in the DRGs of rBoNT/A1-treated animals with CFA inflammation and its simultaneous presence in the lumbar spinal cord. After intraplantar administration of rBoNT/A1, high quantities of c-SNAP25 were observed in the ventral horn and low to moderate levels in the dorsal horn. These data confirm the results in the rats where the effects were abolished by colchicine, a neuronal transport blocker (Matak et al., 2012). Higher targeting of the ventral horn is consistent with the intraplantar route of administration that triggers strong rBoNT/A1 effects in skeletal muscles, as seen in c-SNAP25 staining of the neuromuscular junctions in injected footpads. However, presence of low levels of SNAP25 cleavage in the dorsal horn suggests the targeting of sensory nerves that might be sufficient to reduce nociceptive behavior.

We studied intracellular calcium changes upon mechanical stimulation using a novel custom-made stimulator. The new device allowed to repetitively apply defined levels of pressure onto the inflamed hind paws of our mice. We discovered that, in a subset of cells, increased pressure linearly correlated with the fluorescence intensity changes. These data confirm responses obtained in behavioral studies in rodents testing mechanical hypersensitivity under inflammatory conditions. However, mechano-sensitization evaluated by electrophysiological recordings is controversial. While some groups identified sensitized fibers, others missed these findings (Andrew and Greenspan, 1999; Koltzenburg et al., 1999; Bishop et al., 2010; Lennertz et al., 2012). Here, the simultaneous recording of responses transmitted by hundreds of axons reveals that some but not all fibers are sensitized under inflammation.

In conclusion, this study demonstrates that local rBoNT/A1 application ameliorates mechanical hypersensitivity in mice with local inflammation. Though, assessment of molecular mechanisms with *in vivo* calcium imaging of DRG neurons connected to the peripheral nerve endings of the hind paw revealed that the signal transmission from the periphery towards the soma remained unchanged. In the spinal cord, cleaved SNAP25 is clearly present in rBoNT/A1-treated animals. The data suggest that the efficacy of BoNT for the treatment of inflammatory pain possibly mediated *via* a more central mode of action.

DATA AVAILABILITY STATEMENT

The raw data supporting the conclusions of this article will be made available by the authors, without undue reservation.

ETHICS STATEMENT

The animal study was reviewed and approved by Ethics Committees of the Royal Veterinary College, London and King's College London.

AUTHOR CONTRIBUTIONS

The study was designed by BO, CP, MK, and SM. BO, VM, SL, and AF performed the experiments. The manuscript was prepared and written by BO, SL, VM, and MK. Except SM, who sadly passed away, all authors reviewed and approved the manuscript.

FUNDING

The study was funded by Ipsen.

ACKNOWLEDGMENTS

I gratefully thank my supervisor Professor SM who passed away while preparing the manuscript. Roberto de Col constructed the mechanical stimulator.

SUPPLEMENTARY MATERIAL

The Supplementary Material for this article can be found online at: https://www.frontiersin.org/articles/10.3389/fnmol.2022.909835/full#supplementary-material.

Supplementary Figure 1 | Immunohistochemical analysis of SNAP25 and cleaved-SNAP25 in the footpad. **(A–E)** Representative images of SNAP25 positive nerve endings identified in various skin structures and at the neuromuscular junction (NMJ) in footpad muscles in control animals. **(F–J)** Representative images of cleaved SNAP25 only detected at the NMJ **(F)** in CFA/rBoNT/A1-treated animals. **(K–O)** An isotype control antibody confirmed the specificity of the staining in CFA/rBoNT/A1-treated animals. Bars: 20 μm. N = 5/group (CFA/vehicle, CFA/rBoNT/A1) and N = 3 (absolute control). **(P)** Quantification of cleaved SNAP25 in the injected hind paw indicated by a cumulative score of cleaved SNAP25 in the neuromuscular junctions of the skin in mice treated with CFA and either rBoNT/A or vehicle (gelatine phosphate buffer; GPB; N = 5/group) and in absolute control animals (N = 3). Mean ± SEM. $^{****}p < 0.0001$ CFA/rBoNT/A1 vs. CFA/vehicle; Mann-Whitney test.

Supplementary Figure 2 | Histopathological evaluation rBoNT/A1 on CFA-induced inflammation in the footpad. **(A–E)** Representative images of Hematoxylin-Eosin (H&E) staining of the footpad taken from CFA-injected mice. **(A)** Inflammatory lesions at low magnification (dashed line). **(B)** Inflammatory lesions are composed of macrophages and mixed neutrophil infiltrates (arrow) with empty lipidic vacuoles (*). **(C)** Some areas present foamy macrophage infiltrates containing droplets of CFA (arrowheads). **(D,E)** H&E staining of the footpad collected from untreated (absolute control) animals. **(F)** Overall inflammatory process grading and **(G)** neutrophil infiltrate grading in CFA/rBoNT/A1, CFA/vehicle, and absolute control animals. Bars: (**A,D**; 200 μm; **B,C,E**; 20 μm). **(A–C)** CFA/vehicle treated animals, N = 5/group (CFA/vehicle, CFA/rBoNT/A1) and N = 3 (absolute control). Mean ± SEM. Mann-Whitney test.

REFERENCES

Andrew, D., and Greenspan, J. D. (1999). Mechanical and heat sensitization of cutaneous nociceptors after peripheral inflammation in the rat. *J. Neurophysiol.* 82, 2649–2656. doi: 10.1152/jn.1999.82.5.2649

Aoki, K. R. (2005). Review of a proposed mechanism for the antinociceptive action of botulinum toxin type A. *Neurotoxicology* 26, 785–793. doi: 10.1016/j.neuro.2005.01.017

Bishop, T., Marchand, F., Young, A. R., Lewin, G. R., and McMahon, S. B. (2010). Ultraviolet-B-induced mechanical hyperalgesia: a role for peripheral sensitisation. *Pain* 150, 141–152. doi: 10.1016/j.pain.2010.04.018

Blumenfeld, A. M., Stark, R. J., Freeman, M. C., Orejudos, A., and Manack Adams, A. (2018). Long-term study of the efficacy and safety of OnabotulinumtoxinA for the prevention of chronic migraine: COMPEL study. *J. Headache Pain* 19:13. doi: 10.1186/s10194-018-0840-8

Burstein, R., Zhang, X., Levy, D., Aoki, K. R., and Brin, M. F. (2014). Selective inhibition of meningeal nociceptors by botulinum neurotoxin type A: therapeutic implications for migraine and other pains. *Cephalalgia* 34, 853–869. doi: 10.1177/0333102414527648

Cao, L.-F., Si, M., Huang, Y., Chen, L.-H., Peng, X.-Y., Qin, Y.-Q., et al. (2017). Long-term anti-itch effect of botulinum neurotoxin A is associated with downregulation of TRPV1 and TRPA1 in the dorsal root ganglia in mice. *Neuroreport* 28, 518–526. doi: 10.1097/WNR.0000000000000779

Chisholm, K. I., Khovanov, N., Lopes, D. M., La Russa, F., and McMahon, S. B. (2018). Large scale *in vivo* recording of sensory neuron activity with GCaMP6. *eNeuro* 5:ENEURO.0417-17.2018. doi: 10.1523/ENEURO.0417-17.2018

Chuang, Y.-C., Yoshimura, N., Huang, C.-C., Chiang, P.-H., and Chancellor, M. B. (2004). Intravesical botulinum toxin a administration produces analgesia against acetic acid induced bladder pain responses in rats. *J. Urol.* 172, 1529–1532. doi: 10.1097/01.ju.0000137844.77524.97

Clark, R. A., Shoaib, M., Hewitt, K. N., Stanford, S. C., and Bate, S. T. (2012). A comparison of InVivoStat with other statistical software packages for analysis of data generated from animal experiments. *J. Psychopharmacol.* 26, 1136–1142. doi: 10.1177/0269881111420313

Cui, M., Khanijou, S., Rubino, J., and Aoki, K. R. (2004). Subcutaneous administration of botulinum toxin A reduces formalin-induced pain. *Pain* 107, 125–133. doi: 10.1016/j.pain.2003.10.008

Djouhri, L., Koutsikou, S., Fang, X., McMullan, S., and Lawson, S. N. (2006). Spontaneous pain, both neuropathic and inflammatory, is related to frequency of spontaneous firing in intact C-fiber nociceptors. *J. Neurosci.* 26, 1281–1292. doi: 10.1523/JNEUROSCI.3388-05.2006

Durham, P. L., Cady, R., and Cady, R. (2004). Regulation of calcitonin gene-related peptide secretion from trigeminal nerve cells by botulinum toxin type A: implications for migraine therapy. *Headache* 44, 35–42. doi: 10.1111/j.1526-4610.2004.04007.x

Egeo, G., Fofi, L., and Barbanti, P. (2020). Botulinum neurotoxin for the treatment of neuropathic pain. *Front. Neurol.* 11:716. doi: 10.3389/fneur.2020.00716

Fan, C., Chu, X., Wang, L., Shi, H., and Li, T. (2017). Botulinum toxin type A reduces TRPV1 expression in the dorsal root ganglion in rats with adjuvant-arthritis pain. *Toxicon* 133, 116–122. doi: 10.1016/j.toxicon.2017.05.001

Faul, F., Erdfelder, E., Buchner, A., and Lang, A.-G. (2009). Statistical power analyses using G*Power 3.1: tests for correlation and regression analyses. *Behav. Res. Methods* 41, 1149–1160. doi: 10.3758/BRM.41.4.1149

Favre-Guilmard, C., Auguet, M., and Chabrier, P.-E. (2009). Different antinociceptive effects of botulinum toxin type A in inflammatory and peripheral polyneuropathic rat models. *Eur. J. Pharmacol.* 617, 48–53. doi: 10.1016/j.ejphar.2009.06.047

Favre-Guilmard, C., Chabrier, P.-E., and Kalinichev, M. (2017). Bilateral analgesic effects of abobotulinumtoxinA (Dysport®) following unilateral administration in the rat. *Eur. J. Pain* 21, 927–937. doi: 10.1002/ejp.995

Finnerup, N. B., Attal, N., Haroutounian, S., McNicol, E., Baron, R., Dworkin, R. H., et al. (2015). Pharmacotherapy for neuropathic pain in adults: a systematic review and meta-analysis. *Lancet Neurol.* 14, 162–173. doi: 10.1016/S1474-4422(14)70251-0

Friedrich, J., Zhou, P., and Paninski, L. (2017). Fast online deconvolution of calcium imaging data. *PLoS Comput. Biol.* 13:e1005423. doi: 10.1371/journal.pcbi.1005423

GBD 2019 Diseases and Injuries Collaborators (2020). Global burden of 369 diseases and injuries in 204 countries and territories, 1990-2019: a systematic analysis for the Global Burden of Disease Study 2019. *Lancet* 396, 1204–1222. doi: 10.1016/S0140-6736(20)30925-9

Herd, C. P., Tomlinson, C. L., Rick, C., Scotton, W. J., Edwards, J., Ives, N., et al. (2018). Botulinum toxins for the prevention of migraine in adults. *Cochrane Database Syst. Rev.* 6:CD011616. doi: 10.1002/14651858.CD011616.pub2

Hooker, A., Palan, S., and Beard, M. (2016). Recombinant botulinum neurotoxin serotype A1 (SXN102342): protein engineering and process development. *Toxicon* 123:S40. doi: 10.1016/j.toxicon.2016.11.113

Intiso, D., Basciani, M., Santamato, A., Intiso, M., and Di Rienzo, F. (2015). Botulinum toxin type A for the treatment of neuropathic pain in neuro-rehabilitation. *Toxins (Basel)* 7, 2454–2480. doi: 10.3390/toxins7072454

Joussain, C., Le Coz, O., Pichugin, A., Marconi, P., Lim, F., Sicurella, M., et al. (2019). Botulinum neurotoxin light chains expressed by defective herpes simplex virus type-1 vectors cleave SNARE proteins and inhibit CGRP release in rat sensory neurons. *Toxins (Basel)* 11:123. doi: 10.3390/toxins11020123

Kim, D.-W., Lee, S.-K., and Ahnn, J. (2015). Botulinum toxin as a pain killer: players and actions in antinociception. *Toxins (Basel)* 7, 2435–2453. doi: 10.3390/toxins7072435

Koltzenburg, M., Bennett, D. L. H., Shelton, D. L., and McMahon, S. B. (1999). Neutralization of endogenous NGF prevents the sensitization of nociceptors supplying inflamed skin. *Eur. J. Neurosci.* 11, 1698–1704. doi: 10.1046/j.1460-9568.1999.00590.x

Kuehn, B. (2018). Chronic pain prevalence. *JAMA* 320:1632. doi: 10.1001/jama.2018.16009

Lennertz, R. C., Kossyreva, E. A., Smith, A. K., and Stucky, C. L. (2012). TRPA1 Mediates Mechanical Sensitization in Nociceptors during Inflammation. *PLoS One* 7:e43597. doi: 10.1371/journal.pone.0043597

Li, X., and Coffield, J. A. (2016). Structural and functional interactions between transient receptor potential vanilloid subfamily 1 and botulinum neurotoxin serotype A. *PLoS One* 11:e0143024. doi: 10.1371/journal.pone.0143024

Macfarlane, G. (2016). The epidemiology of chronic pain. *Pain* 157, 2158–2159. doi: 10.1097/j.pain.0000000000000676

Maiarù, M., Leese, C., Certo, M., Echeverria-Altuna, I., Mangione, A. S., Arsenault, J., et al. (2018). Selective neuronal silencing using synthetic botulinum molecules alleviates chronic pain in mice. *Sci. Transl. Med.* 10:eaar7384. doi: 10.1126/scitranslmed.aar7384

Mangione, A. S., Obara, I., Maiarú, M., Geranton, S. M., Tassorelli, C., Ferrari, E., et al. (2016). Nonparalytic botulinum molecules for the control of pain. *Pain* 157, 1045–1055. doi: 10.1097/j.pain.0000000000000478

Marinelli, S., Vacca, V., Ricordy, R., Uggenti, C., Tata, A. M., Luvisetto, S., et al. (2012). The analgesic effect on neuropathic pain of retrogradely transported botulinum neurotoxin A involves Schwann cells and astrocytes. *PLoS One* 7:e47977. doi: 10.1371/journal.pone.0047977

Martin, C., Stoffer, C., Mohammadi, M., Hugo, J., Leipold, E., Oehler, B., et al. (2018). NaV1.9 potentiates oxidized phospholipid-induced TRP responses only under inflammatory conditions. *Front. Mol. Neurosci.* 11:7. doi: 10.3389/fnmol.2018.00007

Matak, B., Bach-Rojecky, L., Bölcskei, K., and Helyes, Z. (2019). Mechanisms of botulinum toxin type A action on pain. *Toxins (Basel)* 11:459. doi: 10.3390/toxins11080459

Matak, I., Riederer, P., and Lackovi'c, Z. (2012). Botulinum toxin's axonal transport from periphery to the spinal cord. *Neurochem. Int.* 61, 236–239. doi: 10.1016/j.neuint.2012.05.001

Matak, I., Rossetto, O., and Lackovi'c, Z. (2014). Botulinum toxin type A selectivity for certain types of pain is associated with capsaicin-sensitive neurons. *Pain* 155, 1516–1526. doi: 10.1016/j.pain.2014.04.027

Matak, I., Tékus, V., Bölcskei, K., Lackovi'c, Z., and Helyes, Z. (2017). Involvement of substance P in the antinociceptive effect of botulinum toxin type A: evidence from knockout mice. *Neuroscience* 358, 137–145. doi: 10.1016/j.neuroscience.2017.06.040

Mendes, J. G., Natour, J., Nunes-Tamashiro, J. C., Toffolo, S. R., Rosenfeld, A., and Furtado, R. N. V. (2019). Comparison between intra-articular Botulinum toxin type A corticosteroid and saline in knee osteoarthritis: a randomized

controlled trial. *Clin. Rehabil.* 33, 1015–1026. doi: 10.1177/0269215519827996

Meng, J., Wang, J., Steinhoff, M., and Dolly, J. O. (2016). TNFα induces co-trafficking of TRPV1/TRPA1 in VAMP1-containing vesicles to the plasmalemma via Munc18-1/syntaxin1/SNAP-25 mediated fusion. *Sci. Rep.* 6:21226. doi: 10.1038/srep21226

Merskey, H., and Bogduk, N. (1994). "IASP Terminology," in *IASP Task Force on Taxonomy*, 2nd Edn., (Seattle: IASP press), 209–214. Available online at: https://www.iasp-pain.org/publications/free-ebooks/classification-of-chronic-pain-second-edition-revised/.

Montecucco, C., Papini, E., and Schiavo, G. (1996). Bacterial protein toxins and cell vesicle trafficking. *Experientia* 52, 1026–1032. doi: 10.1007/BF01952098

Pachitariu, M., Stringer, C., Schröder, S., Dipoppa, M., Rossi, L. F., Carandini, M., et al. (2016). Suite2p: beyond 10,000 neurons with standard two-photon microscopy. *bioRxiv* [Preprint]. doi: 10.1101/061507

Papagiannopoulou, D., Vardouli, L., Dimitriadis, F., and Apostolidis, A. (2016). Retrograde transport of radiolabelled botulinum neurotoxin type A to the CNS after intradetrusor injection in rats. *BJU Int.* 117, 697–704. doi: 10.1111/bju.13163

Park, J., and Park, H. J. (2017). Botulinum toxin for the treatment of neuropathic pain. *Toxins (Basel)* 9:260. doi: 10.3390/toxins9090260

Paterson, K., Lolignier, S., Wood, J. N., McMahon, S. B., and Bennett, D. L. H. (2014). Botulinum toxin-A treatment reduces human mechanical pain sensitivity and mechanotransduction. *Ann. Neurol.* 75, 591–596. doi: 10.1002/ana.24122

Périer, C., Martin, V., Cornet, S., Favre-Guilmard, C., Rocher, M.-N., Bindler, J., et al. (2021). Recombinant botulinum neurotoxin serotype A1 *in vivo* characterization. *Pharmacol. Res. Perspect.* 9:e00857. doi: 10.1002/prp2.857

Purkiss, J., Welch, M., Doward, S., and Foster, K. (2000). Capsaicin-stimulated release of substance P from cultured dorsal root ganglion neurons: involvement of two distinct mechanisms. *Biochem. Pharmacol.* 59, 1403–1406. doi: 10.1016/s0006-2952(00)00260-4

Shi, X., Gao, C., Wang, L., Chu, X., Shi, Q., Yang, H., et al. (2020). Botulinum toxin type A ameliorates adjuvant-arthritis pain by inhibiting microglial activation-mediated neuroinflammation and intracellular molecular signaling. *Toxicon* 178, 33–40. doi: 10.1016/j.toxicon.2019.12.153

Singh, J. A., Mahowald, M. L., and Noorbaloochi, S. (2010). Intraarticular botulinum toxin A for refractory painful total knee arthroplasty: a randomized controlled trial. *J. Rheumatol.* 37, 2377–2386. doi: 10.3899/jrheum.100336

Xiao, L., Cheng, J., Zhuang, Y., Qu, W., Muir, J., Liang, H., et al. (2013). Botulinum toxin type A reduces hyperalgesia and TRPV1 expression in rats with neuropathic pain. *Pain Med.* 14, 276–286. doi: 10.1111/pme.12017

Yoo, K. Y., Lee, H. S., Cho, Y. K., Lim, Y. S., Kim, Y. S., Koo, J. H., et al. (2014). Anti-inflammatory effects of botulinum toxin type a in a complete Freund's adjuvant-induced arthritic knee joint of hind leg on rat model. *Neurotox. Res.* 26, 32–39. doi: 10.1007/s12640-013-9447-7

Conflict of Interest: Authors CP, MK, VM, and SL were employed by Ipsen. AF was employed by Transpharmation.

The remaining authors declare that the research was conducted in the absence of any commercial or financial relationships that could be construed as a potential conflict of interest.

The authors declare that this study received funding from Ipsen. The funder had the following involvement with the study: provided the recombinant botulinum neurotoxin, suggested the dose being used and approved the manuscript.

Publisher's Note: All claims expressed in this article are solely those of the authors and do not necessarily represent those of their affiliated organizations, or those of the publisher, the editors and the reviewers. Any product that may be evaluated in this article, or claim that may be made by its manufacturer, is not guaranteed or endorsed by the publisher.

frontiers | Frontiers in Molecular Neuroscience

ORIGINAL RESEARCH
published: 02 June 2022
doi: 10.3389/fnmol.2022.892870

Analgesic Activity of Cinnabarinic Acid in Models of Inflammatory and Neuropathic Pain

*Serena Notartomaso[1†], Serena Boccella[2†], N. Antenucci[3], Flavia Ricciardi[2], Francesco Fazio[4], F. Liberatore[1], P. Scarselli[1], M. Scioli[1], Giada Mascio[1], V. Bruno[1,3], Giuseppe Battaglia[1,3], Ferdinando Nicoletti[1,3], Sabatino Maione[2,5] and Livio Luongo[2,5]**

[1] Department of Molecular Pathology, Istituto di Ricovero e Cura a Carattere Scientifico (IRCCS) Neuromed, Pozzilli, Italy, [2] Department of Experimental Medicine, University of Campania Luigi Vanvitelli, Naples, Italy, [3] Department of Physiology and Pharmacology, Sapienza University of Rome, Rome, Italy, [4] Department of Psychiatry and Health Science, University of California, San Diego, La Jolla, CA, United States, [5] Istituto di Ricovero e Cura a Carattere Scientifico (IRCCS) Neuromed, Pozzilli, Italy

OPEN ACCESS

Edited by:
Cyril Goudet, INSERM U1191 Institut de Génomique Fonctionnelle (IGF), France

Reviewed by:
Dietmar Benke, University of Zurich, Switzerland
Sara Marinelli, Institute of Biochemistry and Cell Biology (CNR), Italy

***Correspondence:**
Livio Luongo
livio.luongo@gmail.com

† These authors have contributed equally to this work

Specialty section:
This article was submitted to Pain Mechanisms and Modulators, a section of the journal Frontiers in Molecular Neuroscience

Received: *09 March 2022*
Accepted: *05 May 2022*
Published: *02 June 2022*

Citation:
Notartomaso S, Boccella S, Antenucci N, Ricciardi F, Fazio F, Liberatore F, Scarselli P, Scioli M, Mascio G, Bruno V, Battaglia G, Nicoletti F, Maione S and Luongo L (2022) Analgesic Activity of Cinnabarinic Acid in Models of Inflammatory and Neuropathic Pain. Front. Mol. Neurosci. 15:892870. doi: 10.3389/fnmol.2022.892870

Cinnabarinic acid (CA) is a trace kynurenine metabolite, which activates both type-4 metabotropic glutamate (mGlu4) and arylic hydrocarbon (Ah) receptors. We examined the action of CA in models of inflammatory and neuropathic pain moving from the evidence that mGlu4 receptors are involved in the regulation of pain thresholds. Systemic administration of low doses of CA (0.125 and 0.25 mg/kg, i.p.) reduced nocifensive behaviour in the second phase of the formalin test. CA-induced analgesia was abrogated in mGlu4 receptor knockout mice, but was unaffected by treatment with the Ah receptor antagonist, CH223191 (1 mg/Kg, s.c.). Acute injection of low doses of CA (0.25 mg/kg, i.p.) also caused analgesia in mice subjected to Chronic Constriction Injury (CCI) of the sciatic nerve. Electrophysiological recording showed no effect of CA on spinal cord nociceptive neurons and a trend to a lowering effect on the frequency and duration of excitation of the rostral ventromedial medulla (RVM) ON cells in CCI mice. However, local application of CH223191 or the group-III mGlu receptor antagonist, MSOP disclosed a substantial lowering and enhancing effect of CA on both populations of neurons, respectively. When repeatedly administered to CCI mice, CA retained the analgesic activity only when combined with CH223191. Repeated administration of CA *plus* CH223191 restrained the activity of both spinal nociceptive neurons and RVM ON cells, in full agreement with the analgesic activity. These findings suggest that CA is involved in the regulation of pain transmission, and its overall effect depends on the recruitment of mGlu4 and Ah receptors.

Keywords: analgesia, neuropathic pain, cinnabarinic acid, metabotropic glutamate receptor 4, inflammatory pain

INTRODUCTION

The kynurenine pathway of tryptophan metabolism generates a number of neuroactive compounds, and, therefore, has been extensively studied in experimental animal models of CNS disorders in the last several years. In the first step of the pathway, L-tryptophan is converted by type-1 and -2 indoleamine 2,3-dioxygenase (IDO-1 ad -2) or by tryptophan 2,3-dioxygenase into formyl-kynurenine, which is transformed into L-kynurenine. IDO-1 and -2 are induced

by proinflammatory cytokines. L-kynurenine can be transformed into 3-hydroxykynurenine by kynurenine monooxygenase (KMO), or, alternatively, it can be transaminated into kynurenic acid (KYNA) by different isoforms of kynurenine aminotransferase (KAT). 3-Hydroxykyurenine is converted by kynureninase into 3-hydroxyanthranilic acid or, alternatively, is converted by KATs into xanthurenic acid (XA). 3-Hydroxyanthranilic acid can be converted in two steps into quinolinic acid (QUINA), which is further metabolized to produce nicotinic acid ribonucleoside, the precursor of nicotinamide adenine dinucleotide (NAD). Alternatively, 3-hydroxyanthraylic acid may give rise to cinnabarinic acid (CA), a trace kynurenine metabolite, which is increasingly attracting the interest of neurobiologists (Schwarcz et al., 2012). QUINA is an orthosteric agonist of NMDA receptors, whereas KYNA acts as an antagonist at the glycine site of NMDA receptors (Stone, 1993). At least in one study, XA was found to activate type-2 and -3 metabotropic glutamate receptors (mGlu2 and -3 receptors) (Fazio et al., 2017). CA is a pleiotropic molecule, and its action is only partially elucidated. We have found that CA behaves as an orthosteric agonist of mGlu4 receptors (Fazio et al., 2012), a presynaptic receptor that negatively modulates glutamate release (Nicoletti et al., 2011). However, CA can also interact with the aryl hydrocarbon receptor (Ah receptor), a transcription factor known for its ability to bind arylic xenobiotics, such as benzo(a)pirene (Lowe et al., 2014). A large body of evidence supports the involvement of the kynurenine pathway in the regulation of pain thresholds and in the pathophysiology of chronic pain. Both L-kynurenine and 3-hydroxykynurenine are detectable in dorsal horns of the spinal cord (Godefroy et al., 1990), and a number of kynurenine metabolites, including L-kynurenine, KYNA, QUINA, and anthranilic acid modulate pain thresholds in the hot plate ad tail flick tests (Heyliger et al., 1998). In the chronic constriction injury (CCI) model of neuropathic pain, IDO-2, KMO, and 3-hydroxyanthranilate dioxygenase (HAOO) were found to be up-regulated in the spinal cord as result of neuroinflammation and microglia activation, and IDO-2 and KMO inhibitors attenuated mechanical and thermal hyperalgesia (Ciapała et al., 2021). Similar findings were obtained using the KMO inhibitor, Ro 61-8048, in a rat model of neuropathic pain (Laumet et al., 2017). It is generally believed that the influence of the kynurenine pathway on pain transmission is mediated by QUINA or KYNA acting at NMDA receptors and that, for example, KMO inhibitors cause analgesia by shunting L-kynurenine metabolism toward the formation of KYNA (Németh et al., 2005). However, there is increasing evidence that mGlu4 receptors, which are targeted by CA, modulate pain thresholds in different stations of the pain neuraxis, with the overall effect of reducing pain (Pereira and Goudet, 2019). Cyril Goudet, Jean-Philippe Pin, and their associates were first to demonstrate that mGlu4 receptors are located on nerve terminals of unmyelinated C fibres in the dorsal horns of the spinal cord where they negatively modulate glutamate release through coupling to $Ca_v2.2$ voltage-sensitive calcium channels (Goudet et al., 2009). In addition, they found that genetic deletion of mGlu4 receptors enhances nocifensive behaviour in the formalin test and that pharmacological activation of mGlu4 receptors with subtype-selective agonists attenuates hyperalgesia in animal models of inflammatory or neuropathic pain (Vilar et al., 2013). An elegant follow-up of these findings was the demonstration that mGlu4 receptors are localized on neurons neighbouring intercalated cell clusters in the mouse amygdala, and that optical control of endogenous mGlu4 receptors with a photo switchable positive allosteric modulator rapidly and reversibly inhibited sensory and emotional behaviours associated with persistent inflammatory pain (Zussy et al., 2018). mGlu4 and other group-III mGlu receptors are also found in brainstem regions involved in the top-down control of pain, such as the periaqueductal grey (PAG) and the rostral ventromedial medullary (RVM) nucleus, where they modulate the activity of ON and OFF cells (Ohishi et al., 1995; Drew and Vaughan, 2004). This gave us the impetus to examine the effect of CA in two established mouse pain models: the formalin model of inflammatory pain and the CCI model of neuropathic pain. Using the latter model, we extended the analysis to *in vivo* recording of secondary order sensory neurons in the dorsal horn of the spinal cord and ON and OFF cells in the RVM in an attempt to disclose the electrophysiological mechanisms underlying the effect of CA on pain transmission.

MATERIALS AND METHODS

Drugs

CA and CH223191 were purchased by Sigma-Aldrich (Italy). MSOP was purchased by Tocris Cookson Ltd., (Bristol, United Kingdom). For systemic treatments, CA was dissolved in saline and administered i.p. at doses ranging from 0.125 to 3 mg/Kg (Ulivieri et al., 2020), whereas, CH223191 was dissolved in sesame oil and administered s.c. at the dose of 1 mg/Kg (Ulivieri et al., 2020). For local applications in the VL-PAG or spinal cord, CH223191 and MSOP were dissolved in ACSF containing 0.05% DMSO and used at concentrations of 30 nM and 100 uM, respectively. The concentration of MSOP was chosen on the basis of previous studies in which MSOP was microinjected into the VL-PAG and showed no effect on its own (Maione et al., 1998; Berrino et al., 2001; Palazzo et al., 2001; Marabese et al., 2007a,b). Control mice received the same volume of vehicle (ACSF containing 0.05% DMSO).

Animals

Experiments were performed following the Guidelines for Animal Care and Use of the National Institutes of Health to minimize the number of animals and animal suffering. The experimental protocol was approved by the Ethical Committee of Neuromed Institute (Pozzilli, Italy), by the Italian Ministry of Health (515/2021-PR), and by the Ethical Committee of University of Campania "Luigi Vanvitelli" (Naples, Italy) and by the Italian Ministry of Health (713/2021-PR). All efforts were made to minimize animal suffering and the number of animals used. In most of the experiments, we used adult male C57BL/6J mice (20–25 g, b.w.) and mGlu4 receptor knockout mice (B6.129-Grm4tm1Hpn/J). Mice were housed in an animal care facility at

23°C on a 12 h light/12 h dark cycle with food and water provided *ad libitum*.

Drug Treatment

In the formalin test, CA was administered i.p. at doses of 0.125, 0.25, 0.5, or 3 mg/kg always 5 min prior to formalin injection (see below). The respective controls were treated with vehicle. In one experiment, mice were treated s.c. CH223191 (1 mg/kg) or vehicle followed, 5 min later, by i.p. injections of CA (0.25 mg/kg) or vehicle. In another experiment, CA (0.25 mg/kg) or vehicle were injected i.p. in wild-type (WT) and mGlu4$^{-/-}$ mice.

In CCI mice we tested the effects of single or repeated injections of CA (0.25 mg/kg) on mechanical pain thresholds and activity of nociceptive spinal cord neurons and ON RVM cells. In experiments with single injections, either vehicle or CA were administered once i.p. and mechanical thresholds were measured every 15 min from 15 to 120 min following injections. For electrophysiological analysis, either MSOP or CH223191 were locally applied in the spinal cord or in the VL-PAG. In experiments with repeated injections, vehicle, s.c. + vehicle, i.p.; vehicle, s.c. + CA (0.25 mg/kg), i.p.; CH223191 (1 mg/kg), s.c., + vehicle, i.p.; or CH223191, s.c. + CA, i.p. were administered once a day for 7 days starting from day 7 following nerve ligation. Subcutaneous injections were always carried out 5 min prior to i.p. injections. Mechanical thresholds were determined only once 15 min after the last i.p. injection.

Formalin Test

Acute inflammatory pain was assessed using the formalin test. Ten μl of a formalin solution (2%) was injected s.c. into the plantar surface of the right hind paw. After injection, mice were immediately placed in a plexiglass box (20 cm × 15 cm × 15 cm) surrounded by mirrors to allow the observation of nociceptive responses that include licking, lifting and shaking of the injected paw. After formalin injection, mice were observed for 1 h and their behaviour was recorded by researchers blind to genotypes and drug treatments. Formalin scores were separated into two phases, phase I (0–10 min) and phase II (30–60 min).

Induction of Chronic Constriction Injury of the Sciatic Nerve

Chronic constriction of the sciatic nerve was carried out under isoflurane anesthesia (5% for induction and 2% for maintenance), as described by Bennett and Xie (1988). In brief, the biceps femoris and the gluteus superficialis were separated by blunt dissection, and the left sciatic nerve was exposed. CCI was produced by tying two ligatures around the sciatic nerve. The ligatures were tied loosely around the nerve with 1 mm spacing, until they elicited a brief twitch in the respective hind limb, which prevented over-tightening of the ligations, taking care to preserve epineural circulation. The incision was cleaned and the skin was closed with 2–3 ligatures of non-absorbable silk suture size 5–0. Mice were then placed on a warmed surface and, following recovery, they were returned to their home cages and checked routinely for 72 h. In Sham-operated mice (SO) mice, the left sciatic nerve was exposed without ligature. Mechanical allodynia (see below) was assessed 14 days after surgery. The development of mechanical allodynia was evaluated by using the von Frey filaments. All animals were tested before surgery and then 14 days after surgery. Mechanical allodynia was quantified by measuring the hind paw withdrawal response to von Frey filament stimulation.

Assessment of Mechanical Allodynia (Von Frey Test)

Mechanical allodynia was measured by a series of calibrated von Frey filaments (Stoelting, Wood Dale, IL, United States), ranging from 0.02 to 2 gr. Neuropathic mice were placed in plastic cages with a wire-mesh floor approximately 1 h before testing to allow behavioural accommodation. The von Frey filaments were applied in ascending order to the mid-plantar surface of the hind paw through the mesh floor. If the use of the filament three times did not induce a reaction, the next filament with higher pressure was used. The time interval before the application of each filament was at least 5 s. Data were expressed as mean ± S.E.M. of the mechanical withdrawal threshold (MWT) in grams.

Extracellular Recordings of Spinal Nociceptive Specific Neurons *in vivo*

For *in vivo* single unit extracellular recording, mice were initially anesthetized with Avertin (1.25%). After tracheal cannulation, a catheter was placed into the right external jugular vein to allow continuous infusion of propofol (5–10 mg/kg/h, i.v.). Spinal cord segments L4–L6 were exposed medially by laminectomy, near the dorsal root entry zone, up to a depth of 1 mm. An elliptical rubber ring (about 3 mm × 5 mm) was tightly sealed with silicone gel onto the surface of the cord. This ring formed a trough with about 50 μL capacity over the spinal segments used for topical spinal drug application.

It also provided access to the spinal neurons that receive input from the ipsilateral paw, where the mechanical stimulation was applied. Animals were then secured in a stereotaxic apparatus (David Kopf Instruments, Tujunga, CA, United States) supported by clamps attached to the vertebral processes on either side of the exposure site. The exposed area of the spinal cord was initially framed by agar and then filled with mineral oil. Body temperature was maintained at 37°C with a temperature-controlled heating pad. A glass-insulated tungsten filament electrode (3–5 MΩ; FHC Frederick Haer & Co., Bowdoin, ME, United States) was used to record single unit extracellular activity of dorsal horn NS neurons. NS neurons were defined as those neurons that respond only to high-intensity (noxious) stimulation. To confirm NS response patterns, each neuron was characterized while applying a mechanical stimulation to the ipsilateral hind paw using a von Frey filament with 97.8 mN bending force (noxious stimulation) for 2 s until it buckled slightly. Only neurons that responded specifically to the noxious hind paw stimulation, without responding to stimulation of the surrounding tissue, were included in sham and neuropathic mice recordings. The recorded signals were amplified and displayed on a digital storage oscilloscope to ensure that the unit under study was unambiguously discriminated throughout the experiment.

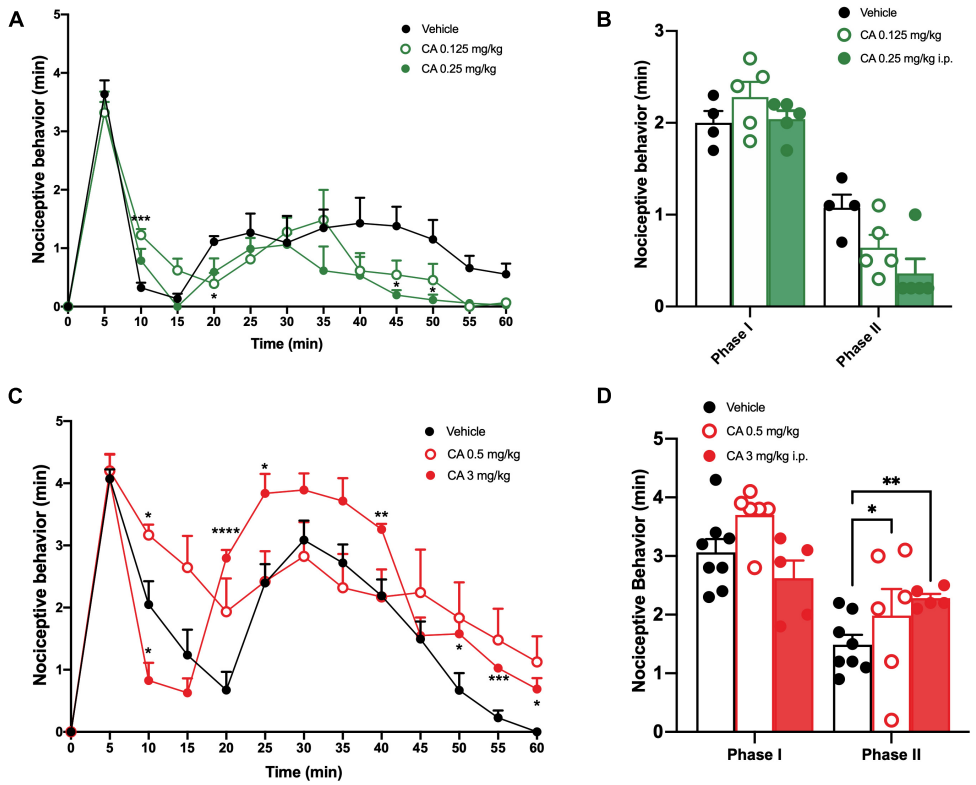

FIGURE 1 | Low doses of cinnabarinic acid significantly reduced formalin-induced nocifensive response in wild-type (WT) mice. **(A)** Effect of lowest doses of cinnabarinic acid (0.125 and 0.25 mg/Kg) on formalin-induced pain behaviours, including lifting, flinching, and licking, observed for 60 min at 5 min intervals. **(B)** Total pain scores were classified as phase I (0–10 min) and phase II (30–60 min) in formalin-injected mice treated with vehicle or with cinnabarinic acid (0.125 and 0.25 mg/Kg). **(C)** Effect of highest doses of cinnabarinic acid (0.5 and 3 mg/Kg) on formalin-induced pain behaviours, including lifting, flinching, and licking, observed for 60 min at 5 min intervals. **(D)** Total pain scores were classified as phase I (0–10 min) and phase II (30–60 min) in formalin-injected mice treated with vehicle or with cinnabarinic acid (0.5 and 3 mg/Kg). Data are expressed as the means ± SEMs (two-way ANOVA for repeated measures with Tukey's *post-hoc* test, $^{*}p < 0.05$, $^{**}p < 0.01$, and $^{****}p < 0.0001$ vs. vehicle, $n = 6–8$).

Signals were also fed into a window discriminator, whose output was processed by an interface CED 1401 (Cambridge Electronic Design Ltd., Milton, United Kingdom) connected to a Pentium III PC. Spike2 software (CED, version 4) was used to create peristimulus rate histograms online and to store and analyse digital records of single unit activity offline. Configuration, shape, and height of the recorded action potentials were monitored and recorded continuously using a window discriminator and Spike2 software for online and offline analysis. This study only included neurons whose spike configuration remained constant and could be clearly discriminated from activity in the background throughout the experiment, indicating that the activity from one neuron only and from the same neuron was measured. The neuronal activity was expressed as spikes/s (Hz). At the end of the experiment, each animal was killed with a lethal dose of urethane. The spontaneous and noxious-evoked neuronal activity was expressed as spikes/s (Hz) and the effect of drugs was analyzed as % variation of firing rate, frequency and duration of excitation. For acute experiments, after recording a stable basal activity (10 min), topical spinal application of vehicle or drugs was performed, and each extracellular recording was monitored until 45-60 min post-injection. In particular, groups of animals were divided as following: (1) Vehicle (sesame oil or 0.05% DMSO in ACSF), (2) Cinnabarinic acid (CA) 0.25 mg/Kg (the anti-nociceptive or analgesic dose), (3) MSOP (100 uM), (4) MSOP (100 uM/5 ul)+CA (0.25 mg/Kg, i.p.), (5) CH223191 (30 nM) and (6) CH223191 (30 nM)+ CA 0.25 mg/Kg (i.p.). Vehicle or drugs were applied on the spinal cord in a volume of 5 μl and at the end of the experiment, each animal was killed with a lethal dose of urethane.

Surgical Preparation for Intra-PAG Microinjections

Control and CCI mice were anesthetized with pentobarbital (50 mg/kg, i.p.), and a 26-gauge, 8 mm-long stainless steel guide cannula was stereotaxically lowered until its tip was 1.0 mm above the VL PAG (AP: -4.7 mm and L: 0.5 mm from bregma, V: 1.78 mm below the dura) (Paxinos and Franklin, 2001). The cannula was anchored with dental cement to a stainless steel screw in the skull. We used a David Kopf stereotaxic apparatus (David Kopf Instruments, Tujunga, CA, United States) with the animal positioned on a homeothermic temperature control blanket (Harvard Apparatus Limited, Edenbridge,

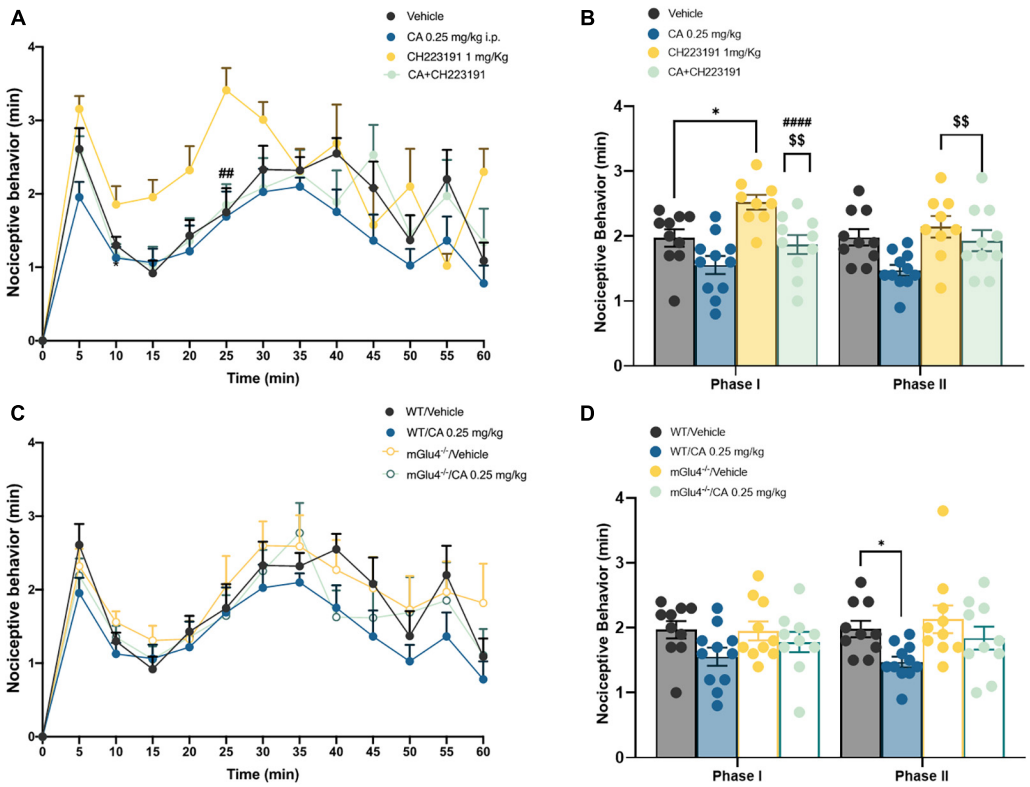

FIGURE 2 | Cinnabarinic acid-induced analgesia was mediated by the activation of mGlu4 receptor in WT and mGlu4$^{-/-}$ mice. **(A)** Effect of cinnabarinic acid (0.25 mg/Kg) alone or in combination with CH223191 (1 mg/Kg) on formalin-induced pain behaviours, including lifting, flinching, and licking, observed for 60 min at 5 min intervals. **(B)** Total pain scores were classified as phase I (0–10 min) and phase II (30–60 min) in formalin-injected mice treated with vehicle or with cinnabarinic acid (0.25 mg/Kg) alone or in combination with CH223191 (1 mg/Kg). **(C)** Effect of cinnabarinic acid (0.25 mg/Kg) on formalin-induced pain behaviours, in WT and in mGlu4$^{-/-}$ mice, observed for 60 min at 5 min intervals. **(D)** Total pain scores were classified as phase I (0–10 min) and phase II (30–60 min) in WT and in mGlu4$^{-/-}$ mice formalin-injected mice treated with vehicle or with cinnabarinic acid (0.25 mg/Kg). Data are expressed as the means ± SEMs (two-way ANOVA for repeated measures with Tukey's *post-hoc* test, $^{*}p < 0.05$ vs. vehicle, $^{\$\$}p < 0.01$ vs. CH223191, and $^{\#\#\#\#}p < 0.0001$ vs. CA, $n = 8$–10).

United Kingdom). Intra-VL PAG administration was conducted with a stainless steel cannula connected by a polyethylene tube to an SGE 1-μl syringe, inserted through the guide cannula, and extended 1.0 mm beyond the tip of the guide cannula to reach the VL PAG. Groups of animals were divided as following: (1) Vehicle (sesame oil or 0.05% DMSO in ACSF), (2) CA 0.25 mg/Kg (the anti-nociceptive or analgesic dose), (3) MSOP (100 uM), (4) MSOP (100 uM/5ul)+CA (0.25 mg/Kg, i.p.), (5) CH223191 (30 nM), and (6) CH223191 (30 nM)+ CA 0.25 mg/Kg (i.p.). Vehicle or drugs were injected in a volume of 0.5 μl into the VL PAG for 60 s and the injection cannula gently removed 2 min later. At the end of the experiment, each animal was killed with a lethal dose of urethane.

Extracellular Recordings of Rostral Ventromedial Medulla ON Cell *in vivo*

Single unit extracellular recordings have been carried out in the RVM while microinjecting MSOP, CH223191 or vehicle into the VL PAG in sham and CCI mice. We implanted the cannula in the ventrolateral subregion of the PAG because output neurons from VL PAG project directly to RVM (Sandkühler and Gebhart, 1984; Moreau and Fields, 1986). A glass-insulated tungsten filament electrode (3–5 MW) (FHC Frederick Haer& Co., Bowdoin, ME, United States) was lowered into the RVM using the stereotaxic coordinates (AP: -6.48 mm and L: 0.3–0.5 mm from bregma, and V: 4.5–6.0 mm below the dura) from the atlas of Paxinos and Franklin (2001). Pain-responding neurons were identified by the characteristic ON cell burst of activity evoked by the noxious stimulus. In particular, neurons showing an abrupt acceleration of firing activity just prior to the pain-evoked nocifensive reaction were identified as ON cells. Neurons showing no change in activity just before the nocifensive reaction were identified as neutral cells and were not recorded (Fields et al., 1983). The recorded signals were amplified and displayed on both, analogue and a digital storage oscilloscope to ensure that the unit under study was unambiguously discriminated throughout the experiment. Signals were sampled by a CED 1401 interface (Cambridge Electronic Design Ltd., United Kingdom) and analyzed by Spike2 window software (CED, version 4) to create peristimulus rate histograms online and to store and analyze digital records of single-unit activity offline. The configuration, shape, and height of the recorded action potentials were monitored and recorded continuously

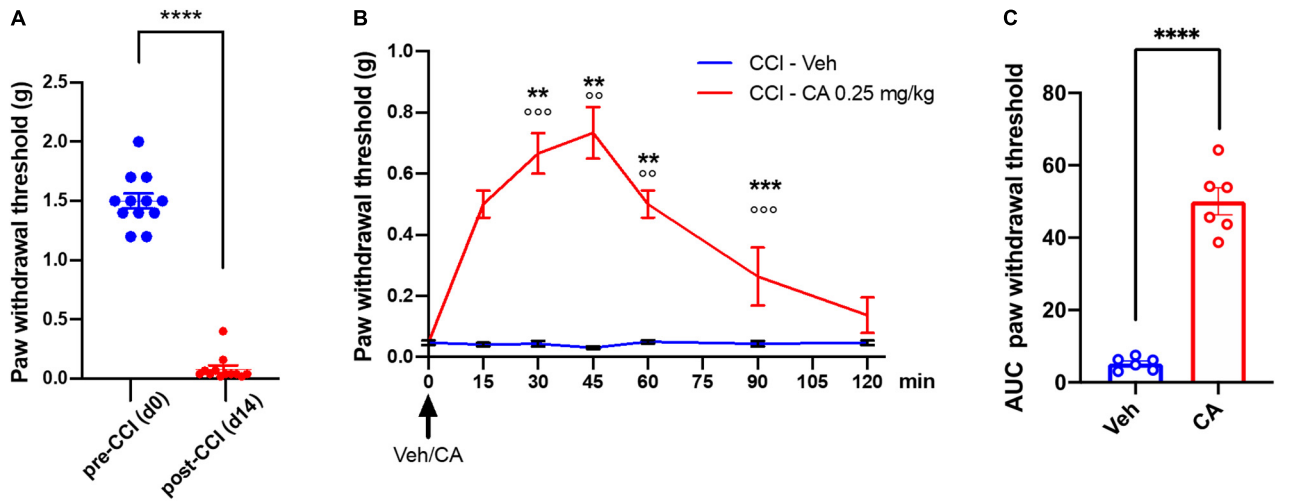

FIGURE 3 | Single injection of cinnabarinic acid showed analgesic effect in WT CCI mice. **(A)** Paw withdrawal thresholds in CCI mice recorded before (day 0) and after (day 14) CCI surgery. Data are expressed as the means ± SEMs [paired *t*-student test, ****$p < 0.0001$ vs. pre-CCI (d0), $n = 12$]. **(B)** Time-course of paw withdrawal threshold (g) measurements before and after single injection of vehicle or CA (0. 25 mg/Kg) in CCI mice, recorded for 120 min at 15 min intervals. Data are expressed as the means ± SEMs [two-way ANOVA for repeated measures with Tukey's or Sidak *post-hoc* test for differences within and between group of animals, **$p < 0.01$, ***$p < 0.001$ and ****$p < 0.0001$ vs. pre-drug (time 0), $^{\circ\circ}p < 0.01$ and $^{\circ\circ\circ}p < 0.001$ vs. vehicle, $n = 6$]. **(C)** The area under curve (AUC) analysis (normalized to -1 d values) of paw withdrawal threshold differences in between vehicle and CA-injected CCI mice. Data are expressed as the means ± SEMs (unpaired *t*-student test, ****$p < 0.0001$ vs. CCI-Veh, $n = 6$).

using Spike2 software for online and offline analyses. Once an ON cell was identified from its background activity, we optimized spike size before all treatments. This study only included neurons whose spike configuration remained constant and could clearly be discriminated from the background activity throughout the entire experiment. By doing so, we were able to determine the activity of a single neuron only. In each mouse, the activity of only a single neuron was recorded before and after vehicle or drug administration. The ongoing activity, the average of the firing rate (spikes/s) for 50 s before the noxious stimulus (which was carried out every 5 min), and noxious stimulus-evoked activity, the peak height (spikes/s) of the noxious stimulus-evoked burst and the onset of the ON cell burst (the time elapsing between the onset of noxious stimulus application and the increase in the frequency rate, which was at least twofold higher than its baseline) were quantified for the ON cells, before and after the VL PAG microinjection of vehicle or drugs. At the end of the experiment, a volume of 200 nl of neutral red (0.1%) was injected into the VL PAG for 30 min before killing the mice with a lethal dose of urethane. Mice were then perfused intracardially with 20 ml phosphate buffer solution (PBS) followed by 20 ml of 10% formalin solution in PBS. The brains were removed and immersed in a saturated formalin solution for 2 days. After fixation, the microinjection and recording sites were identified. The injection sites were ascertained using two consecutive sections (40 μm), one stained with cresyl violet to identify the microinjection site within the VL PAG, and the other unstained to determine dye spreading. The recording site was marked with a 20 μA DC current applied for 20 s immediately prior to the end of the electrophysiological recordings. Only the data from drug microinjection and diffusion sites located within the VL PAG and those from the recording sites in RVM neurons were included in the results.

Statistics

Statistical analysis was performed using GraphPad Prism 9 (GraphPad Software). Behavioural data were expressed as mean ± standard error of the mean (SEM). Electrophysiological data were represented as percentage change from baseline. Test for normal distribution was performed by Kolmogorov-Smirnov test with Lilliefors significance correction. The *t*-test was used to test differences between two means of paired/unpaired data. Under condition of normal distribution, ANOVA for repeated measures was performed followed by Sidak's *post-hoc* test to compare post-injection *vs.* pre-injection values or Tukey's *post-hoc* test to calculate significant differences between the different groups of mice. One Two-way ANOVA followed by Tukey's *post-hoc* test for multiple comparisons was used. $P < 0.05$ was considered statistically significant. Using G*Power3 software (Faul et al., 2007) with $\alpha = 0.05$ and power equal to 80%, sample size requirements for testing the efficacy of CA at 0.25 mg/Kg was $n = 5$.

RESULTS

Effect of Cinnabarinic Acid in the Formalin Test

Inflammatory Pain in C57BL/6J Mice, Wild-Type, and mGlu4$^{-/-}$ Mice

We induced inflammatory pain by injecting a 2% formalin solution in the right hind paw. Control mice (C57BL/6J mice

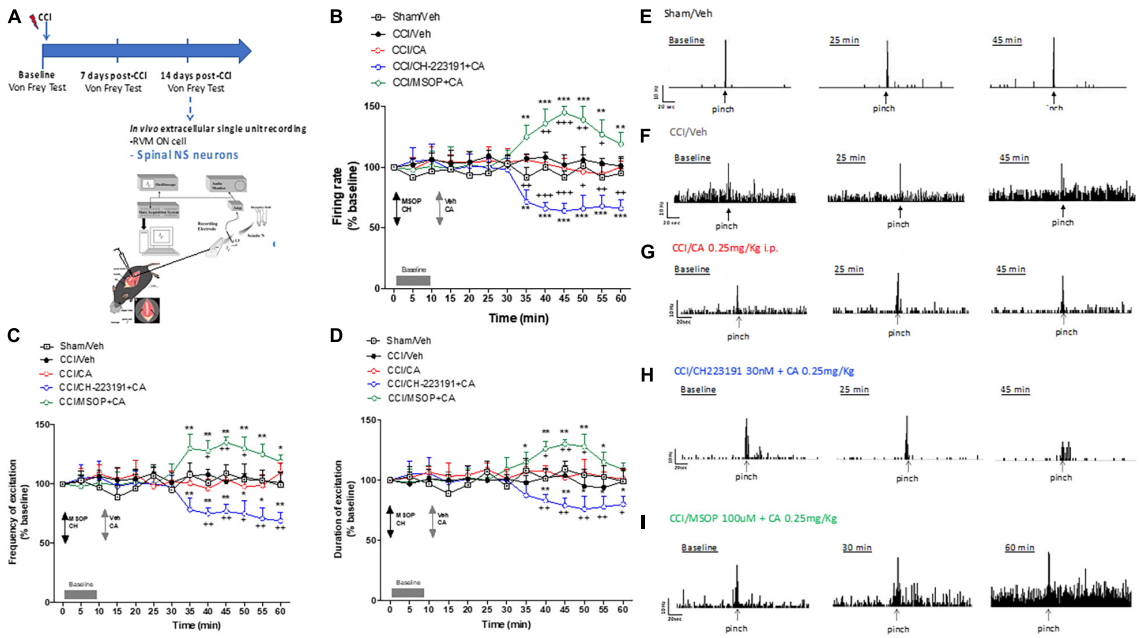

FIGURE 4 | Spinal cord neuronal hyperexcitability is oppositely modulated by mGlu4 or aryl hydrocarbon receptor in WT CCI mice. **(A)** Experimental timeline (top) and graphical representation of extracellular recordings of spinal NS neurons in anesthetized mice. **(B–D)** Mean ± S.E.M population data of spinal cord application of MSOP (100 uM) or CH223191 (30 nM) in presence of single systemic injection of cinnabarinic acid (CA, 0.25 mg/Kg) on firing rate **(B)**, frequency **(C)**, and duration of excitation **(D)** of NS neurons, in CCI mice. Black arrows indicate MSOP or CH223191 spinal application. Grey arrows indicate vehicle or CA spinal application. Grey bars indicate interval recordings of basal neuronal activity. Each point represents the mean of five different mice per group (one neuron recorded per each mouse). $^{*}p < 0.05$, $^{**}p < 0.01$, and $^{***}p < 0.001$ indicate statistically significant difference vs. baseline, $^{+}p < 0.05$, $^{++}p < 0.01$, and $^{+++}p < 0.001$ indicate statistically significant difference vs. CCI/CA. Two-way ANOVA for repeated measures followed by Tukey's *post-hoc* test was used for comparison between groups. Two-way ANOVA for repeated measures followed by Sidak *post-hoc* test was used for comparison between pre-drug and post-drug values. **(E–I)** Representative ratemeters showing spontaneous and noxious-evoked activity of NS neurons in Sham mice **(E)** or in CCI mice before and after treatment with vehicle **(F)**, CA (0.25 mg/Kg) **(G)**, CH223191+CA **(H)**, and MSOP+CA **(I)**.

injected i.p. with vehicle) showed a first phase of nocifensive behaviour in the first 0–10 min after formalin injection, followed by a second phase (30–60 min), which reflects the development of nociceptive sensitization in the dorsal horns of the spinal cord (Coderre and Melzack, 1992; Tjølsen et al., 1992). Very low doses of CA (0.125 or 0.25 mg/kg, i.p.) significantly reduced nocifensive behaviour in the second phase of the formalin test (**Figures 1A,B**), whereas, doses of 0.5 or 3 mg/kg, i.p. were inactive (**Figures 1C,D**). Indeed, mice treated with 0.125 or 0.25 mg/kg of CA, showed a nocifensive response in the second phase post-formalin injection of 0.64 ± 0.14 min ($p = 0.046$) and 0.36 ± 0.16 min ($p = 0.002$), respectively, as compared to vehicle-injected mice (1.07 ± 0.14 min) (**Figures 1A,B**). On the contrary, mice treated with 0.5 or 3 mg/kg of CA, showed a nocifensive response in the second phase post-formalin injection of 1.98 ± 0.45 and 2.28 ± 0.073 min, respectively, as compared to vehicle-injected mice (1.48 ± 0.16 min) (**Figures 1C,D**).

Formalin tests show different nocifensive responses during the first phase, between vehicle or CA-injected mice; this is likely due to diverse experimental settings among research laboratories where studies have been carried out. However, these discrepancies were not statistically different, as reported by t-test analysis. To examine whether CA-induced analgesia was mediated by the activation of mGlu4 receptors, we used mGlu4$^{-/-}$ mice. mGlu4$^{-/-}$ mice treated with vehicle showed no difference in nocifensive behaviour (1.97 ± 0.13 min in the I phase and 1.98 ± 0.12 min in the II phase) with respect to corresponding group of WT mice [see Vilar et al. (2013); **Figures 2A,B**]. Systemic injection of low doses of CA (0.25 mg/kg, i.p.) reduced nocifensive behaviour in WT (1.47 ± 0.08 min, $p = 0.047$), but not in mGlu4$^{-/-}$ mice (1.84 ± 0.17 min, $p = 0.56$) (**Figures 2A–D**). These findings suggest that, at least in the formalin test, CA-induced analgesia was mediated by the activation of mGlu4 receptors.

We also examined whether Ah receptor activation could contribute to the overall effect of CA in the formalin test by injecting C57BL/6J mice with the Ah receptor antagonist, CH-223191 (1 mg/kg, s.c.). This treatment caused a slight, but significant increase in nocifensive behaviour in the second phase of the formalin test (1.93 ± 0.16 min, $p = 0.048$) (**Figures 2C,D**). Low doses of CA (0.25 mg/kg) caused a similar reduction in nocifensive behaviour in control mice and in mice pre-treated with CH-223191 (2.14 ± 0.16 min, $p = 0.68$), indicating that the Ah receptor was not involved in CA-induced analgesia in the formalin test (**Figures 2A,B**).

Taken together these findings demonstrate that: (i) CA causes analgesia in the second phase of the formalin test; (ii) that CA is

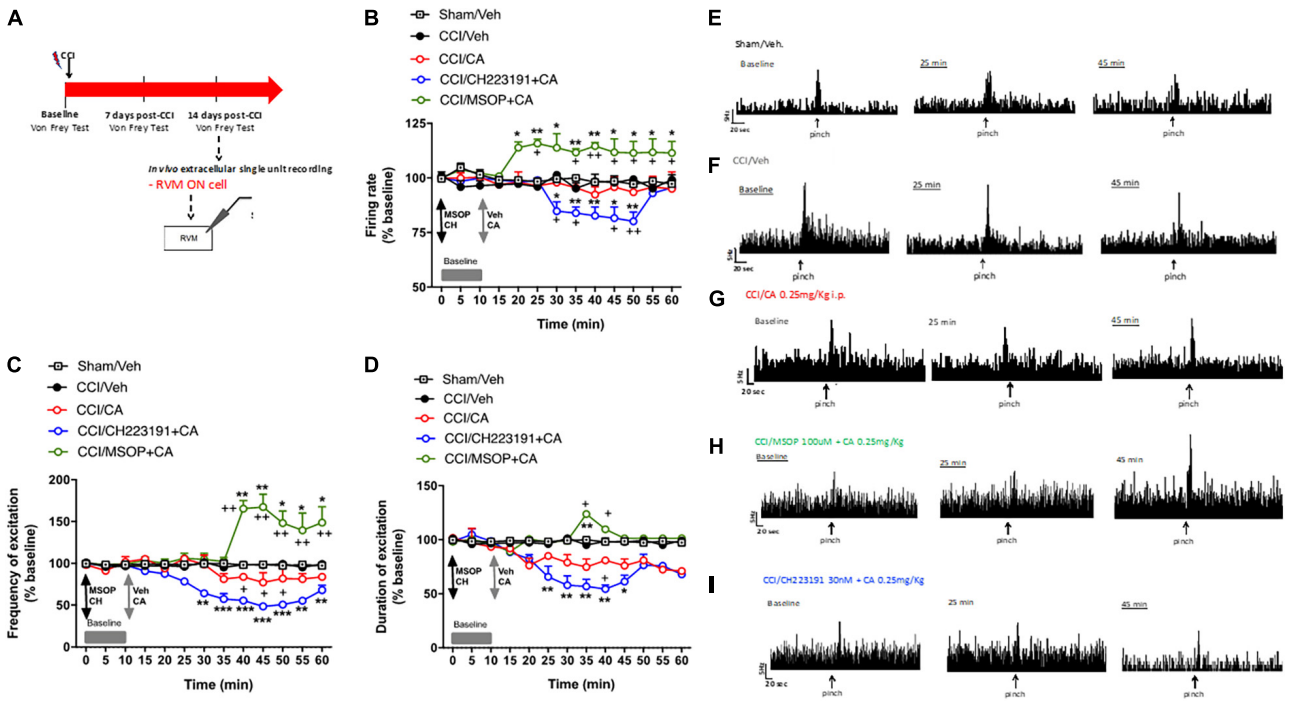

FIGURE 5 | Rostral ventromedial medullary (RVM) ON cell increased activity is oppositely modulated by mGlu4 or aryl hydrocarbon receptor in WT CCI mice. **(A)** Experimental timeline (top) and graphical representation of extracellular recordings of RVM ON cell in anesthetized mice. **(B–D)** Mean ± S.E.M population data of intra vl-PAG of MSOP (100 uM) or CH223191 (30 nM) in presence of single systemic injection of cinnabarinic acid (CA, 0.25 mg/Kg) on firing rate **(B)**, frequency **(C)**, and duration of excitation **(D)** of ON cell, in CCI mice. Black arrows indicate MSOP or CH223191 intra vl-PAG microinjections. Grey arrows indicate vehicle or CA intra vl-PAG microinjections. Grey bars indicate interval recordings of basal neuronal activity. Each point represents the mean of 5 different mice per group (one neuron recorded per each mouse). *textitp < 0.05, **$p < 0.01$, and ***$p < 0.001$ indicate statistically significant difference vs. baseline, $^{+}p < 0.05$ and $^{++}p < 0.01$ indicate statistically significant difference vs. CCI/CA. Two-way ANOVA for repeated measures followed by Tukey's *post-hoc* test was used for comparison between groups. Two-way ANOVA for repeated measures followed by Sidak *post-hoc* test was used for comparison between pre-drug and post-drug values. **(E–I)** Representative ratemeters showing spontaneous and noxious-evoked activity of ON cell in Sham mice **(E)** or in CCI mice before and after treatment with vehicle **(F)**, CA (0.25 mg/Kg) **(G)**, CH223191+CA **(H)**, and MSOP+CA **(I)**.

active at very low doses; and, (iii) that the action of CA in this test requires the presence of mGlu4 receptors and does not involve the Ah receptor.

Effect of Acute Cinnabarinic Acid Injection in the Chronic Constriction Injury Model of Neuropathic Pain

Mechanical Pain Thresholds in Wild-Type Chronic Constriction Injury Mice

Mice were subjected to CCI and treated i.p. with an acute injection of either saline or CA (0.25 mg/kg) after 14 days, when mechanical pain thresholds were markedly reduced as compared to basal values (0.11 ± 0.06 g *vs.* 1.5 ± 0.07 g, $p < 0.0001$) (**Figure 3A**). Treatment with CA, 14 days-post-CCI, caused substantial analgesia from 15 min up to 60 min post-CA, as compared to vehicle-treated mice (0.73 ± 0.084 g *vs.* 0.030 ± 0.084 g, $p = 0.0032$, at 45 min post-injection corresponding to peak of analgesia induced by CA) and it returned back to baseline values at 120 min (**Figure 3B**). Calculation of the AUC, as a measure of the effect of CA during the complete period of observation, showed that the antiallodynic effect of cinnabarinic acid resulted statistically significant ($p < 0.0001$) (**Figure 3C**).

Electrophysiological Activity of Spinal Nociceptive Specific Neurons in Wild-Type Chronic Constriction Injury Mice

In addition, to examine the regional specificity of the analgesic action of acute CA injection we recorded neuronal activity in two regions of the pain neuraxis: the dorsal horns of the spinal cord, and the RVM.

We recorded the activity of NS neurons (one cell recorded from each animal per treatment) at a depth of 0.7–1.0 mm from the surface of the spinal cord. This cell population was characterized by a mean rate of spontaneous firing of 0.015 ± 0.002 spikes/s and only cells showing this pattern of basal firing were chosen for the experiment. We confirmed an overall NS neuron hyperexcitability in CCI mice as compared with sham-operated mice (mice which underwent surgery but not nerve ligation) [see Boccella et al. (2015)]. In particular, we found a significant increase in spontaneous activity (12.33 ± 2.7 spikes/sec, $p = 0.003$, $n = 5$), and in the frequency (29 ± 3.2 spikes/sec, $p = 0.006$, $n = 5$) and duration of the excitation

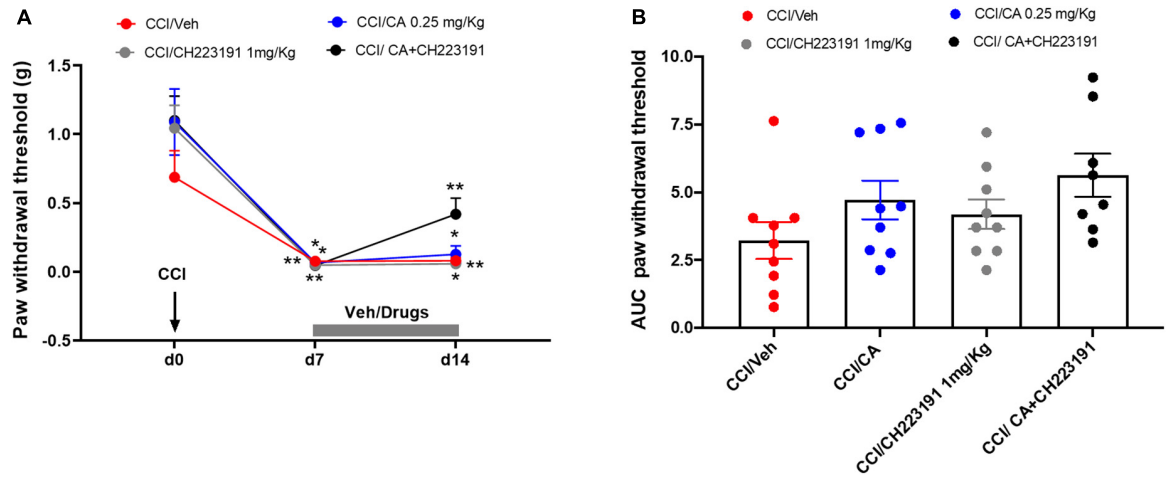

FIGURE 6 | Analgesic activity of chronic treatment with CA was disclosed when the drug was combined with systemic CH223191 in WT CCI mice. **(A)** Effect of repeated administrations of cinnabarinic acid (0.25 mg/Kg) alone or in combination with CH223191 (1 mg/Kg) on paw withdrawal threshold (g) in CCI mice (n = 7–9 mice per group). Black arrow indicates chronic constriction surgery (d0). Grey bar indicate the duration of drug treatment (from d7 to d14). **(B)** The area under curve (AUC) analysis (normalized to -1 d values) of paw withdrawal thresholds in CCI mice treated with vehicle, CA, CH223191 or CA+CH223291 (n = 7–9 mice per group). Two-way ANOVA for repeated measures followed by Sidak *post-hoc* test was used for comparison between pre-drug and post-drug values. $^{*}p < 0.05$ and $^{**}p < 0.01$ indicate statistically significant difference vs. baseline (d0).

(11 ± 2.2 sec, p = 0.003, n = 5) of NS neurons, 14 days after CCI (**Figures 4B–D,F**). Sham-operated animals showed a firing rate of 0.1 ± 0.03 spikes/s (p = 0.003, n = 5), a frequency of excitation of 10.7 ± 1.2 spikes/s (p = 0.003, n = 5), and a duration of excitation of 3.6 ± 0.9 s (p = 0.003, n = 5) (**Figures 4B–E**). A single injection of CA (0.25 mg/kg, i.p.) did not change any of these parameters in CCI mice. In particular, NS neurons showed a mean percentage of spontaneous activity of 102.9 ± 5% (p = 0.99), a frequency of excitation of 96.19 ± 8% (p = 0.85) and a duration of excitation of 108.12 ± 4% (p = 0.95) 30 min following CA injection (**Figures 4B–D**), a time at which CA-induced analgesia was substantial (**Figures 4B–D,G**). We therefore examined whether pharmacological manipulation of spinal mGlu4 or Ah receptor receptors could disclose an activity of systemic CA on spinal NS neurons of CCI mice. We topically applied either the group-III mGlu receptor antagonist, MSOP (100 μM), or the Ah receptor antagonist, CH223191 (30 nM) 10 min prior to systemic CA administration. Neither MSOP nor CH223191 showed any effect on the activity of NS neurons prior to CA injection. However, spinal application of MSOP significantly increased the mean percentage of firing rate (136 ± 12%, p = 0.0002, n = 5), frequency of excitation (128 ± 9%, p = 0.006, n = 5) and the duration of excitation (126 ± 6%, p = 0.0009, n = 5) in CCI mice starting from 20 min post-CA injection until the end of recording (60 min), as compared to CCI mice injected with CA alone (**Figures 4B–D,I**). Opposite results were obtained with CH223191, which significantly reduced the mean frequency of firing rate (66 ± 5%, p = 0.0004, n = 5), frequency of excitation (75 ± 5%, p = 0.0023, n = 5) and the duration of excitation (83 ± 4.5%, p = 0.004, n = 5) in CCI mice starting from 20 min post-CA injection (**Figures 4B–D,H**).

Electrophysiological Activity of the Rostral Ventromedial Medulla ON Cell in Wild-Type Chronic Constriction Injury Mice

In a separate experiment, we recorded the activity of ON cells in the RVM after acute systemic injection of CA in CCI mice. In sham-operated mice, the population of ON cells had a firing rate of 7.1 ± 0.4 spikes/s, a burst of excitation of 13.28 ± 0.64 spikes/s and a duration of excitation of 4 ± 0.37 s (n = 5) (**Figures 5A–C**). In CCI mice, the population of ON cells had a firing rate of 16 ± 2 spikes/s (p = 0.03, n = 5), a frequency of excitation of 26.2 ± 1.4 spikes/s (p = 0.005, n = 5) and a duration of excitation of 12 ± 2.4 s (p = 0.0021, n = 5) that were higher compared to sham mice (**Figures 5B–D**). Systemic injection of CA in CCI mice did not change the firing rate of ON cells (**Figure 5B**), but caused a trend to a decreased in the frequency (**Figure 5C**), and duration (**Figure 5D**) of excitation of ON cells. ON cell showed a mean frequency of spontaneous activity of 92.4 ± 3.59% (p = 0.0021, n = 5), a frequency of excitation of 83.99 ± 1.74% (p = 0.11, n = 5) and the duration of excitation of 80.93 ± 0.096% (p = 0.095, n = 5) of noxious-evoked activity of NS neurons. Recordings of RVM ON cell in CCI mice in which MSOP or CH223191 had been locally applied in the VL-PAG produced results similar to those observed after application of the two drugs in the spinal cord. In particular, intra-PAG microinjection of MSOP (100 uM), 10 min before CA, significantly increased the firing rate (114.67 ± 1.57%, p = 0.003, n = 5) and the frequency of excitation (165.45 ± 9.54%, p = 0.0022, n = 5), as compared to CCI mice injected with CA alone (**Figures 5A–C**), whereas only a slight and transient effect was observed on the duration of excitation (109.69 ± 0.1%, p = 0.049, n = 5) of ON cell in CCI mice (**Figures 5B–D**). In contrast, intra-PAG microinjection of CH223191 (30 nM), 10 min before CA, caused a significant reduction of all three

electrophysiological parameters of RVM ON cell in CCI mice (**Figures 5B–D**). In particular, ON cell showed a spontaneous activity of 82.69 ± 4% ($p = 0.038$, $n = 5$), a frequency of excitation of 55.57 ± 3.25% ($p = 0.044$, $n = 5$) and the duration of excitation of 54.43 ± 3.58% ($p = 0.041$, $n = 5$) in CCI mice starting from 25 to 30 min post-CA injection until the end of recording (60 min) as compared to CCI mice injected with CA alone (**Figures 5A–C**). Neither MSOP nor CH223191 caused any change in the activity of RVM ON cells by themselves (i.e., prior to CA administration) (**Figures 5B–D**). Spontaneous and noxious-evoked activity of a single ON cell in Sham mice (**Figure 5E**) or in CCI mice before and after treatment with vehicle (**Figure 5F**), CA (0.25 mg/Kg) (**Figure 5G**), CH223191+CA (**Figure 5H**), and MSOP+CA (**Figure 5I**) are represented by ratematers recordings.

Taken together these findings demonstrate that (i) acute CA administration causes analgesia in the CCI model of neuropathic pain; and, (ii) the effect of acute CA on the activity of nociceptive spinal neurons and RVM ON cells is disclosed by pharmacological blockade of group-III mGlu receptors or Ah receptors.

Effect of Repeated Administrations of Cinnabarinic Acid in the Chronic Constriction Injury Model of Neuropathic Pain

Mechanical Pain Thresholds in Wild-Type Chronic Constriction Injury Mice

Chronic constriction injury mice were treated daily for 7 days with (i) saline, i.p. + sesame oil, s.c.; (ii) CA (0.25 mg/kg), i.p. + sesame oil, s.c.; (iii) saline, i.p. + CH223191 (1 mg/kg), s.c.; or CA (0.25 mg/kg), i.p. + CH223191 (1 mg/kg), s.c., starting from 7 days after nerve ligation. We did not use MSOP in these experiments because the drug is not systemically active. We assessed mechanical pain threshold before ligation of the sciatic nerve, 1 day prior to the onset of drug treatments, and 1 h after the last administration (day 14 after nerve ligation). As opposed to what observed after a single injection, repeated CA injections did not cause analgesia in CCI mice (0.127 ± 0.062 g, $p = 0.89$) as compared to CCI mice treated with vehicle (0.08 ± 0.021 g) (**Figure 6**), suggesting the development of tolerance. However, the analgesic activity of CA was disclosed when the drug was combined with systemic CH223191 (0.419 ± 0.11 g), which was inactive on its own (0.058 ± 0.015 g) (**Figure 6**).

Electrophysiological Activity of Spinal Nociceptive Specific Neurons in Wild-Type Chronic Constriction Injury Mice

Repeated injections of CA or CH223191 alone did not affect the activity of spinal NS neurons in CCI mice. However, the combination of the two drugs was able to significantly attenuate CCI-induced spinal hyperexcitability. NS neurons of CCI mice treated with vehicle showed a spontaneous activity of 8.34 ± 1.39 spikes/s, a frequency of excitation of 35.92 ± 6.39 spikes/s and the duration of excitation of 15.52 ± 0.6 s (**Figures 7F–H**). In response to a combined treatment with CA and CH223191, NS neurons showed a spontaneous activity of 1.21 ± 0.63 spikes/s ($p < 0.0001$, $n = 5$), a frequency of excitation of 21.72 ± 0.76 spikes/s ($p = 0.09$, $n = 5$), and a duration of excitation of 8.18 ± 0.75 s ($p < 0.0001$, $n = 5$) (**Figures 7F–H**). NS neurons of mice treated with CA alone showed a spontaneous activity of 6.41 ± 0.6 spikes/s ($p = 0.36$, $n = 5$), a frequency of excitation of 32 ± 2.85 spikes/s ($p = 0.94$, $n = 5$) and the duration of excitation of 14.15 ± 1.33 s ($p = 0.76$, $n = 5$) (**Figures 7F–H**), whereas, NS neurons of CCI mice treated with CH223191 showed a spontaneous activity of 7.73 ± 1 spikes/s ($p = 0.98$, $n = 5$), a frequency of excitation of 32.26 ± 3.15 spikes/s ($p = 0.94$, $n = 5$), and a duration of excitation of 14.05 ± 0.71 s ($p = 0.65$, $n = 5$) (**Figures 7F–H**). Population data of NS neurons in Sham mice or in CCI mice before and after treatment with vehicle, CA (0.25 mg/Kg), CH 223191, CH223191+CA are represented in **Figures 7F,G**.

Electrophysiological Activity of Rostral Ventromedial Medulla ON Cells in Wild-Type Chronic Constriction Injury Mice

As opposed to data obtained in the spinal cord, repeated injections with CA significantly reduced the firing rate of ON cells (10.37 ± 0.71 spikes/s, $p = 0.0005$, $n = 5$) in the RVM of CCI mice (**Figures 7L–N**), as compared to vehicle-injected CCI mice (19.38 ± 3.66 spikes/s, $n = 5$) (**Figures 7I,J**). No differences were observed neither in the frequency nor in the duration of excitation between CCI mice treated with vehicle (40.67 ± 8.49 spikes/s for frequency and 16.08 ± 2.80 s for duration of excitation, respectively) or with CA (35.66 ± 1.24 spikes/s for frequency, $p = 0.90$ and 13.11 ± 1.19 s, for duration of excitation, $p = 0.56$) (**Figures 7K–M**). Repeated injections of CH223191 alone did not change any of these parameters (17.03 ± 1.47 spikes/s, 46.66 ± 6 spikes/s, and 16.86 ± 1.18 s) (**Figures 7K–M**). In contrast, the combined treatment with CA and CH223191 markedly reduced the firing rate (2.15 ± 0.23 spikes/s, $p < 0.0001$) and the frequency (13.16 ± 0.49 spikes/s, $p < 0.0001$) and duration (19.86 ± 1.18 s, $p = 0.038$) of excitation of RVM ON cells in CCI mice (**Figures 7K–M**). In Sham mice treated with vehicle, ON cell showed a spontaneous activity of 19.38 ± 3.66 spikes/s ($p = 0.0005$, $n = 5$), a frequency of excitation of 40.67 ± 8.49 spikes/s ($p = 0.90$, $n = 5$) and a duration of excitation of 16.08 ± 2.80 spikes/s ($p < 0.0001$, $n = 5$). Population data of ON cell in Sham mice or in CCI mice before and after treatment with vehicle, CA (0.25 mg/Kg), CH 223191, CH223191+CA are represented in **Figures 7N–P**.

Taken together, these findings demonstrate that (i) repeated CA injections fail to cause analgesia in the CCI model of neuropathic pain unless combined with pharmacological blockade of Ah receptors; and (ii) this combination causes a large reduction in the activity of nociceptive spinal cord neurons and ON RVM cells.

DISCUSSION

We moved from the evidence that the mGlu4 receptor, one of the putative CA receptor target (Fazio et al., 2012), has been found

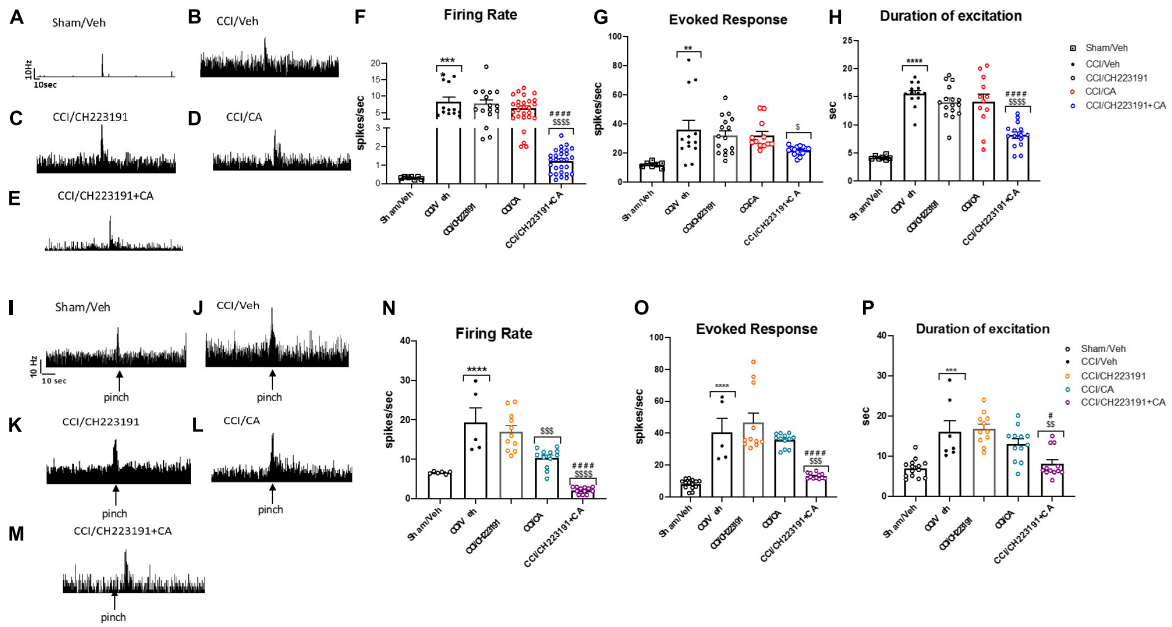

FIGURE 7 | Spinal NS neurons and RVM ON cell hyperexcitability is significantly attenuated by repeated administration of CA in combination with CH223191, in WT CCI mice. **(A–E)** Representative ratemeters showing spontaneous and noxious-evoked activity of spinal NS neurons in Sham mice **(A)** or in CCI mice before and after treatment with vehicle **(B)**, CH223191 **(C)**, CA (0.25 mg/Kg) **(D)**, CH223191+CA (E). **(F–H)** Mean ± S.E.M population data of systemic repeated administrations of CH223191 (1 mg/Kg) in presence of cinnabarinic acid (CA, 0.25 mg/Kg) on firing rate **(F)**, evoked response **(G)** and duration of excitation **(H)** of spinal NS neurons, in CCI mice **(I–M)** representative ratemeters showing spontaneous and noxious-evoked activity of RVM ON cell in Sham mice **(I)** or in CCI mice before and after treatment with vehicle **(J)**, CH223191 **(K)**, CA (0.25 mg/Kg) **(L)**, CH223191+CA **(M)**. **(N–P)** Mean ± S.E.M population data of systemic repeated administrations of CH223191 (1 mg/Kg) in presence of cinnabarinic acid (CA, 0.25 mg/Kg) on firing rate **(N)**, evoked response **(O)** and duration of excitation **(P)** of RVM ON cell, in CCI mice. Each point represents the mean of five different mice per group (one neuron recorded per each mouse). $^{**}p < 0.01$, $^{***}p < 0.001$ and $^{****}p < 0.0001$ indicate statistically significant difference vs. Sham/Veh, $^{\$}p < 0.05$, $^{\$\$}p < 0.01$, $^{\$\$\$}p < 0.001$ and $^{\$\$\$\$}p < 0.0001$ indicate statistically significant difference vs. CCI/CH223191, $^{\#}p < 0.05$ and $^{\#\#\#\#}p < 0.0001$ indicate statistically significant difference vs. CCI/CA. One-way ANOVA followed by Tukey's *post-hoc* test for multiple comparisons was used.

to be involved in the pathophysiology of tonic and chronic pain in several regions of the pain neuraxis (Vilar et al., 2013; Zussy et al., 2018). Here, we have shown for the first time that CA causes analgesia in the formalin model of inflammatory pain, and in the CCI model of neuropathic pain. Different doses of CA were tested in the formalin test, and we were surprised to find that the compound caused analgesia at doses of 0.125 and 0.25 mg/kg, but not at higher doses. This is unusual for a kynurenine metabolite, because most of the kynurenines are behaviourally active at doses >10 mg/kg (Lapin, 1998; Fazio et al., 2015; Varga et al., 2015). CA displayed also a great potency in behavioural models predictive of antipsychotic-like activity in which, however, the compound retained its action at doses of 0.5, 1, and 5 mg/kg (Ulivieri et al., 2020). It is possible that doses of CA > 0.25 mg/kg cause a rapid desensitization of the receptor(s) responsible for CA-induced analgesia, or, alternatively, recruit additional targets that counterbalance the analgesic activity. CA can also activate the aryl hydrocarbon receptor (Ah receptor), an intracellular receptor, which is known to translocate into the nucleus and regulate gene expression in response to agonist activation (Joshi et al., 2017). For example, CA can enhance IL-22 production in human T cells by activating Ah receptor (Godefroy et al., 1990). CA-induced analgesia in the formalin test was abrogated in mGlu4 knockout mice, but was unaffected by treatment with the Ah receptor antagonist, CH223191. Thus, it appear that CA-induced analgesia in the second phase of the formalin test was mediated by activation of mGlu4 receptors, but did not involve the Ah receptor. It is intriguing that CA shows a lower potency than glutamate in activating mGlu4 receptors (Fazio et al., 2012), and that low doses of CA caused analgesia in spite of the competition with synaptically released glutamate. One possibility is that CA is not cleared from the synapse as efficiently as glutamate, and activation of mGlu4 receptors by CA is long-lasting. This might reinforce the ability of presynaptic mGlu4 receptors to restrain the release of glutamate and other neurotransmitters/neuropeptides involved in pain transmission.

We examined in more detail the action of CA in the CCI model of neuropathic pain, in which nociceptive sensitization reflects maladaptive changes in synaptic plasticity different stations of the pain neuraxis associated with neuroinflammation mediated by astrocytes and microglia in the spinal cord (Li et al., 2016; Dubovı et al., 2018; Shu et al., 2020). We could confirm the analgesic activity of acute CA injection CCI model. To further strengthen the behavioural data, we also measured the ongoing and evoked activity of (i) nociceptive specific neurons (NS) in the spinal cord, and (ii) RVM ON following PAG stimulation. Interestingly, CA injection did not change the activity of nociceptive neurons in the spinal cord, but reduced the duration of excitation of RVM ON cells. Thus, it is likely

that CA acted in the RVM and perhaps in other supraspinal regions to enhance mechanical thresholds in the CCI model. The RVM is a key region in the top-down regulation of pain, and inhibition of RVM ON cells fits nicely with the analgesic activity of CA. Interestingly, however, an action of CA in the spinal cord was disclosed by local application of MSOP or CH223191, which were inactive on their own, but respectively enhanced and reduced the activity of spinal neurons when combined with systemic CA. MSOP is a non-selective antagonist of mGlu4, - 6-, -7, and -8 receptors (Nicoletti et al., 2011), however the interaction with CA likely involves the mGlu4 receptor because CA has no activity at mGlu6, -7 or -8 receptors (Fazio et al., 2012). The effects of MSOP and CH223191 in the spinal cord suggest that the two receptors (mGlu4 and Ah receptor) recruited by CA have opposite function in pain control, and a suppressive activity of CA on nociceptive neurons can only be unmasked if the Ah receptor is pharmacologically inhibited. A similar scenario was seen in the PAG/RVM, where CA largely reduced all parameters of ON cell activity when Ah receptor was blocked by application of CH223191 in the PAG.

As opposed to the acute treatment, repeated injections of CA did not affect pain thresholds in the CCI model, suggesting the development of tolerance. Mechanisms of pharmacokinetic tolerance, pharmacodynamics tolerance, or pseudo-tolerance may account for the loss of analgesia in response to repeated injections of CA. In mice injected i.p. with 0.25 mg/kg CA, serum CA levels peak after 15 min, are largely reduced at 60 min, and returned back to normal values at 120 min, whereas levels in the cerebral cortex and cerebellum remain high for at least 12 h (Ulivieri et al., 2020). An accurate PK analysis is needed to establish whether CA exposure decreases in response to repeated injections. Interestingly, CA-induced analgesia was unmasked when the AhR antagonist, CH223191, was co-injected with CA for 7 days. This was paralleled by the activity of nociceptive spinal neurons and RVM ON cells, which was largely reduced in CCI mice treated with CA *plus* CH223191, although CA alone significantly reduced the firing rate of RVM ON cells. A possible explanation is that the Ah receptor is up-regulated in the pain neuraxis in response to CA administration, or, alternatively, that the "analgesic" mGlu4 receptor is down-regulated. This hypotheses warrant further investigation. Finally, we cannot exclude that CA accumulating in brain tissue as a result of repeated injections reaches the threshold to recruit additional targets that counteract CA-induced analgesia. The existence of these targets has been hypothesized (Fazio et al., 2012), but their identity is unknown.

Taken together these data show for the first time that the trace kynurenine, CA, causes analgesia through a mechanism mediated, at least in part, by the activation of mGlu4 receptors. The high potency of CA in reducing nocifensive behaviour in the formalin test or enhancing mechanical thresholds in the CCI model suggests that the small amounts of CA endogenously produced by the kynurenine pathway of tryptophan metabolism may act physiologically to regulate pain transmission. The translational value of our findings for pain treatment in humans is limited because of the lack of analgesia with increasing doses of CA and the development of tolerance in response to repeated administrations. However, it will be interesting to examine whether changes in endogenous CA levels, which are detectable in the peripheral blood, are associated with inter-individual variability in pain sensitivity. Because activation of the kynurenine pathway is one of the putative communication systems in the gut-brain axis (Dehhaghi et al., 2019; Roth et al., 2021), the evidence that CA modulates pain transmission may provide a novel link between the gut microbiota and inflammatory or neuropathic pain.

PERSPECTIVES

Studying the role of the endogenous metabolite cinnabarinic acid, in the pain pathways as a new neurotransmitter of the central nervous system can lay the foundations for new therapies in the treatment of painful pathologies, as well as increase the available knowledge about new pain-related endogenous processes.

DATA AVAILABILITY STATEMENT

The raw data supporting the conclusions of this article will be made available by the authors, without undue reservation.

ETHICS STATEMENT

The animal study was reviewed and approved by Italian Ministry of Health 5015/2021-PR.

AUTHOR CONTRIBUTIONS

FN, SM, LL, GB, and VB: conceptualization and writing. SN, SB, NA, FR, GM, FF, MS, PS, and FL: experiments, data analysis, and writing. All authors contributed to the article and approved the submitted version.

REFERENCES

Bennett, G. J., and Xie, Y. K. (1988). A peripheral mononeuropathy in rat that produces disorders of pain sensation like those seen in man. *Pain* 33, 87–107. doi: 10.1016/0304-3959(88)90209-6

Berrino, L., Oliva, P., Rossi, F., Palazzo, E., Nobili, B., and Maione, S. (2001). Interaction between metabotropic and NMDA glutamate receptors in the periaqueductal grey pain modulatory system. *Naunyn Schmiedeberg's Arch. Pharmacol.* 364, 437–443. doi: 10.1007/s0021001 00477

Boccella, S., Vacca, V., Errico, F., Marinelli, S., Squillace, M., Guida, F., et al. (2015). D-aspartate modulates nociceptive-specific neuron activity and pain threshold in inflammatory and neuropathic pain condition in mice. *BioMed Res. Int.* 2015:905906. doi: 10.1155/2015/905906

Ciapała, K., Mika, J., and Rojewska, E. (2021). The kynurenine pathway as a potential target for neuropathic pain therapy design: from basic research

to clinical perspectives. *Int. J. Mol. Sci.* 22:11055. doi: 10.3390/ijms222011055

Coderre, T. J., and Melzack, R. (1992). The contribution of excitatory amino acids to central sensitization and persistent nociception after formalin-induced tissue injury. *J. Neurosci.* 12, 3665–3670. doi: 10.1523/JNEUROSCI.12-09-03665.1992

Dehhaghi, M., Kazemi Shariat Panahi, H., and Guillemin, G. J. (2019). Microorganisms, tryptophan metabolism, and kynurenine pathway: a complex interconnected loop influencing human health status. *Int. J. Trypt. Res. IJTR* 12:1178646919852996. doi: 10.1177/1178646919852996

Drew, G. M., and Vaughan, C. W. (2004). Multiple metabotropic glutamate receptor subtypes modulate GAB aergic neurotransmission in rat periaqueductal grey neurons in vitro. *Neuropharmacology* 46, 927–934. doi: 10.1016/j.neuropharm.2004.01.015

Dubovı, P., Klusáková, I., Hradilová-Svíženská, I., Joukal, M., and Boadas-Vaello, P. (2018). Activation of astrocytes and microglial cells and CCL2/CCR2 upregulation in the dorsolateral and ventrolateral nuclei of periaqueductal gray and rostral ventromedial medulla following different types of sciatic nerve injury. *Front. Cell. Neurosci.* 12:40. doi: 10.3389/fncel.2018.00040

Faul, F., Erdfelder, E., Lang, A., and Buchner, A. (2007). G*Power 3: a flexible statistical power analysis program for the social, behavioral, and biomedical sciences. *Behav. Res. Methods* 39, 175–191. doi: 10.1098/rstb.1976.0044

Fazio, F., Lionetto, L., Curto, M., Iacovelli, L., Cavallari, M., Zappulla, C., et al. (2015). Xanthurenic acid activates mGlu2/3 metabotropic glutamate receptors and is a potential trait marker for schizophrenia. *Sci. Rep.* 5:17799. doi: 10.1038/srep17799

Fazio, F., Lionetto, L., Curto, M., Iacovelli, L., Copeland, C. S., Neale, S. A., et al. (2017). Cinnabarinic acid and xanthurenic acid: two kynurenine metabolites that interact with metabotropic glutamate receptors. *Neuropharmacology* 112(Pt. B), 365–372. doi: 10.1016/j.neuropharm.2016.06.020

Fazio, F., Lionetto, L., Molinaro, G., Bertrand, H. O., Acher, F., Ngomba, R. T., et al. (2012). Cinnabarinic acid, an endogenous metabolite of the kynurenine pathway, activates type 4 metabotropic glutamate receptors. *Mol. Pharmacol.* 81, 643–656. doi: 10.1124/mol.111.074765

Fields, H. L., Bry, J., Hentall, I., and Zorman, G. (1983). The activity of neurons in the rostral medulla of the rat during withdrawal from noxious heat. *J. Neurosci.* 3, 2545–2552. doi: 10.1523/JNEUROSCI.03-12-02545.1983

Godefroy, F., Matson, W. R., Gamache, P. H., and Weil-Fugazza, J. (1990). Simultaneous measurements of tryptophan and its metabolites, kynurenine and serotonin, in the superficial layers of the spinal dorsal horn. study in normal and arthritic rats. *Brain Res.* 526, 169–172. doi: 10.1016/0006-8993(90)90267-f

Goudet, C., Magnaghi, V., Landry, M., Nagy, F., Gereau, R. W., and Pin, J. P. (2009). Metabotropic receptors for glutamate and GABA in pain. *Brain Res. Rev.* 60, 43–56. doi: 10.1016/j.brainresrev.2008.12.007

Heyliger, S. O., Goodman, C. B., Ngong, J. M., and Soliman, K. F. (1998). The analgesic effects of tryptophan and its metabolites in the rat. *Pharmacol. Res.* 38, 243–250. doi: 10.1006/phrs.1998.0362

Joshi, A. D., Hossain, E., and Elferink, C. J. (2017). Epigenetic regulation by agonist-specific aryl hydrocarbon receptor recruitment of metastasis-associated protein 2 selectively induces stanniocalcin 2 expression. *Mol. Pharmacol.* 92, 366–374. doi: 10.1124/mol.117.108878

Lapin, I. P. (1998). Antagonism of kynurenic acid to anxiogens in mice. *Life Sci.* 63, L231–L236. doi: 10.1016/s0024-3205(98)00404-4

Laumet, G., Zhou, W., Dantzer, R., Edralin, J. D., Huo, X., Budac, D. P., et al. (2017). Upregulation of neuronal kynurenine 3-monooxygenase mediates depression-like behavior in a mouse model of neuropathic pain. *Brain Behav. Immun.* 66, 94–102. doi: 10.1016/j.bbi.2017.07.008

Li, X. Y., Wan, Y., Tang, S. J., Guan, Y., Wei, F., and Ma, D. (2016). Maladaptive plasticity and neuropathic pain. *Neural Plasticity* 2016:4842159. doi: 10.1155/2016/4842159

Lowe, M. M., Mold, J. E., Kanwar, B., Huang, Y., Louie, A., Pollastri, M. P., et al. (2014). Identification of cinnabarinic acid as a novel endogenous aryl hydrocarbon receptor ligand that drives IL-22 production. *PLoS One* 9:e87877. doi: 10.1371/journal.pone.0087877

Maione, S., Palazzo, E., de Novellis, V., Stella, L., Leyva, J., and Rossi, F. (1998). Metabotropic glutamate receptors modulate serotonin release in the rat periaqueductal gray matter. *Naunyn Schmiedeberg's Arch. Pharmacol.* 358, 411–417. doi: 10.1007/pl00005272

Marabese, I., de Novellis, V., Palazzo, E., Scafuro, M. A., Vita, D., Rossi, F., et al. (2007a). Effects of (S)-3,4-DCPG, an mGlu8 receptor agonist, on inflammatory and neuropathic pain in mice. *Neuropharmacology* 52, 253–262. doi: 10.1016/j.neuropharm.2006.04.006

Marabese, I., Rossi, F., Palazzo, E., de Novellis, V., Starowicz, K., Cristino, L., et al. (2007b). Periaqueductal gray metabotropic glutamate receptor subtype 7 and 8 mediate opposite effects on amino acid release, rostral ventromedial medulla cell activities, and thermal nociception. *J. Neurophysiol.* 98, 43–53. doi: 10.1152/jn.00356.2007

Moreau, J. L., and Fields, H. L. (1986). Evidence for GABA involvement in midbrain control of medullary neurons that modulate nociceptive transmission. *Brain Res.* 397, 37–46. doi: 10.1016/0006-8993(86)91367-3

Németh, H., Toldi, J., and Vécsei, L. (2005). Role of kynurenines in the central and peripheral nervous systems. *Curr. Neuro. Res.* 2, 249–260. doi: 10.2174/1567202054368326

Nicoletti, F., Bockaert, J., Collingridge, G. L., Conn, P. J., Ferraguti, F., Schoepp, D. D., et al. (2011). Metabotropic glutamate receptors: from the workbench to the bedside. *Neuropharmacology* 60, 1017–1041. doi: 10.1016/j.neuropharm.2010.10.022

Ohishi, H., Akazawa, C., Shigemoto, R., Nakanishi, S., and Mizuno, N. (1995). Distributions of the mRNAs for L-2-amino-4-phosphonobutyrate-sensitive metabotropic glutamate receptors, mGluR4 and mGluR7, in the rat brain. *J. Comparat. Neurol.* 360, 555–570. doi: 10.1002/cne.903600402

Palazzo, E., Marabese, I., de Novellis, V., Oliva, P., and Rossi, F. (2001). Metabotropic and NMDA glutamate receptors participate in the cannabinoid-induced antinociception. *Neuropharmacology* 40, 319–326. doi: 10.1016/s0028-3908(00)00160-x

Paxinos, G., and Franklin, K. B. J. (2001). *The Mouse Brain in Stereotaxic Coordinates*. San Diego, CA: Academic Press.

Pereira, V., and Goudet, C. (2019). Emerging trends in pain modulation by metabotropic glutamate receptors. *Front. Mol. Neurosci.* 11:464. doi: 10.3389/fnmol.2018.00464

Roth, W., Zadeh, K., Vekariya, R., Ge, Y., and Mohamadzadeh, M. (2021). Tryptophan metabolism and gut-brain homeostasis. *Int. J. Mol. Sci.* 22:2973. doi: 10.3390/ijms22062973

Sandkühler, J., and Gebhart, G. F. (1984). Relative contributions of the nucleus raphe magnus and adjacent medullary reticular formation to the inhibition by stimulation in the periaqueductal gray of a spinal nociceptive reflex in the pentobarbital-anesthetized rat. *Brain Res.* 305, 77–87. doi: 10.1016/0006-8993(84)91121-1

Schwarcz, R., Bruno, J. P., Muchowski, P. J., and Wu, H. Q. (2012). Kynurenines in the mammalian brain: when physiology meets pathology. *Nat. Rev. Neurosci.* 13, 465–477. doi: 10.1038/nrn3257

Shu, B., He, S. Q., and Guan, Y. (2020). Spinal cord stimulation enhances microglial activation in the spinal cord of nerve-injured rats. *Neurosci. Bull.* 36, 1441–1453. doi: 10.1007/s12264-020-00568-6

Stone, T. W. (1993). Neuropharmacology of quinolinic and kynurenic acids. *Pharmacol. Rev.* 45, 309–379.

Tjølsen, A., Berge, O. G., Hunskaar, S., Rosland, J. H., and Hole, K. (1992). The formalin test: an evaluation of the method. *Pain* 51, 5–17. doi: 10.1016/0304-3959(92)90003-T

Ulivieri, M., Wierońska, J. M., Lionetto, L., Martinello, K., Cieslik, P., and Chocyk, A. (2020). The trace kynurenine, cinnabarinic acid, displays potent antipsychotic-like activity in mice and its levels are reduced in the prefrontal cortex of individuals affected by schizophrenia. *Schizophrenia Bull.* 46, 1471–1481. doi: 10.1093/schbul/sbaa074

Varga, D., Herédi, J., Kánvási, Z., Ruszka, M., Kis, Z., Ono, E., et al. (2015). Systemic L-kynurenine sulfate administration disrupts object recognition memory, alters open field behavior and decreases c-fos immunopositivity

in C57Bl/6 mice. *Front. Behav. Neurosci.* 9:157. doi: 10.3389/fnbeh.2015.00157

Vilar, B., Busserolles, J., Ling, B., Laffray, S., Ulmann, L., Malhaire, F., et al. (2013). Alleviating pain hypersensitivity through activation of type 4 metabotropic glutamate receptor. *J. Neurosci.* 33, 18951–18965. doi: 10.1523/JNEUROSCI.1221-13.2013

Zussy, C., Gómez-Santacana, X., Rovira, X., De Bundel, D., Ferrazzo, S., Bosch, D., et al. (2018). Dynamic modulation of inflammatory pain-related affective and sensory symptoms by optical control of amygdala metabotropic glutamate receptor 4. *Mol. Psychiatry* 23, 509–520. doi: 10.1038/mp.2016.223

Conflict of Interest: The authors declare that the research was conducted in the absence of any commercial or financial relationships that could be construed as a potential conflict of interest.

Publisher's Note: All claims expressed in this article are solely those of the authors and do not necessarily represent those of their affiliated organizations, or those of the publisher, the editors and the reviewers. Any product that may be evaluated in this article, or claim that may be made by its manufacturer, is not guaranteed or endorsed by the publisher.

frontiers | Frontiers in Molecular Neuroscience

ORIGINAL RESEARCH
published: 03 June 2022
doi: 10.3389/fnmol.2022.928587

Sex Differences in CGRP Regulation and Function in the Amygdala in a Rat Model of Neuropathic Pain

Peyton Presto[1] *and Volker Neugebauer*[1,2,3]*

[1]Department of Pharmacology and Neuroscience, Texas Tech University Health Sciences Center, Lubbock, TX, United States, [2]Center of Excellence for Translational Neuroscience and Therapeutics, Texas Tech University Health Sciences Center, Lubbock, TX, United States, [3]Garrison Institute on Aging, Texas Tech University Health Sciences Center, Lubbock, TX, United States

The amygdala has emerged as a key player in the emotional response to pain and pain modulation. The lateral and capsular regions of the central nucleus of the amygdala (CeA) represent the "nociceptive amygdala" due to their high content of neurons that process pain-related information. These CeA divisions are the targets of the spino-parabrachio-amygdaloid pain pathway, which is the predominant source of calcitonin gene-related peptide (CGRP) within the amygdala. Changes in lateral and capsular CeA neurons have previously been observed in pain models, and synaptic plasticity in these areas has been linked to pain-related behavior. CGRP has been demonstrated to play an important role in peripheral and spinal mechanisms, and in pain-related amygdala plasticity in male rats in an acute arthritis pain model. However, the role of CGRP in chronic neuropathic pain-related amygdala function and behaviors remains to be determined for both male and female rats. Here we tested the hypothesis that the CGRP1 receptor is involved in neuropathic pain-related amygdala activity, and that blockade of this receptor can inhibit neuropathic pain behaviors in both sexes. CGRP mRNA expression levels in the CeA of male rats were upregulated at the acute stage of the spinal nerve ligation (SNL) model of neuropathic pain, whereas female rats had significantly higher CGRP and CGRP receptor component expression at the chronic stage. A CGRP1 receptor antagonist (CGRP 8-37) administered into the CeA in chronic neuropathic rats reduced mechanical hypersensitivity (von Frey and paw compression tests) in both sexes but showed female-predominant effects on emotional-affective responses (ultrasonic vocalizations) and anxiety-like behaviors (open field test). CGRP 8-37 inhibited the activity of CeA output neurons assessed with calcium imaging in brain slices from chronic neuropathic pain rats. Together, these findings may suggest that CGRP1 receptors in the CeA are involved in neuropathic pain-related amygdala activity and contribute to sensory aspects in both sexes but to emotional-affective pain responses predominantly in females. The sexually dimorphic function of CGRP in the amygdala would make CGRP1 receptors a potential therapeutic target for neuropathic pain relief, particularly in females in chronic pain conditions.

Keywords: amygdala, CGRP, sex differences, plasticity, behavior, neuropathic pain (NP)

OPEN ACCESS

Edited by:
Fabien Marchand, INSERM U1107 Douleur et Biophysique Neurosensorielle (Neuro-Dol), France

Reviewed by:
Yuan-Xiang Tao, Rutgers, The State University of New Jersey, United States
Livio Luongo, University of Campania Luigi Vanvitelli, Italy

***Correspondence:**
Volker Neugebauer
volker.neugebauer@ttuhsc.edu

Specialty section:
This article was submitted to Pain Mechanisms and Modulators, a section of the journal Frontiers in Molecular Neuroscience

Received: *25 April 2022*
Accepted: *12 May 2022*
Published: *03 June 2022*

Citation:
Presto P and Neugebauer V (2022) Sex Differences in CGRP Regulation and Function in the Amygdala in a Rat Model of Neuropathic Pain. Front. Mol. Neurosci. 15:928587. doi: 10.3389/fnmol.2022.928587

INTRODUCTION

Interactions between sensory, emotional-affective, and cognitive dimensions comprise the highly complex, intense pain experience. The intricate interplay of each of these pain components presents a challenge to identifying effective therapeutic strategies for chronic pain relief, as many therapeutic options are associated with variable efficacy and undesirable side effects (Attal, 2019; Bates et al., 2019). One barrier to the discovery of effective treatment options is the lack of full understanding of mechanisms and targets that are involved in a chronic pain state, particularly with regard to potential sex differences. It is estimated that chronic pain impacts 20% of the global population each year (Breivik et al., 2013; Fayaz et al., 2016; Dahlhamer et al., 2018), with females greatly outnumbering males as chronic pain patients (Ruau et al., 2012). However, many currently available analgesics have limited effectiveness in female patients due to the targeting of male-specific pain processing mechanisms (Mogil, 2020; Shansky and Murphy, 2021). Therefore, there is an urgent need to identify sex-specific targets that can lead to the development of improved therapeutic options for pain treatment in male and female patients.

The amygdala is a limbic brain structure that has been revealed to play a critical role in the emotional-affective dimension of pain and pain modulation (Veinante et al., 2013; Neugebauer, 2015, 2020; Neugebauer et al., 2020). The amygdala attaches emotional significance to sensory information from various pain states (Neugebauer et al., 2004; Thompson and Neugebauer, 2017) and connects to descending pain modulatory system structures and other nervous system structures involved in behavioral, emotional, and cognitive functions (Becker and Carrasquillo, 2019; Hua et al., 2020; Liu et al., 2021; Weera et al., 2021). The amygdala is comprised of functionally and anatomically distinct nuclei. The central nucleus of the amygdala (CeA) serves as the primary amygdala output center, and its lateral and capsular divisions receive nociceptive information through the spino-parabrachio-amygdaloid pain pathway (Gauriau and Bernard, 2002; Thompson and Neugebauer, 2017; Kato et al., 2018; Neugebauer, 2020). As neurons in the lateral and capsular regions predominately respond to noxious stimuli (Bernard et al., 1992; Neugebauer and Weidong, 2002), these divisions are often said to comprise the "nociceptive amygdala" (Neugebauer et al., 2004).

Calcitonin gene-related peptide (CGRP) is a 37 amino acid peptide that binds to the G-protein-coupled CGRP1 receptor to activate adenylyl cyclase and protein kinase A (PKA; Russo, 2015). The CGRP1 receptor is composed of three predominant subunits: the seven-transmembrane calcitonin-like receptor (CLR) protein; a receptor activity modifying protein (Ramp1), which is critical for the specificity of CGRP binding and cell surface receptor expression; and the CGRP receptor component protein (RCP), which facilitates coupling to cAMP signaling (Poyner et al., 2002; Barwell et al., 2013; Dickerson, 2013; Russo, 2015; Iyengar et al., 2017; Neugebauer et al., 2020). In the amygdala, CGRP serves as an important molecular marker of the lateral and capsular regions of the CeA due to the CGRP-immunoreactive terminals of fibers from the lateral parabrachial nucleus that synapse in these areas (Kruger et al., 1988; Shimada et al., 1989; Dobolyi et al., 2005; D'Hanis et al., 2007; Palmiter, 2018). CGRP modulates synaptic input from the parabrachial nucleus to the CeA (Han et al., 2005, 2015; Okutsu et al., 2017; Shinohara et al., 2017) and plays a critical role in synaptic plasticity in the CeA in an arthritis pain model (Han et al., 2005). CeA cell types targeted by CGRP input from the parabrachial area include neurons expressing protein kinase C delta or corticotropin releasing factor (CRF; Neugebauer et al., 2020). We have previously shown that the administration of a selective CGRP1 receptor antagonist (CGRP 8-37) into the CeA can inhibit pain behaviors in an acute arthritis model (Han et al., 2005), suggesting that CGRP-mediated mechanisms may influence pain-related amygdala function. However, the role of CGRP in CeA pain mechanisms and sex differences in a chronic neuropathic pain state remains to be determined.

The purpose of this study was to examine the role of CGRP in neuropathic pain-related CeA function and behaviors with regard to sex and stage of neuropathic pain development. We characterized mRNA expression profiles of CGRP and CGRP1 receptor components in adult male and female rats at the acute and chronic phases of the rat spinal nerve ligation (SNL) model of neuropathic pain. We also subjected adult male and female neuropathic rats to behavioral tests before and after the blockade of the CGRP1 receptor in the CeA, and we examined the effects of this blockade on CeA-CRF neuronal cell activity. Our previous work implicated CeA-CRF neurons in pain modulation (Mazzitelli et al., 2021, 2022). Our findings point to a previously unexplored, sexually dimorphic role of CGRP in neuropathic pain-related processing within the CeA.

MATERIALS AND METHODS

Animals

Adult male and female Sprague-Dawley rats (150–300 g, 12 weeks of age at time of testing) were group-housed in a temperature-controlled room under a 12 h day/night cycle with unrestricted access to food and water. On each experimental day, rats were transferred from the animal facility and allowed to acclimate to the laboratory for at least 1 h prior to testing. All experimental procedures were approved by the Institutional Animal Care and Use Committee (IACUC, protocol #14006) of Texas Tech University Health Sciences Center (TTUHSC) and conformed to the guidelines of the International Association for the Study of Pain (IASP) and of the National Institutes of Health (NIH).

Experimental Protocol

mRNA expression levels of CGRP and two of the CGRP1 receptor components, CLR and Ramp1, were measured (see Section "qRT-PCR") in the right CeA of rats in the acute and chronic phases of neuropathic pain (see Section "Neuropathic Pain Model"). The effects of the selective CGRP1 receptor peptide antagonist (CGRP 8-37) compared to artificial cerebrospinal fluid (ACSF) vehicle control were tested in chronic neuropathic rats in behavioral (see Section "Behaviors") and multiphoton calcium imaging (see Section

"Calcium Imaging") experiments. For behavioral experiments, a guide cannula was implanted (see Section "Drug Application in Awake Animals") 1 week before stereotaxic drug application into the CeA by microdialysis. Behavioral assays were performed at 20 min during continued drug (or vehicle) administration. For calcium imaging experiments, CGRP 8-37 or ACSF was applied directly to the brain slice *via* gravity-driven superfusion. The right CeA was targeted in all molecular, behavioral, and calcium imaging experiments, as evidence suggests right-hemispheric lateralization of pain processing and modulation (Carrasquillo and Gereau IV, 2008; Ji and Neugebauer, 2009; Gonçalves and Dickenson, 2012; Simons et al., 2014; Nation et al., 2018; Phelps et al., 2019; Allen et al., 2021).

Neuropathic Pain Model

The well-established spinal nerve ligation (SNL) model of neuropathic pain (Ho Kim and Mo Chung, 1992) was used to create a stable and long-lasting peripheral neuropathy. Rats were anesthetized with isoflurane (2%–3%; precision vaporizer, Harvard Apparatus, Holliston, MA, USA) and underwent surgery in which the left L5 spinal nerve was exposed and tightly ligated using 6–0 sterile silk. In the sham-operated control group, the spinal nerve was exposed but not ligated.

qRT-PCR

At either the acute phase (1 week post-SNL) or chronic phase (4 weeks post-SNL) of neuropathic pain (see Section "Neuropathic Pain Model"), rats were euthanized by decapitation. Brains were rapidly extracted and oxygenated in ice-cold sucrose-based physiological solution (87 NaCl, 75 sucrose, 25 glucose, 5 KCl, 21 $MgCl_2$, 0.5 $CaCl_2$, and 1.25 NaH_2PO_4). Coronal brain slices (1,000 μm) containing the CeA were prepared using a Vibratome (VT1200S, Leica Biosystems, Nussloch, Germany) as described previously (Thompson et al., 2018; Navratilova et al., 2019; Hein et al., 2021; Mazzitelli et al., 2021). The right CeA was dissected from freshly harvested slices for mRNA analysis. RNA was extracted using the MagMAX-96 Total RNA Isolation Kit (Life Technologies, Carlsbad, CA, USA) and quantified on a NanoDrop 8000 spectrophotometer (Thermo Fisher Scientific, Rockford, IL, USA). Total RNA was reverse transcribed using the High-Capacity cDNA Reverse Transcription Kit with RNase Inhibitor (Thermo Fisher Scientific), and then Taqman Fast Advanced Master Mix (Thermo Fisher Scientific) was used to perform quantitative reverse transcription polymerase chain reactions (qRT-PCR). Applied Biosystems Taqman Gene Expression Assays included (CGRP; *Calca*; Rn01511353_g1), CLR (*Calcrl*; Rn00562334_m1), Ramp1 (*Ramp1*; Rn01427056_m1), β-actin (*Actb*; Rn00667869_m1), Rpl3 (*Rpl3*; Rn01505100_g1), and Rpl29 (*Rpl29*; Rn00820801_g1). Reactions containing 5 ng of cDNA were performed in triplicate using the CFX384 Real-Time System (BioRad, Hercules, CA, USA). Relative expression was determined using the $2^{-\Delta\Delta Ct}$ method with samples normalized to the geometric mean of β-actin, Rpl3, and Rpl29, as this normalization strategy utilized the three genes with the most stable expression in a rat neuropathic pain model (Wan et al., 2010).

Drug Application in Awake Animals

Stereotaxic drug administration into the CeA by microdialysis was performed 4 weeks after SNL surgery as described before (Kiritoshi et al., 2016; Kim et al., 2017; Thompson et al., 2018; Mazzitelli and Neugebauer, 2019; Hein et al., 2021). Rats were anesthetized with isoflurane (2%–3%; precision vaporizer, Harvard Apparatus) and a small unilateral craniotomy was performed. Using a stereotaxic apparatus (David Kopf Instruments, Tujunga, CA, USA), a guide cannula (CMA/Microdialysis, Solna, Sweden) was inserted into the CeA using the following coordinates (Paxinos and Watson, 1998): 2.5 mm caudal to the bregma, 4.0 mm lateral to the midline, and 7.5 mm deep. The cannula was fixed to the skull using dental acrylic (Plastic One, Roanoke, VA, USA), and local anesthetic (Lidocaine) and antibiotic ointment (Bacitracin) were applied to reduce inflammation and prevent infection. Rats were allowed to recover from cannula implantation for 1 week prior to experimental testing. On the day of the experiment, a microdialysis probe (CMA/Microdialysis 12) protruding 1 mm from the guide cannula was inserted and connected to an infusion pump (Harvard Apparatus) with polyethylene tubing. A selective CGRP1 receptor antagonist (CGRP 8-37; TOCRIS, Minneapolis, MN, USA) was diluted in ACSF (in mM: 117 NaCl, 4.7 KCl, 1.2 NaH_2PO_4, 2.5 $CaCl_2$, 1.2 $MgCl_2$, 25 $NaHCO_3$, and 11 glucose) to the final concentration (100 μM), which is 100-fold greater than the target concentration in the tissue to account for the concentration gradient across the dialysis membrane and diffusion in brain tissue. CGRP 8-37 (100 μM) or ACSF was administered at 5 μl/min for at least 20 min prior to behavioral testing to establish equilibrium in the tissue.

Behaviors

Mechanosensitivity

Mechanical withdrawal thresholds were measured using a plantar electronic von Frey anesthesiometer (IITC Life Sciences, Woodland Hills, CA, USA) with the tip applied perpendicularly to the base of the 3rd toe of the left hind paw as described before (Mazzitelli et al., 2022). The tip was applied with increasing force until a flexion reflex was provoked, which was automatically recorded as the paw withdrawal threshold (in grams). Three measurements were recorded and averaged. As the least invasive test, this was always performed prior to any other behavioral assay. Mechanosensitivity was also measured using a paw compression test on the affected hindlimb in the recording system that was also used for vocalization measurements. For that, rats were briefly anesthetized with isoflurane (2%–3%; precision vaporizer, Harvard Apparatus) and placed slightly restrained in a customized holding chamber that allowed hindlimb access (U.S. Patent 7,213,538). Hindlimb withdrawal thresholds were measured after 30 min of habituation to the holding chamber by using a calibrated forceps with a force transducer (see Section "Emotional-Affective Responses") to compress the left hindpaw with gradually increasing intensity until a reflex response was evoked, as described in our previous

studies (Hein et al., 2021; Presto et al., 2021). The withdrawal threshold, defined as the force required to evoke a reflex response, was calculated using the average value from three trials. The combination of mechanosensitivity tests was used to address both the static (von Frey test; mediated by sensitized peripheral nociceptors) and dynamic (paw compression test; mediated by primary afferent inputs from deep tissue into the central nervous system) components of mechanical hyperalgesia (Koltzenburg et al., 1992; Ochoa and Yarnitsky, 1993; La and Chung, 2017).

Emotional-Affective Responses

Emotional-affective responses were assessed by measuring vocalizations in the ultrasonic (25 ± 4 kHz) range, as described in our previous studies (Ji et al., 2018; Mazzitelli and Neugebauer, 2019; Hein et al., 2021; Mazzitelli et al., 2021; Presto et al., 2021). Rats were briefly anesthetized with isoflurane (2%–3%; precision vaporizer, Harvard Apparatus) and placed in the custom-designed recording chamber for stable recordings of vocalizations evoked by noxious stimulation. After the rat recovered from anesthesia and was habituated to the recording chamber for 30 min, the hindlimb withdrawal thresholds were evaluated in the paw pressure test (see Section "Mechanosensitivity") before the calibrated forceps with a force transducer was used for vocalization assays. Vocalizations were evoked by a brief (10 s) noxious (500 g/6 mm^2) stimulus applied to the left hind paw. These vocalizations were automatically detected for 1 min using a full-spectrum USB microphone (max sampling rate: 384 kHz), and the ultrasonic component of the vocalizations following the onset of the mechanical stimulus was analyzed using UltraVox 3.2 software (Noldus Information Technology, Leesburg, VA, USA). At the conclusion of each experiment, the durations (in ms) of each individual ultrasonic call were summed for each 1-min recording period to give the total duration of ultrasonic vocalizations for each rat.

Anxiety-Like Behavior

The open field test (OFT) was used to measure exploratory behavior in the peripheral and central zones of an open arena (70 cm × 70 cm) with acrylic walls (height, 45 cm). Rat movements were recorded for 15 min using a computerized video tracking and analysis system (EthoVision XT 11 software, Noldus Information Technology) as described previously (Ji et al., 2018; Hein et al., 2021; Presto et al., 2021). Time spent in the center of the arena was calculated during the first 5 min of each experimental trial. Avoidance of the center of the arena is interpreted as anxiety-like behavior (Prut and Belzung, 2003; Seibenhener and Wooten, 2015).

Calcium Imaging

Rats were anesthetized with isoflurane (2%–3%; precision vaporizer, Harvard Apparatus) and a stereotaxic frame (David Kopf Instruments) was used to inject AAV5-Syn-Flex-GCaMP7 s into the right CeA 5–6 weeks before brain slices were obtained to allow viral vector-mediated expression of a fluorescent calcium sensor. SNL surgery was performed 4 weeks before brain slices were obtained (chronic neuropathic pain stage). On the day of the experiment, coronal brain slices (400 μm) were quickly removed and immersed in oxygenated ACSF at 35°C for at least 1 h before being transferred to the recording chamber and superfused with ACSF (∼2 ml/min) as described previously (Hein et al., 2021). One or two brain slices per animal were used. A multiphoton system (Intelligent Imaging Innovations, Inc., 3i, Denver, CO, USA) equipped with a VIVO^{TM}2-Photon 200 Microscopy Workstation was utilized to record calcium transients evoked in CeA-CRF neurons by electrical stimulation (1.5 mA, 0.6 ms) of the dorsomedial fiber tract containing presumed axons from the parabrachial area (Neugebauer et al., 2003; Ikeda et al., 2007). CeA-CRF neurons receive CGRP input from the parabrachial nucleus (Neugebauer et al., 2020) and modulate pain behaviors (Mazzitelli et al., 2021, 2022). The 2-photon excitation light was generated by a mode-locked Ti: Sapphire laser (920 nm; model Mai-Tai DeepSee, Spectra-Physics, Santa Clara, CA, USA). A 20×/1.0 NA water-immersion lens (Zeiss, Germany) was used for neuronal cluster imaging. Images were acquired at a rate of 0.85 frames/s with a resolution of 512 × 512 pixels, which corresponded to an image plane of 350 × 350 μm. The CeA-CRF neurons that responded to electrical stimulus were selected for further analysis. Fluorescent activity and background ($\Delta F/F_0$) were analyzed using SlideBook 6 (3i, Denver, CO, USA). CeA-CRF neuronal responses were recorded 10 min before and 20 min during CGRP 8-37 application (1 μM), followed by washout with ACSF for 40 min. Neuronal responses could also be blocked by the application of an AMPA/kainate receptor antagonist (6-cyano-7-nitroquinoxaline-2,3-dione, CNQX; 20 μM dissolved in ACSF), consistent with a glutamatergic synaptic drive onto CeA-CRF neurons.

Statistical Analysis

Statistical significance was accepted at the level $P < 0.05$. All averaged values are presented as means ± SEM. GraphPad Prism 9.0 software (Graph-Pad Software, San Diego, CA, USA) was used for all statistical analyses. For qRT-PCR experiments, two-way ANOVA with Tukey *post-hoc* tests were used for multiple comparisons since sample sizes for each group were equal. For behavioral experiments, two-way ANOVA (repeated measures if appropriate) with Bonferroni *post-hoc* tests was used for multiple comparisons. As behavioral experiments consisted of groups with unequal sample sizes, Bonferroni *post-hoc* tests were used due to the effect of unequal sample sizes on Tukey's *post-hoc* method (Smith, 1971; Shingala and Rajyaguru, 2015). For calcium imaging experiments, paired *t*-tests were used for the comparison of calcium transients data sets before and during drug application, which had Gaussian distribution and similar variance as indicated. Repeated measures one-way ANOVA with Dunnett *post-hoc* tests were used for time course analysis of calcium transients compared to predrug ACSF vehicle administration at 10 min, as the Dunnett *post-hoc* method is used to test multiple experimental groups against a single control group (Dunnett, 1955; McHugh, 2011).

RESULTS

Previous anatomical data have demonstrated that CGRP is an important molecular marker of the CeLCand the parabrachial

nucleus is the exclusive source of CGRP to the CeA (Schwaber et al., 1988; Honkaniemi et al., 1990; Dobolyi et al., 2005; Lu et al., 2015; Chen et al., 2018; Huang et al., 2021). We have previously shown that CGRP in the amygdala can exacerbate nocifensive and behavioral responses in normal rats (Han et al., 2010), and selective CGRP1 receptor antagonists can reverse pain-related plasticity in male rats in an arthritis pain model (Han et al., 2005). In this study, we investigated the role of CGRP in neuropathic pain-related amygdala function and behaviors in both sexes. We tested the hypothesis that the CGRP1 receptor is involved in neuropathic pain-related amygdala activity, and that blockade of this receptor in the amygdala could inhibit neuropathic pain behaviors in male and female rats.

Expression Levels of CGRP and CGRP1 Receptor Components in the CeA in Neuropathic Pain

We first examined mRNA expression levels of CGRP in the right CeA at the 1-week acute stage and 4-week chronic stage of the SNL model of neuropathic pain (see Section "Neuropathic Pain Model"). We found that SNL significantly increased CGRP mRNA expression in the CeA of male rats ($n = 6$) compared to sham ($n = 6$) at the acute phase ($P < 0.05$, $F_{3,20} = 5.608$, two-way ANOVA with Tukey *post-hoc* tests; **Figure 1A**), but no significant differences in CGRP expression levels were seen between female SNL ($n = 6$) and female sham ($n = 6$) rats at this stage. In fact, female SNL rats had significantly lower CGRP expression than male SNL rats at the acute phase ($P < 0.05$, $F_{3,20} = 7.127$, two-way ANOVA with Tukey *post-hoc* tests; **Figure 1A**). We also examined mRNA expression levels in the CeA of two CGRP1 receptor components, CLR and Ramp1 (McLatchie et al., 1998; Dickerson, 2013; Edvinsson and Warfvinge, 2013; Edvinsson et al., 2020). No significant differences in CLR or Ramp1 expression were found in the SNL model at the acute phase for males or females.

Interestingly, the opposite pattern of CGRP mRNA expression was seen at the chronic 4-week stage of neuropathic pain. Female SNL rats ($n = 6$) had significantly upregulated CGRP expression in the CeA compared to sham ($n = 6$; $P < 0.05$, $F_{3,20} = 9.053$, two-way ANOVA with Tukey *post-hoc* tests; **Figure 1B**), while there were no significant differences in CGRP expression levels between male SNL ($n = 6$) and male sham ($n = 6$) rats. CGRP mRNA expression was significantly higher in female SNL rats than male SNL rats at the chronic phase ($P < 0.01$, $F_{3,20} = 6.779$, two-way ANOVA with Tukey *post-hoc* tests; **Figure 1B**). For both CGRP receptor components, female SNL rats also had significantly upregulated mRNA expression in the CeA compared to that of female sham rats (CLR: $P < 0.05$, $F_{3,20} = 11.24$, two-way ANOVA with Tukey *post-hoc* tests; Ramp1: $P < 0.05$, $F_{3,20} = 11.59$, two-way ANOVA with Tukey *post-hoc* tests; **Figure 1B**) as well as significantly higher expression compared to male SNL rats (CLR: $P < 0.01$, $F_{3,20} = 7.259$, two-way ANOVA with Tukey *post-hoc* tests; Ramp1: $P < 0.01$, $F_{3,20} = 7.681$; **Figure 1B**). There were no significant differences in expression levels of either CLR or Ramp1 between male SNL and male sham rats during the chronic phase.

Effects of CGRP1 Receptor Blockade in the CeA on Chronic Neuropathic Pain Behaviors

To investigate the role of CGRP in the CeA in chronic neuropathic pain-related behavior, we administered a selective CGRP1 receptor antagonist (CGRP 8-37, 100 μM in microdialysis probe) into the CeA of male and female rats 4 weeks after SNL surgery (see Section "Drug Application in Awake Animals"). The concentration of CGRP 8-37 in the microdialysis probe was 100-fold higher than the intended target concentration in the brain tissue to account for the concentration gradient across the dialysis membrane and diffusion in the brain tissue (Mazzitelli and Neugebauer, 2019; Hein et al., 2021).

We first examined mechanical sensitivity using an electronic von Frey anesthesiometer (see Section "Mechanosensitivity"). CGRP 8-37 administration significantly increased the hindlimb withdrawal thresholds in both male ($n = 12$, $P < 0.001$) and female ($n = 24$, $P < 0.0001$) SNL rats compared to ACSF vehicle (see **Figure 2A**). There was a significant effect of CGRP1 receptor blockade ($P < 0.0001$, $F_{1,29} = 58.56$) but not sex ($P = 0.5587$, $F_{1,29} = 0.3500$) in the Von Frey test. Similarly, CGRP 8-37 administration into the CeA significantly decreased mechanical sensitivity in the paw compression test (reflex response evoked by gradually increasing the intensity of left hindpaw compression with a calibrated forceps, see Section "Mechanosensitivity") in both male ($P < 0.01$) and female ($P < 0.0001$) SNL rats compared to ACSF vehicle (see **Figure 2B**). There was a significant effect of CGRP1 receptor blockade ($P < 0.0001$, $F_{1,29} = 49.63$) but not sex ($P = 0.6238$, $F_{1,29} = 0.2459$) on withdrawal thresholds using the paw compression test. For the statistical analyses of mechanical withdrawal thresholds in both the von Frey and paw compression tests, repeated measures two-way ANOVA with Bonferroni *post-hoc* tests was used (see Section "Statistical Analysis").

We then examined emotional responses by measuring ultrasonic vocalizations in response to a noxious stimulus on the left hindpaw (see Section "Emotional-Affective Responses"). CGRP 8-37 administration significantly decreased the total duration of ultrasonic vocalizations in female SNL rats ($n = 24$, $P < 0.0001$, $F_{3,29} = 8.226$; see **Figure 2C**), but not in male SNL rats ($n = 12$) compared to ACSF vehicle. For the statistical analysis of ultrasonic vocalization durations in males and females, repeated-measures two-way ANOVA with Bonferroni *post-hoc* tests was used (see Section "Statistical Analysis").

Finally, we examined anxiety-like behaviors by measuring the time spent in the center zone of the OFT (see Section "Anxiety-Like Behavior"). Female SNL rats that received CGRP 8-37 in the CeA ($n = 24$) spent significantly more time in the center of the OFT compared to female SNL rats that received ACSF vehicle ($n = 24$, $P < 0.01$, $F_{3,65} = 6.369$; **Figure 2D**). In contrast, CGRP 8-37 administration into CeA had no significant effect in male SNL rats ($n = 12$) compared to ACSF vehicle ($n = 12$). Importantly, no significant differences in locomotor activity were

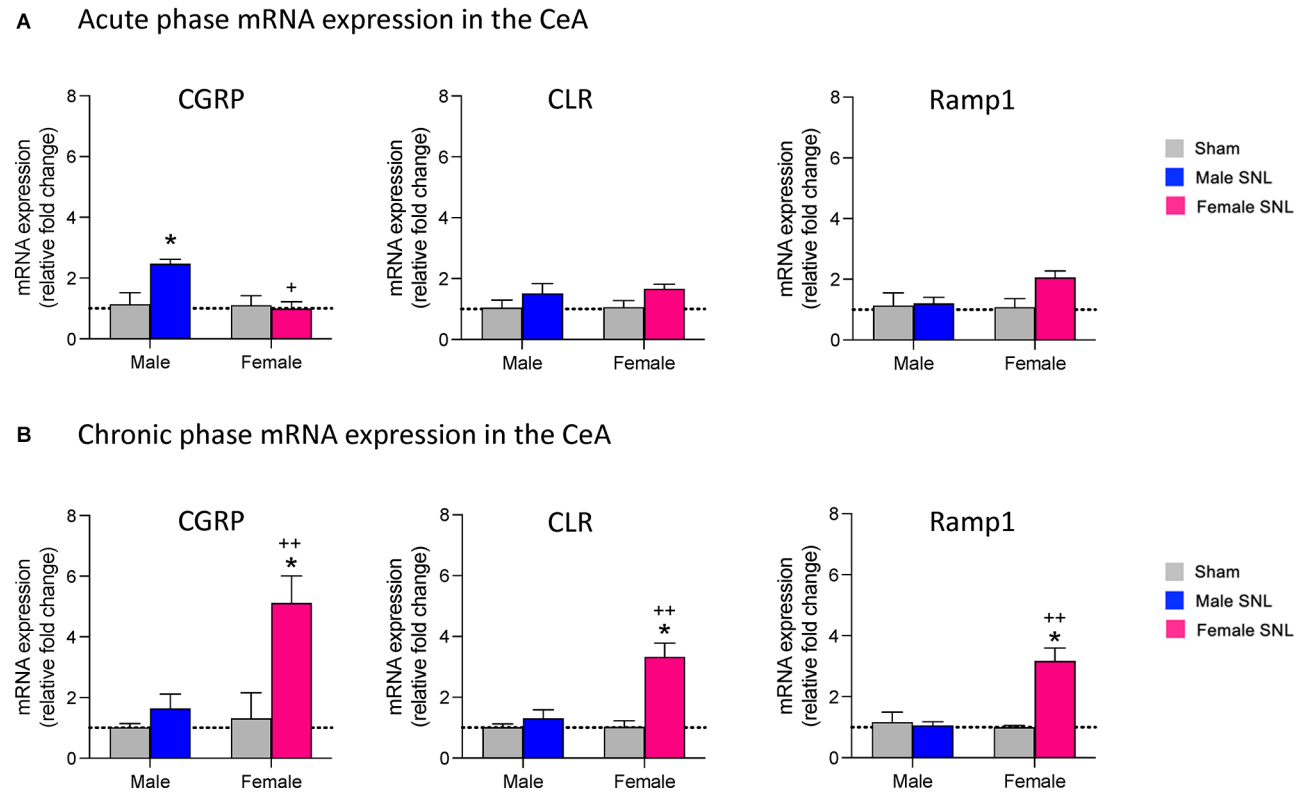

FIGURE 1 | mRNA expression levels of CGRP and CGRP1 receptor components in the spinal nerve ligation (SNL) model of neuropathic pain. At both the acute (1 week) **(A)** and chronic (4 week) **(B)** phases of the SNL model, brains were extracted and the CeA dissected out for mRNA analysis. qRT-PCR analysis of mRNA expression levels for CGRP and two CGRP1 receptor components (calcitonin receptor-like receptor, CLR; receptor activity-modifying protein 1, Ramp1) was performed on CeA tissue at both time points. Data were normalized to the male sham group in both the acute and chronic phases. **(A)** CGRP mRNA expression in the acute phase was upregulated only in male SNL rats ($n = 6$). Female SNL rats ($n = 6$) had significantly lower CGRP expression than male SNL rats. No significant changes of CGRP1 receptor component expression were found. **(B)** CGRP mRNA expression in the chronic phase was significantly upregulated in female ($n = 6$) but not male ($n = 6$) SNL rats. CLR and Ramp1 receptor components were also upregulated only in female SNL rats. Gene expression fold change was calculated using the delta-delta Ct method, geometric mean of β-actin, Rpl3, and Rpl29 used as internal marker. Two-way ANOVA with Tukey *post-hoc* tests was used as sample sizes were equal for each group (see Section "Statistical Analysis"). Bar histograms show mean ± SEM. $^{*}P < 0.05$, compared to male sham; $^{+}$, $^{++}$ $P < 0.05$, 0.01 compared to male SNL. See "Results" ("Expression Levels of CGRP and CGRP1 Receptor Components in the CeA in Neuropathic Pain") Section for details of the statistical analysis.

observed between the ACSF-treated group and the CGRP 8-37-treated group (male, $P > 0.9999$; female, $P = 0.9878$), indicating that the differences in anxiety-like behavior were not due to an increase in spontaneous activity. For the statistical analysis of center duration in the OFT for males and females, two-way ANOVA with Bonferroni *post-hoc* tests was used (see Section "Statistical Analysis").

Effects of CGRP1 Receptor Blockade in the CeA on CeA-CRF Neuronal Activity in Chronic Neuropathic Pain

To determine the neuronal effects of CGRP 8-37 in the amygdala as a potential basis of the inhibitory behavioral effects described in Section "Effects of CGRP1 Receptor Blockade in the CeA on Chronic Neuropathic Pain Behaviors", we measured synaptically-evoked calcium signals in CeA-CRF neurons, which receive CGRP input from the parabrachial area and can modulate pain (Neugebauer et al., 2020; Mazzitelli et al., 2021, 2022), before and after drug application (**Figure 3**). Calcium transients were evoked in CRF neurons expressing a fluorescent calcium indicator (GCaMP7s) by electrical stimulation (1.5 mA, 0.6 ms) of presumed parabrachial afferents (see Section "Calcium Imaging"). Evoking CeA neuronal activity through the stimulation of parabrachial afferents has been a well-documented technique in previous studies from our group (Neugebauer et al., 2003; Fu and Neugebauer, 2008; Han et al., 2010; Ren et al., 2013; Thompson et al., 2018; Hein et al., 2021) and others (Ikeda et al., 2007; Watabe et al., 2013; Miyazawa et al., 2018; Yamamoto et al., 2021). The organization of parabrachial afferents to the amygdala has been well-characterized, with parabrachial fiber tracts shown to run dorsomedial to the CeA and ventral to but outside of the caudate-putamen area (Sarhan et al., 2005). The parabrachial afferent pathway to the CeA can be activated either by electrical (Neugebauer et al., 2003; Ikeda et al., 2007; Hein et al., 2021) or optogenetic (Sugimura et al., 2016; Hein et al., 2021) stimulation. Here neurons were visualized and

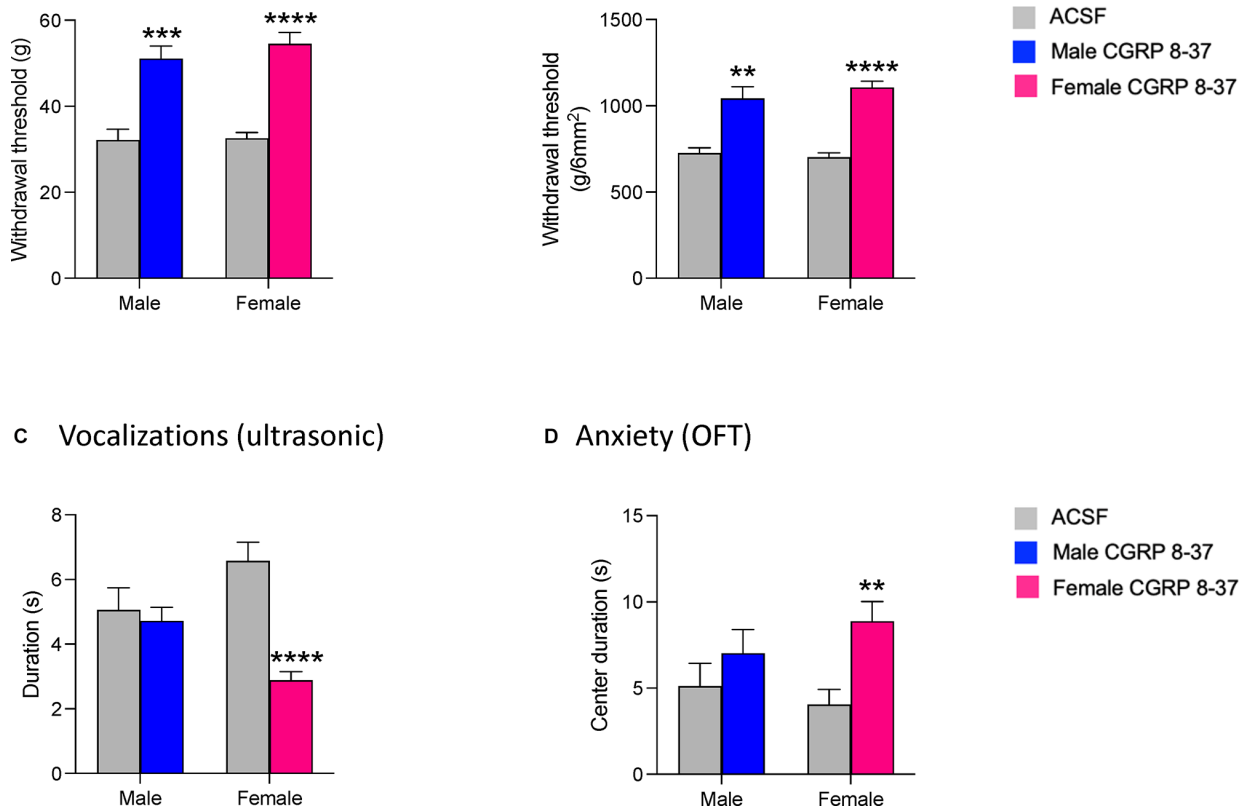

FIGURE 2 | Effects of CGRP1 receptor blockade in the CeA on chronic neuropathic pain behaviors. Pain-related behavioral assays were performed 4 weeks after SNL surgery. Mechanical withdrawal thresholds were measured by electronic von Frey **(A)** and paw compression **(B)** tests. CGRP 8-37 (100 μM in microdialysis probe) administration into the CeA significantly increased withdrawal thresholds in both male (n = 12) and female (n = 24) SNL rats. **, ***, ****$P < 0.01$, 0.001, 0.0001, repeated measures ANOVA with Bonferroni *post-hoc* tests, compared to predrug ACSF vehicle. **(C)** Duration of ultrasonic vocalizations evoked by brief (10 s) noxious (500 g /6 mm^2) mechanical compression of the affected hindpaw. CGRP 8-37 administration into CeA significantly decreased ultrasonic vocalizations in female (n = 24) but not male (n = 12) SNL rats compared to predrug ACSF vehicle. ****$P < 0.0001$, repeated measures ANOVA with Bonferroni *post-hoc* tests. **(D)** CGRP 8-37 administration into CeA significantly decreased anxiety-like behaviors in female (n = 24) but not male (n = 12) SNL rats as measured by increased duration (s) of time spent in the center of the open field test (OFT). **$P < 0.01$, ANOVA with Bonferroni *post-hoc* tests. Bonferroni *post-hoc* tests were used as sample sizes were unequal for each group (see Section "Statistical Analysis"). Bar histograms show mean ± SEM.

signals were recorded following electrical stimulation using a multiphoton imaging system. Neurons that showed an increase in calcium signals in response to electrical stimulation were selected for further analysis. CGRP 8-37 (1 μM, 20 min) significantly decreased calcium transients in CeA-CRF neurons ($n = 18$ neurons from four rats; $P < 0.001$, paired t-test, compared to predrug ACSF vehicle; **Figure 3C**). Time course analysis revealed a significant effect of CGRP 8-37 treatment on calcium signals from CeA-CRF neurons ($P < 0.0001$, $F_{15,150} = 15.60$, one-way ANOVA with repeated measures and Dunnett *post-hoc* test; see Section "Statistical Analysis"; **Figure 3D**).

DISCUSSION

This study explored the role of CGRP in sensory and affective pain-related behaviors as well as in pain-related amygdala function in male and female rats in a neuropathic pain model. We previously showed that selective CGRP1 receptor antagonists (CGRP 8-37 and BIBN4096BS) can inhibit CeA neuronal excitability *in vitro* and can reduce withdrawal reflexes and vocalizations in awake male animals in an acute arthritis pain model (Han et al., 2005). However, it is unclear if these findings extend to a chronic pain condition and whether this inhibition elicits similar behavioral responses in the female sex. The key novelties in this study are the sex-specific characterizations of CGRP and CGRP1 receptor component expression levels in the CeA at both acute and chronic stages of neuropathic pain, the differential behavioral modulation by CGRP1 signaling in the CeA between males and females at the chronic stage, and the effects of CGRP1 receptor blockade on CeA-CRF neurons in chronic neuropathic pain.

Abundant preclinical (Neugebauer et al., 2009; Veinante et al., 2013; Neugebauer, 2015, 2020; Thompson and Neugebauer, 2017; Allen et al., 2021) and clinical (Baliki et al., 2006, 2008;

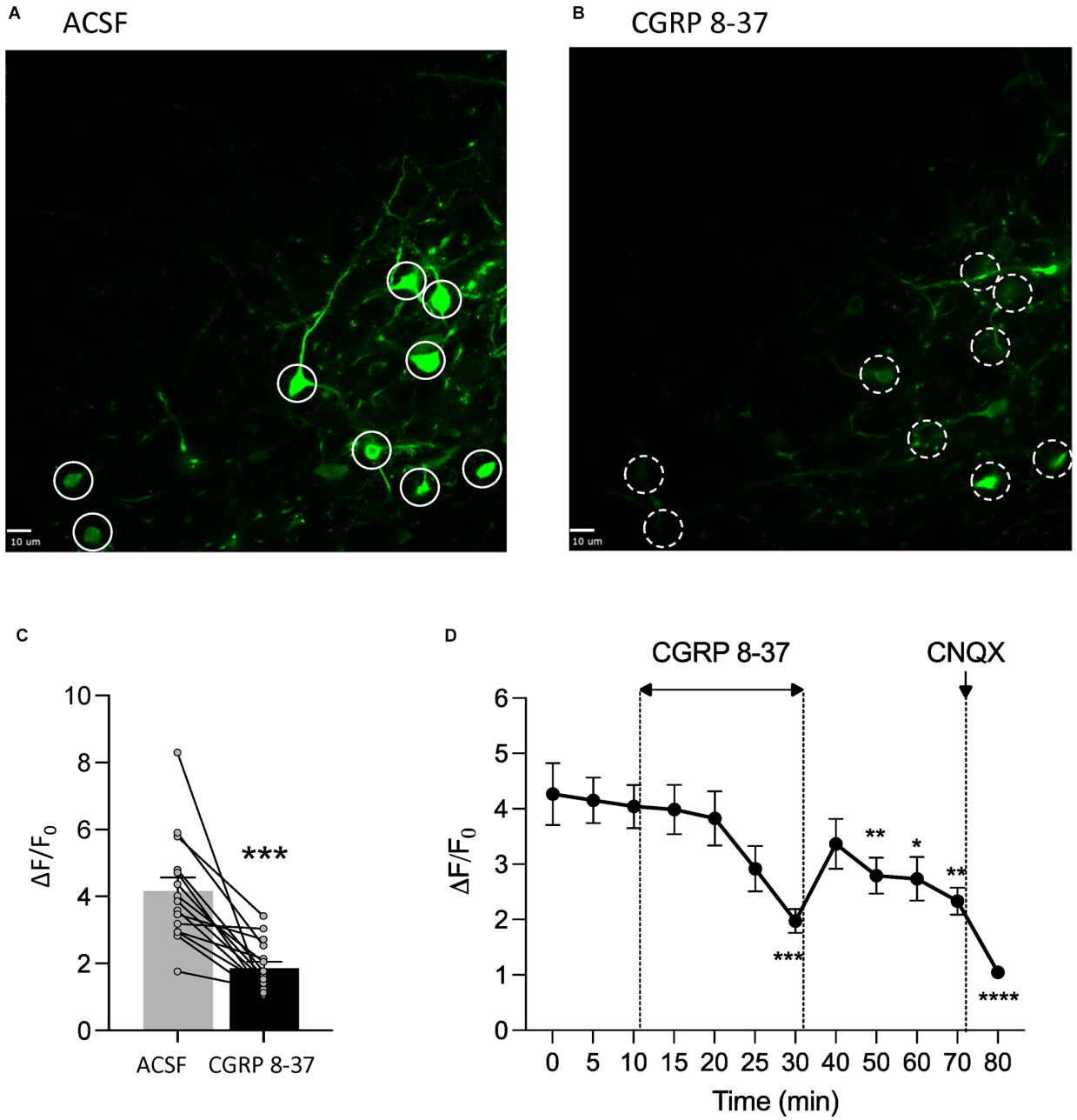

FIGURE 3 | CGRP1 receptor blockade inhibits calcium transients in CeA-CRF neurons in chronic neuropathic pain. *In vitro* calcium imaging of CeA-CRF neurons in brain slices from chronic SNL rats was performed using a multiphoton imaging system (see Section "Calcium Imaging"). **(A,B)** Images show calcium transients in CeA-CRF neurons expressing a fluorescent calcium indicator (GCaMP7s) in response to electrical stimulation (1.5 mA, 0.6 ms) of presumed parabrachial afferents. Solid white circles **(A)** indicate neurons showing synaptically evoked fluorescence in the presence of ACSF vehicle; dashed white circles **(B)** indicate the same neurons after application of CGRP 8-37 (1 μM, 20 min). Scale bars represent 10 μM. **(C)** CGRP 8-37 decreased calcium transients in CeA-CRF neurons (n = 18 neurons from four rats) expressing GCaMP7s. ***$P < 0.001$, paired t-test, compared to predrug ACSF vehicle. **(D)** Time course analysis of calcium signals from CeA-CRF neurons during application of ACSF, CGRP 8-37, washout in ACSF, and CNQX (20 μM). *, **, ***, ****$P < 0.05$, 0.01, 0.001, 0.0001, repeated measures ANOVA with Dunnett *post-hoc* tests, compared to predrug ACSF vehicle at 10 min (see Section "Statistical Analysis"). Bar histograms show mean ± SEM.

Geha et al., 2007; Kulkarni et al., 2007; Liu et al., 2010; Vachon-Presseau et al., 2012, 2016; Simons et al., 2014) evidence has linked the amygdala to the emotional-affective aspects of pain and pain modulation. The lateral and capsular regions of the CeAconstitute the "nociceptive amygdala" due to the high content of neurons encoding nociceptive information and modulating pain-related behaviors (Neugebauer et al., 2004, 2020; Neugebauer, 2015). Changes in the activity of these neurons have been demonstrated inacute inflammatory pain (Adedoyin et al., 2010; Sugimura et al., 2016;

Shinohara et al., 2017; Miyazawa et al., 2018), in colitis (Han and Neugebauer, 2004), in muscle pain (Cheng et al., 2011), in neuropathic pain (Ikeda et al., 2007; Gonçalves and Dickenson, 2012; Nakao et al., 2012; Ji et al., 2017), and in arthritis pain models (Neugebauer and Li, 2003; Bird et al., 2005; Han et al., 2005; Li and Neugebauer, 2006; Ji and Neugebauer, 2007, 2009; Fu and Neugebauer, 2008; Fu et al., 2008; Ji et al., 2009; Ren and Neugebauer, 2010; Ren et al., 2011, 2013). Decreasing amygdala activity has been shown to inhibit pain-related behavior in arthritic (Han and Neugebauer, 2005; Ji et al., 2007, 2010; Fu and Neugebauer, 2008; Palazzo et al., 2008; Ji and Neugebauer, 2009; Grégoire and Neugebauer, 2013; Ren et al., 2013; Medina et al., 2014; Thompson et al., 2015; Kim et al., 2017; Mazzitelli and Neugebauer, 2019; Mazzitelli et al., 2021), acute inflammatory (Kolber et al., 2010; Palazzo et al., 2011; Sugimoto et al., 2021), visceral (Crock et al., 2012), widespread nociplastic (Yajima et al., 2022), and neuropathic (Pedersen et al., 2007; Ansah et al., 2010; Jiang et al., 2014; Ji et al., 2017; Seno et al., 2018; Wilson et al., 2019; Mazzitelli et al., 2022) pain models.

The lateral and capsular divisions of the CeA are the targets of nociceptive input from the spino-parabrachio-amygdaloid pain pathway (Gauriau and Bernard, 2002), where neurons from the lateral pontine parabrachial area provide the main if not exclusive source of CGRP within the amygdale (Dobolyi et al., 2005; D'Hanis et al., 2007; Shinohara et al., 2017; Palmiter, 2018). CGRP has previously been suggested to act as an important modulator of synaptic plasticity within the amygdala, as its exogenous application onto brain slices from normal rats increased both excitatory transmission at the parabrachio-amygdaloid synapse as well as excitability of neurons in the lateral and capsular CeA through N-methyl-D-aspartate (NMDA)- and PKA-dependent mechanisms (Han et al., 2010). Furthermore, the stereotaxic administration of CGRP into the right CeA of awake rats increased emotional responses (audible and ultrasonic vocalizations) to noxious stimuli and induced mechanical hypersensitivity (lowered hindlimb withdrawal thresholds; Han et al., 2010), and CGRP1 receptor blockade in the CeA reduced mechanical hypersensitivity and emotional responses in an acute arthritis pain model (Han et al., 2005). Similarly, mechanical sensitivity in the formalin test was significantly decreased 6 h post-inflammation in CGRP knockout mice, while acute nociceptive behavior was reduced only at 20–25 min after injection (Shinohara et al., 2017). The role of CGRP is therefore a critical link to investigate in the mechanistic analysis of pain-related processing in the amygdala.

A substantial portion (35%–42%) of CRF neurons, which serve output functions in the lateral and capsular regions of the CeA, receive input from CGRP-containing parabrachial afferents (Kruger et al., 1988; Shimada et al., 1989; Harrigan et al., 1994; Dobolyi et al., 2005; D'Hanis et al., 2007; Chen et al., 2018; Palmiter, 2018). As such, CGRP may strengthen the synaptic drive onto CRF neurons and influence amygdala output activity (Han et al., 2010; Okutsu et al., 2017; Shinohara et al., 2017). Here our multiphoton calcium imaging experiments revealed that CGRP1 receptor blockade in a chronic neuropathic pain model decreased CeA-CRF neuronal activity, which indicates endogenous CGRP release and would translate into decreased output from these neurons. As CRF neurons project to numerous extra-amygdalar targets involved in the modulation of averse-affective pain behaviors (Beckerman et al., 2013; Pomrenze et al., 2015, 2019; Dedic et al., 2018; de Guglielmo et al., 2019; Neugebauer et al., 2020), we expect that the deactivation of CeA-CRF neurons would correspond with beneficial behavioral effects observed here in a neuropathic pain model. This is consistent with our previous studies showing that optogenetic silencing of CeA-CRF neurons inhibits pain behaviors (Mazzitelli et al., 2021, 2022). Our data implicate CGRP1 receptors in the pain facilitating role of CRF neurons. The calcium imaging data complement data from our behavioral experiments to suggest that reduced CeA-CRF neuronal activity plays a critical contribution to the facilitatory behavioral responses that we saw from CGRP1 receptor antagonism in chronic neuropathic pain. However, the full downstream consequences of reduced CeA-CRF neuronal output remain to be determined.

Information about sex-specific roles for CGRP in pain modulation is rather limited, though a few studies have focused on sex-differential expression levels in the spinal cord. In the spinal trigeminal nucleus caudalis (SpVc), naïve male rats showed higher baseline mRNA levels of CLR, Ramp1, and the third receptor component, RCP, but not of CGRP when compared to female counterparts (Stucky et al., 2011). Surprisingly, expression of the CGRP-related genes increased in both sexes 30 min after dural application of either an inflammatory cocktail or a vehicle control, though this upregulation was larger in females than in males. As both the inflammatory and control treatments promoted increased CGRP-related gene expression, the authors attributed this upregulation to mechanical stimulation from cannula implantation as opposed to meningeal inflammation (Stucky et al., 2011). However, a later study found SpVc protein levels of RCP but not CLR were higher in naïve females than in males (Ji et al., 2019). In the periphery, naïve female rats were shown to have fewer CGRP-immunoreactive dorsal root ganglion (DRG) neurons than their male counterparts, though ovariectomy produced a significant increase in immunoreactive neurons (Yang et al., 1998). A recent study reported no significant sex differences in CGRP-immunostaining cells in the DRG 7 days after the induction of neuropathic pain using the spared nerve injury (SNI) model (Ahlström et al., 2021). To our knowledge, this study is the first to report neuropathic pain stage-specific sex differences in mRNA expression levels of CGRP and its receptor components within the brain. Additional investigation is needed to confirm sex differences in CGRP and CGRP receptor expression at the protein level and characterize pain-related transcriptional and translational regulatory mechanisms of CGRP and its receptor components at each level of the neuraxis in male and female animals. As a note of caution, we did not determine or analyze separately the different stages of the estrous cycle because previous evidence because our previous work (Chen et al., 2020) and the current study found that sexually dimorphic effects were robust, readily detectable, and statistically significant, even though we did not control for the estrous stage of females, suggesting that the estrous cycle may not be a major factor in the outcomes of our studies. Actually, the value of

testing female rodents at different stages of the estrous cycle is somewhat debatable (Greenspan et al., 2007).

Potential sex differences in CGRP-related pain behaviors have also been explored. Within the brain, a migraine model of dural CGRP administration produced hypersensitivity responses in female but not male rats (Avona et al., 2019). In the SpVc, knockdown of RCP expression with short hairpin RNA (shRNA) attenuated mechanical facial allodynia produced by noxious chemical stimulation of the meninges in both male and female rats (Ji et al., 2019). However, another group found that intrathecal injection of CGRP receptor antagonists (CGRP 8-37 orolcegepant) attenuated mechanical hypersensitivity in a female-specific manner in both a hyperalgesic priming model and at the chronic phase of the SNI neuropathic pain model (Paige et al., 2022). In the same study, intrathecal injection of CGRP caused prolonged mechanical hypersensitivity only in female mice, an effect that was blocked by systemic pretreatment with olcegepant (Paige et al., 2022). These data are consistent with our current finding that CGRP receptor antagonism reduces mechanical hypersensitivity in a neuropathic pain model to a greater extent in female animals. Additionally, since we found that this treatment strategy alleviated other dimensions of pain (emotional-affective responses and anxiety-like behaviors) more strongly in female rats, our collective data provide support for the utilization of CGRP receptor-blocking therapies in the central nervous system for female chronic neuropathic pain patients.

Increasing evidence across the pain field has revealed sexually dimorphic mechanisms that contribute to pain development and maintenance (recently reviewed in Presto et al., 2022). Studies from the periphery and spinal cord have illustrated a male-predominant reliance on macrophage-related (Liu et al., 2020; Rudjito et al., 2021) and microglia-related (Sorge et al., 2011, 2015; Taves et al., 2016; Agalave et al., 2021) pain processing mechanisms. However, the underlying pain modulatory processes for females are complex and not well-characterized. Particularly within the brain, sex-specific signaling mechanisms are largely unknown. Our data may be the first to show sex differences in pain-related behavior following CGRP receptor blockade within the brain, which may be attributed to sex-specific molecular expression profiles throughout neuropathic pain development. Though CGRP expression in the CeA was not upregulated in male rats at the chronic stage, blockade of the CGRP1 receptor at this phase still showed inhibitory effects on sensory pain responses. This may reflect a more tonic role of CGRP signaling in males during the chronic phase, as CGRP also exhibits several physiological properties within the brain (Abushik et al., 2017; Borkum, 2019; Tian et al., 2020). As pain-related CGRP signaling in the CeA of male rats appears to play a significant role during the induction phase but primarily sensory role at the chronic stage of neuropathic pain modulation, our study could provide support that other mechanisms, such as those involved in neuroimmune signaling, may be more relevant for brain-related pain processing in males. Importantly, the impact of CGRP-related pain mechanisms may differ across the pain time course. Our previous studies have highlighted the beneficial effects of CGRP1 receptor blockade in the CeA on pain-related behaviors in males in relatively acute (arthritis) pain conditions (Han et al., 2005, 2010). The role of CGRP in the arthritis model may be more comparable to the acute 1-week stage of the SNL model presented here, in which a stronger upregulation of CGRP mRNA expression was observed in male compared to female SNL rats. The current data suggest that while CGRP signaling may play a critical role in brain-related pain processing at an acute stage in males, other modulatory mechanisms may take on a more predominant role with regard to pain chronicity and maintenance. This illustrates the urgent need to investigate potential sexual dimorphisms in pain-related amygdala function across all stages of neuropathic pain development.

CONCLUSION

The data may suggest that while CGRP-related signaling mechanisms play an important role in neuropathic-pain-related amygdala function, this influence likely differs with respect to the time course of pain development in males and females. CGRP1 receptor blockade in the amygdala may serve as a novel therapeutic strategy for chronic neuropathic pain relief, particularly among female chronic pain patients. Future investigation into the contributions of other pain modulatory mechanisms, such as the role of neuroimmune signaling in the transition from acute to chronic pain, is warranted in both sexes. Ultimately, our work provides support for the investigation of therapeutic targets, such as CGRP receptors, in both male and female subjects across different stages of neuropathic pain.

DATA AVAILABILITY STATEMENT

The original contributions presented in the study are included in the article, further inquiries can be directed to the corresponding author.

ETHICS STATEMENT

The animal study was reviewed and approved by Institutional Animal Care and Use Committee (IACUC, protocol #14006) of Texas Tech University Health Sciences Center (TTUHSC).

AUTHOR CONTRIBUTIONS

PP: methodology, molecular, behavioral and imaging experiments, data analysis, writing original draft. VN: conceptualization, methodology, experimental design, supervision, editing and finalizing the manuscript, project administration, funding acquisition. All authors contributed to the article and approved the submitted version.

FUNDING

Work in the authors' laboratory is supported by National Institutes of Health (NIH) grants R01 NS038261, R01 NS106902, R01 NS109255, R01 NS118731, and R01 NS120395, and USDA grant 2021-67017-34026.

REFERENCES

Abushik, P. A., Bart, G., Korhonen, P., Leinonen, H., Giniatullina, R., Sibarov, D. A., et al. (2017). Pro-nociceptive migraine mediator CGRP provides neuroprotection of sensory, cortical and cerebellar neurons via multi-kinase signaling. *Cephalalgia* 37, 1373–1383. doi: 10.1177/0333102416681588

Adedoyin, M. O., Vicini, S., and Neale, J. H. (2010). Endogenous N-acetylaspartylglutamate (NAAG) inhibits synaptic plasticity/transmission in the amygdala in a mouse inflammatory pain model. *Mol. Pain* 6:60. doi: 10.1186/1744-8069-6-60

Agalave, N. M., Rudjito, R., Farinotti, A. B., Khoonsari, P. E., Sandor, K., Nomura, Y., et al. (2021). Sex-dependent role of microglia in disulfide high mobility group box 1 protein-mediated mechanical hypersensitivity. *Pain* 162:446. doi: 10.1097/j.pain.0000000000002033

Ahlström, F. H. G., Mätlik, K., Viisanen, H., Blomqvist, K. J., Liu, X., Lilius, T. O., et al. (2021). Spared nerve injury causes sexually dimorphic mechanical allodynia and differential gene expression in spinal cords and dorsal root ganglia in rats. *Mol. Neurobiol.* 58:5396. doi: 10.1007/s12035-021-02447-1

Allen, H. N., Bobnar, H. J., and Kolber, B. J. (2021). Left and right hemispheric lateralization of the amygdala in pain. *Prog. Neurobiol.* 196:101891. doi: 10.1016/j.pneurobio.2020.101891

Ansah, O. B., Bourbia, N., Gonçalves, L., Almeida, A., and Pertovaara, A. (2010). Influence of amygdaloid glutamatergic receptors on sensory and emotional pain-related behavior in the neuropathic rat. *Behav. Brain Res.* 209, 174–178. doi: 10.1016/j.bbr.2010.01.021

Attal, N. (2019). Pharmacological treatments of neuropathic pain: the latest recommendations. *Rev. Neurol. (Paris)* 175, 46–50. doi: 10.1016/j.neurol.2018.08.005

Avona, A., Burgos-Ega, C., Burton, M. D., Akopian, A. N., Price, T. J., Dussor, G., et al. (2019). Dural calcitonin gene-related peptide produces female-specific responses in rodent migraine models. *J. Neurosci.* 39:4323. doi: 10.1523/JNEUROSCI.0364-19.2019

Baliki, M. N., Chialvo, D. R., Geha, P. Y., Levy, R. M., Harden, R. N., Parrish, T. B., et al. (2006). Chronic pain and the emotional brain: specific brain activity associated with spontaneous fluctuations of intensity of chronic back pain. *J. Neurosci.* 26:12165. doi: 10.1523/JNEUROSCI.3576-06.2006

Baliki, M. N., Geha, P. Y., Jabakhanji, R., Harden, N., Schnitzer, T. J., Apkarian, A. V., et al. (2008). A preliminary fMRI study of analgesic treatment in chronic back pain and knee osteoarthritis. *Mol. Pain* 4:47. doi: 10.1186/1744-8069-4-47

Barwell, J., Wheatley, M., Conner, A. C., Taddese, B., Vohra, S., Reynolds, C. A., et al. (2013). The activation of the CGRP receptor. *Biochem. Soc. Trans.* 41, 180–184. doi: 10.1042/BST20120251

Bates, D., Carsten Schultheis, B., Hanes, M. C., Jolly, S. M., Chakravarthy, K. V., Deer, T. R., et al. (2019). A comprehensive algorithm for management of neuropathic pain. *Pain Med.* 20, S2–S12. doi: 10.1093/pm/pnz075

Becker, J. J., and Carrasquillo, Y. (2019). Projections, where art thou: the state and future of the central amygdala. *J. Physiol.* 597:365. doi: 10.1113/JP277196

Beckerman, M. A., Van Kempen, T. A., Justice, N. J., Milner, T. A., and Glass, M. J. (2013). Corticotropin-releasing factor in the mouse central nucleus of the amygdala: ultrastructural distribution in NMDA-NR1 receptor subunit expressing neurons as well as projection neurons to the bed nucleus of the stria terminalis. *Exp. Neurol.* 239:120. doi: 10.1016/j.expneurol.2012.10.009

Bernard, J. F., Huang, G. F., and Besson, J. M. (1992). Nucleus centralis of the amygdala and the globus pallidus ventralis: electrophysiological evidence for an involvement in pain processes. *J. Neurophysiol.* 68, 551–569. doi: 10.1152/jn.1992.68.2.551

Bird, G. C., Lash, L. L., Han, J. S., Zou, X., Willis, W. D., Neugebauer, V., et al. (2005). Protein kinase A-dependent enhanced NMDA receptor function in pain-related synaptic plasticity in rat amygdala neurones. *J. Physiol.* 564:907. doi: 10.1113/jphysiol.2005.084780

Borkum, J. M. (2019). CGRP and brain functioning: cautions for migraine treatment. *Headache* 59, 1339–1357. doi: 10.1111/head.13591

Breivik, H., Eisenberg, E., and O'Brien, T. (2013). The individual and societal burden of chronic pain in Europe: the case for strategic prioritisation and action to improve knowledge and availability of appropriate care. *BMC Public Health* 13:1229. doi: 10.1186/1471-2458-13-1229

Carrasquillo, Y., and Gereau IV, R. W. (2008). Hemispheric lateralization of a molecular signal for pain modulation in the amygdala. *Mol. Pain* 4:24. doi: 10.1186/1744-8069-4-24

Chen, J. Y., Campos, C. A., Jarvie, B. C., and Palmiter, R. D. (2018). Parabrachial CGRP neurons establish and sustain aversive taste memories. *Neuron* 100:891. doi: 10.1016/j.neuron.2018.09.032

Chen, Y., Moutal, A., Navratilova, E., Kopruszinski, C., Yue, X., Ikegami, M., et al. (2020). The prolactin receptor long isoform regulates nociceptor sensitization and opioid-induced hyperalgesia selectively in females. *Sci. Transl. Med.* 12:eaay7550. doi: 10.1126/scitranslmed.aay7550

Cheng, S. J., Chen, C. C., Yang, H. W., Chang, Y. T., Bai, S. W., Chen, C. C., et al. (2011). Role of extracellular signal-regulated kinase in synaptic transmission and plasticity of a nociceptive input on capsular central amygdaloid neurons in normal and acid-induced muscle pain mice. *J. Neurosci.* 31:2258. doi: 10.1523/JNEUROSCI.5564-10.2011

Crock, L. W., Kolber, B. J., Morgan, C. D., Sadler, K. E., Vogt, S. K., Bruchas, M. R., et al. (2012). Central amygdala metabotropic glutamate receptor 5 in the modulation of visceral pain. *J. Neurosci.* 32:14217. doi: 10.1523/JNEUROSCI.1473-12.2012

D'Hanis, W., Linke, R., and Yilmazer-Hanke, D. M. (2007). Topography of thalamic and parabrachial calcitonin gene-related peptide (CGRP) immunoreactive neurons projecting to subnuclei of the amygdala and extended amygdala. *J. Comp. Neurol.* 505, 268–291. doi: 10.1002/cne.21495

Dahlhamer, J., Lucas, J., Zelaya, C., Nahin, R., Mackey, S., DeBar, L., et al. (2018). Prevalence of chronic pain and high-impact chronic pain among adults — united states, 2016. *Morb. Mortal. Wkly. Rep.* 67:1001. doi: 10.15585/mmwr.mm6736a2

de Guglielmo, G., Kallupi, M., Pomrenze, M. B., Crawford, E., Simpson, S., Schweitzer, P., et al. (2019). Inactivation of a CRF-dependent amygdalofugal pathway reverses addiction-like behaviors in alcohol-dependent rats. *Nat. Commun.* 10:1238. doi: 10.1038/s41467-019-09183-0

Dedic, N., Kühne, C., Jakovcevski, M., Hartmann, J., Genewsky, A. J., Gomes, K. S., et al. (2018). Chronic CRH depletion from GABAergic, long-range projection neurons in the extended amygdala reduces dopamine release and increases anxiety. *Nat. Neurosci.* 21, 803–807. doi: 10.1038/s41593-018-0151-z

Dickerson, I. M. (2013). Role of CGRP-receptor component protein (RCP) in CLR/RAMP function. *Curr. Protein Pept. Sci.* 14, 407–415. doi: 10.2174/13892037113149990057

Dobolyi, A., Irwin, S., Makara, G., Usdin, T. B., and Palkovits, M. (2005). Calcitonin gene-related peptide-containing pathways in the rat forebrain. *J. Comp. Neurol.* 489, 92–119. doi: 10.1002/cne.20618

Dunnett, C. W. (1955). A multiple comparison procedure for comparing several treatments with a control. *J. Am. Stat. Assoc.* 50:1096.

Edvinsson, L., and Warfvinge, K. (2013). CGRP receptor antagonism and migraine therapy. *Curr. Protein Pept. Sci.* 14, 386–392. doi: 10.2174/13892037113149990055

Edvinsson, L., Grell, A. S., and Warfvinge, K. (2020). Expression of the CGRP family of neuropeptides and their receptors in the trigeminal ganglion. *J. Mol. Neurosci.* 70, 930–944. doi: 10.1007/s12031-020-01493-z

Fayaz, A., Croft, P., Langford, R. M., Donaldson, L. J., and Jones, G. T. (2016). Prevalence of chronic pain in the UK: a systematic review and meta-analysis of population studies. *BMJ Open* 6:e010364. doi: 10.1136/bmjopen-2015-010364

Fu, Y., and Neugebauer, V. (2008). Differential mechanisms of CRF1 and CRF2 receptor functions in the amygdala in pain-related synaptic facilitation and behavior. *J. Neurosci.* 28:3861. doi: 10.1523/JNEUROSCI.0227-08.2008

Fu, Y., Han, J., Ishola, T., Scerbo, M., Adwanikar, H., Ramsey, C., et al. (2008). PKA and ERK, but not PKC, in the amygdala contribute to pain-related synaptic plasticity and behavior. *Mol. Pain* 4:26. doi: 10.1186/1744-8069-4-26

Gauriau, C., and Bernard, J. F. (2002). Pain pathways and parabrachial circuits in the rat. *Exp. Physiol.* 87, 251–258. doi: 10.1113/eph8702357

Geha, P. Y., Baliki, M. N., Chialvo, D. R., Harden, R. N., Paice, J. A., Apkarian, A. V., et al. (2007). Brain activity for spontaneous pain of postherpetic neuralgia and its modulation by lidocaine patch therapy. *Pain* 128:88. doi: 10.1016/j.pain.2006.09.014

Gonçalves, L., and Dickenson, A. H. (2012). Asymmetric time-dependent activation of right central amygdala neurones in rats with peripheral neuropathy and pregabalin modulation. *Eur. J. Neurosci.* 36, 3204–3213. doi: 10.1007/s00417-022-05653-2

Greenspan, J. D., Craft, R. M., LeResche, L., Arendt-Nielsen, L., Berkley, K. J., Fillingim, R. B., et al. (2007). Studying sex and gender differences in pain and analgesia: a consensus report. *Pain* 132, S26–S45. doi: 10.1016/j.pain.2007.10.014

Grégoire, S., and Neugebauer, V. (2013). 5-HT2CR blockade in the amygdala conveys analgesic efficacy to SSRIs in a rat model of arthritis pain. *Mol. Pain* 9:41. doi: 10.1186/1744-8069-9-41

Han, J. S., Adwanikar, H., Li, Z., Ji, G., and Neugebauer, V. (2010). Facilitation of synaptic transmission and pain responses by CGRP in the amygdala of normal rats. *Mol. Pain* 6:10. doi: 10.1186/1744-8069-6-10

Han, J. S., and Neugebauer, V. (2004). Synaptic plasticity in the amygdala in a visceral pain model in rats. *Neurosci. Lett.* 361, 254–257. doi: 10.1016/j.neulet.2003.12.027

Han, J. S., and Neugebauer, V. (2005). mGluR1 and mGluR5 antagonists in the amygdala inhibit different components of audible and ultrasonic vocalizations in a model of arthritic pain. *Pain* 113, 211–222. doi: 10.1016/j.pain.2004.10.022

Han, J. S., Li, W., and Neugebauer, V. (2005). Critical role of calcitonin gene-related peptide 1 receptors in the amygdala in synaptic plasticity and pain behavior. *J. Neurosci.* 25, 10717–10728. doi: 10.1523/JNEUROSCI.4112-05.2005

Han, S., Soleiman, M., Soden, M., Zweifel, L., and Palmiter, R. D. (2015). Elucidating an affective pain circuit that creates a threat memory. *Cell* 162, 363–374. doi: 10.1016/j.cell.2015.05.057

Harrigan, E. A., Magnuson, D. J., Thunstedt, G. M., and Gray, T. S. (1994). Corticotropin releasing factor neurons are innervated by calcitonin gene-related peptide terminals in the rat central amygdaloid nucleus. *Brain Res. Bull.* 33, 529–534. doi: 10.1016/0361-9230(94)90079-5

Hein, M., Ji, G., Tidwell, D., D'Souza, P., Kiritoshi, T., Yakhnitsa, V., et al. (2021). Kappa opioid receptor activation in the amygdala disinhibits CRF neurons to generate pain-like behaviors. *Neuropharmacology* 185:108456. doi: 10.1016/j.neuropharm.2021.108456

Ho Kim, S., and Mo Chung, J. (1992). An experimental model for peripheral neuropathy produced by segmental spinal nerve ligation in the rat. *Pain* 50, 355–363. doi: 10.1016/0304-3959(92)90041-9

Honkaniemi, J., Pelto-Huikko, M., Isola, J., and Rechardt, L. (1990). Simultaneous localization of calcitonin gene-related peptide and neurotensin in rat central amygdaloid nucleus. *Neurosci. Lett.* 113, 1–6. doi: 10.1016/0304-3940(90)90484-q

Hua, T., Chen, B., Lu, D., Sakurai, K., Zhao, S., Han, B. X., et al. (2020). General anesthetics activate a potent central pain-suppression circuit in the amygdala. *Nat. Neurosci.* 23, 854–868. doi: 10.1038/s41593-020-0632-8

Huang, D., Grady, F. S., Peltekian, L., Laing, J. J., and Geerling, J. C. (2021). Efferent projections of CGRP/Calca-expressing parabrachial neurons in mice. *J. Comp. Neurol.* 529, 2911–2957. doi: 10.1002/cne.25136

Ikeda, R., Takahashi, Y., Inoue, K., and Kato, F. (2007). NMDA receptor-independent synaptic plasticity in the central amygdala in the rat model of neuropathic pain. *Pain* 127, 161–172. doi: 10.1016/j.pain.2006.09.003

Iyengar, S., Ossipov, M. H., and Johnson, K. W. (2017). The role of calcitonin gene-related peptide in peripheral and central pain mechanisms including migraine. *Pain* 158, 543–559. doi: 10.1097/j.pain.0000000000000831

Ji, G., and Neugebauer, V. (2007). Differential effects of CRF1 and CRF2 receptor antagonists on pain-related sensitization of neurons in the central nucleus of the amygdala. *J. Neurophysiol.* 97, 3893–3904. doi: 10.1152/jn.00135.2007

Ji, G., and Neugebauer, V. (2009). Hemispheric lateralization of pain processing by amygdala neurons. *J. Neurophysiol.* 102:2253. doi: 10.1152/jn.00166.2009

Ji, G., Fu, Y., Ruppert, K. A., and Neugebauer, V. (2007). Pain-related anxiety-like behavior requires CRF1 receptors in the amygdala. *Mol. Pain* 3:13. doi: 10.1186/1744-8069-3-13

Ji, G., Horváth, C., and Neugebauer, V. (2009). NR2B receptor blockade inhibits pain-related sensitization of amygdala neurons. *Mol. Pain* 5:21. doi: 10.1186/1744-8069-5-21

Ji, G., Sun, H., Fu, Y., Li, Z., Pais-Vieira, M., Galhardo, V., et al. (2010). Cognitive impairment in pain through amygdala-driven prefrontal cortical deactivation. *J. Neurosci.* 30, 5451–5464. doi: 10.1523/JNEUROSCI.0225-10.2010

Ji, G., Yakhnitsa, V., Kiritoshi, T., Presto, P., and Neugebauer, V. (2018). Fear extinction learning ability predicts neuropathic pain behaviors and amygdala activity in male rats. *Mol. Pain* 14:1744806918804441. doi: 10.1177/1744806918804441

Ji, G., Zhang, W., Mahimainathan, L., Narasimhan, M., Kiritoshi, T., Fan, X., et al. (2017). 5-HT2C receptor knockdown in the amygdala inhibits neuropathic-pain-related plasticity and behaviors. *J. Neurosci.* 37, 1378–1393. doi: 10.1523/JNEUROSCI.2468-16.2016

Ji, Y., Rizk, A., Voulalas, P., Aljohani, H., Akerman, S., Dussor, G., et al. (2019). Sex differences in the expression of calcitonin gene-related peptide receptor components in the spinal trigeminal nucleus. *Neurobiol. Pain* 6:100031. doi: 10.1016/j.ynpai.2019.100031

Jiang, H., Fang, D., Kong, L. Y., Jin, Z. R., Cai, J., Kang, X. J., et al. (2014). Sensitization of neurons in the central nucleus of the amygdala *via* the decreased GABAergic inhibition contributes to the development of neuropathic pain-related anxiety-like behaviors in rats. *Mol. Brain* 7:72. doi: 10.1186/s13041-014-0072-z

Kato, F., Sugimura, Y. K., and Takahashi, Y. (2018). Pain-associated neural plasticity in the parabrachial to central amygdala circuit. *Adv. Exp. Med. Biol.* 1099, 157–166. doi: 10.1007/978-981-13-1756-9_14

Kim, H., Thompson, J., Ji, G., Ganapathy, V., and Neugebauer, V. (2017). Monomethyl fumarate (MMF) inhibits pain behaviors and amygdala activity in a rat arthritis model. *Pain* 158, 2376–2385. doi: 10.1097/j.pain.0000000000001042

Kiritoshi, T., Ji, G., and Neugebauer, V. (2016). Rescue of Impaired mGluR5-Driven endocannabinoid signaling restores prefrontal cortical output to inhibit pain in arthritic rats. *J. Neurosci.* 36, 837–850. doi: 10.1523/JNEUROSCI.4047-15.2016

Kolber, B. J., Montana, M. C., Carrasquillo, Y., Xu, J., Heinemann, S. F., Muglia, L. J., et al. (2010). Activation of metabotropic glutamate receptor 5 in the amygdala modulates pain-like behavior. *J. Neurosci.* 30, 8203–8213. doi: 10.1523/JNEUROSCI.1216-10.2010

Koltzenburg, M., Lundberg, L. E. R., and Torebjörk, H. E. (1992). Dynamic and static components of mechanical hyperalgesia in human hairy skin. *Pain* 51, 207–219. doi: 10.1016/0304-3959(92)90262-A

Kruger, L., Sternini, C., Brecha, N. C., and Mantyh, P. W. (1988). Distribution of calcitonin gene-related peptide immunoreactivity in relation to the rat central somatosensory projection. *J. Comp. Neurol.* 273, 149–162. doi: 10.1002/cne.902730203

Kulkarni, B., Bentley, D. E., Elliott, R., Julyan, P. J., Boger, E., Watson, A., et al. (2007). Arthritic pain is processed in brain areas concerned with emotions and fear. *Arthritis Rheum.* 56, 1345–1354. doi: 10.1002/art.22460

La, J. H., and Chung, J. M. (2017). Peripheral afferents and spinal inhibitory system in dynamic and static mechanical allodynia. *Pain* 158, 2285–2289. doi: 10.1097/j.pain.0000000000001055

Li, W., and Neugebauer, V. (2006). Differential changes of group II and group III mGluR function in central amygdala neurons in a model of arthritic pain. *J. Neurophysiol.* 96, 1803–1815. doi: 10.1152/jn.00495.2006

Liu, C. C., Ohara, S., Franaszczuk, P., Zagzoog, N., Gallagher, M., Lenz, F. A., et al. (2010). Painful stimuli evoke potentials recorded from the medial temporal lobe in humans. *Neuroscience* 165, 1402–1411. doi: 10.1016/j.neuroscience.2009.11.026

Liu, J., Hu, T., Zhang, M. Q., Xu, C. Y., Yuan, M. Y., Li, R. X., et al. (2021). Differential efferent projections of GABAergic neurons in the basolateral and central nucleus of amygdala in mice. *Neurosci. Lett.* 745:135621. doi: 10.1016/j.neulet.2020.135621

Liu, L., Karagoz, H., Herneisey, M., Zor, F., Komatsu, T., Loftus, S., et al. (2020). Sex differences revealed in a mouse CFA inflammation model with macrophage targeted nanotheranostics. *Theranostics* 10, 1694–1707. doi: 10.7150/thno.41309

Lu, Y. C., Chen, Y. Z., Wei, Y. Y., He, X. T., Li, X., Hu, W., et al. (2015). Neurochemical properties of the synapses between the parabrachial nucleus-derived CGRP-positive axonal terminals and the GABAergic neurons in the lateral capsular division of central nucleus of amygdala. *Mol. Neurobiol.* 51, 105–118. doi: 10.1007/s12035-014-8713-x

Mazzitelli, M., and Neugebauer, V. (2019). Amygdala group II mGluRs mediate the inhibitory effects of systemic group II mGluR activation on behavior and spinal neurons in a rat model of arthritis pain. *Neuropharmacology* 158:107706. doi: 10.1016/j.neuropharm.2019.107706

Mazzitelli, M., Marshall, K., Pham, A., Ji, G., and Neugebauer, V. (2021). Optogenetic manipulations of amygdala neurons modulate spinal nociceptive

processing and behavior under normal conditions and in an arthritis pain model. *Front. Pharmacol.* 12:668337. doi: 10.3389/fphar.2021.668337

Mazzitelli, M., Yakhnitsa, V., Neugebauer, B., and Neugebauer, V. (2022). Optogenetic manipulations of CeA-CRF neurons modulate pain- and anxiety-like behaviors in neuropathic pain and control rats. *Neuropharmacology* 210:109031. doi: 10.1016/j.neuropharm.2022.109031

McHugh, M. L. (2011). Multiple comparison analysis testing in ANOVA. *Biochem. Medica* 21, 203–209. doi: 10.11613/bm.2011.029

McLatchie, L. M., Fraser, N. J., Main, M. J., Wise, A., Brown, J., Thompson, N., et al. (1998). RAMPs regulate the transport and ligand specificity of the calcitonin-receptor-like receptor. *Nature* 393, 333–339. doi: 10.1038/30666

Medina, G., Ji, G., Grégoire, S., and Neugebauer, V. (2014). Nasal application of neuropeptide S inhibits arthritis pain-related behaviors through an action in the amygdala. *Mol. Pain* 10:32. doi: 10.1186/1744-8069-10-32

Miyazawa, Y., Takahashi, Y., Watabe, A. M., and Kato, F. (2018). Predominant synaptic potentiation and activation in the right central amygdala are independent of bilateral parabrachial activation in the hemilateral trigeminal inflammatory pain model of rats. *Mol. Pain* 14:1744806918807102. doi: 10.1177/1744806918807102

Mogil, J. S. (2020). Qualitative sex differences in pain processing: emerging evidence of a biased literature. *Nat. Rev. Neurosci.* 21, 353–365. doi: 10.1038/s41583-020-0310-6

Nakao, A., Takahashi, Y., Nagase, M., Ikeda, R., and Kato, F. (2012). Role of capsaicin-sensitive C-fiber afferents in neuropathic pain-induced synaptic potentiation in the nociceptive amygdala. *Mol. Pain* 8:51. doi: 10.1186/1744-8069-8-51

Nation, K. M., Felice, M., De Hernandez, P. I., Dodick, D. W., Neugebauer, V., Navratilova, E., et al. (2018). Lateralized kappa opioid receptor signaling from the amygdala central nucleus promotes stress-induced functional pain. *Pain* 159:919. doi: 10.1097/j.pain.0000000000001167

Navratilova, E., Ji, G., Phelps, C., Qu, C., Hein, M., Yakhnitsa, V., et al. (2019). Kappa opioid signaling in the central nucleus of the amygdala promotes disinhibition and aversiveness of chronic neuropathic pain. *Pain* 160:824. doi: 10.1097/j.pain.0000000000001458

Neugebauer, V. (2015). Amygdala pain mechanisms. *Handb. Exp. Pharmacol.* 227:261. doi: 10.1007/978-3-662-46450-2_13

Neugebauer, V. (2020). Amygdala physiology in pain. *Handb. Behav. Neurosci.* 26, 101–113. doi: 10.1016/b978-0-12-815134-1.00004-0

Neugebauer, V., and Li, W. (2003). Differential sensitization of amygdala neurons to afferent inputs in a model of arthritic pain. *J. Neurophysiol.* 89, 716–727. doi: 10.1152/jn.00799.2002

Neugebauer, V., and Weidong, L. I. (2002). Processing of nociceptive mechanical and thermal information in central amygdala neurons with knee-joint input. *J. Neurophysiol.* 87, 103–112. doi: 10.1152/jn.00264.2001

Neugebauer, V., Galhardo, V., Maione, S., and Mackey, S. C. (2009). Forebrain pain mechanisms. *Brain Res. Rev.* 60, 226–242. doi: 10.1016/j.brainresrev.2008.12.014

Neugebauer, V., Li, W., Bird, G. C., and Han, J. S. (2004). The amygdala and persistent pain. *Neuroscientist* 10, 221–234. doi: 10.1177/1073858403261077

Neugebauer, V., Li, W., Bird, G. C., Bhave, G., and Gereau IV, R. W. (2003). Synaptic plasticity in the amygdala in a model of arthritic pain: differential roles of metabotropic glutamate receptors 1 and 5. *J. Neurosci.* 23, 52–63. doi: 10.1523/JNEUROSCI.23-01-00052.2003

Neugebauer, V., Mazzitelli, M., Cragg, B., Ji, G., Navratilova, E., Porreca, F., et al. (2020). Amygdala, neuropeptides and chronic pain-related affective behaviors. *Neuropharmacology* 170:108052. doi: 10.1016/j.neuropharm.2020.108052

Ochoa, J. L., and Yarnitsky, D. (1993). Mechanical hyperalgesias in neuropathic pain patients: dynamic and static subtypes. *Ann. Neurol.* 33, 465–472. doi: 10.1002/ana.410330509

Okutsu, Y., Takahashi, Y., Nagase, M., Shinohara, K., Ikeda, R., Kato, F., et al. (2017). Potentiation of NMDA receptor-mediated synaptic transmission at the parabrachial-central amygdala synapses by CGRP in mice. *Mol. Pain* 13:1744806917709201. doi: 10.1177/1744806917709201

Paige, C., Plasencia-Fernandez, I., Kume, M., Papalampropoulou-Tsiridou, M., Lorenzo, L. E., David, E. T., et al. (2022). A female-specific role for calcitonin gene-related peptide (CGRP) in rodent pain models. *J. Neurosci.* 42, 1930–1944. doi: 10.1523/JNEUROSCI.1137-21.2022

Palazzo, E., Fu, Y., Ji, G., Maione, S., and Neugebauer, V. (2008). Group III mGluR7 and mGluR8 in the amygdala differentially modulate nocifensive and affective pain behaviors. *Neuropharmacology* 55:537. doi: 10.1016/j.neuropharm.2008.05.007

Palazzo, E., Marabese, I., Soukupova, M., Luongo, L., Boccella, S., Giordano, C., et al. (2011). Metabotropic glutamate receptor subtype 8 in the amygdala modulates thermal threshold, neurotransmitter release and rostral ventromedial medulla cell activity in inflammatory pain. *J. Neurosci.* 31, 4687–4697. doi: 10.1523/JNEUROSCI.2938-10.2011

Palmiter, R. D. (2018). The parabrachial nucleus: CGRP neurons function as a general alarm. *Trends Neurosci.* 41:280. doi: 10.1016/j.tins.2018.03.007

Paxinos, G., and Watson, C. (1998). *The Rat Brain in Stereotaxic Coordinates*. New York, NY: Academic Press.

Pedersen, L. H., Scheel-Krüger, J., and Blackburn-Munro, G. (2007). Amygdala GABA-A receptor involvement in mediating sensory-discriminative and affective-motivational pain responses in a rat model of peripheral nerve injury. *Pain* 127, 17–26. doi: 10.1016/j.pain.2006.06.036

Phelps, C. E., Navratilova, E., Dickenson, A. H., Porreca, F., and Bannister, K. (2019). Kappa opioid signaling in the right central amygdala causes hind paw specific loss of diffuse noxious inhibitory controls in experimental neuropathic pain. *Pain* 160, 1614–1621. doi: 10.1097/j.pain.0000000000001553

Pomrenze, M. B., Giovanetti, S. M., Maiya, R., Gordon, A. G., Kreeger, L. J., Messing, R. O., et al. (2019). Dissecting the roles of GABA and neuropeptides from rat central amygdala CRF neurons in anxiety and fear learning. *Cell Rep.* 29:13. doi: 10.1016/j.celrep.2019.08.083

Pomrenze, M. B., Millan, E. Z., Hopf, F. W., Keiflin, R., Maiya, R., Blasio, A., et al. (2015). A transgenic rat for investigating the anatomy and function of cortic otrophin releasing factor circuits. *Front. Neurosci.* 9:487. doi: 10.3389/fnins.2015.00487

Poyner, D. R., Sexton, P. M., Marshall, I., Smith, D. M., Quirion, R., Born, W., et al. (2002). International union of pharmacology. XXXII. The mammalian calcitonin gene-related peptides, adrenomedullin, amylin and calcitonin receptors. *Pharmacol. Rev.* 54, 233–246. doi: 10.1124/pr.54.2.233

Presto, P., Ji, G., Junell, R., Griffin, Z., and Neugebauer, V. (2021). Fear extinction-based inter-individual and sex differences in pain-related vocalizations and anxiety-like behaviors but not nocifensive reflexes. *Brain Sci.* 11:1339. doi: 10.3390/brainsci11101339

Presto, P., Mazzitelli, M., Junell, R., Griffin, Z., and Neugebauer, V. (2022). Sex differences in pain along the neuraxis. *Neuropharmacology* 210:109030. doi: 10.1016/j.neuropharm.2022.109030

Prut, L., and Belzung, C. (2003). The open field as a paradigm to measure the effects of drugs on anxiety-like behaviors: a review. *Eur. J. Pharmacol.* 463, 3–33. doi: 10.1016/s0014-2999(03)01272-x

Ren, W., and Neugebauer, V. (2010). Pain-related increase of excitatory transmission and decrease of inhibitory transmission in the central nucleus of the amygdala are mediated by mGluR1. *Mol. Pain* 6:93. doi: 10.1186/1744-8069-6-93

Ren, W., Kiritoshi, T., Grégoire, S., Ji, G., Guerrini, R., Calo, G., et al. (2013). Neuropeptide S: a novel regulator of pain-related amygdala plasticity and behaviors. *J. Neurophysiol.* 110, 1765–1781. doi: 10.1152/jn.00874.2012

Ren, W., Palazzo, E., Maione, S., and Neugebauer, V. (2011). Differential effects of mGluR7 and mGluR8 activation on pain-related synaptic activity in the amygdala. *Neuropharmacology* 61, 1334–1344. doi: 10.1016/j.neuropharm.2011.08.006

Ruau, D., Liu, L. Y., Clark, J. D., Angst, M. S., and Butte, A. J. (2012). Sex differences in reported pain across 11,000 patients captured in electronic medical records. *J. Pain* 13:228. doi: 10.1016/j.jpain.2011.11.002

Rudjito, R., Agalave, N. M., Farinotti, A. B., Lundbäck, P., Szabo-Pardi, T. A., Price, T. J., et al. (2021). Sex- and cell-dependent contribution of peripheral high mobility group box 1 and TLR4 in arthritis-induced pain. *Pain* 162:459. doi: 10.1097/j.pain.0000000000002034

Russo, A. F. (2015). Calcitonin gene-related peptide (CGRP): a new target for migraine. *Annu. Rev. Pharmacol. Toxicol.* 55:533. doi: 10.1146/annurev-pharmtox-010814-124701

Sarhan, M., Freund-Mercier, M. J., and Veinante, P. (2005). Branching patterns of parabrachial neurons projecting to the central extended amgydala: single axonal reconstructions. *J. Comp. Neurol.* 491, 418–442. doi: 10.1002/cne.20697

Schwaber, J. S., Sternini, C., Brecha, N. C., Rogers, W. T., and Card, J. P. (1988). Neurons containing calcitonin gene-related peptide in the parabrachial nucleus project to the central nucleus of the amygdala. *J. Comp. Neurol.* 270, 416–426. doi: 10.1002/cne.902700310

Seibenhener, M. L., and Wooten, M. C. (2015). Use of the open field maze to measure locomotor and anxiety-like behavior in mice. *J. Vis. Exp.* 52434:e52434. doi: 10.3791/52434

Seno, M. D. J., Assis, D. V., Gouveia, F., Antunes, G. F., Kuroki, M., Oliveira, C. C., et al. (2018). The critical role of amygdala subnuclei in nociceptive and depressive-like behaviors in peripheral neuropathy. *Sci. Rep.* 8:13608. doi: 10.1038/s41598-018-31962-w

Shansky, R. M., and Murphy, A. Z. (2021). Considering sex as a biological variable will require a global shift in science culture. *Nat. Neurosci.* 24, 457–464. doi: 10.1038/s41593-021-00806-8

Shimada, S., Inagaki, S., Kubota, Y., Kito, S., Funaki, H., Takagi, H., et al. (1989). Light and electron microscopic studies of calcitonin gene-related peptide-like immunoreactive terminals in the central nucleus of the amygdala and the bed nucleus of the stria terminalis of the rat. *Exp. Brain Res.* 77, 217–220. doi: 10.1007/BF00250584

Shingala, M. C., and Rajyaguru, A. (2015). Comparison of post hoc tests for unequal variance. *Int. J. New Technol. Sci. Eng.* 2, 22–33. Available online at: https://www.ijntse.com/upload/1447070311130.pdf.

Shinohara, K., Watabe, A. M., Nagase, M., Okutsu, Y., Takahashi, Y., Kurihara, H., et al. (2017). Essential role of endogenous calcitonin gene-related peptide in pain-associated plasticity in the central amygdala. *Eur. J. Neurosci.* 46:2149. doi: 10.1111/ejn.13662

Simons, L. E., Moulton, E. A., Linnman, C., Carpino, E., Becerra, L., Borsook, D., et al. (2014). The human amygdala and pain: evidence from neuroimaging. *Hum. Brain Mapp.* 35:527. doi: 10.1002/hbm.22199

Smith, R. A. (1971). The effect of unequal group size on Tukey's HSD procedure. *Psychometrika* 36, 31–34. doi: 10.1007/BF02291420.

Sorge, R. E., LaCroix-Fralish, M. L., Tuttle, A. H., Sotocinal, S. G., Austin, J. S., Ritchie, J., et al. (2011). Spinal cord toll-like receptor 4 mediates inflammatory and neuropathic hypersensitivity in male but not female mice. *J. Neurosci.* 31:15450. doi: 10.1523/JNEUROSCI.3859-11.2011

Sorge, R. E., Mapplebeck, J. C. S., Rosen, S., Beggs, S., Taves, S., Alexander, J. K., et al. (2015). Different immune cells mediate mechanical pain hypersensitivity in male and female mice. *Nat. Neurosci.* 18:1081. doi: 10.1038/nn.4053

Stucky, N. L., Gregory, E., Winter, M. K., He, Y. Y., Hamilton, E. S., McCarson, K. E., et al. (2011). Sex differences in behavior and expression of cgrp-related genes in a rodent model of chronic migraine. *Headache* 51, 674–692. doi: 10.1111/j.1526-4610.2011.01882.x

Sugimoto, M., Takahashi, Y., Sugimura, Y. K., Tokunaga, R., Yajima, M., Kato, F., et al. (2021). Active role of the central amygdala in widespread mechanical sensitization in rats with facial inflammatory pain. *Pain* 162, 2273–2286. doi: 10.1097/j.pain.0000000000002224

Sugimura, Y. K., Takahashi, Y., Watabe, A. M., and Kato, F. (2016). Synaptic and network consequences of monosynaptic nociceptive inputs of parabrachial nucleus origin in the central amygdala. *J. Neurophysiol.* 115:2721. doi: 10.1152/jn.00946.2015

Taves, S., Berta, T., Liu, D. L., Gan, S., Chen, G., Kim, Y. H., et al. (2016). Spinal inhibition of p38 MAP kinase reduces inflammatory and neuropathic pain in male but not female mice: sex-dependent microglial signaling in the spinal cord. *Brain. Behav. Immun.* 55, 70–81. doi: 10.1016/j.bbi.2015.10.006

Thompson, J. M., and Neugebauer, V. (2017). Amygdala plasticity and pain. *Pain Res. Manag.* 2017:8296501. doi: 10.1155/2017/8296501

Thompson, J. M., Ji, G., and Neugebauer, V. (2015). Small-conductance calcium-activated potassium (SK) channels in the amygdala mediate pain-inhibiting effects of clinically available riluzole in a rat model of arthritis pain. *Mol. Pain* 11:51. doi: 10.1186/s12990-015-0055-9

Thompson, J. M., Yakhnitsa, V., Ji, G., and Neugebauer, V. (2018). Small conductance calcium activated potassium (SK) channel dependent and independent effects of riluzole on neuropathic pain-related amygdala activity and behaviors in rats. *Neuropharmacology* 138:219. doi: 10.1016/j.neuropharm.2018.06.015

Tian, J., Yang, L., Wang, P., Yang, L., and Fan, Z. (2020). Exogenous CGRP regulates apoptosis and autophagy to alleviate traumatic brain injury through Akt/mTOR signalling pathway. *Neurochem. Res.* 45, 2926–2938. doi: 10.1007/s11064-020-03141-9

Vachon-Presseau, E., Centeno, M. V., Ren, W., Berger, S. E., Tétreault, P., Ghantous, M., et al. (2016). The emotional brain as a predictor and amplifier of chronic pain. *J. Dent. Res.* 95, 605–612. doi: 10.1177/0022034516638027

Vachon-Presseau, E., Roy, M., Martel, M. O., Albouy, G., Chen, J., Budell, L., et al. (2012). Neural processing of sensory and emotional-communicative information associated with the perception of vicarious pain. *Neuroimage* 63, 54–62. doi: 10.1016/j.neuroimage.2012.06.030

Veinante, P., Yalcin, I., and Barrot, M. (2013). The amygdala between sensation and affect: a role in pain. *J. Mol. Psychiatry* 1:9. doi: 10.1186/2049-9256-1-9

Wan, G., Yang, K., Lim, Q. E., Zhou, L., He, B. P., Wong, H. K., et al. (2010). Identification and validation of reference genes for expression studies in a rat model of neuropathic pain. *Biochem. Biophys. Res. Commun.* 400, 575–580. doi: 10.1016/j.bbrc.2010.08.106

Watabe, A. M., Ochiai, T., Nagase, M., Takahashi, Y., Sato, M., Kato, F., et al. (2013). Synaptic potentiation in the nociceptive amygdala following fear learning in mice. *Mol. Brain* 6:11. doi: 10.1186/1756-6606-6-11

Weera, M. M., Shackett, R. S., Kramer, H. M., Middleton, J. W., and Gilpin, N. W. (2021). Central amygdala projections to lateral hypothalamus mediate avoidance behavior in rats. *J. Neurosci.* 41:61. doi: 10.1523/JNEUROSCI.0236-20.2020

Wilson, T. D., Valdivia, S., Khan, A., Ahn, H. S., Adke, A. P., Gonzalez, S. M., et al. (2019). Dual and opposing functions of the central amygdala in the modulation of pain. *Cell Rep.* 29:332. doi: 10.1016/j.celrep.2019.09.011

Yajima, M., Sugimoto, M., Sugimura, Y. K., Takahashi, Y., and Kato, F. (2022). Acetaminophen and pregabalin attenuate central sensitization in rodent models of nociplastic widespread pain. *Neuropharmacology* 210:109029. doi: 10.1016/j.neuropharm.2022.109029

Yamamoto, S., Takahashi, Y., and Kato, F. (2021). Input-dependent synaptic suppression by pregabalin in the central amygdala in male mice with inflammatory pain. *Neurobiol. Pain* 10:100078. doi: 10.1016/j.ynpai.2021.100078

Yang, Y., Ozawa, H., Lu, H., Yuri, K., Hayashi, S., Nihonyanagi, K., et al. (1998). Immunocytochemical analysis of sex differences in calcitonin gene-related peptide in the rat dorsal root ganglion, with special reference to estrogen and its receptor. *Brain Res.* 791, 35–42. doi: 10.1016/s0006-8993(98)00021-3

Conflict of Interest: The authors declare that the research was conducted in the absence of any commercial or financial relationships that could be construed as a potential conflict of interest.

frontiers | Frontiers in Molecular Neuroscience

ORIGINAL RESEARCH
published: 13 June 2022
doi: 10.3389/fnmol.2022.913990

The Human *SCN9A*^{R185H} Point Mutation Induces Pain Hypersensitivity and Spontaneous Pain in Mice

Yaping Xue[1], Mélanie Kremer[2], Maria del Mar Muniz Moreno[1], Celeste Chidiac[1], Romain Lorentz[3], Marie-Christine Birling[3], Michel Barrot[2], Yann Herault[1,3†] and Claire Gaveriaux-Ruff[1,4*†]*

[1] Centre National de la Recherche Scientifique (CNRS), Institut de la Santé et de la Recherche Médicale (INSERM), Institut de Génétique et de Biologie Moléculaire et Cellulaire (IGBMC), Université de Strasbourg, Illkirch, France, [2] Centre National de la Recherche Scientifique (CNRS), Institut des Neurosciences Cellulaires et Intégratives (INCI), Université de Strasbourg, Strasbourg, France, [3] Centre National de la Recherche Scientifique (CNRS), Institut de la Santé et de la Recherche Médicale (INSERM), CELPHEDIA-PHENOMIN-Institut Clinique de la Souris, (PHENOMIN-ICS), Université de Strasbourg, Illkirch, France, [4] Centre National de la Recherche Scientifique (CNRS) UMR 7242, Université de Strasbourg, Illkirch, France

OPEN ACCESS

Edited by:
Fabien Marchand, INSERM U1107 Douleur et Biophysique Neurosensorielle (Neuro-Dol), France

Reviewed by:
James Cox, University College London, United Kingdom
David Bennett, University of Oxford, United Kingdom

***Correspondence:**
Yann Herault
herault@igbmc.fr
Claire Gaveriaux-Ruff
c.gaveriaux@unistra.fr

† These authors have contributed equally to this work

Specialty section:
This article was submitted to Pain Mechanisms and Modulators, a section of the journal Frontiers in Molecular Neuroscience

Received: *06 April 2022*
Accepted: *04 May 2022*
Published: *13 June 2022*

Citation:
Xue Y, Kremer M, Muniz Moreno MdM, Chidiac C, Lorentz R, Birling M-C, Barrot M, Herault Y and Gaveriaux-Ruff C (2022) The Human SCN9A^{R185H} Point Mutation Induces Pain Hypersensitivity and Spontaneous Pain in Mice. Front. Mol. Neurosci. 15:913990. doi: 10.3389/fnmol.2022.913990

The voltage-gated sodium channel Nav1.7 is encoded by *SCN9A* gene and plays a critical role in pain sensitivity. Several *SCN9A* gain-of-function (GOF) mutations have been found in patients with small fiber neuropathy (SFN) having chronic pain, including the R185H mutation. However, for most of these variants, their involvement in pain phenotype still needs to be experimentally elucidated. In order to delineate the impact of R185H mutation on pain sensitivity, we have established the *Scn9a*^{R185H} mutant mouse model using the CRISPR/Cas9 technology. The *Scn9a*^{R185H} mutant mice show no cellular alteration in the dorsal root ganglia (DRG) containing cell bodies of sensory neurons and no alteration of growth or global health state. Heterozygous and homozygous animals of both sexes were investigated for pain sensitivity. The mutant mice were more sensitive than the wild-type mice in the tail flick and hot plate tests, acetone, and von Frey tests for sensitivity to heat, cold, and touch, respectively, although with sexual dimorphic effects. The newly developed bioinformatic pipeline, Gdaphen is based on general linear model (GLM) and random forest (RF) classifiers as well as a multifactor analysis of mixed data and shows the qualitative and quantitative variables contributing the most to the pain phenotype. Using Gdaphen, tail flick, Hargreaves, hot plate, acetone, cold plate, and von Frey tests, sex and genotype were found to be contributing most to the pain phenotype. Importantly, the mutant animals displayed spontaneous pain as assessed in the conditioned place preference (CPP) assay. Altogether, our results indicate that *Scn9a*^{R185H} mice show a pain phenotype, suggesting that the *SCN9A*^{R185H} mutation identified in patients with SFN having chronic pain contributes to their symptoms. Therefore, we provide genetic evidence for the fact that this mutation in Nav1.7 channel plays an important role in nociception and in the pain experienced by patients with SFN who have this mutation. These findings should aid in exploring further pain treatments based on the Nav1.7 channel.

Keywords: *SCN9A*, sodium channel, nociception, pain, spontaneous pain, data analysis, statistical modeling, Gdaphen

INTRODUCTION

Painful small fiber neuropathy (SFN) is a disorder of Aδ-fibers and C-fibers characterized by neuropathic pain symptoms and autonomic complaints. Several common diseases, such as diabetes mellitus and HIV have been reported to complicate SFN (Themistocleous et al., 2014; Cazzato and Lauria, 2017). The Nav1.7 channel is a voltage-gated sodium channel that plays a critical role in the generation and conduction of action potentials and is thus important for electrical signaling exhibited by the most excitable cells. It is preferentially expressed in the peripheral nervous system within sensory dorsal root ganglia (DRG) and sympathetic ganglia neurons (Black et al., 2012; Kanellopoulos et al., 2018; Cummins et al., 2020). Interestingly, gain-of-function (GOF) mutations in the *SCN9A* gene encoding for the α-subunit of Nav1.7 sodium channel have been identified in 5% of patients with painful idiopathic SFN (Waxman et al., 2014; Eijkenboom et al., 2019). However, the phenotype of these patients is complex and the impact of Nav1.7 channel mutations on these patients remains to be clarified. Faber et al. (2012) found the heterozygous c.554G > A, p.R185H mutation in the *SCN9A* gene of two unrelated patients with painful SFN (Faber et al., 2012). This mutation resulted in the hyperexcitability of rat DRG neurons when transfected into these neurons (Han et al., 2012). Later, the same mutation was also found to be associated with painful diabetic peripheral neuropathy (Blesneac et al., 2018). On the opposite, *SCN9A* loss-of-function bi-allelic mutations are known to result in congenital insensitivity to pain (CIP) while the mono-allelic carriers have normal pain sensitivity (Bennett et al., 2019; McDermott et al., 2019).

In order to explore the Nav1.7-R185H genotype-phenotype association and the underlying mechanisms for Nav1.7-R185H sodium channel mutation in idiopathic SFN, we have created a *Scn9a*^{R185H} mouse model and characterized this model for nociceptive behavior. This mouse line was generated using the CRISPR/Cas9 technology. We found that *Scn9a*^{R185H} mRNA and protein were both expressed at comparable levels in the mutant mice as wild-type (wt) control mice. Pain sensitivity of the mutant mouse line was investigated using behavioral tests of sensitivity to thermal and mechanical stimuli and in an ongoing spontaneous pain model. As sex is known to be an important variable in pain (Sadler et al., 2022), pain behavior was evaluated in both sexes. Our results indicate that the *Scn9a*^{R185H} mice show a pain phenotype, suggesting that the *SCN9A*^{R185H} mutation identified in patients with SFN contributes to their pain symptoms. Therefore, altogether we provide genetic evidence for the fact that the *SCN9A*-encoded Nav1.7 channel plays a crucial role in pain behavior.

MATERIALS AND METHODS

Animals

Experimental Subjects and Ethical Approval

Animal experiments were performed in agreement with the EC directive, 2010/63/UE86/609/CEE and in compliance with the animal Welfare policies of the French Ministry of Agriculture (law 87 848) and with protocols approved by local ethical committees (Com'Eth, « Comité d'Ethique pour l'Expérimentation Animale IGBMC-ICS », with the agreement number 20880; or CREMEAS). C57BL/6NCrl mice were used for the mutant line generation, and C57BL/6NCrl was the genetic background throughout the study. The number of mice that were used followed the 3R principles. Mice were bred at the ICS animal facility and the behavioral experiments were performed at «Institut de Génétique et de Biologie Moléculaire et Cellulaire» (IGBMC), at the « Chronobiotron UMS3415 » and at « Institut des Neurosciences Cellulaires et Intégratives » (INCI) (see Section below). The mice were housed under a 12-h/12-h light/dark cycle (lights on at 7 a.m.) and at 21 ± 1°C, 55 ± 10% humidity condition. Food and autoclaved tap water were available *ad libitum*. Each cage housed 2–5 mice. All mice were habituated to the experimental environment.

Establishment of the Genetic Animal Model

The *Scn9a*^{R185H} mouse line was generated by using the CRISPR/Cas9 system. The CRISPOR online software was used to select high specificity-score sgRNAs with a low number of predicted off-target sequences. A single-stranded oligonucleotide was used that contained the CGT to CAT change encoding for the R185H mutation with 2 additional silent mutations, one to mutate the PAM sequence and the other to generate a new *Bsp*HI diagnostic restriction site (**Figure 1A**). Before injecting sgRNAs into eggs, the efficiency of sgRNA was tested *in vitro* on the targeted DNA by polymerase chain reaction (PCR). After checking sgRNA efficiency *in vitro*, sgRNA, Cas9, and ssODN were microinjected into the cytoplasm and into the pronucleus of the fertilized oocytes of C57BL/6NCrl. The surviving embryos were implanted into the oviducts of pseudo-pregnant CD1 mice. Resulting pups were screened by PCR followed by *Bsp*HI digestion to detect the expected mutation (R185H) and T7 endonuclease to detect indels. Potential founders were identified and were confirmed by Sanger sequencing. Selected founders were bred with wt C57BL/6NCrl mice to generate F1 heterozygous animal. All F1 mice were analyzed for their confirmed genotype by Sanger Sequencing to establish the *Scn9a*^{R185H} mouse line. These mice were also checked for off-target effects, by using the PCR primers described in **Supplementary Table 1**. Thereafter, the F1 founder (53-11) was backcrossed with C57BL/6NCrl wt mice for four generations to generate the *Scn9a*^{R185H} mutant line containing mutant and wt mice of both sexes for further experiments. Finally, heterozygous *Scn9a*$^{+/R185H}$ males and females were crossed to generate *Scn9a*$^{+/+}$ (wt), heterozygous *Scn9a*$^{+/R185H}$ (het), and homozygous *Scn9*$^{R185H/R185H}$ (homo) mice. This breeding strategy led to 24.2% wt, 50.5% het, and 25.3% homo individuals.

Determination of Genotype

Genotype was determined from tail biopsies on 10-day old pups. Crude genomic DNA was extracted by DirectPCR Lysis Reagent-Tail (Viagen Biotech, Cat # 101-T) according to the manufacturer's instructions. Phusion Hot Start II High-Fidelity DNA polymerase kit (Thermo Scientific) was used. The PCR reaction contained 5 μl of diluted genomic DNA, 4 μl of 5 × Phusion HF Buffer, 0.4 μl of dNTP mix (dATP, dCTP, dGTP,

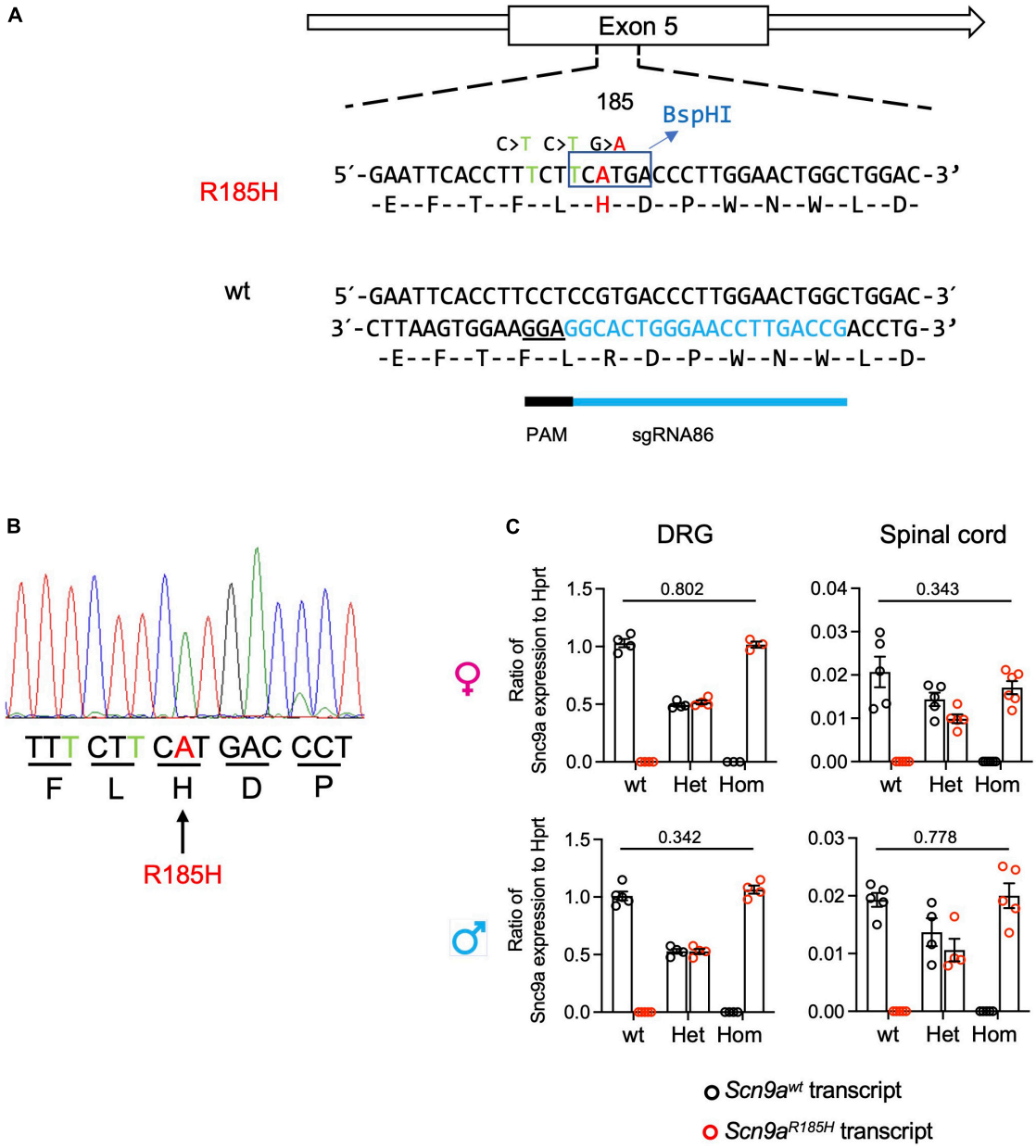

FIGURE 1 | Generation of *Scn9a*^{R185H} mutant mice and *Scn9a* transcript expression in wild-type (wt) and mutant mice. **(A)** Scheme for *Scn9a* targeting strategy. The sgRNA86 guide RNA and protospacer adjacent motif (PAM) are shown. The ssODN contained three basic mutations including two silent mutations and one-point mutation. The first silence mutation, C > T was PAM mutation designed to avoid Cas9 recut. The second mutation, C > T, was designed for *Bsp*HI enzyme restriction site for genotyping. The third G > A mutation was designed to get the R185H found in human patients. **(B)** Mutant allele sequence characterized through Sanger sequencing of F0 founder DNA. The silence-mutated nucleotides are indicated in green and targeted point mutant nucleotide in red. **(C)** *Scn9a* micro-RNA (mRNA) expression in dorsal root ganglia (DRG) and spinal cord, of wt and *Scn9a*^{R185H} mutant mice of both sexes. There was no significant effect of genotype. DRG. females: wt $n = 4$; Het $n = 4$; Homo $n = 3$; males: wt $n = 5$; Het $n = 4$; Homo $n = 4$; Spinal cord. Females: wt $n = 5$; Het $n = 5$; Homo $n = 6$; males: wt $n = 5$; Het $n = 4$; Homo $n = 5$. Scn9a transcript expression was normalized to *Hprt* expression. Results are shown as means ± SEM. Two-tailed unpaired *t*-test for wt allele transcript expression in wt mice vs. mutant allele transcript expression in homozygous mutant mice. Refer to **Supplementary Table 5** for statistics.

and dTTP at 10 mM, Thermo Scientific), 2 μl of each primer at 0.5 nM, and 0.2 μl of Phusion polymerase and H_2O in a total volume of 20 ml. PCRs were done under the following conditions: 98°C for 30 s followed by 30 cycles of 98°C for 8 s, 62°C for 30 s, and 72°C for 1 min and a final elongation step for 5 min at 72°C in a T100 thermocycler (Bio-Rad). Ten microliters of PCR product were then digested in a final volume of 20 μl added to 0.2 μl of *Bsp*HI enzyme and 2 μl of enzyme buffer. PCR outcome was analyzed on a 2% agarose gel. Information about primer sequences is shown in **Supplementary Table 2**.

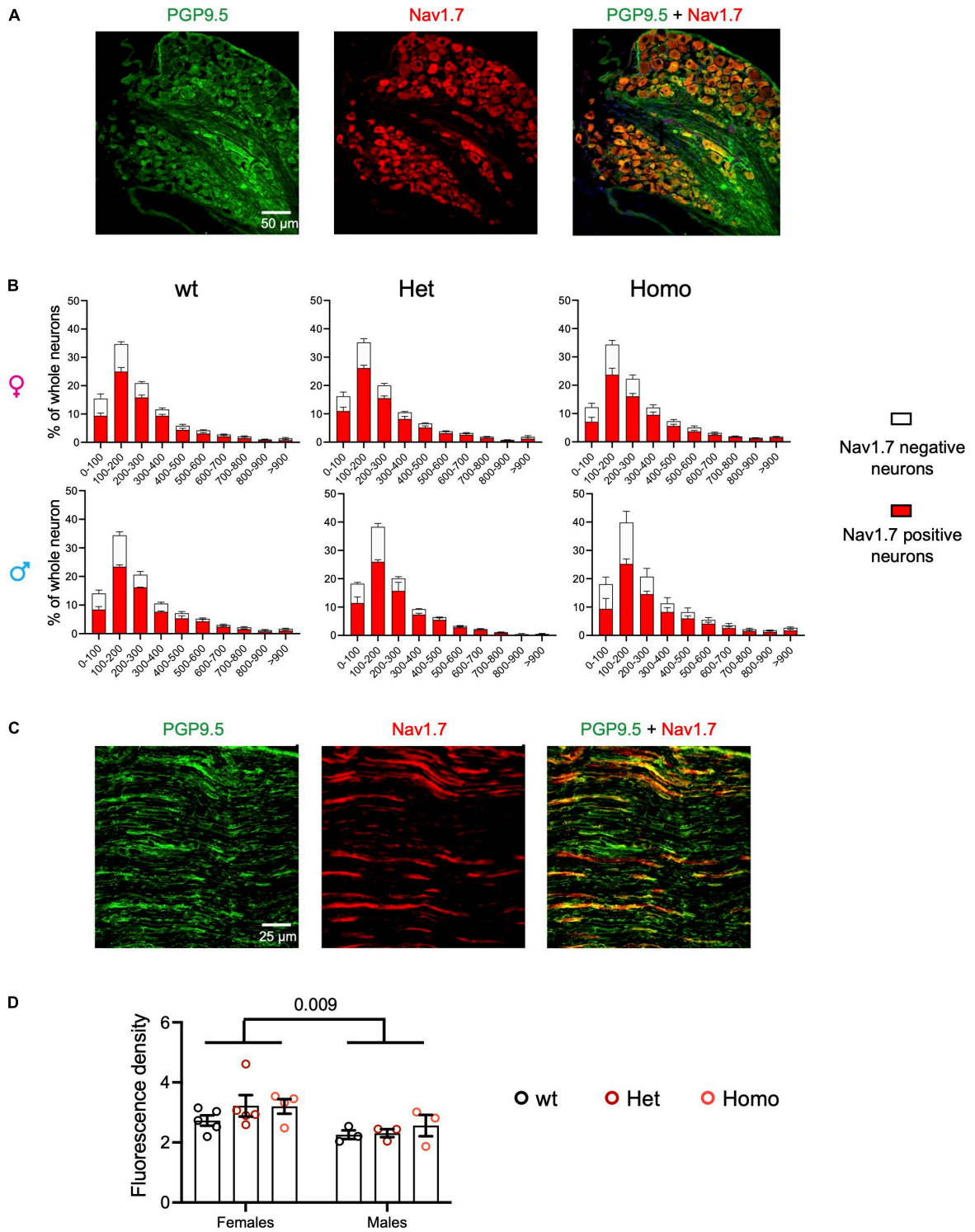

FIGURE 2 | Nav1.7 protein expression of DRG and sciatic nerve in *Scn9a*^{R185H} mutant mice. **(A)** Representative images of PGP9.5 (green) and Nav1.7 (red) fluorescent immunostaining for all neurons (PGP9.5-positive) and Nav1.7-positive neurons in lumbar DRG of wt animals. Scale bar 50 μm. **(B)** Size distribution for Nav1.7-positive (red) and negative (white) neuron cross-sectional areas in *wt,* het, and homo female and male mice. Females: $n = 5$/group; male: $n = 3$/group. Results are shown as means ± SEM. The two-way ANOVAs for genotype and neuron size effects in each sex showed a size effect and no genotype effect. **(C)** Representative images of fluorescent PGP9.5 (green) and Nav1.7 (red) immunostaining of sciatic nerves of *wt* animals. Scale bar of 25 μm. **(D)** Mean fluorescence density Nav1.7 immunostaining of sciatic nerves in wt, het, and homo female and male mice. Females, $n = 4$–5/group; males, $n = 3$/group. Results are shown as means ± SEM. The two-way ANOVA for genotype and sex indicated a sex effect and no genotype effect. The *P* value of 0.009 is for sex effect. See **Supplementary Table 6** for statistics.

Determination of Transcript Expression by Reverse Transcriptase Digital Droplet Polymerase Chain Reaction

The DRGs from both sides, the spinal cord, and half brain, were collected from the mutant and wt mice and flash-frozen in liquid nitrogen. All samples were disrupted with Precellys® CK14 Lysing Kit in TRIzol Reagent, and the total RNA was purified using the RNeasy Fibrous Tissue Mini Kit (Qiagen) according to the manufacturer's instructions. The quality of the samples was checked using an Agilent 2100 Bioanalyzer (Agilent Technologies). Complementary DNA (cDNA) synthesis was performed using the SuperScript™ VILO™ cDNA Synthesis Kit (Invitrogen). Digital droplet PCR (ddPCR) was performed in 20 μL reactions containing 1 × ddPCR Supermix for probes (No dUTP), 250 nM of each probe, 900 nM of specific primers, and 50 ng of DNA according to the manufacturer's recommendations (PCR conditions: 10 min at 95°C, 40 cycles of 30 s at 94°C, 30 s at 55°C, and 10 min at 98°C), in a QX200 Droplet Digital PCR System (Bio-Rad) and analyzed by QuantaSoft Software (Bio-Rad). Sequences of probes and primers are shown in **Supplementary Table 3**.

Histological Analysis

Tissue Preparation

Mice were anesthetized with ketamine/xylazine and perfused intracardially with 40 ml of phosphate buffer saline (PBS) with 0.1 M pH 7.4 followed by 4% of paraformaldehyde (PFA) in PBS with 0.1 M pH 7.4. Both sides of L4 to L6 lumbar DRG and sciatic nerve samples were dissected out and post-fixed for overnight at 4°C in 4% of PFA in PBS, thereafter cryoprotected at 4°C in 30% of sucrose in PB for 3–7 days, embedded in optimal cutting temperature (OCT) medium, frozen, and kept at −80°C. DRG (8 μm thick) and sciatic nerves (10 μm thick) were longitudinally cut with a cryostat and kept at −20°C.

Immunohistochemistry

Light antigen retrieval was performed in 0.1 M of PB with pH 7.3, 0.2% of hydrogen peroxide, and 0.05% of Triton X-100 for 25 min at room temperature (RT). Sections were then washed twice in PBS and incubated in a blocking solution of tris-buffered saline (TBS) with 0.05% of Tween 20, 2% of bovine serum albumin (BSA), and 2% of normal donkey serum (NDS) for 1 h before applying primary antibodies overnight at 4°C. The following primary antibodies (diluted in the blocking solution) were used: Rabbit anti-SCN9A-ATTO Fluor-663 antibody (1:100, ASC-008-FR, Alomone Labs, Jerusalem, Israel), Mouse anti-PGP9.5 antibody (1:200, ab8189, Abcam, Cambridge, United Kingdom), and rabbit anti-PGP9.5 (1:500, ab108986, Abcam). For the detection of the primary antibody, secondary antibody raised in donkey and conjugated with Alexa-647 fluorophore was used (1:500, Molecular Probes, Fisher Scientific, Illkirch, France) for 1 h at RT. DAPI staining (1:2000, Molecular Probes, Thermofisher, Illkirch, France) was performed at the same time as in the secondary antibody. Sections were then washed twice with PBS then placed on superfrost glass slides. One drop of Immu-Mount (Fisher Scientific, Illkirch, France) was added over the tissue sections and a coverglass was placed over the slide.

Image Acquisition and Analysis

Dorsal root ganglia and sciatic nerve images were acquired with the Leica fluorescence microscope using a 20 × (DRG) and 40 × (sciatic nerves) dry objective, the 20 × and 40 × resolution were achieved with a digital zoom factor. Image acquisitions in the sequential mode (single excitation beams: 405, 488, and 633 nm) were used for marker co-localization to avoid potential crosstalk between the different fluorescence emissions. Images were acquired with the LCS (Leica) software using randomly selected sections. The ImageJ software cell counter (approximately 4 non-adjacent sections per condition and per animal) was used to count on-screen neurons expressing a given fluorescent marker manually and blindly. Only neurons from L4 to L6 DRGs with a visible nucleus were considered. Cells expressing a given fluorescence were analyzed separately. During the analysis, we recorded all cross-sectional areas of cell profiles for Nav1.7 positive and negative neurons in PGP9.5-positive total neurons, that were categorized to different sizes based on their area. Sciatic nerves were analyzed for fluorescence density by using the same Nav1.7 and PGP9.5 antibodies, by applying a threshold of fluorescence detection. The mean of fluorescence density (total fluorescence density/area) was calculated to determine the Nav1.7 fluorescence.

Behavioral Characterization

A series of behavioral experiments were conducted on mutants and wt littermates in order to evaluate the nociceptive behavior and motor condition. All behavioral tests were done between 9:00 a.m. and 5:00 p.m. Animals were transferred to the experimental room 30 min before each experimental test. The behavioral tests were performed in the following order: String test, crenelated bar, von Frey, Hargreaves Plantar, tail flick, tail pressure, hot plate, acetone test, cold plate, and odor habituation and discrimination. Mice were tested at 2-month-age. Between two nociceptive tests, there was a gap of at least 2 days. Both females and males of the different genotypes were analyzed. The behavioral analysis was done with an experimenter who was unaware of the genotype of the mouse.

String Test

The grip string test (home-made) was used to measure the muscle strength. The equipment used was a wire stretched horizontally 40 cm above a table. The time required for a forelimb-hanging mouse to gain hindlimb traction as latency was measured, with 20 s cutoffs. Three consecutive trials were done by 5 min intervals.

Crenelated Bar

The notched/crenelated bar test was used for motor coordination and balance. The method described by Carter et al. (2001) was used. Briefly, mice were kept on an elevated crenelated bar and they had to traverse a distance from far away to a distance closer to the home cage. Thereafter, the time to traverse the whole crenelated bar were recorded.

Odor Habituation and Discrimination

This test is adapted from the one described by Duchon et al. (2011). Briefly, mice were placed 5 times for 2 min in a small cage (22 cm × 15 cm). Perforated tubes containing a small piece of Whatman paper soaked with orange flower water were placed in the center of each cage. The time of sniffing was recorded on six trials of 2 min each with the orange flower extract. Thereafter, the orange flower extract was replaced by vanilla extract for the last trial. Inter-trial time ranged from 8 to 10 min. The time spent on sniffing the odors was recorded.

Hot Plate

Hot plate response refers to the method reported by Huang et al. (2019). Mice were habituated on the plate (reference BIO-HC1.00, Bioseb, Vitrolles, France) at RT one day before the test. Mice were placed on the plate at 48, 52, and 56°C with respective cutoff times to avoid tissue damage: 2 min for 48°C, 1 min for 52°C, and 30 s for 56°C. The latency to the first hindlimb reaction and to jump as well as the coping reactions (flicking, licking, and jumping) were recorded until cutoff.

Tail Flick

The tail flick test was performed at Panlab (L7306, Panlab, Bioseb, Vitrolles, France) as described by Weibel et al. (2013). Mice were habituated for 30 min in the procedure room prior to test. During the test, mice were wrapped into 50 ml tube with the whole tail exposed. Three different distances from the tail tip were tested for the reaction to the light beam. The mean of these three measurements of latency was calculated.

Hargreaves Plantar

The Hargreaves Plantar test (Bioseb, Vitrolles, France) was used to quantify the responses of mice to noxious heat at the hind paw by applying a radiant infrared heat stimulus (Weibel et al., 2013). Before the test, the mice were habituated to the glass plate in bottom-opened transparent plexiglass boxes (7 × 9 × 7 cm) so that withdrawal latencies could be clearly determined, usually taking 30 to 45 min. A radiant heat beam was positioned underneath the paws of the mice. The withdrawal latencies were recorded for both right and left hind paws. The time between testing the first and the second paw was at least 5 min. For each mouse, the response assays were tested for a maximum of 4 times. The means of all measurements of both hind paws were calculated.

Thermal Gradient Ring

The analysis of thermal preference in mice was performed with the thermal gradient ring (UgoBasile, Gemonio, Italy) (Touska et al., 2016) at INCI. All mice were adapted to the equipment on day 1 with the ring adjusted to RT for 30 min. Mice were recorded on day 2 for 4 consecutive periods of 15 min for a total of 60 min using the 15–40°C ring gradient. Behavior was videotaped with camera and analyzed with the ANY-maze Software (V5, UgoBasile. Gemonio, Italy). Temperature preference was calculated as the percent of time spent above the surface at a given temperature. Temperature preference was averaged for each 15-min period. The temperature preference over the first 30 min was calculated as the mean of temperature preference from the first two 15-min periods.

Acetone Test

The acetone test was performed to evaluate the behavioral response to cooling as described by Deuis et al. (2017). Mice were placed and habituated in bottom-opened transparent plexiglass boxes (7 × 9 × 7 cm) on a mesh grid floor. One day before the test, the mice were habituated to the boxes for 1 h. On the day of testing, the mice were allowed to habituate for 30 min and then 10 μL of acetone was applied to the center of the plantar surface of each hind paw. Acetone was applied on three successive testing sessions for each paw. The interval between each application was at least 5 min. The number of flicking and licking of affected paw were counted for 30 s after acetone application. The duration of these paw reactions was also recorded.

Cold Plate

The cold plate assay (Bioseb, Vitrolles, France) was used to assess the sensitivity of the mice to the cold 5°C temperature as described by Reiss et al. (2021). One day before the test, the animals were habituated to the plate at RT in transparent plastic boxes as described above. A 5-min cutoff time was used. The number of hind paw lifts and their duration were recorded on each paw and the mean per animal was calculated.

Von Frey Test

The evaluation of sensitivity to touch by the von Frey test was performed on different cohorts at IGBMC (I) or INCI (II). At IGBMC, mice were placed in the same transparent plastic boxes and habituated as described for the acetone test. A series of eight von Frey filaments (with the bending force of 0.008 to 2 g) (Bioseb, Vitrolles, France) was applied to the hind paw using the up-and-down method. Each paw was scored on two successive testing sessions. The withdrawal threshold was calculated by the Excel program generously provided by A. Basbaum (University of California San Francisco). The mean of the sensitivity of the two hind paws was calculated. At INCI, the mechanical threshold of hind paw withdrawal was evaluated using von Frey hairs (Aniphy Vivo-Tech, Salon-de-Provence, France). Mice were placed in clear Plexiglas boxes (7 × 9 × 7 cm) on an elevated mesh screen. After a habituation time of around 10 min, the filaments were applied to the plantar surface of each hind paw in a series of ascending forces (0.6 to 8 grams). Each filament was applied five times per paw, being applied until it just bent, and the threshold was defined as 3 or more withdrawals observed out of the 5 trials. The mean of the sensitivity of the two hind paws was calculated.

Tail Pressure

A gradually increasing pressure was applied to the tail using the equipment Pressure AnalgesiMeter (Ugo Basile, Italy) as previously done by Weibel et al. (2013). The tail withdrawal threshold was recorded for each mouse in three successive testing sessions, with a 500 g cutoff.

Conditioned Place Preference

All experiments were conducted by using the single trial conditioned place preference (CPP) protocol at INCI as

previously described by Barthas et al. (2015). The apparatus (Imetronic, Pessac, France) consists of 3 Plexiglas chambers separated by manually operated doors. Two chambers (size 15 cm × 24 cm × 33 cm) distinguished by the texture of the floor and by the wall patterns are connected by a central chamber (size 15 cm × 11 cm × 33 cm). On the first, second, and third days (pre-conditioning), the animals were free to explore the apparatus during 30 min, and the time spent in each chamber was recorded to control for the lack of spontaneous preference for one compartment. Animals spending more than 75% or less than 25% of the total time in one chamber were excluded from the study. On the 4th day (conditioning), the animals were intrathecally injected with either saline solution (10 μL in the morning) or clonidine solution (10 μL in the afternoon) and restricted in one chamber during 15 min, switching the chamber between the morning and the afternoon. The delay between the two injections was 4 h. On the 5th day, the animals were free to explore the 3 chambers and the time spent in each chamber was recorded for 30 min.

Dark-Light Test

The anxiety-like behavior was evaluated with the dark-light test (Vogt et al., 2016) at INCI with a two-compartment testing box (18 cm × 18 cm × 14.5 cm). One compartment was brightly illuminated (1,500 lux), whereas the other was dark. Mice were placed in the dark compartment at the beginning of the test, and the time spent in the lit compartment was recorded for 5 min.

Forced Wimming Test

This test was performed at INCI to evaluate despair-like behavior (Porsolt et al., 1977). The mice were lowered into a glass cylinder (height 17.5 cm, diameter 12.5 cm) containing 11.5 cm of water (23–25°C). The test duration was 6 min, and since only little immobility is usually observed during the first 2 min, the duration of immobility was quantified during the last 4 min of the test. The mice were considered to be immobile when they floated upright in the water, with only minor movements to keep its head above the water.

Gdaphen Analysis for the Identification of the Variables Contributing the Most to the Genotype or Sex Discrimination

The Gdaphen R pipeline was applied for the identification of the major variables contributing to the genotype or sex discrimination as described previously by Chidiac et al. (2021). Gdaphen is a public R package (Muniz et al., available on github https://github.com/munizmom) developed to identify the explanatory variables from the experimental data. We considered 18 variables, genotype, and sex as well as the following 16 behavioral variables: hot plate 48°C latency to the first response (s), hot plate 48°C latency to jump (s), hot plate 48°C coping reactions (nb), hot plate 52°C latency to the first response (s), hot plate 52°C latency to jump (s), hot plate 52°C coping reactions (nb), hot plate 56°C latency to the first response (s), hot plate 56°C latency to jump (s), hot plate 56°C coping reactions (nb), tail-flick latency (s), Hargreaves latency (s), acetone duration of paw reactions (s), acetone paw reactions (nb), cold plate 5°C paw lifts (nb), von Frey threshold (g), and tail pressure threshold (g). The analysis included the identification of the variables contributing the most to the genotype or sex discrimination by using two classifiers, the supervised algorithm generalized linear model (GLM) and the unsupervised algorithm, random forest (RF). The weight of each individual variable and the overall weight for each test was predicted and visualized by using multiple factor analysis (MFA).

Statistical Analysis

Results are expressed as means ± SEM. Statistical analyses were performed using GraphPad Prism 9 software. Results were analyzed using two-tailed unpaired Student's *t*-test to assess differences between two groups for normally distributed data or by Mann–Whitney test if the data did not pass the normality test. Genotype and age effects, and genotype and sex effects were analyzed using two-way ANOVA. The genotype effect in each sex was analyzed by one-way ANOVA followed by Dunnett's multiple comparison test, when appropriate. A *P*-value less than 0.05 was considered as statistically significant. The detailed statistics are presented in **Supplementary Tables 6–14**. *P*-values for genotype differences are shown in figures when significant or close to significance.

RESULTS

Generation and Characterization of *Scn9a*^{R185H} Mutant Mice

The $Scn9a^{R185H}$ mouse line was generated by using the CRISPR/Cas9 technology. After checking sgRNA validity *in vitro*, different concentrations of sgRNA, Cas9, and ssODN were microinjected into eggs. Sixty F0 mice born were screened by PCR. The different product sizes found by gel analysis suggested a variety of alleles that were confirmed by Sanger sequencing (refer to **Supplementary Figure 1**). Several F0 individuals showed point mutation and high mosaicism in both alleles. Finally, five potential F0 founders were used to cross with C57BL/6NCrl wt mice to generate F1 founders. We successfully got germline transmission to the F1 generation (**Figure 1B**). We selected the F1 animal 53-11 to establish the $Scn9a^{R185H}$ mouse line. There has been much concern raised in the scientific community over the specificity of the CRISPR/Cas9 system. Therefore, we analyzed several predicted off-target sites that were based on the number of mismatches to the target sequences and the homologous genes by the CRISPR design tool.[1] No evidence of Cas9-mediated deletions or base-pair changes in any of the seven mostly predicted off-target sites (**Supplementary Table 4**) was found after comparing with wt sequences in Ensembl genome database[2] (**Supplementary Figure 2**). Thereafter, the heterozygous F1 (53-11) was used as the founder to generate the $Scn9a^{R185H}$ mutant line.

When evaluating *Scn9a* transcript expression in the $Scn9a^{R185H}$ mice, the two-way ANOVA showed a strong

[1] http://crispor.tefor.net/crispor.py

[2] http://www.ensembl.org/index.html

effect of genotype, and there was no effect of sex on expression in both the DRG and spinal cord. $Scn9a^{wt}$ and $Scn9a^{R185H}$ transcripts were equally expressed in the DRG and spinal cord of wt and homozygous mutant mice, respectively, and in both sexes (**Figure 1C** and **Supplementary Table 5**). Heterozygous animals expressed 50% wt and 50% mutant transcript alleles. Globally, these results show that *Scn9* transcripts are expressed equally in the mutant and wt mice, suggesting that the $Scn9a^{R185H}$ mutation does not impact on *Scn9a* transcript expression.

Nav1.7 Protein Expression in Dorsal Root Ganglia and Sciatic Nerves of $Scn9a^{R185H}$ Mice

The impact of the $Scn9a^{R185H}$ mutation on $NA_V1.7$/SCN9A protein expression was analyzed in the DRG and sciatic nerves by immunofluorescent staining of Nav1.7, together with labeling neurons with PGP9.5. The SCN9A protein was found expressed in 78.4 ± 3.4% of neurons in wt and mutant DRGs and with a comparable profile according to cell-size distribution (**Figures 2A,B** and **Supplementary Table 6**). The size distribution of all DRG neurons was also similar in the three genotypes, with most neurons of small and medium size, as expected. No genotype difference was detected (**Supplementary Figure 3** and **Supplementary Table 6**), indicating that the mutation did not impact on neuron size distribution. Sciatic nerves were analyzed for fluorescence density of Nav1.7 and of PGP9.5 protein as a nerve marker (**Figure 2C**) and Nav1.7 density was compared in wt and mutant mice of both sexes. The two-way ANOVA showed a sex effect and no genotype effect, with females expressing globally more Nav1.7 in sciatic nerves than males (**Figure 2D** and **Supplementary Table 6**). Overall, these results indicate that Nav1.7 protein is expressed similarly in mutant and wt mice, suggesting that the *Scn9a*-R185H mutation does not alter Nav1.7 protein expression.

Normal Body Weight and Motor Function in $Scn9a^{R185H}$ Mice

First, as *Scn9a* deletion in hypothalamic neurons was reported to disrupt body weight regulation (Branco et al., 2016), we measured body weight in mutant mice on a weekly basis from week 1 to week 31 of age. There was no difference between mutant and wt animals for body weight (**Supplementary Figure 4A**). To determine whether muscle strength and motor coordination were affected in the mutant line, string test and crenelated bar tests were performed. As shown by two-way ANOVA, there was no effect of genotype and sex for both string test and crenelated bar test. Therefore, no major signs of behavioral abnormalities were found in mutant mice in these tests (**Supplementary Figure 4B**). Previous studies on *Scn9a* loss-of-function models showed that Nav1.7 was necessary for pain sensation (Xue et al., 2021) and was also an essential requirement for odor perception in both mice and humans (Weiss et al., 2011). We then assessed the olfactory function using an odor habituation and discrimination test in mutant mice. We found that the homozygous females had lower sniffing time in the first trial as compared to wt controls while all other parameters including the response of a new olfactory stimulus were comparable in mutant and wt animals, indicating that $Scn9a^{R185H}$ mutants had a normal odor discrimination capacity (**Supplementary Figure 4C**).

Enhanced Heat Pain Sensitivity in $Scn9a^{R185H}$ Mice

The two heterozygous patients with R185H having chronic pain were a man and a woman, respectively, who had abnormal warm pain sensation even when they were 23–24-year-old (Faber et al., 2012). To investigate whether the R185H mutation alters heat pain sensitivity in mutant mice, we tested mutants of both sexes on the hot plate at 48, 52, and 56°C, respectively, as well as in the tail flick, Hargreaves plantar tests, and thermal preference tests (**Figure 3**). First, on the hot plate, there was no genotype or sex effect for the first response latencies at the three temperatures (**Figure 3A** and **Supplementary Table 7**). We also analyzed the jump latencies of the $Scn9a^{R185H}$ line. The two-way ANOVA revealed an effect of sex at 52°C and an effect of sex as well as an interaction between sex and genotype at 56°C. At this temperature, the homozygous females had shorter jump latency as compared to their wt counterparts (**Figure 3B** and **Supplementary Table 7**). Until recently, only the latency to the first hind paw response or to jump were used as outcomes for the hot plate test. Still, in 2019, it was found that mutant mice lacking spinal preprotachykinin-positive neurons had normal first response latency on the hot plate but had reduced coping reactions (Huang et al., 2019), indicating that defensive reactions that limit injury may constitute valuable measures of pain. Therefore, we scored coping reactions (number of flicks, licks, and jumps) in addition to the first response and jump latencies. At 48°C, there was no effect of genotype or sex in the two-way ANOVA (**Figure 3C** and **Supplementary Table 7**). At 52°C, there was a trend for genotype effect as analyzed by two-way ANOVA, a genotype effect in females as shown by one-way ANOVA, and increased coping reactions in homozygous females. At 56°C, both genotype and sex effects were evidenced by two-way ANOVA, with a trend toward more coping reactions in homozygous males (**Figure 3C** and **Supplementary Table 7**). The mutant mice were also tested for their sensitivity to a radiant heat stimulus in the tail flick and Hargreaves plantar tests. In the tail flick test, the mutant females were found to be more sensitive than wt controls, with shorter reaction latencies (**Figure 3D** and **Supplementary Table 8**), while male mutants had no phenotype. In the Hargreaves test, no effect of genotype or sex was found (**Figure 3E** and **Supplementary Table 8**). Additionally, the mutant animals were evaluated in the thermal gradient ring, a novel device that allows for the analysis of thermal preference. Thermal preference was tested at non-noxious temperatures ranging from 15 to 40°C. In this setting, wt males showed a plateau-shaped temperature preference at 26.4–30.9°C which was comparable in male mutants, and wt females showed a peak-like preference for 35.5°C which did not statistically differ in mutant females (**Figure 3F**, **Supplementary Figure 5**, and **Supplementary Table 9**). Overall, the mutant animals, especially females were

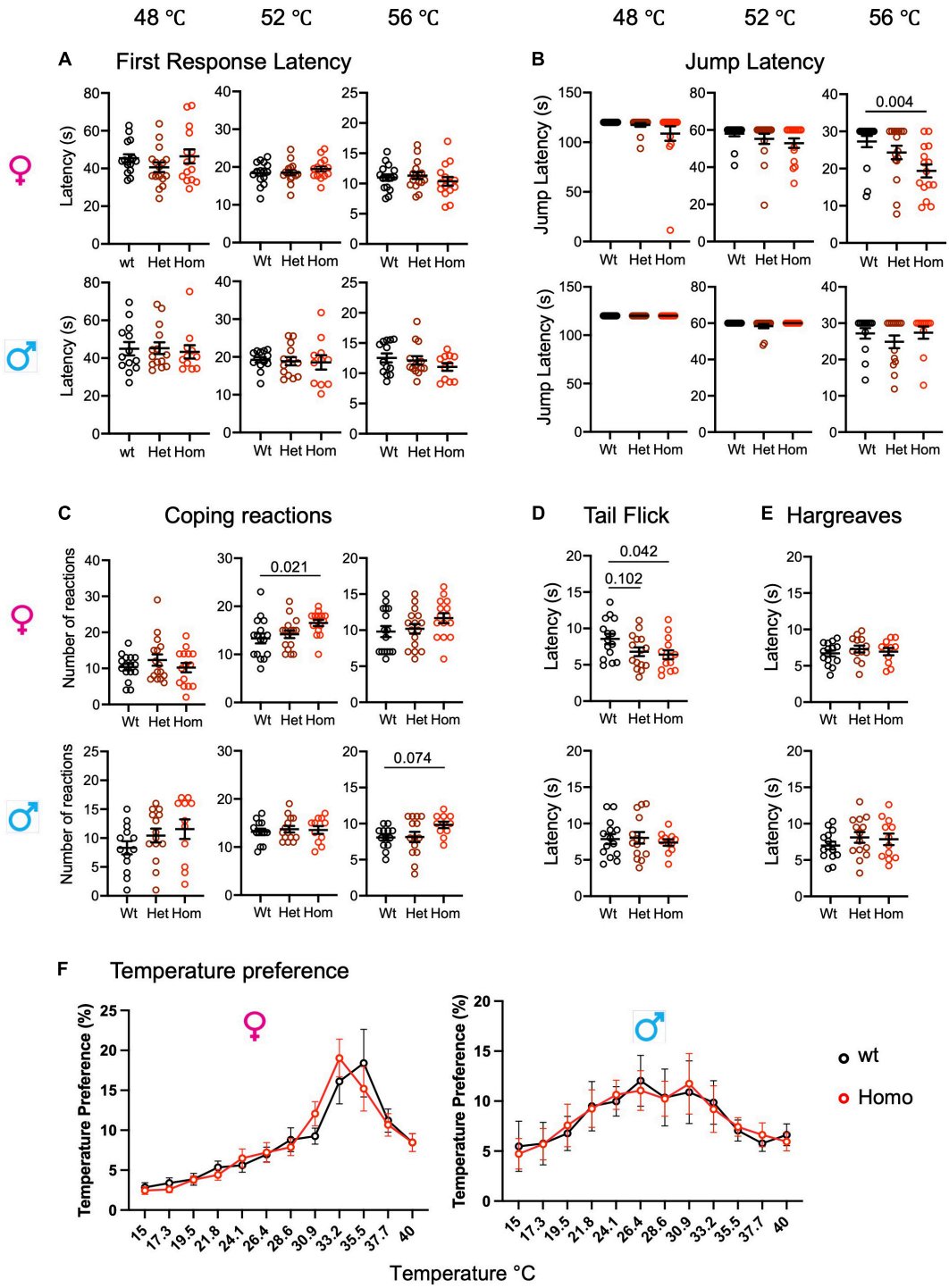

FIGURE 3 | Enhanced heat pain sensitivity in *Scn9a*^{R185H} mice. **(A)** Wild-type and *Scn9a*^{R185H} mice showed comparable first response latency on the hot plate. **(B)** Homozygous *Scn9a*^{R185H} females had decreased jump latency in 56°C Hot Plate. **(C)** Homozygous *Scn9a*^{R185H} female mice showed more coping reactions on the 52°C hot plate. **(D)** Heterozygous and homozygous *Scn9a*^{R185H} females had lower tail latency in the tail flick test. **(E)** No difference was found between wt and mutant mice in the Hargreaves test. **(F)** Control wt and mutant mice showed the same temperature preference. Results are shown as means ± SEM. Hot plate, females: wt, $n = 16$; Het, $n = 16$; Homo, $n = 15$; males: wt, $n = 13$; Het, $n = 14$; Homo, $n = 11$. Tail flick: females: wt, $n = 15$; Het, $n = 15$; Homo, $n = 14$; males: wt, $n = 14$; Het, $n = 14$; Homo, $n = 11$. Hargreaves: females: wt, $n = 14$; Het, $n = 13$; Homo, $n = 11$; males: wt, $n = 14$; Het, $n = 14$; Homo, $n = 11$. Temperature preference: females: wt, $n = 12$; Homo, $n = 12$; males: wt, $n = 11$; Homo, $n = 11$. One-way ANOVA on females and males and Dunnett's multiple comparison tests for hot plate, tail flick, and Hargreaves tests; two-way ANOVA for the thermal preference ring test. *P*-values for genotype difference are shown when significant or close to significance. See **Supplementary Tables 7–9** for statistics.

more sensitive to noxious heat in the tail flick test and in the hot plate assay at the highest temperatures for jump latency and coping reactions.

Sensitivity to Cool and Cold Stimuli in Scn9a^{R185H} Mice

To determine whether *Scn9a*^{R185H} mutants had altered cold sensation, we performed the acetone and cold plate tests for assessing the reactions to cool (12∼15°C) and cold (5°C) stimuli. In the acetone test, the two-way ANOVA showed a strong effect of sex and an effect of genotype for both the number and the duration of paw reactions. The genotype effect was confirmed for males by one-way ANOVA on separate sexes (**Supplementary Table 10A**). As shown in **Figures 4A,B**, homozygous mutant males showed increased paw reaction duration as compared to wt controls indicating a hypersensitivity to cool temperatures. In the cold plate test, the two-way ANOVA for the number of paw lifts evidenced no sex effect and a trend for genotype effect which did not reach significance in the one-way ANOVA on separate sexes (**Figure 4C** and **Supplementary Table 10B**). Overall, the *Scn9a*^{R185H} mutant mice showed an increased sensitivity to cool temperatures.

Scn9a^{R185H} Mice Are More Sensitive to Touch Stimuli

In order to evaluate mechanical sensitivity in *Scn9a* mutant mice, the von Frey and tail pressure tests were applied as models for touch and noxious mechanical stimuli. For the von Frey test, the two-way ANOVAs showed the effect of genotype, with both homo females and males showing enhanced sensitivity (**Supplementary Figure 6A** and **Supplementary Table 11**). In the tail pressure test, wt and *Scn9a*^{R185H} mice had similar sensitivity thresholds (**Figure 4E** and **Supplementary Table 11**).

Gdaphen Analysis for the Identification of the Variables Contributing the Most to the Genotype or Sex Discrimination

We analyzed how much each behavioral variable could discriminate between the three genotypes (wt, heterozygous noted as het, and homozygous noted as homo) and between the two sexes. To perform the Gdaphen analysis, we considered 18 variables in total, genotype, sex, and 16 behavioral variables. Among these 18 variables, 6 were detected as the most relevant ($>$ 30%) to discriminate among the 3 genotypes. These variables were sex, von Frey threshold, cold plate paw lifts, number of paw reactions, and paw reaction duration in the acetone test and tail flick latency. For discriminating between the three genotypes, the GLM classifier identified the von Frey threshold, cold plate paw lifts, and the number of paw reactions in the acetone test as the major variables discriminating between the three genotypes following a linear gene dosage effect. Instead, the RF classifier found von Frey threshold and the number and duration of paw reactions in the acetone test as the most discriminating parameters (**Figure 5A**). Interestingly sex dimorphism was shown to be contributing to the homozygous genotype discrimination by RF. For sex discrimination, GLM and RF (**Figure 5B**) identified paw reaction duration in the acetone test as the most important variable, followed by Hargreaves threshold. In addition, GLM identified von Frey threshold and cold plate paw lifts as important discriminant variables and RF identified tail pressure. The 3D-PCA plots (**Figure 5C**) show the clustering of individual animals in the 3D space based on PCA analyses performed with all the phenotypic variables and colored them based on the genotype and sex. A clear genotype clustering can be seen in the left panel showing the three genotypes and two-sex individuals, in the middle plot for female data only, and in the right plot for male data. As can be seen in **Figure 5D**, based on the qualitative variable discrimination 2D component map, the genotype effect was stronger than the sex effect for the correct clustering of individuals. Furthermore, the PCA component 1 was mostly explaining the variability accounting to the wt and homozygous genotypes and the component 3 denotes the heterozygous genotype. Dimension 2 was strongly explaining the sex effect in females and males. Finally, all three PCA components explained the variability accounting to the genotype and von Frey variables, components 2 and 1 for sex, component 1 for behavior in the acetone and tail flick tests, and components 2 and 3 for cold plate (**Figure 5E**).

The *Scn9a*^{R185H} Mice Show Spontaneous Ongoing Pain

In order to assess the presence of ongoing pain in *Scn9a*^{R185H} mice, we employed a CPP test. This assay is based on the positive reinforcement provided by the non-rewarding analgesic, clonidine. Animals with ongoing pain prefer the compartment where they received clonidine as compared to the compartment where they got the saline control solution.

The three-way ANOVA showed an interaction between the genotype, solutionpaired chamber (saline vs clonidine), and trial (pre-test vs. test) in both males and females (**Figure 6** and **Supplementary Table 12**). Additional two-way ANOVA of time spent in the clonidine-paired chamber compared to the saline-paired chamber in pre-test vs. test trials showed a strong treatment effect (clonidine vs. saline) in homozygous animals and not in wt animals, of both sexes (**Figure 6** and **Supplementary Table 12**).

The wt mice showed no preference for either compartment, while homozygous mice of both sexes preferred the clonidine-paired chamber. These results indicate the presence of ongoing pain in both female and male homozygous mutants.

Influence of Sex on Pain Behavioral Responses in Wild-Type Animals

For all pain behavioral tests, the effects of both mutation and sex have been analyzed by two-way ANOVAs as described above. In order to better apprehend the influence of sex on these pain responses, the behavior of wt females and males was compared (refer to **Supplementary Figure 7** and **Supplementary Table 13**). This shows that, concerning the heat modality, wt females tend to be more sensitive than wt males on the 56°C hot plate for the first response latency and coping reactions (**Supplementary Figures 7A,B**), and equally sensitive for all

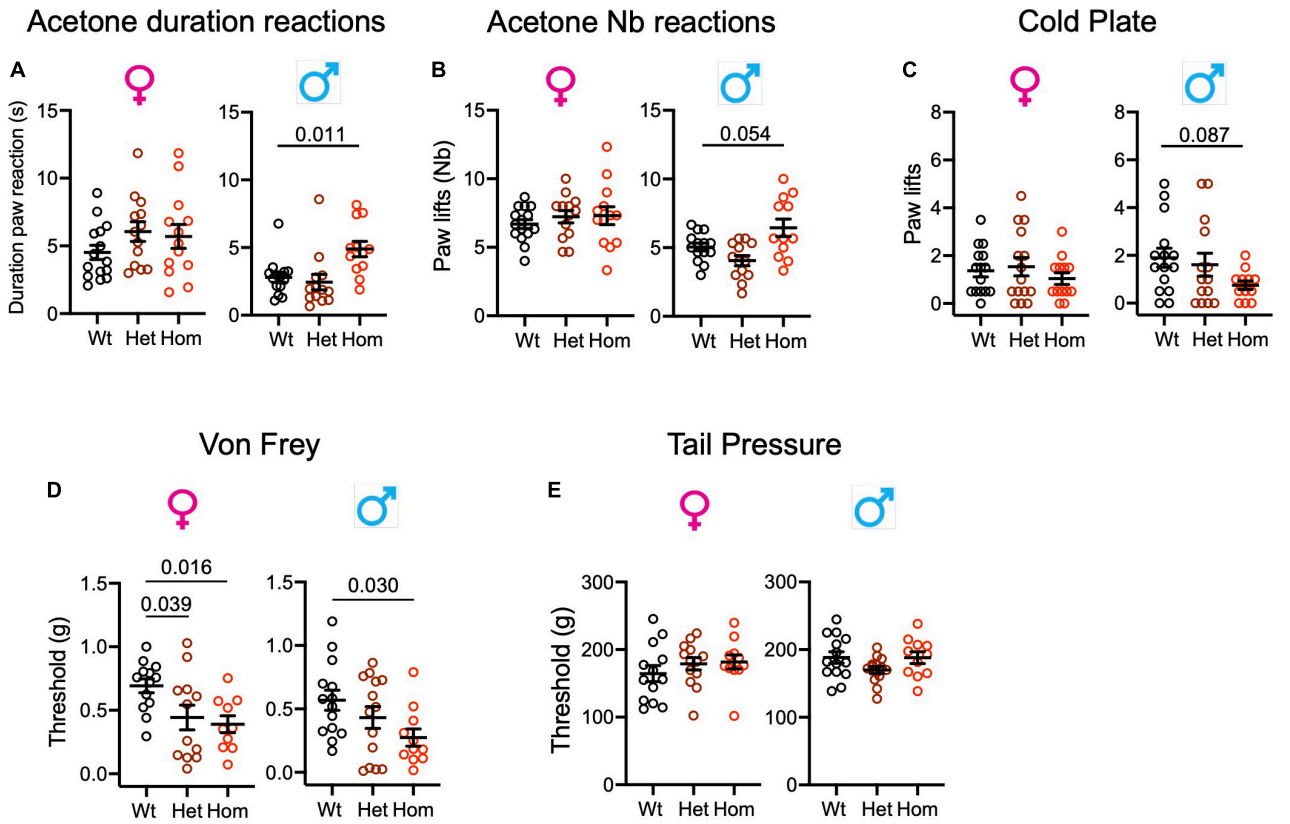

FIGURE 4 | *Scn9a*^{R185H} mice show enhanced sensitivity to cooling and touch stimuli. **(A,B)** Homozygous mutant males show increased duration and number of paw reactions in the acetone test. **(C)** Male mutant mice show a trend to reduced number of paw lifts on the cold plate. **(D)** Mutant mice display lower sensitivity threshold in the von Frey test. **(E)** Mutant mice show no difference to wt mice in the tail pressure test. Results are shown as means ± SEM. Acetone duration of paw reactions and number of paw reactions: females: wt, $n = 15$; Het, $n = 13$; Homo, $n = 13$; males: wt, $n = 14$; Het, $n = 13$; Homo, $n = 12$. Cold plate: females: wt, $n = 15$; Het, $n = 15$; Homo, $n = 13$; males: wt, $n = 15$; Het, $n = 14$; Homo, $n = 12$. Von Frey: females: wt, $n = 13$; Het, $n = 13$; Homo, $n = 10$; males: wt, $n = 14$; Het, $n = 14$; Homo, $n = 11$. Tail pressure: females: wt, $n = 13$; Het, $n = 13$; Homo, $n = 11$; males: wt, $n = 14$; Het, $n = 14$; Homo, $n = 11$. One-way ANOVA on females and males and Dunnett's multiple comparison tests. *P*-values for genotype difference are shown when significant or close to significance. See **Supplementary Tables 10, 11** for statistics.

other hot plate parameters and in the tail flick and Hargreaves models (**Supplementary Figures 7A–D**). The wt females and males showed a different temperature preference profile in the thermal gradient ring (**Supplementary Figure 7E**). For sensitivity to cool temperatures, wt females showed longer durations of paw reactions as compared to males in the acetone test, and no sex influence was detected in the cold plate assay (**Supplementary Figures 7F,G**). In response to non-noxious mechanical stimulation as assessed by the von Frey test, wt females were shown to be more sensitive than wt males in the INCI institute (**Supplementary Figure 7H**). Regardless of this sex difference, homozygous mutant animals of both sexes were found more sensitive than their wt counterparts, indicating that the *Scn9a*^{R185H} mutation has a strong impact on sensitivity to touch. No sex difference in the sensitivity to pressure was detected in wt animals (**Supplementary Figure 7I**).

When spontaneous pain was evaluated in the CPP, the two-way ANOVA showed no clonidine-paired chamber preference in wt animals (**Supplementary Figure 7J**), indicating the absence of spontaneous pain. Also, no sex bias for the time spent in the clonidine-paired chamber as compared to the saline-paired chamber was found. The spontaneous pain evidenced in mutants of both sexes thus suggests that the *Scn9a*^{R185H} mutation induces pain in both males and females which is not paired to a sex susceptibility in wt animals.

The *Scn9a*^{R185H} Mice Do Not Show Anxio-Depressive Behavioral Consequences of Chronic Pain

The homozygous *Scn9a*^{R185H} mutants were evaluated for the anxio-depressive consequences of chronic pain in two classical paradigms, the light-dark box for anxiety-like behavior and the forced-swim test for despair-like behavior. The mutants behaved comparably to their wt counterparts when analyzed in the light-dark box (**Supplementary Figure 6B** and **Supplementary Table 14**). Similarly, mutant mice spent similar immobility time as their wt controls in the forced-swim test (**Supplementary Figure 6C** and **Supplementary Table 14**). These results suggest that the *Scn9a*^{R185H} mutation alters sensitivity to thermal and

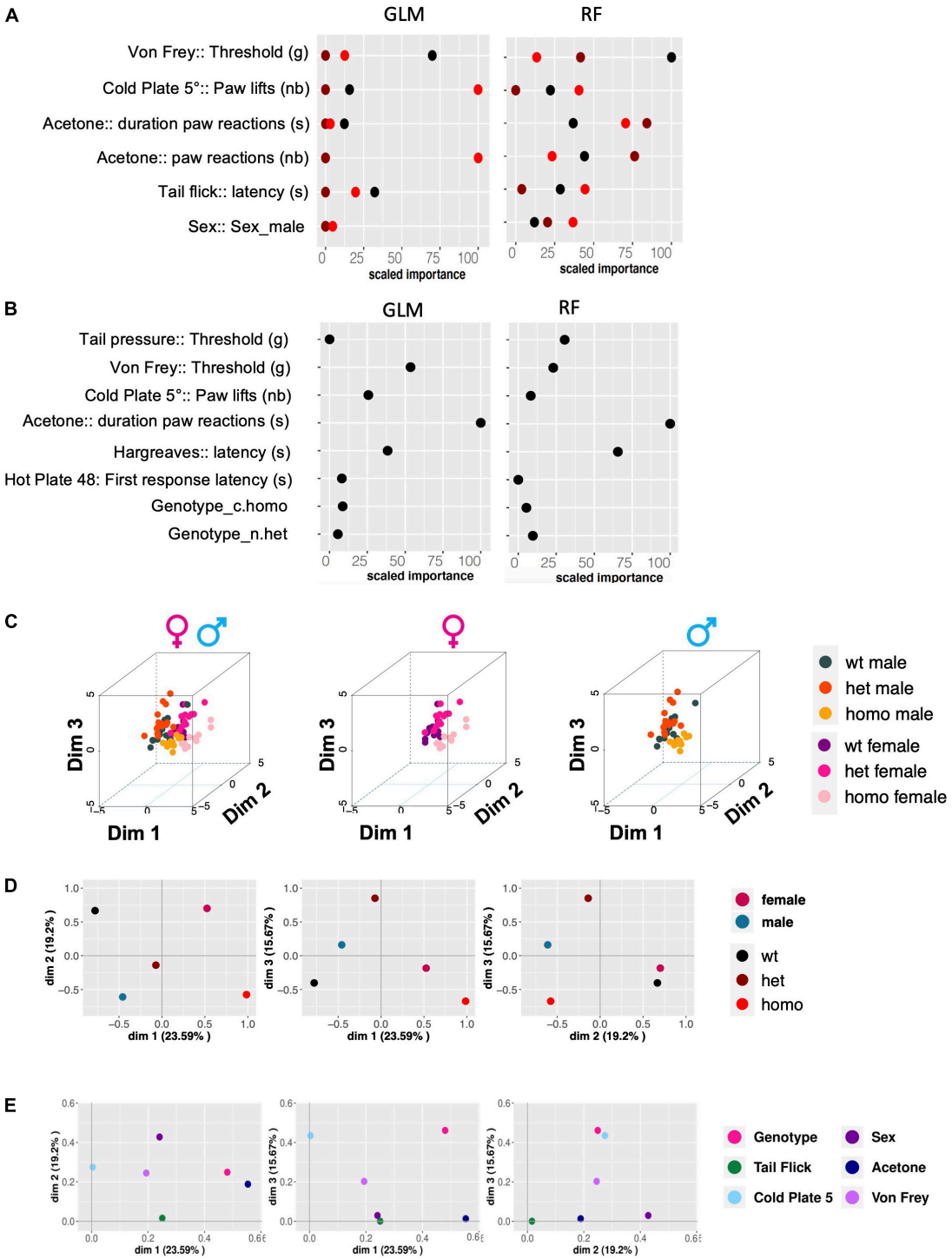

FIGURE 5 | Gdaphen analyses to identify the variables contributing the most to genotype and sex discrimination. **(A)** Identification of the power of each explanatory phenotypic variable to the genotype discrimination. GLM, Generalized Linear Model; RF, Random Forest. The explanatory variables selected were the ones found to contribute more than a 30% to the genotype discrimination. **(B)** Identification of the power of the explanatory phenotypic variables contributing to more than 30% to the genotype discrimination, analyzed to see for different responses based on sex and using the two different statistical GLM and RF classifiers. **(C)** 3D-PCA plots showing the individual animals clustering in 3D space based on PCA analyses performed with all the phenotypic variables and colors based on the genotype and sex. Left panel shows individuals of both sexes, the middle plots female data, and the right plot male data. **(D,E)** The qualitative variable discrimination component maps show the distribution in 2D space of the qualitative variables coordinates calculated based on PCA analysis performed with the multifactor analysis of mixed data (MFA). In panel **(D)**, the variables female, male, wt, het, and homo are represented. In panel **(E)**, the variables genotype, sex, tail flick, acetone, cold plate, and von Frey are shown.

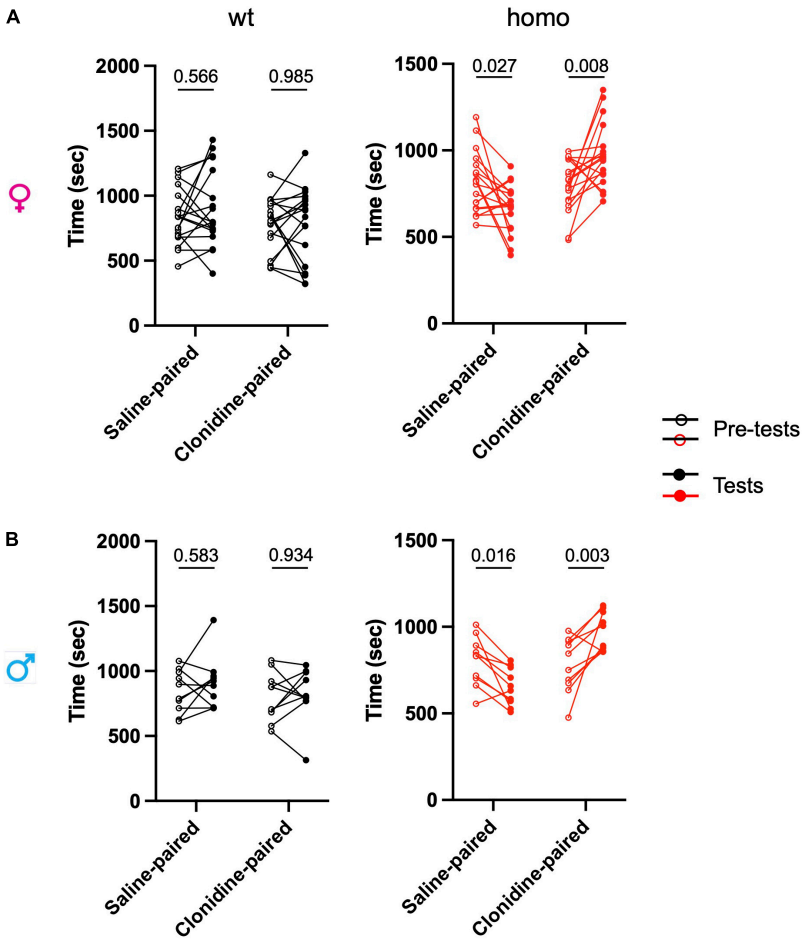

FIGURE 6 | *Scn9a*^{R185H} mutant mice show spontaneous ongoing pain. Ongoing pain was assessed in a conditioned place preference test. After pre-test/habituation for chamber preference on days 1 to 3, conditioning was made on day 4 by intrathecal treatment with either saline solution in the morning or clonidine solution in the afternoon with a restriction in one chamber. On day 5, the animals were free to explore the chambers and the time spent in each chamber was recorded for 30 min. **(A)** Females. **(B)** Males. The time spent in each chamber before conditioning (pre-test) and after conditioning with clonidine or saline (test) are shown. Homozygous mice of both sexes spent more time in clonidine-paired chamber while wt mice spent on average equal time in saline-paired and clonidine-paired chambers. Dots represent individual data points. females: wt, $n = 18$; Homo, $n = 18$; males: wt, $n = 10$; Homo, $n = 10$. Two-way ANOVA for treatment and trial (pretest and test) on each genotype and sex group, Sidak's multiple comparison test. $P =$ values for comparing pre-test and test values are shown. Refer to **Supplementary Table 12** for statistics.

mechanical stimuli and produces spontaneous ongoing pain but does not induce anxiodepressive-like consequences along the tests used in this study.

DISCUSSION

In this study, we successfully established, by using the CRISPR-Cas9 technique, the *Scn9a*^{R185H} mutant mouse line as a model for the human *SCN9A*^{R185H} mutation found in patients with SFN having chronic pain. The wt control mice highly expressed *Scn9a* mRNA in DRG and less in spinal cord, in agreement with previous findings. No alteration of *Scn9a* mRNA or protein expression level was detected in *Scn9a*^{R185H} mutant mice, suggesting that the behavioral changes in mutants may not be attributed to alterations in Nav1.7 expression. Our results indicate that *Scn9a*^{R185H} mice show a pain phenotype in a mutation-dosage dependent manner, suggesting that the *Scn9a*^{R185H} mutation identified in patients with SFN having chronic pain contributes for their pain symptoms. This is confirmed in a different species, the *SCN9A*^{R185H} mutation, as a pathogenic mutation.

Three patients with *SCN9A*^{R185H} having chronic pain had decreased intraepidermal nerve fibers density (IENFD). Although IENFD still remains to be investigated in *Scn9a*^{R185H} mice, the impact of the mutation was investigated on both DRGs and sciatic nerves. Size distribution of DRG neurons was similar in the three genotypes, indicating that the mutation did not induce a selective loss of small size DRG neurons. In addition, the density of PGP9.5 and Nav1.7 labeling was comparable in sciatic nerves of all three genotypes, suggesting that the mutation did not lead to a decrease in sciatic fibers. This is the first description of sensory neurons in the *Scn9a*^{R185H} GOF mutant mice, while DRG and sciatic nerves cannot be

investigated in patients and healthy individuals. Taken globally, the R185H mutation produced neuron hyperexcitability when transfected *in vitro* into rat DRG neurons (Han et al., 2012) and, when introduced in mice, leading to no obvious sensory nerve damage, an increased sensitivity in several pain tests and ongoing spontaneous pain. On the other hand, another mutation found in patients with chronic pain having reduced IENFD, the $SCN9A^{I228M}$ mutation, also led to DRG neuron hyperexcitability *in vitro* but to no neuropathy and no pain behavior phenotype when introduced into mice (Chen et al., 2021). The $SCN10A^{G1662S}$ mutation found in pain patients with normal IENFD did produce hyperexcitability when transfected into DRG neurons (Han et al., 2014; Xiao et al., 2019) as well as normal IENFD and increased pain sensitivity in $Scn10a^{G1663S}$ mice (Chidiac et al., 2021). Therefore, the comparison of these data on the three mutations indicates no strict correlation between *in vitro* hyperexcitability of DRG neurons, neuropathy, and pain phenotype of mutant mice. A difference between patients with chronic pain and the *in vitro* and *in vivo* animal models described above resides in different time courses, in terms of days, weeks, and years, which may possibly lead to different adaptative mechanisms. The different genetic backgrounds in these species may also differentially impact on the mutation effects. Of note, the study by Bianca de Greef et al. (2018) showed that, out of 921 patients with possible SFN diagnosis, 614 had normal IENFD and abnormal temperature sensitivity threshold, demonstrating that abnormal IENFD is a secondary criterion for painful SFN in these patients, and the consequences of the $Scn9a^{R185H}$ GOF mutation on the spinal and brain pain pathways may be further investigated. More generally, the link between Nav channels GOF mutations, sensory neuron activity, neuropathy, and pain feeling will be further investigated when more tools become available.

Heat Pain in $Scn9a^{R185H}$ Mice

Patients with SFN s harboring the $SCN9A^{R185H}$ mutation complained of pain and paresthesias with burning feet and abnormal warm and cold pain sensation as evaluated by quantitative sensory testing (Faber et al., 2012). In $Scn9a^{R185H}$ mutant mice, pain behavior phenotype was observed in the hot plate and tail flick tests. This suggests that we successfully transferred the heat pain symptoms with $SCN9A^{R185H}$ mutation in our mutant line. The heat-sensitivity phenotype was found with a gene dosage effect, strengthening the conclusion on the impact of the mutation. Mutant females were found more sensitive than male littermates and the sex effect will be further discussed below. In addition, temperature preference as assessed between 15 and 40°C was not affected by the mutation, indicating that this mutation does not change the temperature sensing profile at non-noxious temperatures. As compared, deleting Nav1.7 in C-low threshold mechanoreceptors (C-LTMs) led to a shift in preferred temperature from 28.8 to 24°C (Middleton et al., 2021). Taken together, we showed hypersensitivity to noxious heat in $Scn9a^{R185H}$ mice while former studies had demonstrated an analgesic phenotype in *Scn9a* KO mouse lines (Xue et al., 2021). Taken globally, this suggests that the $Scn9a^{R185H}$ mutation induces hypersensitivity to heat.

Cold Pain in $Scn9a^{R185H}$ Mice

In the $Scn9a^{R185H}$ line, males and not females showed more reactions to cooling in the acetone test. Interestingly, the "acetone duration paw reaction" is one of the most discriminating variables linked to the genotype. The increased sensitivity to cooling as assessed in the acetone test is in agreement with previous findings which showed that Nav1.8 and Nav1.9 channels in sensory neurons display unusual biophysical adaptations to operate during extreme cold while Nav1.7 channels are necessary for cooling but not extreme cold sensation as well as for surgery-induced neuropathic cool allodynia (Minett et al., 2012, 2014a,b; Pereira et al., 2018; Shields et al., 2018). Also, the genetic mouse cKO models have globally shown that *Scn9a* is involved in acetone cool pain rather than cold plate cold behavioral responses (Xue et al., 2021). The findings of altered cool responses in $Scn9a^{R185H}$ mice are consistent with the description of the two patients with *R185H* presenting cold impaired modalities in quantitative sensory tests (Faber et al., 2012).

Mechanical Hypersensitivity in $Scn9a^{R185H}$ Mice

Both $Scn9a^{R185H}$ males and females showed a reduced mechanical threshold in the von Frey test with a mutation-dosage effect. They had normal noxious thresholds in tail pressure, indicating that $Scn9a^{R185H}$ mutation may cause mechanical allodynia rather than hyperalgesia. Regarding genetic rodent models, rats with *Scn9a* loss-of-function and global *Scn9a* KO mice were reported to display reduced sensitivity to von Frey and pinprick tests as well as to the Randall-Selitto or tail clip tests (Gingras et al., 2014; Grubinska et al., 2019; Chen L. et al., 2020; Xue et al., 2021). Altogether, our current findings and the cited previous results suggest that lack of *Scn9a* leads to less responses to both innocuous and noxious mechanical stimuli, whereas the $Scn9a^{R185H}$ mutation induces mechanical-touch allodynia rather than hyperalgesia to noxious pressure. These results on $Scn9a^{R185H}$ mice coincide with *R185H* patients' complaint of sheet intolerance.

Spontaneous Ongoing Pain in $Scn9a^{R185H}$ Mice

Measures of reflexive behaviors, such as withdrawals from noxious stimuli have been used for decades to examine pain behaviors. Here, we successfully validated the $Scn9a^{R185H}$ mutant mouse model and found a pain phenotype by examining reflexive pain behaviors. However, pain is a multidimensional experience of sensory-discriminative, cognitive, and affective processes. More recently, preference for the compartment paired with analgesia as measured by the CPP, or avoidance for evoked stimuli as recorded by the conditioned place avoidance test, have been used to assess spontaneous pain behavior, i.e., the presence of ongoing pain in experimentally induced inflammatory and neuropathic pain conditions (King et al., 2009; Barrot, 2012; Barthas et al., 2015). The $Scn9a^{R185H}$ mutant mice show a preference for the analgesia-paired chamber in the CPP test, indicating ongoing pain. These results together with our findings on the other behaviors indicate that $Scn9a^{R185H}$ mutant mice

do not only have altered nociceptive levels but also experience spontaneous pain, that corresponds more closely to the verbal reports of patients.

Sex Influence on Behaviors of *Scn9a*^{R185H} Mutants

This first evaluation of the behavioral consequences of the *Scn9a*^{R185H} mutation showed specific sex differences. Indeed, *Scn9a*^{R185H} females show more pain-like behaviors to heat (jump latency, coping reactions on hot plate and tail flick) while mutant males display more cool-related reactions (acetone). And notably, the increased sensitivity to touch and spontaneous pain were not sexually dimorphic. The study by Faber et al. (2012) comprising both male and female patients with *SCN9A*^{R185H} showed that the mutation was associated with pain in individuals of both sexes. In fact, this analysis was done in rare patients, one man with complaints and pain abnormalities similar to his brother and grand-father, and one woman whose father had similar complaints; thus, a quantitative conclusion cannot be drawn. Although these were rare patients and a quantitative conclusion cannot be drawn, generally, a majority of patients with chronic pain who visited the clinics are found to be women.

The current available evidence indicates hormonal, genetic, neuroimmune, cognitive, and social factors for the establishment and maintenance of chronic pain. Concerning rodents, sex differences or no sex differences in pain were reported in some strains but not in others (Mogil, 2020; Sadler et al., 2022). Interestingly, sex effects in *Scn9a*^{R185H} mutant mice may be explained by a differential effect of the mutation on Nav1.7 localization at the plasma membrane. Indeed, recently Nav1.7 membrane localization was shown to be regulated by the SUMOylation of the collapsin response mediator protein 2 (CRMP2) in female but not in the male sensory neurons (Moutal et al., 2020). This sex-specific mechanism may be tested on *Scn9a*^{R185H} animals on further investigations.

Perspectives

The present new genetic model, together with previous Nav1.7/*Scn9a* models and investigations have shown that Nav1.7 plays important roles in nociception and chronic pain. Although there are differences between rodents and humans, the present genetic mouse model may help to understand the impact of *Scn9a*^{R185H} mutation. Pain is a multifaceted and diverse experience that can be categorized into several types and modalities depending on the presentation and triggering stimulus of the pain event. The analyzed behaviors could provide a first phenotyping of the *Scn9a*^{R185H} mutant animals, and the study may be extended to other clinically relevant behavioral assays to capture the full spectrum of pain in these mice and open new visions for pain therapies based on Nav1.7. In addition, functional magnetic resonance imaging (fMRI) could be used next to study the neural activity underlying *Scn9a*^{R185H} mutation-induced pain. Recently, several emerging imaging methods have been developed (Geha et al., 2016; Chen X. et al., 2020; Markicevic et al., 2021) which may be applied to investigate the consequences of *Scn9a*^{R185H} mutation in the brain of the mouse.

In addition, *Scn9a*^{R185H} mice may constitute a tool to further define mechanisms linked to Nav1.7 interaction with other proteins. As mentioned above, Nav1.7 interacts with SUMOylated CRMP2 to regulate its membrane location (Moutal et al., 2020). The impact of *Scn9a*^{R185H} mutation on cell location may be explored further to elucidate the increased pain observed in the mutant animals. Also, targeted *in situ* repression of Nav1.7 in primary afferent mice led to long-lasting analgesia (Moreno et al., 2021) and the pain insensitivity found in *Scn9a* null mice was shown to be associated to elevated opioid receptors activity (Pereira et al., 2018; MacDonald et al., 2021). This revealed the requirement of both Nav1.7 absence and elevated opioid activity for a full analgesia. Also, the lack of success in developing Na_V channel blockers was reported to be due to their lack of specificity to Nav1.7 but previous findings on *Scn9a* null mice suggested that this may also be due to their lack of effect on the endogenous opioids. Thus, profiling of the endogenous opioid analgesic system could be next addressed in *Scn9a*^{R185H} mice. Another component of neuropathic pain lies in neuroinflammation (Sommer et al., 2018; Sisignano et al., 2022). The impact of *Scn9a*^{R185H} mutation on neuroinflammation or on a broader scale may be further explored by omics approaches.

Also, the limited results of clinical trials with Na_V channel blockers may reside in the differences between human and rodent DRG neurons. Hence, the development of iPSC-derived human sensory neurons, including those from *SCN9A*^{R185H} patients may provide a new preclinical platform for the *in vitro* design of next pain therapies (Alsaloum and Waxman, 2022). Altogether, the combination of rodent genetic models and other molecular, genetic, cellular, and pharmacological approaches will allow to identify additional components of chronic pain and to design new therapeutic strategies (Calvo et al., 2019; Kingwell, 2021).

DATA AVAILABILITY STATEMENT

The original contributions presented in this study are included in the article/**Supplementary Material**, further inquiries can be directed to the corresponding authors.

ETHICS STATEMENT

The animal study was reviewed and approved by Com'Eth, «Comité d'Ethique pour l'Expérimentation Animale IGBMC-ICS, and CREMEAS».

AUTHOR CONTRIBUTIONS

YX, MK, MM, CC, RL, M-CB, MB, YH, and CG-R contributed to the conception and design of the study. YX, MK, and RL performed the experiments. YX, MK, MM, RL, M-CB, MB, and CG-R analyzed data. All authors contributed to the writing of the manuscript and approved the submitted version.

FUNDING

This work has been funded by the Molecule-to-Man Pain Network, a European Commission Multi-Center Collaborative Project through the European Union's Horizon 2020 research and innovation program under grant agreement No. 721841—Pain-Net. This work has been supported by the National Centre for Scientific Research (CNRS, contract UPR3212), the French National Institute of health and medical research (INSERM), the University of Strasbourg (Unistra), the French state funds through the "Agence Nationale de la Recherche" under the frame of Programme Investissements d'Avenir labeled ANR-10-IDEX-0002-02, ANR-10-LABX-0030-INRT, ANR-10-INBS-07 PHENOMIN and ANR-17-EURE-0022 (Euridol), and the Region Grand Est through "Fonds Régional de Coopération pour la Recherche" (CLueDol project).

ACKNOWLEDGMENTS

We wish to thank Pr. Giuseppe Lauria and PAIN-Net members for all discussions. We thank Laurence Schaeffer and Valerie Erbs in the genetic engineering team, Sylvie Jacquot and Amélie Jeanblanc in the ICS genotyping team for their help to create and genotype the mutant mouse line. We thank Loïc Lindner and Pauline Cayrou for their help in ddPCR design and training. We thank the animal caretakers, Sophie Brignon, Charley Pinault, Dalila Ali-Hadji, and Gilles Duval at PHENOMIN-ICS and IGBMC animal facilities, and the Chronobiotron UMS3415 facilities for animal care. We wish to thank Quentin Leboulleux and Aurélia Cès and the ComptOpt plateform (Comportement et Optogénétique, INCI CNRS UPR 3212) for experiments on thermal ring, and ongoing pain. We thank Elvire Guiot for her help with the imaging facility and David Reiss for training on pain-behavioral tests. We wish to thank the Physiopathology of aneuploidy, gene dosage effect, and Down syndrome team for their help and in particular, Ameer Abu Bakr Rasheed, Michel Roux, Maria-Victoria Hinckelman, Claire Chevalier, and Arnaud Duchon.

SUPPLEMENTARY MATERIAL

The Supplementary Material for this article can be found online at: https://www.frontiersin.org/articles/10.3389/fnmol.2022.913990/full#supplementary-material

REFERENCES

Alsaloum, M., and Waxman, S. G. (2022). iPSCs and DRGs: stepping stones to new pain therapies. *Trends Mol. Med.* 28, 110–122. doi: 10.1016/j.molmed.2021.11.005

Barrot, M. (2012). Tests and models of nociception and pain in rodents. *Neuroscience* 211, 39–50. doi: 10.1016/j.neuroscience.2011.12.041

Barthas, F., Sellmeijer, J., Hugel, S., Waltisperger, E., Barrot, M., and Yalcin, I. (2015). The anterior cingulate cortex is a critical hub for pain-induced depression. *Biol. Psychiatry* 77, 236–245. doi: 10.1016/j.biopsych.2014.08.004

Bennett, D. L., Clark, A. J., Huang, J., Waxman, S. G., and Dib-Hajj, S. D. (2019). The role of voltage-gated sodium channels in pain signaling. *Physiol. Rev.* 99, 1079–1151. doi: 10.1152/physrev.00052.2017

Black, J. A., Frezel, N., Dib-Hajj, S. D., and Waxman, S. G. (2012). Expression of Nav1.7 in DRG neurons extends from peripheral terminals in the skin to central preterminal branches and terminals in the dorsal horn. *Mol. Pain* 8:82. doi: 10.1186/1744-8069-8-82

Blesneac, I., Themistocleous, A. C., Fratter, C., Conrad, L. J., Ramirez, J. D., Cox, J. J., et al. (2018). Rare NaV1.7 variants associated with painful diabetic peripheral neuropathy. *Pain* 159, 469–480. doi: 10.1097/j.pain.0000000000001116

Branco, T., Tozer, A., Magnus, C. J., Sugino, K., Tanaka, S., Lee, A. K., et al. (2016). Near-Perfect synaptic Integration by Nav1.7 in Hypothalamic Neurons Regulates Body Weight. *Cell* 165, 1749–1761. doi: 10.1016/j.cell.2016.05.019

Calvo, M., Davies, A. J., Hebert, H. L., Weir, G. A., Chesler, E. J., Finnerup, N. B., et al. (2019). The genetics of neuropathic pain from model organisms to clinical application. *Neuron* 104, 637–653. doi: 10.1016/j.neuron.2019.09.018

Carter, R. J., Morton, J., and Dunnett, S. B. (2001). Motor coordination and balance in rodents. *Curr. Protoc. Neurosci.* 8:12. doi: 10.1002/0471142301.ns0812s15

Cazzato, D., and Lauria, G. (2017). Small fibre neuropathy. *Curr. Opin. Neurol.* 30, 490–499. doi: 10.1097/WCO.0000000000000472

Chen, L., Effraim, P. R., Carrara, J., Zhao, P., Dib-Hajj, F. B., Dib-Hajj, S. D., et al. (2020). Pharmacological characterization of a rat Nav1.7 loss-of-function model with insensitivity to pain. *Pain* 161, 1350–1360. doi: 10.1097/j.pain.0000000000001807

Chen, L., Wimalasena, N. K., Shim, J., Han, C., Lee, S. I., Gonzalez-Cano, R., et al. (2021). Two independent mouse lines carrying the Nav1.7 I228M gain-of-function variant display dorsal root ganglion neuron hyperexcitability but a minimal pain phenotype. *Pain* 162, 1758–1770. doi: 10.1097/j.pain.0000000000002171

Chen, X., Tong, C., Han, Z., Zhang, K., Bo, B., Feng, Y., et al. (2020). Sensory evoked fMRI paradigms in awake mice. *Neuroimage* 204:116242. doi: 10.1016/j.neuroimage.2019.116242

Chidiac, C., Xue, Y., Muniz Moreno, M. D. M., Bakr Rasheed, A. A., Lorentz, R., Birling, M. C., et al. (2021). The Human SCN10A(G1662S) point mutation established in mice impacts on mechanical, heat, and cool sensitivity. *Front. Pharmacol.* 12:780132. doi: 10.3389/fphar.2021.780132

Cummins, T. R., Waxman, S. G., and Wood, J. N. (2020). "Sodium channels and Pain," in *The Oxford Handbook of the Neurobiology of Pain*, ed. J. N. Wood (Oxford: Oxford University Press), 232–262.

de Greef, B. T. A., Hoeijmakers, J. G. J., Gorissen-Brouwers, C. M. L., Geerts, M., Faber, C. G., and Merkies, I. S. J. (2018). Associated conditions in small fiber neuropathy - a large cohort study and review of the literature. *Eur. J. Neurol.* 25, 348–355. doi: 10.1111/ene.13508

Deuis, J. R., Dvorakova, L. S., and Vetter, I. (2017). Methods used to evaluate pain behaviors in rodents. *Front. Mol. Neurosci.* 10:284. doi: 10.3389/fnmol.2017.00284

Duchon, A., Pothion, S., Brault, V., Sharp, A. J., Tybulewicz, V. L., Fisher, E. M., et al. (2011). The telomeric part of the human chromosome 21 from Cstb to Prmt2 is not necessary for the locomotor and short-term memory deficits observed in the Tc1 mouse model of Down syndrome. *Behav. Brain Res.* 217, 271–281. doi: 10.1016/j.bbr.2010.10.023

Eijkenboom, I., Sopacua, M., Otten, A. B. C., Gerrits, M. M., Hoeijmakers, J. G. J., Waxman, S. G., et al. (2019). Expression of pathogenic SCN9A mutations in the zebrafish: a model to study small-fiber neuropathy. *Exp. Neurol.* 311, 257–264. doi: 10.1016/j.expneurol.2018.10.008

Faber, C. G., Hoeijmakers, J. G., Ahn, H. S., Cheng, X., Han, C., Choi, J. S., et al. (2012). Gain of function Nanu1.7 mutations in idiopathic small fiber neuropathy. *Ann. Neurol.* 71, 26–39. doi: 10.1002/ana.22485

Geha, P., Yang, Y., Estacion, M., Schulman, B. R., Tokuno, H., Apkarian, A. V., et al. (2016). Pharmacotherapy for pain in a family with inherited erythromelalgia guided by genomic analysis and functional profiling. *JAMA Neurol.* 73, 659–667. doi: 10.1001/jamaneurol.2016.0389

Gingras, J., Smith, S., Matson, D. J., Johnson, D., Nye, K., Couture, L., et al. (2014). Global Nav1.7 knockout mice recapitulate the phenotype of human congenital indifference to pain. *PLoS One* 9:e105895. doi: 10.1371/journal.pone.0105895

Grubinska, B., Chen, L., Alsaloum, M., Rampal, N., Matson, D. J., Yang, C., et al. (2019). Rat NaV1.7 loss-of-function genetic model: Deficient nociceptive and neuropathic pain behavior with retained olfactory function and intra-epidermal nerve fibers. *Mol. Pain* 15:1744806919881846. doi: 10.1177/1744806919881846

Han, C., Hoeijmakers, J. G., Liu, S., Gerrits, M. M., Te Morsche, R. H., Lauria, G., et al. (2012). Functional profiles of SCN9A variants in dorsal root ganglion neurons and superior cervical ganglion neurons correlate with autonomic symptoms in small fibre neuropathy. *Brain* 135, 2613–2628. doi: 10.1093/brain/aws187

Han, C., Vasylyev, D., Macala, L. J., Gerrits, M. M., Hoeijmakers, J. G., Bekelaar, K. J., et al. (2014). The G1662S NaV1.8 mutation in small fibre neuropathy: impaired inactivation underlying DRG neuron hyperexcitability. *J. Neurol. Neurosurg. Psychiatry* 85, 499–505. doi: 10.1136/jnnp-2013-306095

Huang, T., Lin, S. H., Malewicz, N. M., Zhang, Y., Zhang, Y., Goulding, M., et al. (2019). Identifying the pathways required for coping behaviours associated with sustained pain. *Nature* 565, 86–90. doi: 10.1038/s41586-018-0793-8

Kanellopoulos, A. H., Koenig, J., Huang, H., Pyrski, M., Millet, Q., Lolignier, S., et al. (2018). Mapping protein interactions of sodium channel NaV1.7 using epitope-tagged gene-targeted mice. *EMBO J.* 37, 427–445. doi: 10.15252/embj.201796692

King, T., Vera-Portocarrero, L., Gutierrez, T., Vanderah, T. W., Dussor, G., Lai, J., et al. (2009). Unmasking the tonic-aversive state in neuropathic pain. *Nat. Neurosci.* 12, 1364–1366. doi: 10.1038/nn.2407

Kingwell, K. (2021). Navigating a new path to Nav1.7 for pain. *Nat. Rev. Drug. Discov.* 21:18. doi: 10.1038/d41573-021-00197-2

MacDonald, D. I., Sikandar, S., Weiss, J., Pyrski, M., Luiz, A. P., Millet, Q., et al. (2021). A central mechanism of analgesia in mice and humans lacking the sodium channel NaV1.7. *Neuron* 109, 1497–1512. doi: 10.1016/j.neuron.2021.03.012

Markicevic, M., Savvateev, I., Grimm, C., and Zerbi, V. (2021). Emerging imaging methods to study whole-brain function in rodent models. *Transl. Psychiatry* 11:457. doi: 10.1038/s41398-021-01575-5

McDermott, L. A., Weir, G. A., Themistocleous, A. C., Segerdahl, A. R., Blesneac, I., Baskozos, G., et al. (2019). Defining the functional Role of NaV1.7 in human nociception. *Neuron* 101, 905–919. doi: 10.1016/j.neuron.2019.01.047

Middleton, S. J., Perini, I., Andreas, C. T., Weir, G. A., Mccann, K., Barry, A. M., et al. (2021). Nav1.7 is required for normal C-low threshold mechanoreceptor function in humans and mice. *Brain* 27:awab482. doi: 10.1093/brain/awab482

Minett, M. S., Eijkelkamp, N., and Wood, J. N. (2014a). Significant determinants of mouse pain behaviour. *PLoS One* 9:e104458. doi: 10.1371/journal.pone.0104458

Minett, M. S., Falk, S., Santana-Varela, S., Bogdanov, Y. D., Nassar, M. A., Heegaard, A. M., et al. (2014b). Pain without nociceptors? Nav1.7-independent pain mechanisms. *Cell Rep.* 6, 301–312. doi: 10.1016/j.celrep.2013.12.033

Minett, M. S., Nassar, M. A., Clark, A. K., Passmore, G., Dickenson, A. H., Wang, F., et al. (2012). Distinct Nav1.7-dependent pain sensations require different sets of sensory and sympathetic neurons. *Nat. Commun.* 3:791. doi: 10.1038/ncomms1795

Mogil, J. S. (2020). Qualitative sex differences in pain processing: emerging evidence of a biased literature. *Nat. Rev. Neurosci.* 21, 353–365. doi: 10.1038/s41583-020-0310-6

Moreno, A. M., Aleman, F., Catroli, G. F., Hunt, M., Hu, M., Dailamy, A., et al. (2021). Long-lasting analgesia via targeted in situ repression of NaV1.7 in mice. *Sci. Transl. Med.* 13:eaay9056. doi: 10.1126/scitranslmed.aay9056

Moutal, A., Cai, S., Yu, J., Stratton, H. J., Chefdeville, A., Gomez, K., et al. (2020). Studies on CRMP2 SUMOylation-deficient transgenic mice identify sex-specific NaV1.7 regulation in the pathogenesis of chronic neuropathic pain. *Pain* 161, 2629–2651. doi: 10.1097/j.pain.0000000000001951

Pereira, V., Millet, Q., Aramburu, J., Lopez-Rodriguez, C., Gaveriaux-Ruff, C., and Wood, J. N. (2018). Analgesia linked to Nav1.7 loss of function requires micro- and delta-opioid receptors. *Wellcome Open Res.* 3:101. doi: 10.12688/wellcomeopenres.14687.1

Porsolt, R. D., Bertin, A., and Jalfre, M. (1977). Behavioral despair in mice: a primary screening test for antidepressants. *Arch. Int. Pharmacodyn. Ther.* 229, 327–336.

Reiss, D., Maurin, H., Audouard, E., Martinez-Navarro, M., Xue, Y., Herault, Y., et al. (2021). Delta opioid receptor in astrocytes contributes to neuropathic cold pain and analgesic tolerance in female mice. *Front. Cell Neurosci.* 15:745178. doi: 10.3389/fncel.2021.745178

Sadler, K. E., Mogil, J. S., and Stucky, C. L. (2022). Innovations and advances in modelling and measuring pain in animals. *Nat. Rev. Neurosci.* 23, 70–85. doi: 10.1038/s41583-021-00536-7

Shields, S. D., Deng, L., Reese, R. M., Dourado, M., Tao, J., Foreman, O., et al. (2018). Insensitivity to Pain upon Adult-Onset Deletion of Nav1.7 or Its Blockade with Selective Inhibitors. *J. Neurosci.* 38, 10180–10201. doi: 10.1523/JNEUROSCI.1049-18.2018

Sisignano, M., Gribbon, P., and Geisslinger, G. (2022). Drug repurposing to target neuroinflammation and sensory neuron-dependent pain. *Drugs* 82, 353–373. doi: 10.1007/s40265-022-01689-0

Sommer, C., Leinders, M., and Uceyler, N. (2018). Inflammation in the pathophysiology of neuropathic pain. *Pain* 159, 595–602. doi: 10.1097/j.pain.0000000000001122

Themistocleous, A. C., Ramirez, J. D., Serra, J., and Bennett, D. L. (2014). The clinical approach to small fibre neuropathy and painful channelopathy. *Pract. Neurol.* 14, 368–379. doi: 10.1136/practneurol-2013-000758

Touska, F., Winter, Z., Mueller, A., Vlachova, V., Larsen, J., and Zimmermann, K. (2016). Comprehensive thermal preference phenotyping in mice using a novel automated circular gradient assay. *Temperature (Austin)* 3, 77–91. doi: 10.1080/23328940.2015.1135689

Vogt, M. A., Mallien, A. S., Pfeiffer, N., Inta, I., Gass, P., and Inta, D. (2016). Minocycline does not evoke anxiolytic and antidepressant-like effects in C57BL/6 mice. *Behav. Brain Res.* 301, 96–101. doi: 10.1016/j.bbr.2015.12.015

Waxman, S. G., Merkies, I. S. J., Gerrits, M. M., Dib-Hajj, S. D., Lauria, G., Cox, J. J., et al. (2014). Sodium channel genes in pain-related disorders: phenotype-genotype associations and recommendations for clinical use. *Lancet Neurol.* 13, 1152–1160. doi: 10.1016/S1474-4422(14)70150-4

Weibel, R., Reiss, D., Karchewski, L., Gardon, O., Matifas, A., Filliol, D., et al. (2013). Mu opioid receptors on primary afferent nav1.8 neurons contribute to opiate-induced analgesia: insight from conditional knockout mice. *PLoS One* 8:e74706. doi: 10.1371/journal.pone.0074706

Weiss, J., Pyrski, M., Jacobi, E., Bufe, B., Willnecker, V., Schick, B., et al. (2011). Loss-of-function mutations in sodium channel Nav1.7 cause anosmia. *Nature* 472, 186–190. doi: 10.1038/nature09975

Xiao, Y., Barbosa, C., Pei, Z., Xie, W., Strong, J. A., Zhang, J. M., et al. (2019). Increased resurgent Sodium Currents in Nav1.8 contribute to nociceptive sensory neuron hyperexcitability associated with peripheral neuropathies. *J. Neurosci.* 39, 1539–1550. doi: 10.1523/JNEUROSCI.0468-18.2018

Xue, Y., Chidiac, C., Herault, Y., and Gaveriaux-Ruff, C. (2021). Pain behavior in SCN9A (Nav1.7) and SCN10A (Nav1.8) mutant rodent models. *Neurosci. Lett.* 753:135844. doi: 10.1016/j.neulet.2021.135844

Conflict of Interest: The authors declare that the research was conducted in the absence of any commercial or financial relationships that could be construed as a potential conflict of interest.

Publisher's Note: All claims expressed in this article are solely those of the authors and do not necessarily represent those of their affiliated organizations, or those of the publisher, the editors and the reviewers. Any product that may be evaluated in this article, or claim that may be made by its manufacturer, is not guaranteed or endorsed by the publisher.

frontiers | Frontiers in Molecular Neuroscience

ORIGINAL RESEARCH
published: 14 June 2022
doi: 10.3389/fnmol.2022.880651

Single Subcutaneous Injection of Lysophosphatidyl-Choline Evokes ASIC3-Dependent Increases of Spinal Dorsal Horn Neuron Activity

*Ludivine Pidoux[1], Kevin Delanoe[1], Julie Barbier[2], Fabien Marchand[2], Eric Lingueglia[1] and Emmanuel Deval[1]**

[1] Université Côte d'Azur, CNRS, IPMC, LabEx ICST, FHU InovPain, Valbonne, France, [2] Université Clermont Auvergne, Inserm U1107 Neuro-Dol, Pharmacologie Fondamentale et Clinique de la Douleur, Clermont-Ferrand, France

Lysophosphatidyl-choline (LPC), a member of the phospholipid family, is an emerging player in pain. It is known to modulate different pain-related ion channels, including Acid-Sensing Ion Channel 3 (ASIC3), a cationic channel mainly expressed in peripheral sensory neurons. LPC potentiates ASIC3 current evoked by mild acidifications, but can also activate the channel at physiological pH. Very recently, LPC has been associated to chronic pain in patients suffering from fibromyalgia or osteoarthritis. Accordingly, repetitive injections of LPC within mouse muscle or joint generate both persistent pain-like and anxiety-like behaviors in an ASIC3-dependent manner. LPC has also been reported to generate acute pain behaviors when injected intraplantarly in rodents. Here, we explore the mechanism of action of a single cutaneous injection of LPC by studying its effects on spinal dorsal horn neurons. We combine pharmacological, molecular and functional approaches including *in vitro* patch clamp recordings and *in vivo* recordings of spinal neuronal activity. We show that a single cutaneous injection of LPC exclusively affects the nociceptive pathway, inducing an ASIC3-dependent sensitization of nociceptive fibers that leads to hyperexcitabilities of both high threshold (HT) and wide dynamic range (WDR) spinal neurons. ASIC3 is involved in LPC-induced increase of WDR neuron's windup as well as in WDR and HT neuron's mechanical hypersensitivity, and it participates, together with TRPV1, to HT neuron's thermal hypersensitivity. The nociceptive input induced by a single LPC cutaneous rather induces short-term sensitization, contrary to previously described injections in muscle and joint. If the effects of peripheral LPC on nociceptive pathways appear to mainly depend on peripheral ASIC3 channels, their consequences on pain may also depend on the tissue injected. Our findings contribute to a better understanding of the nociceptive signaling pathway activated by peripheral LPC *via* ASIC3 channels, which is an important step regarding the ASIC3-dependent roles of this phospholipid in acute and chronic pain conditions.

Keywords: pain, lysophosphatidyl-choline, acid-sensing ion channel 3, spinal cord neurons, sodium channel, TRPV1

OPEN ACCESS

Edited by:
Felix Viana, Institute of Neurosciences (CSIC), Spain

Reviewed by:
Zoltán Hegyi, University of Debrecen, Hungary
Pascal Fossat, Université de Bordeaux, France

****Correspondence:***
Emmanuel Deval
deval@ipmc.cnrs.fr

Specialty section:
This article was submitted to Pain Mechanisms and Modulators, a section of the journal Frontiers in Molecular Neuroscience

Received: *21 February 2022*
Accepted: *05 May 2022*
Published: *14 June 2022*

Citation:
Pidoux L, Delanoe K, Barbier J, Marchand F, Lingueglia E and Deval E (2022) Single Subcutaneous Injection of Lysophosphatidyl-Choline Evokes ASIC3-Dependent Increases of Spinal Dorsal Horn Neuron Activity. Front. Mol. Neurosci. 15:880651. doi: 10.3389/fnmol.2022.880651

INTRODUCTION

Lysophosphatidyl-choline (LPC) is an emerging lipid involved in pain (Gentry et al., 2010; Marra et al., 2016; Hung et al., 2020; Rimola et al., 2020; Sadler et al., 2021; Jacquot et al., 2022). It is an endogenous lysophospholipid that can be produced following plasma membrane hydrolysis due to PLA2 enzymes (Murakami et al., 2020) or oxydative stress (Karabina and Ninio, 2006; Choi et al., 2011), but it also serves as an intermediate for the synthesis of phosphatidyl-choline (PC) lipids (D'Arrigo and Servi, 2010). We initially identified LPC in the synovial fluids of patients suffering from painful joint diseases, as a positive modulator of the pain-related Acid-Sensing Ion Channel 3 (ASIC3) (Marra et al., 2016). More recently, we demonstrated that the synovial fluid levels of LPC16:0 species was correlated with pain outcomes in patients with osteoarthritis (Jacquot et al., 2022), and a correlation between the serum levels of LPC16:0 and pain symptoms has also been found in fibromyalgia patients (Hung et al., 2020). Interestingly, injecting LPC16:0 in either muscles (Hung et al., 2020) or joints (Jacquot et al., 2022) generates ASIC3-dependent persistent pain-like states in mice, indicating that this LPC species is a potential triggering factor of chronic pain associated to human musculoskeletal diseases, at least in osteoarthritis (Jacquot et al., 2022) and fibromyalgia (Hung et al., 2020). LPC has also been shown to generate acute pain when injected cutaneously/intraplantarly in rodents (Gentry et al., 2010; Marra et al., 2016; Rimola et al., 2020), including ASIC3-dependent acute pain-like behaviors (Marra et al., 2016).

Acid-sensing ion channel 3 belongs to the Acid-Sensing Ion Channels' family, which are depolarizing cation channels known for their ability to sense extracellular protons (Waldmann et al., 1997a). Several ASIC subunits have been identified in mammals, including ASIC1, ASIC2, ASIC3, and ASIC4, with several variants [for reviews, see Deval and Lingueglia (2015) and Lee and Chen (2018)]. A functional ASIC channel results from the trimeric assembly of these subunits (Jasti et al., 2007), at least for ASIC1, ASIC2, and ASIC3, leading to homomeric and/or heteromeric channels with different biophysical properties and regulations (Hesselager et al., 2004). ASICs are widely distributed in the nervous system and all along the pain pathway. Most ASIC subunits are expressed in sensory neurons, where ASIC3 and ASIC1b subunits have been shown to be important players in several pain models (Sluka et al., 2003; Deval et al., 2008, 2011; Diochot et al., 2012, 2016; Verkest et al., 2018; Chang et al., 2019). If ASICs are extracellular pH sensors, their activity and/or expression are nevertheless highly regulated by various endogenous factors associated with ischemia, inflammation, and pain (Immke and McCleskey, 2001; Mamet et al., 2002; Deval et al., 2004, 2008; Sherwood and Askwith, 2009; Li et al., 2010). This is particularly true for ASIC3 channels (Waldmann et al., 1997b), which seems to behave as "coincidence detectors" of several pain-related mediators, including mild extracellular acidification, hypertonicity, ATP and/or lipids (Deval et al., 2008; Birdsong et al., 2010; Li et al., 2010). LPC, alone or in combination with arachidonic acid (AA), induced a sustained ASIC3 current at physiological pH 7.4, in addition to the potentiation of its current evoked by mild acidifications (Marra et al., 2016; Jacquot et al., 2022).

Here, we investigate how a hindpaw local cutaneous injection of LPC affects the nociceptive pathway and the activity of spinal dorsal horn neurons, as well as the contribution of ASIC3 to this process. We combine *in vivo* and *in vitro* approaches to (i) explore the mechanism of action associated with LPC effect, (ii) determine the role of peripheral ASIC3 to the generation of the pain message, and (iii) study how this message is integrated at the spinal cord level. We show that LPC, which activates and potentiates ASIC3 *in vitro*, positively modulates both spontaneous and evoked activities of particular subsets of spinal dorsal horn neurons. Cutaneous hindpaw injection of LPC in rats or mice enhances the firing of high threshold (HT) and wide-dynamic range (WDR) neurons, leaving low threshold (LT) neurons unaffected. Hindpaw LPC injection is associated to short-term sensitization of nociceptive fibers, which is significantly reduced by the local pharmacological inhibition of ASIC3, and almost abolished in ASIC3 knockout mice. This work shows how a single local cutaneous administration of LPC induces peripheral sensitization of ASIC3-expressing nociceptive fibers that drive hyperexcitability of neurons within the dorsal spinal cord.

MATERIALS AND METHODS

Cell Culture and Transfections

HEK293 cell line was grown in DMEM medium supplemented with 10% of heat-inactivated fetal bovine serum (BioWest) and 1% of antibiotics (penicillin + streptomycin, BioWhittaker). One day after plating, cells were transfected with either pIRES2-rASIC1a-EGFP (rat ASIC1a), pIRES2-rASIC1b-EGFP (rat ASIC1b), or pIRES2-rASIC3-EGFP (rat ASIC3) vectors using the JetPEI reagent according to supplier's protocol (Polyplus transfection SA, Illkirch, France). Fluorescent cells were used for patch clamp recordings 2–4 days after transfection.

Patch Clamp Experiments

Whole cell configuration of the patch clamp technique was used to record membrane currents at a holding potential of −80 mV (voltage clamp mode). Recordings were made at room temperature using an axopatch 200B amplifier (Axon Instruments) with a 2 kHz low-pass filter. Data were digitized by a Digidata 1550 A-D/D-A converter (Axon Instruments), sampled at 20 kHz and recorded on a hard disk using pClamp software (version 11; Axon Instruments). The patch pipettes (2–6 MΩ) were filled with an intracellular solution containing (in mM): 135 KCl, 2 $MgCl_2$, 5 EGTA, and 10 HEPES (pH 7.25 with KOH). The extracellular solution bathing the cells contained (in mM) the following: 145 NaCl, 5 KCl, 2 $MgCl_2$, 2 $CaCl_2$, 10 HEPES (pH 7.4 with *N*-methyl-D-glucamine). ASIC currents were induced by shifting one out of eight outlets of a homemade microperfusion system driven by solenoid valves, from a holding control solution (i.e., pH 7.4) to an acidic test solution (pH 7.0 or pH 6.6). Cells were considered as positively transfected when they exhibited a visible GFP fluorescence and a transient pH 6.6-evoked current

of at least 300 pA (IpH 6.6 $\geq$ 300 pA). Non-transfected (NT) cells were used as controls and they were selected in Petri dishes having undergone the transfection protocol described above, but with no visible GFP fluorescence and no significant pH 6.6-evoked current.

Animals

Experiments were performed on adult male Wistar Han rats (Charles River, age > 6 weeks), adult male C57Bl6J wild type mice (WT, Janvier Lab, age > 7 weeks), and ASIC3 knockout mice (ASIC3 KO, internal animal husbandry, age > 7 weeks). The protocol was approved by the local ethical committee and the French government (agreement n° 02595.02). Animals were kept with a 12 h light/dark cycle with access to food and water *ad libitum*, and were acclimated to housing and husbandry conditions for at least a week before experiments.

Surgery

Anesthesia was induced with a mix of air and isoflurane 4% (Anesteo, Lunel, France). Animals were then placed in a stereotaxic frame (M2E, Montreuil, France) and kept under anesthesia using a mask diffusing a mix of oxygen and isoflurane 2%. The head and vertebral column of the animal were stabilized by ear bars and vertebral clamps, respectively, while a limited laminectomy was performed between vertebrae T13 and L2. Dura was carefully removed, and the spinal cord was immerged with artificial cerebrospinal fluid (ACSF containing 119 mM NaCl, 2.5 mM KCl, 1.25 mM NaH_2PO_4, 1.3 mM $MgSO_4$, 2.5 mM $CaCl_2$, 26 mM $NaHCO_3$, 11 mM glucose, and 10 mM HEPES, pH adjusted to 7.4 with NaOH) before starting electrophysiological recordings.

In vivo Electrophysiological Recordings of Spinal Cord Neurons

Single-unit extracellular recordings of spinal dorsal horn neurons were made with tungsten paralyn-coated electrodes (0.5 MΩ, WPI, Hertfordshire, Europe) and using Spike2 acquisition system (Cambridge Electronic Design, Cambridge, United Kingdom). The tip of a recording electrode was initially placed on the dorsal surface of the spinal cord using a micromanipulator (M2E, Montreuil, France) and this initial position determined the zero on the micromanipulator's micrometer. The electrode was then progressively moved down into the dorsal horn until the receptive field of a spinal neuron was localized on the ipsilateral plantar hindpaw using mechanical stimulations. Neuronal signals were bandpass filtered (0.3–30 kHz) and amplified using a DAM80 amplifier (WPI, Hertfordshire, Europe), digitized with a 1401 data acquisition system (Cambridge Electronic Design, Cambridge, United Kingdom), sampled at 20 kHz and finally stored on a computer.

Once a spinal neuron was isolated with its receptive field, non-noxious (brushing) and noxious (pinching) stimulations were used to characterize the neuronal type (**Figures 1A–C**, **2A**). Classically, spinal neurons were differentiated depending on the peripheral input received (Almeida et al., 2004; Xu and Brennan, 2009; Xu et al., 2013): (i) LT neurons (**Figure 1B**), receiving input from non-nociceptive fibers and essentially responding to non-noxious brushing (**Figure 1B1**), with only modest and non-dynamic responses to noxious pinching (**Figure 1B2**), (ii) HT neurons (**Figure 1C**), receiving input from nociceptive fibers and dynamically responding to noxious pinching by a high frequency activity lasting the whole time of the stimulation (**Figures 1C1,C2**), and (iii) WDR neurons (**Figure 2A**), responding to both noxious and non-noxious stimulations (Aβ, Aδ, and C inputs, **Figures 2A1,A2**), and known to exhibit a facilitatory process (Latremoliere and Woolf, 2009) called windup (**Figures 2A3,A4**).

Stimulation Protocols of Dorsal Horn Neuron Receptive Fields

Receptive fields of dorsal horn neurons were stimulated every 10 min by applying 10 consecutive non-noxious brushings, using a soft paint brush, and/or 5 consecutive noxious pinches, using either calibrated forceps (300 g stimulations, Bioseb, Vitrolles, France) or classical forceps (Moria MC40/B, Fine Science Tools, Heidelberg, Germany) for rats and mice, respectively. In addition to these mechanical stimuli, receptive field of WDR neurons also received repetitive electrical stimulations (protocol of 16 supraliminar 4 ms pulses, Dagan S900 stimulator) to induce windup. Intensity of currents injected for windup was determined as the intensity required to evoke less than 10 action potentials (APs) at the first stimulation, corresponding to 1.2–3 times the AP thresholds.

The evoked responses of dorsal horn neurons to non-noxious and noxious mechanical stimulations were also assessed using von Frey filaments. Different filaments were used to determine the mechanical sensitivity of HT and WDR neurons in rats (1 g; 8 g; 26 g; 60 g; 180 g; 300 g) and mice (0.40 g, 1 g, 2 g, 4 g, 6 g, 8 g, 10 g, 15 g). Each filament was applied three times during 3 s.

Finally, the response of dorsal horn neurons to thermal stimulation was assessed by applying heat ramps onto animal hindpaws. Heat ramps were applied by running a trickle of warm water on the neuron's receptive field using a temperature controller (CL-100, Warner Instruments, Holliston, MA, United States). A temperature probe was placed on the center of the receptive field and temperature was monitored for the entire duration of the experiment. Temperature was initially set at 30°C and heat ramps were delivered for 47 s up to 47°C, every 10 min, before and after injection of LPC or vehicle.

Peripheral Injection of Lipids and Drugs

Subcutaneous injection in the receptive field of dorsal horn neurons (20 μl and 10 μl for rats and mice, respectively) was made using a 28-gauge needle connected to a 50 μl Hamilton syringe. LPC16:0 and LPC18:1 were purchased from Anvanti (Coger, France), prepared as stock solutions in ethanol, and injected either alone (4.8 nmoles and 9.6 nmoles diluted in NaCl 0.9% for rats and mice, respectively) or in combination with pharmacological inhibitors: APETx2 (0.2 nmoles; purchased from Smartox Biotechnology, France, and prepared as stock solution in NaCl 0.9%) or capsazepine (0.2 nmoles, purchased from Smartox Biotechnology, France, and prepared as stock solution in DMSO). Ethanol or DMSO, diluted in NaCl 0.9%, were used as vehicle control solutions (ranging from 0.48 to 5%).

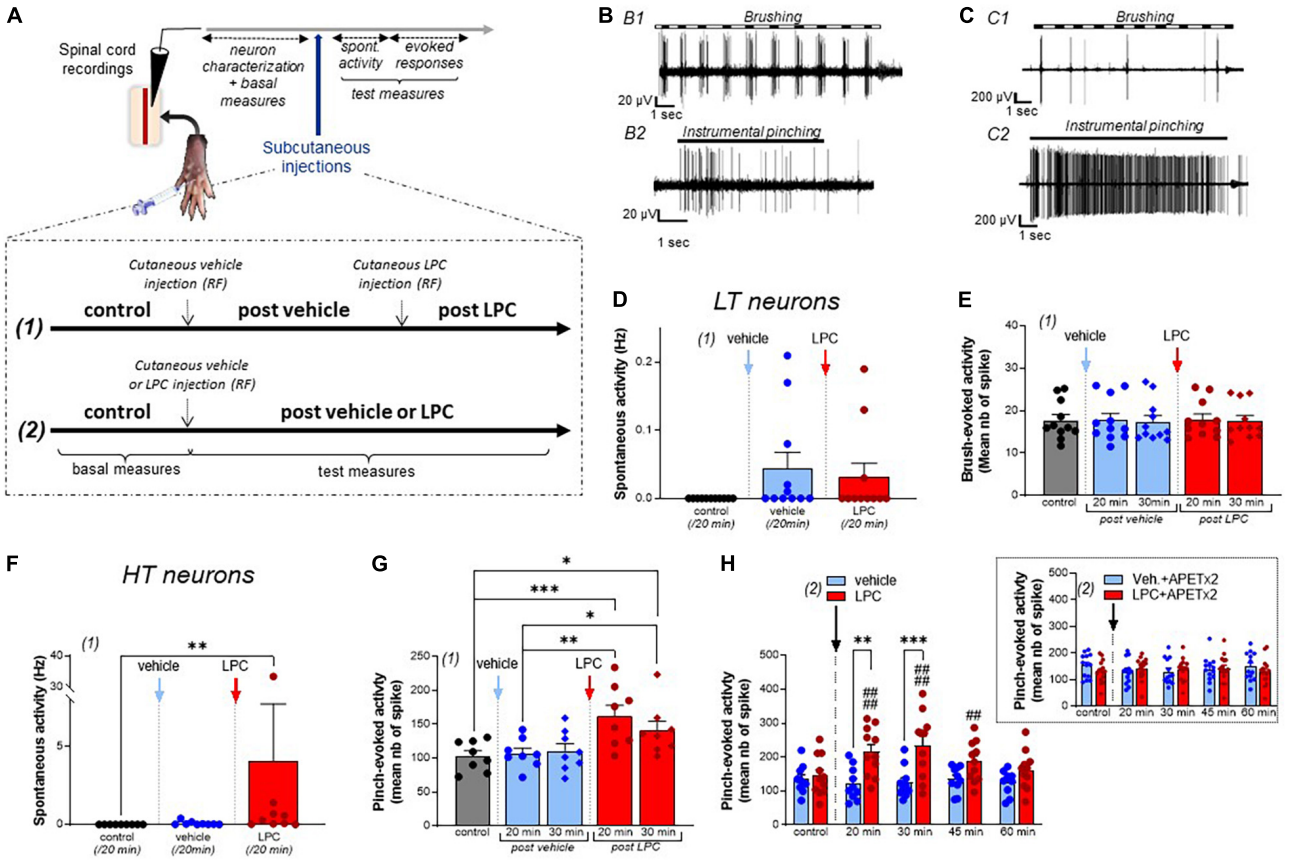

FIGURE 1 | Effect of LPC cutaneous injection on low threshold (LT) and high threshold (HT) spinal neuron activity. **(A)** Protocol used for spinal dorsal horn neuron recordings. After neuron characterization in the spinal cord, vehicle, and/or LPC were subcutaneously injected in the hindpaw using two protocols described in the inset. **(B)** Typical discharge of a rat low threshold (LT) neuron responding to non-noxious brushing **(B1)**, but not to noxious pinching (**B2**, instrumental pinching, 300 g). **(C)** Typical discharge of a rat high threshold (HT) neuron that did not respond to brush **(C1)** but emitted a sustained discharge in response to pinch (**C2**, instrumental pinching, 300 g). **(D)** Global spontaneous activity of LT neurons assessed with protocol (1) over 20 min-periods following vehicle (blue bar and points) and LPC16:0 (red bar and points) subcutaneous injection within the neuron's receptive fields (n = 11 neurons from 7 rats, Friedman test with p = 0.0988). **(E)** Brushing-evoked responses of LT neurons before (control) and after vehicle/LPC16:0 subcutaneous injection in their receptive fields [n = 11 neurons from 7 rats, no significant differences with p = 0.9822, Friedman test; protocol (1) used]. **(F)** Global spontaneous discharge of HT neurons after vehicle (blue bar and points) and LPC16:0 (red bar and points) injections [n = 9 neurons from 7 rats, Friedman test with $p < 0.0001$ followed by a Dunn's multiple comparison test: $^{**}p = 0.0012$; protocol (1) used]. **(G)** Pinch-evoked responses of HT neurons (instrumental pinching, 300 g) before and after vehicle/LPC16:0 subcutaneous injection in their receptive fields [n = 8 neurons from 6 rats, Friedman test with $p < 0.0001$ followed by a Dunn's multiple comparison test: $^{*}p < 0.05$, $^{**}p < 0.01$, and $^{***}p < 0.001$; protocol (1) used]. **(H)** Duration of the LPC effect on pinch-evoked activity of HT neurons [n = 10 and 11 neurons for vehicle and LPC, respectively; two-way ANOVA test with p = 0.0156 and $p < 0.0001$ for treatment and time after injection, respectively; $^{**}p < 0.01$ and $^{***}p < 0.001$, Sidak's multiple comparison *post-hoc* test; $\#\#p < 0.01$ and $\#\#\#\#p < 0.0001$ compared to control before LPC injection, Dunnet's multiple comparison *post-hoc* test; protocol (2) used]. The potentiation by cutaneous LPC was still significant 45 min after injection. Inset: The effect of LPC was abolished when APETx2 (0.2 nmol) was co-injected together with the lipid. Note that APETx2 had no effect by itself (vehicle + APETx2) on pinch-evoked activity of HT neurons [n = 13 and 15 for vehicle + APETx2 and LPC + APETx2, respectively; two-way ANOVA test with p = 0.8062 and p = 0.7850 for treatment and time after injection, respectively; protocol (2) used].

Spike Sorting and Analysis

Off-line analyses of *in vivo* electrophysiological recordings were made using Spike2 (Cambridge Electronic Design, Cambridge, United Kingdom) and Matlab (MathWorks, Natick, MA, United States) softwares. The spike sorting was first performed with Spike2, using principal component analysis of spike waveforms. The spikes and associated stimulation train were then exported to Matlab to perform further analysis. For each neuron, both spontaneous activities and evoked responses to noxious or non-noxious stimulations were quantified as the number of spikes emitted at rest and during the different stimulations, respectively. Matlab codes were used to calculate mean number of spikes. Spontaneous activities were calculated over 20 min periods starting immediately after peripheral injections. For non-noxious brushings, the mean number of spikes was calculated over 10 consecutive stimulations. For noxious pinching, the mean number of spikes was calculated over the 5 consecutive 5 s stimulations. For windup analysis of WDR neurons, each interval between repetitive electrical stimulations was divided into periods, so that the spikes evoked by Aδ and C-fibers can be distinguished (**Supplementary Figure 4A**). Indeed, spikes emitted within the 20–90 ms interval after the stimulation artifact

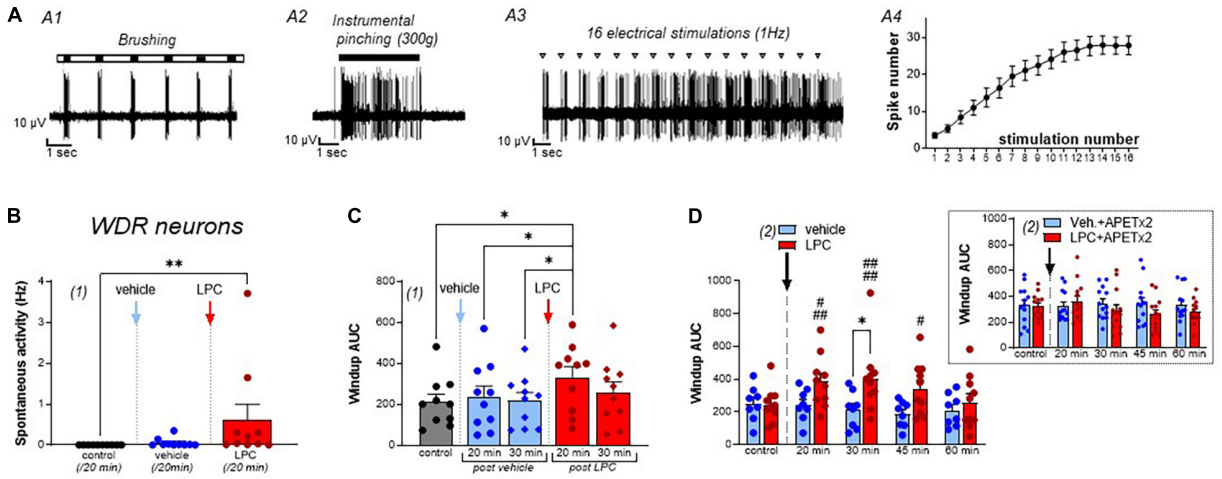

FIGURE 2 | Effect of LPC cutaneous injection on spinal wide dynamic range (WDR) neuron activity. **(A)** Typical discharge of a rat wide dynamic range (WDR) neuron, which responded to both brushing **(A1)** and pinching (**A2**, instrumental pinching, 300 g). WDR neuron also exhibited windup **(A3)** following repetitive electrical stimulations of its receptive field (gray triangle). Typically, windup is characterized by a progressive increase in the number of C-fiber evoked spikes as the number of stimulations increase (**A4**, data from 22 neurons). Maximal windup was reached between the 13th and 16th stimulation, from 3.48 ± 0.72 spikes at the first stimulation to 27.86 ± 2.5 spikes at the 16th stimulation. **(B)** Global spontaneous discharge of WDR neurons after vehicle (blue bar and points) and LPC16:0 (red bar and points) subcutaneous injections in their receptive fields (n = 10 neurons from 8 rats, Friedman test with p = 0.0008 followed by a Dunn's multiple comparison test: $^{**}p$ = 0.0036). **(C)** WDR neuronal windup before and after vehicle (blue bars and points) and LPC16:0 (red bars and points) subcutaneous injections in their receptive fields. C-fiber-induced windup is represented as the area under curve (AUC) determined from classical windup curves (see Section "Materials and Methods," n = 10 neurons from 8 rats, Friedman test with p = 0.0111 followed by a Dunn's multiple comparison test: $^{*}p < 0.05$). **(D)** The potentiating effect of LPC on WDR neuronal windup was significant for 45 min (n = 10 neurons from 8 rats and n = 8 neurons from 7 rats for LPC and vehicle, respectively, two-way ANOVA test with p = 0.0835 and p = 0.0047 for treatment and time after injection, respectively; $^{*}p < 0.05$, Sidak's multiple comparison *post-hoc* test; $\#p < 0.05$, $\#\#\#p < 0.001$, and $\#\#\#\#p < 0.0001$ compared to control before LPC injection, Dunnet's multiple comparison *post-hoc* test), and was abolished when APETx2 (0.2 nmol) was co-injected together with LPC. Note that APETx2 had no effect by itself (vehicle + APETx2) on WDR neuron windup (inset: n = 13 and 13 for vehicle + APETx2 and LPC + APETx2, respectively; two-way ANOVA test with p = 0.4594 and p = 0.3816 for treatment and time after injection, respectively).

were attributed to Aδ-fibers, whereas those emitted during the 90–1,000 ms interval were attributed to C-fibers (90–350 ms) and the after depolarization (AD) period (350–1,000 ms). Windup curves were established by counting the number of spikes emitted during C-fiber + AD periods for each of the 16 repetitive electrical stimulations. Windup was then expressed as the area under curve (AUC), which was calculated with the baseline set at the Y value corresponding to the first number of spikes for each windup protocol.

For experiments using von Frey filaments, the mean number of emitted spikes was calculated over three consecutive 3 s stimulations.

c-Fos Immunohistochemistry on the Spinal Cord Following Intraplantar Vehicle or LPC16:0 Injection

Following intraplantar vehicle (n = 6) or LPC16:0 (n = 5) administration, mice were maintained under isoflurane (1.5%) anesthesia during 1 h. Mice were then terminally anesthetized using a mixture of ketamine/xylazine and quickly perfused transcardially with saline followed by 4% paraformaldehyde (PFA). The lumbar spinal cord was excised and post fixed in 4% PFA in phosphate buffer (0.1 M, pH 7.4) for 24 h at 4°C. After cryoprotection (PB-Sucrose 30%) for at least 48 h, samples were included in tissue freezing medium (O.C.T.). Twenty µm cryostat thick frozen sections of the lumbar spinal cord were processed, mounted on Superfrost slides, blocked with PBS, BSA 1% and, incubated with a rabbit primary antibody against c-Fos (1:1,000; 9F6#2250, Cell Signaling) in PBS + BSA 1% + Triton 0.2% overnight at room temperature following three washes in PBS. After washes in PBS, sections were incubated with the corresponding secondary antibody (1:1,000, AlexaFluor 488 Molecular Probes, United States). After PBS washes, sections were then cover-slipped with fluorescent mounting medium (Dako) and observed with Nikon Eclipse Ni-E microscope. Quantitative analyses were performed with NIS-Elements software and a minimum of 7 sections per animal (n = 5–6 per group) were quantified by a blinded investigator and an average of the number of c-Fos positive neurons of the ipsilateral and contralateral dorsal horn (layers I & II and IV & V) counts was taken.

Statistical Analysis of Data

Graphs and statistical analysis were made using GraphPad Prism software (GraphPad Software, San Diego, CA, United States). Numerical values are given as mean ± SEM, unless otherwise stated. Statistical differences between sets of data were assessed using either parametric or non-parametric tests followed by *post-hoc* tests, when appropriate. In all cases, the significance level was set at $p \leq 0.05$. Statistical test used and significant p-values are indicated in each figure legend.

RESULTS

In vivo Cutaneous Injection of Lysophosphatidyl-Choline Affects Spinal High Threshold, but Not Low Threshold, Neurons

Lysophosphatidyl-choline has been associated to acute pain behaviors when injected cutaneously/intraplantarly in rodents (Gentry et al., 2010; Marra et al., 2016; Rimola et al., 2020). We thus performed *in vivo* recordings of spinal dorsal horn neuron activity to investigate how the acute pain message generated by subcutaneous injection of LPC, and more particularly LPC16:0 species (Marra et al., 2016; Jacquot et al., 2022), is integrated at the spinal level (see Section "Materials and Methods"). To determine whether LPC affects the firing of spinal dorsal horn neurons, both spontaneous activity and evoked neuronal responses to non-noxious and/or noxious stimuli were recorded in rats before and after vehicle or LPC injections (**Figures 1A–C**, **2A**). Two different protocols were used for vehicle and LPC administration (**Figure 1A**): (1) consecutive administration of vehicle and LPC within the same animals, which allowed paired analyses, and (2) single administration of vehicle or LPC in different animals. With protocol (1), no significant effect of LPC on low threshold (LT) neurons was observed on either spontaneous activity (**Figure 1D**, 0.04 ± 0.02 Hz and 0.03 ± 0.02 Hz after vehicle and LPC16:0 injections, respectively), or non-noxious brush-evoked activity (**Figure 1E**). The spiking activity evoked by brushing remained unchanged 20 and 30 min after vehicle or LPC injection, compared to the evoked activity in control condition before any injection (**Figure 1E**, +0.6%, and −1.6% compared to control at 20 and 30 min, respectively, after vehicle injection, and +1.2% and −0.7% compared to control at 20 and 30 min, respectively, after LPC16:0 injection).

Lysophosphatidyl-choline was next tested on spinal high threshold (HT) neurons (**Figures 1F–H**). Both the spontaneous and pinch–evoked activities of HT neurons were significantly increased by LPC cutaneous injection (**Figure 1F**, Spontaneous activity: 0.07 ± 0.04 Hz for vehicle vs. 4.05 ± 3.67 Hz for LPC16:0; **Figure 1G**, Pinch-evoked activity: +3.8% and +7.4% compared to control at 20 and 30 min, respectively, after vehicle injection, and +57.1% and +36.5% compared to control at 20 and 30 min, respectively, after LPC16:0 injection). These results were confirmed using protocol (2) in which vehicle or LPC were administered in different animals. The HT neuron hyperexcitability induced by LPC lasted up to 45 min after its injection, demonstrating short-term sensitization to noxious mechanical stimuli (**Figure 1H**, −9.9, −7.5, +0.5, and −6.8% compared to control at 20, 30, 45, and 60 min, respectively, after vehicle injection, and +49.4, +61.9, +28.9, and +11.7% compared to control at 20, 30, 45, and 60 min, respectively, after LPC16:0 injection). A similar sensitization of HT neuron activity was also observed following cutaneous injection of LPC18:1 (**Supplementary Figure 1A**), another LPC species that has recently been involved in nociceptor activation and pain in rodents (Rimola et al., 2020). A maximal effect on HT neurons' pinch-evoked activity was reached between ∼5 and ∼15 nmoles of LPC16:0 (**Supplementary Figure 1B**), with a decrease at 50 nmoles that could be related to desensitization or additional effects of LPC at high doses, for instance on the hyperpolarizing potassium channels TREK1 and TRAAK (Maingret et al., 2000).

Because LPC16:0 has been shown to activate/potentiate ASIC3 (Marra et al., 2016; Jacquot et al., 2022; **Supplementary Figure 2**), the ASIC3 blocker APETx2 (Diochot et al., 2004) was next co-injected with the lipid (**Figure 1H**, Inset). APETx2 prevented LPC-induced short-term sensitization of spinal HT neurons (−14.7, −14.7, −9.0, and −1.7% compared to control at 20, 30, 45, and 60 min, respectively, after vehicle + APETx2 injections, and +8.7, +5.5, +7.4, and −1.4% compared to control at 20, 30, 45, and 60 min, respectively, after LPC16:0 + APETx2 injections), supporting a role of ASIC3 channels in this effect. LPC has also been shown to activate some TRP channels, including TRPV1 and TRPM8 (Andersson et al., 2007; Gentry et al., 2010; Rimola et al., 2020). We thus tested the effect of capsazepine, which has been reported to block both channels (Weil et al., 2005; Messeguer et al., 2006). The hyperexcitability of HT neurons induced by peripheral injection of LPC was not significantly reduced by capsazepine (**Supplementary Figure 3**), suggesting that TRPV1 and TRPM8 channels were not involved in the increase of HT neuron spontaneous activity nor in their hypersensivity to pinch following cutaneous injection of LPC16:0.

In vivo Cutaneous Injection of Lysophosphatidyl-Choline Affects Spinal Wide Dynamic Range Neurons

The spontaneous activity of spinal WDR neurons was significantly increased by LPC cutaneous injection, compared to vehicle (**Figure 2B**, 0.02 ± 0.01 Hz for vehicle vs. 0.66 ± 0.41 Hz for LPC16:0). Moreover, the C-fiber-evoked activity of WDR neurons was also enhanced by LPC, as illustrated by its effect on windup (**Figures 2C,D** and **Supplementary Figures 4A,C**), whereas WDR activity related to non-noxious brushing was unaffected (**Supplementary Figures 4A,B**, Aδ-evoked activity: 2.71 ± 0.26 spikes, 2.49 ± 0.29 spikes, and 3.10 ± 0.51 spikes for control, vehicle and LPC16:0 injection, respectively; **Supplementary Figure 4D**, Brush-evoked activity: 3.86 ± 0.24 spikes, 3.83 ± 0.36 spikes, and 4.47 ± 0.40 spikes for control, vehicle and LPC16:0 injection, respectively). Thus, LPC significantly increased windup compared to vehicle and control conditions (**Figure 2C**, +13.0% and +2.9% compared to control at 20 and 30 min, respectively, after vehicle injection, and +57.7% and +22.7% compared to control at 20 and 30 min, respectively, after LPC16:0 injection), with an effect that lasted at least 45 min (**Figure 2D**). Finally, as observed for the LPC potentiation of HT neuron evoked-activity, the potentiating effect on WDR neuron windup was abolished by APETx2, further supporting a role of ASIC3 channels (**Figure 2D**, Inset, −2.3, +4.5, +4.2, and +0.6% compared to control at 20, 30, 45, and 60 min, respectively, after vehicle + APETx2 injections, and +11.4, −10.6, −19.8, and −14.3% compared to control at 20, 30, 45, and 60 min, respectively, after LPC16:0 + APETx2 injections).

Lysophosphatidyl-Choline-Induced Mechanical Hypersensitivity of Spinal High Threshold Neurons Is Dependent on Peripheral Acid-Sensing Ion Channel 3

To further explore the contribution of ASIC3 in the effect of cutaneous LPC, experiments were performed in WT and ASIC3 knockout mice. The spontaneous and evoked activities of HT neurons were both significantly potentiated following LPC cutaneous injection in WT mice (**Figures 3A,B**), whereas those of LT neurons remained unaffected (**Supplementary Figures 5A,B**), as observed in rats. HT neuron spontaneous activity was significantly higher following LPC injection compared to vehicle (**Figure 3A**, 0.23 ± 0.12 Hz for vehicle vs. 0.53 ± 0.17 Hz for LPC16:0). Moreover, response of HT neurons to noxious pinch in WT mice was also enhanced by LPC, with a 52.4% and 53.9% increase of evoked-activity 20 and 30 min, respectively, after LPC16:0 injection, compared to vehicle (**Figure 3B**). This potentiating effect of LPC lasted up to 45 min (**Supplementary Figure 5E**), similarly to what has been observed in rats (**Figure 1H**). Importantly, both effects on spontaneous and pinch-evoked activities of HT neurons were lost in ASIC3 knockout mice (ASIC3 KO, **Figure 3C**, 0.25 ± 0.23 Hz for vehicle vs. 0.09 ± 0.09 Hz for LPC16:0; **Figure 3D**, +19.2% and +10.2% compared to control at 20 and 30 min, respectively, after vehicle injection, −3.3% and +9.2% compared to control at 20 and 30 min, respectively, after LPC16:0 injection), further supporting the involvement of ASIC3 channels in LPC-induced hyperexcitability of spinal HT neurons.

The mechanical sensitivity of spinal HT neurons was next assessed using von Frey filaments in both mice (**Figure 3E**) and rats (**Figure 3F**). A set of filaments ranging from 0.4 to 15 g was applied successively (see Section "Materials and Methods") in both WT and ASIC3 KO mice, before and after LPC cutaneous injection into HT neuron receptive fields (**Figure 3E**). Before LPC injection, HT neurons of both genotypes responded similarly to von Frey stimulations, with an increase of emitted spikes as a function of filament strength (**Figure 3E**, From 0.31 ± 0.21 to 81.04 ± 10.19 spikes for WT mice, and from 1.2 ± 1.12 to 51.87 ± 13.74 spikes for ASIC3 KO mice), showing no significant difference in their basal mechanical sensitivities. Following LPC injection, the mechanical sensitivity of WT HT neurons was significantly increased from filaments ≥ 4 g, an effect that was not observed in ASIC3 KO mice (**Figure 3E**, After LPC16:0 injection: from 1.63 ± 1.38 to 109.50 ± 11.48 spikes for WT mice, and from 2.26 ± 2.10 to 53.93 ± 10.97 spikes for ASIC3 KO mice).

The basal von Frey sensitivity of HT neurons in rats, determined with filaments ranging from 1 to 300 g, was also enhanced after LPC cutaneous injection (**Figure 3F**, From 0.62 ± 0.21 to 83.55 ± 6.24 spikes in control condition, and from 0.87 ± 0.40 to 131.93 ± 18.23 spikes after LPC16:0 injection), demonstrating a significant LPC-induced mechanical hypersensitivity from filaments ≥ 26 g. Similar results were also observed for rat WDR neurons from filaments ≥8 g (**Supplementary Figure 5F**, From 4.58 ± 0.80 to 83.73 ± 6.93 spikes in control condition, and from 4.20 ± 1.75 to 146.67 ± 21.15 spikes after LPC16:0 injection). Mechanical hypersensitivity in rats was prevented by the co-administration of the ASIC3 blocker APETx2 with LPC into the receptive fields of both HT (**Figure 3F**, From 0.76 ± 0.42 to 88.10 ± 14.18 spikes after LPC16:0 + APETx2 injection) and WDR neurons (**Supplementary Figure 5F**, From 11.77 ± 2.10 to 99.44 ± 14.72 spikes after LPC16:0 + APETx2 injection), fully consistent with a role of peripheral ASIC3 channels in cutaneous LPC effects.

Lysophosphatidyl-Choline-Induced Hypersensitivity of Spinal High Threshold Neurons Is Not Restricted to Mechanical Stimuli

Thermal sensitivity of spinal HT neurons was also tested to determine whether LPC induced-sensitization was dependent of the stimulus modality. Heat temperature ramps were applied onto rat HT neuron receptive fields, before and after LPC or vehicle injections (**Figure 4A**). As expected in control condition, the number of spike emitted by HT neurons increased as a function of temperature (from 0 spikes at 30°C to 186.08 ± 22.70 spikes at temperatures above 46°C; **Figure 4B** control). The discharge pattern was significantly enhanced following LPC16:0 cutaneous injection, especially for temperatures above 42°C (from 88.75 ± 43.82 spikes at 42°C to 513.05 ± 106.69 spikes at temperatures above 46°C; **Figure 5B**), compared to both control (from 2.22 ± 1.28 spikes at 42°C to 186.08 ± 22.67 spikes at temperatures above 46°C; **Figure 5B**) and vehicle injection (from 1.06 ± 1.06 spikes at 42°C to 187.61 ± 36.24 spikes at temperatures above 46°C; **Figure 4B**). Co-injection of APETx2 prevented LPC-induced thermal hypersensitivity, similarly to what has been observed for mechanical hypersensitivity. Thus, thermal-evoked activity of HT neurons was significantly reduced in the LPC16:0 + APETx2 condition (from 4.06 ± 3.63 spikes at 42°C to 196.44 ± 37.84 spikes at temperatures above 46°C; **Figure 5B**) compared to LPC16:0 alone (from 88.75 ± 43.82 spikes at 42°C to 513.05 ± 106.69 spikes at temperatures above 46°C; **Figure 4B**). Finally, a significant decrease of the temperature threshold triggering HT neuron's spiking was also observed following LPC cutaneous injection (40.7 ± 0.4°C for LPC16:0 vs. 44.3 ± 0.2°C and 43.4 ± 0.3°C for control and vehicle, respectively; **Figure 4C**), which was also abolished by the co-injection of APETx2 (43.8 ± 0.7°C for LPC16:0 + APETx2; **Figure 4C**).

Finally, we assessed the potential role of TRPV1 channels in heat hypersensitivity of spinal HT neurons following LPC cutaneous injection. Capsazepine had no effect on basal heat sensitivity, but partially and significantly prevented LPC-induced thermal hypersensitivity of spinal HT neurons (**Figure 4D**). The lack of effect of capsazepine on the basal heat sensitivity of HT neurons does not exclude the involvement of TRPV1 that was previously demonstrated (Caterina et al., 2000), but rather illustrates the low efficacy of the drug on channel responses to heat (Savidge et al., 2001). Nevertheless, the use of capsazepine demonstrates an involvement of peripheral TRPV1 channels to LPC-induced heat hypersensitivity of spinal HT neurons (**Figure 4D**). Indeed, thermal evoked activity after LPC16:0 + capsazepine cutaneous injection (from 27.75 ± 12.28

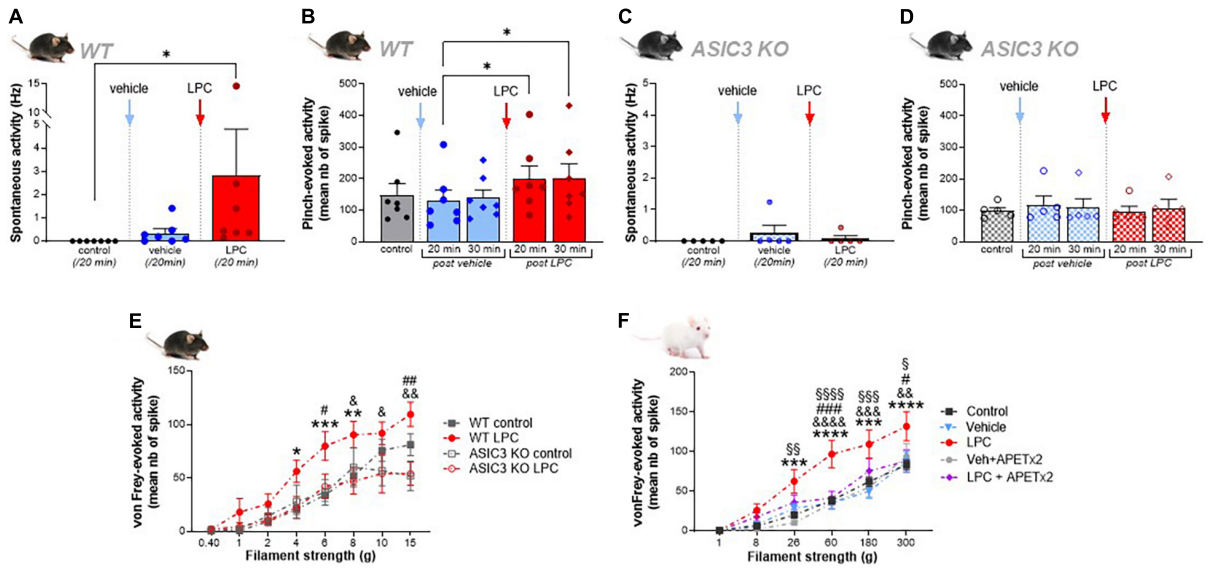

FIGURE 3 | Effect of LPC cutaneous injection on spinal HT neuron on both spontaneous and mechanically evoked activity. **(A)** Global spontaneous discharge of HT neurons before and after vehicle (blue bar and points) and LPC (red bar and point) subcutaneous injections in wild-type mice receptive fields (n = 7 neurons from 6 WT mice, Friedman test with $p < 0.0001$ followed by a Dunn's multiple comparison test: $^{*}p < 0.05$ for control vs. LPC comparison). **(B)** Evoked responses of HT neurons to nociceptive stimulation (pinch) in WT mice after vehicle (blue bars and points) and LPC16:0 (red bars and points) subcutaneous injections. Effects were measured 20 min (circle point) and 30 min (diamond point) after respective injections (n = 7 neurons from 6 WT mice, Friedman test with $p = 0.0025$ followed by a Dunn's multiple comparison test: $^{*}p < 0.05$). **(C)** Global spontaneous discharge of HT neurons of ASIC3 KO mice before and after vehicle (blue bar and points) and LPC (red bar and points) subcutaneous injections (n = 5 neurons from 4 ASIC3 KO mice, no significant difference, $p = 0.3333$, Friedman test). **(D)** HT neuron responses of ASIC3 KO mice to nociceptive stimulation (pinch) before and after vehicle and LPC16:0 subcutaneous injections (n = 5 neurons from 4 ASIC3 KO mice, no significant difference, Friedman test with $p = 0.3848$). **(E)** Curves representing the mechanical sensitivity of mouse HT neurons following von Frey filament applications on their receptive fields before (black curves) and after LPC16:0 injection (red curves). Experiments were performed in both WT (full symbols, n = 15 neurons from 10 mice and 10 neurons from 6 mice for control and LPC, respectively) and ASIC3 KO mice (empty symbols, n = 5 neurons) (two way ANOVA with $p = 0.0106$ and $p < 0.0001$ for treatment and von Frey filaments effects, respectively, followed by Tukey's multiple comparison test: $^{*}p < 0.05$, $^{**}p < 0.01$, and $^{***}p < 0.001$ for WT LPC vs. WT control; &$p < 0.05$ and &&$p < 0.01$ for WT LPC vs. ASIC3 KO LPC; #$p < 0.05$ and ##$p < 0.01$ for WT LPC vs. ASIC3 KO control). **(F)** Mechanical sensitivity of rat HT neurons to von Frey filaments before (control, n = 39 neurons) and after injection of vehicle (n = 10 neurons from 9 rats), vehicle + APETx2 (n = 9 neurons from 5 rats), LPC (n = 10 neurons from 9 rats), and LPC + APETx2 (n = 10 neurons from 6 rats; two way ANOVA with $p = 0.0004$ and $p < 0.0001$ for treatment and von Frey filaments effects, respectively, followed by Tukey's multiple comparison test: $^{***}p < 0.001$ and $^{****}p < 0.0001$ for LPC vs. control; &&$p < 0.01$, &&&$p < 0.001$, and &&&&$p < 0.0001$ for LPC vs. vehicle; #$p < 0.05$ and ###$p < 0.001$ for LPC vs. LPC + APETx2; §$p < 0.05$, §§$p < 0.01$, §§§$p < 0.001$, and §§§§$p < 0.0001$ for LPC vs. vehicle + APETx2).

spikes at 42°C to 409.08 ± 93.12 spikes at temperatures above 46°C) was significantly reduced compared to LPC16:0 alone (from 123.66 ± 29.73 spikes at 42°C to 745.00 ± 87.74 spikes at temperatures above 46°C), but was still significantly increased compared to control (from 0 spikes at 42°C to 188.33 ± 28.15 spikes at temperatures above 46°C). As observed previously (**Figure 4C**), LPC significantly decreased the temperature threshold triggering HT neuron's spiking compared to control (**Figure 4E**, 44.3 ± 0.2°C vs. 40.0 ± 0.5°C for control and LPC16:0, respectively), but this effect was not reduced by capsazepine (**Figure 4E**, 40.4 ± 0.8°C for LPC16:0 + capsazepine).

Lysophosphatidyl-Choline-Induced Hypersensitivity of Spinal High Threshold Neurons Displays Some, but Not All, Central Sensitization Features

To characterize the mechanism by which peripheral LPC affects spinal dorsal horn neuron activity, we assessed c-Fos expression in the lumbar spinal cord following cutaneous LPC injection (**Figure 5**). C-Fos expression was significantly increased in both ipsilateral layers I & II and layers IV & V of the spinal cord following LPC administration (**Figure 5C**), consistent with the increased neuronal activity observed for *in vivo* electrophysiological recordings. The number of c-Fos-positive cells was significantly higher after LPC cutaneous injection (**Figures 5A,C**, 7.81 ± 0.63 cells for layers I & II, 5.75 ± 0.70 cells for layers IV & V) compared to vehicle (**Figures 5B,C**, 5.29 ± 0.41 cells for layers I & II, 3.40 ± 0.54 cells for layers IV & V). C-Fos positive cell number after LPC peripheral injection was also significantly different between the ipsilateral (7.81 ± 0.63 cells) and contralateral (4.82 ± 0.61 cells) sides in layer I & II of the dorsal horn, suggesting that spinal neurons on the contralateral side were not activated by ipsilateral LPC injection.

Additional experiments have been made to determine whether neuronal activation in the spinal cord following peripheral LPC cutaneous injection could induce central sensitization features. Among the features particular to central sensitization, we already demonstrated hyperexcitability of spinal HT and

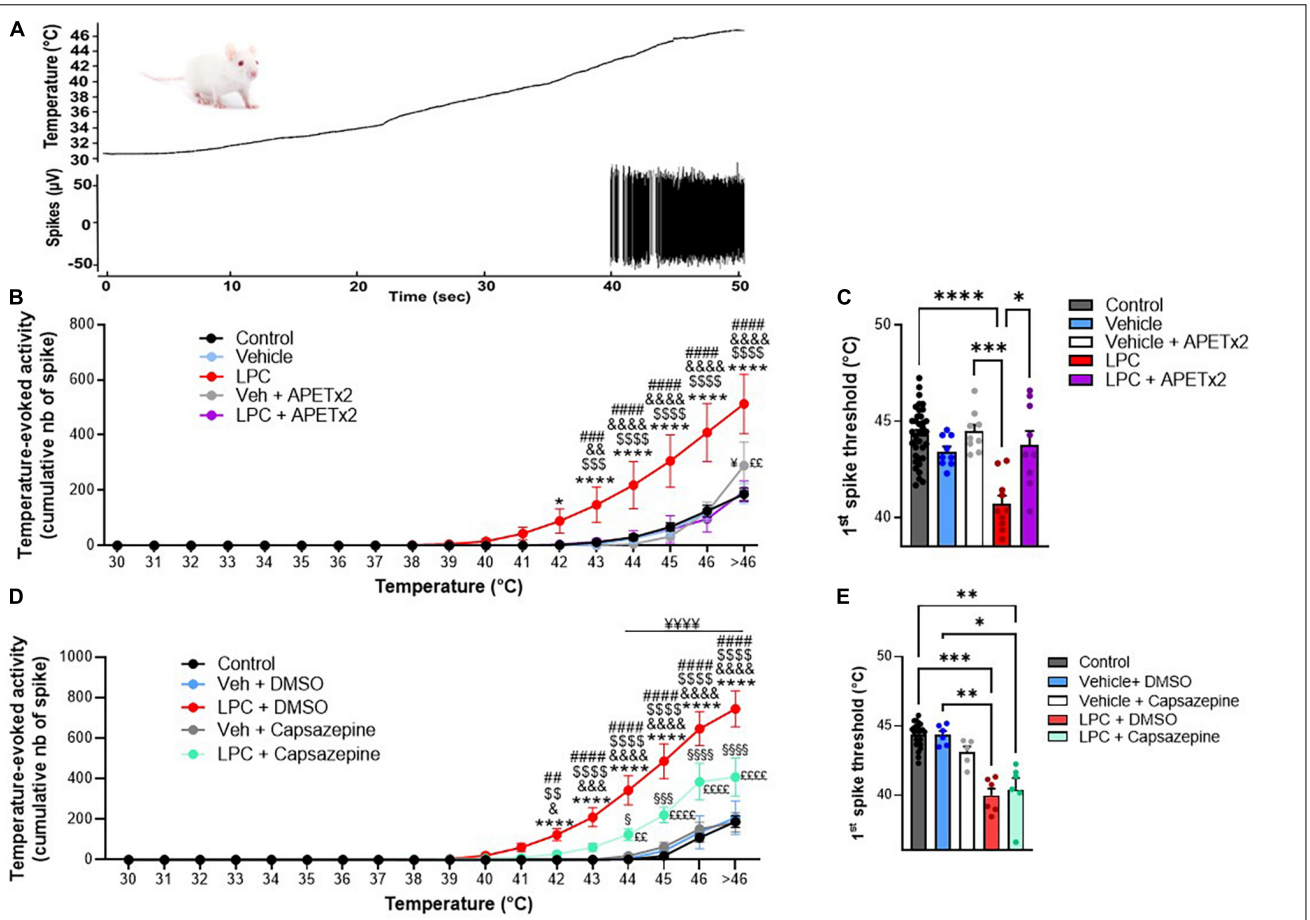

FIGURE 4 | Effect of cutaneous LPC injection on heat sensitivity of spinal HT neuron. **(A)** Typical trace of a rat HT neuron response following heat ramp stimulation. Heat ramps from 30 to 46°C were applied onto neuron receptive field (top panel, black curve) while neuronal evoked activity was recorded (bottom panel). **(B)** Cumulative representation of the number of spikes evoked by heat ramps as a function of the temperature. Experiments were performed before (control, black dots, $n = 37$ neurons from 17 rats) and 20 min after cutaneous injection of vehicle (light blue dots, $n = 9$ neurons from 6 rats), LPC16:0 (red bar dots, $n = 10$ neurons from 6 rats), vehicle + APETx2 (gray dots, $n = 9$ neurons from 6 rats) or LPC16:0 + APETx2 (purple dots, $n = 9$ neurons from 7 rats; two-way ANOVA with $p < 0.0001$ for both treatment and temperature effects, followed by a Tukey's multiple comparison test: $^{*}p < 0.05$ and $^{****}p < 0.0001$ for LPC vs. control; $\$\$p < 0.001$ and $\$\$\$\$p < 0.0001$ for LPC vs. vehicle; $\&\&p < 0.01$ and $\&\&\&\&p < 0.0001$ for LPC vs. LPC + APETx2; $\#\#\#p < 0.001$ and $\#\#\#\#p < 0.0001$ for LPC vs. vehicle + APETx2; $¥p < 0.05$ for vehicle vs. vehicle + APETx2; $££p < 0.01$ for control vs. vehicle + APETx2). **(C)** Histogram of temperature thresholds that triggered the first spiking activity of HT neurons in response to heat ($n = 37$, 9, 10, 9, 9 and for control, vehicle, LPC, LPC + APETx2 and vehicle + APETx2, respectively, Kruskal-Wallis test with $p < 0.0001$, followed by a Dunn's multiple comparison test: $^{*}p < 0.05$, $^{***}p < 0.001$, and $^{****}p < 0.0001$). **(D)** Cumulative representation of the number of spikes evoked by heat ramps as a function of the temperature. Experiments were performed before (control, black dots, $n = 23$ neurons from 12 rats) and 20 min after cutaneous injection of vehicle + DMSO (light blue dots, $n = 6$ neurons from 4 rats), LPC16:0 + DMSO (red bar dots, $n = 6$ neurons from 5 rats), vehicle + capsazepine (gray dots, $n = 5$ neurons from 4 rats), or LPC16:0 + capsazepine (green dots, $n = 6$ neurons from 5 rats; two-way ANOVA with $p < 0.0001$ for both treatment and temperature effects, followed by a Tukey's multiple comparison test: $^{****}p < 0.0001$ for LPC + DMSO vs. control; $\&p < 0.05$, $\&\&\&p < 0.001$, and $\&\&\&\&p < 0.0001$ for LPC + DMSO vs. LPC + capsazepine; $\$\$p < 0.01$ and $\$\$\$\$p < 0.0001$ for LPC + DMSO vs. vehicle + capsazepine; $\#\#p < 0.01$ and $\#\#\#\#p < 0.0001$ for LPC + DMSO vs. vehicle + DMSO; $§p < 0.05$, $§§§p < 0.001$, and $§§§§p < 0.0001$ for LPC + capsazepine vs. vehicle + capsazepine; $¥¥¥¥p < 0.0001$ for LPC + capsazepine vs. control; $ŁŁp < 0.01$ and $ŁŁŁŁp < 0.0001$ for LPC + capsazepine vs. vehicle + DMSO). **(E)** Histogram of temperature thresholds that triggered the first spiking activity of HT neurons in response to heat ($n = 23$, 6, 6, 6, 5 and for control, vehicle + DMSO, LPC + DMSO, LPC + capsazepine and vehicle + capsazepine, respectively, Kruskal-Wallis test with $p < 0.0001$, followed by a Dunn's multiple comparison test: $^{*}p > 0.05$, $^{**}p < 0.01$ and $^{***}p < 0.001$).

WDR neurons (**Figures 1–4**). We then studied two other features that could be possibly affected by LPC (**Figure 6A**): the conversion of nociceptive-specific neurons to WDR neuronal type (**Figures 6B,C**), as well as the enlargement of the receptive field of spinal neurons (**Figures 6D,E**) that are typically associated with central sensitization (Latremoliere and Woolf, 2009).

Nociceptive-specific spinal neurons, i.e., HT neurons, only respond to noxious stimuli in control condition. If central sensitization is induced in spinal HT neurons following LPC cutaneous injection, they should be converted to WDR neurons and also respond to non-noxious stimulation such as brushing. The number of spikes emitted by HT neurons in response to non-noxious stimulations after LPC cutaneous injection (**Figures 6B,C**) was not significantly different from control and vehicle (**Figure 6C**), indicating that HT neurons were not converted to WDR neurons in our conditions.

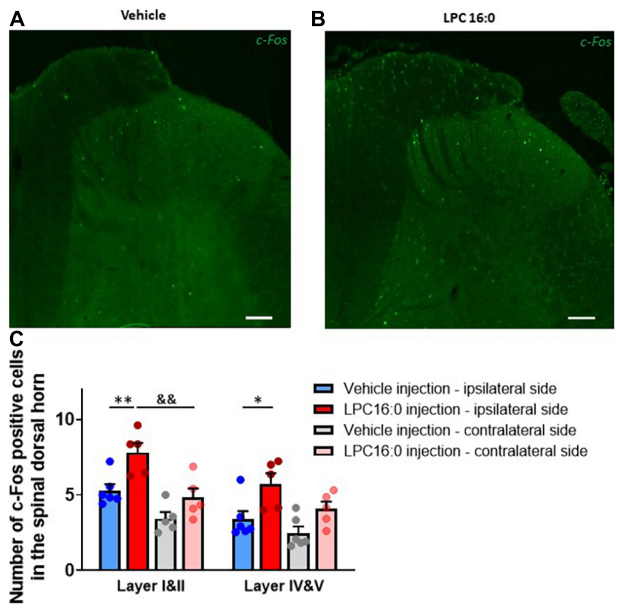

FIGURE 5 | C-Fos immunohistochemistry in dorsal spinal cord. **(A,B)** Representative photomicrographs of c-Fos labeling following vehicle **(A)** and LPC16:0 **(B)** peripheral injection. Scale bar: 100 μm. **(C)** Quantification of the number of c-Fos positive cells in the spinal dorsal horn in I&II and IV&V spinal cord layers. Quantifications were done on both ipsilateral and contralateral spinal cord side after peripheral injections of LPC 16:0 ($n = 5$ for both) and vehicle ($n = 6$ and 5, respectively). Two-way ANOVA with $p < 0.0001$ for treatment effects, followed by a Tukey's multiple comparison test: $^{*}p < 0.05$; $^{**}p < 0.01$ for LPC 16:0 injection vs. vehicle injection and $\&\&p < 0.01$ for ipsilateral vs. contralateral side.

Receptive fields were defined as the areas inside which noxious pinching induced strong responses of HT neurons before LPC injection (**Figures 6A,D**, upper-left trace). Noxious stimulations were then applied 5 mm and 10 mm outside the receptive field (**Figure 6A**). In control condition, HT neuronal responses to pinch were weak 5 mm and absent 10 mm away from the receptive field (**Figure 6D**, Middle and bottom left traces). Following LPC cutaneous injection, HT neuronal responses were significantly increased following stimulation within their receptive field (**Figure 6D**, Upper-right trace and **Figure 6E**), as observed previously (**Figures 2**, **4**). However, no significant change was observed in our conditions when stimulations were applied 5 mm or 10 mm away from the receptive field (**Figure 6D**, Middle- and bottom-right traces, and **Figure 6E**). However, the dose of LPC used in these experiments has been identified based on dose-dependency of the pinch-evoked activity of HT neurons (**Supplementary Figure 1B**), and it remains possible that a transition of HT to WDR and/or an increase of receptive field could occur at higher (or lower) doses of LPC.

DISCUSSION

The production of LPC *via* the activation of phospholipase A2 (PLA2), oxidative stress, or as an intermediate product of phosphatidylcholine metabolism occurs in many tissues, including the nervous system. Interestingly, elevated levels of LPC have been detected in the synovial fluids and plasma of patients suffering from rheumatic diseases and fibromyalgia (Hung et al., 2020; Jacquot et al., 2022), where they were correlated with patient pain symptoms, supporting a peripheral role of this endogenous phospholipid in pain in humans. Moreover, local injection of LPC induces acute and chronic pain in rodents through its effects on pain-related ion channels, including some TRPs and ASIC3 (Gentry et al., 2010; Marra et al., 2016; Hung et al., 2020; Rimola et al., 2020; Sadler et al., 2021; Jacquot et al., 2022). The aim of this work was to (i) study the pain message generated by peripheral LPC when injected in the skin, (ii) determine the contribution of peripheral ASIC3 to the generation of this message and, (iii) investigate how this message is processed by spinal dorsal horn neurons.

Our data show that peripheral cutaneous LPC injection exclusively affects the nociceptive pathway by inducing an ASIC3-dependent sensitization of peripheral nociceptive fibers, ultimately leading to increased spontaneous and evoked-activities of spinal HT and WDR neurons. The activity of spinal LT neurons remained unaffected by cutaneous injection of LPC, consistent with a lack of effect of this lysolipid on non-nociceptive fibers. The sensitizing effect of LPC on HT and WDR neurons occurs following a single cutaneous injection and lasts approximately 45 min. It is also modality-independent since neuronal responses to noxious heat and mechanical stimulations are both potentiated. This is consistent with the recent description of an acute mechanical hypersensitivity after cutaneous injection of LPC in mice (Rimola et al., 2020). Basal mechanical and thermal sensitivities are not affected by either pharmacological or genetic inhibition of ASIC3, in agreement with previous studies using ASIC3 KO mice to test behavioral responses following noxious thermal or mechanical stimulations (Price et al., 2001; Chen et al., 2002; Borzan et al., 2010). However, the mechanical and thermal hypersensitivity of spinal HT neurons induced by cutaneous injection of LPC is clearly dependent on peripheral ASIC3 activation. The persistent depolarizing ASIC3 current generated by LPC is likely to participate in this ASIC3-dependent sensitization of nociceptive fibers, as demonstrated in primary cultures of dorsal root ganglia neurons (Deval et al., 2003; Jacquot et al., 2022). Interestingly, LPC does not seem to produce the same effect on non-nociceptive fibers where ASIC3 is also largely expressed (Molliver et al., 2005; Lin et al., 2016), suggesting some cell-specific roles of this channel. The augmented peripheral nociceptive inputs is likely to drive the increase of spinal activities from HT and WDR neurons.

Lysophosphatidyl-choline displays a good specificity for ASIC3 compared to other pain-related ASICs also expressed in peripheral sensory neurons such as ASIC1a and ASIC1b, as shown here and in Marra et al. (2016). LPC not only modulates ASIC3 (Marra et al., 2016), but also affects other pain-related channels, including TREK1 and TRAAK (Maingret et al., 2000), TRPM8 (Andersson et al., 2007; Gentry et al., 2010), TRPC5 (Flemming et al., 2006; Sadler et al., 2021), and TRPV1 (Rimola et al., 2020). Our data demonstrated that at least TRPV1 and TRPM8 channels did not significantly contribute to the effect

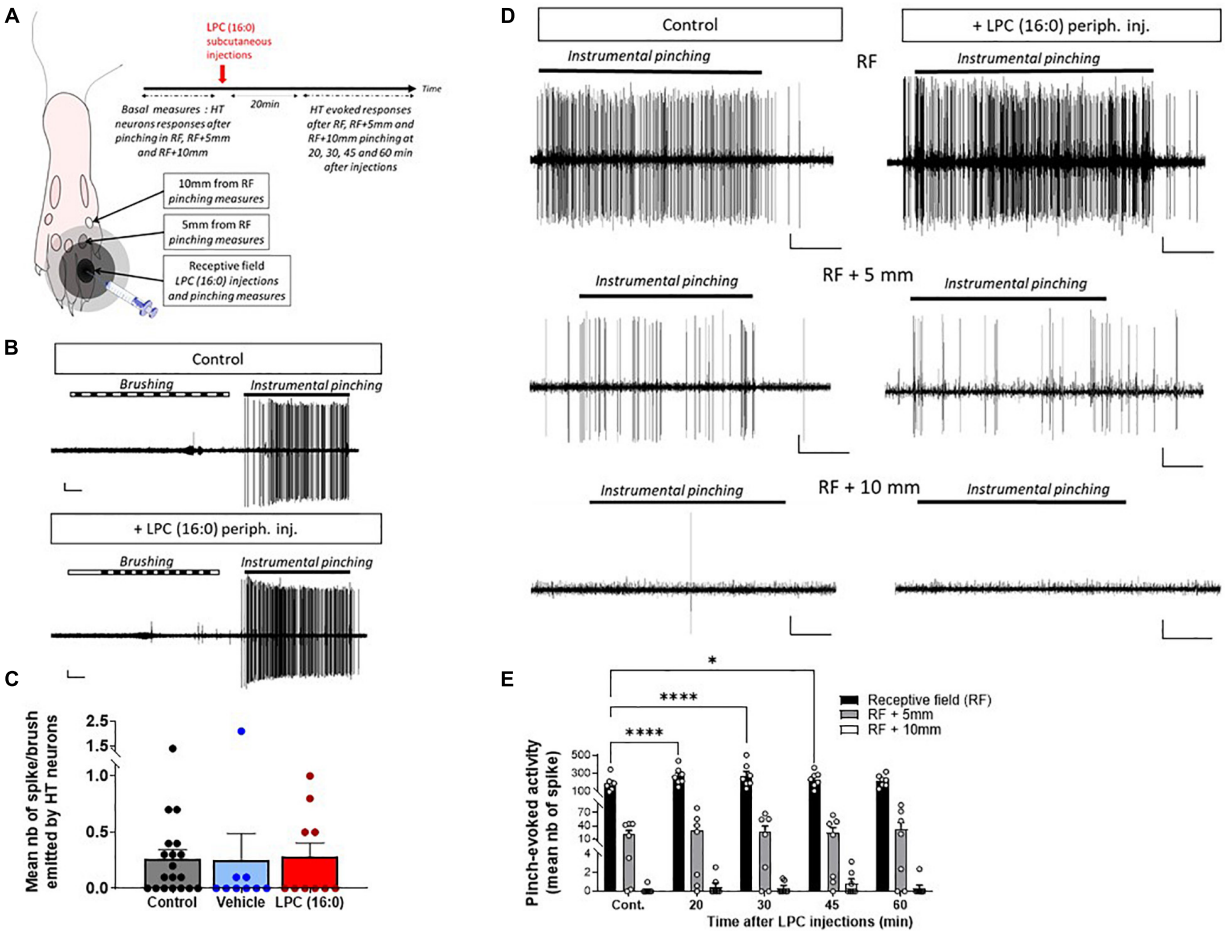

FIGURE 6 | Effect of cutaneous LPC injection on the size of HT neuron receptive field. **(A)** Experimental protocol used to test the possible enlargement of rat spinal HT neuron receptive fields (RF). Different areas were initially determined: RF, RF + 5 mm and RF + 10 mm. Noxious pinches (instrumental pinching, 300 g) were then applied onto these different areas. **(B)** Typical traces of a HT neuron not responding to brush but to instrumental pinching (indicating by black lines) before (top panel) and after LPC16:0 peripheral injection (bottom panel). Scale bars: 50 μV–1 s. **(C)** Population data showing non-noxious responses of HT neuron before (gray bar, n = 19 neurons/19 rats) and after vehicle (blue bar, n = 9 neurons/9 rats) or LPC16:0 (red bar, n = 10 neurons/10 rats) peripheral injections. Kruskal and Wallis test with $p = 0.4190$. **(D)** Representative recordings of HT neuronal discharge following pinching of RF, RF + 5 mm, or RF + 10 mm areas before (left panels) and 20 min after LPC16:0 peripheral injection (right panels, scale bars: 10 μV–1 s). **(E)** HT neuronal responses following RF (black bar), RF + 5 mm (gray bar) and RF + 10 mm (white bar) noxious stimulations, before and after LPC16:0 cutaneous injection. LPC only enhanced HT neurons evoked response when pinches were applied within the RF and not at RF + 5 mm or RF + 10 mm (n = 7 neurons from 7 rats, two-way ANOVA with $p = 0.0043$ and $p < 0.0001$ for time after LPC and RF area effects, followed by a Dunnet's multiple comparison test: $^{*}p < 0.05$ and $^{****}p < 0.0001$ as compared to control).

of LPC on HT neuron mechanical hyperexcitability. However, TRPV1 was involved in heat thermal hypersensitivity, as expected for this heat-sensitive channel. Indeed, pharmacological experiments with capsazepine and APETx2 are consistent with a direct role of TRPV1 in thermal transduction and a more pivotal role of ASIC3 in setting the overall neuronal excitability. This does not, however, preclude the participation of other LPC-modulated channels to the cutaneous effects of this lipid in physiological or pathophysiological conditions.

An increase spinal activity can result from both peripheral and central sensitization processes. Spinal dorsal horn neurons subject to central sensitization exhibit typical features, such as increased spontaneous activity, lower activation threshold to peripheral stimuli, increase response to suprathreshold stimulations, and an enlargement of the neuronal receptive field (Latremoliere and Woolf, 2009). We demonstrate here that spinal HT and WDR neurons exhibited enhanced spontaneous activities following LPC cutaneous injections as well as reduced temperature threshold triggering spikes in HT neurons. Moreover, the facilitation process of windup was potentiated by LPC. On the other hand, experiments using von Frey stimuli did not reveal any significant responses of HT and WDR neurons to subthreshold stimulations, at least for the filaments used that were at or below rat and mouse thresholds. It seems therefore that a single LPC subcutaneous injection would elicit rather hyperalgesia than allodynia. Finally, the increased response of spinal neurons to suprathreshold stimuli is rather short (45 min) and, importantly, no enlargement of spinal neuron receptive

fields, nor conversion of HT to WDR neuron or bilateral activation of spinal dorsal horn neurons have been observed at the dose of LPC used. However, we cannot completely exclude such phenomena at different doses. Thus, spinal neuron activity displayed some, but not all, the features of central sensitization, rather suggesting short-term than long-term central sensitization following subcutaneous LPC. This effect is driven by peripheral ASIC3 channels activation, which increase nociceptive inputs, leading to the enhancement of both spontaneous firing and evoked responses of spinal neurons to noxious stimuli.

It is interesting to compare the effects of LPC subcutaneous injection with those recently reported for intra-articular or intramuscular administrations of LPC (Hung et al., 2020; Jacquot et al., 2022). If the single subcutaneous injection of LPC described here only induces short-term hypersensitivity of the nociceptive pathway, in agreement with other studies (Gentry et al., 2010; Rimola et al., 2020), a single knee injection of LPC generates a secondary mechanical allodynia lasting for several days (Jacquot et al., 2022). Most importantly, two consecutive injections of LPC within muscles or joints induce chronic pain states associated to a sensitization of spinal HT neurons (Hung et al., 2020; Jacquot et al., 2022), in agreement with the high level of LPC detected in patients with established joint or muscle painful diseases (Marra et al., 2016; Hung et al., 2020; Jacquot et al., 2022). Such a difference in LPC effects between skin and joint/muscle may be related to different ASIC3 levels in the peripheral fibers innervating these tissues (Molliver et al., 2005), and/or to different processing of the pain information associated with superficial and deep tissues (Sluka, 2002; Prato et al., 2017).

Our study demonstrates how a single cutaneous injection of LPC can generate a short-term peripheral sensitization of nociceptive fibers. The underlying mechanism mainly involves pain-related ASIC3, but also TRPV1 channels, which can be both activated by this lipid. The nociceptive input induced by a single LPC cutaneous injection did not appear to be sufficient to drive long-term spinal synaptic plasticity, contrary to injections in muscle and joint (Hung et al., 2020; Jacquot et al., 2022). If LPC effects on nociceptive pathways clearly depend on peripheral ASIC3 channels, their consequences on pain may be tissue-dependent.

DATA AVAILABILITY STATEMENT

The raw data supporting the conclusions of this article will be made available by the authors, without undue reservation.

ETHICS STATEMENT

This study was reviewed and approved by CIEPAL-Azur and the French Ministry of Research, approval number 02595.02.

AUTHOR CONTRIBUTIONS

LP: conception and design, acquisition, and analysis and interpretation of *in vivo* data. KD: acquisition and analysis and interpretation of *in vitro* data. EL: interpretation of data. JB and FM: perform c-Fos immunohistochemistry. ED: conception and design and analysis and interpretation of data. All the authors have contributed to drafting the manuscript and have given approval to its final version.

FUNDING

This work was supported by the Centre National de la Recherche Scientifique, the Institut National de la Santé et de la Recherche Médicale, the Association Française contre les Myopathies (AFM grant #19618 and AFM grant #23731), the Agence Nationale de la Recherche (ANR-11-LABX-0015-01 and ANR-17-CE16-0018), and the NeuroMod Institute of University Côte d'Azur (UCA). This work has also been supported by the French government, through the UCAJEDI Investments in the future project managed by the National Research Agency (ANR) with the reference number ANR-15-IDEX-01.

ACKNOWLEDGMENTS

We thank A. Baron, S. Diochot, J. Noël, M. Salinas, and P. Inquimbert for helpful discussions, V. Friend and J. Salvi-Leyral for technical support, and V. Berthieux for secretarial assistance.

SUPPLEMENTARY MATERIAL

The Supplementary Material for this article can be found online at: https://www.frontiersin.org/articles/10.3389/fnmol.2022.880651/full#supplementary-material

REFERENCES

Almeida, T. F., Roizenblatt, S., and Tufik, S. (2004). Afferent pain pathways: a neuroanatomical review. *Brain Res.* 1000, 40–56. doi: 10.1016/j.brainres.2003.10.073

Andersson, D. A., Nash, M., and Bevan, S. (2007). Modulation of the cold-activated channel TRPM8 by lysophospholipids and polyunsaturated fatty acids. *J. Neurosci.* 27, 3347–3355. doi: 10.1523/JNEUROSCI.4846-06.2007

Birdsong, W. T., Fierro, L., Williams, F. G., Spelta, V., Naves, L. A., Knowles, M., et al. (2010). Sensing muscle ischemia: coincident detection of acid and ATP via interplay of two ion channels. *Neuron* 68, 739–749. doi: 10.1016/j.neuron.2010.09.029

Borzan, J., Zhao, C., Meyer, R. A., and Raja, S. N. (2010). A role for acid-sensing ion channel 3, but not acid-sensing ion channel 2, in sensing dynamic mechanical stimuli. *Anesthesiology* 113, 647–654. doi: 10.1097/ALN.0b013e3181eaa58a

Caterina, M. J., Leffler, A., Malmberg, A. B., Martin, W. J., Trafton, J., Petersen-Zeitz, K. R., et al. (2000). Impaired nociception and pain sensation in mice lacking the capsaicin receptor. *Science* 288, 306–313. doi: 10.1126/science.288.5464.306

Chang, C.-T., Fong, S. W., Lee, C.-H., Chuang, Y.-C., Lin, S.-H., and Chen, C.-C. (2019). Involvement of acid-sensing ion channel 1b in the development of acid-induced chronic muscle pain. *Front. Neurosci.* 13:1247. doi: 10.3389/fnins.2019.01247

Chen, C.-C., Zimmer, A., Sun, W.-H., Hall, J., Brownstein, M. J., and Zimmer, A. (2002). A role for ASIC3 in the modulation of high-intensity pain stimuli. *Proc. Natl. Acad. Sci. U.S.A.* 99, 8992–8997. doi: 10.1073/pnas.122245999

Choi, J., Zhang, W., Gu, X., Chen, X., Hong, L., Laird, J. M., et al. (2011). Lysophosphatidylcholine is generated by spontaneous deacylation of oxidized phospholipids. *Chem. Res. Toxicol.* 24, 111–118. doi: 10.1021/tx100305b

D'Arrigo, P., and Servi, S. (2010). Synthesis of lysophospholipids. *Molecules* 15, 1354–1377. doi: 10.3390/molecules15031354

Deval, E., and Lingueglia, E. (2015). Acid-sensing ion channels and nociception in the peripheral and central nervous systems. *Neuropharmacology* 94, 49–57. doi: 10.1016/j.neuropharm.2015.02.009

Deval, E., Baron, A., Lingueglia, E., Mazarguil, H., Zajac, J.-M., and Lazdunski, M. (2003). Effects of neuropeptide SF and related peptides on acid sensing ion channel 3 and sensory neuron excitability. *Neuropharmacology* 44, 662–671. doi: 10.1016/s0028-3908(03)00047-9

Deval, E., Noël, J., Gasull, X., Delaunay, A., Alloui, A., Friend, V., et al. (2011). Acid-sensing ion channels in postoperative pain. *J. Neurosci.* 31, 6059–6066. doi: 10.1523/JNEUROSCI.5266-10.2011

Deval, E., Noël, J., Lay, N., Alloui, A., Diochot, S., Friend, V., et al. (2008). ASIC3, a sensor of acidic and primary inflammatory pain. *EMBO J.* 27, 3047–3055. doi: 10.1038/emboj.2008.213

Deval, E., Salinas, M., Baron, A., Lingueglia, E., and Lazdunski, M. (2004). ASIC2b-dependent regulation of ASIC3, an essential acid-sensing ion channel subunit in sensory neurons via the partner protein PICK-1. *J. Biol. Chem.* 279, 19531–19539. doi: 10.1074/jbc.M313078200

Diochot, S., Alloui, A., Rodrigues, P., Dauvois, M., Friend, V., Aissouni, Y., et al. (2016). Analgesic effects of mambalgin peptide inhibitors of acid-sensing ion channels in inflammatory and neuropathic pain. *Pain* 157, 552–559. doi: 10.1097/j.pain.0000000000000397

Diochot, S., Baron, A., Rash, L. D., Deval, E., Escoubas, P., Scarzello, S., et al. (2004). A new sea anemone peptide, APETx2, inhibits ASIC3, a major acid-sensitive channel in sensory neurons. *EMBO J.* 23, 1516–1525. doi: 10.1038/sj.emboj.7600177

Diochot, S., Baron, A., Salinas, M., Douguet, D., Scarzello, S., Dabert-Gay, A.-S., et al. (2012). Black mamba venom peptides target acid-sensing ion channels to abolish pain. *Nature* 490, 552–555. doi: 10.1038/nature11494

Flemming, P. K., Dedman, A. M., Xu, S.-Z., Li, J., Zeng, F., Naylor, J., et al. (2006). Sensing of lysophospholipids by TRPC5 calcium channel. *J. Biol. Chem.* 281, 4977–4982. doi: 10.1074/jbc.M510301200

Gentry, C., Stoakley, N., Andersson, D. A., and Bevan, S. (2010). The roles of iPLA2, TRPM8 and TRPA1 in chemically induced cold hypersensitivity. *Mol. Pain* 6:4. doi: 10.1186/1744-8069-6-4

Hesselager, M., Timmermann, D. B., and Ahring, P. K. (2004). PH Dependency and desensitization kinetics of heterologously expressed combinations of acid-sensing ion channel subunits. *J. Biol. Chem.* 279, 11006–11015. doi: 10.1074/jbc.M313507200

Hung, C.-H., Lee, C.-H., Tsai, M.-H., Chen, C.-H., Lin, H.-F., Hsu, C.-Y., et al. (2020). Activation of acid-sensing ion channel 3 by lysophosphatidylcholine 16:0 mediates psychological stress-induced fibromyalgia-like pain. *Ann. Rheum. Dis.* 79, 1644–1656. doi: 10.1136/annrheumdis-2020-218329

Immke, D. C., and McCleskey, E. W. (2001). Lactate enhances the acid-sensing Na+ channel on ischemia-sensing neurons. *Nat. Neurosci.* 4, 869–870. doi: 10.1038/nn0901-869

Jacquot, F., Khoury, S., Labrum, B., Delanoe, K., Pidoux, L., Barbier, J., et al. (2022). Lysophosphatidylcholine 16: 0 mediates chronic joint pain associated to rheumatic diseases through acid-sensing ion channel 3. *Pain*. doi: 10.1097/j.pain.0000000000002596 [Epub ahead of print].

Jasti, J., Furukawa, H., Gonzales, E. B., and Gouaux, E. (2007). Structure of acid-sensing ion channel 1 at 1.9 A resolution and low pH. *Nature* 449, 316–323. doi: 10.1038/nature06163

Karabina, S.-A., and Ninio, E. (2006). Plasma PAF-acetylhydrolase: an unfulfilled promise? *Biochim. Biophys. Acta* 1761, 1351–1358. doi: 10.1016/j.bbalip.2006.05.008

Latremoliere, A., and Woolf, C. J. (2009). Central sensitization: a generator of pain hypersensitivity by central neural plasticity. *J. Pain* 10, 895–926. doi: 10.1016/j.jpain.2009.06.012

Lee, C.-H., and Chen, C.-C. (2018). Roles of ASICs in nociception and proprioception. *Adv. Exp. Med. Biol.* 1099, 37–47. doi: 10.1007/978-981-13-1756-9_4

Li, M., Inoue, K., Branigan, D., Kratzer, E., Hansen, J. C., Chen, J. W., et al. (2010). Acid-sensing ion channels in acidosis-induced injury of human brain neurons. *J. Cereb. Blood Flow Metab.* 30, 1247–1260. doi: 10.1038/jcbfm.2010.30

Lin, S.-H., Cheng, Y.-R., Banks, R. W., Min, M.-Y., Bewick, G. S., and Chen, C.-C. (2016). Evidence for the involvement of ASIC3 in sensory mechanotransduction in proprioceptors. *Nat. Commun.* 7:11460. doi: 10.1038/ncomms11460

Maingret, F., Patel, A. J., Lesage, F., Lazdunski, M., and Honoré, E. (2000). Lysophospholipids open the two-pore domain mechano-gated K(+) channels TREK-1 and TRAAK. *J. Biol. Chem.* 275, 10128–10133. doi: 10.1074/jbc.275.14.10128

Mamet, J., Baron, A., Lazdunski, M., and Voilley, N. (2002). Proinflammatory mediators, stimulators of sensory neuron excitability via the expression of acid-sensing ion channels. *J. Neurosci.* 22, 10662–10670. doi: 10.1523/JNEUROSCI.22-24-10662.2002

Marra, S., Ferru-Clément, R., Breuil, V., Delaunay, A., Christin, M., Friend, V., et al. (2016). Non-acidic activation of pain-related Acid-Sensing Ion Channel 3 by lipids. *EMBO J.* 35, 414–428. doi: 10.15252/embj.201592335

Messeguer, A., Planells-Cases, R., and Ferrer-Montiel, A. (2006). Physiology and pharmacology of the vanilloid receptor. *Curr. Neuropharmacol.* 4, 1–15. doi: 10.2174/157015906775202995

Molliver, D. C., Immke, D. C., Fierro, L., Paré, M., Rice, F. L., and McCleskey, E. W. (2005). ASIC3, an acid-sensing ion channel, is expressed in metaboreceptive sensory neurons. *Mol. Pain* 1:35. doi: 10.1186/1744-8069-1-35

Murakami, M., Sato, H., and Taketomi, Y. (2020). Updating phospholipase A2 biology. *Biomolecules* 10:1457. doi: 10.3390/biom10101457

Prato, V., Taberner, F. J., Hockley, J. R. F., Callejo, G., Arcourt, A., Tazir, B., et al. (2017). Functional and molecular characterization of mechanoinsensitive "silent" nociceptors. *Cell Rep.* 21, 3102–3115. doi: 10.1016/j.celrep.2017.11.066

Price, M. P., McIlwrath, S. L., Xie, J., Cheng, C., Qiao, J., Tarr, D. E., et al. (2001). The DRASIC cation channel contributes to the detection of cutaneous touch and acid stimuli in mice. *Neuron* 32, 1071–1083. doi: 10.1016/s0896-6273(01)00547-5

Rimola, V., Hahnefeld, L., Zhao, J., Jiang, C., Angioni, C., Schreiber, Y., et al. (2020). Lysophospholipids contribute to oxaliplatin-induced acute peripheral pain. *J. Neurosci.* 40, 9519–9532. doi: 10.1523/JNEUROSCI.1223-20.2020

Sadler, K. E., Moehring, F., Shiers, S. I., Laskowski, L. J., Mikesell, A. R., Plautz, Z. R., et al. (2021). Transient receptor potential canonical 5 mediates inflammatory mechanical and spontaneous pain in mice. *Sci. Transl. Med.* 13:eabd7702. doi: 10.1126/scitranslmed.abd7702

Savidge, J. R., Ranasinghe, S. P., and Rang, H. P. (2001). Comparison of intracellular calcium signals evoked by heat and capsaicin in cultured rat dorsal root ganglion neurons and in a cell line expressing the rat vanilloid receptor, VR1. *Neuroscience* 102, 177–184. doi: 10.1016/s0306-4522(00)00447-4

Sherwood, T. W., and Askwith, C. C. (2009). Dynorphin opioid peptides enhance acid-sensing ion channel 1a activity and acidosis-induced neuronal death. *J. Neurosci.* 29, 14371–14380. doi: 10.1523/JNEUROSCI.2186-09.2009

Sluka, K. A. (2002). Stimulation of deep somatic tissue with capsaicin produces long-lasting mechanical allodynia and heat hypoalgesia that depends on early activation of the cAMP pathway. *J. Neurosci.* 22, 5687–5693. doi: 10.1523/JNEUROSCI.22-13-05687.2002

Sluka, K. A., Price, M. P., Breese, N. M., Stucky, C. L., Wemmie, J. A., and Welsh, M. J. (2003). Chronic hyperalgesia induced by repeated acid injections in muscle is abolished by the loss of ASIC3, but not ASIC1. *Pain* 106, 229–239. doi: 10.1016/s0304-3959(03)00269-0

Verkest, C., Piquet, E., Diochot, S., Dauvois, M., Lanteri-Minet, M., Lingueglia, E., et al. (2018). Effects of systemic inhibitors of acid-sensing ion channels 1 (ASIC1) against acute and chronic mechanical allodynia in a rodent model of migraine. *Br. J. Pharmacol.* 175, 4154–4166. doi: 10.1111/bph.14462

Waldmann, R., Bassilana, F., de Weille, J., Champigny, G., Heurteaux, C., and Lazdunski, M. (1997b). Molecular cloning of a non-inactivating proton-gated Na+ channel specific for sensory neurons. *J. Biol. Chem.* 272, 20975–20978. doi: 10.1074/jbc.272.34.20975

Waldmann, R., Champigny, G., Bassilana, F., Heurteaux, C., and Lazdunski, M. (1997a). A proton-gated cation channel involved in acid-sensing. *Nature* 386, 173–177. doi: 10.1038/386173a0

Weil, A., Moore, S. E., Waite, N. J., Randall, A., and Gunthorpe, M. J. (2005). Conservation of functional and pharmacological properties in the distantly related temperature sensors TRPV1 and TRPM8. *Mol. Pharmacol.* 68, 518–527. doi: 10.1124/mol.105.012146

Xu, J., and Brennan, T. J. (2009). Comparison of skin incision vs. Skin plus deep tissue incision on ongoing pain and spontaneous activity in dorsal horn neurons. *Pain* 144, 329–339. doi: 10.1016/j.pain.2009.05.019

Xu, Q., Li, W.-Y., and Guan, Y. (2013). Mu-opioidergic modulation differs in deep and superficial wide-dynamic range dorsal horn neurons in mice. *Neurosci. Lett.* 549, 157–162. doi: 10.1016/j.neulet.2013.05.059

Conflict of Interest: The authors declare that the research was conducted in the absence of any commercial or financial relationships that could be construed as a potential conflict of interest.

frontiers | Frontiers in Molecular Neuroscience

ORIGINAL RESEARCH
published: 04 July 2022
doi: 10.3389/fnmol.2022.903087

Modulation of GABAergic Synaptic Transmission by NMDA Receptors in the Dorsal Horn of the Spinal Cord

Benjamin Leonardon[1,2], *Lou Cathenaut*[1,2], *Louise Vial-Markiewicz*[1,2], *Sylvain Hugel*[1], *Rémy Schlichter*[1,2] *and Perrine Inquimbert*[1,2]*

[1]Centre National de la Recherche Scientifique, UPR 3212 Institute of Cellular and Integrative Neurosciences, Strasbourg, France, [2]Université de Strasbourg, Strasbourg, France

The dorsal horn (DH) of the spinal cord is an important structure involved in the integration of nociceptive messages. Plastic changes in the properties of neuronal networks in the DH underlie the development of analgesia as well as of hyperalgesia and allodynia in acute and chronic pain states. Two key mechanisms are involved in these chronic pain states: increased electrical activities and glutamate release leading to the recruitment of NMDAr and plastic changes in the synaptic inhibition. Although: (1) the balance between excitation and inhibition is known to play a critical role in the spinal network; and (2) plastic changes in spinal excitation and inhibition have been studied separately, the relationship between these two mechanisms has not been investigated in detail. In the present work, we addressed the role of NMDA receptors in the modulation of GABAergic synaptic transmission in the DH network. Using tight-seal whole-cell recordings on adult mice DH neurons, we characterized the effect of NMDAr activation on inhibitory synaptic transmission and more especially on the GABAergic one. Our results show that, in a subset of neurons recorded in lamina II, NMDAr activation facilitates spontaneous and miniature GABAergic synaptic transmission with a target specificity on GABAergic interneurons. In contrast, NMDA reduced the mean amplitude of evoked GABAergic IPSCs. These results show that NMDAr modulate GABAergic transmission by a presynaptic mechanism of action. Using a pharmacological approach, we investigated the composition of NMDAr involved in this modulation of GABAergic synaptic transmission. We found that the NMDA-induced facilitation was mediated by the activation of NMDAr containing GluN2C/D subunits. Altogether, our results bring new insights on nociceptive information processing in the spinal cord network and plastic changes in synaptic inhibition that could underlie the development and maintenance of chronic pain.

Keywords: dorsal horn, synaptic inhibition, NMDA receptors, nociception, pain

OPEN ACCESS

Edited by:
Fabien Marchand, INSERM U1107 Douleur et Biophysique Neurosensorielle (Neuro-Dol), France

Reviewed by:
Hugues Petitjean, Benephyt, France
Rita Bardoni, University of Modena and Reggio Emilia, Italy

***Correspondence:**
Perrine Inquimbert
inquimbert@unistra.fr

Specialty section:
This article was submitted to Pain Mechanisms and Modulators, a section of the journal Frontiers in Molecular Neuroscience

Received: *23 March 2022*
Accepted: *31 May 2022*
Published: *04 July 2022*

Citation:
Leonardon B, Cathenaut L, Vial-Markiewicz L, Hugel S, Schlichter R and Inquimbert P (2022) Modulation of GABAergic Synaptic Transmission by NMDA Receptors in the Dorsal Horn of the Spinal Cord. Front. Mol. Neurosci. 15:903087. doi: 10.3389/fnmol.2022.903087

INTRODUCTION

The dorsal horn (DH) of the spinal cord is an important structure involved in the integration and transmission of nociceptive messages from the inner and outer environment. Spinal integration of this information relies on the interplay between different DH neurons forming a complex and functionally plastic neuronal network (Cordero-Erausquin et al., 2016).

The DH neuronal network is composed of inhibitory and excitatory interneurons. A fine-tuning of the excitatory/inhibitory balance is crucial in the control of the transmission of nociceptive messages from the DH to the supraspinal structures where it may lead to pain perception. Imbalance between excitation and inhibition in DH networks is known to be one of the mechanisms leading to enhanced pain sensation and underlying the development and maintenance of pathological pain, such as neuropathic pain. Impairment of DH inhibitory synaptic transmission plays a pivotal role in this disruption of the excitation/inhibition balance (Sivilotti and Woolf, 1994; Coull et al., 2003; Harvey et al., 2004; Torsney and MacDermott, 2006). Indeed, pharmacological blockade of ionotropic $GABA_A$ and glycine receptors induces thermal hyperalgesia and mechanical allodynia (Beyer et al., 1985; Roberts et al., 1986).

The major excitatory transmitter released by primary afferent fibers is glutamate. Under physiological conditions, fast glutamatergic transmission in the DH is mediated by postsynaptic AMPA receptors (AMPAr). Sustained or repeated afferent fiber stimulation leads to an increased release of glutamate in the DH and consequently to the recruitment of NMDA receptors (NMDAr; Woolf and Thompson, 1991). In the DH, NMDAr activation is critically involved in long-term potentiation of excitatory synapses (Woolf and Salter, 2000; Sandkuhler, 2007; Latremoliere and Woolf, 2009). Moreover activation of presynaptic NMDAr expressed on afferent fiber terminals facilitates glutamate release in the DH (Liu et al., 1994, 1997; Bardoni, 2013) and modulates transmission of nociceptive messages in the spinal cord (Bardoni, 2013; Deng et al., 2019). Interestingly, one study demonstrated that 37% of GABAergic synaptic terminals in the DH of the rat spinal cord expressed NMDAr (Lu et al., 2005), but the subunit composition as well as the role of these presynaptic receptors has not been investigated so far.

Plastic changes in the strength of inhibitory synaptic transmissions play a crucial role in information processing and tuning of neural activity. In several regions of the CNS, activity-dependent long-term plasticities (LTP and LTD) of inhibitory synapses have been described (Kullmann et al., 2012). In the DH, one study has described a heterosynaptic plasticity at GABAergic synapses in lamina I neurons, after activation of metabotropic glutamate receptors (Fenselau et al., 2011) and one recent study described an NMDAr-dependent potentiation of glycinergic synapses (Kloc et al., 2019). In other structures, postsynaptic and presynaptic NMDAr have been shown to be key players in the modulation of GABA release (Glitsch and Marty, 1999; Duguid and Smart, 2004; Crabtree et al., 2013) and in the functional plasticity of inhibitory synapses (Nugent et al., 2007; Mapelli et al., 2016). It is known that changes in spinal inhibition are crucial in the processing of nociceptive information and that NMDAr are activated by an increased activity in the DH network. However, nothing is known about the possibility that activity-dependent modulation at inhibitory synapses engaging NMDAr could take place in the DH.

In the present work, we addressed the role of NMDAr in the modulation of GABAergic synaptic transmission in the DH network. Using patch-clamp recordings on adult mice DH neurons, we characterized the effect of NMDAr activation on inhibitory synaptic transmission and more especially on the GABAergic one. Our results indicate that NMDAr activation differentially modulates spontaneous and electrically-evoked GABA release and that this effect targets preferentially GABAergic synapses established with GABAergic interneurons.

MATERIALS AND METHODS

Animals

All procedures were performed in accordance with European directives and were approved by the regional ethics committee and the French Ministry of Agriculture (license No. 2015030911301894). We used C57BL/6j (n = 118) and GAD65-eGFP mice (n = 28). GAD65-eGFP were obtained from Ferenc Erdelyi and Gabor Szabo (Institute of Experimental Medicine, Budapest) and have been described previously (Cui et al., 2011). The mice were interbred, born and housed in the animal house of the laboratory (Chronobiotron, agreement No. A67-2018-38) at room temperature with a 12 h light/dark cycle and with free access to food and water. Experiments were performed with male adult mice (5–10 weeks old).

Slice Preparation

Mice were anesthetized by intraperitoneal injection of urethane (1.9 g/kg body weight) prior to realizing a laminectomy. The lumbar spinal cord was removed and immediately immersed in ice-cold sucrose-based artificial cerebrospinal fluid (sACSF) containing in mM: sucrose (252), KCl (2.5), $NaCl_2$ (2), $MgCl_2$ (2), glucose (10), $NaHCO_3$ (26), and NaH_2PO_4 (1.25) continuously gassed with carbogen (5% CO_2 and 95% O_2). The spinal cord was embedded in agarose (5%) and 300 μm-thick transverse slices were cut through lumbar 3–5 segments using a Leica VT1200S vibratome (Leica Microsystems Inc.). Slices were stored at room temperature (22°C–24°C) in a chamber filled with ACSF containing (in mM): NaCl (126), $NaHCO_3$ (26), $NaCl_2$ (2), KCl (2.5), NaH_2PO_4 (1.25), $MgCl_2$ (2), glucose (10), and continuously gassed with carbogen.

Electrophysiology

Slices were transferred to the recording chamber and continuously perfused with oxygenated ACSF. Recordings were performed from lamina II neurons.

Patch pipettes were pulled from borosilicate glass capillaries (1.2 mm o.d. 0.69 mm i.d.; Harvard Apparatus) using a P-1000 puller (Sutter Instruments, Novato, CA, USA) and had final tip resistances between 3 and 6 MΩ. Pipettes were filled with an intracellular solution containing (in mM): CsCl (130), HEPES (10), and $MgCl_2$ (2). The intracellular solution had a pH of 7.3 adjusted with CsOH and an osmolarity of 300 mOsm adjusted with sucrose. In these conditions, the theoretical equilibrium potential for Cl^- anions was 0 mV.

Whole-cell patch-clamp recordings were performed from neurons identified under visual control using an infrared differential interface contrast optics. Gad65-eGFP neurons were identified using epifluorescent illumination.

Voltage-clamp recordings were performed with an Axopatch 200 B amplifier (Molecular Devices, San Jose, CA) at a holding potential fixed at −60 mV allowing visualization of excitatory postsynaptic currents and inhibitory postsynaptic currents (EPSCs; IPSCs) as inward currents. Recordings were low-pass filtered (5 kHz) and acquired with Clampex software (Molecular Devices, San Jose, USA). Current traces were digitized (10 kHz) and stored on the hard drive of a personal computer. All experiments were performed at room temperature (22°C–24°C).

Paired-pulse ratio experiments were performed by stimulation of a presynaptic neuron with a 0.25 mA current injection with an extracellular electrode filled with ACSF.

The stimulation was performed as described in Cathenaut et al by applying current steps (0.25 ms; 0.10–0.40 mA) through a patch pipette filled with ACSF (Cathenaut et al., 2022). This stimulation electrode was placed at 20–150 μm from the cell body of the recorded neuron. For each recorded neuron, the lowest amplitude of stimulation evoking IPSCs was determined and was increased by 0.05 mA to evoke IPSCs for each stimulation applied. Synaptic contacts were identified as monosynaptic unitary connections when the following criteria were satisfied: (1) all-or-none eIPSCs appearance; (2) absence of increase in eIPSC amplitude when minimal stimulation amplitude was increased by 0.05 mA; (3) disappearance of eIPSCs when stimulation polarity was inverted; and (4) constant latency of the eIPSCs.

Three different interstimulus intervals of stimulation were realized: 20, 50, and 100 ms and were repeated every 3 s. Paired-pulse ratio was determined as the amplitude ratio of the second to the first IPSC evoked in the postsynaptic neuron.

Pharmacological Substances

Different drugs were used in order to study NMDA effects on inhibitory synaptic transmission. We recorded spontaneous IPSCs in the presence of antagonist of AMPA and Kainate receptors, 6-cyano-7-nitroquinoxaline-2,3-dione (CNQX, 10 μM, Tocris). To isolate GABAergic or glycinergic currents, we used strychnine (1 μM, Sigma) or bicuculline methiodine (10 μM, Sigma), respectively. Miniature IPSCs were recorded in the presence of tetrodotoxin (TTX; 0.5 μM, Latoxan) to block voltage gated sodium channels.

To assess the role of NMDAr, we used the specific agonist N-Methyl-D-aspartic acid (NMDA, 100 μM, Tocris). The specific antagonist of NMDAr, D-2-amino-5-phosphonovalerate (APV 50 μM; Abcam), was used to block all NMDAr. Two specific antagonists of NMDAr containing GluN2C/D subunits were used, (2R,3S)-1-[(phenanthren-3-yl)carbonyl]piperazine-2,3-dicarboxylic acid) (UBP141 10 μM and 25 μM) and (4-((1H-Indol-7yl)carbamoyl)phenyl diethylcarbamate) NAB14 (10 μM, from Abcam and Aobious respectively). Ifenprodil (10 μM, Sigma) was used to block NMDAr containing GluN2B subunits. Zinc (100 nM, Sigma) was used to inhibit NMDAr containing GluN2A subunits. Finally, we also used a channel blocker of NMDAr, dizocilpine (MK-801; 2 mM in the intracellular solution, Tocris). Drugs were prepared as 1,000× or 10,000× concentrated stock solutions in dimethylsulphoxide (DMSO), water or ethanol in accordance with indications from the manufacturer. The stocks were stored at −20°C. All substances were diluted to their final concentration in ACSF at the beginning of each experiment and applied by general bath perfusion (flow rate: 1.0 ml/min; total chamber volume: 2 ml).

Data Analysis

Synaptic events were detected using WinEDR with an amplitude threshold detection algorithm and visually inspected for validity. The analysis of frequency has been performed as described in a previous study of our lab (Petitjean et al., 2012). For each neuron analyzed, the cumulative number, N, of synaptic events was plotted as a function of time. A two-linear-segment curve was fitted by non-linear regression (KyPlot 2.15; KyensLab, Tokyo, Japan) using the following equation:

$$N = fo \times t \times a$$

for $t < tc$ and

$$N = fc \times t + (fo - fc) \times tc + a$$

for $t > tc$

Where the slope "fo" represents an estimation of the average frequency under control conditions and "fc" provides an estimation of the mean frequency following the application of the drug. "tc" is the time at which the change in frequency occurs. Drugs were considered to have an effect when "tc" occurred around 100 s following the beginning of the application of the substance and when the change in frequency exceeded 20% of the recorded basal frequency.

The percentage of increase in frequency was calculated as follows:

$$\text{Change in frequency (\%)} = \left(\frac{(fc - fo)}{fo}\right) \times 100$$

Peak amplitude was determined by using WinWCP (waveform measurements) to determine the exact value of the peak. Tau rise and Tau decay were determined by fitting the trace with an exponential decay (EPC endplate current-fitting function of WinWCP) using the following equation:

$$y(t) = 0.5 * A * (1 + \text{erf}(x - \tau\text{rise})) * \exp\left(\frac{-x}{\tau\text{decay}}\right)$$

Where A is the amplitude (in pA), τrise is the rise time (in ms) and τdecay is the decay time (in ms). Following these analyses, each neuron was classified either as displaying a change in EPSCs or IPSCs frequency, amplitude or kinetics in response to the application of the substance or as being non-responsive to this substance.

Statistics

Data are represented as mean ± Standard Error to the Mean (SEM). Statistical analyses were performed with GraphPad Prism (GraphPad Software 6.07, La Jolla, CA, USA). To compare proportions of neurons, Fisher's exact test was used. For the

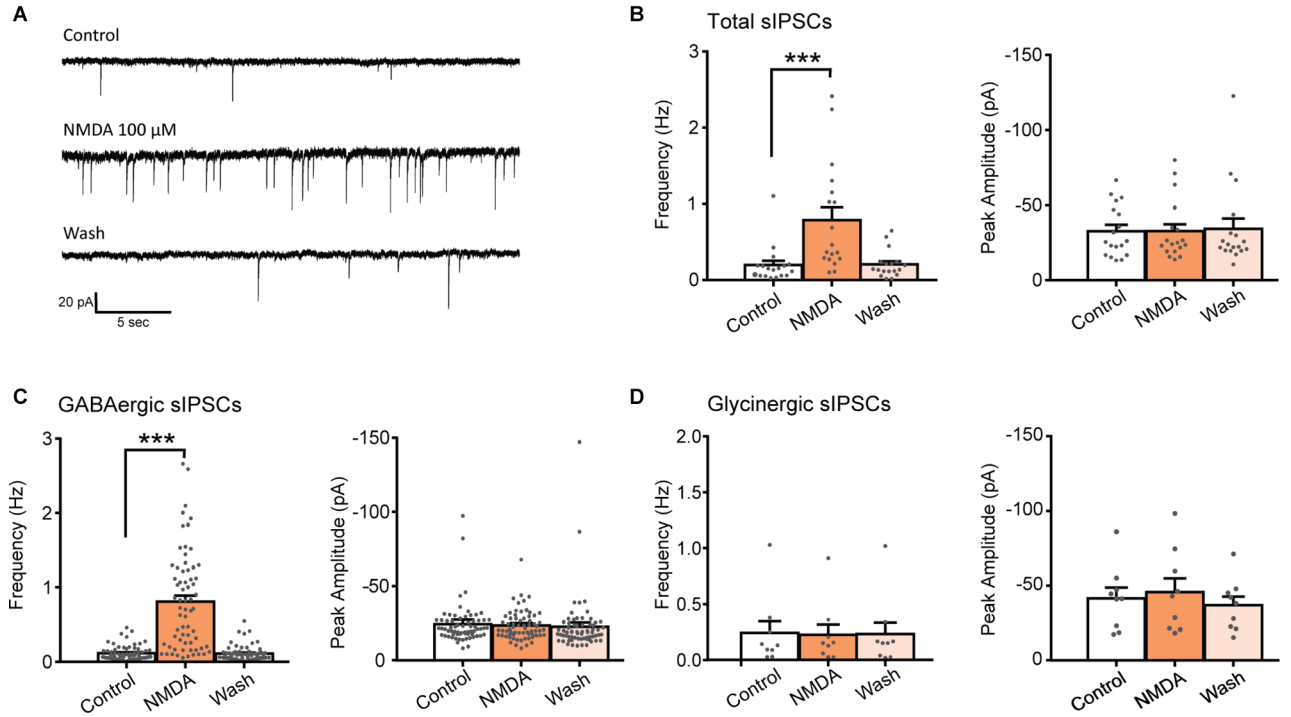

FIGURE 1 | NMDA increases GABA sIPSC frequency in lamina II neurons. **(A)** Representative traces of total sIPSCs recorded from lamina II neuron in spinal cord slice from C57Bl6 mouse before (Control) and during NMDA application (NMDA; 100 s after the beginning of application) and after a washout (wash; 360 s after the beginning of NMDA washout). **(B)** Bar graph showing total sIPSC frequency and peak amplitude before (Control) and during NMDA application (NMDA) and after a washout (wash; $N = 18$). NMDA application resulted in a reversible increase in sIPSC frequency without change in sIPSC amplitude. **(C,D)** Frequency and peak amplitude of GABAergic sIPSCs **(C)** and glycinergic sIPSCs **(D)** isolated pharmacologically. NMDA application enhances GABAergic sIPSC (recorded in presence of strychnine) frequency ($N = 67$) but did not affect glycinergic sIPSCs, recorded in presence of bicuculline **(D)** ($N = 9$). ***$p < 0.001$. Paired t-test was used. Error bars indicate SEM.

effect of drug application, we used the paired t-Test or the Wilcoxon test, and the unpaired t-Test or the Mann-Whitney test were used for unpaired comparisons, depending on the data distribution previously tested with the D'Agostino and Pearson normality test.

RESULTS

NMDA Receptor Activation Leads to an Increase in Spontaneous GABAergic Synaptic Transmission

Bath application of NMDA (100 μM, 60 s) caused a significant increase in the frequency of spontaneous inhibitory postsynaptic currents (sIPSCs) in 75% of the recorded neurons ($N = 18/24$). This facilitation was always followed by a full recovery after a washout (**Figures 1A,B**). In neurons displaying a significant increase in sIPSCs frequency, the increase was of 415% (control: 0.19 ± 0.06 Hz, NMDA: 0.79 ± 0.17 Hz; $N = 18$; $t = 4.147$, $p = 0.0007$, paired t-test). In these neurons, increase in sIPSCs frequency occurred without changes in sIPSCs amplitude (control: −32.5 ± 4.0 pA, NMDA: −32.5 ± 4.7 pA; $N = 18$; $t = 0.003$, $p = 0.9975$, paired t-test; **Figure 1B**).

Fast synaptic inhibition in the dorsal horn of the spinal cord is mediated by GABA and glycine. Effects of NMDA on GABAergic sIPSCs were examined in presence of 1 μM strychnine, a glycine receptor antagonist and effects of NMDA on Glycinergic sIPSCs were examined in presence of 10 μM bicuculline, a $GABA_A$ receptor antagonist. NMDA application induced a reversible increase of GABAergic sIPSCs in 80.7% of the recorded neurons ($N = 67/83$). In neurons displaying a significant effect, NMDA increased GABAergic sIPSCs frequency by 736% (control: 0.11 ± 0.01 Hz, NMDA: 0.81 ± 0.08 Hz; $N = 67$; $t = 4.147$, $p = 0.0007$, paired t-test) without changing sIPCSs amplitude (control: −24.2 ± 1.6 pA, during NMDA: −23.5 ± 1.2 pA; $N = 67$; $t = 0.9188$, paired t-test; **Figure 1C**). NMDA application neither changed glycinergic sIPSCs frequency nor amplitude ($N = 9$) indicating that NMDA modulates specifically GABAergic synaptic transmission (**Figure 1D**).

These results indicate that activation of NMDAr increases the frequency of GABAergic and not glycinergic spontaneous IPSCs.

In neurons in which NMDA facilitated GABAergic sIPSCs, a second application of NMDA yielded a similar effect (relative increase in frequency: NMDA = 0.93 ± 0.29, $N = 6$; **Figure 2A**). Taking advantage of the reproductibility of NMDA effect, we examined the effect of NMDAr antagonists in NMDA-responsive neurons. To this end, a second application of NMDA was

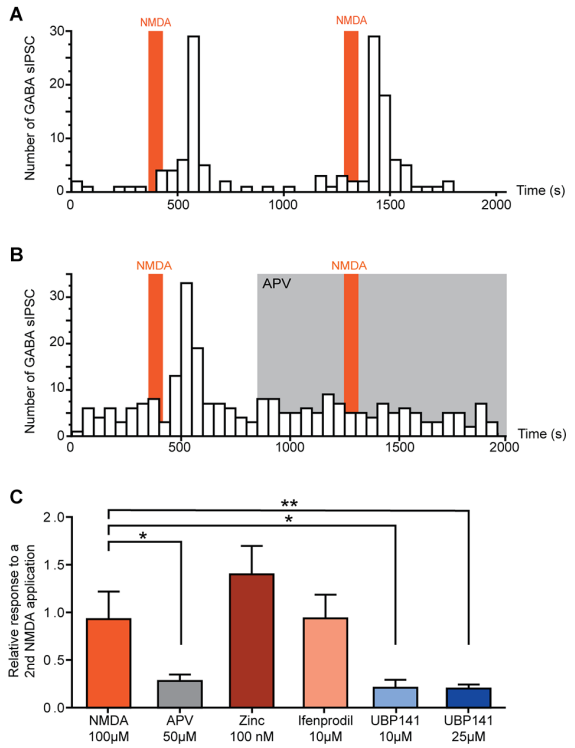

FIGURE 2 | Activation of GluN 2C/D containing NMDA receptors induces increase of spontaneous GABAergic transmission. **(A,B)** Example of the effect of two successive NMDA applications on the number of GABAergic sIPCSs (50 s bin). NMDA effect is reproducible **(A)** and completely blocked in presence of APV (50 μM) **(B)**. **(C)** Effect of a second application of NMDA in presence of different NMDAr selective antagonists. Histogram showing the effect of a second NMDA application normalized to a first application performed in absence of antagonists. NMDA-induced increase in GABA sIPSC frequency was inhibited in presence of APV (50 μM, $N = 8$) and UBP 141 (10 μM, $N = 4$; 25 μM, $N = 9$). Presence of Zinc (100 nM, $N = 4$) or Ifenprodil (10 μM, $N = 8$) did not affect NMDA effect. $^{*}p < 0.05$ and $^{**}p < 0.01$. Mann-Whitney test was used. Error bars indicate SEM.

performed in presence of NMDAr antagonists or modulators, and effects of both applications were compared.

In the presence of 50 μM APV, a selective NMDAr antagonist, NMDA-induced increase in GABAergic sIPSCs frequency was reduced by 72% (relative increase in frequency: NMDA = 0.93 ± 0.29, NMDA+APV = 0.28 ± 0.07, $N = 8$, $p = 0.02$, Mann-Whitney test; **Figure 2B**).

NMDAr is a tetrameric ionotropic glutamate receptor with a most frequent configuration consisting of two mandatory GluN1 and two GluN2 subunits (GluN2 A-D). To assess the composition of NMDAr contributing to the increase in GABAergic sIPSCs frequency, we tested the effect of NMDAr subunit-selective antagonists.

Zinc (100 nM), which blocks specifically NMDAr containing GluN2A subunit, had no effect on NMDA-induced effect (relative increase in frequency: Zinc = 1.40 ± 0.30, $N = 4$), neither did ifenprodil (10 μM), a selective antagonist of GluN2B-containing NMDAr (relative increase in frequency: ifenprodil = 0.94 ± 0.25, $N = 8$). However, NMDA-induced increase in GABAergic sIPSCs frequency was reduced by 79% in presence of UBP 141 (UBP 10 μM: relative increase in frequency = 0.21 ± 0.08, $N = 4$, $p = 0.019$, Mann-Whitney test; UBP 25 μM: relative increase in frequency = 0.20 ± 0.04, $N = 9$, $p = 0.0048$, Mann-Whitney test) a specific antagonist of GluN2C/D-containing NMDAr (**Figure 2C**), indicating the involvement of NMDAr containing these subunits in the effects of NMDA on GABAergic transmission.

NMDA Receptor Activation Selectively Increases GABA Release

We next examined whether NMDA-induced facilitation of spontaneous GABAergic transmission involved a direct effect on presynaptic GABAergic terminals or whether it required action potential firing and propagation in presynaptic interneurons. To this end, we recorded miniature IPSCs (mIPSCs) in the presence of 0.5 μM TTX. In 58% of recorded-neurons ($N = 14/24$), application of NMDA induced a significant increase in mIPSCs frequency (control: 0.04 ± 0.01 Hz, NMDA: 0.21 ± 0.05 Hz; $N = 14$; $t = 3.664$, $p = 0.0029$, paired t-test), without change in mIPSCs amplitude. We next recorded pharmacologically isolated GABAergic mIPSCs in the presence of the channel blocker TTX and the glycine receptor antagonist Strychnine (STR). In 54% of recorded neurons ($N = 35/65$), NMDA induced a significant increase in GABAergic mIPSCs frequency (control: 0.07 ± 0.01 Hz, NMDA: 0.26 ± 0.04 Hz; $N = 36$; $t = 5.364$, $p < 0.0001$, paired t-test) without changes in GABAergic mIPSCs amplitude (**Figures 3A,B**). Moreover, NMDA never induced significant changes neither in amplitude, nor in mIPSCs activation or deactivation kinetics, suggesting that NMDA increased GABA release probability *via* a presynaptic action.

To examine the specificity of the NMDA effect on GABAergic synapses, we examined the effect of NMDA application on mEPSCs or glycinergic mIPSCs. NMDA applications neither changed mEPSCs (recorded without CNQX and in presence of bicuculline and strychnine), nor glycinergic mIPSCs (recorded in absence of Strychnine and in presence of CNQX and bicuculline; data not shown).

As previously performed for spontaneous GABAergic transmission, we observed the effects of NMDAr antagonists on the NMDA-induced increase in mIPSCs frequency.

APV (50 μM) reduced by 72% the NMDA-induced increase in GABAergic mIPSCs frequency (relative response to the first application: NMDA = 0.59 ± 0.11, APV = 0.17 ± 0.04, $N = 6$, $p = 0.0087$, Mann-Whitney test; **Figure 2B**). These results confirm that NMDA acted on NMDAr to increase the frequency of GABAergic mIPSCs.

NMDA-induced increase in GABAergic mIPSCs frequency was reduced by 77% in presence of NAB14 (10 μM) a highly selective antagonist of GluN2C/D-containing NMDAr (relative response: NAB14 = 0.23 ± 0.05, $N = 5$, $p = 0.0173$, Mann-Whitney test) confirming the involvement of GluN2C/D-containing NMDAr in NMDA-induced facilitation of GABAergic synaptic transmission (**Figure 3C**).

The voltage-dependent block of NMDAr by Mg^{2+} is stronger for NMDAr containing GluN2A or GluN2B subunits than for those containing GluN2C/D subunit (Paoletti et al., 2013).

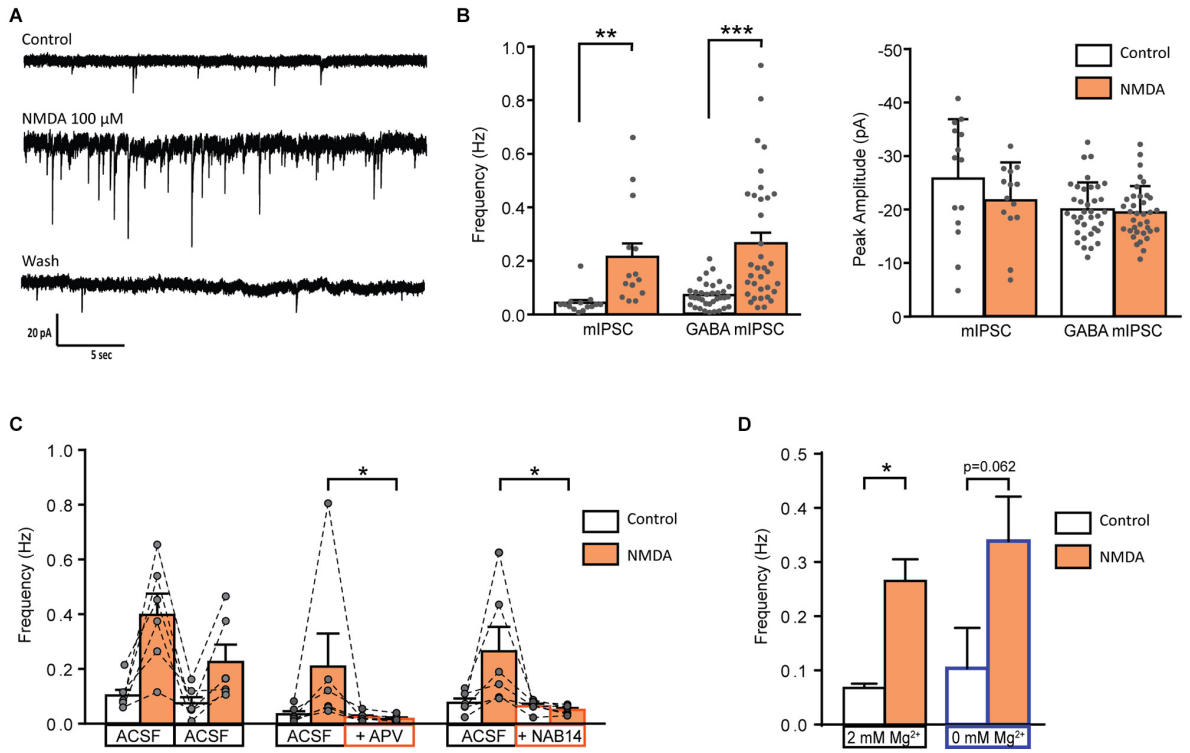

FIGURE 3 | Activation of GluN2C/D containing NMDA receptor increase miniature GABAergic IPSCs. **(A)** Representative traces of mIPSCs recorded from a lamina II neuron in spinal cord slice from C57Bl6 mouse before (Control) during NMDA application (NMDA; 100 s after the beginning of application) and after a washout (wash; 400 s after the beginning of NMDA washout). **(B)** Bar graph showing total mIPSC (N = 14) and GABA mIPSC (N = 36) frequency and peak amplitude before (Control) and during NMDA application (NMDA). **(C)** Effect of APV (50 µM, N = 6) and NAB 14 (10 µM, N = 5) on NMDA-induced increase in GABA mIPSC frequency. Both antagonists blocked effect of NMDA application. **(D)** NMDA-induced increase in GABA mIPSC frequency in presence (2 mM Mg^{2+}, N = 36) or in absence of external Mg^{2+} (0 mM Mg^{2+}, N = 5) is comparable. *$p < 0.05$, **$p < 0.01$, ***$p < 0.001$. Paired t-test **(A)**, Mann-Whitney test **(B)**, and Wilcoxon test **(C)** were used. Error bars indicate SEM.

The experiments described so far were performed in the presence of 2 mM Mg^{2+}. To assess whether the contribution of GluN2A- or GluN2B-containing NMDAr was masked by a Mg^{2+}-dependent block, we assessed the effect of NMDA on GABAergic mIPSCs recorded in absence of extracellular Mg^{2+}. These recordings were performed in presence of MK801 (2 mM) in the recording pipette in order to prevent activation of NMDAr present on the recorded neuron. The stimulatory effect of NMDA on GABAergic mIPSCs was unchanged under these conditions. In 50% of the recorded cells (N = 5/10) NMDA application induced an increase in frequency of GABAergic mIPSCs (control: 0.10 ± 0.07 Hz, during NMDA: 0.34 ± 0.08 Hz; N = 5; p = 0.0625, Wilcoxon test) without any change in mIPSCs amplitude (data not shown; **Figure 3D**).

NMDAr-Dependent Modulation of GABAergic Transmission Depends on the Neurochemical Identity of the Postsynaptic Neuron

The NMDA-induced increase in GABAergic IPSCs frequency was only observed in 80.7% (spontaneous IPSC) and 54.0% (miniature IPSC) of recorded neurons. We therefore wondered whether NMDA-induced facilitation of GABAergic transmission would depend on the excitatory or inhibitory phenotype of the postsynaptic neurons (from which we recorded). To this end, we perfrormed recordings using slices prepared from GAD65-eGFP mice.

NMDA increased the frequency of spontaneous GABAergic IPSCs recorded both in eGFP+ and eGFP-, in similar proportions (eGFP+: 100%, N = 10/10; eGFP-: 85% N = 6/7). These results were similar to those obtained from C57Bl6 mice (**Figure 4A**).

A large majority of eGFP+ neurons displayed a facilitatory effect of NMDA on GABAergic mIPSCs (91%, N = 20/22). However, a significantly lower proportion of eGFP- neurons (22%, N = 2/9, p = 0.00042, Fischer's exact test) showed an effect of NMDA on GABAergic mIPSCs (**Figure 4B**). As previously observed in "unidentified" neurons, NMDA application increased GABAergic mIPSCs frequency (control: 0.07 ± 0.02 Hz, during NMDA: 0.25 ± 0.05 Hz; N = 20; t = 4.880, p = 0.0001, paired t-test) but neither change in mIPSC amplitude (control: −17.5 ± 1.3 pA, during NMDA: −16.8 ± 1.4 pA; N = 20; t = 0.5017, paired t-test) nor kinetics (data not shown; **Figures 4C,D**). In eGFP- neurons displaying an effect, NMDA application also increased GABAergic mIPSCs frequency

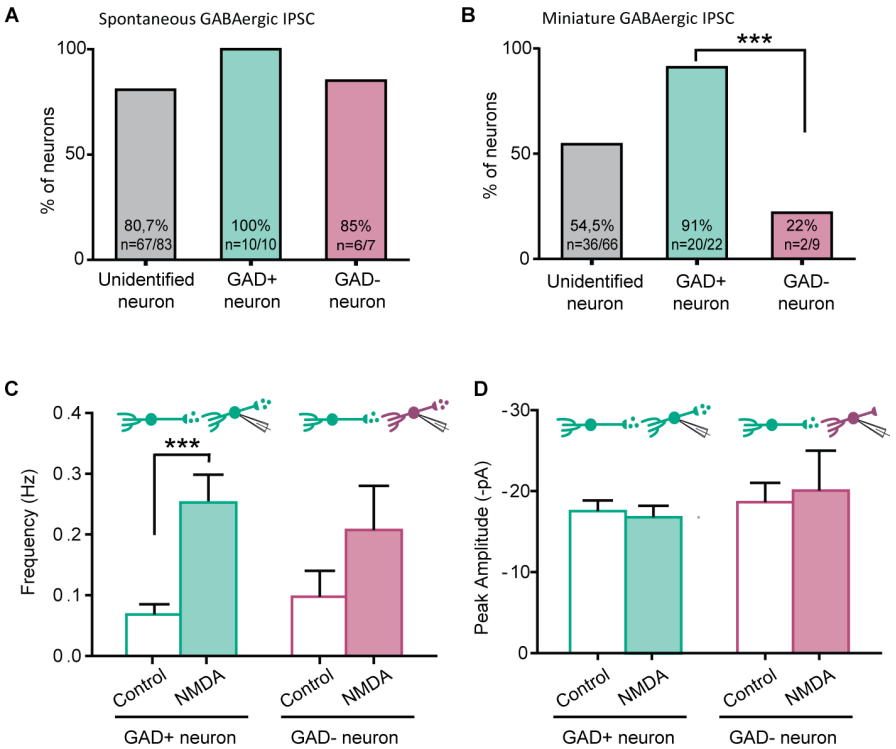

FIGURE 4 | NMDA enhancement of mIPSC frequency target specifically GABAergic interneurons. **(A)** Proportion of recorded neurons showing an increase of GABA sIPCS frequency by NMDA application, in unidentified neurons from C57bl6 mice and GAD positive (GAD+) or GAD negative (GAD-) neurons from GAD65-eGFP mice. **(B)** Proportion of recorded neurons recorded showing an increase of GABA mIPCS frequency by NMDA application is significantly higher in GAD positive (GAD+) neurons than for GAD negative (GAD-). **(C,D)** Frequency **(C)** and peak amplitude **(D)** of GABAergic mIPSCs recorded in GAD+ and GAD- neurons from GAD65-eGFP mice. Effect of NMDA on mIPSC frequency is independent of the neuron type. ***$p < 0.001$. Fischer's exact test **(B)** and Paired t-test **(C)** were used. Error bars indicate SEM.

(control: 0.10 ± 0.04 Hz, during NMDA: 0.21 ± 0.07 Hz; $N = 2$; **Figure 4C**). These results indicate that the facilitation of GABAergic synaptic transmission by presynaptic NMDAr depends on the postsynaptic target: it preferentially occurs in GABAergic connections onto eGFP+ neurons.

NMDA Changes the Paired-Pulse Ratio and Inhibits Evoked GABAergic IPSCs

An increase in mIPSCs frequency with no change in amplitude suggested a presynaptic mechanism of action of NMDA. We further tested this possibility by determining the effect of NMDA on the paired-pulse ratio (PPR) of electrically-evoked IPSCs (eIPSCs) in eGFP+ neurons (**Figure 5A**). The relative change in absolute PPR was consistently different from 0 at all interpusle interval tested: 20 ms interpulse (ΔPPR = 0.19 ± 0.07, $N = 8$, $t = 2.751$, $p = 0.0285$, one sample t-test), 50 ms interpulse (ΔPPR = 0.19 ± 0.06, $N = 9$, $t = 3$, $p = 0.0112$, one sample t-test) or 100 ms interpulse (ΔPPR = 0.19 ± 0.07, $N = 9$, $t = 0.1944$, $p = 0.0205$, one sample t-test; **Figure 5B**).

In these neurons, NMDA reduced the mean amplitude of eIPSCs (control: −37.5 ± 3.9 pA, during NMDA: −24.7 ± 2.6 pA; $N = 17$; $t = 6.029$, $p < 0.0001$, paired t-test). This inhibition remains significant at least during 5 min following NMDA washout (Wash −24.4 ± 2.6 pA, $N = 17$, compared to control $t = 2.440$, $p = 0.0267$, paired t-test; **Figures 5C,D**). These results are consistent with a NMDAr-mediated shunt of action potential dependent release of GABA and confirm that NMDAr modulate GABAergic transmission by a presynaptic mechanism of action.

DISCUSSION

Our results show that activation of NMDAr containing GluN2C/D subunits increased the frequency of GABAergic spontaneous and miniature IPSCs in lamina II neurons. Furthermore, this facilitation of spontaneous and miniature GABAergic IPSCs by NMDAr was preferentially observed for GABAergic connections onto eGFP+ neurons. Interestingly, NMDAr activation reduced the amplitude of electrically-evoked IPSCs recorded.

NMDAr Subunit Composition and Mg^{2+} Sensitivity

NMDAr are abundant in the dorsal horn with GluN1 and GluN2A/B receptors subunits expressed virtually in all lamina I and II neurons (Nagy et al., 2004). Concerning GluN2C/D

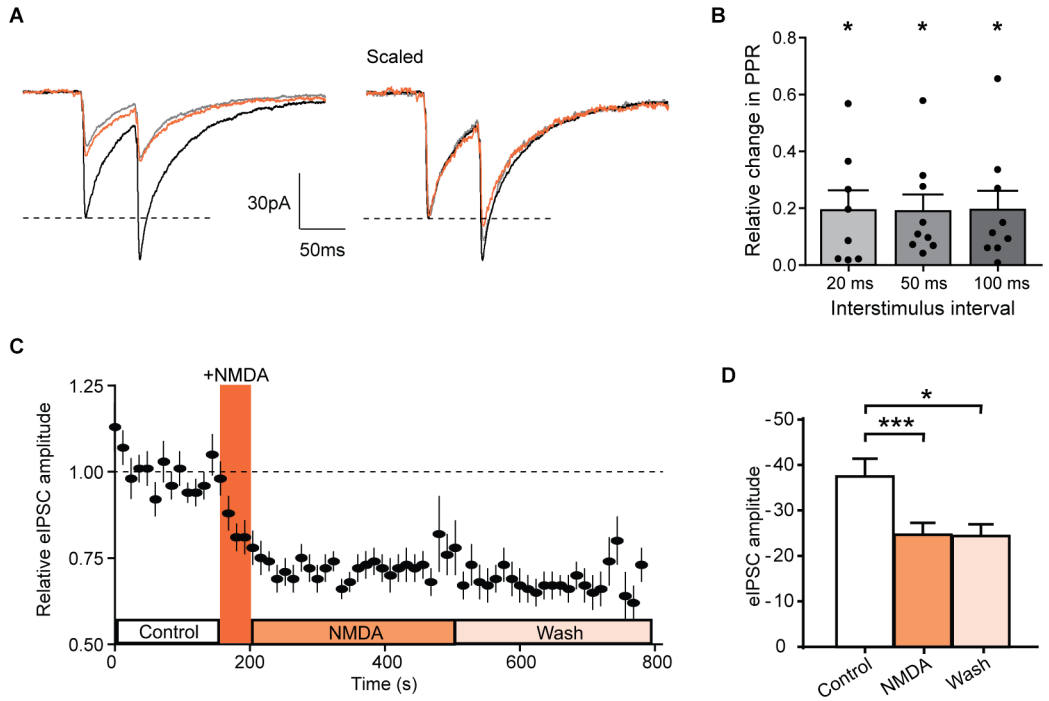

FIGURE 5 | NMDA inhibits evoked IPSCs in GAD-eGFP positive neurons. **(A)** Average of 10 traces representing the response to two successive stimulations separated by 50 ms before (black, control) and during NMDA application (orange, NMDA) and after a washout (gray, wash). **(B)** Histograms showing the relative change in PPR measured in GAD positive cells, for three different paired stimulation interval: 20 ms ($N = 8$), 50 ms ($N = 9$), and 100 ms ($N = 9$). **(C)** Time course of normalized GABAergic eIPSC amplitude before and after NMDA application ($N = 17$). **(D)** Histogram showing average eIPSC amplitude before (control) NMDA application, after NMDA application (NMDA) and after a washout (wash; $N = 17$). $^{*}p < 0.05$ and $^{***}p < 0.001$. One sample t-test **(B)** and paired t-test **(D)** were used. Error bars indicate SEM.

subunits, their level of expression is lower in the dorsal horn compared to other GluN2 subunits. But it has been shown that GABAergic interneurons also express NMDAr containing GluN2C/D subunits. These receptors may play a role in modulating the activity of inhibitory interneurons in the dorsal horn of the spinal cord (Shiokawa et al., 2010). Recently, a sex-specific expression pattern of GluN2D subunit has been reported in young rats (P21), with a larger expression of this subunit in male compared to female in superficial regions of the dorsal horn (Temi et al., 2021). We used only male mice in our study; therefore, the modulation of the GABAergic synaptic transmission by NMDAr activation could be different in female mice and would require further investigation.

Using a pharmacological approach, we identify GluN2C/D containing NMDAr as responsible for the NMDA-induced increase of spontaneous GABA release. The increase in mIPSC frequency was comparable in the presence of 2 mM Mg^{2+} or in the absence of Mg2+ indicating low sensitivity to Mg^{2+} block of the NMDAr. This is in agreement with the fact that the presence of GluN2C/D subunits reduces the voltage-sensitive Mg^{2+} block of NMDAr and therefore allows an activation by endogenous glutamate even without depolarization to relieve the Mg^{2+} block (Paoletti, 2011). These properties of NMDAr are well suited for a presynaptic NMDAr function because it may allow receptors to sense level of ambient glutamate and to be activated in the absence of depolarization, and thus under resting conditions. Inhibition may be thus finely regulated according to the overall level of glutamate and to the excitatory activity in the network (Bouvier et al., 2015).

NMDA Receptor Localization

In the superficial laminae of the dorsal horn, NMDAr are present in virtually every excitatory synapse and therefore in every interneuron (Nagy et al., 2004). NMDA receptors have also been immunocytochemically detected on presynaptic terminals of primary afferents (Liu et al., 1994; Lu et al., 2003) where they regulate neurotransmitter release from the terminals of primary afferent neurons (Bardoni, 2013). Presynaptic localization of NMDAr on GABAergic terminals is less documented. Only one immunohistochemical study has reported that, NMDArs are present on a subset of GABAergic terminals (37%) in rat superficial dorsal horn (Lu et al., 2005); however, the role of these receptors has not been investigated so far.

In other regions of the CNS, such as cerebellum, neocortex, prefrontal cortex, and visual cortex, immunocytochemical and functional studies have documented the presence of presynaptic NMDAr involved in modulation of GABA release (Glitsch and Marty, 1999; Mathew and Hablitz, 2011; Abrahamsson et al., 2017; Pafundo et al., 2018). Some of these studies reported a differential regulation of evoked and spontaneous release by

presynaptic NMDAr (Glitsch and Marty, 1999; Abrahamsson et al., 2017) comparable with our results. Indeed, we showed that NMDA increased the frequency of GABAergic mIPSCs but depressed evoked GABAergic IPSCs recorded in lamina II neurons. Considering a presynaptic localization, NMDAr activation could induce a calcium influx through the NMDAr channel, and thereby facilitate synaptic vesicle exocytosis and spontaneous GABA release. The same presynaptic NMDAr could depress evoked GABA release by decreasing the input resistance, thereby shunting the propagation of incoming action potentials. Presynaptic NMDAr could also depolarize synaptic boutons, inactivate voltage gated Na^+ channels and elevate the threshold for action potential generation. Both mechanisms would result in an increase in transmission failure and a reduction of the probability of evoked GABA release. Finally, presynaptic NMDAr could act *via* distinct and independent pathways to control evoked and spontaneous release separately as recently shown in the visual cortex (Abrahamsson et al., 2017).

However, our results provide indirect evidence for a presynaptic localization of NMDAr with important limitations. We cannot exclude that NMDAr are expressed near the GABAergic synapse and that NMDA might act by an indirect effect implicating a second messenger. Indeed, postsynaptic NMDAr activation could be the source of calcium needed to trigger and/or release a retrograde messenger such as NO. For example, NO could act retrogradely on the presynaptic terminal and facilitate GABA release. Such a mechanism has been reported in the dorsal horn were NO release was triggered by metabotropic glutamate receptor (mGluR1) activation and induced a heterosynaptic LTP of GABAeric synapses (Fenselau et al., 2011). Interestingly, in the dorsal horn, NO synthase is expressed in 17% of GABAergic interneurons (Boyle et al., 2017) and we found that NMDAr-dependent modulation of GABAergic transmission targeted preferentially inputs to GABAergic neurons. However, this mechanism could only explain the facilitatory effect observed on spontaneous transmission but not the depression of evoked IPSCs.

Finally, recent investigations have shown that functional NMDAr were present on astrocytes (Ziak et al., 1998; Lalo et al., 2006; Palygin et al., 2011), and activation of these astroglial NMDAr is involved in neuron-to-glia communication, and in the modulation of inhibitory synaptic transmission (Lalo et al., 2006, 2014). Such astroglial receptors could be involved in our results but once again could not completely explain the differential modulation of spontaneous and evoked GABA release.

However implication of different NMDAr with different localizations can drive bidirectional plasticities at GABAergic synapses (Mapelli et al., 2016) and thus could explain the differential regulation of GABAergic transmission that we observed.

In our experiments, the frequency of glycinergic mIPSCs was unaffected, indicating that presynaptic modulation of inhibitory synaptic transmission by NMDAr activation was exclusively observed at GABAergic nerve terminals and selectively controlled spontaneous GABAergic synaptic transmission. These results are in accordance with a recent study by Kloc and collaborators who showed that NMDAr activation induced LTP at glycinergic synapses that depended upon an increase in the number and/or the properties of Glycinergic receptors but was independent of glycine release (Kloc et al., 2019). In the DH, most dorsal horn neurons receive both GABAergic and glycinergic inputs, but these inputs may arise from neurons having their cell body localized in distinct laminae. Inhibitory interneurons in lamina II are virtually only GABAergic since glycinergic cell bodies were almost absent in this lamina (Zeilhofer et al., 2005; Punnakkal et al., 2014). A selective modulation of GABAergic transmission by NMDAr might therefore correspond to a restricted modulation of inhibition within lamina II processing nociceptive information.

Physiologically, glutamate required to activate NMDAr responsible for GABAergic synapse modulation may originate from neighboring excitatory synapses. In this case, NMDAr activation would depend on glutamate diffusion from neighboring synapses as previously described in the cerebellum (Huang and Bordey, 2004; Duguid and Smart, 2009). In the dorsal neuronal horn network ambient levels of glutamate are tightly regulated by glutamate transporters. These transporters (mainly expressed by glial cells) have a crucial role in limiting glutamate diffusion and crosstalk between neighboring synapses. Interestingly, in pathological states such as during neuropathic pain induced by a nerve injury, disruption of glutamate homeostasis in the DH led to an increase in extracellular levels of glutamate and subsequent spillover (Inquimbert et al., 2012). Therefore the modulation of GABAergic synaptic transmission by NMDA receptors we described in this study could be a new spinal mechanism involved in the development of neuropathic pain. Moreover, subunit composition and properties of NMDAr are altered by inflammation and peripheral nerve injury (Guo and Huang, 2001; Iwata et al., 2007) and consequently the modulation of GABAergic transmission by NMDAr activation could be modified.

Altogether our results strongly suggest that glutamate can directly activate GluN2C/D containing NMDAr which differentially regulate GABA release. This crosstalk between excitation and inhibition could control the excitation/inhibition balance in the spinal neuronal network. It will be critical in future work to clarify the localization of NMDAr involved in the regulation of GABAergic transmission targeting GABAergic neurons and to define their role in the processing of nociceptive information in spinal neuronal network in physiological, inflammatory and neuropathic pain conditions.

DATA AVAILABILITY STATEMENT

The original contributions presented in the study are included in the article, further inquiries can be directed to the corresponding author.

ETHICS STATEMENT

The animal study was reviewed and approved by Regional ethics committee and the French Ministry of Agriculture.

AUTHOR CONTRIBUTIONS

BL, LC, and LV-M performed acquisition and analysis of data. This study was designed by PI, SH, and RS. The manuscript was written by PI, SH, RS, and BL. All authors contributed to the article and approved the submitted version.

FUNDING

This study was supported by the Centre National de la Recherche Scientifique, Université de Strasbourg, the French National Research Agency (ANR) through the Programme d'Investissement d'Avenir under the contract ANR-17-EURE-0022 and Neurex. BL was funded by a fellowship from Région Grand Est and by a fellowship from the Fond Paul Mandel pour les Recherches en Neuroscience. LC and LV-M were recipients of a doctoral fellowship from the Ministère de la Recherche.

ACKNOWLEDGMENTS

We thank Mrs. Catherine Moreau and Mrs. Chantal Fitterer for helpful technical assistance. We thank Chronobiotron UMS 3512 for assistance in animal cares and experimentation. We thank Ferenc Erdelyi and Gabor Szabo for providing GAD65::EGFP mice.

REFERENCES

Abrahamsson, T., Chou, C. Y. C., Li, S. Y., Mancino, A., Costa, R. P., Brock, J. A., et al. (2017). Differential regulation of evoked and spontaneous release by presynaptic NMDA receptors. *Neuron* 96, 839–855.e5. doi: 10.1016/j.neuron.2017.09.030

Bardoni, R. (2013). Role of presynaptic glutamate receptors in pain transmission at the spinal cord level. *Curr. Neuropharmacol.* 11, 477–483. doi: 10.2174/1570159X11311050002

Beyer, C., Roberts, L. A., and Komisaruk, B. R. (1985). Hyperalgesia induced by altered glycinergic activity at the spinal cord. *Life Sci.* 37, 875–882. doi: 10.1016/0024-3205(85)90523-5

Bouvier, G., Bidoret, C., Casado, M., and Paoletti, P. (2015). Presynaptic NMDA receptors: roles and rules. *Neuroscience* 311, 322–340. doi: 10.1016/j.neuroscience.2015.10.033

Boyle, K. A., Gutierrez-Mecinas, M., Polgar, E., Mooney, N., O'Connor, E., Furuta, T., et al. (2017). A quantitative study of neurochemically defined populations of inhibitory interneurons in the superficial dorsal horn of the mouse spinal cord. *Neuroscience* 363, 120–133. doi: 10.1016/j.neuroscience.2017.08.044

Cathenaut, L., Leonardon, B., Kuster, R., Inquimbert, P., Schlichter, R., Hugel, S., et al. (2022). Inhibitory interneurons with differential plasticities at their connections tune excitatory-inhibitory balance in the spinal nociceptive system. *Pain* 163, e675–e688. doi: 10.1097/j.pain.0000000000002460

Cordero-Erausquin, M., Inquimbert, P., Schlichter, R., and Hugel, S. (2016). Neuronal networks and nociceptive processing in the dorsal horn of the spinal cord. *Neuroscience* 338, 230–247. doi: 10.1016/j.neuroscience.2016.08.048

Coull, J. A., Boudreau, D., Bachand, K., Prescott, S. A., Nault, F., Sik, A., et al. (2003). Trans-synaptic shift in anion gradient in spinal lamina i neurons as a mechanism of neuropathic pain. *Nature* 424, 938–942. doi: 10.1038/nature01868

Crabtree, J. W., Lodge, D., Bashir, Z. I., and Isaac, J. T. (2013). GABAA, NMDA and mGlu2 receptors tonically regulate inhibition and excitation in the thalamic reticular nucleus. *Eur. J. Neurosci.* 37, 850–859. doi: 10.1111/ejn.12098

Cui, L., Kim, Y. R., Kim, H. Y., Lee, S. C., Shin, H. S., Szabo, G., et al. (2011). Modulation of synaptic transmission from primary afferents to spinal substantia gelatinosa neurons by group III mGluRs in GAD65-EGFP transgenic mice. *J. Neurophysiol.* 105, 1102–1111. doi: 10.1152/jn.00108.2010

Deng, M., Chen, S. R., and Pan, H. L. (2019). Presynaptic NMDA receptors control nociceptive transmission at the spinal cord level in neuropathic pain. *Cell. Mol. Life Sci.* 76, 1889–1899. doi: 10.1007/s00018-019-03047-y

Duguid, I. C., and Smart, T. G. (2004). Retrograde activation of presynaptic NMDA receptors enhances GABA release at cerebellar interneuron-Purkinje cell synapses. *Nat. Neurosci.* 7, 525–533. doi: 10.1038/nn1227

Duguid, I. C., and Smart, T. G. (2009). "Chapter 14 - Presynaptic NMDA receptors," in *Biology of the NMDA Receptor*, ed A. M. Van Dongen (Boca Raton, FL: CRC Press/Taylor & Francis).

Fenselau, H., Heinke, B., and Sandkuhler, J. (2011). Heterosynaptic long-term potentiation at GABAergic synapses of spinal lamina I neurons. *J. Neurosci.* 31, 17383–17391. doi: 10.1523/JNEUROSCI.3076-11.2011

Glitsch, M., and Marty, A. (1999). Presynaptic effects of NMDA in cerebellar Purkinje cells and interneurons. *J. Neurosci.* 19, 511–519. doi: 10.1523/JNEUROSCI.19-02-00511.1999

Guo, H., and Huang, L. Y. (2001). Alteration in the voltage dependence of NMDA receptor channels in rat dorsal horn neurones following peripheral inflammation. *J. Physiol.* 537, 115–123. doi: 10.1111/j.1469-7793.2001.0115k.x

Harvey, R. J., Depner, U. B., Wassle, H., Ahmadi, S., Heindl, C., Reinold, H., et al. (2004). GlyR alpha3: an essential target for spinal PGE2-mediated inflammatory pain sensitization. *Science* 304, 884–887. doi: 10.1126/science.1094925

Huang, H., and Bordey, A. (2004). Glial glutamate transporters limit spillover activation of presynaptic NMDA receptors and influence synaptic inhibition of Purkinje neurons. *J. Neurosci.* 24, 5659–5669. doi: 10.1523/JNEUROSCI.1338-04.2004

Inquimbert, P., Bartels, K., Babaniyi, O. B., Barrett, L. B., Tegeder, I., Scholz, J., et al. (2012). Peripheral nerve injury produces a sustained shift in the balance between glutamate release and uptake in the dorsal horn of the spinal cord. *Pain* 153, 2422–2431. doi: 10.1016/j.pain.2012.08.011

Iwata, H., Takasusuki, T., Yamaguchi, S., and Hori, Y. (2007). NMDA receptor 2B subunit-mediated synaptic transmission in the superficial dorsal horn of peripheral nerve-injured neuropathic mice. *Brain Res.* 1135, 92–101. doi: 10.1016/j.brainres.2006.12.014

Kloc, M. L., Pradier, B., Chirila, A. M., and Kauer, J. A. (2019). NMDA receptor activation induces long-term potentiation of glycine synapses. *PLoS One* 14:e0222066. doi: 10.1371/journal.pone.0222066

Kullmann, D. M., Moreau, A. W., Bakiri, Y., and Nicholson, E. (2012). Plasticity of inhibition. *Neuron* 75, 951–962. doi: 10.1016/j.neuron.2012.07.030

Lalo, U., Pankratov, Y., Kirchhoff, F., North, R. A., and Verkhratsky, A. (2006). NMDA receptors mediate neuron-to-glia signaling in mouse cortical astrocytes. *J. Neurosci.* 26, 2673–2683. doi: 10.1523/JNEUROSCI.4689-05.2006

Lalo, U., Rasooli-Nejad, S., and Pankratov, Y. (2014). Exocytosis of gliotransmitters from cortical astrocytes: implications for synaptic plasticity and aging. *Biochem. Soc. Trans.* 42, 1275–1281. doi: 10.1042/BST20140163

Latremoliere, A., and Woolf, C. J. (2009). Central sensitization: a generator of pain hypersensitivity by central neural plasticity. *J. Pain* 10, 895–926. doi: 10.1016/j.jpain.2009.06.012

Liu, H., Mantyh, P. W., and Basbaum, A. I. (1997). NMDA-receptor regulation of substance p release from primary afferent nociceptors. *Nature* 386, 721–724. doi: 10.1038/386721a0

Liu, H., Wang, H., Sheng, M., Jan, L. Y., Jan, Y. N., Basbaum, A. I., et al. (1994). Evidence for presynaptic N-methyl-D-aspartate autoreceptors in the spinal cord dorsal horn. *Proc. Natl. Acad. Sci. U S A* 91, 8383–8387. doi: 10.1073/pnas.91.18.8383

Lu, C. R., Hwang, S. J., Phend, K. D., Rustioni, A., and Valtschanoff, J. G. (2003). Primary afferent terminals that express presynaptic NR1 in rats are mainly from myelinated, mechanosensitive fibers. *J. Comp. Neurol.* 460, 191–202. doi: 10.1002/cne.10632

Lu, C. R., Willcockson, H. H., Phend, K. D., Lucifora, S., Darstein, M., Valtschanoff, J. G., et al. (2005). Ionotropic glutamate receptors are expressed in GABAergic terminals in the rat superficial dorsal horn. *J. Comp. Neurol.* 486, 169–178. doi: 10.1002/cne.20525

Mapelli, J., Gandolfi, D., Vilella, A., Zoli, M., and Bigiani, A. (2016). Heterosynaptic GABAergic plasticity bidirectionally driven by the activity of pre- and postsynaptic NMDA receptors. *Proc. Natl. Acad. Sci. U S A* 113, 9898–9903. doi: 10.1073/pnas.1601194113

Mathew, S. S., and Hablitz, J. J. (2011). Presynaptic NMDA receptors mediate IPSC potentiation at GABAergic synapses in developing rat neocortex. *PLoS One* 6:e17311. doi: 10.1371/journal.pone.0017311

Nagy, G. G., Watanabe, M., Fukaya, M., and Todd, A. J. (2004). Synaptic distribution of the NR1, NR2A and NR2B subunits of the N-methyl-d-aspartate receptor in the rat lumbar spinal cord revealed with an antigen-unmasking technique. *Eur. J. Neurosci.* 20, 3301–3312. doi: 10.1111/j.1460-9568.2004.03798.x

Nugent, F. S., Penick, E. C., and Kauer, J. A. (2007). Opioids block long-term potentiation of inhibitory synapses. *Nature* 446, 1086–1090. doi: 10.1038/nature05726

Pafundo, D. E., Miyamae, T., Lewis, D. A., and Gonzalez-Burgos, G. (2018). Presynaptic effects of N-methyl-D-aspartate receptors enhance parvalbumin cell-mediated inhibition of pyramidal cells in mouse prefrontal cortex. *Biol. Psychiatry* 84, 460–470. doi: 10.1016/j.biopsych.2018.01.018

Palygin, O., Lalo, U., and Pankratov, Y. (2011). Distinct pharmacological and functional properties of NMDA receptors in mouse cortical astrocytes. *Br. J. Pharmacol.* 163, 1755–1766. doi: 10.1111/j.1476-5381.2011.01374.x

Paoletti, P. (2011). Molecular basis of NMDA receptor functional diversity. *Eur. J. Neurosci.* 33, 1351–1365. doi: 10.1111/j.1460-9568.2011.07628.x

Paoletti, P., Bellone, C., and Zhou, Q. (2013). NMDA receptor subunit diversity: impact on receptor properties, synaptic plasticity and disease. *Nat. Rev. Neurosci.* 14, 383–400. doi: 10.1038/nrn3504

Petitjean, H., Rodeau, J. L., and Schlichter, R. (2012). Interactions between superficial and deep dorsal horn spinal cord neurons in the processing of nociceptive information. *Eur. J. Neurosci.* 36, 3500–3508. doi: 10.1111/j.1460-9568.2012.08273.x

Punnakkal, P., von Schoultz, C., Haenraets, K., Wildner, H., and Zeilhofer, H. U. (2014). Morphological, biophysical and synaptic properties of glutamatergic neurons of the mouse spinal dorsal horn. *J. Physiol.* 592, 759–776. doi: 10.1113/jphysiol.2013.264937

Roberts, L. A., Beyer, C., and Komisaruk, B. R. (1986). Nociceptive responses to altered GABAergic activity at the spinal cord. *Life Sci.* 39, 1667–1674. doi: 10.1016/0024-3205(86)90164-5

Sandkuhler, J. (2007). Understanding LTP in pain pathways. *Mol. Pain* 3:9. doi: 10.1186/1744-8069-3-9

Shiokawa, H., Kaftan, E. J., MacDermott, A. B., and Tong, C. K. (2010). NR2 subunits and NMDA receptors on lamina II inhibitory and excitatory interneurons of the mouse dorsal horn. *Mol. Pain* 6:26. doi: 10.1186/1744-8069-6-26

Sivilotti, L., and Woolf, C. J. (1994). The contribution of GABAA and glycine receptors to central sensitization: disinhibition and touch-evoked allodynia in the spinal cord. *J. Neurophysiol.* 72, 169–179. doi: 10.1152/jn.1994.72.1.169

Temi, S., Rudyk, C., Armstrong, J., Landrigan, J. A., Dedek, C., Salmaso, N., et al. (2021). Differential expression of GluN2 NMDA receptor subunits in the dorsal horn of male and female rats. *Channels (Austin)* 15, 179–192. doi: 10.1080/19336950.2020.1871205

Torsney, C., and MacDermott, A. B. (2006). Disinhibition opens the gate to pathological pain signaling in superficial neurokinin 1 receptor-expressing neurons in rat spinal cord. *J. Neurosci.* 26, 1833–1843. doi: 10.1523/JNEUROSCI.4584-05.2006

Woolf, C. J., and Salter, M. W. (2000). Neuronal plasticity: increasing the gain in pain. *Science* 288, 1765–1769. doi: 10.1126/science.288.5472.1765

Woolf, C. J., and Thompson, S. W. (1991). The induction and maintenance of central sensitization is dependent on N-methyl-D-aspartic acid receptor activation; implications for the treatment of post-injury pain hypersensitivity states. *Pain* 44, 293–299. doi: 10.1016/0304-3959(91)90100-C

Zeilhofer, H. U., Studler, B., Arabadzisz, D., Schweizer, C., Ahmadi, S., Layh, B., et al. (2005). Glycinergic neurons expressing enhanced green fluorescent protein in bacterial artificial chromosome transgenic mice. *J. Comp. Neurol.* 482, 123–141. doi: 10.1002/cne.20349

Ziak, D., Chvatal, A., and Sykova, E. (1998). Glutamate-, kainate- and NMDA-evoked membrane currents in identified glial cells in rat spinal cord slice. *Physiol. Res.* 47, 365–375.

Conflict of Interest: The authors declare that the research was conducted in the absence of any commercial or financial relationships that could be construed as a potential conflict of interest.

Publisher's Note: All claims expressed in this article are solely those of the authors and do not necessarily represent those of their affiliated organizations, or those of the publisher, the editors and the reviewers. Any product that may be evaluated in this article, or claim that may be made by its manufacturer, is not guaranteed or endorsed by the publisher.

frontiers | Frontiers in Molecular Neuroscience

BRIEF RESEARCH REPORT
published: 06 July 2022
doi: 10.3389/fnmol.2022.946159

5-HT$_7$ Receptors Regulate Excitatory-Inhibitory Balance in Mouse Spinal Cord Dorsal Horn

*Antonella Comitato[1], Enza Lacivita[2], Marcello Leopoldo[2] and Rita Bardoni[1]**

[1] Department of Biomedical, Metabolic and Neural Sciences, University of Modena and Reggio Emilia, Modena, Italy,
[2] Department of Pharmacy – Drug Sciences, University of Bari Aldo Moro, Bari, Italy

Serotonergic receptors of the 5-HT$_7$ type (5-HT$_7$Rs) are widely expressed in the central nervous system (CNS), where they modulate several functions, such as pain. Behavioral experiments *in vivo* have shown both anti- and pro-nociceptive actions of 5-HT$_7$Rs, although an analgesic effect seems to be prevalent. In the spinal cord dorsal horn, the mechanisms involved in 5-HT$_7$R-mediated synaptic modulation are still poorly understood, especially those regarding the control of synaptic inhibition. The present study investigated the modulation exerted by 5-HT$_7$Rs on dorsal horn excitatory and inhibitory synaptic circuits, by performing patch-clamp recordings from lamina II neurons in mouse spinal cord slices. Our results show that applying the selective 5-HT$_7$ agonist LP-211 facilitates glutamatergic release by enhancing the frequency of spontaneous postsynaptic currents (sEPSCs) and increasing the peak amplitude of excitatory postsynaptic currents (EPSCs) evoked by dorsal root stimulation. The effects on sEPSCs were still observed in the presence of the 5-HT$_{1A}$ antagonist WAY-100635, while the 5-HT$_7$ antagonist SB-269970 blocked them. LP-211 was also able to increase the release of gamma-aminobutyric acid (GABA) and glycine, as shown by the increase of spontaneous inhibitory currents (sIPSC) frequency and evoked inhibitory postsynaptic currents (IPSC) amplitude. LP-211 was proved to be more effective in potentiating synaptic inhibition as compared to excitation: consistently, 5-HT$_7$R activation significantly enhanced the excitability of tonic firing neurons, mainly corresponding to inhibitory interneurons. Our data bring new insights into the mechanisms of synaptic modulation mediated by 5-HT$_7$Rs in the dorsal horn. Stronger impact on synaptic inhibition supports the hypothesis that these receptors may play an anti-nociceptive role in the spinal cord of naïve animals.

Keywords: pain, serotonin, spinal cord, synaptic transmission, GABA, electrophysiology

OPEN ACCESS

Edited by:
Fabien Marchand, INSERM U1107 Douleur et Biophysique Neurosensorielle (Neuro-Dol), France

Reviewed by:
Stephane Doly, University of Auvergne, France
Krzysztof Tokarski, Maj Institute of Pharmacology (PAN), Poland

****Correspondence:***
Rita Bardoni
rita.bardoni@unimore.it

Specialty section:
This article was submitted to Pain Mechanisms and Modulators, a section of the journal Frontiers in Molecular Neuroscience

Received: *17 May 2022*
Accepted: *13 June 2022*
Published: *06 July 2022*

Citation:
Comitato A, Lacivita E, Leopoldo M and Bardoni R (2022) 5-HT$_7$ Receptors Regulate Excitatory-Inhibitory Balance in Mouse Spinal Cord Dorsal Horn. Front. Mol. Neurosci. 15:946159. doi: 10.3389/fnmol.2022.946159

INTRODUCTION

Serotonergic fibers modulate pain transmission in the spinal cord dorsal horn through the activation of several serotonergic receptors (5-HTRs). Among these, the most recently identified 5-HT receptor family, the 5-HT$_7$ receptor (5-HT$_7$R), has been involved in pain modulation, acting at several levels along the pain axis (Cortes-Altamirano et al., 2018; Bardoni, 2019). 5HT$_7$Rs are heterodimeric receptors that stimulate cyclic adenosine monophosphate (cAMP) formation by activating adenylate cyclase through a stimulatory Gs protein, which also causes the activation of RAS-dependent extracellular-regulated kinases (ERKs) (Norum et al., 2003).

Targets of 5-HT$_7$R-mediated modulation are voltage-dependent ion channels, membrane transporters, and synaptic receptors. Indeed, 5-HT$_7$Rs have been reported to induce neuronal depolarization, regulate neurotransmitter release, and modulate synaptic plasticity in several areas of the central nervous system (CNS) (Ciranna and Catania, 2014).

In the nociceptive system, expression of 5-HT$_7$Rs has been detected in dorsal root ganglion cells (DRGs), especially on small- and medium-size cell bodies and in the dorsal horn, on both axons and cell bodies (Meuser et al., 2002; Doly et al., 2005). Labeling for 5-HT$_7$Rs in the spinal cord appeared to be particularly intense in the superficial dorsal horn, compatibly with a role of these receptors in pain transmission.

The effects of 5-HT$_7$Rs on pain have been investigated *in vivo* in different animal models: although an anti-nociceptive action seemed to be prevalent in both inflammatory and neuropathic pain, pro-nociceptive effects have also been reported (reviewed in Cortes-Altamirano et al., 2018; Bardoni, 2019). These discrepancies may depend on the site of 5-HT$_7$R activation (periphery vs. CNS), the use of different pain models and animal species, and the scarce availability of selective 5-HT$_7$R agonists. Recently, more selective agonists for 5-HT$_7$R have become available (Blattner et al., 2019). Among these, the compound LP-211 has been tested in several studies, proving to be specific and effective in activating 5HT$_7$Rs, both *in vivo* and *in vitro* (Leopoldo et al., 2011; Costa et al., 2012; Demirkaya et al., 2016; Lippiello et al., 2016).

Data about the modulatory effects exerted by 5-HT$_7$Rs on nociceptive neurons are limited. An early study had shown that activation of 5-HT$_7$Rs with 5-Carboxamidotryptamine increased the amplitude of Ih current in medium diameter rat DRG neurons (Cardenas et al., 1999). In mouse trigeminal subnucleus caudalis, application of the 5HT$_{1A/7}$ agonist 8-hydroxy-2-(di-n-propylamino)tetralin (8-OH-DPAT; in the presence of a 5-HT$_{1A}$ antagonist) produced a depolarization in a subpopulation of neurons (Yang et al., 2014), while in rat deep dorsal horn 8-OH-DPAT facilitated excitatory synaptic responses (Garraway and Hochman, 2001).

In the spinal cord superficial dorsal horn, the role of 5-HT$_7$Rs in modulating excitatory and inhibitory synaptic circuits has not been clarified. By patch-clamp recording synaptic responses from neurons in mouse spinal cord slices, we have studied the effects of the selective 5-HT$_7$ agonist LP-211 on synaptic transmission in the superficial dorsal horn. Our results show that 5-HT$_7$Rs can potentiate the release of glutamate and gamma-aminobutyric acid (GABA)/glycine in this region, exerting a more powerful effect on synaptic inhibition and excitability of inhibitory interneurons.

Parts of these results have been presented in a preliminary form (Comitato et al., 2021).

MATERIALS AND METHODS

Spinal Cord Slice Preparation

The Italian Ministry of Health approved all the experiments conducted on postnatal CD1 mice of either sex (P18–P28) following the Guide for the Care and Use of Laboratory Animals and the EU and Italian regulations on animal welfare. Spinal cord slices were obtained following the procedure described previously (Betelli et al., 2015; Bardoni et al., 2019). Briefly, the animals were anesthetized with isoflurane and decapitated; the spinal cord and vertebrae were rapidly removed and placed in ice-cold dissecting Krebs' solution (composition in mM: 95 NaCl, 50 sucrose, 2.5 KCl, 1.25 NaH_2PO_4, 26 $NaHCO_3$, 25 glucose, 6 $MgCl_2$, 1.5 $CaCl_2$, and 1 kynurenic acid, pH 7.4, 320 mOsm), bubbled with 95% O_2 and 5% CO_2. The lumbar spinal cord was isolated, embedded in an agarose block (low melting point agarose 3%, Thermo Fisher Scientific, Waltham, MA, United States), and transverse slices (400–500 μm thick) were obtained using a vibrating microtome (WPI, Sarasota, FL, United States). The slices were maintained in oxygenated incubation Krebs' solution (in mM: 125 NaCl, 2.5 KCl, 1.25 NaH_2PO_4, 26 $NaHCO_3$, 25 glucose, 6 $MgCl_2$, and 1 $CaCl_2$, pH 7.4, 320 mOsm) at 35°C for 20 min and then used for recording.

Patch-Clamp Recording and Stimulation

The patch-clamp recording in whole-cell configuration was performed on lamina II neurons at room temperature. The slices were perfused at 2 ml/min with recording Krebs' solution (in mM: 125 NaCl, 2.5 KCl, 1.25 NaH_2PO_4, 26 $NaHCO_3$, 25 glucose, 1 $MgCl_2$, and 2 $CaCl_2$, pH 7.4, 320 mOsm). Recordings of excitatory postsynaptic currents (EPSCs) were performed in voltage-clamp at −70 mV by using a potassium-based intracellular solution with the following composition (in mM): 120 potassium methanesulfonate, 10 NaCl, 10 ethylene glycol bis(2-aminoethyl ether)tetraacetic acid (EGTA), 1 $CaCl_2$, 10 hydroxyethyl piperazineethanesulfonic acid (HEPES), 5 adenosine triphosphate (ATP)-Mg, 0.5 guanosine triphosphate (GTP)-Na, pH adjusted to 7.2 with KOH, and osmolarity 300 mOsm. The data were recorded and acquired using a MultiClamp 700A Amplifier and the pClamp 10 software (Molecular Devices, Sunnyvale, CA, United States). The sampling rate was 10 kHz, and the data were filtered at 2 kHz. Series resistance was not compensated, and cells with a resistance higher than 30 MOhm were discarded. Junction potentials were corrected off-line. Inhibitory postsynaptic currents (IPSCs) were recorded in voltage-clamp at 0 mV by using a cesium-based intracellular solution having the following composition (in mM): 130 cesium methanesulfonate, 10 sodium methanesulfonate, 10 EGTA, 1 $CaCl_2$, 10 HEPES, 2 ATP-Mg, pH adjusted to 7.2 with CsOH, and osmolarity 300 mOsm.

Evoked EPSCs were obtained by stimulating the dorsal root attached to the slice with a suction electrode. The applied stimuli (500 μA intensity and 0.1 ms duration) activated both Aδ and C fibers synapsing onto lamina II neurons. Monosynaptic EPSCs were identified from the absence of failures during a train of 20 stimuli at 1 Hz (Daniele and MacDermott, 2009; Bardoni et al., 2019).

Evoked IPSCs were elicited by focally stimulating the region around the recorded cell with a glass pipette (tip diameter 2–5 μm) at an intensity of 0.1–1 mA and duration of 0.1 ms.

Monosynaptic IPSCs were recognized by constant latency and by the absence of failures at 1 Hz.

Single EPSCs or IPSCs were recorded by stimulating at 0.1 Hz. EPSCs or IPSCs recorded with the paired-pulse protocol were evoked by applying 2 stimuli at 400 ms intervals. The time between consecutive pairs of stimuli was 20–30 s.

Recordings in the current clamp were performed by using the potassium-based intracellular solution. Resting potential was determined within the first 5 min of recording: cells with membrane potential more positive than −50 mV were discarded. The neuronal firing pattern was determined by applying at least 10 current steps (amplitude: 10–20 pA; duration: 500 ms). Between the steps, the membrane potential was held at about −80 mV to unmask the delayed firing pattern better, as previously described (Yasaka et al., 2010; Bardoni et al., 2019). Once the firing pattern was established, root stimulation was performed as described above, using the paired-pulse protocol to record paired excitatory postsynaptic potentials (EPSPs). The neuron potential was maintained at −60/−65 mV.

Data Analysis

Spontaneous EPSCs or IPSCs were analyzed offline using pClamp10 software and Minianalysis (Synaptosoft, United States). The responsivity of individual cells to LP-211 was assessed by performing the Kolmogorov–Smirnov test on cumulative distributions of inter-event intervals (**Figure 1B**). Evoked EPSCs and IPSCs were analyzed using pClamp10 software: sensitivity to LP-211 was established by comparing with an unpaired *t*-test, the peak amplitudes of 5–10 currents in control and in the presence of the 5-HT$_7$ agonist. Paired pulse ratio was determined as the ratio between the second and the first EPSC.

The data are expressed as the mean ± SEM, and differences were considered significant for $p < 0.05$. Comparisons between 2 groups were performed by using an unpaired or paired t-test. Non-parametric tests were applied when the data were not normally distributed. Graphs and statistical analysis were obtained by using GraphPad Prism 9.3 (GraphPad Software, San Diego, CA, United States).

Drugs

All the components of Krebs and intracellular solutions were obtained from Sigma-Aldrich (Merck Group, Darmstadt, Germany). LP-211 tartrate was provided by Prof. Marcello Leopoldo at the University of Bari (Italy). Aliquots of 1 μM stock solution in dimethyl sulfoxide (DMSO) were initially prepared and then diluted to 1 μM in recording Krebs' solution on the day of the experiment. NBQX, D-AP5, and tetrodotoxin (TTX) were provided by Abcam (Cambridge, United Kingdom), and WAY-100635 and SB-269970 were obtained from Sigma-Aldrich.

RESULTS

We have tested the effects of 5-HT$_7$Rs on synaptic transmission in the superficial dorsal horn by recording from 109 lamina II neurons in mouse spinal cord slices. To activate 5-HT$_7$Rs, we have bath-applied the selective agonist LP-211 at 1 μM. Application of LP-211 to the slice for 3–5 min caused a significant increase of glutamate release in a subpopulation of lamina II neurons, recorded in voltage-clamp at −70 mV (**Figures 1A–C**). The responsivity to LP-211 was assessed on individual cells based on the significant change in frequency of spontaneous postsynaptic currents (sEPSCs; **Figure 1B**). The 5-HT$_7$R agonist caused a significant increase in sEPSC frequency

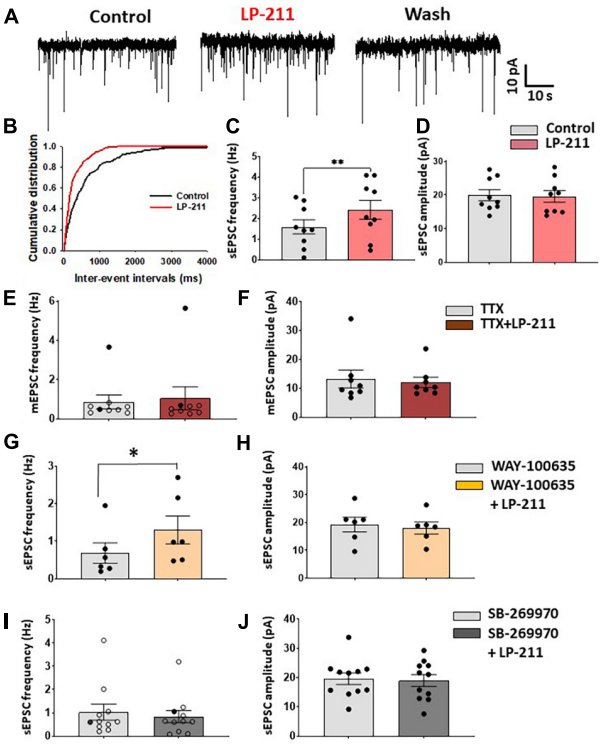

FIGURE 1 | Application of LP 211 increases spontaneous EPSCs in a subpopulation of lamina II neurons. **(A)** Examples of spontaneous EPSC recordings (sEPSCs), obtained in voltage-clamp at –70 mV. LP-211 (1 μM) caused a significant increase in sEPSC frequency, which was reversible in the wash. **(B)** Cumulative distributions of the inter-event intervals determined from the neuron shown in panel **(A)**. LP-211 caused a shift of the curve to the left, indicating an increase in sEPSC frequency (Kolmogorov–Smirnov test, $p = 0.000$). **(C)** Summary graph of sEPSC frequencies obtained from the neurons responsive to LP-211 (9 out 14 tested cells; paired *t*-test, $p < 0.01$); **(D)** LP-211 did not change sEPSC amplitude in the responsive cells (paired *t*-test, $p = 0.69$, $n = 9$). **(E)** Tetrodotoxin (TTX, 1 μM) reduced the effect of LP-211 on spontaneous glutamate release: in only 2 neurons (black circles) out of 9 a significant increase of mEPSC frequency was observed. The overall effect of LP-211 on mEPSC frequency was not significant (Wilcoxon rank-sum test, $p = 0.91$). **(F)** No changes in mEPSC amplitude were observed in LP-211 + TTX (Wilcoxon rank-sum test, $p = 0.96$, $n = 9$). **(G,H)** Co-application of the 5-HT$_{1A}$ antagonist WAY 100-635 (10 μM) did not prevent the increase of sEPSC on 6 out of 10 tested neurons (paired *t*-test on responsive cells, $p < 0.05$, $n = 6$). The sEPSC amplitude was not significantly changed (paired *t*-test, $p = 0.39$, $n = 6$). **(I)** Co-application of LP-211 with the 5-HT$_7$ antagonist SB-269970 (10 μM) blocked both the LP-211 effects on sEPSC frequency [**(I)**: only one responsive cell (black circles) out of 11 tested, Wilcoxon rank-sum test, $p = 0.17$, n = 11] and amplitude [**(J)**: paired *t*-test, $p = 0.4$, $n = 11$]. Asterisks reported in the graphs represent statistical significance: $^*p < 0.05$; $^{**}p < 0.01$; $^{***}p < 0.001$.

in a subpopulation of neurons (mean percentage increase: 86.9 ± 32.9%, n = 9 out of 14), which was reversible in the wash and it was not accompanied by a change in sEPSC amplitude (**Figure 1D**). In some neurons, we also observed a slow inward current during LP-211 application (mean amplitude: 8.9 ± 1.1 pA; mean duration: 3.5 ± 0.3 min; 5 out of 11 neurons), indicating the activation of postsynaptic 5-HT$_7$Rs located on the recorded cell.

LP-211 had been shown to be effective in activating 5-HT$_7$Rs in brain slices at concentrations in the nanomolar range (Costa et al., 2012), so we tested the agonist at 0.1 μM on a sample of 8 neurons. We observed a significant increase in sEPSC frequency only in one neuron, and the analysis of the whole sample did not show a significant effect of 0.1 μM LP-211 (mean frequency in control: 0.58 ± 0.13 Hz; LP-211: 0.57 ± 0.13 Hz; paired t-test $p = 0.93$, $n = 8$).

To test whether the effect of LP-211 on glutamate release was dependent on action potential firing, we applied 1 μM LP-211 in the presence of 1 μM tetrodotoxin (TTX). In these conditions, LP-211 significantly increased miniature EPSC (mEPSC) frequency in only 2 out of 9 tested lamina II neurons, while the mEPSC amplitude was unaffected (**Figures 1E,F**). This would suggest that the potentiating effect exerted by 5-HT$_7$Rs partially involves the generation of action potentials in the excitatory networks. Furthermore, the lack of effect on mEPSC amplitude indicates that 5-HT$_7$Rs act at the presynaptic site.

Since it is known that some 5-HT$_7$ agonists can also activate 5-HT$_{1A}$Rs, we have tested 1 μM LP-211 in the presence of the 5-HT$_{1A}$ antagonist WAY-100635 (10 μM) to exclude the involvement of these receptors in the modulation of glutamate release. As shown in **Figures 1G,H**, a significant increase in sEPSC frequency is still observed in 6 out of 10 tested cells, without any significant alteration in sEPSC amplitude. Conversely, the LP-211 effect on sEPSCs was blocked by applying the 5-HT$_7$ antagonist SB-269970, confirming the selective activation of 5-HT$_7$Rs by the agonist (**Figures 1I,J**).

Activation of 5-HT$_7$Rs by LP-211 was also effective in potentiating spontaneous inhibitory currents (sIPSCs) mediated by GABA and/or glycine and recorded in voltage-clamp at 0 mV (**Figure 2**). In the presence of Alpha-Amino-3-Hydroxy-5-Methyl-4-Isoxazole Propionic Acid (AMPA) and N-methyl-D-aspartate (NMDA) receptor antagonists NBQX and D-AP5 (10 and 50 μM, respectively), 1 μM of LP-211 strongly increased sIPSC frequency in 10 out of 14 lamina II neurons (**Figures 2A,B**; mean percentage increase: 236.7 ± 75.2%), without changing sIPSC amplitude (**Figure 2C**). In the presence of TTX, a significant enhancement of mIPSC frequency was still observed in 6 out of 11 neurons (**Figure 2D**). Although the overall mIPSC amplitude of the responsive cells was not significantly changed by LP-211 (**Figure 2E**), the increase in frequency was accompanied by an enhancement of amplitude in three cells. The analysis of the frequency distributions of mIPSC amplitudes showed that this was likely due to the recruitment of additional GABA/glycinergic synaptic terminals, generating larger mIPSCs.

The effect of LP-211 on inhibitory transmission was blocked by 10 μM SB-269970, confirming the involvement of 5-HT$_7$Rs (**Figure 2F**). Finally, the percentage frequency increase of sIPSCs resulted significantly higher than that observed for sEPSCs, indicating that 5-HT$_7$Rs exert a more effective potentiation on inhibitory synaptic transmission (**Figure 2G**).

Since 5-HT$_7$R expression has been detected on DRG neurons and primary afferent fibers, we have then tested whether LP-211 could modulate EPSCs evoked by dorsal root stimulation. A paired-pulse protocol was applied, recording two EPSCs at an interval of 400 ms; the stimulus intensity was 500 μM, able to recruit both Aδ and C fibers.

As shown in **Figures 3A–C**, a significant increase in the first evoked EPSC is observed in 5 out of 11 lamina II neurons, which is not accompanied by a significant change in the second peak (first peak percentage change: 24.3 ± 3.7%; second peak: 5.3 ± 4.8%, **Figure 3B**). The paired-pulse ratio (PPR) of the evoked EPSCs was significantly decreased, suggesting a presynaptic site of action of 5-HT$_7$Rs on primary afferent terminals (**Figure 3C**).

Evoked IPSCs, mediated by GABA and/or glycine, were strongly facilitated by LP-211 (**Figures 3D–F**). The IPSCs were elicited by focally stimulating lamina II with the paired-pulse protocol and were recorded in the presence of NBQX and D-AP5 to block glutamatergic transmission (**Figure 3D**). The activation of 5-HT$_7$Rs by 1 μM LP-211 induced an increase of both IPSC peaks in 5 out of 11 tested neurons (first peak percentage change: 71.2 ± 21.6%; second peak: 27.9 ± 6.9%, **Figure 3E**). The stronger potentiation of the first IPSC, as compared to the second, resulted in a significant decrease in the PPR (**Figure 3F**). This is consistent with the results on spontaneous IPSCs, suggesting a presynaptic modulation exerted by 5-HT$_7$Rs on inhibitory neurotransmitters. Similar to what was shown above for spontaneous synaptic transmission, a comparison between percentage changes of evoked EPSCs and IPSCs confirmed a stronger potentiation exerted by LP-211 on GABA/glycine mediated transmission (**Figure 3G**).

Based on this consideration, we finally determined whether LP-211 can modify the excitability of lamina II inhibitory interneurons. As shown by previous studies, excitatory and inhibitory lamina II neurons exhibit different action potential firing patterns in response to current steps. While excitatory neurons show a delayed firing pattern, most inhibitory interneurons tend to fire tonically (**Figures 4A,C**). Based on this classification, we established the firing pattern of the recorded neuron at the beginning of the experiment. Afterward, we tested the effect of LP-211 on the number of action potentials evoked by dorsal root stimulation (paired-pulse protocol). The LP-211 did not affect the number of action potentials in delayed firing neurons (**Figures 4B,E**). Still, it effectively increased action potential firing at the first stimulus in tonic neurons (**Figures 4D,F**). The higher impact of 5-HT$_7$R activation on the excitability of tonic firing neurons is consistent with the stronger effect exerted by LP-211 on inhibitory synaptic transmission.

DISCUSSION

This study has investigated the modulatory action exerted by 5-HT$_7$Rs on dorsal horn synaptic transmission. Our results showed

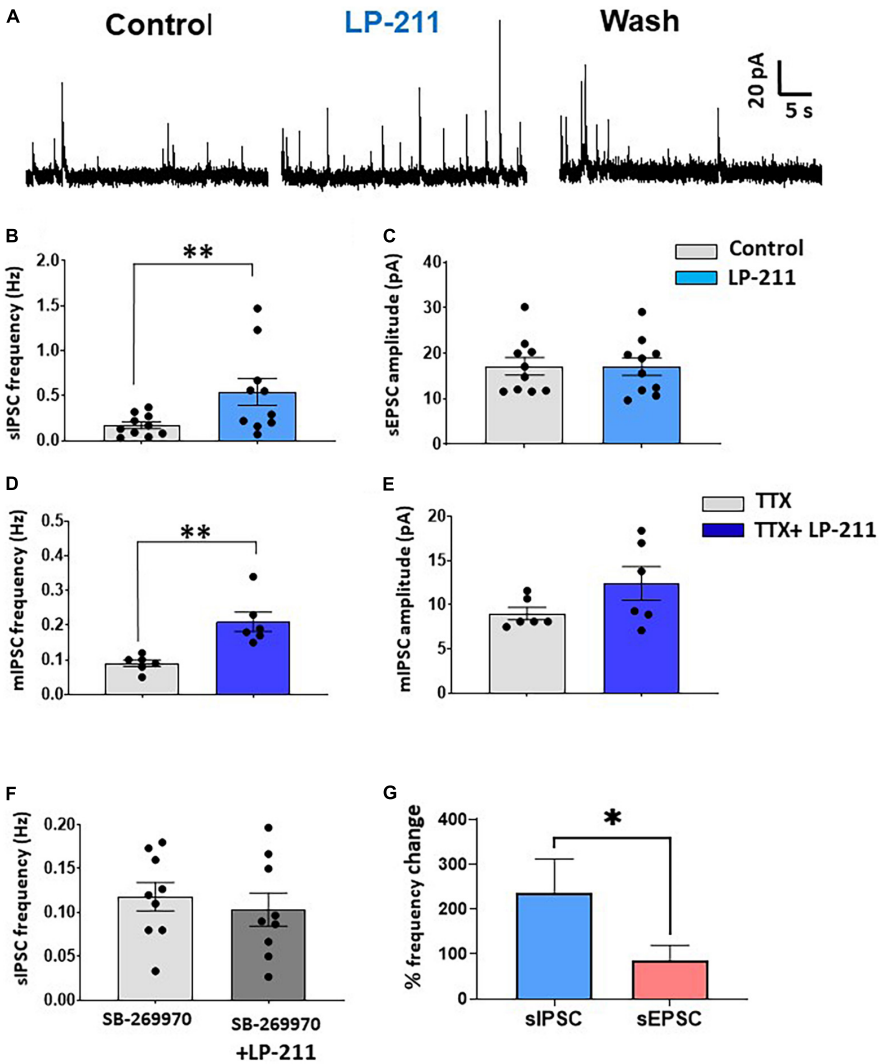

FIGURE 2 | Activation of 5-HT$_7$Rs by LP-211 potentiates spontaneous GABA and glycine release. **(A)** Representative traces of spontaneous inhibitory postsynaptic currents (IPSCs), recorded in voltage-clamp at 0 mV, in the presence of the AMPA and NMDA receptor antagonists NBQX (10 μM) and D-AP5 (50 μM). An increase in sIPSC frequency was evident in the presence of LP-211 (1 μM). **(B,C)** Summary graphs obtained from the lamina II neurons responsive to LP-211. The agonist caused a significant increase of sIPSC frequency in 10 out of 14 tested cells [**(B)** paired *t*-test, $p < 0.01$, $n = 10$], without affecting the mean sIPSC amplitude (paired *t*-test, $p = 0.96$, n = 10). **(D,E)** In the presence of 1 μM TTX, LP-211 still produced a significant increase in mIPSC frequency in 6 out of 11 cells tested [**(D)** paired t-test, $p < 0.01$, $n = 6$], while mean mIPSC was not altered [**(E)** paired *t*-test, $p = 0.12$, $n = 6$]. **(F)** Co-application of LP-211 with SB-269970 (10 μM) inhibited the increase of sEPSC frequency, confirming the involvement of 5-HT$_7$Rs (zero responsive cells out of 9 tested, paired *t*-test, $p = 0.21$, $n = 9$). **(G)** LP-211 exerted a stronger effect on sIPSC frequency as compared to sEPSC (Mann–Whitney test, $p < 0.05$, $n = 10$ and 9, for sIPSCs and sEPSCs, respectively). Asterisks reported in the graphs represent statistical significance: *$p < 0.05$; **$p < 0.01$; ***$p < 0.001$.

that 5-HT$_7$Rs are able to potentiate both excitatory (mediated by glutamate) and inhibitory transmission (mediated by GABA and glycine), with a stronger impact on synaptic inhibition. The increase in frequency of spontaneous excitatory and inhibitory currents, not accompanied by changes in amplitude, and the decrease of PPRs in the evoked currents indicate that 5-HT$_7$Rs act at presynaptic sites modulating neurotransmitter release.

In our experiments, we used the compound LP-211 to activate 5-HT$_7$Rs. This agonist was tested previously in the hippocampus (Costa et al., 2012, 2015, 2018) and the cerebellum (Lippiello et al., 2016), but it was never utilized in studies on spinal cord neurons. In the hippocampus, modulatory effects of 5-HT$_7$Rs have been described by applying very low concentrations of LP-211 (10 nM). We have observed reliable results only administering LP-211 at 1 μM, while 0.1 μM was ineffective. Similarly, LP-211 was tested at 1 μM on cerebellar slices, where 5-HT$_7$Rs were involved in the induction of Long term depression (LTD) (Lippiello et al., 2016). The necessity of using higher concentrations of agonists in spinal cord slices as compared to other preparations could derive from their particular morphology and from the location of the recorded cells. Indeed, most recordings were obtained from neurons

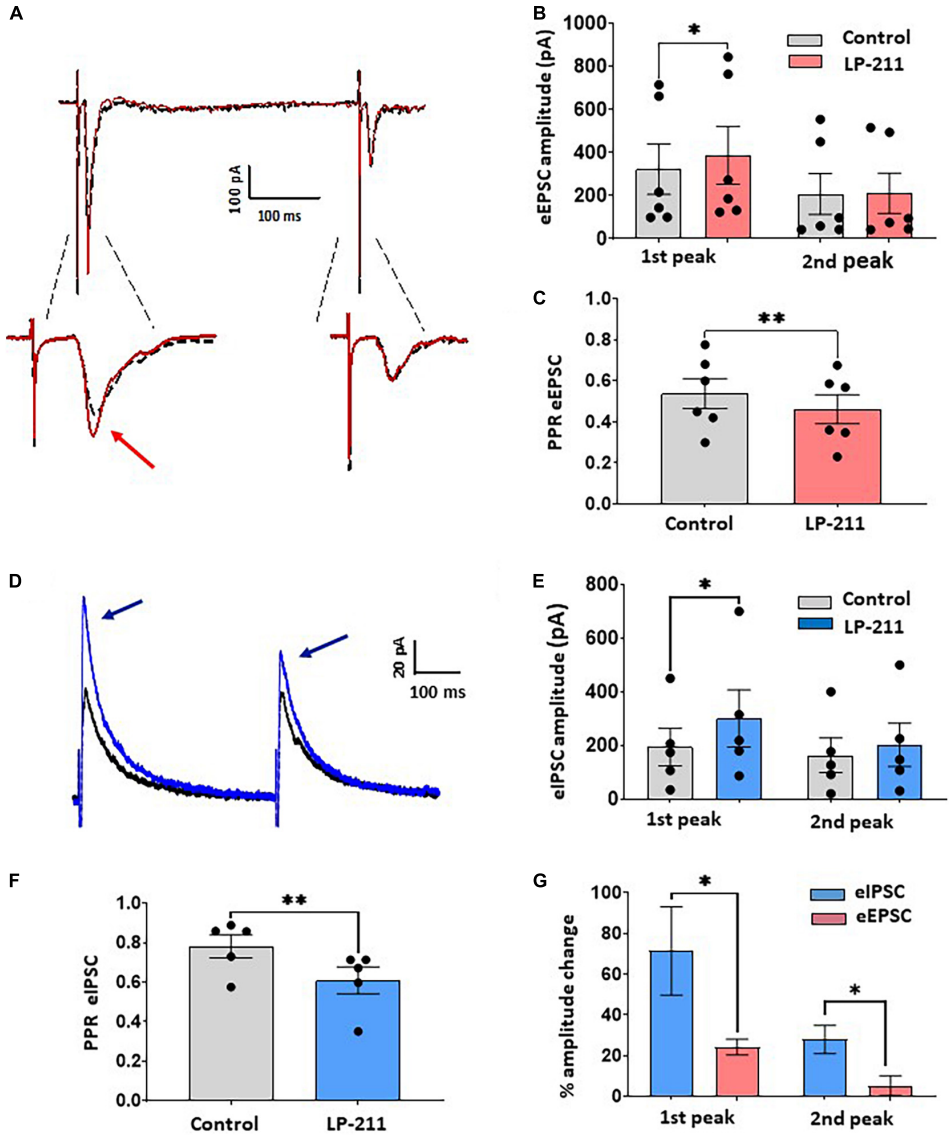

FIGURE 3 | Application of LP-211 facilitates evoked excitatory postsynaptic currents (EPSCs) and Inhibitory postsynaptic currents (IPSCs), exerting a stronger action on inhibitory transmission. **(A)** Example of EPSC recordings (eEPSCs), evoked by dorsal root stimulation (500 mA, 0.1 ms) and recorded at –70 mV. Two stimuli were applied at 400 ms intervals (paired pulse protocol). LP-211 (1 μM, red trace) caused a moderate potentiation of evoked EPSCs in 5 out of 11 cells tested. **(B)** The first EPSC was significantly increased (Wilcoxon rank-sum test, $p < 0.05$, $n = 6$ EPSCs from 5 cells), while the second peak was not changed (Wilcoxon rank-test, $p = 0.76$, $n = 6$). **(C)** Paired pulse ratio (PPR = second EPSC/first EPSC) was significantly decreased by LP-211, suggesting a presynaptic action (paired *t*-test, $p < 0.01$, $n = 6$). **(D)** Recordings of IPSCs evoked by focal stimulation (paired pulse protocol) and recorded at 0 mV, in the presence of NBQX (10 μM) and D-AP5 (50 μM): in this example, LP-211 caused the increase of both IPSCs (blue trace). **(E)** The first IPSC underwent a stronger potentiation than the second peak, as observed in 5 responsive cells out of 11 (first peak, paired *t*-test, $p < 0.05$; second peak: paired *t*-test, $p = 0.07$, $n = 5$). **(F)** Paired pulse ratio was significantly decreased (paired *t*-test, $p < 0.01$, $n = 5$), confirming a presynaptic effect. **(G)** Evoked inhibitory currents were more affected by 5-HT$_7$R activation compared to excitatory responses, as revealed by the higher percentage increase of both evoked IPSC peaks (Mann–Whitney test, $p < 0.05$, $n = 5$ and 6 for IPSCs and EPSCs, respectively). Asterisks reported in the graphs represent statistical significance: *$p < 0.05$; **$p < 0.01$; ***$p < 0.001$.

located quite deep into the slice, where synaptic connections are well preserved.

In our preparation, LP-211 was ineffective in potentiating excitatory transmission in the presence of the 5-HT$_7$ antagonist SB-269970, while it produced significant effects when applied with the 5-HT$_{1A}$ antagonist WAY-100635. SB-269970 was applied at the concentration of 10 μM that could also inhibit the activity 5-HT$_{5A}$Rs. However, these receptors are negatively coupled to adenylate cyclase *via* Gi/o proteins whose activation opens K^+ channels. This mechanism of action is not compatible with the increase of transmitter release and action potential firing observed in our study. Furthermore, SB-269970 administered at similar concentrations has proved to be ineffective on locomotor-like rhythmic activity recorded from *in vitro* spinal cord in

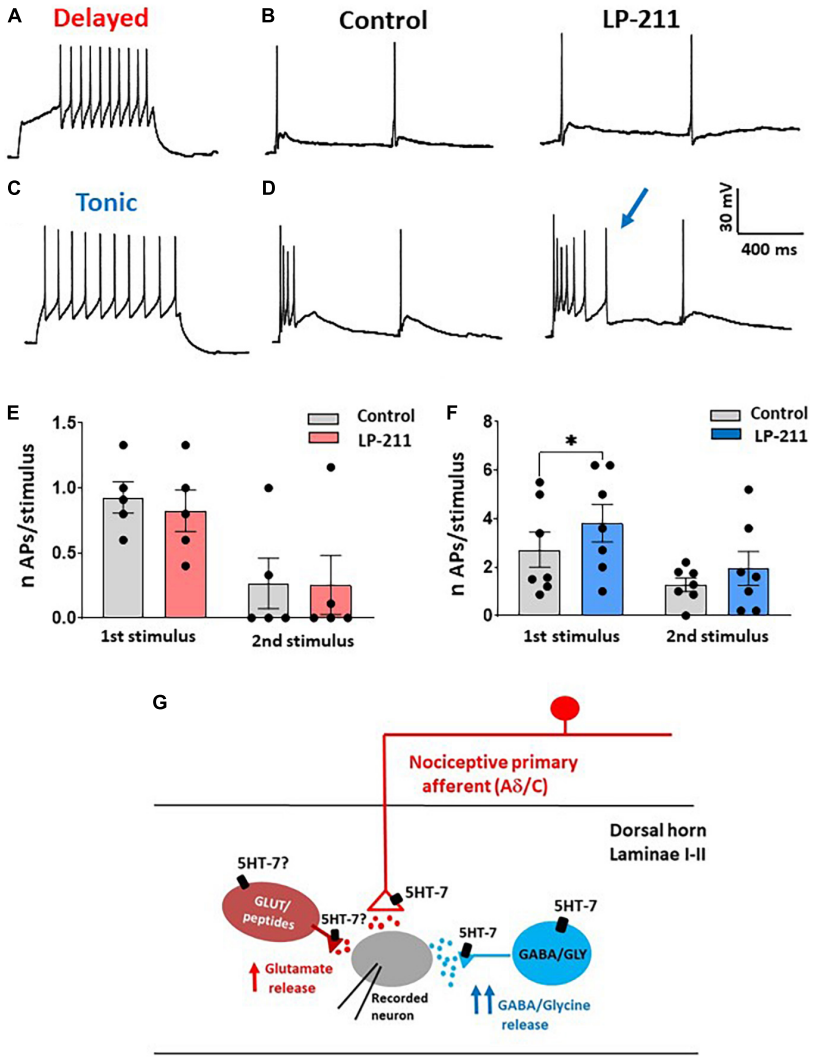

FIGURE 4 | Activation of 5-HT$_7$Rs differently affects the excitability of delayed and tonic firing lamina II neurons. **(A)** Example of a delayed firing neuron, recorded in current clamp at –80 mV. **(B)** In the same neuron, dorsal root stimulation (2 pulses) evoked action potentials (APs) superimposed to the excitatory postsynaptic potentials (EPSPs). The number of APs was not changed in the presence of LP-211 (1 μM). **(C)** Example of a tonic firing neuron, recorded at a potential of about –80 mV. **(D)** In the same neuron, LP-211 increased the number of APs elicited by root stimulation at the first pulse. **(E)** The mean number of APs evoked in delayed firing neurons was not changed by LP-211 (first stimulus: paired *t*-test, $p = 0.08$; second: paired *t*-test, $p = 0.85$, $n = 5$). **(F)** In the tonic firing neurons, the number of APs was significantly increased at the first stimulus (first: Wilcoxon rank-sum test, $p < 0.05$; second: paired t-test, $p = 0.2$, $n = 7$). **(G)** Schematic diagram depicting the hypothetical dorsal horn circuit involved in 5-HT$_7$R-mediated synaptic modulation (see section "Discussion"). Asterisks reported in the graphs represent statistical significance: *$p < 0.05$; **$p < 0.01$; ***$p < 0.001$.

5-HT$_7$R knockout mice (Liu et al., 2009). Interestingly, 5-HT$_2$Rs that are involved in the generation of this activity together with 5-HT$_7$Rs (Pearlstein et al., 2005) were not affected by SB-269970 at these concentrations.

Based on these considerations, we could assume that LP-211 selectively activates 5-HT$_7$Rs in mouse spinal cord slices, even at higher concentrations. Future studies employing 5-HT$_7$ knockout mice, shRNA, or CRISPR viral delivery will be helpful to further clarify the role of 5-HT$_7$Rs in modulating nociceptive transmission in the spinal cord dorsal horn.

In the spinal cord dorsal horn, 5-HT$_7$Rs have been observed on primary afferent fiber terminals (especially small myelinated and unmyelinated fibers), neuronal somas, dendrites, and astrocytes (Doly et al., 2005). Although 5-HT$_7$Rs are expressed in both laminae I and II, we have focused our study on lamina II neurons, since a large number of studies are available to describe the correlation between action potential firing patterns and neuronal types in this region. This allowed us to determine the different effects of LP-211 on excitatory (delayed firing) and inhibitory interneurons (tonic firing, **Figures 4A–F**).

Dorsal horn neurons that express 5-HT$_7$Rs are mainly represented by excitatory peptidergic neurons and GABAergic interneurons (Meuser et al., 2002; Doly et al., 2005). Consistently, we observed a 5-HT$_7$-mediated potentiation of both spontaneous

and evoked glutamate release. Furthermore, the effects of LP-211 on spontaneous and evoked GABA/glycinergic IPSCs confirm the role of 5-HT$_7$Rs expressed on inhibitory interneurons. The diagram shown in **Figure 4G** summarizes our results in relation to a hypothetical dorsal horn circuit: functional 5-HT$_7$Rs are expressed by some nociceptive afferent terminals synapsing onto the recorded lamina II neuron, by a subpopulation of inhibitory interneurons and probably also by some excitatory interneurons. Indeed, the effect of LP-211 on spontaneous EPSCs was reduced in the presence of TTX, suggesting that 5-HT$_7$Rs expressed on excitatory interneurons could contribute to the modulation of glutamate release through an action potential-dependent mechanism.

Several cellular mechanisms could be involved in the synaptic facilitation mediated by 5-HT$_7$Rs (Ciranna and Catania, 2014). As shown in many CNS areas, activation of these receptors can increase neuronal excitability by (i) reducing action potential hyperpolarization (through the inhibition of a Ca^{2+}-dependent potassium current; Goaillard and Vincent, 2002); (ii) inhibiting the I_A potassium current (Siwiec et al., 2020); (iii) enhancing the hyperpolarization-activated cation current (Ih; Larkman and Kelly, 1997; Cardenas et al., 1999; Chapin and Andrade, 2001; Bickmeyer et al., 2002; Tang and Trussell, 2015); and (iv) potentiating the activity of voltage-dependent T-type calcium channels (Lenglet et al., 2002). Our study showed that LP-211 is particularly effective in increasing the excitability of tonic firing neurons, which mainly correspond to inhibitory interneurons (Daniele and MacDermott, 2009; Yasaka et al., 2010; Hughes et al., 2012). Interestingly, tonic-firing cells in lamina II have the highest expression level of Ih, which has also been often associated with inhibitory neuron populations (Hantman and Perl, 2005; Hughes et al., 2012; Smith et al., 2015). Together with the expression of T-type Ca^{2+} channels in some neuron populations (Smith et al., 2015), this property would make tonic firing inhibitory interneurons favorable targets for 5-HT$_7$R-mediated modulation. The persistence of the LP-211 effect on mIPSCs in TTX would also suggest the presence of an action potential-independent, direct modulation at the inhibitory neuron axon terminal, similarly to what was observed in the hippocampus (Tokarski et al., 2011).

The effects of 5-HT$_7$R activation on pain transmission *in vivo* are still under debate. Studies performed in rodents have reported both anti- and pro-nociceptive actions of these receptors. Analgesic effects seem to be prevalent for spinal 5-HT$_7$R, while receptors expressed peripherally could be more involved in enhancing pain (Cortes-Altamirano et al., 2018). An anti-nociceptive action of 5-HT7Rs has been observed, for example, in models of pain hypersensitivity induced by capsaicin injection (Brenchat et al., 2009), sciatic nerve ligation (Brenchat et al., 2010), or chronic constriction injury (Viguier et al., 2012). Similarly, in mice, 5-HT$_7$ agonists LP-211 and LP-44 induce analgesic effects on formalin-induced orofacial pain (Demirkaya et al., 2016). GABAergic interneurons seem to be especially involved in 5-HT$_7$-mediated anti-nociception since the intrathecal administration of the $GABA_A$ antagonist bicuculline prevented the anti-hyperalgesic effect of 5-HT$_7$ agonists in rats with the constriction injury of the sciatic nerve (Viguier et al., 2012, 2013). On the other hand, pro-nociceptive actions of 5-HT$_7$Rs have been described by Rocha-González et al. (2005), reporting an increase of flinching during the second phase of the formalin test after administration of a 5-HT$_7$ agonist. In a different study, tactile allodynia induced by nerve injury was reduced by systemic or spinal administration of a 5-HT$_7$ antagonist (Amaya-Castellanos et al., 2011). These discrepancies in 5-HT$_7$R-mediated effects on animal models of pain *in vivo* could be explained by the differences in the pain models used and the low selectivity of some of the 5-HT$_7$ agonists employed in the studies.

Our results, showing a prevalent effect of LP-211 in potentiating synaptic inhibition in naïve mice, suggest that 5-HT$_7$Rs exert an anti-nociceptive effect in acute pain. However, it is difficult to predict how these modulatory mechanisms could be altered in conditions of chronic pain. As discussed by Bannister et al. (2017) in an interesting study demonstrating the involvement of 5-HT$_7$Rs in spinal diffuse noxious inhibitory control (DNIC), the recruitment and function of dorsal horn 5-HT$_7$Rs can be influenced by several factors, such as the pain state, the amount of serotonin release, the level of receptor expression in primary nociceptors and dorsal horn interneurons, and the relative contribution of other serotonergic receptors. Future experiments performed on identified dorsal horn neuron populations (excitatory or inhibitory interneurons and projection neurons) will allow a better characterization of 5-HT$_7$R modulatory effects on dorsal horn neural circuits. These studies should be carried out in different animal pain models, determining the modifications of receptor expression and function in specific classes of neurons.

DATA AVAILABILITY STATEMENT

The raw data supporting the conclusions of this article will be made available by the authors, without undue reservation.

ETHICS STATEMENT

The animal study was reviewed and approved by Italian Ministry of Health.

AUTHOR CONTRIBUTIONS

AC performed part of the experiments. EL and ML synthesized the compound LP-211 and wrote the manuscript. RB conceived and designed the study, performed part of the experiments, and wrote the manuscript. All authors contributed to the article and approved the submitted version.

FUNDING

This work was supported by the Italian Ministry of University and Research (MIUR, "Department of Excellence program") and by a grant from Banca Popolare dell'Emilia Romagna (BPER).

REFERENCES

Amaya-Castellanos, E., Pineda-Farias, J. B., Castañeda-Corral, G., Vidal-Cantú, G. C., Murbartián, J., Rocha-González, H. I., et al. (2011). Blockade of 5-HT7 receptors reduces tactile allodynia in the rat. *Pharmacol. Biochem. Behav.* 99, 591–597. doi: 10.1016/j.pbb.2011.06.005

Bannister, K., Lockwood, S., Goncalves, L., Patel, R., and Dickenson, A. H. (2017). An investigation into the inhibitory function of serotonin in diffuse noxious inhibitory controls in the neuropathic rat. *Eur. J. Pain* 21, 750–760. doi: 10.1002/ejp.979

Bardoni, R. (2019). Serotonergic modulation of nociceptive circuits in spinal cord dorsal horn. *Curr. Neuropharmacol.* 17, 1133–1145. doi: 10.2174/1570159X17666191001123900

Bardoni, R., Shen, K.-F., Li, H., Jeffry, J., Barry, D. M., Comitato, A., et al. (2019). Pain inhibits GRPR neurons via GABAergic signaling in the spinal cord. *Sci. Rep.* 9:15804. doi: 10.1038/s41598-019-52316-0

Betelli, C., MacDermott, A. B., and Bardoni, R. (2015). Transient, activity dependent inhibition of transmitter release from low threshold afferents mediated by GABAA receptors in spinal cord lamina III/IV. *Mol. Pain* 11:64. doi: 10.1186/s12990-015-0067-5

Bickmeyer, U., Heine, M., Manzke, T., and Richter, D. W. (2002). Differential modulation of I(h) by 5-HT receptors in mouse CA1 hippocampal neurons. *Eur. J. Neurosci.* 16, 209–218. doi: 10.1046/j.1460-9568.2002.02072.x

Blattner, K. M., Canney, D. J., Pippin, D. A., and Blass, B. E. (2019). Pharmacology and therapeutic potential of the 5-HT7 receptor. *ACS Chem. Neurosci.* 10, 89–119. doi: 10.1021/acschemneuro.8b00283

Brenchat, A., Nadal, X., Romero, L., Ovalle, S., Muro, A., Sánchez-Arroyos, R., et al. (2010). Pharmacological activation of 5-HT7 receptors reduces nerve injury-induced mechanical and thermal hypersensitivity. *Pain* 149, 483–494. doi: 10.1016/j.pain.2010.03.007

Brenchat, A., Romero, L., García, M., Pujol, M., Burgueño, J., Torrens, A., et al. (2009). 5-HT7 receptor activation inhibits mechanical hypersensitivity secondary to capsaicin sensitization in mice. *Pain* 141, 239–247. doi: 10.1016/j.pain.2008.11.009

Cardenas, C. G., Mar, L. P., Vysokanov, A. V., Arnold, P. B., Cardenas, L. M., Surmeier, D. J., et al. (1999). Serotonergic modulation of hyperpolarization-activated current in acutely isolated rat dorsal root ganglion neurons. *J. Physiol.* 518, 507–523. doi: 10.1111/j.1469-7793.1999.0507p.x

Chapin, E. M., and Andrade, R. (2001). A 5-HT(7) receptor-mediated depolarization in the anterodorsal thalamus. II. Involvement of the hyperpolarization-activated current I(h). *J. Pharmacol. Exp. Ther.* 297, 403–409.

Ciranna, L., and Catania, M. V. (2014). 5-HT7 receptors as modulators of neuronal excitability, synaptic transmission and plasticity: physiological role and possible implications in autism spectrum disorders. *Front. Cell Neurosci.* 8:250. doi: 10.3389/fncel.2014.00250

Comitato, A., Lacivita, E., Leopoldo, M., and Bardoni, R. (2021). "Serotonergic modulation by 5-HT7 receptors in mouse spinal cord dorsal horn," in *Proceedings of the 44th AISD National Meeting* (Bari: Università di Bari).

Cortes-Altamirano, J. L., Olmos-Hernandez, A., Jaime, H. B., Carrillo-Mora, P., Bandala, C., Reyes-Long, S., et al. (2018). Review: 5-HT1, 5-HT2, 5-HT3 and 5-HT7 receptors and their role in the modulation of pain response in the central nervous system. *Curr. Neuropharmacol.* 16, 210–221. doi: 10.2174/1570159X15666170911121027

Costa, L., Sardone, L. M., Bonaccorso, C. M., D'Antoni, S., Spatuzza, M., Gulisano, W., et al. (2018). Activation of serotonin 5-HT7 receptors modulates hippocampal synaptic plasticity by stimulation of adenylate cyclases and rescues learning and behavior in a mouse model of fragile X syndrome. *Front. Mol. Neurosci.* 11:353. doi: 10.3389/fnmol.2018.00353

Costa, L., Sardone, L. M., Lacivita, E., Leopoldo, M., and Ciranna, L. (2015). Novel agonists for serotonin 5-HT7 receptors reverse metabotropic glutamate receptor-mediated long-term depression in the hippocampus of wild-type and Fmr1 KO mice, a model of Fragile X Syndrome. *Front. Behav. Neurosci.* 9:65. doi: 10.3389/fnbeh.2015.00065

Costa, L., Spatuzza, M., D'Antoni, S., Bonaccorso, C. M., Trovato, C., Musumeci, S. A., et al. (2012). Activation of 5-HT7 serotonin receptors reverses metabotropic glutamate receptor-mediated synaptic plasticity in wild-type and Fmr1 knockout mice, a model of Fragile X syndrome. *Biol. Psychiatry* 72, 924–933. doi: 10.1016/j.biopsych.2012.06.008

Daniele, C. A., and MacDermott, A. B. (2009). Low-threshold primary afferent drive onto GABAergic interneurons in the superficial dorsal horn of the mouse. *J. Neurosci.* 29, 686–695. doi: 10.1523/JNEUROSCI.5120-08.2009

Demirkaya, K., Akgün, ÖM., Şenel, B., Öncel Torun, Z., Seyrek, M., Lacivita, E., et al. (2016). Selective 5-HT7 receptor agonists LP 44 and LP 211 elicit an analgesic effect on formalin-induced orofacial pain in mice. *J. Appl. Oral Sci.* 24, 218–222. doi: 10.1590/1678-775720150563

Doly, S., Fischer, J., Brisorgueil, M.-J., Vergé, D., and Conrath, M. (2005). Pre- and postsynaptic localization of the 5-HT7 receptor in rat dorsal spinal cord: immunocytochemical evidence. *J. Comp. Neurol.* 490, 256–269. doi: 10.1002/cne.20667

Garraway, S. M., and Hochman, S. (2001). Pharmacological characterization of serotonin receptor subtypes modulating primary afferent input to deep dorsal horn neurons in the neonatal rat. *Br. J. Pharmacol.* 132, 1789–1798. doi: 10.1038/sj.bjp.0703983

Goaillard, J.-M., and Vincent, P. (2002). Serotonin suppresses the slow afterhyperpolarization in rat intralaminar and midline thalamic neurones by activating 5-HT(7) receptors. *J. Physiol.* 541, 453–465. doi: 10.1113/jphysiol.2001.013896

Hantman, A. W., and Perl, E. R. (2005). Molecular and genetic features of a labeled class of spinal substantia gelatinosa neurons in a transgenic mouse. *J. Comp. Neurol.* 492, 90–100. doi: 10.1002/cne.20709

Hughes, D. I., Sikander, S., Kinnon, C. M., Boyle, K. A., Watanabe, M., Callister, R. J., et al. (2012). Morphological, neurochemical and electrophysiological features of parvalbumin-expressing cells: a likely source of axo-axonic inputs in the mouse spinal dorsal horn. *J. Physiol.* 590, 3927–3951. doi: 10.1113/jphysiol.2012.235655

Larkman, P. M., and Kelly, J. S. (1997). Modulation of IH by 5-HT in neonatal rat motoneurones in vitro: mediation through a phosphorylation independent action of cAMP. *Neuropharmacology* 36, 721–733. doi: 10.1016/s0028-3908(97)00021-x

Lenglet, S., Louiset, E., Delarue, C., Vaudry, H., and Contesse, V. (2002). Involvement of T-type calcium channels in the mechanism of action of 5-HT in rat glomerulosa cells: a novel signaling pathway for the 5-HT7 receptor. *Endocr. Res.* 28, 651–655. doi: 10.1081/erc-120016981

Leopoldo, M., Lacivita, E., Berardi, F., Perrone, R., and Hedlund, P. B. (2011). Serotonin 5-HT7 receptor agents: structure-activity relationships and potential therapeutic applications in central nervous system disorders. *Pharmacol. Ther.* 129, 120–148. doi: 10.1016/j.pharmthera.2010.08.013

Lippiello, P., Hoxha, E., Speranza, L., Volpicelli, F., Ferraro, A., Leopoldo, M., et al. (2016). The 5-HT7 receptor triggers cerebellar long-term synaptic depression via PKC-MAPK. *Neuropharmacology* 101, 426–438. doi: 10.1016/j.neuropharm.2015.10.019

Liu, J., Akay, T., Hedlund, P. B., Pearson, K. G., and Jordan, L. M. (2009). Spinal 5-HT7 receptors are critical for alternating activity during locomotion: in vitro neonatal and in vivo adult studies using 5-HT7 receptor knockout mice. *J. Neurophysiol.* 102, 337–348. doi: 10.1152/jn.91239.2008

Meuser, T., Pietruck, C., Gabriel, A., Xie, G.-X., Lim, K.-J., and Pierce Palmer, P. (2002). 5-HT7 receptors are involved in mediating 5-HT-induced activation of rat primary afferent neurons. *Life Sci.* 71, 2279–2289. doi: 10.1016/s0024-3205(02)02011-8

Norum, J. H., Hart, K., and Levy, F. O. (2003). Ras-dependent ERK activation by the human G(s)-coupled serotonin receptors 5-HT4(b) and 5-HT7(a). *J. Biol. Chem.* 278, 3098–3104. doi: 10.1074/jbc.M206237200

Pearlstein, E., Mabrouk, F. B., Pflieger, J. F., and Vinay, L. (2005). Serotonin refines the locomotor-related alternations in the in vitro neonatal rat spinal cord. *Eur. J. Neurosci.* 21, 1338–1346. doi: 10.1111/j.1460-9568.2005.03971.x

Rocha-González, H. I., Meneses, A., Carlton, S. M., and Granados-Soto, V. (2005). Pronociceptive role of peripheral and spinal 5-HT7 receptors in the formalin test. *Pain* 117, 182–192. doi: 10.1016/j.pain.2005.06.011

Siwiec, M., Kusek, M., Sowa, J. E., Tokarski, K., and Hess, G. (2020). 5-HT7 receptors increase the excitability of hippocampal CA1 pyramidal neurons by inhibiting the A-type potassium current. *Neuropharmacology* 177:108248. doi: 10.1016/j.neuropharm.2020.108248

Smith, K. M., Boyle, K. A., Madden, J. F., Dickinson, S. A., Jobling, P., Callister, R. J., et al. (2015). Functional heterogeneity of calretinin-expressing neurons

in the mouse superficial dorsal horn: implications for spinal pain processing. *J. Physiol.* 593, 4319–4339. doi: 10.1113/JP270855

Tang, Z.-Q., and Trussell, L. O. (2015). Serotonergic regulation of excitability of principal cells of the dorsal cochlear nucleus. *J. Neurosci.* 35, 4540–4551. doi: 10.1523/JNEUROSCI.4825-14.2015

Tokarski, K., Kusek, M., and Hess, G. (2011). 5-HT7 receptors modulate GABAergic transmission in rat hippocampal CA1 area. *J. Physiol. Pharmacol.* 62, 535–540.

Viguier, F., Michot, B., Hamon, M., and Bourgoin, S. (2013). Multiple roles of serotonin in pain control mechanisms–implications of 5-HT7 and other 5-HT receptor types. *Eur. J. Pharmacol.* 716, 8–16. doi: 10.1016/j.ejphar.2013.01.074

Viguier, F., Michot, B., Kayser, V., Bernard, J.-F., Vela, J.-M., Hamon, M., et al. (2012). GABA, but not opioids, mediates the anti-hyperalgesic effects of 5-HT7 receptor activation in rats suffering from neuropathic pain. *Neuropharmacology* 63, 1093–1106. doi: 10.1016/j.neuropharm.2012.07.023

Yang, E. J., Han, S. K., and Park, S. J. (2014). Functional expression of 5-HT^7 receptor on the substantia gelatinosa neurons of the trigeminal subnucleus caudalis in mice. *Brain Res.* 1543, 73–82.

Yasaka, T., Tiong, S. Y. X., Hughes, D. I., Riddell, J. S., and Todd, A. J. (2010). Populations of inhibitory and excitatory interneurons in lamina II of the adult rat spinal dorsal horn revealed by a combined electrophysiological and anatomical approach. *Pain* 151, 475–488. doi: 10.1016/j.pain.2010.08.008

Conflict of Interest: The authors declare that the research was conducted in the absence of any commercial or financial relationships that could be construed as a potential conflict of interest.

Publisher's Note: All claims expressed in this article are solely those of the authors and do not necessarily represent those of their affiliated organizations, or those of the publisher, the editors and the reviewers. Any product that may be evaluated in this article, or claim that may be made by its manufacturer, is not guaranteed or endorsed by the publisher.

frontiers | Frontiers in Molecular Neuroscience

ORIGINAL RESEARCH
published: 07 July 2022
doi: 10.3389/fnmol.2022.926596

Anatomical Analysis of Transient Potential Vanilloid Receptor 1 (*Trpv1*+) and Mu-Opioid Receptor (*Oprm1*+) Co-expression in Rat Dorsal Root Ganglion Neurons

Wenting Ma[1†], *Matthew R. Sapio*[1†], *Allison P. Manalo*[1], *Dragan Maric*[2], *Mary Kate Dougherty*[1], *Taichi Goto*[1,3], *Andrew J. Mannes*[1] *and Michael J. Iadarola*[1*]

[1] Department of Perioperative Medicine, Clinical Center, National Institutes of Health, Bethesda, MD, United States, [2] National Institute of Neurological Disorders and Stroke, Flow and Imaging Cytometry Core Facility, Bethesda, MD, United States, [3] Symptoms Biology Unit, National Institute of Nursing Research, National Institutes of Health, Bethesda, MD, United States

OPEN ACCESS

Edited by:
Fabien Marchand, INSERM U1107 Douleur et Biophysique Neurosensorielle (Neuro-Dol), France

Reviewed by:
Braulio Alfredo Muñoz Ramirez, Indiana University Bloomington, United States
Claire Gaveriaux-Ruff, Université de Strasbourg, France

***Correspondence:**
Michael J. Iadarola
michael.iadarola@nih.gov

[†] These authors have contributed equally to this work and share first authorship

Specialty section:
This article was submitted to Pain Mechanisms and Modulators, a section of the journal Frontiers in Molecular Neuroscience

Received: 22 April 2022
Accepted: 09 June 2022
Published: 07 July 2022

Citation:
Ma W, Sapio MR, Manalo AP, Maric D, Dougherty MK, Goto T, Mannes AJ and Iadarola MJ (2022) Anatomical Analysis of Transient Potential Vanilloid Receptor 1 (Trpv1+) and Mu-Opioid Receptor (Oprm1+) Co-expression in Rat Dorsal Root Ganglion Neurons. Front. Mol. Neurosci. 15:926596. doi: 10.3389/fnmol.2022.926596

Primary afferent neurons of the dorsal root ganglia (DRG) transduce peripheral nociceptive signals and transmit them to the spinal cord. These neurons also mediate analgesic control of the nociceptive inputs, particularly through the μ-opioid receptor (encoded by *Oprm1*). While opioid receptors are found throughout the neuraxis and in the spinal cord tissue itself, intrathecal administration of μ-opioid agonists also acts directly on nociceptive nerve terminals in the dorsal spinal cord resulting in marked analgesia. Additionally, selective chemoaxotomy of cells expressing the TRPV1 channel, a nonselective calcium-permeable ion channel that transduces thermal and inflammatory pain, yields profound pain relief in rats, canines, and humans. However, the relationship between *Oprm1* and *Trpv1* expressing DRG neurons has not been precisely determined. The present study examines rat DRG neurons using high resolution multiplex fluorescent *in situ* hybridization to visualize molecular co-expression. Neurons positive for *Trpv1* exhibited varying levels of expression for *Trpv1* and co-expression of other excitatory and inhibitory ion channels or receptors. A subpopulation of densely labeled *Trpv1*+ neurons did not co-express *Oprm1*. In contrast, a population of less densely labeled *Trpv1*+ neurons did co-express *Oprm1*. This finding suggests that the medium/low *Trpv1* expressing neurons represent a specific set of DRG neurons subserving the opponent processes of both transducing and inhibiting nociceptive inputs. Additionally, the medium/low *Trpv1* expressing neurons co-expressed other markers implicated in pathological pain states, such as *Trpa1* and *Trpm8*, which are involved in chemical nociception and cold allodynia, respectively, as well as *Scn11a*, whose mutations are implicated in familial episodic pain. Conversely, none of the *Trpv1*+ neurons co-expressed *Spp1*, which codes for osteopontin, a marker for large diameter proprioceptive neurons, validating that nociception and proprioception are governed by separate neuronal populations. Our findings support the hypothesis that the population

of *Trpv1* and *Oprm1* coexpressing neurons may explain the remarkable efficacy of opioid drugs administered at the level of the DRG-spinal synapse, and that this subpopulation of *Trpv1*+ neurons is responsible for registering tissue damage.

Keywords: dorsal root ganglia (DRG), opioid receptor, transient receptor potential vanilloid-1 (TRPV1), nociception, transient receptor potential A1 (TRPA1), mu opioid (MOP) receptor, Kappa opioid receptor (KOR), TRPM8

INTRODUCTION

The nociceptive system is a major target of interest for the design of analgesic drugs. When administered at this level of the pain pathway, analgesic agents such as opioids and local anesthetics ultimately act on primary afferent endings by inhibiting presynaptic release of nociceptive signaling molecules, such as substance P and calcitonin gene-related peptide (CGRP) (Julius and Basbaum, 2001; Kondo et al., 2005). A better understanding of which afferents are required for nociception and what constellation of receptors are expressed by these neurons is an important component of designing alternative strategies to selectively inhibit nociception while preserving other somatosensory functions.

Transient receptor potential vanilloid subfamily, member 1 (TRPV1) is expressed by primary afferent nociceptive neurons (Caterina et al., 1997; Szallasi and Blumberg, 1999; Caterina, 2007), and transduces thermal and inflammatory tissue damage stimuli (Karai et al., 2004a; Mishra and Hoon, 2010; Mitchell et al., 2010, 2014). In the search for novel non-opioid analgesics, much attention has been centered on the TRPV1 molecule as an analgesic target (Jancso et al., 1977; Yaksh et al., 1979; Bevan et al., 1992; Urban et al., 2000; Wong and Gavva, 2009; Iadarola and Gonnella, 2013). Genetic ablation or chemical silencing of *TRPV1*+ afferents has been reported to cause loss of nociceptive responses (Jancso et al., 1977; Karai et al., 2004a; Brown et al., 2005, 2015; Mishra and Hoon, 2010; Brown and Iadarola, 2015; Sapio et al., 2018). However, direct antagonism of the TRPV1 receptor has not led to clinically useful antinociceptive agents, despite promising preclinical rodent studies and demonstrable target engagement in humans (Menéndez et al., 2006; Szallasi et al., 2007; Rowbotham et al., 2011; Quiding et al., 2013). These drugs did not advance in part due to induction of varying degrees of hyperthermia (Wong and Gavva, 2009; Garami et al., 2018; Park et al., 2021), and lack of sustained efficacy (Quiding et al., 2013), as TRPV1 is not the only nociceptive transducing molecule expressed by primary afferents (Goswami et al., 2014). In the complex milieu of tissue damage and inflammation, multiple other algesic mediators remain capable of discharging the primary afferents, even with a high degree of TRPV1 inhibition, which may explain why TRPV1 antagonists are much less analgesic than agonist-mediated chemoaxotomy approaches (Karai et al., 2004a; Iadarola et al., 2018; Sapio et al., 2018). Additionally, patients treated with high concentrations of TRPV1 antagonists become insensitive to noxious hot thermal stimuli, posing a burn risk as they rated temperatures up to 49°C as safe (Rowbotham et al., 2011). Thus, TRPV1+ afferents are the critical transducers of pain associated with tissue damage as well as most forms of warm and hot thermosensation.

Untangling desirable and undesirable pharmacologic effects of TRPV1-based therapies requires clarification of the underlying neurobiology. An interesting observation is that selective lesioning of TRPV1+ nerve endings using the highly potent TRPV1 agonist, resiniferatoxin (RTX), leads to loss of thermal nociceptive sensitivity and with high subcutaneous doses (250 ng intraplantar) can produce near-total insensitivity to tissue-damaging stimuli in the denervated area (Mitchell et al., 2010, 2014). While it is known that TRPV1+ nociceptors comprise several discrete populations of sensory afferent neurons (Sapio et al., 2018), detailed studies of nociceptive cellular neurobiology are needed to elucidate the precise molecular markers of each population. The objective of the present investigations is to delineate the molecular complement of receptors and ion channels in neurons responsible for nociception and analgesic action. Specifically, we hypothesize that we can identify a population of cells using multiplex labeling that contains several nociceptive and analgesic markers, that maybe useful for future studies of pain and analgesia. Delineating these neurons in a quantitative, molecularly-defined fashion enables future studies to directly target these neurons using selective pharmacological analgesic strategies.

MATERIALS AND METHODS

Rat Dorsal Root Ganglia Tissue Procurement and Slide Preparation

Experiments in the present study were approved by the Institutional Animal Care and Use Committee of the Clinical Center, National Institutes of Health (Bethesda, Maryland). Male Sprague-Dawley rats 7–8 weeks old weighing 175–200 g (Charles River Laboratories, Wilmington, MA) were used for all experiments. Rats were housed in pairs with a plastic tube for enrichment/housing. At the time of tissue collection, rats were euthanized under deep isoflurane anesthesia ($\geq$4%) and perfused with cold intracardiac PBS followed by 10% formalin. Bilateral lumbar DRGs were harvested at the level of L3–L6. DRGs were fixed in 10% formalin for 24 h and subsequently transferred to 2.5% formalin before embedding (within 3–4 days). DRG tissues were embedded in paraffin blocks and cut to 6 μm sections and mounted on slides by Histoserv, Inc. (Germantown, MD). For these experiments DRGs from $N = 6$ rats were collected; with $N = 3$ stained, analyzed, and scanned for most analyses. Cell types identified were found in approximately the same proportions in each individual animal. Multiple windows on the sections of DRG were selected to capture representative fields for quantification. Sample sizes were estimated from previous experiments (Sapio et al., 2020b).

Fluorescent Multiplex *in situ* Hybridization and Microscopic Imaging

Fluorescent RNA *in situ* hybridization was performed using RNAScope® Multiplex Fluorescent V2 Assay (Advanced Cell Diagnostics, Newark, CA) in accordance with the manufacturer's instructions for treating formalin-fixed paraffin-embedded tissue. Target retrieval was performed for 15 mins at 100°C. The catalog numbers of the probes used in these experiments are listed in **Table 1**. Note that color balancing was performed based on sFPKM data (Sapio et al., 2016) to put weaker signals in channels with the least background autofluorescence (higher wavelengths) to avoid signal bleed. To avoid cross reaction between opioid receptors, the kappa opioid receptor (*Oprk1*) probe was custom designed to be specific when used together with the other opioid receptor detection probes. This was accomplished by targeting base pairs 1,300–2,293 of NM_017167.3. To validate a neuronal population exhibiting a low signal for *Trpm8* hybridization, a second probe was used against a different region of the transcript. This was targeted to base pairs 2,671–3,590 of NM_134371.3.

Hybridized slides were imaged using an Axio Imager.Z2 scanning fluorescence microscope (Zeiss, Oberkochen, Germany), fitted with an ORCA-Flash4.0s CMOS sensor high resolution digital camera (Hamamatsu, Shizuoka, Japan), 20X/0.8 Plan-Apochromat (Phase-2) non-immersion objective (Zeiss), and 200W X-Cite 200DC broad band lamp source (Excelitas Technologies, Waltham MA). Filter sets (Semrock, Rochester NY) for detecting DAPI, Opal520, Opal570, Opal620, and Opal690 fluorescent dyes (Opal Reagent Systems; PerkinElmer, Waltham MA) were custom furnished as described previously (Maric et al., 2021) (**Supplementary Table 1**). Image tiles sized 600 × 600 μm were captured and seamlessly stitched using ZEN2 imaging software (Zeiss) at 3 pixel/μm spatial resolution. For each emission wavelength, fluorescent microscopy images were captured and displayed as individual layers to generate multi-colored composites. Representative images are enhanced for visibility.

Quantification and Visualization of *in situ* Data

The images were processed with Adobe Photoshop and Fiji (Image J v2.1.0/1.53c) in order to analyze the co-localization patterns of genes that are detected in the multiplex *in situ* hybridization experiments. For quantification of signal intensity inside individual DRG neurons, polygons were drawn based on the bright field image in a multichannel overlay using Fiji, and fluorescence intensity of this polygonal area was measured. The neuronal diameter was extrapolated from the polygonal area using the formula for the diameter of a circle [diameter $= 2\sqrt{}$ (area/π)]. For cell counting, cells were counted manually in Photoshop, and tabulated counts were used to plot visualizations of intersecting sets in R (v4.05) using the UpSet package. In these plots, the number of cells positive for each of the four markers is plotted as "set size" and the number of cells co-positive for each given combination of markers is shown as "intersection size." Cells were identified using a combination of DAPI-labeling and diffusion image contrast imaging which revealed cellular outline. A single 6 μm section was counted for each stain per rat to avoid counting the same cell twice in serial sections. Statistical testing of diameter measurements was conducted using Prism GraphPad (Version 9.3.0, Kruskal-Wallis test with Dunn's multiple comparison test). In these experiments, data from each individual rat was examined before pooling to ensure homogeneity, and the individual values are shown in **Supplementary Figure 1**. Proportions of cells positive for *Oprm1*, *Oprk1*, *Oprd1*, and *Trpv1* markers were determined in a pairwise manner and represented as percentages relative to the total number of cells counted.

To distinguish cell populations by levels of *Trpv1*, *Oprm1*, *Oprd1*, and *Trpm8* expression, a surface plot was generated in Fiji to visualize fluorescence intensity per pixel. Surface plots have three axes, with the x and y axes corresponding to the physical dimension of the slide section, and the z-dimension, or height of the surface representing intensity. Intensity in these plots is also represented by color in a flame scale.

For quantitative graphs, each channel was checked for non-specific signal coming from neighboring channels and subtracted if signal bleed was detected to quantify only specific fluorescent signal.

RESULTS

Co-expression of Transient Receptor Potential Vanilloid 1 (*Trpv1*) and the Three Opioid Receptors (*Oprm1*, *Oprk1*, *Oprd1*)

Semiquantitative analysis was performed to estimate the number of cells present or absent for the mRNA encoding the thermosensory nociceptive ion channel *Trpv1* and each of the three opioid receptors (*Oprm1*, *Oprk1*, and *Oprd1*). This analysis subdivided the sensory afferents into 12 populations, though not all were prevalent (**Figure 1A**). In order to concisely depict the overlap between *Trpv1* and opioid receptor transcripts, a pairwise matrix of percentages was constructed (**Figure 1B**). The most prevalent binary combination of markers was *Trpv1* and *Oprm1*, comprising 60.4% of all neurons (ignoring categorization by the other markers). The κ-opioid receptor (encoded by *Oprk1*) was identified with ∼15% of neurons in combination with either *Trpv1* or *Oprm1*. The δ-opioid receptor (*Oprd1*) was less prevalent, and the rarest combination were neurons co-positive for δ- and κ-opioid receptors (5.4%). These results are based on the aggregated quantification of 755 cells from $N = 3$ rats. The bottom 15 panels show representative images of the distinct co-expressing populations of *Trpv1*+/*Oprm1*+ neurons (**Figure 1C**), *Trpv1*+/*Oprm1*+/*Oprk1*+ neurons (**Figure 1D**), and *Oprm1*+/*Oprd1*+ neurons (**Figure 1E**).

Heterogeneous Levels of *Trpv1* mRNA in Rat DRG

While examining binary expression patterns (presence vs. absence), we noted substantial variation in expression of *Trpv1* transcript. Previously, it has been reported that *Trpv1*

TABLE 1 | Table of genes examined in the present study.

Probes used for *in situ* hybridization			
Gene name	**Symbol**	**Catalog#**	**sFPKM**
Delta Opioid Receptor 1	*Oprd1*	457011-C3	1.5
Kappa Opioid Receptor 1	*Oprk1*	1037891-C1	3.2
Opioid Related Nociceptin Receptor 1	*Oprl1*	576011	25.8
Mu Opioid Receptor 1	*Oprm1*	410691-C2	7.9
Sodium Voltage-Gated Channel Alpha Subunit 11	*Scn11a*	404811-C2	121.5
Secreted Phosphoprotein 1	*Spp1*	405441-C2	1179.0
Transient Receptor Potential Cation Channel, Subfamily A (Ankyrin-like) Member 1	*Trpa1*	312511-C2	23.0
Transient Receptor Potential Cation Channel Subfamily M (Melastatin) Member 8	*Trpm8*	539571 and 1127541	51.4
Transient Receptor Potential Cation Channel Subfamily V (Vanilloid) Member 1	*Trpv1*	501161-C4	58

Expression data in significant fragments per kilobase per million aligned reads (sFPKMs) comes from a previously published study (Sapio et al., 2016). This expression data was used at the experimental design stage for color balancing. Note that two Trpm8 probes were used to validate the low intensity staining result from the Trpm8 stain.

expression level is high in small diameter thermosensitive C-fibers, consistent with our observation that the highest intensity signals were observed within sparsely distributed small diameter neurons (**Figure 2A**, arrows). Based on this variation in *Trpv1* expression levels we quantified the fluorescence intensity for *Trpv1* to further characterize if quantitative expression levels of this ion channel gene indicated cell type differences. A lower intensity of *Trpv1* fluorescent signal was evident in many other cells (**Figures 2B,C**, arrowheads), consistent with the observation of multiple *Trpv1*+ neuronal populations containing a range of expression (**Figure 2D**) (Cavanaugh et al., 2011a; Goswami et al., 2014; Mitchell et al., 2014). Quantification of fluorescence intensity revealed three loosely separated populations (inflection points or "knees," in the plot of **Figure 2D**; $N = 3$ rats, $n = 146$ cells) corresponding to high, medium, and low expressing *Trpv1*+ neurons, consistent with previous findings from single-cell RNA-Seq (Usoskin et al., 2015; Li et al., 2016; Sapio et al., 2018). A surface plot was generated to visualize the range of expression profiles in the DRG neurons. Note that the high expressors appear as isolated peaks in this view, indicating that they are quantitatively separate from other *Trpv1*+ neurons (**Figure 2E**, arrows). Additionally, high intensity *Trpv1*+ neurons were smaller in diameter than the lower intensity *Trpv1*+ neurons (**Figure 2F**). In imaging *Trpv1*+ neurons, the exposure was set to minimize oversaturation of the signal at the highest level of expression, leading to apparent low signal in some cells. This is visualized showing the raw data (**Figure 2G**, upper row) and an enhanced image in which brightness is adjusted (**Figure 2G**, lower row), which shows the wide dynamic range of the signal. Note that even lower expressing *Trpv1*+ neurons contain a high enough density of puncta to distinguish their signal from background.

Analysis of Distribution of Intensity Values for the Opioid Receptor Genes *Oprm1* and *Oprd1*

The finding that *Trpv1* was unevenly distributed in rat DRG prompted an investigation of *Oprm1* and *Oprd1*. We also examined the distribution of expression intensity for two of the analgesic opioid receptors, the μ-opioid receptor transcript (*Oprm1*), and the delta opioid receptor transcript (*Oprd1*), which are responsible for opioid analgesic responses *in vivo* (reviewed in Valentino and Volkow, 2018). In a wide field we show an enhanced zoomed out image (brightened for clarity; **Figures 3A,B**). From this zoomed out field we did not observe a similar evident difference in expression level analogous to what was observed for *Trpv1* in either *Oprm1* or *Oprd1*. Note that *Oprm1* is expressed in a much greater number of neurons than *Oprd1*. In order to quantify this further, we used a surface plot to represent intensity over area for *Oprm1* (**Figures 3C,D**) and *Oprd1* (**Figures 3E,F**). In the angled view, the peaks represent intensity for staining with these labels, and generally fit the overall expression pattern of these receptors with evident peaks corresponding to the majority of positive cells. This is in contrast to what was observed for *Trpv1*, which had a small number of highly evident peaks on a linear axis (**Figure 2E**). Rank order plots were created to quantify expression, and test whether coefficient of variation differed between measured intensity values for *Trpv1*, *Oprm1* and *Oprd1*. These analyses showed a greater coefficient of variation in Trpv1 intensity as compared with *Oprm1* or *Oprd1* (**Supplementary Figure 2**).

Co-labeling of the Nociceptive Ion Channel Genes *Trpv1* and *Trpa1* With the *Oprm1* Opioid Receptor and the Opioid Receptor-Like *GPCR Oprl1*

RNA-Seq of rat dorsal root ganglia showed modest expression of *Oprm1* and comparatively higher expression of the opioid-related nociceptin receptor 1 (*Oprl1*) gene (7.9 and 25.8 sFPKM respectively) (Sapio et al., 2016). This receptor binds the opioid-like heptadecapeptide nociceptin, derived from the pronociceptin precursor and has sequence similarity (Phe-Gly-Gly-Phe-Thr-Gly-Ala-Arg-Lys-Ser-Ala-Arg-Lys-Leu-Ala-Asn-Gln) to dynorphin A1-17 (Tyr-Gly-Gly-Phe-Leu-Arg-Arg-Ile-Arg-Pro-Lys-Leu-Lys-Trp-Asp-Asn-Gln). To assess the overlap between expression of *Oprm1* and *Oprl1* and the nociceptive transducing ion channel genes *Trpv1* and *Trpa1*, multiplex fluorescent *in situ* hybridization was performed for these four transcripts together.

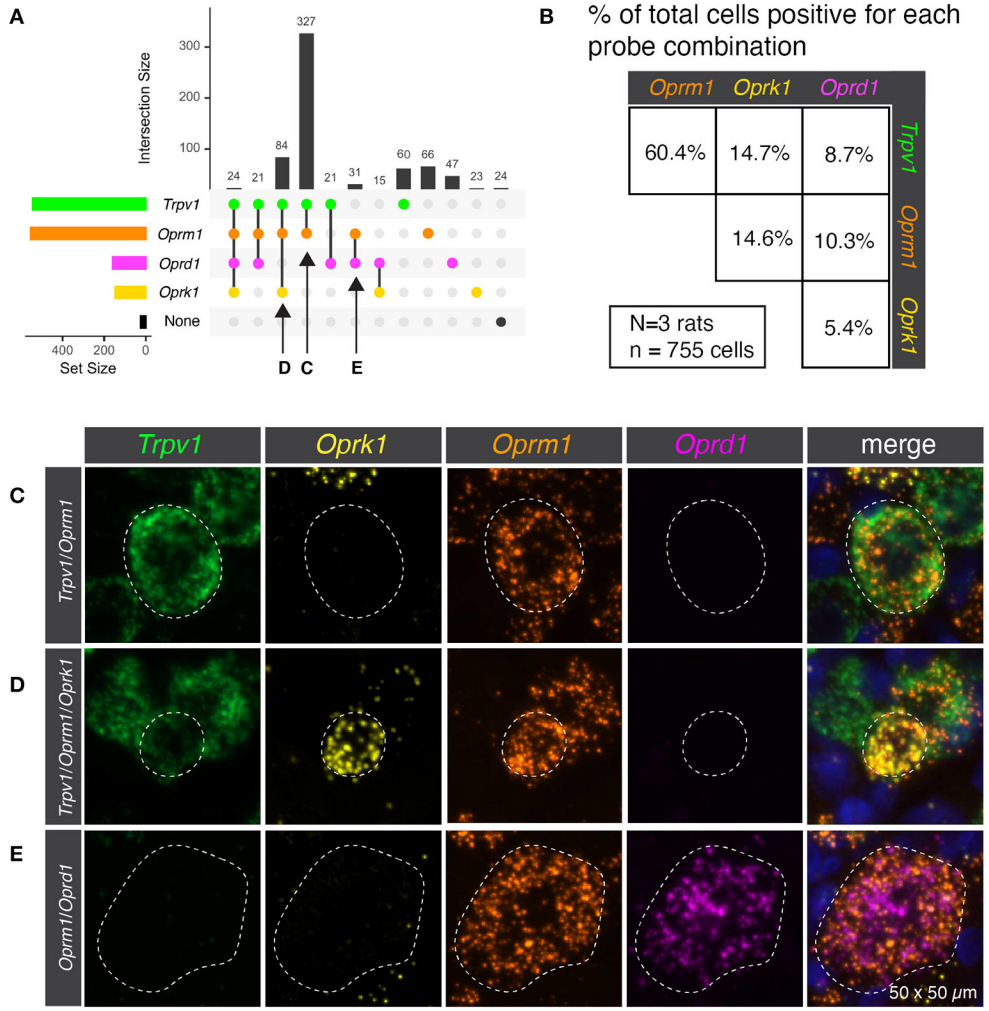

FIGURE 1 | Co-expression of transient receptor potential vanilloid 1 (*Trpv1*) and the three opioid receptors (*Oprm1*, *Oprk1*, *Oprd1*). **(A)** Semiquantitative analysis was performed to count the number of cells present or absent for each of the four marker genes. This analysis subdivided the sensory afferents into 12 populations, although not all of these populations were prevalent. **(B)** In order to simplify the overlap between *Trpv1* and Opioid receptor transcripts, a pairwise matrix of percentages is shown. This shows the total number of neurons positive for each marker (set size) as well as the number of cells positive for combinations of markers (intersection size; see Methods section). This display clarifies that *Trpv1*+/*Oprm1*+ cells were very prevalent in the DRG, comprising 60.4% of all neurons (ignoring categorization by the other markers.). While all possible combinations were identified, some were quite rare, with the population of cells positive for both *Oprk1* and *Oprd1* (the rarest combination) comprising ∼5% of neurons. **(C)** Representative multi-channel microscopy images are shown for three of the populations identified in panel A, the first of which being *Trpv1*+/*Oprm1*+ neurons. These neurons were the most abundant population at 327 of 755 total cells (or 43.3%). **(D)** The *Trpv1*+/*Oprm1*+/*Oprk1*+ population is shown, which is the second most abundant subpopulation at 84/755 cells (11.1%). **(E)** Finally, a representative cell from the *Oprm1*+/*Oprd1*+ population is shown. This population is rare, but is large and expresses very high levels of both *Oprm1* and *Oprd1*. Outlines of neurons are shown to enhance visibility (dotted lines).

The plot in **Figure 4A** is derived from 805 cells, counted in 3 sections from 3 animals. Co-expression was assessed for each of the 4 genes. The most prevalent neuronal type identified by these four labels was *Oprl1* alone neurons, which accounted for 272 cells (33.8%). When coexpression was taken into account, *Oprl1* was observed to be expressed in a majority of DRG neurons (71.6%). Cells positive for all four labels (133 cells, 16.5%) were also among the most prevalent co-expression combinations, indicating a strong overlap between the nociceptive ion channels *Trpv1* and *Trpa1* with opioid receptor genes *Oprm1* and *Oprl1*. Populations containing the nociceptive marker gene *Trpv1* and *Oprm1* with or without *Oprl1* (59 cells with all three and 147 cells with *Trpv1*/*Oprm1* only) were also prevalent, reinforcing the overlap between this thermal nociceptive ion channel and the main opioid analgesia-producing receptor. A representative panel of neurons is shown in **Figure 4B**, with neurons positive for all 4 labels indicated with arrows, and *Trpv1*+/*Oprm1*+ neurons indicated with arrowheads. These arrows/arrowheads are maintained in all four channels to show individual signal. The overlap between the two nociceptive ion channel genes (*Trpv1* and *Trpa1*) is visualized in **Figure 4C**. Within these populations, a wide range of signal intensity was detected for *Oprm1*

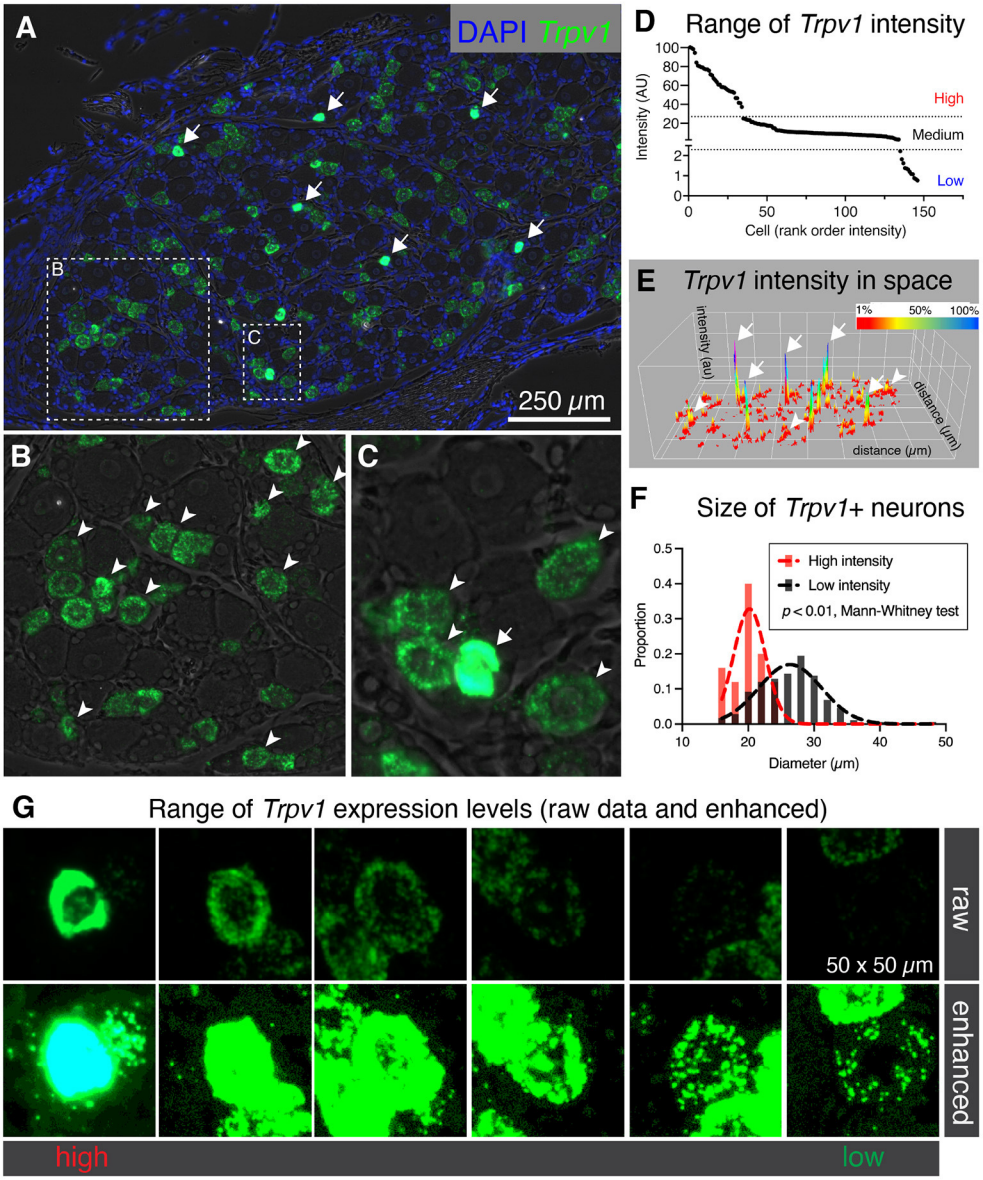

FIGURE 2 | Heterogeneous labeling of *Trpv1* mRNA in rat dorsal root ganglion (DRG). **(A)** Fluorescent *in situ* hybridization was performed and imaged for whole rat DRG sections ($N = 3$). Very high levels of expression were observed in a small number of small diameter neurons (white arrows). **(B)** An enlargement of a neuron-rich region is shown with *Trpv1*+ neurons (arrowheads). **(C)** A second enlargement includes one high-expressing *Trpv1*+ neuron (arrow) and several other Trpv1+ neurons with moderate staining intensity (arrowheads). **(D)** Intensity values for *Trpv1* were plotted by rank order. Based on these values, *Trpv1* expression was divided into high, medium and low expression. **(E)** A surface plot was generated for *Trpv1* intensity (arbitrary units, Z-axis) across the entire DRG section shown in **(A)**. This plot shows the relationship between the high-expressing *Trpv1* DRG neurons and other cells in the ganglion. Note the high peaks indicating a quantitatively separate population (white arrows). **(F)** Diameter of the high intensity *Trpv1*+ neurons was examined by measuring the area in Fiji. High intensity *Trpv1*+ neurons had a stereotyped small diameter as represented by the narrow Gaussian (red) relative to the broader distribution of medium/low *Trpv1*+ neurons (black Gaussian). This difference was significant based on a Mann-Whitney test ($p < 0.01$). **(G)** Representative fields of 6 *Trpv1*+ DRG neurons are shown, spanning a range of expression levels. Scanning parameters are tuned so as not to saturate the brightest cells. Note that the range of expression values is such that when the lower expressing *Trpv1*+ neurons are visible, the highest cells are saturated.

indicating variable expression of the μ-opioid receptor gene in the populations described with this 4-plex labeling scheme. In the visualization of *Oprl1* alone, note the broad labeling of many primary afferent neurons (**Figure 4E**). Analogous to the visualization in **Figure 4C**, the two opioid receptors (*Oprm1* and *Oprl1*) detected in this staining panel were visualized together in **Figure 4F**. Note the incomplete overlap between these two labels.

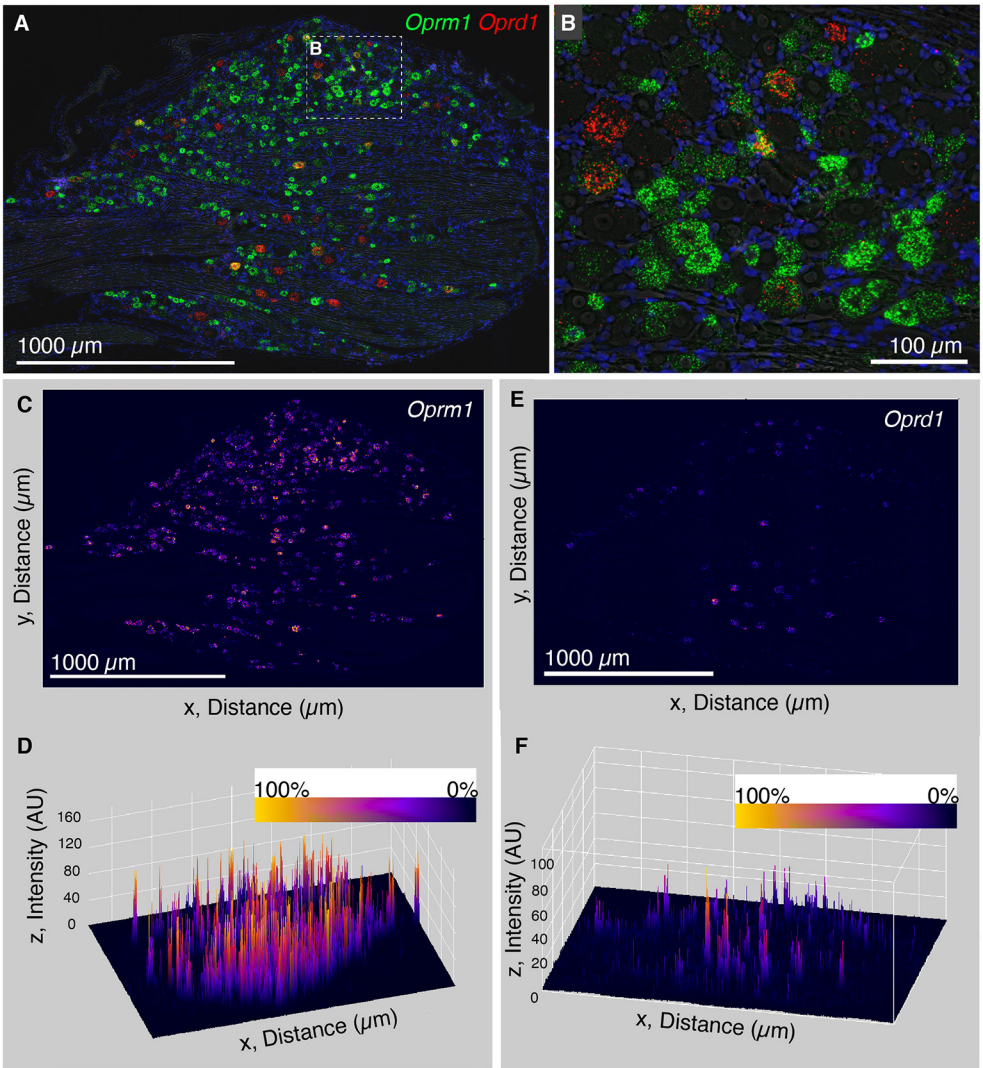

FIGURE 3 | Analysis of intensity distribution for the opioid receptor genes *Oprm1* and *Oprd1*. The finding that *Trpv1* was unevenly distributed in rat DRG prompted an investigation of *Oprm1* and *Oprd1* to answer whether these analgesic opioid receptors were also distributed unevenly across cell populations. **(A)** In a wide field view of a DRG stained for *Oprm1* and *Oprd1*, we did not observe marked differences in expression across the field. The gene encoding the mu-opioid receptor (*Oprm1*) is much more widely expressed than the delta receptor gene (*Opd1*), and both show a range of expression values. **(B)** However, this range appeared qualitative smaller than that observed for *Trpv1*. **(C)** In order to quantify this further, we used a surface plot to represent intensity over area for *Oprm1*. **(D)** When viewed from an angle, this analysis shows many peaks of similar height across the DRG, consistent with the wide expression pattern of *Oprm1*. This is in contrast to *Trpv1*, which showed several very high peaks (**Figure 2E**). **(E)** The same analysis was also performed for *Oprd1*, which is expressed in many fewer cells than either *Trpv1* or *Oprm1*. **(F)** Viewed at an angle, most of these *Oprd1* peaks are evident in the same linear axis. In **Supplementary Figure 2**, we quantified differences in distribution and coefficient of variation in these measurements, showing that *Trpv1* had significantly higher coefficient of variation than either *Oprm1* or *Oprd1*.

Quantitative Co-expression Analysis for the Nociceptive Ion Channel *Trpv1* and *Trpa1* and Opioid Receptor *Oprm1* and *Oprl1* Genes

Individual neuronal perikarya of three distinct populations were examined by multiplex fluorescent *in situ* hybridization (**Figure 5A**). The high *Trpv1* expressing neurons were selected out for separate analysis based on their unique signature of *Trpv1* expression (see **Figure 2**). The major populations colocalizing *Trpv1*+/*Oprm1*+ were low and medium expressing *Trpv1* neurons (middle row, **Figure 5A** *Trpv1* medium). Similarly, while not all low *Trpv1* expressors are positive for all four labels, we focused on such quad+ neurons for visualization (bottom row, **Figure 5A** *Trpv1 low*). This is the population that coexpressed mRNA encoding the chemo-nociceptive ion channel *Trpa1*. As we observed that the cells labeled with all four markers were generally low for *Trpv1*, we examined the relationship between *Trpv1* and *Trpa1* in greater detail. In the representative field (**Figure 5B**), we observed that *Trpv1* and *Trpa1* were

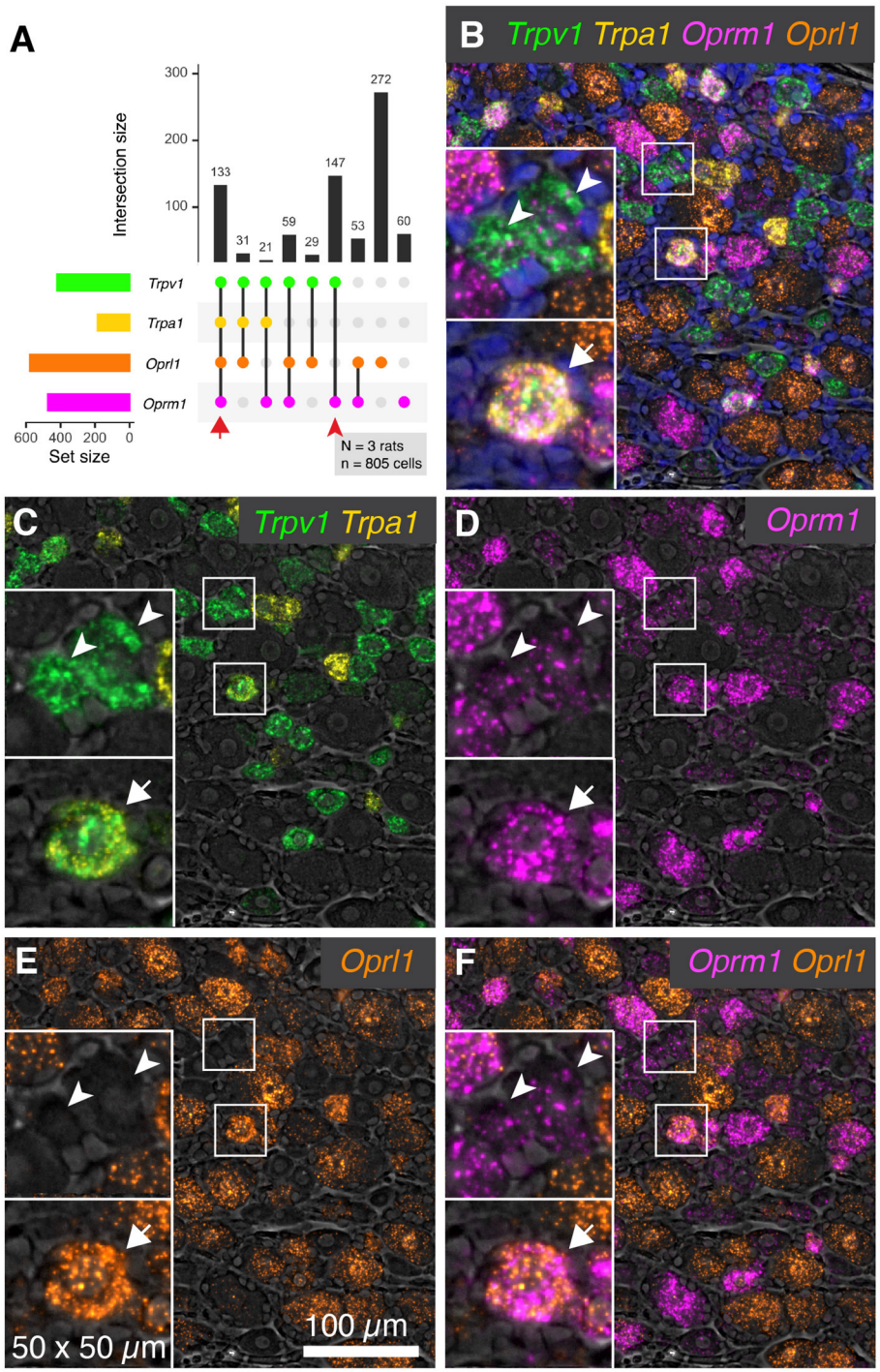

FIGURE 4 | Co-expression patterns of nociceptive ion channels and opioid receptors. To assess the overlap between nociceptive transducing ion channels and opioid receptors, multiplex fluorescent hybridization was performed for *Trpv1*, *Trpa1*, *Oprm1* and *Oprl1*. This analysis was performed in $N = 3$ rats total, and 805 cells. **(A)** Counts were tabulated for co-expression of these four markers in each cell, and the intersections of these are plotted. The most prevalent count group was *Oprl1* alone, due to the near-ubiquitous nature of this marker (272 cells). Cells positive for all four labels (133 cells) were also prevalent, indicating overlap between nociceptive ion channels (*Trpv1* and *Trpa1*) and the mu-opioid receptor *Oprm1* as well as *Oprl1*. Populations containing *Trpv1* and *Oprm1* with or without *Oprl1* (59 cells with all three and 147 cells with *Trpv1*/*Oprm1* only) were also prevalent, reinforcing the overlap between these two markers. **(B)** A representative panel showing a diverse field of cells is shown, with quad-positive neurons highlighted (arrows). Additionally, *Trpv1*+/*Oprm1*+ cells are indicated (arrowheads). **(C–F)** To increase the visibility of the highly multiplexed image, individual channels and channel pairs are shown for the image in **(B)**, with the channel identity found in the bottom right of each panel. **(C)** A panel showing only *Trpv1* and *Trpa1* was selected to show the relationship between these two nociceptive ion channels. **(D)** A range of intensities was observed for *Oprm1*. Note the presence of less prominent puncta in *Trpv1*+/*Oprm1*+ cells (arrowheads). **(E)** *Oprl1* alone. **(F)** *Oprm1* and *Oprl1*. Scale bar applies to all images.

generally not strongly expressed in the same cells, although some co-positive cells were observed with low levels of both markers. Note the cells strongly expressing *Trpv1* (arrowheads) or *Trpa1* (arrows), as well as cells co-expressing both markers (asterisks). Cell counts by marker positivity were performed to evaluate the findings of our peripheral ganglionic comparison study between the nodose, DRG and superior cervical ganglia (Sapio et al., 2020b) (**Figure 5C**). We found that the most prominent populations of cells were *Trpv1*+/*Trpa1*- (*Trpa1*-; 233 cells, 53.8%) followed closely by the faintly labeled *Trpv1*+/*Trpa1*+ (190 cells, 43.9%) population. The *Trpv1*-/*Trpa1*+ cells (10 cells, 2.3%) comprised the rarest subgroup. In a quantitative analysis of expression levels, *Trpv1* and *Trpa1* intensity measurements tended toward the axes (**Figure 5D**, shaded areas), indicating an inverse correlation with expression levels. Note that no cells are identified in the center of the graph, which would indicate bright co-expression of these two markers. Pairwise coincidence is shown for each of the four labels in this experiment (**Figure 5E**). All of these combinations are common (with the rarest being approximately 19.1% of all cells) for *Trpa1* and *Oprm1*. In these analyses, we tried to identify differences among the high *Trpv1*+ population, and noticed that they seemed less likely to express high levels of *Oprm1*. This was formally quantified, and is displayed in pie charts (**Figure 5F**) showing that the subgroup of *Trpv1*+ high-expressing neurons (N = 33) expressed *Oprm1* only 18.1% of the time, whereas *Trpv1*+ neurons overall expressed *Oprm1* 85.7% of the time. We also noted that these cells expressed a low level of *Oprm1* on average (**Supplementary Figure 3**).

Heterogeneous Levels of *Trpm8* mRNA in Rat DRG and Co-expression Analysis With *Trpv1*

In addition to *Trpv1*, several other temperature sensitive ion channels are implicated in noxious stimuli transduction and nociceptive signaling in baseline and disease states (reviewed in Koivisto et al., 2022). These ion channel genes are useful markers of nociceptive cell populations and have been targeted for therapeutic interventions. While Trpv1 responds to temperatures in the warm to hot temperature range, another ion channel, Trpm8 is activated by cold temperatures and participates in cold allodynia (Bautista et al., 2007; Knowlton et al., 2010). Multiplex fluorescent *in situ* hybridization revealed heterogeneous expression of the *Trpm8* mRNA, with most of the signal concentrated within sparsely distributed, small diameter neurons (**Figure 6A**, arrows). The results for *Trpm8* expression were similar to what was observed for *Trpv1* in **Figure 2**, showing a range of expression consisting of a small subpopulation of brightly labeled neurons and a second set of neurons with weaker signal. An enlarged visualization of *Trpm8* alone (**Figures 6B,C**) showed the densely labeled small to medium sized neurons (arrows), as well as additional neurons showing less intense labeling (arrowheads). The convergence of transcripts was examined using multiplex fluorescent *in situ* hybridization with four labels (*Trpv1*, *Trpm8*, and *Oprm1*). This staining combination revealed that virtually all *Trpm8*+ neurons co-expressed *Oprm1*, albeit at a range of expression values as seen in the representative field (**Figure 6D**). A surface plot was generated to visualize the range of expression profiles in the DRG neurons. Note that the high expressors appear as isolated peaks in this view, indicating that they are quantitatively separable from other *Trpm8*+ neurons (**Figure 6E**). Also note that the lower expressing *Trpm8*+ neurons required enhancement for visualization, indicating they express *Trpm8* at a much lower level than the high-expressing neurons. This lower expression was validated by using a second *Trpm8* probe to rule out origination from nonspecific signal (**Supplementary Figure 3**).

We further examined the co-expression pattern of the hot and cold thermosensory ion channel transcripts *Trpv1* and *Trpm8*, respectively. In the representative image (**Figure 6F**), densely labeled *Trpm8*+ (arrows) and *Trpv1*+ neurons (asterisks) are indicated. Co-expression analysis showed that the most prominent population was the *Trpv1*+/*Trpm8*- population (295 cells, 76.0%), as *Trpv1* is more broadly expressed than *Trpm8* (**Figure 5G**). The *Trpv1*+/*Trpm8*+ co-positive cells (42 cells, 10.8%) and *Trpm8*+ populations (37 cells, 9.5%) were less abundant, with approximately half of *Trpm8*+ cells coexpressing *Trpv1*. Similar to what was shown for *Trpv1* and *Trpa1*, fluorescence intensities of *Trpm8* vs. *Trpv1* signals tended to plot along the axes (shaded areas, **Figure 6H**) indicating that strong expression of either marker gene was observed mainly in separate sensory neurons (cell quantification from N=3 rats). This indicates that strongly *Trpv1*+ neurons never strongly expressed *Trpm8*, and strongly *Trpm8*+ neurons never strongly express *Trpv1*.

Co-expression Analysis of the Thermal Nociceptive Ion Channels *Trpv1* and *Trpm8* With the μ-Opioid Receptor (*Oprm1*) and the Voltage-Gated Ion Channel Subunit *Scn11a*

To further assess the overlap between nociceptive transducing ion channels and opioid receptors, multiplex fluorescent *in situ* hybridization was performed for the thermally responsive ion channels *Trpv1* and *Trpm8*, in conjunction with the μ-opioid receptor gene *Oprm1*. An additional marker of nociceptive neurons, the voltage-gated sodium channel subunit ($Na_V1.9$) gene, *Scn11a*, was also included. Human mutations in *SCN11A* cause pain insensitivity or episodic pain syndromes depending on the nature of the mutation (Leipold et al., 2013; Zhang et al., 2013). The total number of cells counted was 570 from N = 3 rats. Upon quantification of co-expression of these four markers, the most prevalent subgroup was composed of neurons co-positive for *Trpv1*, *Oprm1* and *Scn11a* (197 cells 34.6%, **Figure 7A**). Notably, many neurons were also unlabeled (167 cells 29.2%). In a panoramic visualization (**Figure 7B**) of these cell populations, a representative field was chosen to highlight the staining patterns. Examples of the most prevalent cell type (*Trpv1*+/*Oprm1*+/*Scn11a*+) are indicated with arrowheads (**Figures 7C–G**). Large diameter cells with no reactivity for these markers are also indicated (asterisks). A putative thermosensory C-fiber with very high levels of *Trpv1* is indicated (arrow). This

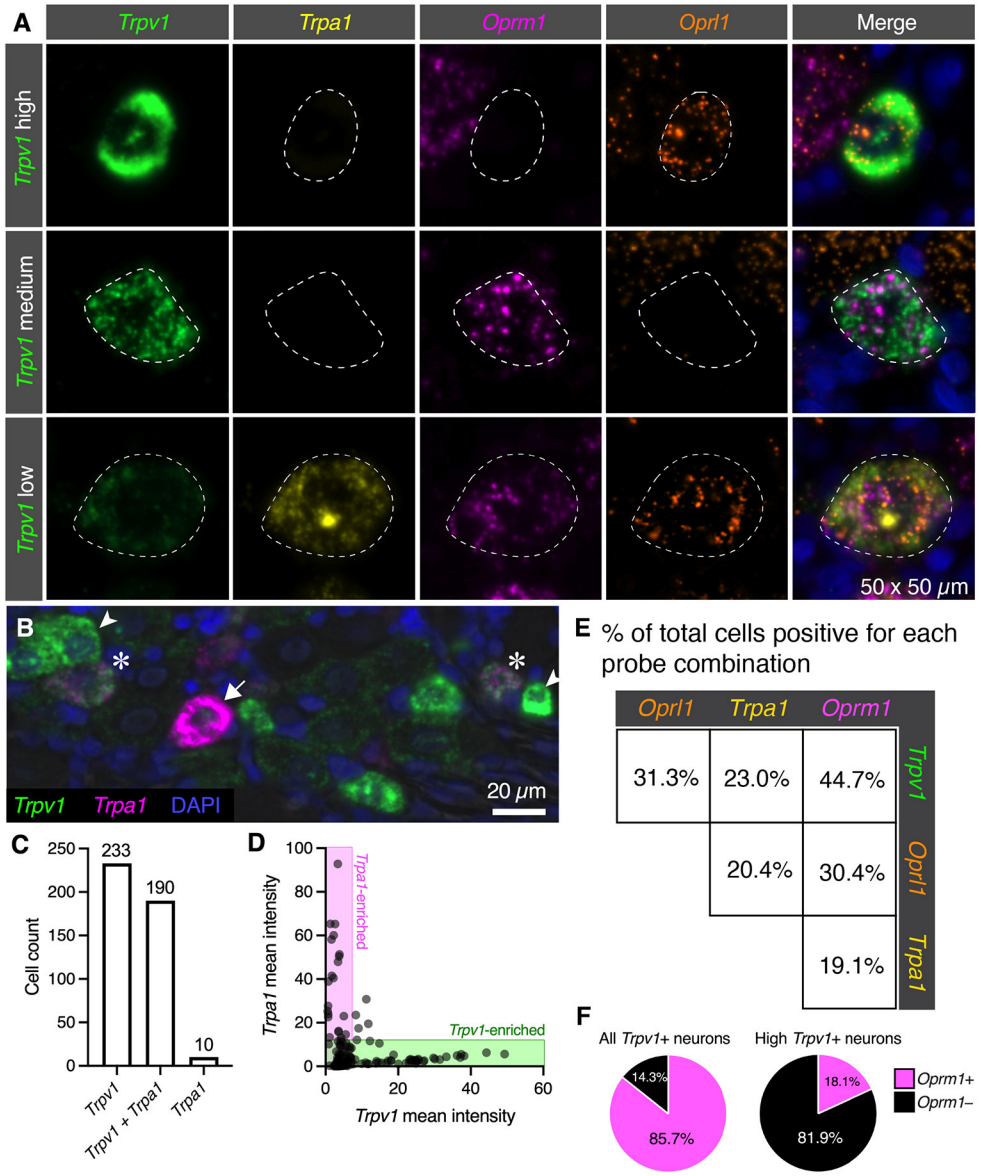

FIGURE 5 | Quantification of nociceptive ion channel and opioid receptors. We further examined the subpopulations of DRG neurons shown in **Figure 3**. **(A)** Enlarged and enhanced fields were shown for each of three representative cell populations corresponding to high, medium and low *Trpv1* expression. Note that several populations of cells have medium *Trpv1* expression, but that one of the most common subtypes (*Trpv1* and *Oprm1* alone), was selected. Similarly, a quad-positive neuron was selected as representative of low *Trpv1* expression. **(B)** To examine the relationship between *Trpv1* and *Trpa1* in particular, expression levels in perikarya of cells expressing either marker were examined in further detail. In this representative field, neurons strongly enriched for *Trpv1* (arrowheads) or *Trpa1* (arrow) are indicated, as well as two neurons (asterisks) that co-express these two ion channel genes. **(C)** Using cell counting, we identified the coincidence of these two markers. More cells express *Trpv1* than *Trpa1* with the majority of *Trpa1*+ cells co-expressing *Trpv1*, and only 10 *Trpa1*+ cells expressing no detectable *Trpv1*. **(D)** However, cells expressing high levels of either *Trpv1* or *Trpa1* express very low levels of the other transcript. Therefore, the expression of these two markers while coincident, appears to be anticorrelated (note that points fall on the axes rather than in the middle of the plot. **(E)** Pairwise coincidence is shown for each of the four labels in this experiment. All of these combinations are common (with the rarest being approximately 19.1% of all cells). High *Trpv1* neurons, in particular, seemed to differ from other *Trpv1* neurons in terms of *Oprm1* expression. **(F)** We addressed this by counting high *Trpv1* neurons separately from other *Trpv1* neurons (shown in pie charts). Whereas average *Trpv1* neurons expressed *Oprm1* the majority of the time (85.7%), the high Trpv1 neurons expressed *Oprm1* only 18.1% of the time. On average, the expression in these cells was also lower (**Supplementary Figure 3**). Outlines (dotted lines) of neuronal perikarya are shown to enhance visbility.

type of cell does not show reactivity for the other three markers, indicating minimum co-localization of either nociceptive or analgesic markers in the highest expressing *Trpv1*+ neurons. Note the varying levels of *Oprm1* in *Trpv1*+/*Oprm1*+/*Scn11a*+ neurons (arrowheads), which could indicate heterogeneity in this labeled class. In an overlay of *Trpv1* and *Trpm8* (**Figure 7E**),

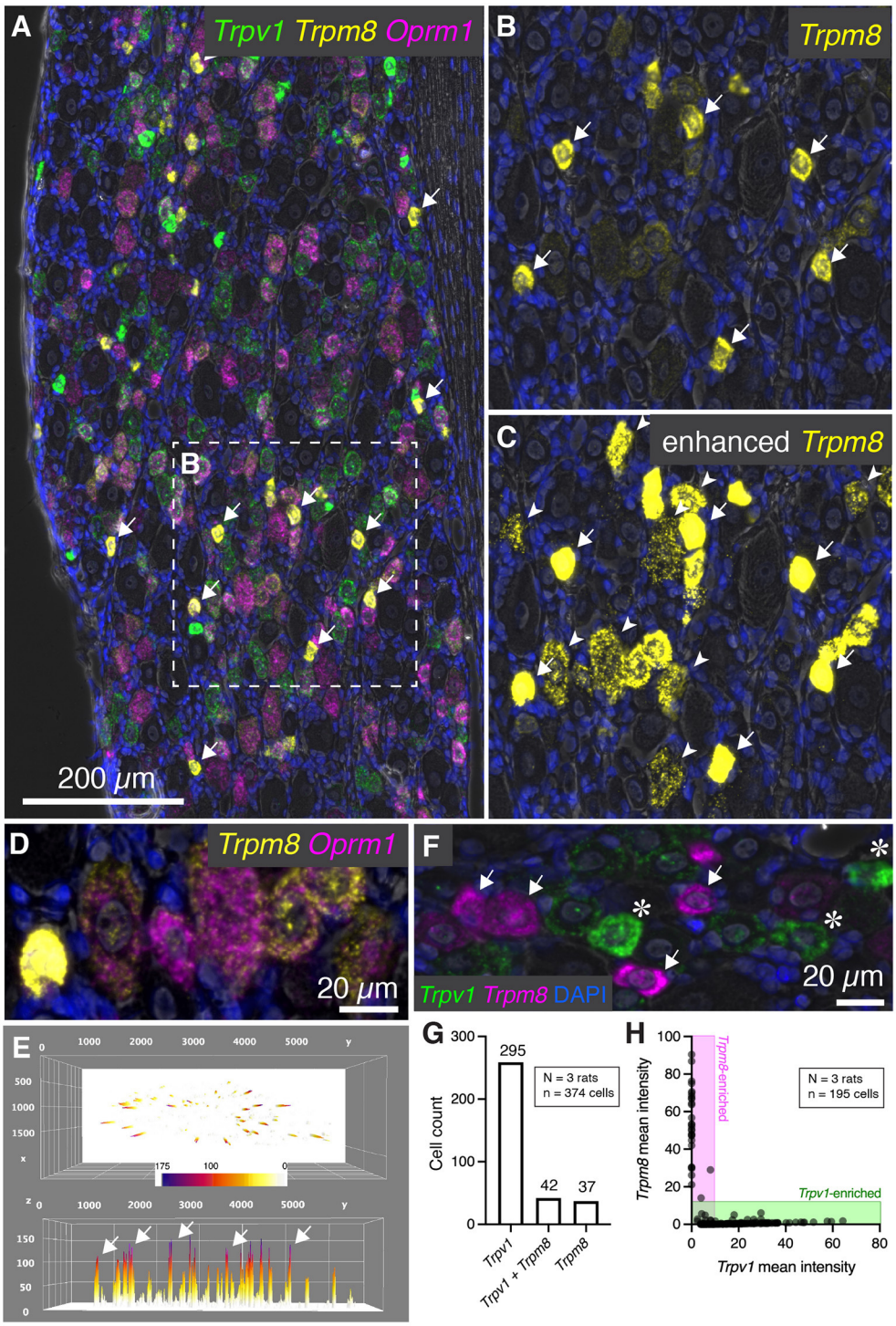

FIGURE 6 | Characterization of *Trpm8* expression levels in rat DRG. To assess the overlap between hot and cold thermal nociceptive transducing ion channels, multiplex fluorescent hybridization was performed for *Trpv1*, and *Trpm8* alongside *Oprm1*. **(A)** Panoramic view of triple-labeled rat DRG. **(B)** Cells positive for *Trpm8* were brightly labeled small diameter neurons (white arrows). However, a number of other neurons were also visible with lower levels of *Trpm8*. **(C)** Similar to what was performed for *Trpv1*, enhancement of the image saturates the high-expressing *Trpm8* neurons, but allows for visualization of the much lower intensity staining observed in other neurons. Note that these neurons still have clear punctate staining pattern and that this staining pattern was reproduced with a different probe for confirmation (**Supplementary Figure 4**). **(D)** Another characteristic of *Trpm8* neurons is that 100% of them co-express *Oprm1* to some extent. This relationship is visualized in the representative field. **(E)** A surface plot of *Trpm8* expression levels is shown with arrows pointing to the highest expressing *Trpm8*+ neurons. Note the lower peaks span a range of expression levels. **(F)** The relationship between *Trpv1* and *Trpm8* was further explored by quantifying levels of expression of these two

(Continued)

FIGURE 6 | thermal transducing ion channels shown in the representative field. **(G)** The *Trpv1*+ population was much larger than the *Trpm8*+ population, and approximately half of *Trpm8*+ neurons co-expressed *Trpv1*. **(H)** However, with quantification we saw that no cell co-expressed these markers strongly, and that their expression was anticorrelated (note that the points fall on the axes rather than in the center of the plot).

note that cells were generally high in one *or* the other but not both markers indicating the specialized role of *Trpm8* in cold thermonociception and cold pain, and its localization within a small, discrete subclass of sensory afferents in the rat. Consistent with its role in nociception, the sodium channel subunit *Scn11a* was prevalent in *Trpv1*+/*Oprm1*+/*Scn11a*+ neurons (arrowheads), as well as strongly expressed in many cells throughout the ganglion. We also considered the *Trpm8*+ cell populations quantitatively (**Supplementary Figure 4**), showing that high/medium *Trm8*+ cells were negative for *Trpv1* and *Scn11a*, whereas low expressing *Trpm8*+ cells have low levels of these markers.

Evaluation of *Trpv1, Oprm1, Oprl1* and the Proprioceptive Neuron Marker Secreted Phosphoprotein 1, Osteopontin (Spp1)

To extend the multiplex fluorescent *in situ* hybridization staining experiments to include a non-nociceptive marker, we examined co-expression of algesic and analgesic markers with osteopontin (*Spp1*), which labels large diameter neurons (with an average diameter of approximately 38 μm). These neurons are thought to be chiefly implicated in proprioception (Ichikawa et al., 2000; Usoskin et al., 2015; Saito-Diaz et al., 2021). In the co-expression plot in **Figure 8A**, all of the *Spp1*+ neurons co-expressed the nociceptin receptor *Oprl1*, while none showed expression of *Trpv1* or *Oprm1* (160 *Spp1*+/*Oprl1*+ neurons, red arrow). In a panoramic view of whole rat DRG, *Spp1*+ neurons constitute a distinct population (**Figure 8B**). Note also that these neurons tended to be spatially arranged in a particular area of the DRG section (**Figures 8C,D**).

Summary Figure of Identified Neurons and Their Properties

While numerous categories of co-expression are documented, five readily distinguishable neuronal groups are shown in **Figure 9** with frequency distributions of their cell diameters. The high *Trpv1*-expressing neurons were the smallest in size with a 20 μm mean diameter ($n = 25$ cells). The *Trpv1*/*Trpa1* cell population ($n = 120$ cells; often "quad positive," as in **Figure 4**; ∼26.8 μm average diameter) contains two algesic-sensing ion channels and the μ-opioid receptor that can confer analgesia. This analysis was performed using the double label as a selection criteria, but note that a subpopulation of these cells (such as that in the representative image) has additional labels. The diameter of the high expressing *Trpm8* cells was on average 33.0 μm ($n = 68$ cells), indicating a larger diameter than high *Trpv1* neurons (21 μm) or *Trpv1*/*Trpa1* cells (26 μm). The largest neuron identified was the co-positive for the μ-δ opioid receptor (*Oprm1*+/*Ord1*+) neurons (44 μm average diameter). These were even larger than the osteopontin (*Spp1*) expressing proprioceptive neurons (38 μm average diameter; $n = 102$ cells). In mouse, the osteopontin immunoreactive neurons give rise to the spiral endings innervating muscle spindles (Ichikawa et al., 2000; Chiu et al., 2014).

We identified a significant difference in diameter between each of the groups ($p < 0.05$). Significance testing was performed between the five groups (all comparisons) using a Kruskal-Wallis test with Dunn's correction for multiple comparisons (Prism 9, GraphPad). These findings were calculated from the same sections as other $N = 3$ analyses in other figures, although sampling was expanded ($n = 117$ cells in **Figure 9**) for this analysis due to the rarity of the *Oprm1*+/*Oprd1*+ population.

DISCUSSION

This study examined rat primary afferent neurons using multiplex fluorescent mRNA *in situ* hybridization to understand nociceptive and analgesia mechanisms in the peripheral nervous system. We consider identifying critical neuronal populations essential knowledge for developing potential peripherally acting non-opioid analgesics that do not exhibit central nervous system side effects. The investigation focused on determining co-expression patterns of nociceptive-, and analgesia-transducing molecular markers in DRG neurons. We hypothesized the conjuncture of these two types of molecules in one or more neuronal subpopulations would provide a colocalization matrix that could be used to generate a molecularly informed approach to peripheral analgesia and analgesic drug development.

The populations of nociceptive *Trpv1*+ neurons were heterogeneous, expressing varying levels of *Trpv1* and the μ-opioid receptor *Oprm1*. Co-expression analysis indicated differing degrees of μ-opioid expression among the two populations of *Trpv1*+ neurons that we hypothesize subserve thermosensory and tissue-injury nociception. We identified a population of very high expressors of *Trpv1* that are absent of *Oprm1*. In contrast, most low and medium expressors of *Trpv1* do express *Oprm1*, and are the evident candidates for the neuronal population inhibited by μ-opioid agonist analgesics, especially when given intrathecally or epidurally, administration paradigms where the injectate bathes the central projection of dorsal root ganglion axons entering the spinal cord. The co-expression of *Trpv1* and *Oprm1* receptors within the same cell types provides both cellular and molecular level explanations for the efficacy of opioid agonists. That is, opioid drugs act by inhibiting the very cells responsible for transmitting certain types of nociceptive stimuli from the periphery to the central nervous system. Available evidence suggests that opioid analgesia occurs, in part, through presynaptic inhibition of transmitter release from *Trpv1*+ DRG afferent terminals in spinal cord and potentially spinal cord μ-expressing neurons (Kondo et al., 2005; Chen and Pan, 2006; Xanthos and Sandkühler, 2014; Che et al., 2021). Co-expression of *Trpv1* was never observed with *Spp1*, a

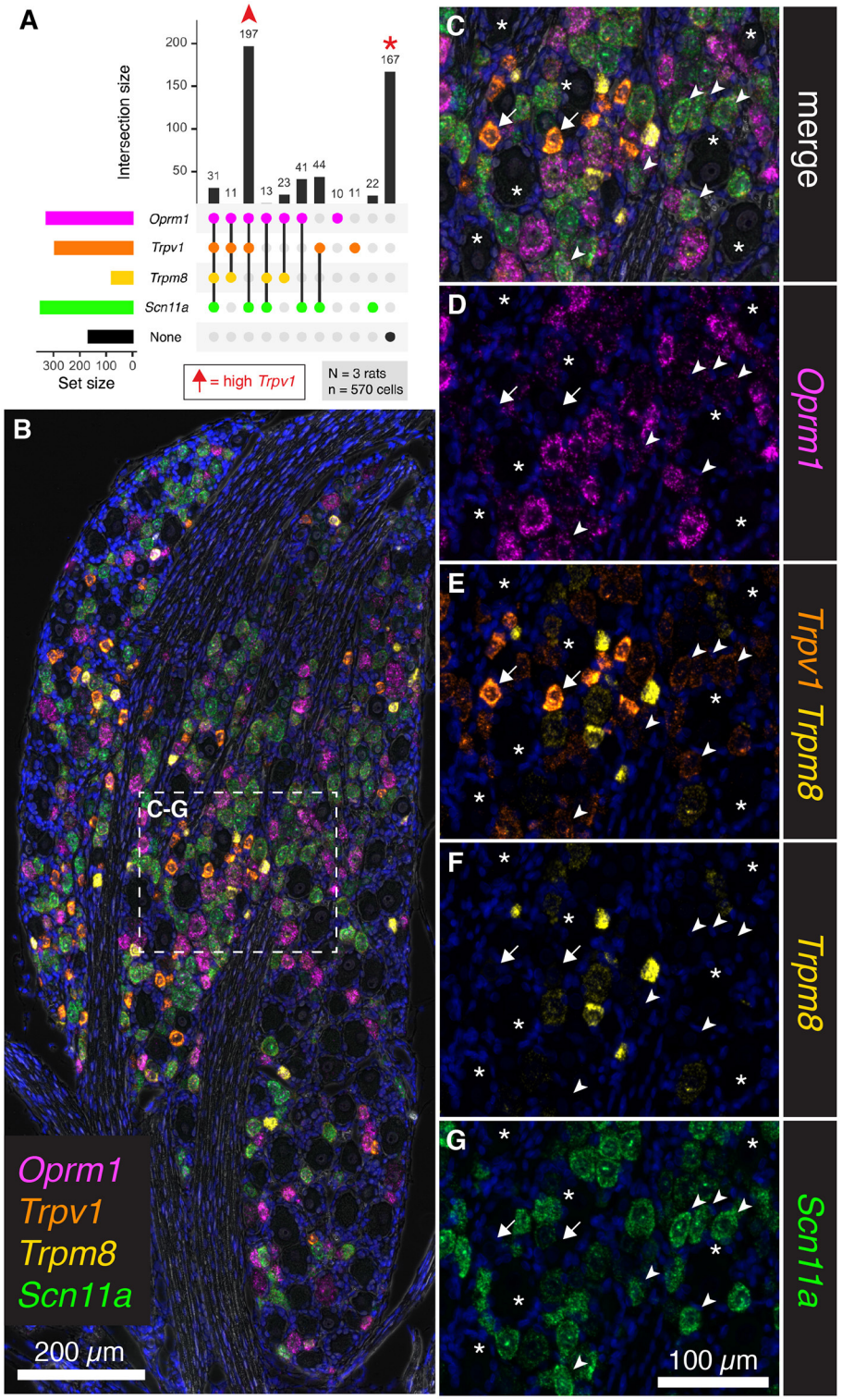

FIGURE 7 | Co-expression analysis for *Trpv1*, *Trpm8*, *Oprm1*, and *Scn11a*. To further assess the overlap between nociceptive transducing ion channels and opioid receptors, multiplex fluorescent hybridization was performed for *Trpv1*, *Trpm8*, *Oprm1* and *Scn11a* in $N = 3$ rats ($n = 570$ cells). In this experiment, we investigated the mRNA coding for the cold-pain transducing nociceptive ion channel Trpm8 as well as the mRNA encoding the voltage-gated ion channel subunit Scn11a. **(A)** Counts were tabulated for co-expression of these four markers as before. The most prevalent group were neurons co-positive for *Trpv1*, *Oprm1* and *Scn11a* (197 cells). Notably, a large number of neurons was also unlabeled (167 cells). Arrows in the plot in **(A)** are used to identify cells in the representative fields in subsequent panels. High *Trpv1* neurons (arrows) are not in the plot in **(A)**, but were highlighted in the representative fields. **(B)** A panoramic stitched image is shown to

(Continued)

FIGURE 7 | demonstrate the anatomical location of these markers within the greater structure. In the center of the field, a representative area was enlarged for subsequent panels. **(C)** Overlay of the 4-plex label with DAPI and brightfield is shown. Note that examples of the most prevalent cell type, *Trpv1+/Oprm1+/Scn11a+* neurons are indicated (arrowheads). Larger diameter cells with no reactivity for these markers are indicated (asterisks). A singular putative thermosensing c-fiber is indicated with very high levels of *Trpv1* (arrow). **(D).** Note the varying levels of *Oprm1* in *Trpv1+/Oprm1+/Scn11a+* neurons (arrowheads), and absence of Oprm1 in the high-expressing Trpv1+ neuron (arrow). **(E)** In an overlay of *Trpv1* and *Trpm8*, note that cells were generally high in one or the other but not both markers. **(F)** Also note the sparse labeling of *Trpm8*, indicative of its specialized function. **(G)** The sodium channel subunit Scn11a was prevalent in *Trpv1+/Oprm1+/Scn11a+* neurons (arrowheads), as well as strongly expressed in many cells throughout the ganglion. Scale bar applies to all images. Scale bar applies to **(C–G)**.

marker for large diameter proprioceptive neurons, a finding that validates that nociception and proprioception are mediated by distinct neuronal populations. Additionally, the lower expressors of *Trpv1* co-expressed other markers implicated in pathological pain states. For example, Trpm8, a nociceptive ion channel implicated in cold thermosensation (Bautista et al., 2007) and cold allodynia (Xing et al., 2007) was identified in some lower-expressing *Trpv1* sensory neurons. Additionally, the ion channel NaV 1.9 (encoded by *SCN11A*), whose gain-of-function mutation leads to familial episodic pain (Leipold et al., 2013), was also identified in the low to medium-expressing *Trpv1* population. In contrast, the small diameter high *Trpv1* expressing neurons were negative for all of these markers, most likely indicating an exclusive role as a dedicated labeled line for thermonociception and/or non-noxious thermosensation (Kobayashi et al., 2005; Craig, 2018). Coexpression analysis is also a critical step for gaining insight into the algesic and analgesic receptors on DRG neurons, and could be important for understanding indirect interactions between painful and analgesic target receptors. In particular, there are established interactions between pain transducing ion channels and opioid receptors (Chew et al., 2019).

The μ-opioid receptor is one of the most clinically important targets for analgesia, with the majority of highly impactful orally and intravenously available analgesic agents acting through this receptor. While there are three canonical opioid receptors (μ, δ, and κ), and a fourth opioid-like paralog (*Oprl1*), only μ-receptor agonists are used clinically at this time, although extensive medicinal chemical and preclinical development on the other receptors has occurred or is in progress (Calo et al., 2000; Floyd et al., 2009; Bardoni et al., 2014; Viscusi et al., 2021). Additionally, some controversy exists over detection of these receptors, as they are frequently expressed to a low degree and difficult to quantify accurately (Imlach and Christie, 2014; Iadarola et al., 2015; Sapio et al., 2016). In this regard, the present study fills a critical knowledge gap by delineating the co-expression matrix of these receptors in detail. We characterize the expression pattern of all four receptors, and, in particular, the canonical three together. One point of contention is the pharmacological relevance of opioid receptor heterodimers. In order for the heterodimer to form (Jordan and Devi, 1999; Erbs et al., 2015; Gaborit and Massotte, 2021), both receptors would, at a minimum, have to be expressed in the same cell. Our data confirm that co-expression of the μ-, δ- and κ-opioid receptors does indeed occur in some combinations, albeit in a very small population of neurons. This heterogeneity is confirmed by recording and staining from rat DRG neurons, although some differences in proportions of cells between the present study and the *in vitro* recording investigation are seen and are likely due to methodological differences (Rau et al., 2005). Interestingly, some large cells were observed with high concentrations of μ- and δ-opioid receptors (**Figure 1E**), consistent with putative mechanosensory nociceptors, based on genetic anatomical tracing studies done in the mouse (Bardoni et al., 2014). These anatomical findings showing colocalization of *Oprm1* and *Oprd1* may be related to the observed analgesic synergy between μ- and δ-opioid agonists in the periphery (Bruce et al., 2019). Another study using genetic labeling in mice showed that the κ-opioid receptor was frequently expressed in myelinated lanceolate or circumferential nerve endings around hair follicles, and demonstrated that κ-opioid receptor function at these afferents modulated pain and itch (Snyder et al., 2018). In our rat study the majority, although not all κ-opioid receptor expressing neurons, also expressed the μ-opioid receptor indicating that this pair of receptors likely functions in the same cell to modulate some modalities of nociception.

Another opioid-like receptor examined in this study is the nociceptin/orphanin FQ receptor (NOP receptor, encoded by *Oprl1*). This is the least studied of the four opioid-like receptors, and although it has been proposed to have multiple avenues toward clinical potential (Lambert, 2008), none have been realized to date. One finding that is particularly relevant to pain and analgesia, is the observation that intrathecal administration of nociceptin, the endogenous agonist at the NOP receptor was analgesic, and this analgesia was not naltrexone reversible, suggesting NOP-dependent analgesic actions are distinct from analgesia mediated at other opioid receptors (Ko et al., 2006). In our staining, we identified signal for *Oprl1* expression in almost all DRG neurons, which does not exclude its utility as an antinociceptive agent, but suggests very broad function(s), and may result in off target side effects on non-nociceptive fibers. Notably, broad action, or expression of an analgesic target outside of the nociceptive neurons is not necessarily indicative of reduced analgesic potential, but the ubiquity of *Oprl1* signal does contradict the supposition that this receptor is involved in endogenous analgesia in a specific fashion.

One of the key nociceptive markers examined in the present study is Trpv1. This receptor is the endogenous receptor for capsaicin, the pungent ingredient in hot peppers and resiniferatoxin, a new analgesic currently undergoing clinical trials (NCT03542838, NCT02522611, NCT00804154, NCT04885972, and others) (Caterina et al., 1997). It has long been appreciated that *Trpv1* is expressed in several subclasses of neurons, and more recently these populations have been described to a greater extent in several species (Goswami et al., 2014; Isensee et al., 2014; Usoskin et al., 2015; Sapio et al., 2018; Tavares-Ferreira et al., 2022). The overall pattern of expression

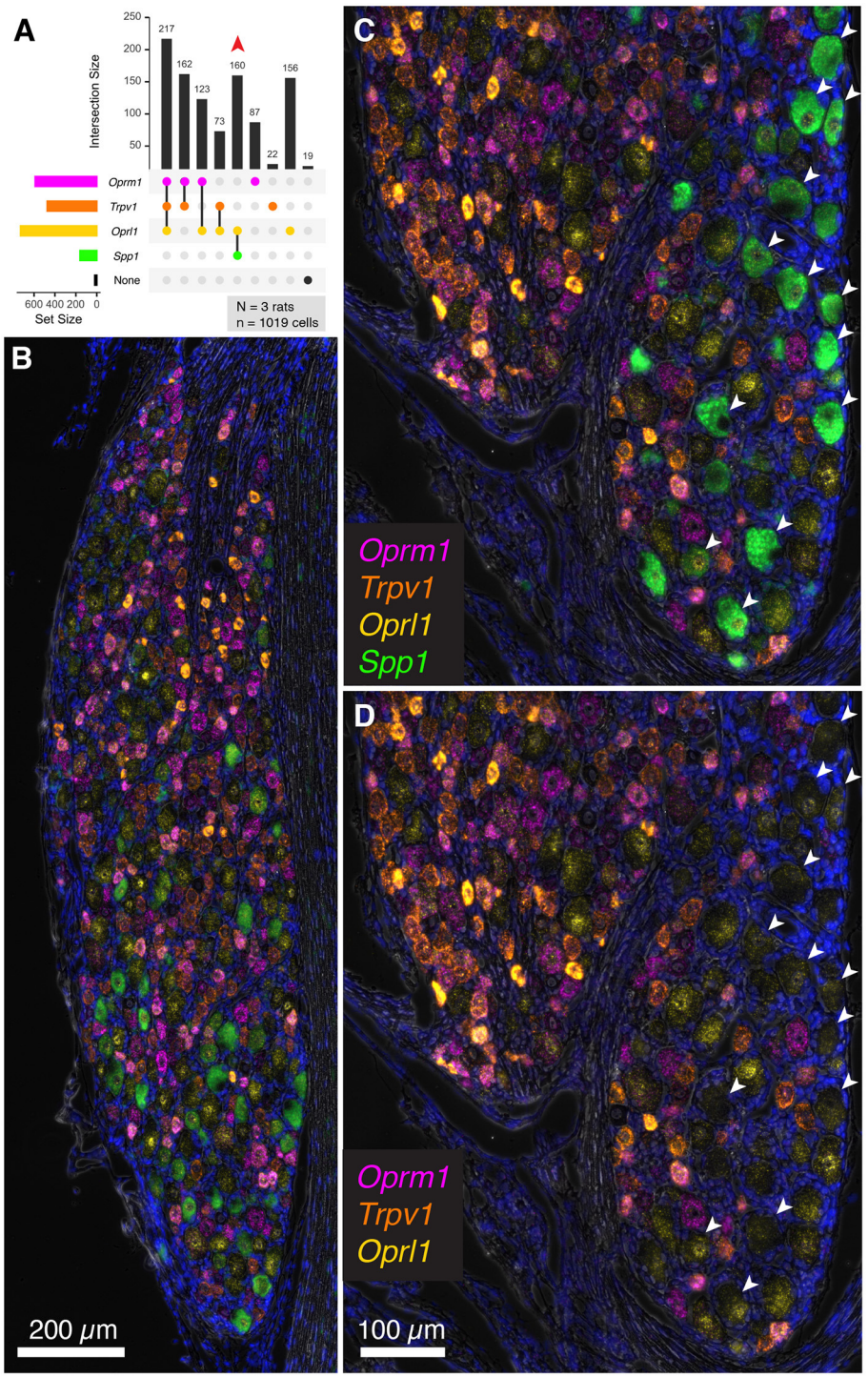

FIGURE 8 | Co-expression of the nociceptive and analgesic markers *Trpv1*, *Oprm1*, and *Oprl1* with Secreted Phosphoprotein 1/Osteopontin (*Spp1*) transcript. Co-expression of *Trpv1*, *Oprm1*, and *Oprl1* with *Spp1*, a marker of DRG neurons thought to be chiefly implicated in proprioception. **(A)** In a co-expression plot, all of the *Spp1*+ neurons co-expressed *Oprl1*, while none showed expression of *Trpv1* or *Oprm1* (83 *Spp1*+/*Oprl1*+ neurons, red arrow). **(B)** A panoramic view of a whole rat DRG stained for this combination of markers. Note the distinct signal for *Spp1*. **(C)** An enlargement of a different DRG neuron shows spatially distinct areas with and without *Spp1* neurons. **(D)** Note that *Spp1*+ neurons (arrows) do not contain any *Trpv1* or *Oprm1* signal.

of *Trpv1* is similar to previous studies, although it appears that the RNAScope procedure, in particular, labels more neurons than most antibody-based approaches (Mitchell et al., 2010, 2014; Goswami et al., 2014; Poulson et al., 2020; Sapio et al., 2020b; Shiers et al., 2020; Hall et al., 2022; Tavares-Ferreira et al., 2022). It is also notable that the percentage of Trpv1+ neurons as assessed

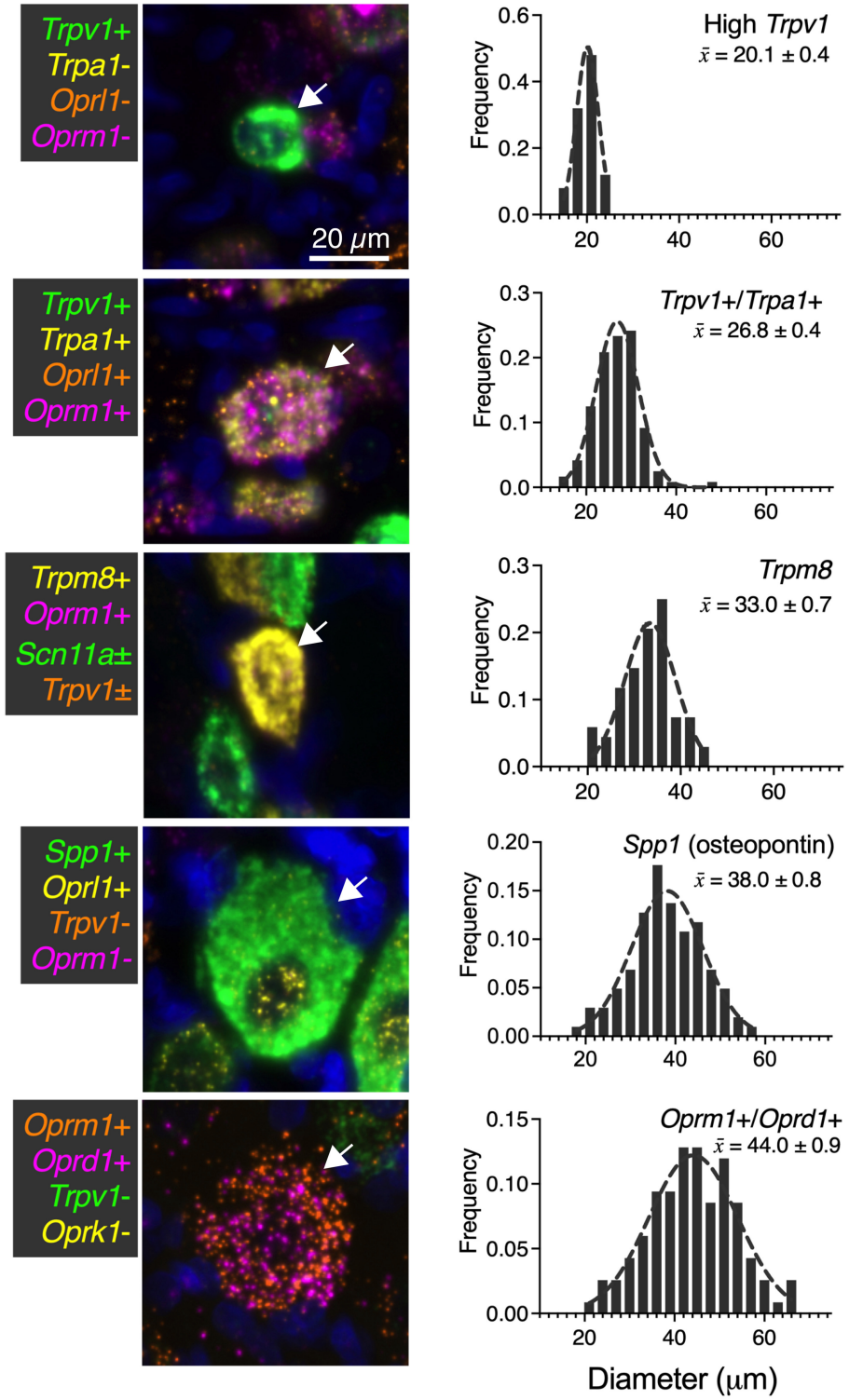

FIGURE 9 | Summary of identified cell types with size analysis. For each of the major identified cell types in the present study, a representative image (66 μm square) is shown. Additionally, histogram information of the cell size for each population is identified in ascending order of mean size ± SEM. High *Trpv1* neurons were the smallest cells (20.1 μm ± 0.4). *Oprm1*+/*Oprd1*+ neurons were the largest cells identified, with an average size of 44.0 μm ± 0.9. Scale bar applies to all images. These analyses were performed with at least $N = 3$ rats.

by a technique as sensitive as RNAScope is not necessarily identical to the number of capsaicin-responsive neurons. For example, the percentage of neurons killed by capsaicin incubation in culture is estimated to be approximately 37% in one study (Wood et al., 1988), which is also similar to the number of cultured mouse lumbar DRG neurons responding to 300 nM capsaicin (39%) (Teichert Russell et al., 2012). Therefore, it appears that at a certain level of expression is required to produce robust enough calcium influx to compromise cellular integrity (Karai et al., 2004b). That is, approximately half of the neurons detected as *Trpv1*+ in our study (presumably the most strongly labeled neurons) are likely to be capsaicin responsive.

Generally, it has been observed that there is a small number of densely immunoreactive small diameter Trpv1+ neurons, as well as a larger number of larger diameter and less densely stained neurons (Tominaga et al., 1998; Cavanaugh et al., 2011b; Goswami et al., 2014). Presumably, this encompasses at least two functionally defined TRPV1+ subclasses: the Trpv1+ C-fibers and A-δ fibers (Mitchell et al., 2010, 2014). The molecular identity of the TRPV1+ A-δ fibers is still being determined (Raithel et al., 2018), in part due to the small percentage of A-δ neurons in DRG (Lawson et al., 2019). Our study suggests that the small diameter high expressing *Trpv1*+ fibers in the rat contain a narrower repertoire of noci-responsive TRP channels, potentially implicating a more exclusive thermal nociceptive role which, at least in the rat, does not appear to be sensitive to opioid-induced analgesia. Differential thermal activation of A-δ and C-fibers suggest that, based on behavioral withdrawal, the C-fiber population is the one that is less sensitive to μ-opioid receptor agonists (Mitchell et al., 2014) and the A-δ neurons are a subpopulation of the medium to low TRPV1 expressing neurons. To some extent, a similar phenomenon has been examined in humans in a study using high dose transdermal capsaicin patch. In this study, sensitivity to noxious (55°C) thermal stimulation was confined to the capsaicin-treated region, while intensity ratings for less noxious (44°C) or non-noxious (38°C) thermal stimuli were *reduced* distal to the patch-treated skin (Van Neerven and Mouraux, 2020). This is potentially consistent with the idea that higher expressing *Trpv1*+ fibers are more capsaicin sensitive and primarily involved in thermonociceptive sensation, while the more broadly, polymodal nociceptive fibers may have less *Trpv1* but co-express multiple noci-responsive channels. However, notably, this type of experiment may also be influenced by other variables such as receptive field size and central modulatory effects. Further studies will be needed in humans to tease out the function of these Trpv1+ populations.

Another TRP channel *Trpa1* was examined in regard to both *Trpv1* and analgesic-related opioid receptors. Trpa1 is the receptor for chemical nociception and is responsible for transducing stimuli such as allyl isothiocyanate, the active pungent ingredient in foods such as wasabi (Jordt et al., 2004; Mcnamara et al., 2007). In our previous study using transcriptomics and multiplex fluorescent *in situ* hybridization, we examined the expression pattern of *Trpv1* and *Trpa1* in DRG and nodose ganglion sensory afferents (Sapio et al., 2020b). In that study, we found that *Trpv1* and *Trpa1* were more highly co-expressed in nodose, whereas in the DRG, neurons that were high in either *Trpv1* or *Trpa1* tended to be low for the other, suggesting a separate, although not exclusive set of sensory pathways for thermal and chemical nociception in the peripheral nervous system. The present study confirms this result (**Figure 6**). The largely differential expression is also consistent with previous studies showing partial depletion of Trpa1 with Trpv1 agonists (Pecze et al., 2009) or coexpression of these receptors. However, *TRPA1* is apparently expressed in low expressing *TRPV1* population, which could explain why these neurons are resistant to TRPV1 agonist actions and could also explain the failure to deplete *TRPA1*-expressing neurons with TRPV1 agonists in some experiments (Isensee et al., 2014; Sapio et al., 2018, 2020b). The functional implication of co-expression of these receptors is being investigated. For example, heteromers have been reported between these two ion channels with different pharmacologic and biophysical properties and have been proposed to be involved in nociceptive sensitization (Fischer et al., 2014; Patil et al., 2020). Cells with both *Trpv1* and *Trpa1* also tended to have moderate to high amounts of *Oprm1* expression (see **Figure 3**, Quad+ neurons), consistent with their proposed dual nociceptive and analgesia-conferring properties (Akopian, 2011).

Trpm8 is the primary receptor for cold and cold pain (Bautista et al., 2007) and serves as a marker for cold-sensing sensory afferents (Renthal, 2020). We describe populations of high and low *Trpm8* expression, where presumably the high *Trpm8* expressing cells are those that have primarily been described in previous studies as cold thermosensory afferents (Le Pichon and Chesler, 2014; Jankowski et al., 2017), and the lower levels of *Trpm8* in other cells are currently of unknown significance. However, these could be polymodal neurons, or cells that become recruited at colder temperatures and/or during cold allodynia. Notably, while *Trpm8*+ afferents have been shown to be involved in responding to environmental cooling, a small population of *Trpm8*+ fibers has been reported to respond to noxious mechanical stimulation (Jankowski et al., 2017), and it has been suggested that in injury states a subpopulation of *Trpm8*+ fibers may become responsive to additional noxious modalities. Additionally, the processes underlying thermal encoding in the DRG can be complex, with populations of cells responding in a graded fashion to various temperatures (Wang et al., 2018). Furthermore, electrical recordings have shown that cooling-responsive cells comprise only about 2.3% of all DRG neurons (Lawson et al., 2019), whereas the total number of *Trpm8*+ cells we quantified was much larger than this estimate. While examining the full range of thermal-encoding cells is beyond the scope of this study, the coincidence of expression of *Trpv1* and *Trpm8*, which encode two major encoding ion channels of temperature, may be useful information for future investigations. This is also an indication that we are examining multiple classes of DRG neurons among the *Trpm8*+ population. This is one area where additional electrical characterization of these subtypes would be informative, as this can elucidate functional response characteristics to further segregate the DRG afferents (Petruska et al., 2000; Rau et al., 2005; Lawson et al., 2019). This is also interesting given that *Trpm8* expression level may be related to tuning thermal responsiveness, which is notable given the

finding that various channels and/or channel combinations may be involved in thermal coding based on mouse studies (Paricio-Montesinos et al., 2020).

The overlap between *Trpm8* and *Oprm1* expression in the rat makes sense given reduction in clinical responses to cold sensation upon morphine (a mu-opioid receptor agonist) administration (Cleeland et al., 1996). This is also corroborated by the finding that morphine alleviated cold allodynia in rat models of chronic pain (Erichsen et al., 2005). Both cases support the idea that *Trpm8*+ cells are inhibited by μ-opioid receptor agonists. The *Trpm8*+ neurons also appear to be largely *Trpv1*-, indicating discrete types of peripheral neurons for the detection of hot and cold. This lack of overlap between *Trpv1* and *Trpm8*, is consistent with previous evidence demonstrating that *Trpm8*+ neurons are (in general) a small-diameter, relatively rare *Trpv1*- population of sensory afferents (Dhaka et al., 2008; Pecze et al., 2009; Le Pichon and Chesler, 2014; Jankowski et al., 2017). Although we did detect *Trpm8*+/*Trpv1*+ neurons, the expression was largely anticorrelated (**Figure 6H**) indicating that these two receptors are never strongly co-expressed. While developmentally, *Trpm8* is co-expressed in a subset of *Trpv1*-lineage neurons in the mouse (Mishra et al., 2011) pharmacologic ablation of Trpv1+ fibers in adult rodents suggests a further differentiation of a distinct subpopulation of *Trpm8*+/*Trpv1*- neurons (Cavanaugh et al., 2009) consistent with our anatomical findings. This is also consistent with ISH and single-cell RNA-Seq in DRG and trigeminal ganglion showing very low levels of *Trpv1* in *Trpm8*+ neurons (Kobayashi et al., 2005; Von Buchholtz et al., 2020). The idea of multiple *Trpm8*+ populations (Xing et al., 2006), where the *Trpv1*-coexpressing population may be more nociceptive in nature would potentially explain our results in context of the broader literature. We also cannot rule out an interaction between these input pathways at the level of the spinal cord, where Trpv1-specific and Trpm8-specific input pathways may be processed together in spinal circuits. For example, it is known that there is some interaction between Trpv1-specific and Trpm8-specific behavioral outcomes (Anderson et al., 2014).

The tetrodotoxin-resistant sodium channel subunit NaV1.9 (encoded by *Scn11a*) has come into focus as a potential nociceptor-specific target for the development of new non-opioid analgesics. Alongside two other sodium channel subunits in this family (*Scn9a* and *Scn10a*), *Scn11a* has been suggested as an interesting and understudied mediator of pain signaling. For example, the related ion channel subunit gene, *Scn9a* has been extensively studied in rodents and humans where it is strongly linked to pain and nociceptive signaling (Hisama et al., 1993; Dib-Hajj et al., 2005, 2007, 2013; Yang et al., 2018). Similarly, *Scn10a* has been used extensively as a nociceptive specific marker (Akopian et al., 1996; Dib-Hajj et al., 1999; Stirling et al., 2005; Shiers et al., 2020). The current study focuses on *Scn11a* largely due to the fact that it has been studied less intensively than *Scn9a* and *Scn10a*, and because mutations in this gene are associated with pain insensitivity or episodic pain syndromes in humans (Leipold et al., 2013; Zhang et al., 2013). For example, NaV1.9 has been found to be enriched in cells in the *Trpv1* lineage (Goswami et al., 2014) or depleted with TRPV1 agonist treatment (Isensee et al., 2014; Sapio et al., 2018), suggesting specificity for the nociceptive population. This channel has also been implicated in nociception and hyperalgesia in animal models, suggesting potential utility as an analgesic pharmacological target (Priest et al., 2005). NaV1.9 is required for cold-triggered nociception in the mouse (Lolignier et al., 2015), consistent with our observation that *Scn11a* is found in high-expressing *Trpm8*+ neurons. However, our staining shows a broad expression pattern of *Scn11a* consistent with involvement in other nociceptive functions. For example, *Scn11a* is frequently co-expressed with *Trpv1*, which is consistent with human mutation studies of NaV1.9 in nociception in which loss or gain of function *SCN11A* mutations can cause pain insensitivity or episodic pain syndromes (Leipold et al., 2013; Zhang et al., 2013). The phenotype depends on the location of mutation in the channel. Importantly, the finding that gain of function mutations that inhibit transmitter release leads to pain insensitivity suggests that NaV1.9 is expressed in enough nociceptive afferents to be sufficient to support a pain insensitive phenotype. These findings are also corroborated by other studies using single cell RNA-Seq showing that *Scn11a* is expressed in *Trpv1*+ cells, but also in several other classes of sensory afferents (Li et al., 2016; Sapio et al., 2018).

In our staining analysis, we examined secreted phosphoprotein 1 (*Spp1*) positive neurons, which are non-nociceptive large diameter primary afferents that innervate muscle spindles. The *Spp1* gene encodes osteopontin (Ichikawa et al., 2000). While the function of osteopontin in neurons has not been determined, it has been suggested as a regulator of myelination, and hypothesized that its expression is related to the maintenance or formation of axons with high conduction velocities (Higo et al., 2010). These neurons are thought to be chiefly implicated in proprioception (Ichikawa et al., 2000; Usoskin et al., 2015; Saito-Diaz et al., 2021). Anatomically, osteopontin immunoreactivity localizes to spiral axon terminals in muscle spindle fibers. In our staining, we found that *Spp1*+ cells were negative for *Trpv1* and *Oprm1*, but co-expressed *Oprl1*. These neurons were also generally large, and their staining pattern, showing distinction from *Trpv1* expressors, further suggests their non-nociceptive nature in the DRG.

The current study has several limitations that must be addressed in future studies. For the present investigation, experiments are conducted in male rats, and as such may not be fully reflective of the neuroanatomy and neurochemistry in the mouse or across both sexes (Sadler et al., 2022). For behavioral studies, the rat has many advantages compared to the mouse, however, at this point in time, a large set of molecular-genetic rat manipulations are not available for investigation as they are for the mouse nervous system (Ellenbroek and Youn, 2016; Homberg et al., 2017). Thus, the use of multiplex fluorescence represents a concerted effort to assemble the combinatorial molecular-cellular expression patterns in rat that mediate algesia and analgesia in sensory ganglia. The ultimate goal of these investigations is to gain insights into conserved molecular biological phenomena in both sexes and in humans. Future studies will concentrate on direct human investigation in male and female organ donor tissue to corroborate and extend these findings into human health, disease, and pharmacology (Iadarola et al., 2022), as such studies are more likely to yield

information that may be more clinically relevant and applicable. As an additional area for future directions, much attention has been paid to the use of single cell and single nucleus RNA-Seq for the determination and characterization of neuronal cell types in the DRG in mouse, monkey and human (Usoskin et al., 2015; Kupari et al., 2021; Tavares-Ferreira et al., 2022). These studies are useful in the determination of cell types but often lack the precision to determine the expression profile of an individual gene. In the existing databases, the opioid receptors are weakly detected, and probably encountered a limit of detection. Additionally, for genes such as *Trpv1* and *Trpm8*, the mouse and monkey databases have shown correlation between *Trpv1* and *Trpm8*, where the cell population with the highest level of one also has the highest level of the other, which is in direct contrast to our findings (Usoskin et al., 2015; Kupari et al., 2021). However, this could be due to multiple technical issues or species differences and is beyond the scope of the current investigation. Finally, another limitation is that this study does not assess the impact of pain and nerve injury on expression and co-expression of these markers. Nerve injury in particular induces strong transcriptional changes and may alter the baseline expression patterns of nociceptive and analgesic targets (Ray et al., 2018; Sapio et al., 2020a). Future studies can expand upon these foundational data to understand pain conditions.

While the field of nociceptive neuroscience has expended substantial effort over many years toward understanding key receptors involved in nociceptive circuits, there is a need for exact delineation of neuronal populations that contribute to clinical pain and pain control as well as identification of molecular signatures which can define these distinct populations. Our study utilized multiplex high sensitivity mRNA *in situ* hybridization, which allowed us to obtain precise answers, leading to enhanced clarity of these issues. Importantly, our findings suggest that the medium to low expressing *Trpv1*+ neurons indeed represent the population that transmit nociceptive signaling associated with tissue-damage and this population is coincident with opioid-induced anti-nociception. Deeper analysis of the coexpression matrix of these nociceptive and analgesic target genes provides additional rationale for identifying susceptible neuronal populations for early-stage novel therapeutics development, with either pharmacological agents or other methods such as *in vivo* gene transfer, by better defining the neuronal populations directly responsible for clinically relevant pain and pain control.

DATA AVAILABILITY STATEMENT

The original contributions presented in the study are included in the article/**Supplementary Material**, further inquiries can be directed to the corresponding author.

ETHICS STATEMENT

The animal study was reviewed and approved by NIH Clinical Center.

AUTHOR CONTRIBUTIONS

The project was conceptualized by MI, WM, and MS. Experiments were performed by WM, with technical involvement from MS, DM, and TG. Staining and slide scanning was performed by WM with assistance from AM and supervision from DM in fluorescence microscopy and image analysis. Stained sections were analyzed in Adobe Photoshop by WM with assistance from AM and MS. Visualizations, final figures, and formal analysis were generated primarily by MS, with assistance from WM, AM, and MD. Initial drafts of the manuscript were prepared by MS, WM, and MI with editing and suggestions from all of the authors. Funding was obtained by WM, DM, MI, and AM. The project was supervised by MS, AM, and MI. All authors revised and approved the final manuscript.

FUNDING

Funding for this work was supported by the Intramural Research Program of the NIH Clinical Center (1ZIACL090033-09, 1ZIACL090034-09, and 1ZIACL090035-08 to AM), and the NINDS. This work was also supported by a funds from the National Center for Complementary and Integrative Health (1ZIAAT000017-03), and the Office of Behavioral and Social Sciences Research. TG was supported by the Japan Society for the Promotion of Science Overseas Research Fellowship. This research was made possible through the National Institutes of Health (NIH) Medical Research Scholars Program, a public-private partnership supported jointly by the NIH and generous contributions to the Foundation for the NIH from the Doris Duke Charitable Foundation, Genentech, the American Association for Dental Research, the Colgate-Palmolive Company, Elsevier, alumni of student research programs, and other individual supporters *via* contributions to the Foundation for the National Institutes of Health.

ACKNOWLEDGMENTS

The authors acknowledge Ms. Pranavi Nara for technical assistance with several of the *in situ* hybridization studies.

SUPPLEMENTARY MATERIAL

The Supplementary Material for this article can be found online at: https://www.frontiersin.org/articles/10.3389/fnmol.2022.926596/full#supplementary-material

REFERENCES

Akopian, A. N., Sivilotti, L., and Wood, J. N. (1996). A tetrodotoxin-resistant voltage-gated sodium channel expressed by sensory neurons. *Nature* 379, 257–262. doi: 10.1038/379257a0

Akopian, A. (2011). Regulation of nociceptive transmission at the periphery *via* TRPA1-TRPV1 interactions. *Curr. Pharm. Biotechnol.* 12, 89–94. doi: 10.2174/138920111793937952

Anderson, E. M., Jenkins, A. C., Caudle, R. M., and Neubert, J. K. (2014). The effects of a co-application of menthol and capsaicin on nociceptive behaviors of

the rat on the operant orofacial pain assessment device. *PLoS ONE* 9, e89137. doi: 10.1371/journal.pone.0089137

Bardoni, R., Tawfik, V. L., Wang, D., Francois, A., Solorzano, C., Shuster, S. A., et al. (2014). Delta opioid receptors presynaptically regulate cutaneous mechanosensory neuron input to the spinal cord dorsal horn. *Neuron* 81, 1312–1327. doi: 10.1016/j.neuron.2014.01.044

Bautista, D. M., Siemens, J., Glazer, J. M., Tsuruda, P. R., Basbaum, A. I., Stucky, C. L., et al. (2007). The menthol receptor TRPM8 is the principal detector of environmental cold. *Nature* 448, 204–208. doi: 10.1038/nature05910

Bevan, S., Hothi, S., Hughes, G., James, I. F., Rang, H. P., Shah, K., et al. (1992). Capsazepine: a competitive antagonist of the sensory neurone excitant capsaicin. *Br. J. Pharmacol.* 107, 544–552. doi: 10.1111/j.1476-5381.1992.tb12781.x

Brown, D. C., Agnello, K., and Iadarola, M. J. (2015). Intrathecal resiniferatoxin in a dog model: efficacy in bone cancer pain. *Pain* 156, 1018–1024. doi: 10.1097/j.pain.0000000000000115

Brown, D. C., and Iadarola, M. J. (2015). "TRPV1 agonist cytotoxicity for chronic pain relief," in: *TRP Channels as Therapeutic Targets*, eds A. Szallasi (Boston: Academic Press).

Brown, D. C., Iadarola, M. J., Perkowski, S. Z., Erin, H., Shofer, F., Laszlo, K. J., et al. (2005). Physiologic and antinociceptive effects of intrathecal resiniferatoxin in a canine bone cancer model. *Anesthesiology* 103, 1052–1059. doi: 10.1097/00000542-200511000-00020

Bruce, D. J., Peterson, C. D., Kitto, K. F., Akgün, E., Lazzaroni, S., Portoghese, P. S., et al. (2019). Combination of a δ-opioid receptor agonist and loperamide produces peripherally-mediated analgesic synergy in mice. *Anesthesiology* 131, 649–663. doi: 10.1097/ALN.0000000000002840

Calo, G., Guerrini, R., Rizzi, A., Salvadori, S., and Regoli, D. (2000). Pharmacology of nociceptin and its receptor: a novel therapeutic target. *Br. J. Pharmacol.* 129, 1261–1283. doi: 10.1038/sj.bjp.0703219

Caterina, M. J. (2007). Transient receptor potential ion channels as participants in thermosensation and thermoregulation. *Am. J. Physiol. Regul. Integr. Comp. Physiol.* 292, R64–76. doi: 10.1152/ajpregu.00446.2006

Caterina, M. J., Schumacher, M. A., Tominaga, M., Rosen, T. A., Levine, J. D., and Julius, D. (1997). The capsaicin receptor: a heat-activated ion channel in the pain pathway. *Nature* 389, 816–824. doi: 10.1038/39807

Cavanaugh, D. J., Chesler, A. T., Braz, J. M., Shah, N. M., Julius, D., and Basbaum, A. I. (2011a). Restriction of transient receptor potential vanilloid-1 to the peptidergic subset of primary afferent neurons follows its developmental downregulation in nonpeptidergic neurons. *J. Neurosci.* 31, 10119–10127. doi: 10.1523/JNEUROSCI.1299-11.2011

Cavanaugh, D. J., Chesler, A. T., Jackson, A. C., Sigal, Y. M., Yamanaka, H., Grant, R., et al. (2011b). Trpv1 reporter mice reveal highly restricted brain distribution and functional expression in arteriolar smooth muscle cells. *J. Neurosci.* 31, 5067–5077. doi: 10.1523/JNEUROSCI.6451-10.2011

Cavanaugh, D. J., Lee, H., Lo, L., Shields, S. D., Zylka, M. J., Basbaum, A. I., et al. (2009). Distinct subsets of unmyelinated primary sensory fibers mediate behavioral responses to noxious thermal and mechanical stimuli. *Proc. Natl. Acad. Sci.* 106, 9075–9080. doi: 10.1073/pnas.0901507106

Che, T., Dwivedi-Agnihotri, H., Shukla, A. K., and Roth, B. L. (2021). Biased ligands at opioid receptors: Current status and future directions. *Sci. Signal.* 14:aav0320. doi: 10.1126/scisignal.aav0320

Chen, S.-R., and Pan, H.-L. (2006). Blocking μ opioid receptors in the spinal cord prevents the analgesic action by subsequent systemic opioids. *Brain Res.* 1081, 119–125. doi: 10.1016/j.brainres.2006.01.053

Chew, L. A., Bellampalli, S. S., Dustrude, E. T., and Khanna, R. (2019). Mining the Nav1.7 interactome: opportunities for chronic pain therapeutics. *Biochem. Pharmacol.* 163, 9–20. doi: 10.1016/j.bcp.2019.01.018

Chiu, I. M., Barrett, L. B., Williams, E. K., Strochlic, D. E., Lee, S., Weyer, A. D., et al. (2014). Transcriptional profiling at whole population and single cell levels reveals somatosensory neuron molecular diversity. *Elife* 3:e34. doi: 10.7554/eLife.04660.034

Cleeland, C. S., Nakamura, Y., Howland, E. W., Morgan, N. R., Edwards, K. R., and Backonja, M. (1996). Effects of oral morphine on cold pressor tolerance time and neuropsychological performance. *Neuropsychopharmacology* 15, 252–262. doi: 10.1016/0893-133X(95)00205-R

Craig, A. D. (2018). "Chapter 19 - Central neural substrates involved in temperature discrimination, thermal pain, thermal comfort, and thermoregulatory behavior," in *Handbook of Clinical Neurology*, ed A. A. Romanovsky (Amsterdam: Elsevier).

Dhaka, A., Earley, T. J., Watson, J., and Patapoutian, A. (2008). Visualizing cold spots: TRPM8-expressing sensory neurons and their projections. *J. Neurosci.* 28, 566–575. doi: 10.1523/JNEUROSCI.3976-07.2008

Dib-Hajj, S. D., Cummins, T. R., Black, J. A., and Waxman, S. G. (2007). From genes to pain: Na v 1.7 and human pain disorders. *Trends Neurosci.* 30, 555–563. doi: 10.1016/j.tins.2007.08.004

Dib-Hajj, S. D., Rush, A. M., Cummins, T. R., Hisama, F. M., Novella, S., Tyrrell, L., et al. (2005). Gain-of-function mutation in Nav1.7 in familial erythromelalgia induces bursting of sensory neurons. *Brain* 128, 1847–1854. doi: 10.1093/brain/awh514

Dib-Hajj, S. D., Tyrrell, L., Cummins, T. R., Black, J. A., Wood, P. M., and Waxman, S. G. (1999). Two tetrodotoxin-resistant sodium channels in human dorsal root ganglion neurons. *FEBS Lett.* 462, 117–120. doi: 10.1016/S0014-5793(99)01519-7

Dib-Hajj, S. D., Yang, Y., Black, J. A., and Waxman, S. G. (2013). The Na(V)1.7 sodium channel: from molecule to man. *Nat. Rev. Neurosci.* 14, 49–62. doi: 10.1038/nrn3404

Ellenbroek, B., and Youn, J. (2016). Rodent models in neuroscience research: is it a rat race? *Dis. Model. Mech.* 9, 1079–1087. doi: 10.1242/dmm.026120

Erbs, E., Faget, L., Scherrer, G., Matifas, A., Filliol, D., Vonesch, J. L., et al. (2015). A mu-delta opioid receptor brain atlas reveals neuronal co-occurrence in subcortical networks. *Brain Struct. Funct.* 220, 677–702. doi: 10.1007/s00429-014-0717-9

Erichsen, H. K., Hao, J. X., Xu, X. J., and Blackburn-Munro, G. (2005). Comparative actions of the opioid analgesics morphine, methadone and codeine in rat models of peripheral and central neuropathic pain. *Pain* 116, 347–358. doi: 10.1016/j.pain.2005.05.004

Fischer, M. J. M., Balasuriya, D., Jeggle, P., Goetze, T. A., Mcnaughton, P. A., Reeh, P. W., et al. (2014). Direct evidence for functional TRPV1/TRPA1 heteromers. *Pflügers Archiv. Eur. J. Physiol.* 466, 2229–2241. doi: 10.1007/s00424-014-1497-z

Floyd, B. N., Camilleri, M., Busciglio, I., Sweetser, S., Burton, D., Wong, G. Y., et al. (2009). Effect of a kappa-opioid agonist, i.v. JNJ-38488502, on sensation of colonic distensions in healthy male volunteers. *Neurogastroenterol. Motil.* 21, 281–290. doi: 10.1111/j.1365-2982.2008.01202.x

Gaborit, M., and Massotte, D. (2021). Therapeutic potential of opioid receptor heteromers in chronic pain and associated comorbidities. *Br. J. Pharmacol.* doi: 10.1111/bph.15772. [Epub ahead of print].

Garami, A., Pakai, E., Mcdonald, H. A., Reilly, R. M., Gomtsyan, A., Corrigan, J. J., et al. (2018). TRPV1 antagonists that cause hypothermia, instead of hyperthermia, in rodents: Compounds' pharmacological profiles, in vivo targets, thermoeffectors recruited and implications for drug development. *Acta Physiol.* 223, e13038. doi: 10.1111/apha.13038

Goswami, S. C., Mishra, S. K., Maric, D., Kaszas, K., Gonnella, G. L., Clokie, S. J., et al. (2014). Molecular signatures of mouse TRPV1-lineage neurons revealed by RNA-Seq transcriptome analysis. *J. Pain* 15, 1338–1359. doi: 10.1016/j.jpain.2014.09.010

Hall, B. E., Macdonald, E., Cassidy, M., Yun, S., Sapio, M. R., Ray, P., et al. (2022). Transcriptomic analysis of human sensory neurons in painful diabetic neuropathy reveals inflammation and neuronal loss. *Sci. Rep.* 12, 4729. doi: 10.1038/s41598-022-08100-8

Higo, N., Sato, A., Yamamoto, T., Nishimura, Y., Oishi, T., Murata, Y., et al. (2010). SPP1 is expressed in corticospinal neurons of the macaque sensorimotor cortex. *J. Comp. Neurol* 518, 2633–2644. doi: 10.1002/cne.22356

Hisama, F. M., Dib-Hajj, S. D., and Waxman, S. G. (1993). "SCN9A-Related Inherited Erythromelalgia," in: *GeneReviews(R)*, eds R. A. Pagon, M. P. Adam, H. H. Ardinger, S. E. Wallace, A. Amemiya, L. J. H. Bean, et al. (Seattle, WA).

Homberg, J. R., Wöhr, M., and Alenina, N. (2017). Comeback of the rat in biomedical research. *ACS Chem. Neurosci.* 8, 900–903. doi: 10.1021/acschemneuro.6b00415

Iadarola, M. J., and Gonnella, G. L. (2013). Resiniferatoxin for pain treatment: an interventional approach to personalized pain medicine. *Open Pain J.* 6, 95–107. doi: 10.2174/1876386301306010095

Iadarola, M. J., Sapio, M. R., and Mannes, A. J. (2015). A new splice of life for the mu-opioid receptor. *J. Clin. Invest.* 125, 2558–2561. doi: 10.1172/JCI82060

Iadarola, M. J., Sapio, M. R., and Mannes, A. J. (2022). Be in it for the long haul: a commentary on human tissue recovery initiatives. *J. Pain*. doi: 10.1016/j.jpain.2022.04.009

Iadarola, M. J., Sapio, M. R., Raithel, S. J., Mannes, A. J., and Brown, D. C. (2018). Long-term pain relief in canine osteoarthritis by a single intra-articular injection of resiniferatoxin, a potent TRPV1 agonist. *Pain* 159, 2105–2114. doi: 10.1097/j.pain.0000000000001314

Ichikawa, H., Itota, T., Nishitani, Y., Torii, Y., Inoue, K., and Sugimoto, T. (2000). Osteopontin-immunoreactive primary sensory neurons in the rat spinal and trigeminal nervous systems. *Brain Res.* 863, 276–281. doi: 10.1016/S0006-8993(00)02126-0

Imlach, W., and Christie, Macdonald, J. (2014). The light touch of delta opioid receptors. *Neuron* 81, 1220–1222. doi: 10.1016/j.neuron.2014.03.004

Isensee, J., Wenzel, C., Buschow, R., Weissmann, R., Kuss, A. W., and Hucho, T. (2014). Subgroup-elimination transcriptomics identifies signaling proteins that define subclasses of TRPV1-positive neurons and a novel paracrine circuit. *PLoS ONE* 9, e115731. doi: 10.1371/journal.pone.0115731

Jancso, G., Kiraly, E., and Jancso-Gabor, A. (1977). Pharmacologically induced selective degeneration of chemosensitive primary sensory neurones. *Nature* 270, 741–743. doi: 10.1038/270741a0

Jankowski, M. P., Rau, K. K., and Koerber, H. R. (2017). Cutaneous TRPM8-expressing sensory afferents are a small population of neurons with unique firing properties. *Physiol. Rep.* 5, e13234. doi: 10.14814/phy2.13234

Jordan, B. A., and Devi, L. A. (1999). G-protein-coupled receptor heterodimerization modulates receptor function. *Nature* 399, 697–700. doi: 10.1038/21441

Jordt, S. E., Bautista, D. M., Chuang, H. H., Mckemy, D. D., Zygmunt, P. M., Högestätt, E. D., et al. (2004). Mustard oils and cannabinoids excite sensory nerve fibres through the TRP channel ANKTM1. *Nature* 427, 260–265. doi: 10.1038/nature02282

Julius, D., and Basbaum, A. I. (2001). Molecular mechanisms of nociception. *Nature* 413, 203–210. doi: 10.1038/35093019

Karai, L., Brown, D. C., Mannes, A. J., Connelly, S. T., Brown, J., Gandal, M., et al. (2004a). Deletion of vanilloid receptor 1-expressing primary afferent neurons for pain control. *J. Clin. Invest.* 113, 1344–1352. doi: 10.1172/JCI20449

Karai, L. J., Russell, J. T., Iadarola, M. J., and Olah, Z. (2004b). Vanilloid receptor 1 regulates multiple calcium compartments and contributes to Ca2+-induced Ca2+ release in sensory neurons. *J. Biol. Chem.* 279, 16377–16387. doi: 10.1074/jbc.M310891200

Knowlton, W. M., Bifolck-Fisher, A., Bautista, D. M., and Mckemy, D. D. (2010). TRPM8, but not TRPA1, is required for neural and behavioral responses to acute noxious cold temperatures and cold-mimetics in vivo. *Pain* 150, 340–350. doi: 10.1016/j.pain.2010.05.021

Ko, M. C. H., Wei, H., Woods, J. H., and Kennedy, R. T. (2006). Effects of intrathecally administered nociceptin/orphanin fq in monkeys: behavioral and mass spectrometric studies. *J. Pharmacol. Exp. Therap.* 318, 1257–1264. doi: 10.1124/jpet.106.106120

Kobayashi, K., Fukuoka, T., Obata, K., Yamanaka, H., Dai, Y., Tokunaga, A., et al. (2005). Distinct expression of TRPM8, TRPA1, and TRPV1 mRNAs in rat primary afferent neurons with aδ/c-fibers and colocalization with trk receptors. *J. Comp. Neurol.* 493, 596–606. doi: 10.1002/cne.20794

Koivisto, A.-P., Belvisi, M. G., Gaudet, R., and Szallasi, A. (2022). Advances in Trp channel drug discovery: from target validation to clinical studies. *Nat. Rev. Drug Discov.* 21, 41–59. doi: 10.1038/s41573-021-00268-4

Kondo, I., Marvizon, J. C., Song, B., Salgado, F., Codeluppi, S., Hua, X. Y., et al. (2005). Inhibition by spinal mu- and delta-opioid agonists of afferent-evoked substance P release. *J. Neurosci.* 25, 3651–3660. doi: 10.1523/JNEUROSCI.0252-05.2005

Kupari, J., Usoskin, D., Parisien, M., Lou, D., HU, Y., Fatt, M., et al. (2021). Single cell transcriptomics of primate sensory neurons identifies cell types associated with chronic pain. *Nat. Commun.* 12, 1510. doi: 10.1038/s41467-021-21725-z

Lambert, D. G. (2008). The nociceptin/orphanin FQ receptor: a target with broad therapeutic potential. *Nat. Rev. Drug Discov.* 7, 694–710. doi: 10.1038/nrd2572

Lawson, S. N., Fang, X., and Djouhri, L. (2019). Nociceptor subtypes and their incidence in rat lumbar dorsal root ganglia (DRGs): focussing on C-polymodal nociceptors, Aβ-nociceptors, moderate pressure receptors and their receptive field depths. *Curr. Opin. Physiol.* 11, 125–146. doi: 10.1016/j.cophys.2019.10.005

Le Pichon, C. E., and Chesler, A. T. (2014). The functional and anatomical dissection of somatosensory subpopulations using mouse genetics. *Front. Neuroanat.* 8, 21. doi: 10.3389/fnana.2014.00021

Leipold, E., Liebmann, L., Korenke, G. C., Heinrich, T., Giesselmann, S., Baets, J., et al. (2013). A de novo gain-of-function mutation in SCN11A causes loss of pain perception. *Nat. Genet.* 45, 1399–1404. doi: 10.1038/ng.2767

Li, C. L., Li, K. C., Wu, D., Chen, Y., Luo, H., Zhao, J. R., et al. (2016). Somatosensory neuron types identified by high-coverage single-cell RNA-sequencing and functional heterogeneity. *Cell Res.* 26, 967. doi: 10.1038/cr.2016.90

Lolignier, S., Bonnet, C., Gaudioso, C., Noël, J., Ruel, J., Amsalem, M., et al. (2015). The Nav1.9 channel is a key determinant of cold pain sensation and cold allodynia. *Cell Rep.* 11, 1067–1078. doi: 10.1016/j.celrep.2015.04.027

Maric, D., Jahanipour, J., LI, X. R., Singh, A., Mobiny, A., Van Nguyen, H., et al. (2021). Whole-brain tissue mapping toolkit using large-scale highly multiplexed immunofluorescence imaging and deep neural networks. *Nat. Commun.* 12, 1550. doi: 10.1038/s41467-021-21735-x

Mcnamara, C. R., Mandel-Brehm, J., Bautista, D. M., Siemens, J., Deranian, K. L., Zhao, M., et al. (2007). TRPA1 mediates formalin-induced pain. *Proc. Natl. Acad. Sci. USA.* 104, 13525–13530. doi: 10.1073/pnas.0705924104

Menéndez, L., Juárez, L., García, E., García-Suárez, O., Hidalgo, A., and Baamonde, A. (2006). Analgesic effects of capsazepine and resiniferatoxin on bone cancer pain in mice. *Neurosci. Lett.* 393, 70–73. doi: 10.1016/j.neulet.2005.09.046

Mishra, S. K., and Hoon, M. A. (2010). Ablation of TrpV1 neurons reveals their selective role in thermal pain sensation. *Mol. Cell. Neurosci.* 43, 157–163. doi: 10.1016/j.mcn.2009.10.006

Mishra, S. K., Tisel, S. M., Orestes, P., Bhangoo, S. K., and Hoon, M. A. (2011). TRPV1-lineage neurons are required for thermal sensation. *EMBO J.* 30, 582–593. doi: 10.1038/emboj.2010.325

Mitchell, K., Bates, B. D., Keller, J. M., Lopez, M., Scholl, L., Navarro, J., et al. (2010). Ablation of rat TRPV1-expressing Adelta/C-fibers with resiniferatoxin: analysis of withdrawal behaviors, recovery of function and molecular correlates. *Mol. Pain* 6, 94. doi: 10.1186/1744-8069-6-94

Mitchell, K., Lebovitz, E. E., Keller, J. M., Mannes, A. J., Nemenov, M. I., and Iadarola, M. J. (2014). Nociception and inflammatory hyperalgesia evaluated in rodents using infrared laser stimulation after Trpv1 gene knockout or resiniferatoxin lesion. *Pain* 155, 733–745. doi: 10.1016/j.pain,.2014.01.007

Paricio-Montesinos, R., Schwaller, F., Udhayachandran, A., Rau, F., Walcher, J., Evangelista, R., et al. (2020). The sensory coding of warm perception. *Neuron* 106, 830-841.e3. doi: 10.1016/j.neuron.2020.02.035

Park, C. W., Kim, B. J., Lee, Y. W., Won, C., Park, C. O., Chung, B. Y., et al. (2021). Asivatrep, a TRPV1 antagonist, for the topical treatment of atopic dermatitis: a phase III, randomized, vehicle-controlled study (CAPTAIN-AD). *J. Allergy Clin. Immunol.* doi: 10.1016/j.jaci.2021.09.024

Patil, M. J., Salas, M., Bialuhin, S., Boyd, J. T., Jeske, N. A., and Akopian, A. N. (2020). Sensitization of small-diameter sensory neurons is controlled by TRPV1 and TRPA1 association. *FASEB J.* 34, 287–302. doi: 10.1096/fj.201902026R

Pecze, L., Pelsoczi, P., Kecskes, M., Winter, Z., Papp, A., Kaszas, K., et al. (2009). Resiniferatoxin mediated ablation of TRPV1+ neurons removes TRPA1 as well. *Can. J. Neurol. Sci.* 36, 234–241. doi: 10.1017/S0317167100006600

Petruska, J. C., Napaporn, J., Johnson, R. D., GU, J. G., and Cooper, B. Y. (2000). Subclassified acutely dissociated cells of rat DRG: histochemistry and patterns of capsaicin-, proton-, and ATP-activated currents. *J. Neurophysiol.* 84, 2365–2379. doi: 10.1152/jn.2000.84.5.2365

Poulson, S. J., Aldarraji, A., Arain, I. I., Dziekonski, N., Motlana, K., Riley, R., et al. (2020). Naked mole-rats lack cold sensitivity before and after nerve injury. *Mol. Pain* 16, 1744806920955103. doi: 10.1177/1744806920955103

Priest, B. T., Murphy, B. A., Lindia, J. A., Diaz, C., Abbadie, C., Ritter, A. M., et al. (2005). Contribution of the tetrodotoxin-resistant voltage-gated sodium channel NaV1.9 to sensory transmission and nociceptive behavior. *Proc. Natl. Acad. Sci. USA.* 102, 9382–9387. doi: 10.1073/pnas.0501549102

Quiding, H., Jonzon, B., Svensson, O., Webster, L., Reimfelt, A., Karin, A., et al. (2013). TRPV1 antagonistic analgesic effect: a randomized study of AZD1386 in pain after third molar extraction. *Pain* 154, 808–812. doi: 10.1016/j.pain.2013.02.004

Raithel, S. J., Sapio, M. R., Iadarola, M. J., and Mannes, A. J. (2018). Thermal A-delta nociceptors, identified by transcriptomics, express higher

levels of anesthesia-sensitive receptors than thermal c-fibers and are more suppressible by low-dose isoflurane. *Anesth. Analg.* 127, 263–266. doi: 10.1213/ANE.0000000000002505

Rau, K. K., Caudle, R. M., Cooper, B. Y., and Johnson, R. D. (2005). Diverse immunocytochemical expression of opioid receptors in electrophysiologically defined cells of rat dorsal root ganglia. *J. Chem. Neuroanat.* 29, 255–264. doi: 10.1016/j.jchemneu.2005.02.002

Ray, P., Torck, A., Quigley, L., Wangzhou, A., Neiman, M., Rao, C., et al. (2018). Comparative transcriptome profiling of the human and mouse dorsal root ganglia: an RNA-seq-based resource for pain and sensory neuroscience research. *Pain* 159, 1325–1345. doi: 10.1097/j.pain.0000000000001217

Renthal, W. (2020). "Chapter 23—pain genetics," in *Rosenberg's Molecular and Genetic Basis of Neurological and Psychiatric Disease (Sixth Edition)*, eds R. N. Rosenberg and J. M. Pascual (New York: Academic Press). doi: 10.1016/B978-0-12-813866-3.00023-0

Rowbotham, M. C., Nothaft, W., Duan, R. W., Wang, Y., Faltynek, C., Mcgaraughty, S., et al. (2011). Oral and cutaneous thermosensory profile of selective TRPV1 inhibition by ABT-102 in a randomized healthy volunteer trial. *Pain* 152, 1192–1200. doi: 10.1016/j.pain.2011.01.051

Sadler, K. E., Mogil, J. S., and Stucky, C. L. (2022). Innovations and advances in modelling and measuring pain in animals. *Nat. Rev. Neurosci.* 23, 70–85. doi: 10.1038/s41583-021-00536-7

Saito-Diaz, K., Street, J. R., Ulrichs, H., and Zeltner, N. (2021). Derivation of peripheral nociceptive, mechanoreceptive, and proprioceptive sensory neurons from the same culture of human pluripotent stem cells. *Stem Cell Rep.* 16, 446–457. doi: 10.1016/j.stemcr.2021.01.001

Sapio, M. R., Goswami, S. C., Gross, J. R., Mannes, A. J., and Iadarola, M. J. (2016). Transcriptomic analyses of genes and tissues in inherited sensory neuropathies. *Exp. Neurol.* 283, 375–395. doi: 10.1016/j.expneurol.2016.06.023

Sapio, M. R., Iadarola, M. J., Loydpierson, A. J., Kim, J. J., Thierry-Mieg, D., Thierry-Mieg, J., et al. (2020a). Dynorphin and enkephalin opioid peptides and transcripts in spinal cord and dorsal root ganglion during peripheral inflammatory hyperalgesia and allodynia. *J. Pain* 21, 988–1004. doi: 10.1016/j.jpain.2020.01.001

Sapio, M. R., Neubert, J. K., Lapaglia, D. M., Maric, D., Keller, J. M., Raithel, S. J., et al. (2018). Pain control through selective chemo-axotomy of centrally projecting TRPV1+ sensory neurons. *J. Clin. Invest.* 128, 1657–1670. doi: 10.1172/JCI94331

Sapio, M. R., Vazquez, F. A., Loydpierson, A. J., Maric, D., Kim, J. J., Lapaglia, D. M., et al. (2020b). Comparative analysis of dorsal root, nodose and sympathetic ganglia for the development of new analgesics. *Front. Neurosci.* 14, 615362. doi: 10.3389/fnins.2020.615362

Shiers, S., Klein, R. M., and Price, T. J. (2020). Quantitative differences in neuronal subpopulations between mouse and human dorsal root ganglia demonstrated with RNAscope *in situ* hybridization. *Pain* 161, 2410–2424. doi: 10.1101/2020.03.06.981597

Snyder, L. M., Chiang, M. C., Loeza-Alcocer, E., Omori, Y., Hachisuka, J., Sheahan, T. D., et al. (2018). Kappa opioid receptor distribution and function in primary afferents. *Neuron* 99, 1274-1288.e6. doi: 10.1016/j.neuron.2018.08.044

Stirling, L. C., Forlani, G., Baker, M. D., Wood, J. N., Matthews, E. A., Dickenson, A. H., et al. (2005). Nociceptor-specific gene deletion using heterozygous NaV1.8-Cre recombinase mice. *Pain* 113, 27–36. doi: 10.1016/j.pain.2004.08.015

Szallasi, A., and Blumberg, P. M. (1999). Vanilloid (Capsaicin) receptors and mechanisms. *Pharmacol. Rev.* 51, 159–212.

Szallasi, A., Cortright, D. N., Blum, C. A., and Eid, S. R. (2007). The vanilloid receptor TRPV1: 10 years from channel cloning to antagonist proof-of-concept. *Nat. Rev. Drug Discov.* 6, 357–372. doi: 10.1038/nrd2280

Tavares-Ferreira, D., Shiers, S., Ray, P. R., Wangzhou, A., Jeevakumar, V., Sankaranarayanan, I., et al. (2022). Spatial transcriptomics of dorsal root ganglia identifies molecular signatures of human nociceptors. *Sci. Transl. Med.* 14, eabj8186. doi: 10.1126/scitranslmed.abj8186

Teichert Russell, W., Smith Nathan, J., Raghuraman, S., Yoshikami, D., Light Alan, R., and Olivera Baldomero, M. (2012). Functional profiling of neurons through cellular neuropharmacology. *Proc. Nat. Acad. Sci.* 109, 1388–1395. doi: 10.1073/pnas.1118833109

Tominaga, M., Caterina, M. J., Malmberg, A. B., Rosen, T. A., Gilbert, H., Skinner, K., et al. (1998). The cloned capsaicin receptor integrates multiple pain-producing stimuli. *Neuron* 21, 531–543. doi: 10.1016/S0896-6273(00)80564-4

Urban, L., Campbell, E. A., Panesar, M., Patel, S., Chaudhry, N., Kane, S., et al. (2000). In vivo pharmacology of SDZ 249-665, a novel, non-pungent capsaicin analogue. *Pain* 89, 65–74. doi: 10.1016/S0304-3959(00)00349-3

Usoskin, D., Furlan, A., Islam, S., Abdo, H., Lonnerberg, P., Lou, D., et al. (2015). Unbiased classification of sensory neuron types by large-scale single-cell RNA sequencing. *Nat. Neurosci.* 18, 145–153. doi: 10.1038/nn.3881

Valentino, R. J., and Volkow, N. D. (2018). Untangling the complexity of opioid receptor function. *Neuropsychopharmacology* 43, 2514–2520. doi: 10.1038/s41386-018-0225-3

Van Neerven, S. G. A., and Mouraux, A. (2020). Capsaicin-induced skin desensitization differentially affects a-delta and c-fiber-mediated heat sensitivity. *Front. Pharmacol.* 11. doi: 10.3389/fphar.2020.00615

Viscusi, E. R., Torjman, M. C., Munera, C. L., Stauffer, J. W., Setnik, B. S., and Bagal, S. N. (2021). Effect of difelikefalin, a selective kappa opioid receptor agonist, on respiratory depression: a randomized, double-blind, placebo-controlled trial. *Clin. Transl. Sci.* 14, 1886–1893. doi: 10.1111/cts.13042

Von Buchholtz, L. J., Lam, R. M., Emrick, J. J., Chesler, A. T., and Ryba, N. J. P. (2020). Assigning transcriptomic class in the trigeminal ganglion using multiplex in situ hybridization and machine learning. *Pain* 161, 2212–2224. doi: 10.1097/j.pain.0000000000001911

Wang, F., Bélanger, E., Côté, S. L., Desrosiers, P., Prescott, S. A., Côt,é, D. C., et al. (2018). Sensory afferents use different coding strategies for heat and cold. *Cell Rep.* 23, 2001–2013. doi: 10.1016/j.celrep.2018.04.065

Wong, G. Y., and Gavva, N. R. (2009). Therapeutic potential of vanilloid receptor TRPV1 agonists and antagonists as analgesics: recent advances and setbacks. *Brain Res. Rev.* 60, 267–277. doi: 10.1016/j.brainresrev.2008.12.006

Wood, J. N., Winter, J., James, I. F., Rang, H. P., Yeats, J., and Bevan, S. (1988). Capsaicin-induced ion fluxes in dorsal root ganglion cells in culture. *J. Neurosci.* 8, 3208–3220. doi: 10.1523/JNEUROSCI.08-09-03208.1988

Xanthos, D. N., and Sandkühler, J. (2014). Neurogenic neuroinflammation: inflammatory CNS reactions in response to neuronal activity. *Nat. Rev. Neurosci.* 15, 43–53. doi: 10.1038/nrn3617

Xing, H., Chen, M., Ling, J., Tan, W., and Gu, J. G. (2007). TRPM8 mechanism of cold allodynia after chronic nerve injury. *J. Neurosci.* 27, 13680–13690. doi: 10.1523/JNEUROSCI.2203-07.2007

Xing, H., Ling, J., Chen, M., and Gu, J. G. (2006). Chemical and cold sensitivity of two distinct populations of TRPM8-expressing somatosensory neurons. *J. Neurophysiol.* 95, 1221–1230. doi: 10.1152/jn.01035.2005

Yaksh, T. L., Farb, D. H., Leeman, S. E., and Jessell, T. M. (1979). Intrathecal capsaicin depletes substance P in the rat spinal cord and produces prolonged thermal analgesia. *Science* 206, 481–483. doi: 10.1126/science.228392

Yang, Y., Mis, M. A., Estacion, M., Dib-Hajj, S. D., and Waxman, S. G. (2018). NaV1.7 as a pharmacogenomic target for pain: moving toward precision medicine. *Trends Pharmacol. Sci.* 39, 258–275. doi: 10.1016/j.tips.2017.11.010

Zhang, X. Y., Wen, J., Yang, W., Wang, C., Gao, L., Zheng, L. H., et al. (2013). Gain-of-function mutations in SCN11A cause familial episodic pain. *Am. J. Hum. Genet.* 93, 957–966. doi: 10.1016/j.ajhg.2013.09.016

Conflict of Interest: The authors declare that the research was conducted in the absence of any commercial or financial relationships that could be construed as a potential conflict of interest.

frontiers | Frontiers in Molecular Neuroscience

TYPE Original Research
PUBLISHED 27 July 2022
DOI 10.3389/fnmol.2022.918321

OPEN ACCESS

EDITED BY
Fabien Marchand,
INSERM U1107 Douleur et Biophysique Neurosensorielle (Neuro-Dol), France

REVIEWED BY
Jie Tu,
Shenzhen Institutes of Advanced Technology (CAS), China
Livio Luongo,
University of Campania Luigi Vanvitelli, Italy

*CORRESPONDENCE
Juan Nacher
juan.nacher@uv.es
Esther Berrocoso
esther.berrocoso@uca.es

SPECIALTY SECTION
This article was submitted to Pain Mechanisms and Modulators, a section of the journal Frontiers in Molecular Neuroscience

RECEIVED 12 April 2022
ACCEPTED 04 July 2022
PUBLISHED 27 July 2022

CITATION
Bravo L, Mariscal P, Llorca-Torralba M, López-Cepero JM, Nacher J and Berrocoso E (2022) Altered expression of vesicular glutamate transporter-2 and cleaved caspase-3 in the locus coeruleus of nerve-injured rats. *Front. Mol. Neurosci.* 15:918321. doi: 10.3389/fnmol.2022.918321

Altered expression of vesicular glutamate transporter-2 and cleaved caspase-3 in the locus coeruleus of nerve-injured rats

Lidia Bravo[1,2,3], Patricia Mariscal[2,3,4], Meritxell Llorca-Torralba[2,3,5], Jose María López-Cepero[5], Juan Nacher[3,6,7]* and Esther Berrocoso[2,3,4]*

[1]Neuropsychopharmacology and Psychobiology Research Group, Department of Neuroscience, University of Cádiz, Cádiz, Spain, [2]Instituto de Investigación e Innovación Biomédica de Cádiz, INiBICA, Hospital Universitario Puerta del Mar, Cádiz, Spain, [3]Centro de Investigación Biomédica en Red de Salud Mental (CIBERSAM), Instituto de Salud Carlos III, Madrid, Spain, [4]Neuropsychopharmacology and Psychobiology Research Group, Department of Psychology, University of Cádiz, Cádiz, Spain, [5]Neuropsychopharmacology and Psychobiology Research Group, Department of Cell Biology and Histology, University of Cádiz, Cádiz, Spain, [6]Neurobiology Unit, Program in Neurosciences and Institute of Biotechnology and Biomedicine (BIOTECMED), Universitat de València, Burjassot, Spain, [7]Fundación Investigación Hospital Clínico de Valencia, INCLIVA, Valencia, Spain

Neuropathic pain is a debilitating chronic condition provoked by a lesion in the nervous system and it induces functional alterations to the noradrenergic locus coeruleus (LC), affecting distinct dimensions of pain, like sensorial hypersensitivity, pain-induced depression, and anxiety. However, the neurobiological changes induced by nerve damage in the LC remain unclear. Here, we analyzed excitatory and inhibitory inputs to the LC, as well as the possible damage that noradrenergic neurons suffer after the induction of neuropathic pain through chronic constriction injury (CCI). Neuropathic pain was induced in male Sprague-Dawley rats, and the expression of the vesicular glutamate transporter 1 or 2 (VGLUT1 or VGLUT2), vesicular GABA transporter (VGAT), and cleaved caspase-3 (CC3) was analyzed by immunofluorescence 7 (CCI7d) or 28 days after the original lesion (CCI28d). While no significant differences in the density of VGLUT1 puncta were evident, CCI7d induced a significant increase in the perisomatic VGLUT2/VGAT ratio relative to Sham-operated and CCI28d animals. By contrast, when the entire region of LC is evaluated, there was a significant reduction in the density of VGLUT2 puncta in CCI28d animals, without changes in VGLUT2/VGAT ratio relative to the CCI7d animals. Additionally, changes in the noradrenergic soma size, and a lower density of mitochondria and lysosomes were evident in CCI28d animals. Interestingly, enhanced expression of the apoptotic marker CC3 was also evident in the CCI28d rats, mainly co-localizing with glial fibrillary acidic protein but not with any neuronal or noradrenergic marker. Overall, short-term

pain appears to lead to an increase of markers of excitatory synapses in the perisomatic region of noradrenergic cells in the LC, an effect that is lost after long-term pain, which appears to activate apoptosis.

KEYWORDS

locus coeruleus, vesicular glutamate transporter 1, vesicular glutamate transporter 2, cleaved caspase 3, neuropathic pain

Introduction

Neuropathic pain is a debilitating chronic pain condition that arises after the nervous system is damaged, and it is associated with a plethora of changes in the peripheral and central nervous systems (PNS and CNS). Indeed, functional plasticity has been reported after nerve injury in the noradrenergic locus coeruleus (LC) that affects all dimensions of pain, including its long-term affective consequences on depression and anxiety. The LC is located on the floor of the fourth ventricle in the rostral pons, and it provides and receives extensive projections throughout the neuroaxis, representing a critical hub for pain neurotransmission (Llorca-Torralba et al., 2016; Suarez-Pereira et al., 2021). It has been demonstrated that lesions and pharmacological or chemogenetic inactivation of the LC exacerbate pain responses soon after nerve injury, suggesting enhanced pain sensitivity when the normal LC-noradrenergic circuit is disrupted (Bodnar et al., 1978; Martin et al., 1999; Camarena-Delgado et al., 2021; Llorca-Torralba et al., 2022). However, when pain becomes long-term (3–8 weeks depending on the species, strain, and animal model), selective destruction or inactivation of noradrenergic neurons appears not to modify or dampen neuropathic pain (Brightwell and Taylor, 2009; Camarena-Delgado et al., 2021; Llorca-Torralba et al., 2022). Furthermore, the depressive phenotype that usually accompanies long-term neuropathic pain (Yalcin et al., 2014; Barthas et al., 2015; Alba-Delgado et al., 2016) is abolished by intra-LC administration of lidocaine (Camarena-Delgado et al., 2021) and through chemogenetic approaches targeting that structure (Llorca-Torralba et al., 2022), suggesting that LC activation contributes to pain-induced depression. As such, it appears that LC activity can contribute to early analgesia but also to late pronociception and depressive-like behavior (Llorca-Torralba et al., 2022) although the mechanisms underlying this plasticity are still unclear.

Glutamate is the primary excitatory neurotransmitter in the synaptic afferents received by noradrenergic neurons and these inputs arrive from different regions of the CNS, such as the paragigantocellularis (PGi) nucleus and neocortex (Ennis and Aston-Jones, 1988; Singewald and Philippu, 1998). Evidence suggests that altered glutamatergic regulation might be involved in LC plasticity in nerve-injured animals and indeed, short-term peripheral nerve injury (1 week) increases NMDAR1 activity and pCAMKII following noxious stimulus in a model of neuropathic pain (Alba-Delgado et al., 2012b). Furthermore, long-term pain after nerve injury (6 weeks) increases the basal extracellular glutamate concentration in the LC by downregulating glutamate transporter 1 (GLT1) expression, an astroglial glutamate transporter (Kimura et al., 2015). In contrast to glutamate, GABA acts as the principal inhibitory neurotransmitter on LC neurons *via* the GABA-A and GABA-B receptors (Shefner and Osmanovic, 1991; Corteen et al., 2011), and it also inhibits evoked glutamate release *via* presynaptic GABA-B receptors (Suto et al., 2014). LC neurons receive direct GABAergic inputs and it has been speculated that this inhibitory contribution originates from local GABAergic neurons (Aston-Jones et al., 2004; Jin et al., 2016). Furthermore, spinal nerve ligated (SNL) rats show increased basal levels of GABA release and more intense immunoreactivity for the GABA-synthesizing enzyme glutamic acid decarboxylase (GAD) in the LC 1 week after SNL (Yoshizumi et al., 2012). Hence, GABA tone appears to be enhanced after nerve injury.

These data suggest that a dysregulation of glutamatergic and GABAergic neurotransmission is associated with neuropathic pain. However, alterations to the vesicular glutamate transporters 1 and 2 (VGLUT1 and VGLUT2), and to the vesicular inhibitory amino acid transporter (VGAT) at different time points of neuropathy have not yet been examined. These transporters are markers of excitatory and inhibitory synapses, respectively. Indeed, fast glutamate release at the neuronal synapse relies on small vesicles carrying one vesicular glutamate transporter for vesicular glutamate storage (Fremeau et al., 2004a,b). Although the expression of VGLUT1 and 2 overlap in some regions, one transcript usually predominates in given regions (Fremeau et al., 2001; Herzog et al., 2001; Sakata-Haga et al., 2001; Kaneko and Fujiyama, 2002). Thus, in adults, VGLUT1 is mainly expressed by excitatory synapses originating from excitatory neurons in the cerebral cortex, cerebellum, and hippocampus, whereas VGLUT2 is most abundant in those coming from principal neurons in the diencephalon (thalamus, hypothalamus), brainstem, and spinal cord (SC). Similarly, VGAT is a marker for synapses from GABA-releasing neurons. We previously reported stronger

expression of tyrosine hydroxylase (TH), pCREB, and c-Fos, as well as increased electrophysiological activity of LC cells in association with long-term pain, coinciding with the onset of anxiodepressive disorders (Alba-Delgado et al., 2013, 2018, 2021; Llorca-Torralba et al., 2019a,b, 2022). Thus, we extended these studies by exploring the expression of markers of excitatory and inhibitory synapses in LC, and also, we evaluated the expression of a marker of apoptosis, cleaved caspase-3 (CC3), because CC3 elevation in the LC and other brain areas has been related to depressive-like behaviors (Gonzalez and Aston-Jones, 2008; Todorovic et al., 2019).

In the light of the above, we have explored the density of puncta expressing excitatory and inhibitory vesicular transporters (VGLUT1, VGLUT2, and VGAT), as well as the marker of apoptosis CC3 in the LC by immunohistochemistry at two different times after neuropathic pain induction. Moreover, ultrastructural features of the noradrenergic LC neurons were evaluated in long-term neuropathic pain animals (CCI28d). In the short-term, 7 days after nerve injury, animals have fully developed sensory hypersensitivity, while after long-term neuropathic pain, 28 days after nerve injury, the pain phenotype is accompanied by anxiety and depressive symptoms.

Materials and methods

Animals and experimental design

All the experimental procedures were approved by the Committee for Animal Experimentation at the University of Cadiz, and were carried out in accordance with guidelines for the care and use of laboratory animals: the European Commission directive 2010/63/EU and the Spanish Royal Decree 53/2013. After 1 week of habituation under standard conditions (water and food *ad libitum*, constant room temperature 22 ± 1°C, 12 h light/dark cycle), male Sprague-Dawley rats (250–300 g) were subjected to neuropathic pain for 7 or 28 days. The experimenter was blind to the animal's status in all the behavioral assessments.

Neuropathic pain: Chronic constriction injury model

Neuropathic pain was induced by chronic constriction injury (CCI) of the common left sciatic nerve (Bennett and Xie, 1988; Bravo et al., 2012). Rats were anesthetized with an intraperitoneal (ip) injection of 100 mg/kg ketamine and 20 mg/kg xylazine, and the common left sciatic nerve was exposed at the mid-thigh level proximal to the sciatic trifurcation and separated from the adjacent tissue. Four loose ligatures were tied around the dissected nerve using chromic catgut sutures (4–0) with a 1.5 mm interval between each pair of ligatures. The overlying muscle was closed in layers with synthetic absorbable surgical suture (4–0) and the skin was sutured with silk thread (2–0). In Sham-operated rats, an identical dissection was performed but the sciatic nerve was not ligated. The animals were analyzed 7 (short-term, CCI7d) or 28 days (long-term, CCI28d) post-surgery.

Sensory pain behavior

Mechanical hypersensitivity (von Frey test)

In order to test whether animals developed neuropathy, at the end of the experiment, mechanical allodynia was measured in rats using an automatic von Frey apparatus (Dynamic Plantar Anesthesiometer Cat. No. 37400-002, Ugo Basile, Italy; Bravo et al., 2013). Animals were randomly placed in plastic cages with an operable metal grid to which they had been habituated for 30 min prior to the test. A vertical force was applied to the hind paw that increased from 0 to 50 g over a period of 20 s, and the threshold was determined as the average of two values that induced a withdrawal response (with a 50 g cut-off).

Cold hypersensitivity (acetone test)

Animals were placed individually into Plexiglas chambers on a metal grid, and a drop of acetone (100 μl) was applied to the center of the ipsilateral and contralateral hind paw with a pipette (Bravo et al., 2012). The acetone was applied four times to each hind paw Alternately at 5 min intervals and the responses were recorded over 1 min according to the following scale: 0, no response; 1, quick withdrawal, flick or stamping of the paw; 2, prolonged withdrawal or repeated flicking of the paw; and 3, repeated flicking of the paw with persistent licking directed at the ventral side of the paw. The cumulative score for each rat was obtained by summing the score and dividing it by the number of assays.

Emotional-like behavior

Elevated zero maze test

Anxiety-like behavior was evaluated in the elevated zero maze (EZM) test (Llorca-Torralba et al., 2018). Animals were placed in a black, 10 cm wide circular track (120 cm in diameter), elevated 70 cm above the ground, with two opposing enclosed arms and two open arms, and with a 7-mm-high edge to prevent falls. The time spent in the open arm (%, a measure of anxiety) was monitored over a 5-min test period using the SMART video software (Spontaneous Motor Activity Recording and Tracking: Panlab, S.L., Barcelona, Spain). Anxiety-like behavior was defined as a decrease in the time spent in the open arm.

Forced swimming test

Depressive-like behavior was evaluated in the forced swimming test (FST) (Llorca-Torralba et al., 2019a). Animals were placed individually in large plastic cylinders filled to a depth of 30 cm with water at 25 ± 1°C, over two different sessions: a 15-min pre-test and a 5-min test performed 24 h later. The predominant behaviors were recorded (climbing, swimming, or immobility) and scored in each 5 s period of the 300 s test session using customized software (Red-Mice, Cadiz, Spain). Immobility behavior was determined when no activity was observed other than the movements necessary to keep the animal's head above water. Climbing behavior was measured when the rats made vigorous upward movements with their forepaws in and out of the water. Swimming was considered the predominant behavior when the rats moved around the cylinder. Depressive-like behavior was defined as an increase in mean immobility.

Perfusion, microtomy, and immunohistochemistry

The distribution of VGLUT1 and VGLUT2 in the LC region was assessed in brain tissue from the rats. Animals were deeply anesthetized with sodium pentobarbital and perfused transcardially with 4% paraformaldehyde (PFA) in phosphate buffer (PB, 0.1 M) for confocal microscopy ($n = 5$–6) studies and with an additional 0.5% glutaraldehyde for electron microscopy (EM) studies ($n = 3$). The rat's brain was removed and cryoprotected in 30% sucrose in PB (0.1 M) for 48 h, and coronal vibratome sections (50 μm thick: Leica VT 1000E) of the region containing the LC were collected in four series and processed "free-floating" for immunohistochemistry. Briefly, sections were washed in phosphate-buffered saline (PBS) and then incubated for 1 h in 10% normal donkey serum (NDS: Abcys) in PBS with 0.3% Triton X-100 (PBST: Sigma-Aldrich). The sections were then incubated for 48 h at 4°C with the appropriate primary antibody or antibody cocktail (see Table 1) diluted in PBST with 0.5% of NDS as follows: (a) triple immunostaining using antibodies against TH, VGLUT2, and VGAT; (b) double staining with antibodies against TH and VGLUT1; (c) double staining using antibodies against dopamine beta hydroxylase (DBH) and CC3. In order to detect the expression of CC3 in $GFAP^+$ or $NeuN^+$ cells, the brains of the second group of animals ($n = 2$–3 per group) were processed and 30-μm-thick coronal sections were triple stained using antibodies against NeuN, CC3, and GFAP, or against DBH, CC3, and GFAP.

After washing, the sections were incubated for 1 h at room temperature (RT) with secondary antibodies conjugated to the appropriate fluorochrome or streptavidin (see Table 1), also diluted in PBST. Finally, sections were washed in PB (0.1 M), mounted on slides, and coverslipped using fluorescence mounting medium (Dako).

Quantification of VGLUT1, VLGUT2, and VGAT puncta in the LC

VGLUT1 was distributed around the pericoerulear region but not specifically surrounding the soma of TH^+ cells (Figure 2; Barr and Van Bockstaele, 2005). Consequently, the density of VGLUT1 puncta was evaluated in the entire LC region. Confocal z-stacks of three to four quadrants in a total of three LC sections per rat were acquired with a 1 μm step size and with a 63× oil immersion objective on a Zeiss Axio Observer Z1 Confocal microscope. The images were analyzed using a Macro generated from ImageJ software that converted the image to RGB color. The density of the VGLUT1 puncta was quantified using a threshold signal intensity (170 on a 0–255 Brightness scale) that maximized the selection of puncta and minimized the background noise. The results were expressed as the number of puncta/μm^2.

VGLUT2 and VGAT were expressed around the pericoerulear region and specifically, surrounding the somata of TH^+ cells. Thus, the density of puncta expressing VGLUT2 or VGAT puncta was evaluated in the entire LC region but also, surrounding noradrenergic somata, using a protocol described previously (Guirado et al., 2018) and adapted to the LC. Confocal z-stack of three to four quadrants in a total of three LC sections per rat were acquired with 1 μm step size with a 63× oil immersion objective by using a confocal microscope (FV 10i; Olympus, Japan). For perisomatic study of VGLUT2 and VGAT markers, a mean of 30 to 35 neurons was randomly selected in the sections acquired. The profile of the noradrenergic soma of these neurons was drawn manually to assess the density of the puncta around the perimeter. This manual selection was enlarged by 0.5 μm in order to define the perisomatic area. The linear density of VGLUT2 and VGAT immunoreactive puncta within an optical section was analyzed manually using ImageJ (National Institutes of Health, Bethesda, Maryland). The results were expressed as the number of puncta/μm^2.

The expression of all the vesicular transporter markers studied was represented along the dorsal–ventral axis of the LC (−9.72 to −9.96 from Bregma, three slices per animal; Llorca-Torralba et al., 2022).

Quantification of the soma size of noradrenergic LC neurons

To detect changes in soma size, the mean soma area per group was calculated in 30–35 randomly selected TH^+ cells per animal. Each TH^+ soma was outlined manually using a

TABLE 1 List of primary and secondary antibodies used in the study.

	Dilution	Company
Primary antibodies		
Guinea pig anti-VGLUT1 (*Vesicular Glutamate Transporter 1*)	1:2,000	Millipore, AB5905
Guinea pig anti-VGLUT2 (*Glutamate Transporter 2*)	1:2,000	Millipore, AB2251-I
Rabbit anti-VGAT (*Vesicular GABA Transporter*)	1:1,000	Synaptic systems, 131 002
Mouse anti-DBH (*Dopamine Beta Hydroxylase*)	1:1,000	Millipore, MAB308
Rabbit anti-CC3 (*Cleaved Caspase-3* (*Asp175*))	1:500	Cell signaling, #9661S
Goat anti-GFAP (*Glial fibrillary acidic protein*)	1:1,000	Abcam Ab53554
Rabbit anti-TH (Tyrosine hydroxylase)	1:1,000	Millipore, AB152
Mouse anti-NeuN	1:500	Millipore MAB377
Secondary antibodies		
Goat anti-Guinea Pig A-647	1:1,000	Invitrogen A-21450
Donkey anti-mouse Alexa-555	1:1,000	Invitrogen A31570
Biotinylated Donkey anti-guinea pig	1:200	Jackson 706-065-148
Biotinylated Donkey anti-goat	1:200	Jackson 705-065-147
Donkey anti-rabbit Alexa-488	1:1,000	Invitrogen A21206
Streptavidin Alexa 568 conjugate	1:1,000	Invitrogen S11226
Donkey anti-mouse Alexa-647	1:1,000	Invitrogen A31571

computer mouse and the cross-sectional area was calculated with ImageJ software. The results were represented in μm^2.

Electron microscopy

For the EM studies, Sprague-Dawley rats (Sham and CCI28d, $n = 3$) were perfused transcardially with fixative containing 4% formaldehyde and 0.5% glutaraldehyde in PB (0.1 M, pH 7.4). Coronal vibratome sections (50 μm thick) through the rostrocaudal extent of the LC were collected in PB (0.1 M) and left for 20 min in 1% sodium borohydride in PB (0.1 M) to remove reactive aldehydes. After rinsing extensively in PB (0.1 M), the sections were then incubated with the primary antibody. TH was detected using the avidin–biotin–peroxidase (ABC) method. The sections were first blocked with 10% NDS in PB (0.1 M) for 45 min at RT and then probed for 48 h at 4°C with a rabbit antiserum against TH (Millipore) diluted 1:1,000 in PB containing 1% NDS and 0.05% sodium azide. A biotinylated donkey anti-rabbit (Thermo Scientific, Fremont, CA, USA) antibody, diluted 1:200 in PB, was used to detect the antibody binding for 2 h at RT, and the sections were then incubated for 2 h at RT with an avidin-biotinylated horseradish peroxidase complex (ABC: Vector Labs. Burlingame, CA, USA) diluted 1:200 in PB. The peroxidase reaction was then developed over 5 min at RT using 0.05% 3,3-diaminobenzidine tetrahydrochloride (DAB: Sigma-Aldrich, St. Louis, MO, USA) and 0.003% hydrogen peroxide in PB. Sections were carefully rinsed in PB after each step.

After performing immunohistochemistry, the sections were treated for 45 min at RT with 1% osmium tetroxide (Electron Microscopy Sciences, Hatfield, PA, USA) containing 7% glucose in PB. Subsequently, the sections destined for EM were stained with uranyl acetate (Electron Microscopy Sciences) in maleate buffer (pH 4.5), dehydrated through a graded ethanol series and in propylene oxide (Fluka AG, Buch, Switzerland), and flat-embedded in Durcupan (Fluka AG) between slides and coverslips. Durcupan was polymerized overnight at 60°C and the flat-embedded sections were examined under a light microscope to select the LC tissue containing TH^+ neurons for further analyses. The selected material was re-embedded in Durcupan and serial ultrathin sections (60 nm thick) were obtained in an ultramicrotome and mounted on formvar-coated nickel grids. The grids were contrasted with 1% uranyl acetate in 70% ethanol for 1 min and then in a 0.2% lead citrate contrasting solution for 5 min (Venable and Coggeshall, 1965). The sections were observed under a transmission electron microscope (Jeol JEM 1010) at 100 kV.

Ultrathin sections of tissue immediately adjacent to the fourth ventricle in the region of the LC were captured by EM at 4,000× magnification. The densities of mitochondria and lysosomes found in a mean of 9 to 10 neurons per animal ($n = 3$ per group) were analyzed and the results were represented in μm^2.

Axons were classified according to the following myelin compaction code (Savigni et al., 2013): (A) normally myelinated, myelin in thick, high-electron density, with no signs of decompaction; (B) marginally decompacted myelin, with axons

presenting small signs of decompaction in ≤20% of the circumference of the myelin sheath; (C) partially decompacted myelin, with ≥20% of the myelin sheath showing signs of decompaction; (D) fully decompacted myelin with the entire axon ensheathed with multiple layers of thin, moderate-electron dense myelin; and (E) unmyelinated.

Quantification of CC3 and GFAP in the LC

Confocal z-stack of three to four quadrants in a total of three LC sections per rat were acquired with a 63× oil immersion objective ($n = 4$–5 rats per group) on a Zeiss LSM 880 Confocal microscope with FAST Airyscan (Carl Zeiss Microscopy GmbH, Germany). $CC3^+$ cells were quantified manually in the LC region using the ImageJ Cell Counter plugin (National Institutes of Health, Bethesda, Maryland). The results were expressed as the mean number of $CC3^+$ cells per animal in the whole LC region and along the dorso-ventral LC axis. The relative $GFAP^+$ area was quantified using a threshold (14 on a 0–255 greyscale) for the signal intensity that maximized the selection of expressing cells while minimizing the background noise. A mean of three to four quadrants per section was represented and expressed as the percentage area occupied by GFAP.

Statistical analysis

All the data were analyzed using Graph-Pad Prism 9.1 (GraphPad San Diego, CA) and Statistic 10.0 software (Statistic, Tulsa, Oklahoma), and they were presented as the mean ± SEM. One-way analysis of variance (ANOVA) was followed by the appropriate post-hoc tests (Tukey test) and an unpaired Student's t-test was used to compare the values between the two groups. In all cases, $p < 0.05$ was considered significant.

Results

Neuropathic pain induces nociceptive responses and anxiodepressive-like behavior

As expected, nerve-injured animals displayed pain hypersensitivity in response to mechanical and thermal stimuli, both at 7- and 28-days post-surgery ($p < 0.001$: Figures 1A,B). No differences were observed in the contralateral paw between the groups when evaluated by the von Frey test (values obtained: Sham 34.79 ± 3.91, CCI7d 38. 57 ± 7.16, CCI28d 39.28 ± 7.10) or acetone test (values obtained: Sham 0.13 ± 0.21, CCI7d 0.25 ± 0.22, CCI28d 0.21 ± 0.25). However, when anxiety and depressive-like behaviors were evaluated (Figures 1C,D), CCI28d animals spent significantly less time in the open arms of the EZM than Sham ($p < 0.05$) and CCI7d ($p < 0.01$) animals, reflecting an anxiogenic state (Figure 1C). In the FST, the CCI28d rats spent more time in the immobile state relative to the Sham and CCI-7d animals ($p < 0.001$), whereas their climbing time decreased ($p < 0.001$), indicative of a depressive-like state. No changes were observed in swimming behavior (Figure 1D).

Expression of VGLUT1, VGLUT2, and VGAT in the LC

As a first approach, we assessed the distribution of excitatory VGLUT1 and VGLUT2 in the entire LC region. In accordance with previous studies, VGLUT1 expression was clearly evident around the pericoerulear region while VGLUT2 expression was prominent in both the pericoerulear region and surrounding the somata (Figures 2A,B: Barr and Van Bockstaele, 2005). When the density of VGLUT1 puncta was quantified across the whole LC region (Figures 2C–E), no significant differences were detected between the three experimental groups (Figures 2F–H). Similarly, there were no significant differences between the different groups in the size of the neuronal somata when the area they occupied was explored (Figures 2I,J). However, the frequency distribution of the soma sizes revealed an increase in the proportion of intermediate cells following CCI, which was significantly different in the CCI28d rats compared to the Sham group (150 μm^2, $p < 0.05$; Figure 2I).

In terms of the density of VGLUT2 or VGAT immunoreactive puncta in the LC region (Figure 3), one-way ANOVA revealed a significant effect of CCI surgery on these parameters ($p < 0.001$), an effect that persisted in the dorsal ($p < 0.01$) and ventral region of the LC ($p < 0.001$). Indeed, there was a significant decrease in $VGLUT2^+$ puncta in the LC of CCI28d rats relative to the Sham ($p < 0.05$) and CCI7d animals ($p < 0.001$; Figure 3D), an effect that was particularly evident in the ventral region of the LC (Figures 3E,F). However, the density of VGAT puncta or the VGLUT2/VGAT ratio was no different between the groups of animals.

In addition, the density of VGLUT2 and VGAT puncta surrounding the soma of noradrenergic neurons was analyzed (Figure 4) and one-way ANOVA of the $VGLUT2^+$ puncta revealed a significant effect of CCI surgery ($p < 0.05$) in the dorsal ($p < 0.05$) but not the ventral region of the LC (Figures 4F,G). Indeed, an overall increase of $VGLUT2^+$ puncta was evident in the LC of CCI7d rats relative to the CCI28d animals ($p < 0.05$: Figure 4E), an effect that was detected in the dorsal but not in the ventral region of the LC ($p < 0.05$: Figures 4F,G). The density of VGAT immunoreactive puncta was not altered in any group, although there was a prominent increase in the VGLUT2/VGAT ratio in CCI7d rats relative to the Sham and CCI28d animals ($p < 0.01$: Figure 4K). This

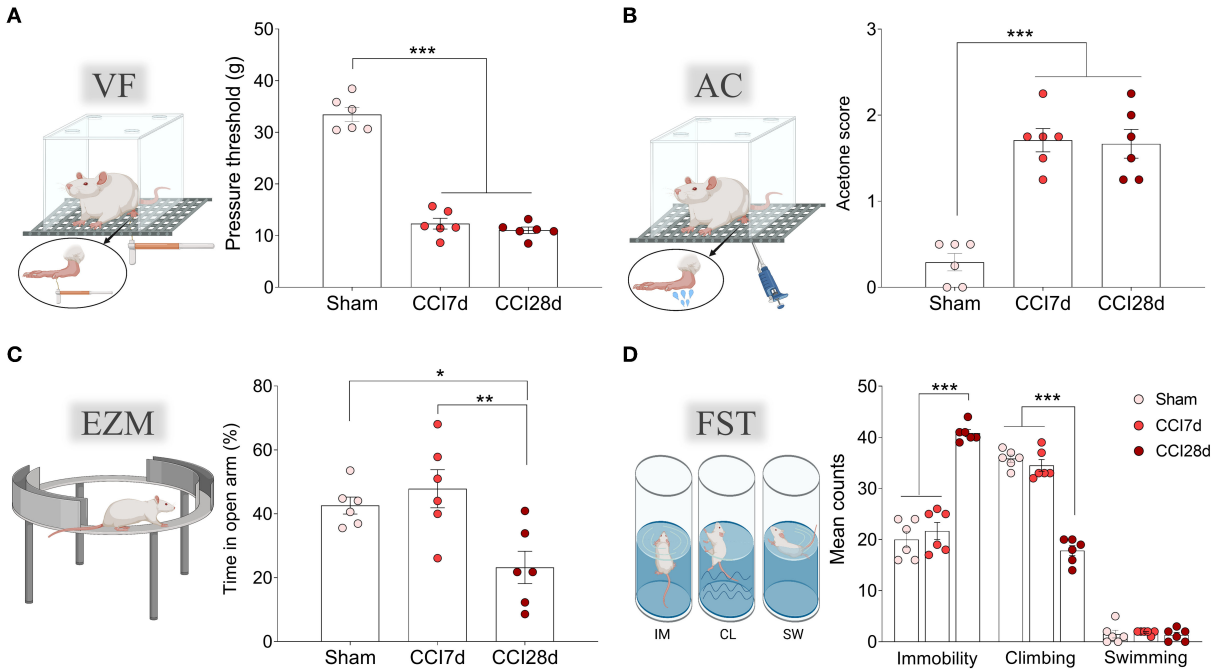

FIGURE 1
Nociceptive and emotional behaviors after chronic constriction injury. **(A)** Mechanical hypersensitivity (g) of the ipsilateral paw in response to von Frey (VF) hair stimulation (0–50 g, 20 s). **(B)** Thermal hypersensitivity of the ipsilateral paw in response to acetone (AC) application (100 μl). **(C)** Anxiety-related behavior in the elevated zero maze test (EZM) and the relative time spent in the open areas (5 min test). **(D)** Depressive-related behavior in the forced swimming test (FST) relative to the predominant behavior (IM, immobility; CL, climbing; SW, swimming: 5 min test). Each bar represents the mean ± SEM of six animals/group: $*p < 0.05$, $**p < 0.01$, $***p < 0.001$ as assessed by one-way ANOVA followed by Tukey's post-test.

increase in the VGLUT2/VGAT ratio was notable in the dorsal ($p < 0.01$: Figure 4L) but not the ventral LC (Figure 4M).

Ultrastructural changes of noradrenergic LC neurons

In a different set of animals, the ultrastructural features of the noradrenergic LC neurons of Sham and CCI28d animals were explored (Figures 5A,B). The EM images from Sham animals were similar to those described previously (Groves and Wilson, 1980), whereas long-term nerve injury (CCI28d) appeared to induce changes in LC neurons evidenced mainly through the presence of more dilated ER and mitochondria in EM images. Mitochondria and lysosomes were quantified in a mean of nine to ten neurons per animal ($n = 3$ per group), revealing a significant decrease in their number/μm^2 ($^{**}p < 0.01$: Figures 5C,D). When myelin compaction was assessed, the percentage of (A) normally myelinated, (B) marginally decompacted myelin, and (C) partially decompacted myelin was similar in Sham and CCI28d rats. However, there was a trend in the CCI28d group toward an increase in the level of (D) fully decompacted myelin (CCI28d 8.96%, Sham 2.94%) and of (E) unmyelinated axons (CCI28d 4.05%, Sham 1.56%: Figures 5E,F).

Expression of CC3 in DBH$^+$ and DBH$^-$ LC cells

In order to determine the cell damage provoked in the LC as a result of CCI, we examined the density of CC3$^+$ cells in this structure (Figures 6A–C). One-way ANOVA revealed a significant effect of CCI surgery on the global LC ($p < 0.001$), which was also evident when the dorsal ($p < 0.05$) and ventral regions of the LC ($p < 0.01$) were analyzed separately. Tukey's multiple comparisons test revealed a significant increase in the density of CC3$^+$ cells in CCI28d rats relative to the Sham ($p < 0.001$) and CCI7d animals ($p < 0.05$) when the LC is considered globally (Figure 6D). This was also the case in the dorsal region of the LC (Figure 6E), whereas in the ventral LC domain, there was an increase in the number of CC3$^+$ cells in CCI28d rats relative to Sham animals ($p < 0.01$), yet not when compared to the LC of CCI7d rats (Figure 6F).

In the images captured, most CC3$^+$ cells did not express DBH, suggesting that another type of cell was expressing

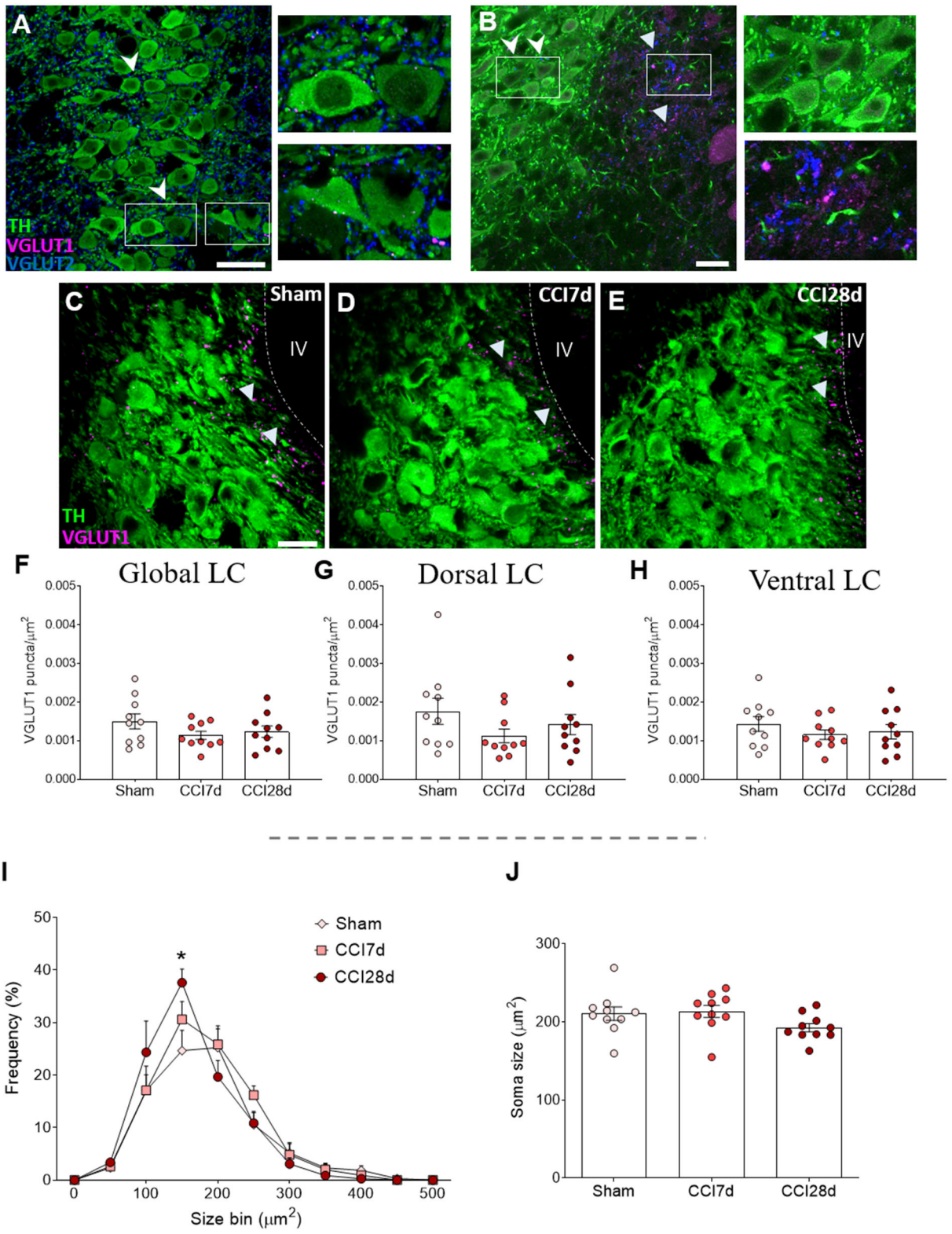

FIGURE 2
Study of VGLUT1 expression in the LC of neuropathic pain rats. **(A,B)** Localization of the vesicular glutamate transporter 1 (VGLUT1) and vesicular transporter 2 (VGLUT2) in the LC region. The arrowheads point to VGLUT2^{+} puncta in both the pericoerulear and perisomatic area (TH green; VGLUT1 magenta; VGLUT2 blue: scale bar, 20 μm). The triangles point to VGLUT1^{+} puncta mainly in the pericoerulear area. **(C–E)**
(Continued)

FIGURE 2
Representative confocal images of the LC showing neurons expressing TH and puncta-expressing VGLUT1 in **(C)** Sham, **(D)** CCI7d, and **(E)** CCI28d rats (TH green; VGLUT1 magenta: scale bar, 20 μm). **(F–H)** Quantification of the density of VGLUT1$^+$ puncta in the **(F)** global, **(G)** dorsal, and **(H)** ventral LC. The data represent the mean ± SEM of the number of the puncta/μm^2 (obtained from three to four quadrants in a total of three LC sections per rat). The graphs depict **(I)** the frequency distribution of the TH$^+$ soma size and **(J)** the mean of soma size for each experimental group. The data are presented as the mean ± SEM of 30–35 random neurons per animal: *$p < 0.05$ vs. Sham, one-way ANOVA followed by a Tukey's post-test.

CC3. When the density of CC3$^+$ in DBH$^+$ and DBH$^-$ was considered, the low density of CC3$^+$ in DBH$^+$ cells was similar in each experimental group (Sham 4.4 ± 2.7, CCI7d 5.1 ± 3.1, CCI28d 7.43± 2.7: Figures 6G–I).

However, in the DBH$^-$ cells, one-way ANOVA revealed a significant effect of CCI surgery in the global ($p < 0.001$) and as well as in the dorsal and ventral region ($p < 0.01$) of LC. Tukey's multiple comparisons tests revealed that CC3 was detected more often in DBH$^-$ cells at CCI28d than in the Sham rats ($p < 0.001$) and this difference was lesser extent compared to CCI7d rats ($p < 0.01$: Figure 6J). The differences between the Sham and CCI28d were also evident in the dorsal but not in the ventral region of the LC ($p < 0.01$: Figures 6K,L).

Expression of CC3 in GFAP$^+$ LC cells

We performed triple immunofluorescence to determine the identity of the CC3$^+$ cells, first combining staining for CC3 with NeuN and GFAP (Figure 7). There was robust co-expression of CC3 with GFAP but not with NeuN in the cells (Figure 7A), suggesting that CC3 was mainly expressed by astrocytes in the LC. As a result, we assessed the co-localization of CC3, DBH, and GFAP (Figures 8A–D), recording the mean number of CC3$^+$ cells, and the number of cells immunostained for both CC3 and DBH or GFAP in both entire LC and the dorsal/ventral regions (Figures 8E–M). One-way ANOVA revealed a significant effect of CCI surgery on the expression of CC3 in the LC as a whole ($p < 0.05$), although this was not evident when the dorsal or ventral LC were considered separately. A Tukey's multiple comparisons test revealed that there were significantly more CC3$^+$ cells in the CCI28d LC than that of the Sham rats ($p < 0.05$), yet not relative to the CCI7d animals (Figure 8E). There were no differences in the proportion of DBH$^+$ cells expressing CC3 between the groups (Figures 8H–J), although as seen previously, the CC3$^+$ cells observed in the CCI28d LC coincided with GFAP$^+$ cells and again there were differences compared to the Sham group ($p < 0.05$, Tukey's test: Figure 8K). However, this effect was no longer evident when the dorsal or ventral LC regions were considered separately (Figures 8L,M). Although CC3 was co-expressed with GFAP, the quantification of GFAP expression in the LC was similar in all three experimental groups (Figures 7E–G).

Discussion

This study shows that short-term peripheral nerve injury (CCI7d) increases the expression of markers of excitatory synapses in perisomatic puncta of noradrenergic cells in the LC relative to long-term pain (CCI28d). In addition, long-term pain is associated with a decrease in the density of mitochondria and lysosomes, and an increase of the CC3 marker in glia but not in noradrenergic cells.

The density of VGLUTs and VGAT in the LC was explored here. Vesicular glutamate or GABA transporters are present in glutamatergic or GABAergic vesicles where they serve to transport the corresponding neurotransmitter into the synapse to ensure the release of glutamate or GABA into the synaptic cleft (Roth and Draguhn, 2012; Siksou et al., 2013). Short-term pain (CCI7d) did not produce significant differences in VGLUT1, VGLUT2, or VGAT compared to Sham animals in the region containing the entire LC. However, when perisomatic puncta expressing excitatory (VGLUT2) or inhibitory (VGAT) markers on noradrenergic cells were considered, an increase in VGLUT2 and a tendency to decrease the expression of VGAT was seen at CCI7d relative to CCI28d animals. The increase in the VGLUT2/VGAT ratio in CCI7d rats relative to Sham and CCI28d animals suggests an increase in the excitatory/inhibitory balance of neurotransmission at this time point of nerve injury. Whereas VGLUT1 is localized in excitatory neurons in the cerebral cortex, VGLUT2 is found mostly in synapses from neurons in the diencephalon (thalamus, hypothalamus), brainstem, or spinal cord (Fremeau et al., 2001, 2004a; Herzog et al., 2001; Kaneko and Fujiyama, 2002; Varoqui et al., 2002). Footpad inflammation was previously seen to increase glutamate release in the LC (Nonaka et al., 2017). Furthermore, glutamate stimulates noradrenaline release in the SC by activating LC AMPA (a-amino-3-hydroxy-5-methylisoxazole-4-propionic acid) receptors (Singewald and Philippu, 1998), suggesting that LC glutamatergic activation is caused by acute nociceptive input. Accordingly, increased NMDAR1 activity and pCAMKII are observed in the LC of CCI7d rats following a noxious stimulus (Alba-Delgado et al., 2012b). We previously demonstrated that 7 days of neuropathy increases PGi activation (Alba-Delgado et al., 2012a), the source of the main glutamatergic afferents to the LC that expresses VGLUT2. This suggests that the PGi could be responsible for the increase in the excitatory marker observed in CCI7d rats, which would be consistent with the

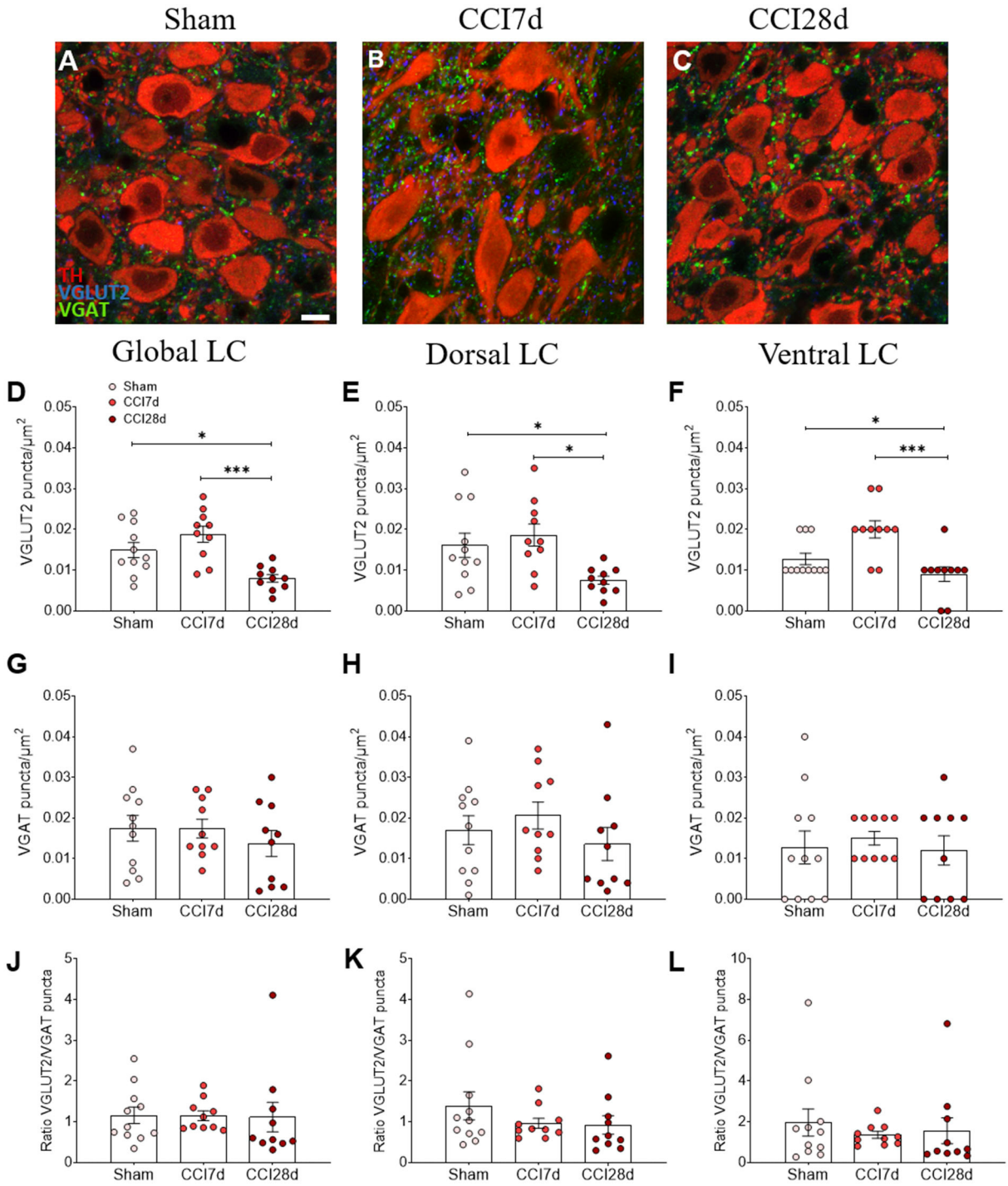

FIGURE 3
VGLUT2 and VGAT expression in the LC of neuropathic pain rats. **(A–C)** Representative confocal images showing the density of puncta expressing VGLUT2 and VGAT in the LC of **(A)** Sham, **(B)** CCI7d, and **(C)** CCI28d rats (TH red; VGLUT2 blue; VGAT green: scale bar, 10 µm). **(D–F)** Quantification of the density of puncta expressing VGLUT2 in the **(D)** global, **(E)** dorsal, and **(F)** ventral LC. **(G–I)** Quantification of the density of VGAT puncta in the **(G)** global, **(H)** dorsal, and **(I)** ventral LC. **(J–L)** Representation of the ratio of VGLUT2/VGAT puncta in the **(J)** global, **(K)** dorsal, and **(L)** ventral LC. The data represent the mean ± SEM of the number of the puncta/µm^2 (obtained from three to four quadrants in a total of three LC sections per rat): *$p < 0.05$, ***$p < 0.001$ vs. the corresponding group, one-way ANOVA followed by a Tukey's post-test.

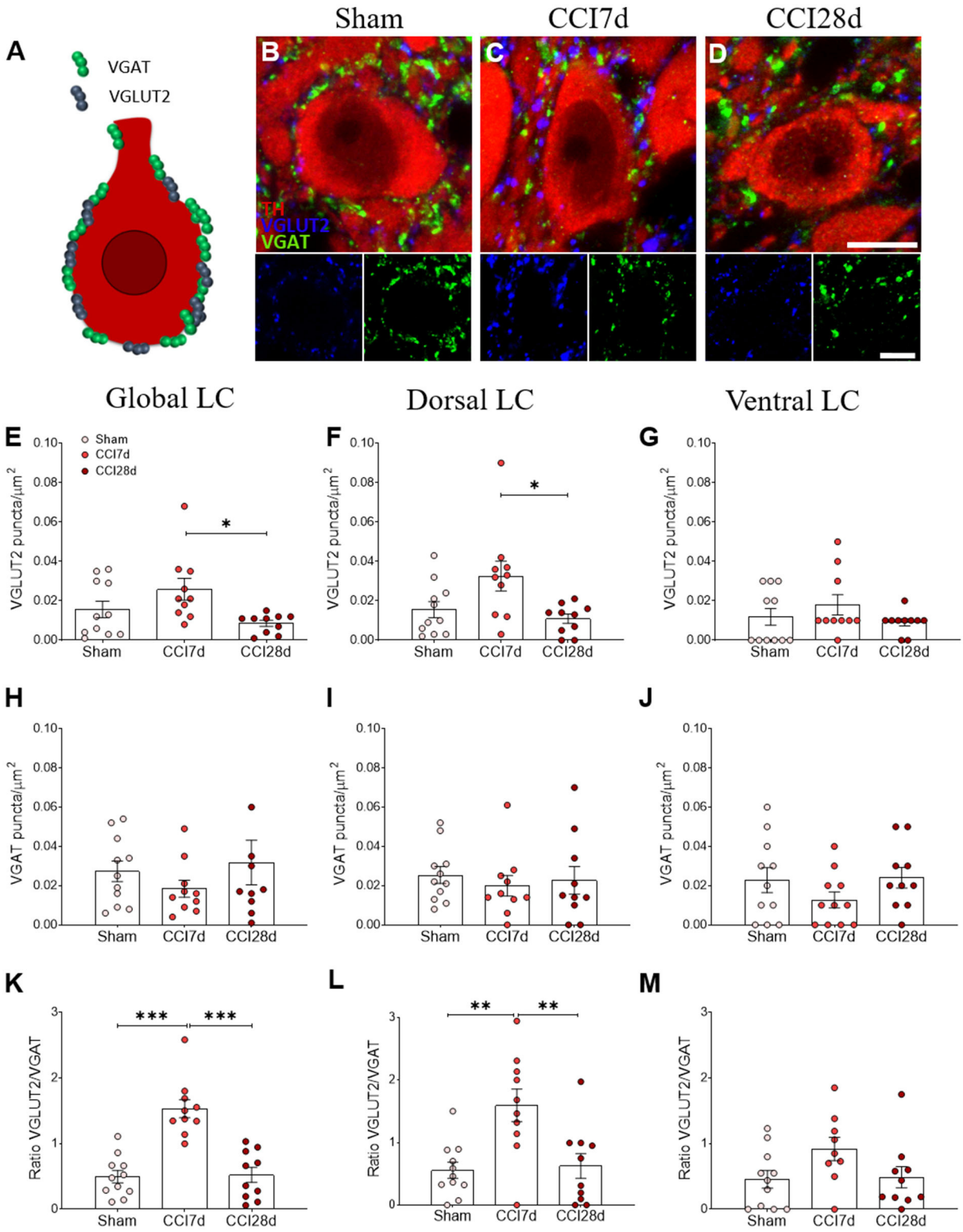

FIGURE 4
Perisomatic puncta expressing VGLUT2 and VGAT in LC neurons of neuropathic pain rats. **(A–D)** Representative confocal images showing perisomatic density of puncta expressing VGLUT2 and VGAT in the LC of **(B)** Sham, **(C)** CCI7d, and **(D)** CCI28d rats (TH red; VGLUT2 blue; VGAT green: scale bar, 10 μm). **(E–G)** Quantification of the VGLUT2 expression in the **(E)** global, **(F)** dorsal, and **(G)** ventral LC. **(H–J)** Quantification of VGAT expression in the **(H)** global, **(I)** dorsal, and **(J)** ventral LC. **(K–M)** Representation of the ratio of VGLUT2/VGAT puncta in the **(K)** global, **(L)** dorsal, and **(M)** ventral LC. The data are presented as the mean ± SEM of the number of the puncta/μm^2 (obtained from 30 to 35 neurons from three LC sections per rat): $^*p < 0.05$, $^{**}p < 0.01$, $^{***}p < 0.001$ vs. the corresponding group, one-way ANOVA followed by a Tukey's post-test.

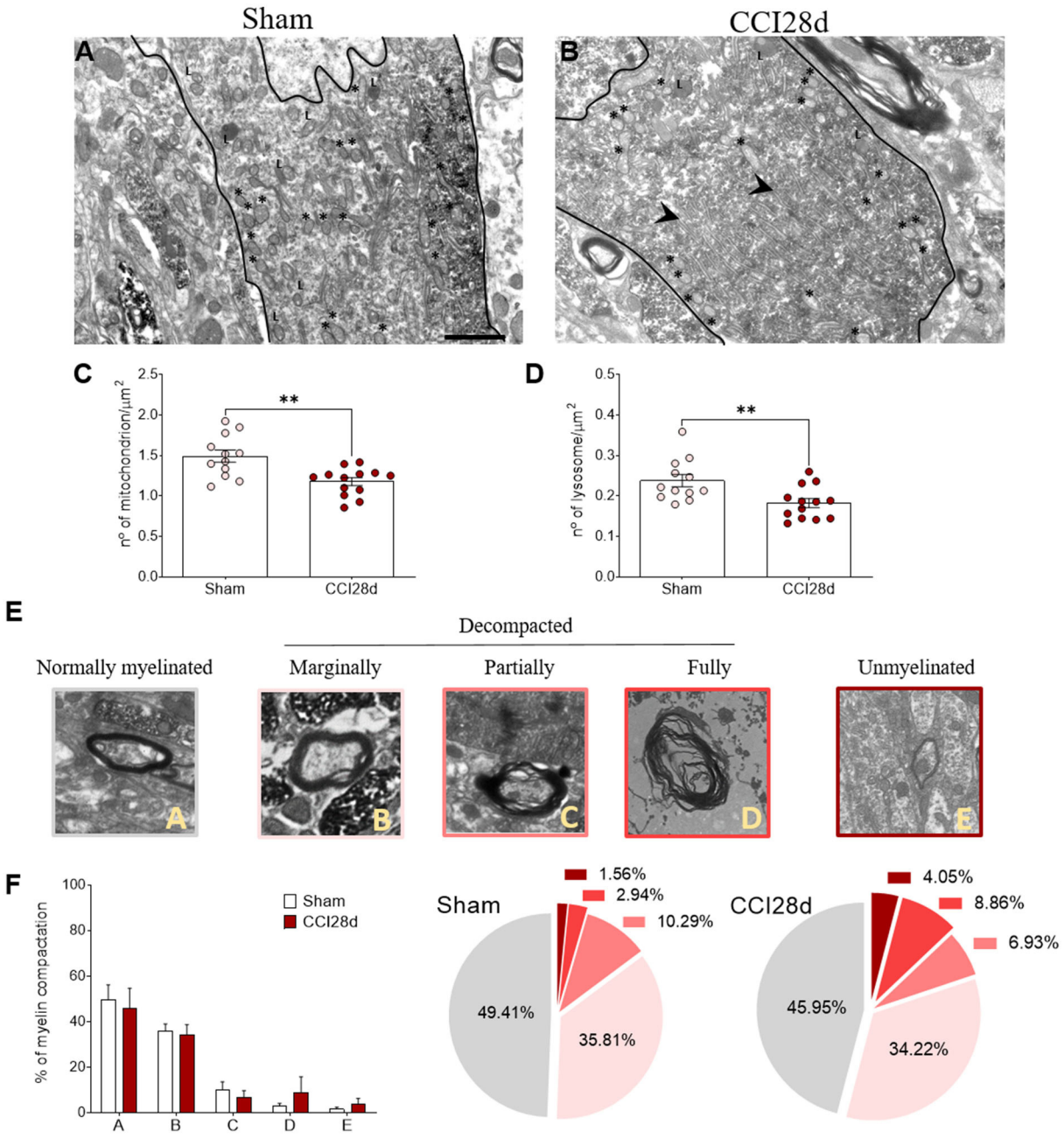

FIGURE 5
Ultrastructural studies of noradrenergic LC neurons in neuropathic pain rats. Representative electron microscopy images of **(A)** Sham and **(B)** CCI28d rats. The asterisks indicate mitochondria and the arrowheads point to the dilated ER: L, lysosome. Scale bar: 2 µm. **(C,D)** Quantification of the number of **(C)** mitochondria and **(D)** lysosomes. **(E,F)** Representative images and quantification of the relative myelin compaction scored from A to E as axons with normal myelin **(A)**, marginally **(B)**, partially **(C)**, fully decompacted **(D)**, and unmyelinated **(E)**.

increase in excitatory synaptic transmission in LC neurons seen previously, 7 days after CCI (Rohampour et al., 2017). On the other hand, an increase in noradrenergic immunoreactivity in the spinal dorsal horn was reported 2 days and 2 weeks after CCI (Ma and Eisenach, 2003). Together, these data might suggest that short-term nerve injury affects excitatory synaptic markers significantly in LC neurons, which could imply a gradual enhancement in the noradrenergic system as an adaptive mechanism to counteract chronic pain transmission.

It was also reported previously that SNL rats increase basal GABA release and the immunoreactivity for the GABA-synthesizing enzyme GAD in the LC 5 days after SNL

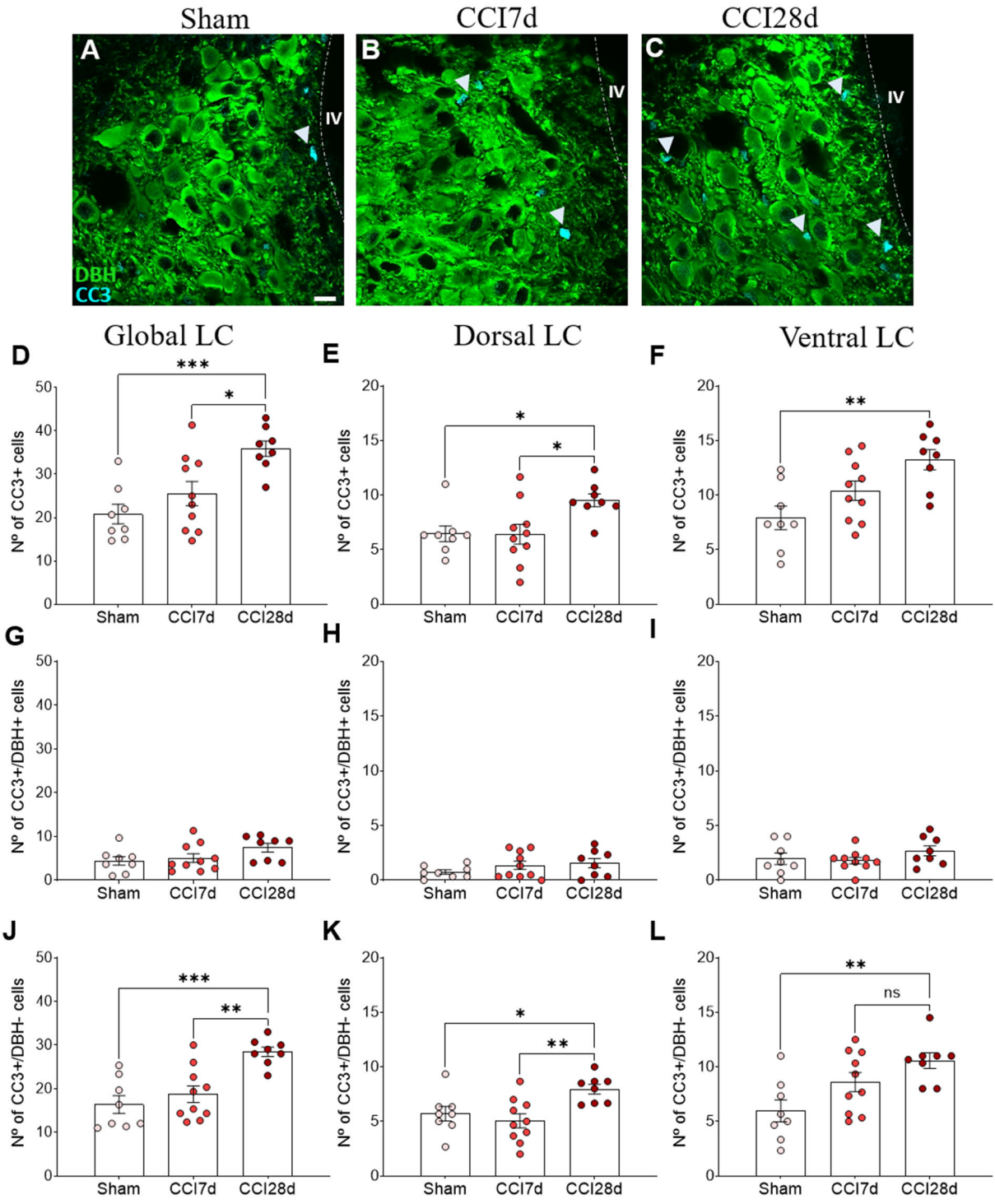

FIGURE 6
Cell damage in the LC of neuropathic pain rats. **(A–C)** Representative confocal images of CC3 expression in DBH^+ neurons of the LC in **(A)** Sham, **(B)** CCI7d, and **(C)** CCI28d rats (DBH green, CC3 blue: scale bar, 10 μm). **(D–F)** Quantification of the number of $CC3^+$ cells in the **(D)** global, **(E)** dorsal, and **(F)** ventral LC. **(G–I)** Quantification of the number of $CC3^+/DBH^+$ cells in the **(G)** global, **(H)** dorsal, and **(I)** ventral LC. **(J–L)** Quantification of the number of $CC3^+/DBH^-$ cells in the **(J)** global, **(K)** dorsal, and **(L)** ventral LC. The data are presented as the mean ± SEM of the number of $CC3^+$ cells (obtained from three to four quadrants in a total of three LC sections per rat): $^*p < 0.05$, $^{**}p < 0.01$, $^{***}p < 0.001$ vs. the indicated group, one-way ANOVA followed by a Tukey's post-test.

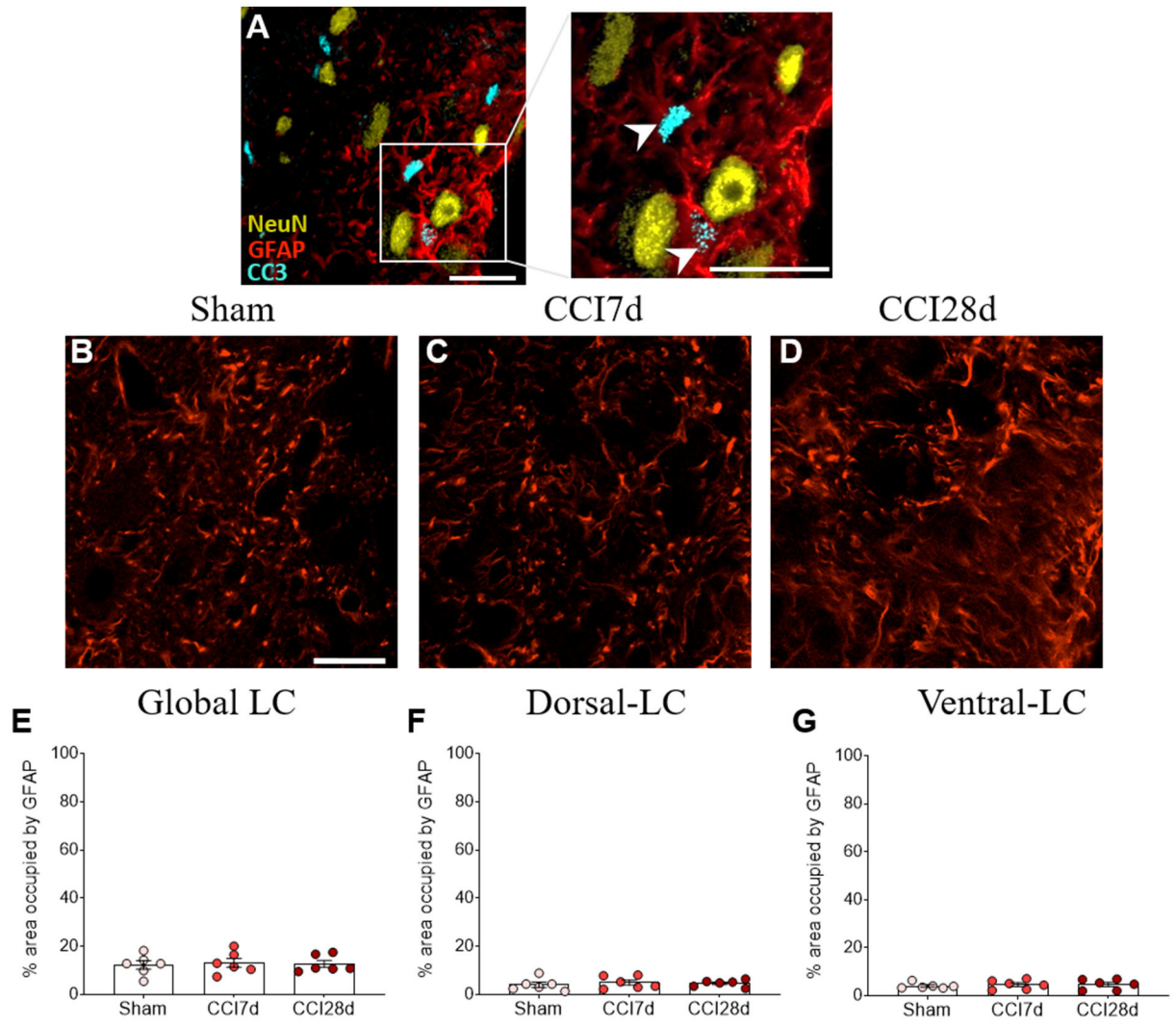

FIGURE 7
Study of the CC3 in GFAP$^+$ or NeuN$^+$ cells in the LC. **(A)** Representative confocal images of CC3$^+$/GFAP$^+$ cells without NeuN (NeuN yellow, GFAP red, CC3 blue; scale bar, 20 μm). **(B–D)** Representative confocal images of GFAP expression in **(B)** Sham, **(C)** CCI7d, and **(D)** CCI28d rats. **(E–G)** Quantification of the area occupied by GFAP in the **(E)** global, **(F)** dorsal, and **(G)** ventral LC. The data are presented as the mean ± SEM of three to four quadrants per section (three slices), one-way ANOVA followed by a Tukey's post-test.

(Yoshizumi et al., 2012), suggesting increased GABA tone after early nerve injury. Similarly, we did not find differences in the density of VGAT$^+$ puncta 7 or 28 days after neuropathy. Our previous studies failed to detect differences in the expression of gephyrin 14 days after neuropathy, a protein selectively located at inhibitory synapses in the LC (Bravo et al., 2013). This discrepancy could be due to the different animal models employed, as different approaches to induce neuropathy may promote similar changes in the LC associated with the instauration of neuropathy but these events could occur over different timescales.

When exploring long-term CCI (CCI28d), we did not find any significant effect on the density of VGLUT1$^+$ puncta. However, evaluating the complete LC region, revealed a decrease in VGLUT2 density without producing a net difference in the VGLUT2/VGAT ratio. Regarding noradrenergic perisomatic study, CCI28d showed a decrease in VGLUT2 density accompanied by a decrease in the ratio VGLUT2/VGAT when compared to CCI7d. That is, short-term neuropathic pain causes an increase in excitatory synaptic markers that falls to normal levels (Sham) in association with long-term pain. In mice, an increase in the VGLUT2 density during early spared nerve injury was also followed by a return to control levels in pain-related brain areas (Wang et al., 2015). Moreover, long-term peripheral nerve injury augments extracellular glutamate by down-regulating GLT-1, thereby inhibiting evoked glutamate release

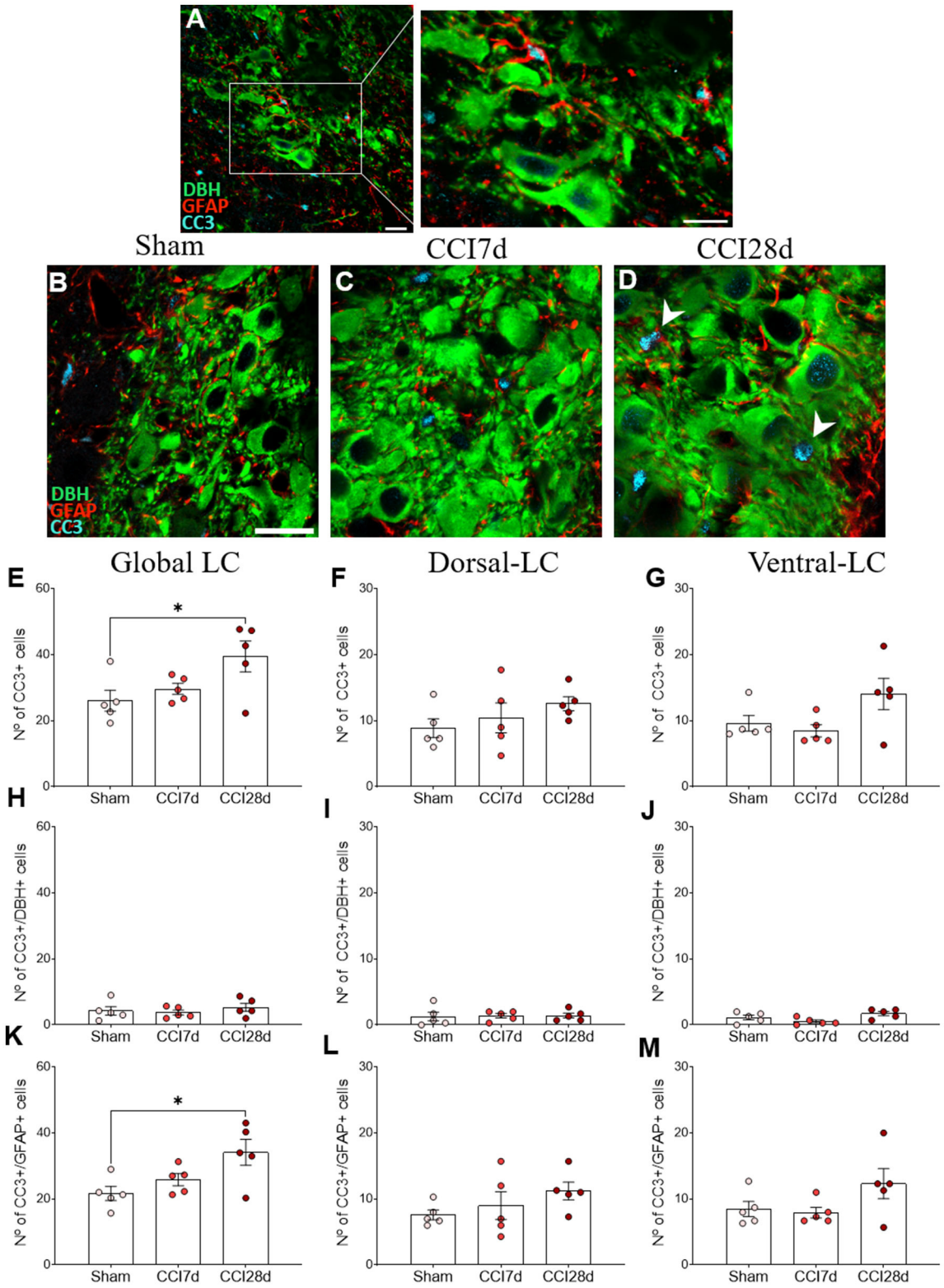

FIGURE 8
CC3 expression in DBH$^+$ and GFAP$^+$ LC cells of neuropathic pain rats. **(A)** Representative confocal images of CC3 expression in DBH$^+$ neurons in the LC of **(B)** Sham, **(C)** CCI7d, and **(D)** CCI28d rats (DBH green; GFAP red; CC3 blue: scale bar, 20 μm). **(E–G)** Quantification of the number of CC3$^+$ cells in the **(E)** global, **(F)** dorsal, and **(G)** ventral LC. **(H–J)** Quantification of the number of CC3$^+$/DBH$^+$ cells in the **(H)** global, **(I)**

(Continued)

FIGURE 8
dorsal, and **(J)** ventral LC. **(K–M)** Quantification of the number of $CC3^+/GFAP^+$ cells in the **(K)** global, **(L)** dorsal, and **(M)** ventral LC. The data are presented as the mean ± SEM of the number of the $CC3^+$ cells/μm^2 obtained from three to four quadrants per section (three slices). $^*p < 0.05$, $^{**}p < 0.01$, $^{***}p < 0.001$ vs. the group indicated, one-way ANOVA followed by a Tukey's post-test.

in the LC *via* the activation of mGluRs. This response would dampen the neuronal activity evoked in the LC in response to a noxious input, which is important when contemplating pain-induced endogenous analgesia (Kimura et al., 2015). These data suggest that the endogenous protective analgesia mediated by the LC may become exhausted. We did not find differences in the density of VGAT at this time point after nerve injury, consistent with previous studies that failed to find any change in GAD immunoreactivity in SNL-6W rats (Yoshizumi et al., 2012). Importantly, the differences in the VGLUT2/VGAT ratio at both CCI7d and CCI28d are mainly due to changes in the dorsal LC as no significant differences were evident in the ventral domain. These findings suggest a topographic distribution in the LC. We recently reported that LC neurons located specifically in the dorsal domain are activated (expressing c-Fos) at early times post-injury but not after long-term injury (Llorca-Torralba et al., 2022). Furthermore, chemogenetic inactivation of LC-SC neurons clearly increases pain sensitivity 2 days after nerve injury. This effect is reduced at 7 days and it is lost at 30 days after neuropathic pain induction (Llorca-Torralba et al., 2022). Although discrepancies might occur between studies regarding the anatomical denomination of the dorsal and ventral domains, and different rat strains were used (Sprague-Dawley vs. Long-Evans rats), these findings suggest that specific subpopulations of noradrenergic neurons mediate pain transmission.

Considering our previous findings following long-term neuropathy, we also evaluated the size of TH^+ cell somas. Although we did not find any significant differences in soma size among nerve-injured animals, there were differences in the frequency distribution of soma sizes, with a higher percentage of neurons with a soma of 150 μm^2 after long-term pain. Chronic stress also produces alterations in soma size, but in the opposite direction. Hence, TH^+ cells had a smaller soma in chronic mild stress (CMS) animals, an effect that was further exaggerated in CCI-CMS rats. Additional ultrastructural studies in long-term pain animals showed the presence of dilated ER and mitochondria, as well as a decrease in the density of mitochondria and lysosomes. These data are consistent with the idea that a loss of mitochondria impairs lysosomal activity (Demers-Lamarche et al., 2016). Mitochondria play a central role in neuron survival and death, and a loss of these structures might mean a reduction in the available energy substrates, which could hinder a cell's ability to withstand insults. Although there is no data about the ultrastructural changes in the LC of neuropathic rats, selective destruction of noradrenergic neurons using the neurotoxins 6-OHDA or DSP-4 induces depressive-like behavior (Szot et al., 2016) and impairs the emotional component of pain (Bravo et al., 2016), classic behaviors related to long-term but not short-term pain.

Interestingly, in animal models of neurodegenerative disorders, the shrinkage of TH^+ cells in the LC has often been described (German et al., 2005; Polak et al., 2011). Also, alterations to mitochondrial function and other microstructural changes in the LC, as well as degeneration of noradrenergic axons, have been demonstrated in the frontal cortex of rats subjected to long-term stress (Kitayama et al., 1997, 2008). An increasing number of studies have reported that mitochondrial activities (apoptosis, oxidative stress, etc.) are altered in anxiety and mood disorders, and it has been suggested that individuals with mitochondrial dysfunction would be vulnerable to stress and psychiatric disorders (Hollis et al., 2015; Filiou and Sandi, 2019). Thus, our findings invite an exploration of mitochondrial function in chronic neuropathic pain models.

We also explored the effect of nerve injury on the number of $CC3^+$ cells in the LC. Increased activation of CC3 is considered a marker of impending neuronal death (Thornberry and Lazebnik, 1998) but also plays non-apoptotic roles related to neuroadaptation, synapse refinement (D'Amelio et al., 2010; Fan et al., 2014), and astrogliosis (Aras et al., 2012). Regarding $CC3^+$ cells, there was a significant increase in the CCI28d LC but such increase was found in DBH^- cells, indicating that noradrenergic neurons were not involved. Indeed, most CC3 expression corresponds to glial $GFAP^+$ cells in spite of GFAP staining did not change among groups. Interestingly, the pattern of CC3 has been detected largely in non-neuronal cell populations without matching with TUNEL death marker (Stevenson et al., 2018). Also, rats submitted to a protocol of brain excitotoxic damage showed astroglial cells positive for CC3 without associated apoptotic death (Acarin et al., 2007). Moreover, CC3 upregulation occurs in absence of cell death in both *in vitro* and *ex vivo* models of astrogliosis (Aras et al., 2012). In this study, the inhibition of CC3 reduced the expression of proteins associated with astrogliosis (glutamine synthetase and fibroblast growth factor-2) without altering astrocytes reactive morphology. Thus, one possibility is that the impact of suffering by LC in response to neuropathic pain activates the CC3 expression in astrocytes as a remodeling process but not of cell death.

Other studies demonstrated that CC3 can be activated *via* the mitochondrial pathway by stimulating NMDA receptors, without causing cell death (Li et al., 2010). Indeed, local

activation of CC3 by photostimulation of mitochondria-targeted KillerRed, which triggers mitochondrial damage induces local spine elimination and dendrite retraction in cultured hippocampal neurons, without inducing full apoptosis (Erturk et al., 2014). Interestingly, we have found an important affectation of the excitatory/inhibitory ratio in the LC of CCI7d that is lost at CCI28d when CC3 is increased in glial cells. These results suggest once again that CC3 should be not considered a marker of death cell but rather a remodeling process in response to early glutamate overstimulation or *via* mitochondria damage.

In summary, this study highlights the importance of considering remodeling process occurring in the LC cells of neuropathic pain animals in a time-dependent manner. First, short-term pain affects excitatory neurotransmission in the LC, probably as an adaptive mechanism against the instauration of chronic pain. Second, long-term pain might induce ultrastructural changes in LC, which activates astroglial CC3 expression as a possible adaptive mechanism that might contribute to LC plasticity in long-term pain. Consequently, these phenomena might drive the negative emotional impact underlying chronic neuropathic pain.

Data availability statement

The raw data supporting the conclusions of this article will be made available by the authors, without undue reservation.

Ethics statement

The animal study was reviewed and approved by Committee for Animal Experimentation at the University of Cadiz.

Author contributions

EB, JN, and LB designed the study and wrote the manuscript. ML-T performed the behavioral experiments. PM and LB performed the tissue extraction and processing, they designed the protocols for immunohistochemistry, and as well as performed the acquisition and analysis of the data. JL-C contributed to the processing of tissue and the image analysis. EB and JN supervised the study. All authors revised and approved the submitted version of the manuscript.

Funding

This study was supported by grants co-financed by the Fondo Europeo de Desarrollo Regional (FEDER)-UE (A way to build Europe) from the Ministerio de Economía y Competitividad (MINECO: RTI2018-099778-B-I00) and the Ministerio de Salud-Instituto de Salud Carlos III (PI18/01691), by the Consejería de Salud de la Junta de Andalucía (PI-0134-2018; Grant No. P20-00958), by the Programa Operativo de Andalucía FEDER, Iniciativa Territorial Integrada ITI 2014-2020 Consejería Salud, Junta de Andalucía (PI-0080-2017), by the Instituto de Investigación e Innovación en Ciencias Biomédicas de Cádiz (INiBICA LI19/06IN-CO22; IN-C09), by the Consejería de Economía, Innovación, Ciencia y Empleo de la Junta de Andalucía (CTS-510), and by the "CIBERSAM": CIBER-Consorcio Centro de Investigación Biomédica en Red-(CB07/09/0033), Instituto de Salud Carlos III, Ministerio de Ciencia e Innovación and the European Union's Horizon 2020 Research and Innovation Programme under the Marie Sklodowska-Curie grant agreement (Grant No. 955684). Figures were created with BioRender.com.

Conflict of interest

The authors declare that the research was conducted in the absence of any commercial or financial relationships that could be construed as a potential conflict of interest.

Publisher's note

References

Acarin, L., Villapol, S., Faiz, M., Rohn, T. T., Castellano, B., and Gonzalez, B. (2007). Caspase-3 activation in astrocytes following postnatal excitotoxic damage correlates with cytoskeletal remodeling but not with cell death or proliferation. *Glia* 55, 954–965. doi: 10.1002/glia.20518

Alba-Delgado, C., Borges, G., Sanchez-Blazquez, P., Ortega, J. E., Horrillo, I., Mico, J. A., et al. (2012a). The function of alpha-2-adrenoceptors in the rat locus coeruleus is preserved in the chronic constriction injury model of neuropathic pain. *Psychopharmacol. (Berl.).* 221, 53–65. doi: 10.1007/s00213-011-2542-7

Alba-Delgado, C., Cebada-Aleu, A., Mico, J. A., and Berrocoso, E. (2016). Comorbid anxiety-like behavior and locus coeruleus impairment in diabetic peripheral neuropathy: a comparative study with the chronic constriction injury model. *Prog. Neuropsychopharmacol. Biol. Psychiatry* 71, 45–56. doi: 10.1016/j.pnpbp.2016.06.007

Alba-Delgado, C., Llorca-Torralba, M., Horrillo, I., Ortega, J. E., Mico, J. A., Sanchez-Blazquez, P., et al. (2013). Chronic pain leads to concomitant noradrenergic impairment and mood disorders. *Biol. Psychiatry* 73, 54–62. doi: 10.1016/j.biopsych.2012.06.033

Alba-Delgado, C., Llorca-Torralba, M., Mico, J. A., and Berrocoso, E. (2018). The onset of treatment with the antidepressant desipramine is critical for the emotional consequences of neuropathic pain. *Pain* 159, 2606–2619. doi: 10.1097/j.pain.0000000000001372

Alba-Delgado, C., Mico, J. A., and Berrocoso, E. (2021). Neuropathic pain increases spontaneous and noxious-evoked activity of locus coeruleus neurons. *Prog. Neuropsychopharmacol. Biol. Psychiatry* 105, 110121. doi: 10.1016/j.pnpbp.2020.110121

Alba-Delgado, C., Mico, J. A., Sanchez-Blazquez, P., and Berrocoso, E. (2012b). Analgesic antidepressants promote the responsiveness of locus coeruleus neurons to noxious stimulation: implications for neuropathic pain. *Pain* 153, 1438–1449. doi: 10.1016/j.pain.2012.03.034

Aras, R., Barron, A. M., and Pike, C. J. (2012). Caspase activation contributes to astrogliosis. *Brain Res.* 1450, 102–115. doi: 10.1016/j.brainres.2012.02.056

Aston-Jones, G., Zhu, Y., and Card, J. P. (2004). Numerous GABAergic afferents to locus ceruleus in the pericerulear dendritic zone: possible interneuronal pool. *J. Neurosci.* 24, 2313–2321. doi: 10.1523/JNEUROSCI.5339-03.2004

Barr, J., and Van Bockstaele, E. J. (2005). Vesicular glutamate transporter-1 colocalizes with endogenous opioid peptides in axon terminals of the rat locus coeruleus. *Anat. Rec. A Discov. Mol. Cell Evol. Biol.* 284, 466–474. doi: 10.1002/ar.a.20184

Barthas, F., Sellmeijer, J., Hugel, S., Waltisperger, E., Barrot, M., and Yalcin, I. (2015). The anterior cingulate cortex is a critical hub for pain-induced depression. *Biol. Psychiatry* 77, 236–245. doi: 10.1016/j.biopsych.2014.08.004

Bennett, G. J., and Xie, Y. K. (1988). A peripheral mononeuropathy in rat that produces disorders of pain sensation like those seen in man. *Pain* 33, 87–107.

Bodnar, R. J., Ackermann, R. F., Kelly, D. D., and Glusman, M. (1978). Elevations in nociceptive thresholds following locus coeruleus lesions. *Brain Res. Bull.* 3, 125–130.

Bravo, L., Alba-Delgado, C., Torres-Sanchez, S., Mico, J. A., Neto, F. L., and Berrocoso, E. (2013). Social stress exacerbates the aversion to painful experiences in rats exposed to chronic pain: the role of the locus coeruleus. *Pain* 154, 2014–2023. doi: 10.1016/j.pain.2013.06.021

Bravo, L., Mico, J. A., Rey-Brea, R., Camarena-Delgado, C., and Berrocoso, E. (2016). Effect of DSP4 and desipramine in the sensorial and affective component of neuropathic pain in rats. *Prog. Neuropsychopharmacol. Biol. Psychiatry* 70, 57–67. doi: 10.1016/j.pnpbp.2016.05.002

Bravo, L., Mico, J. A., Rey-Brea, R., Perez-Nievas, B., Leza, J. C., and Berrocoso, E. (2012). Depressive-like states heighten the aversion to painful stimuli in a rat model of comorbid chronic pain and depression. *Anesthesiology* 117, 613–625. doi: 10.1097/ALN.0b013e3182657b3e

Brightwell, J. J., and Taylor, B. K. (2009). Noradrenergic neurons in the locus coeruleus contribute to neuropathic pain. *Neuroscience* 160, 174–185. doi: 10.1016/j.neuroscience.2009.02.023

Camarena-Delgado, C., Llorca-Torralba, M., Suarez-Pereira, I., Bravo, L., Lopez-Martin, C., Garcia-Partida, J. A., et al. (2021). Nerve injury induces transient locus coeruleus activation over time: role of the locus coeruleus-dorsal reticular nucleus pathway. *Pain* 163, 943–954. doi: 10.1097/j.pain.0000000000002457

Corteen, N. L., Cole, T. M., Sarna, A., Sieghart, W., and Swinny, J. D. (2011). Localization of GABA-A receptor alpha subunits on neurochemically distinct cell types in the rat locus coeruleus. *Eur. J. Neurosci.* 34, 250–262. doi: 10.1111/j.1460-9568.2011.07740.x

D'Amelio, M., Cavallucci, V., and Cecconi, F. (2010). Neuronal caspase-3 signaling: not only cell death. *Cell Death Differ.* 17, 1104–1114. doi: 10.1038/cdd.2009.180

Demers-Lamarche, J., Guillebaud, G., Tlili, M., Todkar, K., Belanger, N., Grondin, M., et al. (2016). Loss of mitochondrial function impairs lysosomes. *J. Biol. Chem.* 291, 10263–10276. doi: 10.1074/jbc.M115.695825

Ennis, M., and Aston-Jones, G. (1988). Activation of locus coeruleus from nucleus paragigantocellularis: a new excitatory amino acid pathway in brain. *J. Neurosci.* 8, 3644–3657.

Erturk, A., Wang, Y., and Sheng, M. (2014). Local pruning of dendrites and spines by caspase-3-dependent and proteasome-limited mechanisms. *J. Neurosci.* 34, 1672–1688. doi: 10.1523/JNEUROSCI.3121-13.2014

Fan, W., Dai, Y., Xu, H., Zhu, X., Cai, P., Wang, L., et al. (2014). Caspase-3 modulates regenerative response after stroke. *Stem Cells* 32, 473–486. doi: 10.1002/stem.1503

Filiou, M. D., and Sandi, C. (2019). Anxiety and brain mitochondria: a bidirectional crosstalk. *Trends Neurosci.* 42, 573–588. doi: 10.1016/j.tins.2019.07.002

Fremeau, R. T. Jr., Kam, K., Qureshi, T., Johnson, J., Copenhagen, D. R., Storm-Mathisen, J., et al. (2004a). Vesicular glutamate transporters 1 and 2 target to functionally distinct synaptic release sites. *Science* 304, 1815–1819. doi: 10.1126/science.1097468

Fremeau, R. T. Jr., Troyer, M. D., Pahner, I., Nygaard, G. O., Tran, C. H., Reimer, R. J., et al. (2001). The expression of vesicular glutamate transporters defines two classes of excitatory synapse. *Neuron* 31, 247–260. doi: 10.1016/S0896-6273(01)00344-0

Fremeau, R. T. Jr., Voglmaier, S., Seal, R. P., and Edwards, R. H. (2004b). VGLUTs define subsets of excitatory neurons and suggest novel roles for glutamate. *Trends Neurosci.* 27, 98–103. doi: 10.1016/j.tins.2003.11.005

German, D. C., Nelson, O., Liang, F., Liang, C. L., and Games, D. (2005). The PDAPP mouse model of Alzheimer's disease: locus coeruleus neuronal shrinkage. *J. Comp. Neurol.* 492, 469–476. doi: 10.1002/cne.20744

Gonzalez, M. M., and Aston-Jones, G. (2008). Light deprivation damages monoamine neurons and produces a depressive behavioral phenotype in rats. *Proc. Natl. Acad. Sci. USA* 105, 4898–4903. doi: 10.1073/pnas.0703615105

Groves, P. M., and Wilson, C. J. (1980). Fine structure of rat locus coeruleus. *J. Comp. Neurol.* 193, 841–852.

Guirado, R., Carceller, H., Castillo-Gomez, E., Castren, E., and Nacher, J. (2018). Automated analysis of images for molecular quantification in immunohistochemistry. *Heliyon* 4, e00669. doi: 10.1016/j.heliyon.2018.e00669

Herzog, E., Bellenchi, G. C., Gras, C., Bernard, V., Ravassard, P., Bedet, C., et al. (2001). The existence of a second vesicular glutamate transporter specifies subpopulations of glutamatergic neurons. *J. Neurosci.* 21, RC181. doi: 10.1523/JNEUROSCI.21-22-j0001.2001

Hollis, F., van der Kooij, M. A., Zanoletti, O., Lozano, L., Canto, C., and Sandi, C. (2015). Mitochondrial function in the brain links anxiety with social subordination. *Proc. Natl. Acad. Sci. USA* 112, 15486–15491. doi: 10.1073/pnas.1512653112

Jin, X., Li, S., Bondy, B., Zhong, W., Oginsky, M. F., Wu, Y., et al. (2016). Identification of a group of GABAergic neurons in the dorsomedial area of the locus coeruleus. *PLoS ONE* 11, e0146470. doi: 10.1371/journal.pone.0146470

Kaneko, T., and Fujiyama, F. (2002). Complementary distribution of vesicular glutamate transporters in the central nervous system. *Neurosci. Res.* 42, 243–250. doi: 10.1016/S0168-0102(02)00009-3

Kimura, M., Suto, T., Morado-Urbina, C. E., Peters, C. M., Eisenach, J. C., and Hayashida, K. (2015). Impaired pain-evoked analgesia after nerve injury in rats reflects altered glutamate regulation in the locus coeruleus. *Anesthesiology* 123, 899–908. doi: 10.1097/ALN.0000000000000796

Kitayama, I., Yaga, T., Kayahara, T., Nakano, K., Murase, S., Otani, M., et al. (1997). Long-term stress degenerates, but imipramine regenerates, noradrenergic axons in the rat cerebral cortex. *Biol. Psychiatry* 42, 687–696.

Kitayama, I. T., Otani, M., and Murase, S. (2008). Degeneration of the locus ceruleus noradrenergic neurons in the stress-induced depression of rats. *Ann. N. Y. Acad. Sci.* 1148, 95–98. doi: 10.1196/annals.1410.059

Li, Z., Jo, J., Jia, J. M., Lo, S. C., Whitcomb, D. J., Jiao, S., et al. (2010). Caspase-3 activation via mitochondria is required for long-term depression and AMPA receptor internalization. *Cell* 141, 859–871. doi: 10.1016/j.cell.2010.03.053

Llorca-Torralba, M., Borges, G., Neto, F., Mico, J. A., and Berrocoso, E. (2016). Noradrenergic locus coeruleus pathways in pain modulation. *Neuroscience* 338, 93–113. doi: 10.1016/j.neuroscience.2016.05.057

Llorca-Torralba, M., Camarena-Delgado, C., Suarez-Pereira, I., Bravo, L., Mariscal, P., Garcia-Partida, J. A., et al. (2022). Pain and depression comorbidity causes asymmetric plasticity in the locus coeruleus neurons. *Brain* 145, 154–167. doi: 10.1093/brain/awab239

Llorca-Torralba, M., Mico, J. A., and Berrocoso, E. (2018). Behavioral effects of combined morphine and MK-801 administration to the locus coeruleus of a rat neuropathic pain model. *Prog. Neuropsychopharmacol. Biol. Psychiatry* 84, 257–266. doi: 10.1016/j.pnpbp.2018.03.007

Llorca-Torralba, M., Pilar-Cuellar, F., Bravo, L., Bruzos-Cidon, C., Torrecilla, M., Mico, J. A., et al. (2019a). Opioid activity in the locus coeruleus is modulated by chronic neuropathic pain. *Mol. Neurobiol.* 56, 4135–4150. doi: 10.1007/s12035-018-1361-9

Llorca-Torralba, M., Suarez-Pereira, I., Bravo, L., Camarena-Delgado, C., Garcia-Partida, J. A., Mico, J. A., et al. (2019b). Chemogenetic silencing of the locus coeruleus-basolateral amygdala pathway abolishes pain-induced anxiety and enhanced aversive learning in rats. *Biol. Psychiatry* 85, 1021–1035. doi: 10.1016/j.biopsych.2019.02.018

Ma, W., and Eisenach, J. C. (2003). Chronic constriction injury of sciatic nerve induces the up-regulation of descending inhibitory noradrenergic innervation to the lumbar dorsal horn of mice. *Brain Res.* 970, 110–118. doi: 10.1016/S0006-8993(03)02293-5

Martin, W. J., Gupta, N. K., Loo, C. M., Rohde, D. S., and Basbaum, A. I. (1999). Differential effects of neurotoxic destruction of descending noradrenergic pathways on acute and persistent nociceptive processing. *Pain* 80, 57–65.

Nonaka, T., Yamada, T., Ishimura, T., Zuo, D., Moffett, J. R., Neale, J. H., et al. (2017). A role for the locus coeruleus in the analgesic efficacy of N-acetylaspartylglutamate peptidase (GCPII) inhibitors ZJ43 and 2-PMPA. *Mol. Pain* 13, 1744806917697008. doi: 10.1177/1744806917697008

Polak, P. E., Kalinin, S., and Feinstein, D. L. (2011). Locus coeruleus damage and noradrenaline reductions in multiple sclerosis and experimental autoimmune encephalomyelitis. *Brain* 134(Pt 3), 665–677. doi: 10.1093/brain/awq362

Rohampour, K., Azizi, H., Fathollahi, Y., and Semnanian, S. (2017). Peripheral nerve injury potentiates excitatory synaptic transmission in locus coeruleus neurons. *Brain Res. Bull.* 130, 112–117. doi: 10.1016/j.brainresbull.2017.01.012

Roth, F. C., and Draguhn, A. (2012). GABA metabolism and transport: effects on synaptic efficacy. *Neural Plast.* 2012, 805830. doi: 10.1155/2012/805830

Sakata-Haga, H., Kanemoto, M., Maruyama, D., Hoshi, K., Mogi, K., Narita, M., et al. (2001). Differential localization and colocalization of two neuron-types of sodium-dependent inorganic phosphate cotransporters in rat forebrain. *Brain Res.* 902, 143–155. doi: 10.1016/S0006-8993(01)02290-9

Savigni, D. L., O'Hare Doig, R. L., Szymanski, C. R., Bartlett, C. A., Lozic, I., Smith, N. M., et al. (2013). Three Ca^{2+} channel inhibitors in combination limit chronic secondary degeneration following neurotrauma. *Neuropharmacology* 75, 380–390. doi: 10.1016/j.neuropharm.2013.07.034

Shefner, S. A., and Osmanovic, S. S. (1991). GABAA and GABAB receptors and the ionic mechanisms mediating their effects on locus coeruleus neurons. *Prog. Brain Res.* 88, 187–195.

Siksou, L., Silm, K., Biesemann, C., Nehring, R. B., Wojcik, S. M., Triller, A., et al. (2013). A role for vesicular glutamate transporter 1 in synaptic vesicle clustering and mobility. *Eur. J. Neurosci.* 37, 1631–1642. doi: 10.1111/ejn.12199

Singewald, N., and Philippu, A. (1998). Release of neurotransmitters in the locus coeruleus. *Prog. Neurobiol.* 56, 237–267.

Stevenson, M. E., Lensmire, N. A., and Swain, R. A. (2018). Astrocytes and radial glia-like cells, but not neurons, display a nonapoptotic increase in caspase-3 expression following exercise. *Brain Behav.* 8, e01110. doi: 10.1002/brb3.1110

Suarez-Pereira, I., Llorca-Torralba, M., Bravo, L., Camarena-Delgado, C., Soriano-Mas, C., and Berrocoso, E. (2021). The role of the locus coeruleus in pain and associated stress-related disorders. *Biol. Psychiatry*. 91, 786–797. doi: 10.1016/j.biopsych.2021.11.023

Suto, T., Severino, A. L., Eisenach, J. C., and Hayashida, K. (2014). Gabapentin increases extracellular glutamatergic level in the locus coeruleus via astroglial glutamate transporter-dependent mechanisms. *Neuropharmacology* 81, 95–100. doi: 10.1016/j.neuropharm.2014.01.040

Szot, P., Franklin, A., Miguelez, C., Wang, Y., Vidaurrazaga, I., Ugedo, L., et al. (2016). Depressive-like behavior observed with a minimal loss of locus coeruleus (LC) neurons following administration of 6-hydroxydopamine is associated with electrophysiological changes and reversed with precursors of norepinephrine. *Neuropharmacology* 101, 76–86. doi: 10.1016/j.neuropharm.2015.09.003

Thornberry, N. A., and Lazebnik, Y. (1998). Caspases: enemies within. *Science* 281, 1312–1316.

Todorovic, N., Micic, B., Schwirtlich, M., Stevanovic, M., and Filipovic, D. (2019). Subregion-specific protective effects of fluoxetine and clozapine on parvalbumin expression in medial prefrontal cortex of chronically isolated rats. *Neuroscience* 396, 24–35. doi: 10.1016/j.neuroscience.2018.11.008

Varoqui, H., Schafer, M. K., Zhu, H., Weihe, E., and Erickson, J. D. (2002). Identification of the differentiation-associated Na+/PI transporter as a novel vesicular glutamate transporter expressed in a distinct set of glutamatergic synapses. *J. Neurosci.* 22, 142–155. doi: 10.1523/JNEUROSCI.22-01-00142.2002

Venable, J. H., and Coggeshall, R. (1965). A simplified lead citrate stain for use in electron microscopy. *J. Cell Biol.* 25, 407–408.

Wang, Z. T., Yu, G., Wang, H. S., Yi, S. P., Su, R. B., and Gong, Z. H. (2015). Changes in VGLUT2 expression and function in pain-related supraspinal regions correlate with the pathogenesis of neuropathic pain in a mouse spared nerve injury model. *Brain Res.* 1624, 515–524. doi: 10.1016/j.brainres.2015.08.010

Yalcin, I., Barthas, F., and Barrot, M. (2014). Emotional consequences of neuropathic pain: insight from preclinical studies. *Neurosci. Biobehav. Rev.* 47, 154–164. doi: 10.1016/j.neubiorev.2014.08.002

Yoshizumi, M., Parker, R. A., Eisenach, J. C., and Hayashida, K. (2012). Gabapentin inhibits gamma-amino butyric acid release in the locus coeruleus but not in the spinal dorsal horn after peripheral nerve injury in rats. *Anesthesiology* 116, 1347–1353. doi: 10.1097/ALN.0b013e318254e6fd

frontiers | Frontiers in Molecular Neuroscience

TYPE Mini Review
PUBLISHED 29 July 2022
DOI 10.3389/fnmol.2022.945450

OPEN ACCESS

EDITED BY
Cyril Goudet,
INSERM U1191 Institut de Génomique Fonctionnelle (IGF), France

REVIEWED BY
Livio Luongo,
University of Campania Luigi Vanvitelli, Italy

*CORRESPONDENCE
Alexandre Charlet
acharlet@unistra.fr
Hugues Petitjean
hugues.petitjean@benephyt.fr

†These authors have contributed equally to this work

SPECIALTY SECTION
This article was submitted to Pain Mechanisms and Modulators, a section of the journal Frontiers in Molecular Neuroscience

RECEIVED 16 May 2022
ACCEPTED 04 July 2022
PUBLISHED 29 July 2022

CITATION
Petitjean H, Héberlé E, Hilfiger L, Łapieś O, Rodrigue G and Charlet A (2022) TRP channels and monoterpenes: Past and current leads on analgesic properties.
Front. Mol. Neurosci. 15:945450.
doi: 10.3389/fnmol.2022.945450

TRP channels and monoterpenes: Past and current leads on analgesic properties

Hugues Petitjean[1*†], Eléa Héberlé[1†], Louis Hilfiger[1,2], Olga Łapieś[2], Guillaume Rodrigue[1] and Alexandre Charlet[2*]

[1]Benephyt, Strasbourg, France, [2]Centre National de la Recherche Scientifique, University of Strasbourg, Institute of Cellular and Integrative Neuroscience, INCI UPR3212, Strasbourg, France

The activation of the transient receptor potential (TRP) channels expressed by sensory neurons is essential to the transduction of thermal and mechanical sensory information. In the setting of chronic inflammatory conditions, the activation of the melastatin family member 8 (TRPM8), the TRP vanilloid 1 (TRPV1), and the TRP ankyrin 1 (TRPA1) is correlated with pain hypersensitivity reactions. Monoterpenes, among which pulegone and menthol, a major class of phytocompounds present in essential oils of medicinal plants, are known modulators of those TRP channels activity. In the present review, we correlate the monoterpene content of plants with their historical therapeutic properties. We then describe how monoterpenes exert their anti-inflammatory and antihyperalgesia effects through modulation of TRP channels activity. Finally, we discuss the importance and the potential of characterizing new plant extracts and reassessing studied plant extracts for the development of ethnopharmacology-based innovative treatments for chronic pain. This review suggests that monoterpene solutions, based on composition from traditional healing herbs, offer an interesting avenue for the development of new phytotherapeutic treatments to alleviate chronic inflammatory pain conditions.

KEYWORDS

monoterpenes, pain, inflammation, TRP, pulegone, menthol, hyperalgesia

Introduction

Chronic inflammatory pain conditions such as osteoarthritis are debilitating diseases that impair the normal life of 14–36% of the population of the USA (Neogi, 2013; Treede et al., 2019). They are characterized by the presence of spontaneous pain, not evenly linked to an injury, and by hypersensitivity to painful stimuli (Raja et al., 2020). Despite the existence of several medications to alleviate chronic pain conditions, such as opioid treatment, which come with their share of unwanted side effects (Opioid Overdose Crisis | National Institute on Drug Abuse, 2022), most debilitating chronic inflammatory states remain uncured (Gilbert, 2021). Phytotherapy, or traditional herbalism, referring to the use of plant-derived preparation in the treatment and prevention of disease, might be a promising lead, with lower rates of adverse effects and efficiencies that might reach those of currently used conventional drugs (Dragos et al., 2017). Across the world, it remains the first intentional solution to diseases, or a preponderant complement to

"conventional" medicine. Phytotherapy has been increasingly supported by the WHO (World Health Organization, 2013), and has been used to treat chronic joint inflammatory disorders such as osteoarthritis (Cameron and Chrubasik, 2014), rheumatoid arthritis (Dragos et al., 2017), and to alleviate chronic low back pain (Oltean et al., 2014).

Regarding their elaborate secondary metabolism, plants are indeed interesting reservoirs of phytocompounds with pharmacological activities (Yang et al., 2018). Among secondary metabolites, monoterpenes, such as menthol, are small volatile and fragrant molecules synthesized through the terpenoid biosynthesis pathway (Bergman and Phillips, 2021). Cyclohexanoids monoterpenes, also known as "p-menthanes," are highly valuable molecules in industry and of important economical value, accounting for the majority of the compounds in essential oils (Tetali, 2018; Bergman et al., 2019). Widespread across the plant kingdom, menthol is, among this compound family, the most studied. It represents a reference molecule (Croteau et al., 2005), especially in the case of the modulation of pain conditions (Galeotti et al., 2002). Menthol is the naturally cyclic monoterpene alcohol found in the peppermint plant *Mentha x piperita* L. that gives the *Mentha* species their distinctive peppermint odor and flavor, and this essential oil triggers cold sensation through the activation of the transient receptor potential (TRP) melastatin family member 8 (TRPM8) channel (Peier et al., 2002). Menthol not only modulates TRPM8 but also several receptors and channels such as other TRP channels [for review (Oz et al., 2017)]; notably the TRP vanilloid 1 (TRPV1) (Takaishi et al., 2014) and the TRP ankyrin 1 (TRPA1) (Karashima et al., 2007) that are both transducers of noxious stimulation and therefore contribute to pain hypersensitivities during inflammation (Julius, 2013). Despite the fact that terpenes are the largest class of secondary metabolites, with over 50,000 compounds with interesting biological activities (such as antibacterial and anti-inflammatory) (Zielińska-Błajet and Feder-Kubis, 2020), less than thirty monoterpenes have been identified to promote analgesia and antihyperalgesia effects (Sousa and Pergentino, 2011; Guimarães et al., 2013; Gouveia et al., 2018). In a recent comparative study, menthol and its precursor, pulegone, have both been demonstrated to bear anti-inflammatory and antihyperalgesic properties in an inflammatory pain rodent model (Hilfiger et al., 2021) suggesting that plant extracts containing pulegone could help alleviate pain conditions, in a synergistic fashion.

In this review, first, we will list the plants containing menthol and pulegone, and enumerate their therapeutic properties mentioned in ethnobotanical data, to define a new plant group as matrices of interest. Second, we will summarize the evidence demonstrating the pain-killer properties of menthol and other monoterpenes. This will be further extended by the description of the current state of knowledge on the modulation of TRP channels by menthol and pulegone leading to reduced nociception. Finally, we will discuss the importance and the potential of characterizing new and reassessing studied plant extracts for the development of ethnopharmacology-based innovative treatments for chronic pain.

A historic standpoint: Lamiaceae, pulegone, and menthol

Menthol and pulegone are monoterpene derivatives synthesized through the conserved terpenoid backbone biosynthesis pathway (Figure 1A). They have been recently characterized and demonstrated to reduce the mechanical and thermal pain hypersensitivities in a rodent inflammatory pain model, thus reinforcing various previous results (de Sousa et al., 2007, 2011).

We first wanted to explore natural products databases to establish a list of plants currently known to contain menthol or pulegone. Because there are many natural products repositories (Sorokina and Steinbeck, 2020), we chose to investigate the LOTUS database, as it is one of the latest intents to harmonize, curate, and validate structure-organism pairs, in an open access fashion (Rutz et al., 2021). Dr. Duke's Phytochemical and Ethnobotanical Database (1992–2016), hosted on the USDA website (https://data.nal.usda.gov/dataset/dr-dukes-phytochemical-and-ethnobotanical-databases), was also consulted for its richness in ethnobotanical mentions for each plant. We started by extracting all plant names mentioned to contain pulegone and/or menthol, and also their precursor piperitone and their associated derivatives: neomenthol, isomenthol, and neoisomenthol (Figure 1B). To avoid any duplicates, their names were converted to their accurate scientific names and botanical families according to the Angiosperm Phylogeny Group IV (2016) and listed on "Plants of the World Online" (POWO, 2022 facilitated by the Royal Botanic Gardens; http://www.plantsoftheworldonline.org/---Retrieved 10 May 2022). Results show that piperitone appears in the highest number of species inventoried in the databases (over 158 species listed), throughout most of the plant families registered, whereas the derivatives of pulegone: (neomenthol, neoisomenthol, and isomenthol) present the lowest occurrence in the catalog (24, 13, and 12 species, respectively) (Figure 1B). The list of all plants recorded for the presence of menthol and pulegone forms a group of 85 and 110 species of plants, respectively (Supplementary Table 1). Among them, the Lamiaceae subgroup is best represented, with pulegone and menthol present in 84 and 56.5% of the Lamiaceae, respectively (Figures 1C,D).

Because of their aromatic properties, plants within this family have been extensively used across the world and for all kinds of purposes: food, aromatics, cosmetics, and healing. A trend to investigate plant properties based on

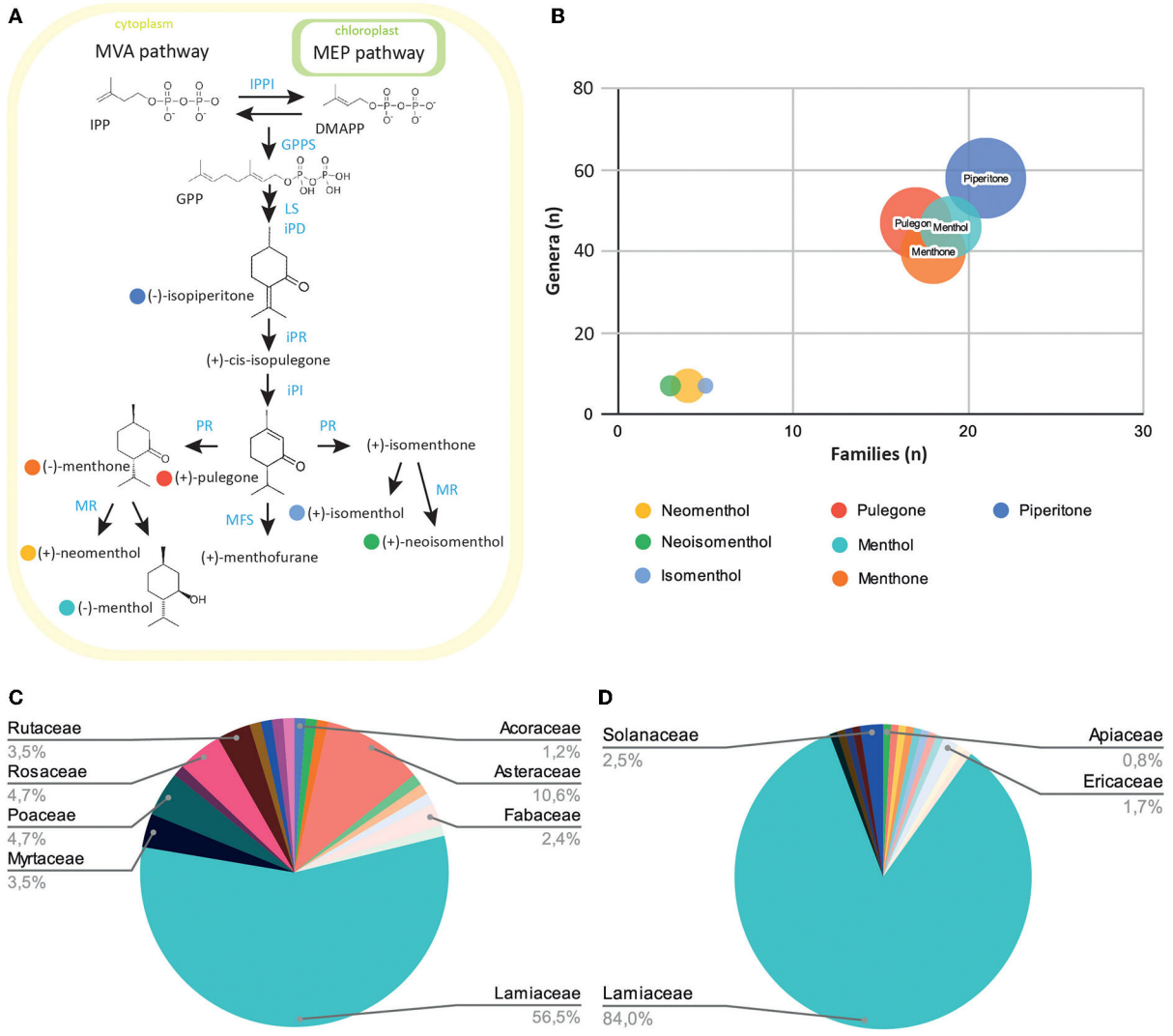

FIGURE 1
Exploration of the prevalence of menthol-like monoterpenes across the plant kingdom. **(A)** Schematic view of the monoterpene biosynthesis pathway leading to menthol, pulegone, and their derivatives. Plants produce the small precursor isopentenyl-pyrophosphate (IPP) through the mevalonate (MVA) pathway in the cytoplasm, or the methylerythritol (MEP) pathway in the plast. IPP can be isomerized into dimethylallyl-pyrophosphate (DMAPP) through the IPP isomerase activity (IPPI). Five-carbon units IPP and DMAPP can be converted into 10-unit geranyl-pyrophosphate (GPP) through the geranyl-pyrophosphate synthase (GPPS) activity. GPP is then converted into limonene, isopiperitone, and cis-isopulegone through limonene synthase (LS), trans-isopiperitenol dehydrogenase (iPD), and isopiperitone reductase (iPR) activity. Pulegone is then produced through cis-isopulegone isomerase (iPI) activity. Pulegone reductase (PR) converts pulegone into isomenthone or menthone, through different activities. These two compounds can then be converted into neomenthol and menthol, or isomenthol and neoisomenthol, respectively, through the menthone reductase activity (MR). The menthofurane synthase (MFS) can also convert pulegone into menthofurane, in an NADP-dependant reaction. **(B)** Bubble diagram representing the number of families (x-axis), genera (y-axis), and species (circle radius) containing monoterpenes precursors or derivatives. **(C)** Diagram of the distribution of menthol-containing plants within plant families. **(D)** Diagram of the distribution of pulegone-containing plants within plant families.

their traditional use has emerged, embodied in the vast discipline of ethnopharmacology and showing promising results (Bruhn and Rivier, 2019). The re-examination of historical texts and traditional pharmacopeias will help to re-evaluate plant species' potential toward new indications that were discarded in the modern pharmacopeias (Heinrich et al., 2006).

During the Greek Antiquity (Leonti and Verpoorte, 2017), as referred to in Theophrastus' Historia Plantarum (Totelin, 2006), *Origanum majorana* and *Origanum sipylaeum* are mentioned as aromatics. *Mentha pulegium* is also mentioned with properties useful for pain treatment that were allegedly "known by all": endemic from Crete and imported to Athens, it had a great reputation in ancient Greece (Totelin, 2006).

In Mattioli's translation of Dioscorides' original texts from AD 50 to 70 (Mattioli, 1590), *Thymbrium* was cited as *Menta romana* for the Italians, and it was stated that leaves could relieve head pain when topically applied as a cataplasm. *Origanum* was described to relieve ear pain, when applied with milk. As for the "*Pulegium*," probably referring to *M. pulegium* L., he stated that when applied with dried sour cherry, it relieved all inflammation and helped patients to support gout (Mattioli, 1590). A cross-observation between the following plants: *M. pulegium*, *Origanum*, and *M. romana*, reveals that they are all reported to contain menthol and pulegone; (Supplementary Table 1) eventually supporting a shared use based on their aromatic properties (Ntalli et al., 2010). Interestingly, 38 plants of the Lamiaceae family are present on the A list of the French Pharmacopeia, among which 22 are sold over the counter. Eight species are on the B list, due to their putative undesirable effects outnumbering the benefits they provide. Very few of them still have an indication for pain alleviation. As plant uses and medical paradigms fluctuate across history, sometimes resulting in loss of knowledge or transformations in the indications, it is important to re-assess plant compositions and their effects on a scientific basis.

Among those, *M. x piperita* L. is a textbook example, having been used for centuries in traditional medicine to reduce numerous ailments such as infections, insomnia, irritable bowel syndrome, and also pain (Farco and Grundmann, 2013). It has been demonstrated that the large quantity of menthol in this plant acts as the major active principle to alleviate joint pain (Topp et al., 2013). Another example is *Clinopodium nepeta* (L.) Kuntze, a plant of the Lamiaceae family, which has been mentioned since Greek Antiquity and in at least two of the most renowned herbals of the 16th and 17th centuries for the treatment of rheumatism (Adams et al., 2009): in Mattioli (1590), it is advised to boil and drink a *C. nepeta* (L.) Kuntze-based broth against gout and slime, while FUCHS (1543) recommends an external application of leaves against hip pain. In this case, the major active substance associated with beneficial effects is pulegone, which is found in large quantities in *C. nepeta* (L.) (BoŽović and Ragno, 2017). Recent evidence points out that pulegone, like menthol, acts as an antihyperalgesic phytocompound in an inflammatory pain animal model (Hilfiger et al., 2021).

Phytotherapy based on *M. x piperita* L. (*Mentha x officinalis* Hull) and *C. nepeta* (L.), Kuntze preparations rich in menthol or pulegone, as a major active compound, shows the potential for studying other members of the Lamiaceae family described throughout history of medicine for pain relief to reveal other analgesic monoterpenes. Chemotaxonomy suggests that other plants, which did not make it to the European traditional pharmacopeia, might also be interesting due to their composition. In our analysis, we found out, for instance, that *Clinopodium serpylifollium* subsp. fruticosum (L.) Bräuchler's [formally *Micromeria fruticosa* (L.) Druce] essential oil contains over 80% of pulegone, along with 36 other compounds. It might therefore be an interesting European plant to investigate (Kinmer et al., 1993). This idea is supported by the fact that essential oils from Lamiaceae do not exclusively contain pulegone or menthol but also other monoterpenes which, although present in low quantities, could act potentially in synergy on different molecular targets to alleviate pain (Maroon et al., 2010). However, as in the case of any molecule under investigation, it is crucial to assess toxicity effects (Wojtunik-Kulesza, 2022). Although pulegone's use as a food additive has been restricted by the FDA, there is no conclusive evidence of its carcinogenicity, and it is still authorized when extracted from natural sources (Food Drug Administration, 2018).

Pulegone and menthol as potent analgesic and anti-inflammatory phytocompounds

Pulegone and menthol are both reported to have analgesic properties, along with 26 other monoterpenes and some of their derivatives (Guimarães et al., 2013; Wang et al., 2017; Dos Santos et al., 2021). To understand their putative pain relief properties, we reduced this group to monoterpenes associated with anti-inflammatory activity (de Cássia da Silveira e Sá et al., 2013) that is mediated at least through an anti-TNF-α activity (Chen et al., 2021; Hilfiger et al., 2021). We combined data reporting a modulation of the TRPV1, TRPA1, or TRPM8 activity to define a group of anti-inflammatory phytocompound modulators of TRP channels (Xu et al., 2005; de Sousa et al., 2010; Ortar et al., 2012; de Cássia da Silveira e Sá et al., 2013; Guimarães et al., 2013; Rufino et al., 2014; Takaishi et al., 2014; Mihara and Shibamoto, 2015; Ohtsubo et al., 2015; Dai, 2016; Kaimoto et al., 2016; Oz et al., 2017; Wang et al., 2017; Chamanara et al., 2019; de Christo Scherer et al., 2019; Quintans et al., 2019; Soleimani et al., 2019; Ghosh et al., 2020; Heblinski et al., 2020; Hilfiger et al., 2020; Islam et al., 2020; Zhu et al., 2020; Chen et al., 2021; Dos Santos et al., 2021; Kashiwadani et al., 2021) (Table 1). Both menthol and pulegone, among other monoterpenes, match these properties (Table 1). Interestingly, *M. pulegium* L. and *Origanum dictamnus* L. have been used in traditional pain-relief preparations and their essential oil analysis revealed that their essential oils contain 5 and 6 of those monoterpenes, respectively (Ntalli et al., 2010) (see Table 1).

However, how monoterpenes, particularly based on menthol and pulegone reports, promote analgesic properties through the modulation of the activities of TRPV1, TRPA1, or TRPM8 channels in the setting of inflammatory pain conditions remains to be explored.

TABLE 1 Anti-inflammatory monoterpenes modulating TRP channel activity compared to the essential oil of *Mentha pulegium* L. and *Origanum dictamnus* L.

	Channel modulation			Plant	
Terpene	**TRPA1**	**TRPV1**	**TRPM8**	***Mentha pulegium* L.**	***Origanum dictamnus***
Borneol	X				
1,8-cineol	X		X		
Camphor	X	X	X		
Carvacrol	X			X	X
Carvone	X	X	X		
Citral	X	X	X		
Citronellol	X	X	X		
p-cymene	X		X		X
Fenchone	X				
Limonene	X			X	
Linalool	X		X		X
L-menthol	X	X	X		
β-myrcene	X	X		X	X
α-pinene	X	X		X	X
Pulegone	X	X	X	X	
Thymol	X		X		X
Thymoquinone	X				

The mark ("**X**") indicates if the monoterpene listed in the left column modulates a TRP channel activity. Each monoterpene is then associated to its presence ("**X**") in the essential oil of *Mentha pulegium* or *Origanum dictamnus* (right columns).

TRP channels in pain, physiologic, and chronic inflammatory conditions

Under normal conditions, nociceptors aim to detect potentially painful stimuli, and the detection and transduction of neuronal messages are less involving: TRPV1, for temperatures $> 42^{\circ}$C; TRPM8, for temperatures around 18°C, and TRPA1, for various noxious and mechanical stimuli (Dai, 2016). Aside from these functional arrangements exists an anatomical differentiation: TRPA1-expressing nociceptors are a subset of TRPV1-expressing nociceptors in rodents, whereas TRPM8 remains more expressed in a different set of specific sensory neurons (Dhaka et al., 2008; Jankowski et al., 2017; Kupari et al., 2021). In addition to their sensor roles, it is important to note that TRP channels are also expressed in immune cells [for review (Khalil et al., 2018)]: TRPM8 activity regulates the TNF-α production by macrophage cells (Khalil et al., 2016). These observations allow considering TRP channels not only as peripheral transducers but also as ionic receptors for endogenous ligands and major actors in pain hypersensitivities: TRPM8, TRPA1, and TRPV1 have a fundamental role in the initiation, regulation, and maintenance of hyperalgesia conditions (Schumacher, 2010).

Moreover, they may have a role in pain-central sensitization due to their expression in different regions and/or cellular subtypes of the central nervous system. Indeed, TRPV1 was reported to be expressed in a subset of sensory neurons (Cavanaugh et al., 2011) and central nervous cells (González-Ramírez et al., 2017). Therefore, rodent TRPV1 is present in brain regions such as the sensory, prefrontal, entorhinal, insular, and anterior cingulate cortices, and also the hippocampus, amygdala, and thalamus (for review see Duitama et al., 2020). Interestingly, those regions are involved in pain integration and/or modulation (Ordás et al., 2021; Wahis et al., 2021). However, it is important to note that human TRPV1 was, up to now, only detected in cortical regions (Morelli et al., 2013). The functional contribution of the central expression of TRPV1 is still debated and its contribution to central synaptic plasticity, especially as part of the endocannabinoid system regulation, is under scrutiny (Hakimizadeh et al., 2012; Li et al., 2021). Functional investigations have demonstrated that TRPV1 expressed in hippocampal neurons (Sun et al., 2013) contributes to strengthening spontaneous synaptic transmission (Anstötz et al., 2018).

Functional TRPA1 is described in the hippocampus and somatosensory cortex (Menigoz and Boudes, 2011; Shigetomi et al., 2011; Kheradpezhouh et al., 2017). In the hippocampus, TRPA1 activation increases extracellular GABA concentration, leading to a downregulation of the astrocyte GABA transport GAT-3 activity and a decreased efficiency of inhibitory synapses (Shigetomi et al., 2011). Finally, TRPM8 is present at least in the hypothalamus, septum, and thalamic reticular nucleus (for

review Ordás et al., 2021). Interestingly, TRPM8 expressing neurons are innervating the hypothalamus, the periaqueductal gray, and the amygdala regions (Ordás et al., 2021), which are major actors of pain regulation (Eliava et al., 2016; Ordás et al., 2021; Iwasaki et al., 2022).

Under inflammatory conditions, TRP channels are overexpressed at the membrane of sensory nerve endings innervating the inflamed joint. In addition, their intrinsic properties, namely, conductance or sensibility to noxious cues, change and contribute directly to abnormal pain symptoms such as hyperalgesia (Schumacher, 2010). Such conclusions are supported through experimental investigation using inflammatory animal pain models based on the administration of the complete Freund's adjuvant (CFA). Consisting of an injection of CFA into the joint or into the plantar surface of the hind paw, this model is characterized by the presence of exaggerated sensitivity to heat and cold stimulations and heightened sensitivity to mechanical tactile stimulations (Hilfiger et al., 2020, 2021). At the inflammation site, the free endings of the nociceptors are in contact with several inflammatory mediators such as proinflammatory cytokines and protein kinases [for review: (Dai, 2016)]. These interactions lead to sensitization of the nociceptors through different molecular pathways, which contribute directly to pain hypersensitivities and are referred to as "peripheral sensitization" (Mizumura, 1997). Peripheral sensitization allows, for example, the overexpression of TRPV1 in nociceptors (Yu et al., 2008). Such condition was investigated, using complementary pharmacological and genetic approaches. It was demonstrated that TRPV1 is essential to thermal hyperalgesia but not to mechanical hypersensitivity of nociceptors (for review (Dai, 2016). Nonetheless, their activation still recruits mechanical allodynia neuronal circuits (Petitjean et al., 2014). Based on the same approaches, it was clearly shown that TRPM8 is involved in cold hyperalgesia (Colburn et al., 2007; Gong and Jasmin, 2017) while TRPA1 is responsible for mechanical hypersensitivity and nocifensive reactions (Kwan et al., 2006; Eid et al., 2008; Kerstein et al., 2009; Vilceanu and Stucky, 2010; Lennertz et al., 2012; Asgar et al., 2015).

Thus, the three following TRP channels act as a complex molecular system that participates in pain hypersensitivities: TRPV1 contributes to thermal hyperalgesia (Caterina et al., 1997; Petitjean et al., 2014; Koivisto et al., 2022), TRPA1 contributes to thermal, mechanical, and chemical hyperalgesia (Koivisto et al., 2022), and TRPM8 contributes to cold allodynia (Koivisto et al., 2022). Expressed by nociceptors, those channels are easily accessible for exogenous molecules and two paths are generally proposed: a blockage of the channel activity through effective antagonists (Dai, 2016) or, paradoxically, overstimulation leading to long-term desensitization. Therefore, TRPV1, TRPM8, and TRPA1 are ideal targets for analgesic molecules.

Monoterpenes and TRP channels: An analgesic combination?

Interestingly, both pulegone and menthol act as strong anti-inflammatory molecules in *in vitro* essay with EC_{50} values of 1.2 ± 0.2 and 1.5 ± 0.1 mM, respectively (Hilfiger et al., 2021). In addition, a single intraperitoneal injection of 100 mg/kg pulegone or menthol in CFA rats exerts a transient antihyperalgesic effect on both mechanical, thermal heat and cold hyperalgesia (Hilfiger et al., 2021). Few studies have focused on pulegone-dependent mechanisms that reduce pain reactions. In chicks, intraplantar injection of pulegone causes nocifensive reactions which are attenuated by TRPA1 antagonists (Majikina et al., 2018). In humans and rodents, pulegone appears as a partial agonist of TRPV1 and an inhibitor of the menthol-induced TRPM8 activity (Jabba and Jordt, 2020) (Table 1). These suggest that pulegone is a strong agonist of TRPA1, and a partial TRPV1 agonist, and inhibits the TRPM8 activity. Interestingly, it is proposed that TRPA1 can be desensitized through different cellular pathways which are regulated by the activation of TRPV1 (Akopian et al., 2007; Ruparel et al., 2011; Kistner et al., 2016).

Molecular targets of menthol have been better investigated [for review (Oz et al., 2017)]. In humans and mouse pain models alike, TRPV1 currents activated by heat and capsaicin were inhibited by menthol, a phenomenon that might partially explain its antinociceptive properties (Takaishi et al., 2014); it also activates the TRPM8 to promote an antihyperalgesic effect (Liu et al., 2013). This activation induces a "cooling" sensation, followed by a TRPM8 channel shift into an inactive state that can be reversed only after the wash-out of the agonist compounds: a phenomenon called transient desensitization (Diver et al., 2019; Perri et al., 2020). Furthermore, menthol exerts in murine cells (*in vitro*) a bimodal modulation of TRPA1, activating it at low concentration (0.3–0.7 mM) and blocking it at high concentration (>3 mM) (Lemon et al., 2019). However, in humans, only the activation of TRPA1 by methanol has been observed (Xiao et al., 2008). This suggests that menthol is a strong agonist of TRPM8, and a partial TRPA1 agonist or blocker, and that it inhibits the TRPV1 activity.

In conclusion, both pulegone and menthol strongly interact with TRPM8, TRPA1, and TRPV1 (Table 1) (Takaishi et al., 2014; Oz et al., 2017; Jabba and Jordt, 2020). These pharmacological properties remain to be explored in the setting of TRPV1/TRPA1 channel heterodimers (Fischer et al., 2014). These heterodimers contribute also to pain symptoms (Galindo et al., 2018; Souza Monteiro de Araujo et al., 2020). Based on those properties, monoterpene activating the TRP channel with antihyperalgesic properties may be explained by an initial activation and then desensitization of TRP channels expressed in sensory neurons.

Prospects of new phytotherapy treatment to alleviate pain conditions

In prospect, beyond plants extracts or essential oils preparations, new treatments relying on specific monoterpenes mixes open an interesting avenue to treat pain. Monoterpenes are very volatile and have the capacity to cross the skin and the blood–brain barrier—thus enabling the modulation of peripheral and central neuronal, and immune cell receptors (Zhang et al., 2015; Weston-Green, 2019).

Based on these properties, commercial topical creams for pain relief were developed, for example, containing a mix of 3 monoterpenes: camphor, 1,8-cineole, and menthol (product NPN 02248563 RUB-A533 Antiphlogistine). To define the efficiency of a new putative mix, for new topical preparations, for instance, the reassessment of compounds found in traditional/popular medicine treatments and investigation of other bioactive principles that could alleviate chronic pain conditions seems a promising path. With an aim to develop a local and effective treatment to alleviate chronic conditions, this work intends to demonstrate the potential for the discovery of new antinociceptive drugs: there are already 50,000 terpenes identified (Breitmaier, 2006; Yamada et al., 2015) and their putative synergistic analgesic effects remain to be explored. This approach will further enable us to discover new uses for local plant species and to consider meaningful actions toward their valorization on environmental and patrimonial levels. Therefore, efforts toward the translation, annotation, and promotion of old folk books to a large audience are still worthy enterprises [for review (UNESCO World Heritage Center, 2010)]. Although ethnobotanical studies have been booming since the 1980s, few initiatives managed to share the results with traditional communities or raise awareness of local plant materials (Reyes-García et al., 2021; Schultz et al., 2021).

In the era of open science and open data sharing and within the logic of the "one health" theory, it is of the utmost importance to share this knowledge with citizens and professionals and to protect our plant heritage increasing our global commitment to biodiversity, as advised by international organizations (UNESCO, 2018; Mackenzie and Jeggo, 2019). We believe that this approach will bring new virtuous and resilient cycles of innovation, while increasing citizens' commitment and engagement toward their ecosystems.

Author contributions

EH performed the plant databases analysis. HP and LH performed the monoterpene databases analysis. EH, HP, and AC coordinated and produced the review. All authors discussed and elaborated the ideas, wrote the first draft, corrected it until the final version was obtained, and approved the manuscript.

Funding

This work was supported by the Centre National de la Recherche Scientifique contract UPR3212, the Université de Strasbourg contract UPR3212, the Graduate School of Pain EURIDOL, ANR-17-EURE-0022, and the ANRT CIFRE Grants No. 2018/1140 (to AC and HP) and no. 2016/047 (to HP).

Conflict of interest

HP, EH, LH, and GR are salaried employees at the private company Benephyt.

The remaining authors declare that the research was conducted in the absence of any commercial or financial relationships that could be construed as a potential conflict of interest.

Publisher's note

Supplementary material

The Supplementary Material for this article can be found online at: https://www.frontiersin.org/articles/10.3389/fnmol.2022.945450/full#supplementary-material

References

Adams, M., Berset, C., Kessler, M., and Hamburger, M. (2009). Medicinal herbs for the treatment of rheumatic disorders–a survey of European herbals from the 16th and 17th century. *J. Ethnopharmacol.* 121, 343–359. doi: 10.1016/j.jep.2008.11.010

Akopian, A. N., Ruparel, N. B., Jeske, N. A., and Hargreaves, K. M. (2007). Transient receptor potential TRPA1 channel desensitization in sensory neurons is agonist dependent and regulated by TRPV1-directed internalization. *J. Physiol.* 583, 175–193. doi: 10.1113/jphysiol.2007.133231

Angiosperm Phylogeny Group IV (2016). *An Update of the Angiosperm Phylogeny Group Classification for the Orders and Families of Flowering Plants*. APG IV. Botanical Journal of the Linnean Society (Wiley Online Library). Available online at: https://onlinelibrary.wiley.com/doi/abs/10.1111/boj.12385 (accessed May 10, 2022).

Anstötz, M., Lee, S. K., and Maccaferri, G. (2018). Expression of TRPV1 channels by Cajal-Retzius cells and layer-specific modulation of synaptic transmission by capsaicin in the mouse hippocampus. *J. Physiol.* 596, 3739–3758. doi: 10.1113/JP275685

Asgar, J., Zhang, Y., Saloman, J. L., Wang, S., Chung, M.-K., and Ro, J. Y. (2015). The role of TRPA1 in muscle pain and mechanical hypersensitivity under inflammatory conditions in rats. *Neuroscience* 310, 206–215. doi: 10.1016/j.neuroscience.2015.09.042

Bergman, M. E., Davis, B., and Phillips, M. A. (2019). Medically useful plant terpenoids: biosynthesis, occurrence, and mechanism of action. *Molecules* 24, 3961. doi: 10.3390/molecules24213961

Bergman, M. E., and Phillips, M. A. (2021). Structural diversity and biosynthesis of plant derived p-menthane monoterpenes. *Phytochem. Rev.* 20, 433–459. doi: 10.1007/s11101-020-09726-0

BoŽović, M., and Ragno, R. (2017). Calamintha nepeta (L.) savi and its main essential oil constituent pulegone: biological activities and chemistry. *Molecules* 22, 290. doi: 10.3390/molecules22020290

Breitmaier, E. (2006). "Terpenes: Importance, general structure, and biosynthesis," in *Terpenes* (John Wiley and Sons Ltd), 1–9. doi: 10.1002/9783527609949.ch1

Bruhn, J. G., and Rivier, L. (2019). Ethnopharmacology - a journal, a definition and a society. *J. Ethnopharmacol.* 242, 112005. doi: 10.1016/j.jep.2019.112005

Cameron, M., and Chrubasik, S. (2014). Oral herbal therapies for treating osteoarthritis. *Cochrane Database Syst. Rev.* 2014, CD002947. doi: 10.1002/14651858.CD002947.pub2

Caterina, M. J., Schumacher, M. A., Tominaga, M., Rosen, T. A., Levine, J. D., and Julius, D. (1997). The capsaicin receptor: a heat-activated ion channel in the pain pathway. *Nature* 389, 816–824. doi: 10.1038/39807

Cavanaugh, D. J., Chesler, A. T., Bráz, J. M., Shah, N. M., Julius, D., and Basbaum, A. I. (2011). Restriction of transient receptor potential vanilloid-1 to the peptidergic subset of primary afferent neurons follows its developmental downregulation in nonpeptidergic neurons. *J. Neurosci.* 31, 10119–10127. doi: 10.1523/JNEUROSCI.1299-11.2011

Chamanara, M., Abdollahi, A., Rezayat, S. M., Ghazi-Khansari, M., Dehpour, A., Nassireslami, E., et al. (2019). Thymol reduces acetic acid-induced inflammatory response through inhibition of NF-kB signaling pathway in rat colon tissue. *Inflammopharmacology* 27, 1275–1283. doi: 10.1007/s10787-019-00583-8

Chen, M., Zheng, J., Zou, X., Ye, C., Xia, H., Yang, M., et al. (2021). Ligustrum robustum (Roxb.) blume extract modulates gut microbiota and prevents metabolic syndrome in high-fat diet-fed mice. *J. Ethnopharmacol.* 268, 113695. doi: 10.1016/j.jep.2020.113695

Colburn, R. W., Lubin, M. L., Stone, D. J., Wang, Y., Lawrence, D., D'Andrea, M. R., et al. (2007). Attenuated cold sensitivity in TRPM8 null mice. *Neuron* 54, 379–386. doi: 10.1016/j.neuron.2007.04.017

Croteau, R. B., Davis, E. M., Ringer, K. L., and Wildung, M. R. (2005). (-)-Menthol biosynthesis and molecular genetics. *Naturwissenschaften* 92, 562–577. doi: 10.1007/s00114-005-0055-0

Dai, Y. (2016). TRPs and pain. *Semin. Immunopathol.* 38, 277–291. doi: 10.1007/s00281-015-0526-0

de Cássia da Silveira e Sá, R., Andrade, L. N., and de Sousa, D. P. (2013). A review on anti-inflammatory activity of monoterpenes. *Mol. Basel Switz.* 18, 1227–1254. doi: 10.3390/molecules18011227

de Christo Scherer, M. M., Marques, F. M., Figueira, M. M., Peisino, M. C. O., Schmitt, E. F. P., Kondratyuk, T. P., et al. (2019). Wound healing activity of terpinolene and α-phellandrene by attenuating inflammation and oxidative stress in vitro. *J. Tissue Viability* 28, 94–99. doi: 10.1016/j.jtv.2019.02.003

de Sousa, D. P., Camargo, E. A., Oliveira, F. S., and de Almeida, R. N. (2010). Anti-inflammatory activity of hydroxydihydrocarvone. *Z. Naturforschung C J. Biosci.* 65, 543–550. doi: 10.1515/znc-2010-9-1003

de Sousa, D. P., Júnior, E. V. M., Oliveira, F. S., de Almeida, R. N., Nunes, X. P., and Barbosa-Filho, J. M. (2007). Antinociceptive activity of structural analogues of rotundifolone: structure-activity relationship. *Z. Naturforschung C J. Biosci.* 62, 39–42. doi: 10.1515/znc-2007-1-207

de Sousa, D. P., Nóbrega, F. F. F., de Lima, M. R. V., and de Almeida, R. N. (2011). Pharmacological activity of (R)-(+)-pulegone, a chemical constituent of essential oils. *Z. Naturforschung C J. Biosci.* 66, 353–359. doi: 10.1515/znc-2011-7-806

Dhaka, A., Earley, T. J., Watson, J., and Patapoutian, A. (2008). Visualizing cold spots: TRPM8-expressing sensory neurons and their projections. *J. Neurosci.* 28, 566–575. doi: 10.1523/JNEUROSCI.3976-07.2008

Diver, M. M., Cheng, Y., and Julius, D. (2019). Structural insights into TRPM8 inhibition and desensitization. *Science* 365, 1434–1440. doi: 10.1126/science.aax6672

Dos Santos, E., Leitão, M. M., Aguero Ito, C. N., Silva-Filho, S. E., Arena, A. C., Silva-Comar, F. M., et al. (2021). Analgesic and anti-inflammatory articular effects of essential oil and camphor isolated from Ocimum kilimandscharicum Gürke leaves. *J. Ethnopharmacol.* 269, 113697. doi: 10.1016/j.jep.2020.113697

Dragos, D., Gilca, M., Gaman, L., Vlad, A., Iosif, L., Stoian, I., et al. (2017). Phytomedicine in joint disorders. *Nutrients* 9, E70. doi: 10.3390/nu9010070

Dr. Duke's Phytochemical and Ethnobotanical Database (1992–2016). Dr. Duke's Phytochemical and Ethnobotanical Databases (U.S. Department of Agriculture, Agricultural Research Service). Home Page. Available online at: http://phytochem.nal.usda.gov/ (accessed June 30, 2022).

Duitama, M., Vargas-López, V., Casas, Z., Albarracin, S. L., Sutachan, J.-J., and Torres, Y. P. (2020). TRP channels role in pain associated with neurodegenerative diseases. *Front. Neurosci.* 14, 782. doi: 10.3389/fnins.2020.00782

Eid, S. R., Crown, E. D., Moore, E. L., Liang, H. A., Choong, K.-C., Dima, S., et al. (2008). HC-030031, a TRPA1 selective antagonist, attenuates inflammatory- and neuropathy-induced mechanical hypersensitivity. *Mol. Pain* 4, 1744-8069-4–48. doi: 10.1186/1744-8069-4-48

Eliava, M., Melchior, M., Knobloch-Bollmann, H. S., Wahis, J., Gouveia, M., da, S., et al. (2016). A new population of parvocellular oxytocin neurons controlling magnocellular neuron activity and inflammatory pain processing. *Neuron* 89, 1291–1304. doi: 10.1016/j.neuron.2016.01.041

Farco, J. A., and Grundmann, O. (2013). Menthol – pharmacology of an important naturally medicinal "cool." *Mini-Rev. Med. Chem.* 13, 124–131. doi: 10.2174/138955713804484686

Fischer, M. J. M., Balasuriya, D., Jeggle, P., Goetze, T. A., McNaughton, P. A., Reeh, P. W., et al. (2014). Direct evidence for functional TRPV1/TRPA1 heteromers. *Pflugers Arch.* 466, 2229–2241. doi: 10.1007/s00424-014-1497-z

Food and Drug Administration (2018). Food Additive Regulations; Synthetic Flavoring Agents and Adjuvants. *Fed. Regist.* Available online at: https://www.federalregister.gov/documents/2018/10/09/2018-21807/food-additive-regulations-synthetic-flavoring-agents-and-adjuvants (accessed May 10, 2022).

FUCHS, L. (1543). New Kreüterbuch. Available online at: https://docnum.unistra.fr/digital/collection/coll13/id/219002/rec/555 (accessed June 30, 2022).

Galeotti, N., Di Cesare Mannelli, L., Mazzanti, G., Bartolini, A., and Ghelardini, C. (2002). Menthol: a natural analgesic compound. *Neurosci. Lett.* 322, 145–148. doi: 10.1016/S0304-3940(01)02527-7

Galindo, T., Reyna, J., and Weyer, A. (2018). Evidence for transient receptor potential (TRP) channel contribution to arthritis pain and pathogenesis. *Pharm. Basel Switz.* 11, E105. doi: 10.3390/ph11040105

Ghosh, M., Schepetkin, I. A., Özek, G., Özek, T., Khlebnikov, A. I., Damron, D. S., et al. (2020). Essential oils from monarda fistulosa: chemical composition and activation of transient receptor potential A1 (TRPA1) channels. *Molecules* 25, 4873. doi: 10.3390/molecules25214873

Gilbert, S. (2021). "Chronic pain and dependence," in *Textbook of Addiction Treatment: International Perspectives*, eds N. el-Guebaly, G. Carrà, M. Galanter, and A. M. Baldacchino (Cham: Springer International Publishing), 1255–1267.

Gong, K., and Jasmin, L. (2017). Sustained morphine administration induces TRPM8-dependent cold hyperalgesia. *J. Pain* 18, 212–221. doi: 10.1016/j.jpain.2016.10.015

González-Ramírez, R., Chen, Y., Liedtke, W. B., and Morales-Lázaro, S. L. (2017). "TRP channels and pain," in *Neurobiology of TRP Channels Frontiers in Neuroscience*, ed T. L. R. Emir (Boca Raton, FL: CRC Press/Taylor & Francis). Available online at: http://www.ncbi.nlm.nih.gov/books/NBK476120/ (accessed July 1, 2022).

Gouveia, D. N., Pina, L. T. S., Rabelo, T. K., da Rocha Santos, W. B., Quintans, J. S. S., and Guimaraes, A. G. (2018). Monoterpenes as perspective to chronic pain management: a systematic review. *Curr. Drug Targets* 19, 960–972. doi: 10.2174/1389450118666170711145308

Guimarães, A. G., Quintans, J. S. S., and Quintans, L. J. (2013). Monoterpenes with analgesic activity–a systematic review. *Phytother. Res. PTR* 27, 1–15. doi: 10.1002/ptr.4686

Hakimizadeh, E., Oryan, S., Hajizadeh Moghaddam, A., Shamsizadeh, A., and Roohbakhsh, A. (2012). Endocannabinoid system and TRPV1 receptors in the dorsal hippocampus of the rats modulate anxiety-like behaviors. *Iran. J. Basic Med. Sci.* 15, 795–802.

Heblinski, M., Santiago, M., Fletcher, C., Stuart, J., Connor, M., McGregor, I. S., et al. (2020). Terpenoids commonly found in cannabis sativa do not modulate the actions of phytocannabinoids or endocannabinoids on TRPA1 and TRPV1 channels. *Cannabis Cannabinoid Res.* 5, 305–317. doi: 10.1089/can.2019.0099

Heinrich, M., Kufer, J., Leonti, M., and Pardo-de-Santayana, M. (2006). Ethnobotany and ethnopharmacology–interdisciplinary links with the historical sciences. *J. Ethnopharmacol.* 107, 157–160. doi: 10.1016/j.jep.2006.05.035

Hilfiger, L., Triaux, Z., Marcic, C., Héberl,é, E., Emhemmed, F., Darbon, P., et al. (2021). Anti-hyperalgesic properties of menthol and pulegone. *Front. Pharmacol.* 12, 3248. doi: 10.3389/fphar.2021.753873

Hilfiger, L., Zhao, Q., Kerspern, D., Inquimbert, P., Andry, V., Goumon, Y., et al. (2020). A nonpeptide oxytocin receptor agonist for a durable relief of inflammatory pain. *Sci. Rep.* 10, 3017. doi: 10.1038/s41598-020-59929-w

Islam, A. U. S., Hellman, B., Nyberg, F., Amir, N., Jayaraj, R. L., Petroianu, G., et al. (2020). Myrcene attenuates renal inflammation and oxidative stress in the adrenalectomized rat model. *Mol. Basel Switz.* 25, E4492. doi: 10.3390/molecules25194492

Iwasaki, M., Lefevre, A., Althammer, F., Łapieś, O., and Hilfiger, L., Kerspern, D., et al. (2022). A novel analgesic pathway from parvocellular oxytocin neurons to the periaqueductal gray. *BioRxiv [Preprint]*. doi: 10.1101/2022.02.23.481531

Jabba, S. V., and Jordt, S. E. (2020). "Activation of respiratory irritant receptors by pulegone, a toxic flavor chemical in mint- or menthol-flavored electronic cigarettes," in *B18. E-Cigarette and Vaping Induced Respiratory Health Outcomes - It Is Not That Simple American Thoracic Society International Conference Abstracts* (American Thoracic Society), A2767.

Jankowski, M. P., Rau, K. K., and Koerber, H. R. (2017). Cutaneous TRPM8-expressing sensory afferents are a small population of neurons with unique firing properties. *Physiol. Rep.* 5, e13234. doi: 10.14814/phy2.13234

Julius, D. (2013). TRP channels and pain. *Annu. Rev. Cell Dev. Biol.* 29, 355–384. doi: 10.1146/annurev-cellbio-101011-155833

Kaimoto, T., Hatakeyama, Y., Takahashi, K., Imagawa, T., Tominaga, M., and Ohta, T. (2016). Involvement of transient receptor potential A1 channel in algesic and analgesic actions of the organic compound limonene. *Eur. J. Pain Lond. Engl.* 20, 1155–1165. doi: 10.1002/ejp.840

Karashima, Y., Damann, N., Prenen, J., Talavera, K., Segal, A., Voets, T., et al. (2007). Bimodal action of menthol on the transient receptor potential channel TRPA1. *J. Neurosci.* 27, 9874–9884. doi: 10.1523/JNEUROSCI.2221-07.2007

Kashiwadani, H., Higa, Y., Sugimura, M., and Kuwaki, T. (2021). Linalool odor-induced analgesia is triggered by TRPA1-independent pathway in mice. *Behav. Brain Funct. BBF* 17, 3. doi: 10.1186/s12993-021-00176-y

Kerstein, P. C., del Camino, D., Moran, M. M., and Stucky, C. L. (2009). Pharmacological blockade of TRPA1 inhibits mechanical firing in nociceptors. *Mol. Pain* 5, 19. doi: 10.1186/1744-8069-5-19

Khalil, M., Alliger, K., Weidinger, C., Yerinde, C., Wirtz, S., Becker, C., et al. (2018). Functional role of transient receptor potential channels in immune cells and epithelia. *Front. Immunol.* 9, 174. doi: 10.3389/fimmu.2018.00174

Khalil, M., Babes, A., Lakra, R., Försch, S., Reeh, P. W., Wirtz, S., et al. (2016). Transient receptor potential melastatin 8 ion channel in macrophages modulates colitis through a balance-shift in TNF-alpha and interleukin-10 production. *Mucosal Immunol.* 9, 1500–1513. doi: 10.1038/mi.2016.16

Kheradpezhouh, E., Choy, J. M. C., Daria, V. R., and Arabzadeh, E. (2017). TRPA1 expression and its functional activation in rodent cortex. *Open Biol.* 7, 160314. doi: 10.1098/rsob.160314

Kinmer, N., Özek, T., Baser, K. H. C., and Tümen, G. (1993). The essential oil of *Micromeria fruticosa* (L.) Druce subsp. barbata (Boiss. et Kotschy) P.H. Davis of Turkish origin. *Acta Hortic.* 5, 239–244. doi: 10.17660/ActaHortic.1993.333.28

Kistner, K., Siklosi, N., Babes, A., Khalil, M., Selescu, T., Zimmermann, K., et al. (2016). Systemic desensitization through TRPA1 channels by capsazepine and mustard oil - a novel strategy against inflammation and pain. *Sci. Rep.* 6, 28621. doi: 10.1038/srep28621

Koivisto, A.-P., Belvisi, M. G., Gaudet, R., and Szallasi, A. (2022). Advances in TRP channel drug discovery: from target validation to clinical studies. *Nat. Rev. Drug Discov.* 21, 41–59. doi: 10.1038/s41573-021-00268-4

Kupari, J., Usoskin, D., Parisien, M., Lou, D., Hu, Y., Fatt, M., et al. (2021). Single cell transcriptomics of primate sensory neurons identifies cell types associated with chronic pain. *Nat. Commun.* 12, 1510. doi: 10.1038/s41467-021-21725-z

Kwan, K. Y., Allchorne, A. J., Vollrath, M. A., Christensen, A. P., Zhang, D.-S., Woolf, C. J., et al. (2006). TRPA1 contributes to cold, mechanical, and chemical nociception but is not essential for hair-cell transduction. *Neuron* 50, 277–289. doi: 10.1016/j.neuron.2006.03.042

Lemon, C. H., Norris, J. E., and Heldmann, B. A. (2019). The TRPA1 ion channel contributes to sensory-guided avoidance of menthol in mice. *eNeuro* 6, ENEURO.0304-19.2019. doi: 10.1523/ENEURO.0304-19.2019

Lennertz, R. C., Kossyreva, E. A., Smith, A. K., and Stucky, C. L. (2012). TRPA1 Mediates Mechanical Sensitization in Nociceptors during Inflammation. *PLoS ONE* 7, e43597. doi: 10.1371/journal.pone.0043597

Leonti, M., and Verpoorte, R. (2017). Traditional Mediterranean and European herbal medicines. *J. Ethnopharmacol.* 199, 161–167. doi: 10.1016/j.jep.2017.01.052

Li, Y., Chen, X., Nie, Y., Tian, Y., Xiao, X., and Yang, F. (2021). Endocannabinoid activation of the TRPV1 ion channel is distinct from activation by capsaicin. *J. Biol. Chem.* 297, 101022. doi: 10.1016/j.jbc.2021.101022

Liu, B., Fan, L., Balakrishna, S., Sui, A., Morris, J. B., and Jordt, S.-E. (2013). TRPM8 is the principal mediator of menthol-induced analgesia of acute and inflammatory pain. *Pain* 154, 2169–2177. doi: 10.1016/j.pain.2013.06.043

Mackenzie, J. S., and Jeggo, M. (2019). The one health approach—why is it so important? *Trop. Med. Infect. Dis.* 4, 88. doi: 10.3390/tropicalmed4020088

Majikina, A., Takahashi, K., Saito, S., Tominaga, M., and Ohta, T. (2018). Involvement of nociceptive transient receptor potential channels in repellent action of pulegone. *Biochem. Pharmacol.* 151, 89–95. doi: 10.1016/j.bcp.2018.02.032

Maroon, J. C., Bost, J. W., and Maroon, A. (2010). Natural anti-inflammatory agents for pain relief. *Surg. Neurol. Int.* 1, 80. doi: 10.4103/2152-7806.73804

Mattioli, P. A. (1590). *Kreutterbuch*. Available online at: https://docnum.unistra.fr/digital/collection/coll13/id/4668/rec/436 (accessed February 11, 2022).

Menigoz, A., and Boudes, M. (2011). The expression pattern of TRPV1 in brain. *J. Neurosci.* 31, 13025–13027. doi: 10.1523/JNEUROSCI.2589-11.2011

Mihara, S., and Shibamoto, T. (2015). The role of flavor and fragrance chemicals in TRPA1 (transient receptor potential cation channel, member A1) activity associated with allergies. *Allergy Asthma Clin. Immunol.* 11, 11. doi: 10.1186/s13223-015-0074-0

Mizumura, K. (1997). Peripheral mechanism of hyperalgesia–sensitization of nociceptors. *Nagoya J. Med. Sci.* 60, 69–87.

Morelli, M. B., Amantini, C., Liberati, S., Santoni, M., and Nabissi, M. (2013). TRP channels: new potential therapeutic approaches in CNS neuropathies. *CNS Neurol. Disord. Drug Targets* 12, 274–293. doi: 10.2174/1871527311312 9990056

Neogi, T. (2013). The epidemiology and impact of pain in osteoarthritis. *Osteoarthritis Cartilage* 21, 1145–1153. doi: 10.1016/j.joca.201 3.03.018

Ntalli, N. G., Ferrari, F., Giannakou, I., and Menkissoglu-Spiroudi, U. (2010). Phytochemistry and nematicidal activity of the essential oils from 8 Greek Lamiaceae aromatic plants and 13 terpene components. *J. Agric. Food Chem.* 58, 7856–7863. doi: 10.1021/jf100797m

Ohtsubo, S., Fujita, T., Matsushita, A., and Kumamoto, E. (2015). Inhibition of the compound action potentials of frog sciatic nerves by aroma oil compounds having various chemical structures. *Pharmacol. Res. Perspect.* 3, e00127. doi: 10.1002/prp2.127

Oltean, H., Robbins, C., van Tulder, M. W., Berman, B. M., Bombardier, C., and Gagnier, J. J. (2014). Herbal medicine for low-back pain. *Cochrane Database Syst. Rev.* 2014, CD004504. doi: 10.1002/14651858.CD004504.pub4

Opioid Overdose Crisis | National Institute on Drug Abuse (2022). NIDA. Available online at: https://nida.nih.gov/drug-topics/opioids/opioid-overdose-crisis (accessed April 27, 2022).

Ordás, P., Hernández-Ortego, P., Vara, H., Fernández-Peña, C., Reimúndez, A., Morenilla-Palao, C., et al. (2021). Expression of the cold thermoreceptor TRPM8 in rodent brain thermoregulatory circuits. *J. Comp. Neurol.* 529, 234–256. doi: 10.1002/cne.24694

Ortar, G., Morera, L., Moriello, A. S., Morera, E., Nalli, M., Di Marzo, V., et al. (2012). Modulation of thermo-transient receptor potential (thermo-TRP) channels by thymol-based compounds. *Bioorg. Med. Chem. Lett.* 22, 3535–3539. doi: 10.1016/j.bmcl.2012.03.055

Oz, M., El Nebrisi, E. G., Yang, K.-H. S., Howarth, F. C., and Al Kury, L. T. (2017). Cellular and molecular targets of menthol actions. *Front. Pharmacol.* 8, 472. doi: 10.3389/fphar.2017.00472

Peier, A. M., Moqrich, A., Hergarden, A. C., Reeve, A. J., Andersson, D. A., Story, G. M., et al. (2002). A TRP channel that senses cold stimuli and menthol. *Cell* 108, 705–715. doi: 10.1016/S0092-8674(02)00652-9

Perri, F., Coricello, A., and Adams, J. D. (2020). Monoterpenoids: the next frontier in the treatment of chronic pain? *Journals* 3, 195–214. doi: 10.3390/j3020016

Petitjean, H., Hugel, S., Barthas, F., Bohren, Y., Barrot, M., Yalcin, I., et al. (2014). Activation of transient receptor potential vanilloid 2-expressing primary afferents stimulates synaptic transmission in the deep dorsal horn of the rat spinal cord and elicits mechanical hyperalgesia. *Eur. J. Neurosci.* 40, 3189–3201. doi: 10.1111/ejn.12688

POWO (2022). Plants of the World Online. *Facilitated by the Royal Botanic Gardens, Kew*. Available online at: http://www.plantsoftheworldonline.org/ (accessed May 10, 2022).

Quintans, J. S. S., Shanmugam, S., Heimfarth, L., Araújo, A. A. S., Almeida, J. R. G., da, S., et al. (2019). Monoterpenes modulating cytokines - a review. *Food Chem. Toxicol. Int. J. Publ. Br. Ind. Biol. Res. Assoc.* 123, 233–257. doi: 10.1016/j.fct.2018.10.058

Raja, S. N., Carr, D. B., Cohen, M., Finnerup, N. B., Flor, H., Gibson, S., et al. (2020). The revised International Association for the Study of Pain definition of pain: concepts, challenges, and compromises. *Pain* 161, 1976–1982. doi: 10.1097/j.pain.0000000000001939

Reyes-García, V., Benyei, P., Aceituno-Mata, L., Gras, A., Molina, M., Tardío, J., et al. (2021). Documenting and protecting traditional knowledge in the era of open science: Insights from two Spanish initiatives. *J. Ethnopharmacol.* 278, 114295. doi: 10.1016/j.jep.2021.114295

Rufino, A. T., Ribeiro, M., Judas, F., Salgueiro, L., Lopes, M. C., Cavaleiro, C., et al. (2014). Anti-inflammatory and chondroprotective activity of (+)-α-pinene: structural and enantiomeric selectivity. *J. Nat. Prod.* 77, 264–269. doi: 10.1021/np400828x

Ruparel, N. B., Patwardhan, A. M., Akopian, A. N., and Hargreaves, K. M. (2011). Desensitization of transient receptor potential ankyrin 1 (TRPA1) by the TRP vanilloid 1-selective cannabinoid arachidonoyl-2 chloroethanolamine. *Mol. Pharmacol.* 80, 117–123. doi: 10.1124/mol.110.068940

Rutz, A., Sorokina, M., Galgonek, J., Mietchen, D., Willighagen, E., Gaudry, A., et al. (2021). The lotus initiative for open natural products research: Knowledge management through wikidata. *BioRxiv [Preprint]*. doi: 10.1101/2021.02.28.433265

Schultz, F., Dworak-Schultz, I., Olengo, A., Anywar, G., and Garbe, L.-A. (2021). Transferring ethnopharmacological results back to traditional healers in rural indigenous communities – the Ugandan greater Mpigi region example: research translation. *Video J. Educ. Pedagogy* 6, 1–15. doi: 10.1163/23644583-bja10018

Schumacher, M. A. (2010). Transient receptor potential channels in pain and inflammation: therapeutic opportunities. *Pain Pract.* 10, 185–200. doi: 10.1111/j.1533-2500.2010.00358.x

Shigetomi, E., Tong, X., Kwan, K. Y., Corey, D. P., and Khakh, B. S. (2011). TRPA1 channels regulate astrocyte resting calcium and inhibitory synapse efficacy through GAT-3. *Nat. Neurosci.* 15, 70–80. doi: 10.1038/nn.3000

Soleimani, M., Sheikholeslami, M. A., Ghafghazi, S., Pouriran, R., and Parvardeh, S. (2019). Analgesic effect of α-terpineol on neuropathic pain induced by chronic constriction injury in rat sciatic nerve: involvement of spinal microglial cells and inflammatory cytokines. *Iran. J. Basic Med. Sci.* 22, 1445–1451. doi: 10.22038/IJBMS.2019.14028

Sorokina, M., and Steinbeck, C. (2020). Review on natural products databases: where to find data in 2020. *J. Cheminformatics* 12, 20. doi: 10.1186/s13321-020-00424-9

Sousa, D., and Pergentino, D. (2011). Analgesic-like activity of essential oils constituents. *Molecules* 16, 2233–2252. doi: 10.3390/molecules16032233

Souza Monteiro de Araujo, D., Nassini, R., Geppetti, P., and De Logu, F. (2020). TRPA1 as a therapeutic target for nociceptive pain. *Expert Opin. Ther. Targets* 24, 997–1008. doi: 10.1080/14728222.2020.1815191

Sun, F.-J., Guo, W., Zheng, D.-H., Zhang, C.-Q., Li, S., Liu, S.-Y., et al. (2013). Increased expression of TRPV1 in the cortex and hippocampus from patients with mesial temporal lobe epilepsy. *J. Mol. Neurosci.* 49, 182–193. doi: 10.1007/s12031-012-9878-2

Takaishi, M., Uchida, K., Fujita, F., and Tominaga, M. (2014). Inhibitory effects of monoterpenes on human TRPA1 and the structural basis of their activity. *J. Physiol. Sci.* 64, 47–57. doi: 10.1007/s12576-013-0289-0

Tetali, S. D. (2018). Terpenes and isoprenoids: a wealth of compounds for global use. *Planta* 249, 1–8. doi: 10.1007/s00425-018-3056-x

Topp, R., Brosky, J. A., and Pieschel, D. (2013). The effect of either topical menthol or a placebo on functioning and knee pain among patients with knee OA. *J. Geriatr. Phys. Ther.* 36, 92–99. doi: 10.1519/JPT.0b013e318268dde1

Totelin, L. M. V. (2006). Review of: Théophraste. Recherches sur les plantes. Tome V. Livre IX. *Bryn Mawr Class. Rev.* Available online at: https://bmcr.brynmawr.edu/2006/2006.07.24/ (accessed January 8 2022).

Treede, R.-D., Rief, W., Barke, A., Aziz, Q., Bennett, M., Benoliel, R., et al. (2019). Chronic pain as a symptom or a disease: the IASP classification of chronic pain for the international classification of diseases (ICD-11). *Pain* 160, 19–27. doi: 10.1097/j.pain.0000000000001384

UNESCO World Heritage Center (2010). n°56 - World Heritage Review n°56
 Biodiversity. *UNESCO World Herit. Cent.* Available online at: https://whc.unesco.org/en/review/56/ (accessed May 12, 2022).

UNESCO. (2018). UNESCO's Commitment to Biodiversity: Connecting People and Nature For An Inspiring Future. Available online at: https://unesdoc.unesco.org/ark:/48223/pf0000265200 (accessed May 12, 2022).

Vilceanu, D., and Stucky, C. L. (2010). TRPA1 mediates mechanical currents in the plasma membrane of mouse sensory neurons. *PLoS ONE* 5, e12177. doi: 10.1371/journal.pone.0012177

Wahis, J., Baudon, A., Althammer, F., Kerspern, D., Goyon, S., Hagiwara, D., et al. (2021). Astrocytes mediate the effect of oxytocin in the central amygdala on neuronal activity and affective states in rodents. *Nat. Neurosci.* 24, 529–541. doi: 10.1038/s41593-021-00800-0

Wang, S., Zhang, D., Hu, J., Jia, Q., Xu, W., Su, D., et al. (2017). A clinical and mechanistic study of topical borneol-induced analgesia. *EMBO Mol. Med.* 9, 802–815. doi: 10.15252/emmm.201607300

Weston-Green, K. (2019). "The united chemicals of cannabis: beneficial effects of cannabis phytochemicals on the brain and cognition," in *Recent Advances in Cannabinoid Research*, eds W. J. Costain and R. B. Laprairie (Wollongong, NSW: IntechOpen).

Wojtunik-Kulesza, K. A. (2022). Toxicity of selected monoterpenes and essential oils rich in these compounds. *Mol. Basel Switz.* 27, 1716. doi: 10.3390/molecules27051716

World Health Organization (2013). *WHO Traditional Medicine Strategy: 2014-2023*. World Health Organization. Available online at: https://apps.who.int/iris/handle/10665/92455 (accessed May 10, 2022).

Xiao, B., Dubin, A. E., Bursulaya, B., Viswanath, V., Jegla, T. J., and Patapoutian, A. (2008). Identification of transmembrane domain 5 as a critical molecular determinant of menthol sensitivity in mammalian TRPA1 channels. *J. Neurosci.* 28, 9640–9651. doi: 10.1523/JNEUROSCI.2772-08.2008

Xu, H., Blair, N. T., and Clapham, D. E. (2005). Camphor activates and strongly desensitizes the transient receptor potential vanilloid subtype 1 channel in a vanilloid-independent mechanism. *J. Neurosci.* 25, 8924–8937. doi: 10.1523/JNEUROSCI.2574-05.2005

Yamada, Y., Kuzuyama, T., Komatsu, M., Shin-Ya, K., Omura, S., Cane, D. E., et al. (2015). Terpene synthases are widely distributed in bacteria. *Proc. Natl. Acad. Sci. U. S. A.* 112, 857–862. doi: 10.1073/pnas.1422108112

Yu, L., Yang, F., Luo, H., Liu, F.-Y., Han, J.-S., Xing, G.-G., et al. (2008). The role of TRPV1 in different subtypes of dorsal root ganglion neurons in rat chronic inflammatory nociception induced by complete Freund's adjuvant. *Mol. Pain* 4, 61. doi: 10.1186/1744-8069-4-61

Zhang, Q., Wu, D., Wu, J., Ou, Y., Mu, C., Han, B., et al. (2015). Improved blood-brain barrier distribution: effect of borneol on the brain pharmacokinetics of kaempferol in rats by in vivo microdialysis sampling. *J. Ethnopharmacol.* 162, 270–277. doi: 10.1016/j.jep.2015.01.003

Zhu, X., Wang, G., Wu, S., and Li, C. (2020). Protective effect of D-carvone against dextran sulfate sodium induced ulcerative colitis in Balb/c mice and LPS induced RAW cells via the inhibition of COX-2 and TNF-α. *J. Environ. Pathol. Toxicol. Oncol.* 39, 235–245. doi: 10.1615/JEnvironPatholToxicolOncol.2020031860

Zielińska-Błajet, M., and Feder-Kubis, J. (2020). Monoterpenes and their derivatives—recent development in biological and medical applications. *Int. J. Mol. Sci.* 21, 7078. doi: 10.3390/ijms21197078

Advantages of publishing in Frontiers

OPEN ACCESS
Articles are free to read for greatest visibility and readership

FAST PUBLICATION
Around 90 days from submission to decision

HIGH QUALITY PEER-REVIEW
Rigorous, collaborative, and constructive peer-review

TRANSPARENT PEER-REVIEW
Editors and reviewers acknowledged by name on published articles

Frontiers
Avenue du Tribunal-Fédéral 34
1005 Lausanne | Switzerland

Visit us: www.frontiersin.org
Contact us: frontiersin.org/about/contact

REPRODUCIBILITY OF RESEARCH
Support open data and methods to enhance research reproducibility

DIGITAL PUBLISHING
Articles designed for optimal readership across devices

FOLLOW US
@frontiersin

IMPACT METRICS
Advanced article metrics track visibility across digital media

EXTENSIVE PROMOTION
Marketing and promotion of impactful research

LOOP RESEARCH NETWORK
Our network increases your article's readership